Electric Manipulation and Impedance Analysis of Adherent Cells on Gold-Film Electrodes

DISSERTATION

Zur Erlangung des

DOKTORGRADES DER NATURWISSENSCHAFTEN

(Dr. rer. Nat.)

der Fakultät für Chemie und Pharmazie

der Universität Regensburg

vorgelegt von

Diplom-Biotechnologin

Judith Anthea Stolwijk

aus Leonberg

2011

Diese Arbeit wurde angeleitet von Prof. Dr. Joachim Wegener

Prüfungsgesuch eingereicht am: _____

Tag der mündlichen Prüfung: 05.07.2011

Prüfungsausschuss: Vorsitzender: Prof. Dr. Jens Schlossmann

Prof. Dr. Joachim Wegener

Prof. Dr. Otto S. Wolfbeis

Prof. Dr. Achim Göpferich

Meiner Familie

Contents

1 Introduction

During the last decade biosensors based on living cells have gained increasing interest. Especially in toxicology and environmental analysis as well as biotechnology, biomedicine and the pharmaceutical screening industry whole-cell biosensors have found many applications. The possibility to obtain information on the biological activity of an analyte rather than the bare analytical information on concentration, binding strength and kinetics is the most important reason for using biosensors based on living cells.
Cell-based biosensors (chapter 1.1) are capable of detecting and analyzing different forms of cellular responses that occur upon exposure to a broad variety of physical, biological and chemical stimuli (Fig. 1.1). In experimental procedures of basic cell biology research and pharmaceutical drug development cells are routinely exposed to substances of biological or chemical origin. The cell response to this exposure is then further analyzed by a suitable sensing technique. Also the impact of certain physical stimuli, like mechanical shear forces, electromagnetic or electric fields, are of fundamental biological and medical interest. The enormous potential of physical manipulation, like for lab-on-a-chip developments using microfluidics or their use in changing cellular properties, make the biosensor based research on physical challenges even more interesting. Two highly relevant techniques used to manipulate cells with respect to the cellular content and properties are electroporation and electrofusion that both rely on the transient permeabilization of the cell membrane by application of short invasive electric field pulses (chapter 1.2). The effect of these kinds of invasive electric fields on animal cells has already been investigated extensively. Whole-cell biosensing techniques, however, have not been used for this, yet. *In situ* approaches for electroporation and electrofusion deserve special attention, as the cells maintain anchored to their growth substrate during manipulation and, moreover, enable a technical combination with substrate-integrated sensor techniques that are suited for chip technology. Combining the capabilities of highly sensitive biosensing with the versatile options to manipulate cellular properties by electric field induced permeabilization of the cell membrane may provide novel valuable tools for basic cell biology research as well as drug discovery and biotechnological engineering.

1.1 Cell-Based Biosensors

In contrast to chemical sensors biosensors use a biological component as the sensitive detection element. Biological recognition elements can be classified by hierarchy of complexity into those using isolated biomolecules, organelles or membrane fragments, whole cells, tissues, organs or even a whole organism (Luong et al., 1988; Keusgen, 2002). The wide field of the classical molecular biosensors using enzymes, antibodies, antigens, nucleic acids etc. is capable of detecting a large variety of target molecules with high sensitivity and it has especially been widely used in clinical diagnostics and drug discovery (Comley, 2008b).

However, the analytical response is detected independently of the complex environment of a living cell. No information about its actual biological activity is provided by most of these target-directed approaches.

Therefore, cell-based biosensors were developed using living cells – the smallest self-sustaining living unit – as the biological recognition element (Bousse, 1996; Ziegler, 2000; Wang et al., 2005). Whole-cell biosensors allow for measuring the biofunctionality and bioavailability of an analyte, since the biological recognition element is embedded in its natural environment and associated with all essential signaling and processing networks of the relevant living system. This allows, for example, distinguishing analytes which bind to cellular structures without causing a cellular response (e.g. antagonist in drug discovery) from molecular candidates that really trigger a cellular reaction (e.g. agonist). One molecule or certain kind of extracellular stimuli can trigger various forms of cellular responses. Changes in cell metabolism are detectable due to altered O_2 and glucose consumption or changes in pH (Owiki and Parce, 1992). Also alterations of cell shape as a result of a redistribution of the cytoskeleton or changes in the cell-cell and cell-substrate contact areas are common responses to external stimuli (Giaever and Keese, 1993).

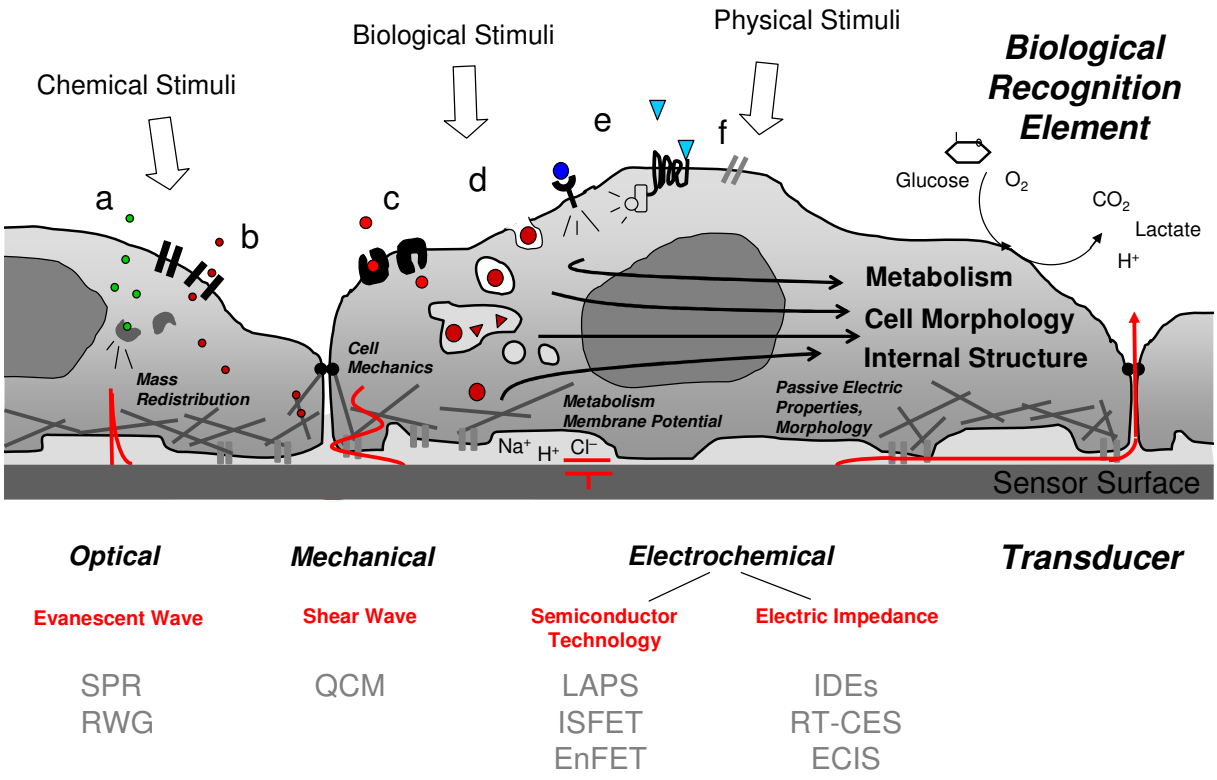

Fig. 1.1: Schematic overview of label-free substrate-integrated whole-cell biosensors using anchorage-dependent mammalian cells as the biological recognition element. The cells are influenced by various chemical, biological and physical stimuli from their environment by different cellular uptake and recognition mechanisms: Uptake can proceed via (**a**) free diffusion across the semipermeable membrane, (**b**) channels, (**c**) carriers or (**d**) endocytosis. Binding of xenomolecules to intracellular key molecules can activate cellular processes after uptake. Alternatively, the extracellular signal is transferred via (**e**) specific binding to surface receptors, unspecific binding to other surface structures or (**f**) physical stimulation of surface receptors. Activation of surface receptors may trigger signaling cascades inside the cell. Different optical, mechanical and electrochemical transducer techniques allow for detection of various forms of cellular responses, like changes in metabolism, internal cell structure and cell morphology.

A certain cellular parameter like cell morphology, in turn, can be altered by a magnitude of different influences. An integral readout of generic cellular properties enables the detection of so called "group effects" like pharmaceutical activity, cytotoxicity or mutagenicity (Bousse, 1996). Cell-based biosensors are typically capable of monitoring the complete kinetics of a cellular reaction with high sensitivity and temporal resolution. Therefore, sensor techniques (Fig. 1.1) in addition to conventional biochemical and optical methods can essentially contribute to the analysis and investigation of cellular processes, which accounts for the growing popularity of cell-based biosensors in fundamental cell biology.

For sensor applications the biological recognition element, i.e. the cell, is connected to a transducer or detector, which translates the biological response into an easily quantifyable signal. Most common signal transduction platforms for cell-based biosensors rely on optical, mechanical or electrochemical detection (Keusgen, 2002).
The most promising label-free optical approaches to be exploited for cell-based sensors rely on surface plasmon resonance (SPR) (Homola, 2008) or resonant waveguide grating (RWG) (Fang et al., 2006). These techniques are able to detect changes in the refractive index near the sensor surface (~ 200 nm). Refractive index changes in the bottom portion of cells are assumed to occur due to a redistribution of proteins (e.g. the cytoskeleton) and other cellular components, commonly termed as dynamic mass redistribution (DMR) (Fang, 2006; Fang et al., 2009; Yanase et al., 2007; Chen et al., 2010).
For mechanical whole-cell biosensing the mass and viscoelasticity sensitive QCM (quartz crystal microbalance) technique has found promising applications (Gryte et al., 1993; Marx, 2007). Due to its penetration depth of about 250 nm (Martin et al., 1991) the QCM can be used for sensitive monitoring of cell adhesion (Redepenning et al., 1993; Wegener et al., 1998; Heitmann and Wegener, 2007; Michaelis, 2010) or manipulations on the viscoelastic properties of a cell, e.g. the cytoskeleton (Wegener et al., 2000c; Marx et al., 2007).
Electrochemical biosensors transduce the biorecognition response of the detection unit to a quantifyable signal by means of electrochemical principles (Grieshaber et al., 2008; Thévenot et al., 2001). Cell-based electrochemical biosensors can be subdivided into two classes with respect to the kind of cellular changes they detect (Ziegler, 2000). Metabolic biosensors measure metabolic products (chapter 1.1.1), while biosensors for cell morphology detect morphological parameters of cells (chapter 1.1.2). Different types of chip-based electrochemical biosensors can even be combined to multi-parameter "physiocontrol" systems (Birschwein et al., 1996; Baumann et al., 1999).

1.1.1 Metabolic Biosensors

It was found that cells respond with a change in metabolism to many stimuli including for example certain ligand-receptor binding events. Metabolic changes can be defined by acidification of the cellular environment, the O_2 or CO_2 concentration as well as the glucose or lactate content. Changing ion concentrations as for Na^+ or Ca^{2+} can be interesting parameters when investigating electrogenic cells that respond to certain external stimuli with

changes in their membrane potential by the opening of ion channels. Aside from several electrochemical dipping microelectrodes suitable for use in cell culture (Jung et al., 1999; Lee, 1981) various chip-based approaches have been realized (Spegel et al., 2008).
The light-addressable potentiometric sensor (LAPS) technique interfaces living cells with a silicon-based sensor for the detection of pH in the cellular environment (Hafner, 2000) (Fig. 1.2 A). Protons secreted by the cells change the local H^+ concentration of a pH-sensitive thin nitride or oxynitride layer deposited on the silicon substrate and change its surface charge. The altered surface charge establishes a change in voltage, which is linearily related to the pH in the medium. Regions of interest can be selectively addressed, since conducting electrons are produced in the light sensitive silicon by illumination with light. Additionally, multi LAPS (MLAPS) were developed for the simultaneous measurement of ions as H^+, Na^+, K^+ and Ca^{2+} (Wu et al., 2001; Wang et al., 2005).

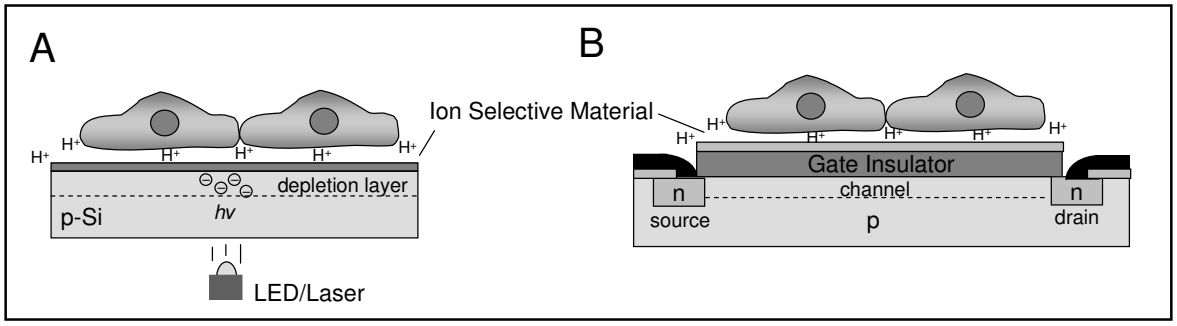

Fig. 1.2: Schematic illustration of the most common types of metabolic cell-based biosensors based on semiconductor technology. **A:** LAPS (light-addressable potentiometric sensor). **B:** ISFET (ion selective field-effect transistor).

Another well-established transducer principle is based on field-effect transistor (FET) technology (Kimura and Kuriyama, 1990; Zhou et al., 2009). FETs measure the accumulation of charged species at the gate electrode, which controls current flow between the source and drain electrode by the creation of an electric field within the semiconductor material (Fig. 1.2 B). Among the multitude of FET variants available, cell-based biosensor applications commonly rely on ISFET (ion selective field-effect transistors) technology (Fig. 1.2 B). ISFETs are used to measure pH (Martinoia et al., 2001) and several other ions (e.g. Na^+, Ca^{2+}) using ion selective membranes on top of the gate (Ziegler, 2000). Integration of immobilized enzymes to an ISFET creates a so-called EnFET (enzyme field-effect transistor) sensor which allows for detecting metabolites like glucose or lactate (Shulga et al., 1992; Schöning and Poghossian, 2002; Baumann et al., 1999).

1.1.2 Biosensors for Cell Morphology

Although cell morphology changes are conventionally observed by microscopic means, the temporal and spatial resolution does not allow to visualize very small and fast morphological changes. Electrochemical biosensors sensitive for cell morphology can be used to detect these kind of small changes in cell shape, based on the fact that cellular bodies act as insulating

particles that force the current to flow around them. Current flow is essentially limited to the paracellular pathways and, thus, the passive electric properties of cells, like cell shape and junctions to neighboring cells, define the resistance (DC) or complex impedance (AC) that is measured for the cells in their experimental environment. Especially impedimetric cell-based biosensors have found wide applicability for functional analysis of barrier forming epithelia and endothelia as well as for monitoring processes like cell attachment, proliferation and detachment as well as specific responses to certain stimuli.
Although many recent developments focus on single-cell impedance spectroscopy suitable for lab-on-a-chip systems and microfluidics (Cho et al., 2007; Han et al., 2007; Park et al., 2010; Sun and Morgan, 2010) this work concentrates on the analysis of confluent cell layers of anchorage-dependent cells. Several measurement setups for impedimetric monitoring of adherent cells can be distinguished (Fig. 1.3).

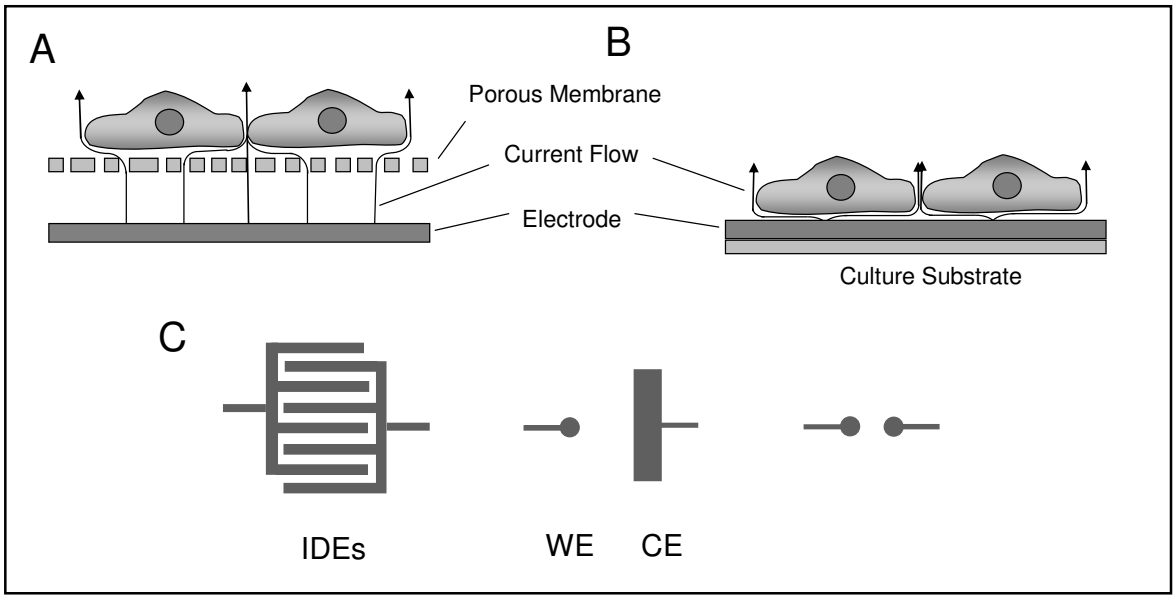

Fig. 1.3: Schematic illustration of experimental setups for electric impedance spectroscopy in cell-based biosensors. **A:** Cell layers are cultivated on a permeable filter support, separating an upper and lower chamber. Electrodes are placed below and above the cell layer. **B:** Substrate-integrated electrodes: cells are directly cultured on the electrode surface deposited on a common culture substrate. **C:** Interdigitated electrodes (IDEs) or small working electrodes (WE) in combination with a significantly larger counter electrode (CE) are the most common layouts for substrate-integrated electrodes. Alternatively, two small same-sized electrodes can be used (e.g. this work).

The cells can be cultivated on a porous filter membrane, which separates two fluid compartments (Fig. 1.3 A). Electrodes on either side of the filter membrane measure the overall resistance or impedance across the entire cell layer (Cereijido et al., 1986; Hein et al., 1992; Gitter et al., 1997; Wegener et al., 2004). Impedance measurements with cells grown on filters are successfully used in research addressing the regulation of barrier forming epithelia and endothelia, like the blood brain barrier (Malina et al., 2009; von Wedel-Parlow et al., 2010), the renal (Rehder et al., 2006) or colon (Karczewski et al., 2010) barrier as well as drug delivery across such epithelia (Pramentier et al., 2010).
Alternatively, cells are directly cultured on planar electrodes made of various conductive materials (gold, indium tin oxide: ITO, iridium, etc.) which are deposited on common cell

culture substrates by thin-film preparation processes (Spegel et al., 2008). In these approaches the substrate-integrated electrode serves as both, growth substrate and signal transducer to translate the morphological cell response into an impedimetric signal (Fig. 1.3 B). Several geometric arrangements have been developed, using either a dipping counter electrode (Jahnke et al., 2009) or a coplanar setup of working and counter electrode, as is more suited for chip fabrication (Wegener et al., 1996; Giaever and Keese, 1984; Rahman et al., 2006; Wolf et al., 2008; Pähnke et al., 2011) (Fig. 1.3 C). Using an electrode layout of interdigitated comb structures the working and counter electrode are equally large (Ehret et al., 1997; Moore et al., 2009). The contribution of the cell layer to the overall impedance is equal on both electrodes and a large fraction of the growth surface can be covered by the electrodes (~ 70 %) (Solly et al., 2004; Atienza et al., 2006; Peters et al., 2007).
Other systems use small working electrodes in combination with a large counter electrode, having a negligible contribution to the overall impedance signal. These rather small circular (Ø ~ 30 – 250 µm) or rectangular working electrodes made from ITO, platinum or gold are either arranged in groups on the bottom of one well, providing many individual measuring spots of one cell layer (Wolf et al., 2008; Pänke et al., 2011; Rahman et al., 2006; Liu et al., 2009) or are separated by individual chambers (Giaever and Keese, 1984, 1993).
The system commonly referred to as ECIS (electric cell-substrate impedance sensing) developed by Giaever and Keese (1984) classically uses a small circular working electrode (Ø ~ 250 µm) and an about 500 times larger counter electrode. The extremely sensitive and versatile ECIS biosensor technique commercialized by Applied BioPhysics Inc. (Troy / NY, USA) is the main technique used in this work.

1.1.3 ECIS – A Versatile Impedimetric Biosensor for Adherent Cells

The ECIS technique, which is explained in more detail in chapter 3.1.2, has already found many applications in basic cell biology research and has potential to become a versatile platform for pharmaceutical screening and drug discovery.
Monitoring of cell adhesion and spreading on either untreated electrodes (Giaever and Keese, 1984) or on electrodes pre-coated with different components of the extracellular matrix provided insights into basic cell adhesion kinetics of different anchorage-dependent cells (Wegener et al., 2000b; Heitmann et al., 2008; Hartmann et al., 2007). The technique is especially well-suited for the analysis of epithelial and endothelial cells with respect to their barrier forming properties, since individual impedance contributions arising in the intercellular cleft, the cell-electrode junction or the cell membrane can be distinguished. Cell morphology in confluent cell layers can be quantified applying a physical model that uses the three model parameters α, R_b and C_m (Giaever and Keese, 1991; Wegener et al., 2000a). Measurements with a time resolution of only a few hundred milliseconds moreover allow for sensitive investigation of cell dynamics within a confluent cell layer, since even microscopic shape fluctuations can be detected (Giaever and Keese, 1991). This “micromotion” was found

to correlate with metabolic activity and cell vitality serving as a sensitive indicator for the response to various external stimuli (Lo et al., 1993, 1994).

The sensitive response of cell shape to a myriad of different chemical, biological and physical stimuli provides a broad spectrum of possible applications (Giaever and Keese, 1993). Chemical stimuli can modulate cell shape and barrier properties of a cell layer by activation of various molecular reorganizations of the cytoskeleton or proteins involved in cell-cell contacts or the cell-electrode junction. For example, the influence of hydrocortisone on the barrier function of brain endothelial cells has been investigated (Weidenfeller et al., 2005). The enhanced barrier properties upon hydrocortisone exposure were found to result from changes in the distribution of tight junction proteins at the cell borders and rearrangements of the actin cytoskeleton. Severe cell morphology changes are associated with apoptosis and necrosis that finally lead to cell detachment. Apoptosis induced by cycloheximide (Arndt et al., 2004) as well as the concentration-dependent cytotoxicity of cadmium, mercury, arsenate, trinitrobenzene or benzalkonium ions (Xiao et al., 2002; Xiao and Luong, 2003, 2005) were monitored by ECIS with high sensitivity. During the last decade special interest focused on the evaluation of the cytotoxicity of new materials, like nanoparticles (Male et al., 2008; Tarantola et al., 2009, 2010b) or polyelectrolytes (Chanana et al., 2005) that were designed for the use *in vitro* and *in vivo*.

The cellular response to various biological stimuli has been increasingly probed with ECIS in many recent studies. For example, the transmigration of different tumor cell lines across confluent epithelial cell layers (Keese et al., 2002; Tarantola et al., 2010a) as well as the role of molecular factors that determine the metastatic potential of certain tumor cell lines (Saxena et al., 2007; Chen et al., 2008; Davies and Jiang, 2010) have been analyzed. Measuring cell layer responses to viral infection (McCoy et al., 2005; Campbell et al., 2007) or malaria-activated blood cells (Treeratanapiboon et al., 2005) moreover provided useful contributions to the research of infectious diseases. Of general interest is the study of signal transduction cascades that rely on the activation of cell surface receptors, because these are often important targets for drug development (Reddy et al., 1998; Triupatthi et al., 2000; Hug, 2003; Qiao, 2006).

Impacts of physical forces on mammalian cell layers have also been investigated. The mechanical stimulation of endothelial cells by fluid convection was for example found to play an essential role in their barrier formation (DePaola et al., 2001). The effect of short invasive electric field pulses, which were applied to confluent cell layers via the working electrode, were also monitored (Gosh et al., 1993; Wegener et al., 2002). Strong invasive electric fields, in contrast, were shown to result in cell death of the population on the electrode (Keese et al., 2004).

1.2 Electric Manipulation of Cells

For cells subjected to an electric field, various observations have been made that have paved the way to versatile tools for cell manipulations. First studies with suspended cells in electric fields revealed the damaging impact of strong electric pulses leading to irreversible perforation of the cell membrane (Neumann and Rosenheck, 1972). In contrast, weak, non-invasive electric fields can induce deforming, electrophoretic and dielectric forces, which are based on the dielectric polarization of a cell (Sukhorukov et al., 1998). Especially polarization induced dielectrophoresis and electrorotation phenomena can be utilized to transport and guide suspended cells within microfluidic systems and to separate cell mixtures (Voldmann et al., 2006). The enormous biotechnological relevance of dielectrophoresis has been realized in combination with hybridoma production, where the "pearl-chain"-alignment of suspended cells mediates the essential close cell-cell contact prior to cell fusion (Schmidt et al., 2001).
Cells that are anchored to a substrate prevent such passive translational or rotational forces to be effective. However, it has been observed that non-invasive electric fields can provoke cellular responses in adherent cells (McCaig et al., 2005). Reorientation of the cellular axis in parallel or perpendicular to the field direction has been observed, which included phenomena like synchronized alignment of the mitosis and cytokinesis plane during cell division (Zhao et al., 1999) or the directed axon growth of neurites (Rajnick et al., 2006a, b; Yao et al., 2009). Electric field induced movements of single adherent cells (Yan et al., 2009; Li et al., 2011) or even cell sheets (Zaho et al., 1996) have also been observed. All these non-invasive electric field phenomena are attributed to electrophoretic or electroosmotic effects, which change the lateral distribution of mobile membrane receptors, carriers or channels within the lipid matrix causing intracellular concentration gradients (Zaho et al., 1999). Electric fields were even found to interfere with metabolism (Huang et al., 1997) and cell cycle control (Wang et al., 2003). Findings that weak electric fields play an essential role in development and tissue repair make electric field effects an interesting issue in biomedicine (McCaig et al., 2009; Zhao et al., 2006). However, these weak electric fields have to be applied to the cells over hours in order to evoke a cellular response.
In addition to the short, highly invasive electric pulses and the long-lasting, weak electric fields, a third type of electric manipulation of cells can be distinguished. Invasive electric field pulses with a limited amount of energy, which are applied for only a short period of time, make the cell membrane transiently permeable (cp. chapter 3.2). This permeabilized state of the membrane was found to be associated with two biotechnologically useful phenomena:
(i) Electroporation: The permeabilized membrane provides exogenous molecules, which cannot pass the membrane under normal circumstances, access to the interior of the cell. Under defined, well-adjusted conditions the membrane reseals after pulse application and the cell survives the process without membrane rupture. The exogenous molecule is captured inside the cell and can perform its specific action inside the cytoplasm. This opens up a new possibility of cell manipulation, since the membrane normally forms a selective barrier,

strictly controlling the exchange of substances and signals between the cellular interior and the environment.
(ii) Electrofusion: The destabilized structure of electropermeabilized membranes transfers it to a fusogenic state. Destabilized cell membranes of adjacent cells easily intermix lipids and fuse. As a result the cytoplasmic content and genetic material are brought together, creating new cellular properties.

1.2.1 Electroporation: Delivery of Membrane-Impermeable Molecules to the Cytoplasm

Free diffusion across the membrane is only possible for small or lipophilic molecules, whereas the membrane hinders free entrance of most hydrophilic molecules. Controlled uptake of small hydrophilic molecules proceeds via membrane channels or carriers, while macromolecules can be incorporated by endocytosis (cp. Fig. 1.1).
The transfer of certain molecules across the plasma membrane allows one to manipulate the properties of living cells for purposes of basic research as well as medical and biotechnological applications. The delivery of foreign genetic material has always played a central role in creating cells with tailored properties, driving the continuous development of gene transfer strategies on the basis of biological, chemical and physical methods (Colosimo et al., 2000). Also the cytoplasmic delivery of other biomolecules like proteins – signaling peptides, enzymes and antibodies in particular – or nanoparticles have found increasing applications and created the need for suitable transfer strategies. Not to forget the ongoing search for drug delivery strategies that might enable targeted and efficient therapy of diseases. Most molecules relevant in cellular manipulation are, however, too polar to cross the cell membrane via simple diffusion and too big in size to be transported via membrane proteins having a size exclusion in the range of ~ 500 Da.

1.2.1.1 Survey of Delivery Strategies

The techniques for delivery of membrane-impermeable macromolecules across the membrane either rely on the inherent cellular uptake mechanisms leaving the membrane intact or they are based on the transient perforation of the membrane. Many biological and chemical transfection mechanisms exploit endocytosis, cellular mechanisms for uptake of exogenous macromolecules and particles by internalization of cargo loaded vesicles from the membrane surface (Luo and Saltzman, 2000; Conner and Schmid, 2003; Doherty and McMahon, 2009). Endocytotic mechanisms typically involve fusion of the endosome with the lysosome and enzymatic degradation of entrapped cargo molecules in a low pH environment (Conner and Schmid, 2003). Alternatively, endocytotic vesicles are recycled to the membrane or targeted to the Golgi or ER (Doherty and McMahon, 2009; Khalil et al., 2006).
The concept of most chemical transfection reagents is the formation of a condensed complex between the transfection reagent and the cargo molecule (e.g. DNA) by non-covalent, mostly

electrostatic interactions. The complex binds to the membrane surface and stimulates non-specific or receptor-mediated endocytosis. Classical DNA delivery reagents are calcium phosphate (Graham and van der Eb, 1973) and diethylaminoethyl- (DEAE)-dextran (Mc Cutchan and Pagano, 1968). In recent years many cationic polymers have been increasingly used in mammalian cell transfection like polyethyleneimine (PEI) (Boussif et al., 1995), poly-L-lysin (PLL) (Liu et al., 2001) and polyamidoamine- (PAMAM) dendrimers (Kukowasaka-Latallo et al., 1996; Tang et al., 1996). Alternatively, DNA and other macromolecules can be complexed with artificial cationic lipids, which are to date the most efficient and versatile non-viral synthetic transfection system (Felgner 1987, 1994; Friend et al., 1996; Pack et al., 2005). In addition to the transfer of DNA, liposome formulations enable the efficient intracellular delivery of RNA (Malone et al., 1989), proteins (Colosimo et al., 2000) and various drugs (Gregoriadis, 1995; Sharma and Sharma, 1997). Uptake of liposomes is most likely mediated by endocytosis and subsequent release of cargo from the endosome (de Lima et al., 2001; Zabner et al., 1995; Xu and Szoka, 1996; Friend et al., 1996). Also solid inorganic and polymeric nanoparticles are increasingly used for intracellular delivery of drugs, nucleic acids, proteins and peptides as well as for sensor purposes (Mohanraj and Chen, 2006; de Jong and Brom, 2008; Link et al., 2007; Rao et al., 2010). They are mostly incorporated by endocytotic pathways (Verma and Stelacci, 2010; Zhang et al., 2009).

In order to save the endosomal cargo from lysosomal degradation it has to escape from the endocytotic pathway (Doherty and Mc Mahon, 2009). Different strategies to promote the early escape from the endosomes have been developed (Varkouhi et al., 2010). These include the use of certain chemicals like chloroquine (Wagner et al., 1992) and branched cationic polymers like PEI (Godbey et al., 1999a, 2000) or dendrimers (Kukowsako-Latolla et al., 1996) that promote endosomal rupture by the so-called proton sponge effect (Akinc et al., 2004). The use of pH triggered liposomes (Guo and Szoka, 2003) or photosensitizers (Berg et al., 1999; Matsushita et al., 2004) are further strategies. Moreover, synthetic and biologically derived proteins and peptides capable of disrupting the endosome are utilized (Duguid et al., 1996; Plank et al., 1994). After uptake in the endosome they either create pore structures or induce fusion of the lipid coat of a cargo complex with the endosomal membrane (Varkouhi et al., 2010).

In contrast to endocytosis mediated uptake, direct delivery of molecules into the cytoplasm can be achieved by penetration of the membrane, by fusion of membrane coated cavities with the plasma membrane or by permeabilization of the membrane (Khalil et al., 2006). The so-called cell penetrating peptides (CPPs) were shown to efficiently mediate the intracellular delivery of biologically active peptides, proteins and nucleic acids as well as liposomes and nanoparticles (Temsamani and Vidal, 2004; Trabulo et al., 2010; Varkouhi et al., 2010). However, it is yet unclear in how far cargo-loaded cell penetrating peptides are capable to completely bypass endocytotic pathways (Trabulo et al., 2010; Patel et al., 2007). Although direct transfer of molecules could be principally mediated by fusion of liposomes with the plasma membrane, it was found that fusion only contributes to a small degree compared to endocytotic uptake of the liposomes (Khalil et al., 2006; Zuhorn et al., 2002; Gregoriadis, 1995). The permeabilization of the membrane with chemical or biological agents, like viral

and bacterial proteins, is often associated with high toxicity and irreversible damage (Khalil et al., 2006).

The most efficient methods that allow a direct transfer of various types of molecules into the cytoplasm of cells are based on physical techniques. Mechanical approaches like particle bombardment (Uchida et al., 2009; Zelenin et al., 1989; Yang et al., 1990) and microinjection (Graessmann, 1983; de Pamphilis et al., 1988; Soreq and Seidmann, 1992) are based on a transient mechanical penetration of the membrane. Whereas particle bombardment is rather limited to the transfer of nucleic acids, microinjection can be used to transfer a wide variety of molecules into the cytoplasm or into the nucleus of cells. However, microinjection is laborious and therefore not suited for the intracellular manipulation of large cell populations. Other physical methods use short pulses of laser light (optoporation) (Kurata et al., 1986; Tao et al., 1987) or ultrasonic cavitation (sonoporation) (Miller et al., 2002), thereby making the membrane permeable for the incorporation of exogenous material. In a similar way short electric pulses can bring the membrane to a transient permeable state (electroporation). Due to its simplicity and versatility electroporation became one of the most widely applied techniques for the intracellular delivery of exogenous molecules.

1.2.1.2 Electroporation

First experimental protocols for electroporation of mammalian cells, which were predominantly developed to mediate gene transfer, have been described by Neumann et al. (1982). Nowadays, this method can be applied to facilitate cellular uptake of molecules like DNA, RNA, peptides, antibodies, enzymes, therapeutic chemicals, dyes, radioactive molecules and even nanoparticles (Gehl, 2003).

Still, electroporation is predominantly used to transfer recombinant genes and other nucleic acids into the cell (Gazdhar et al., 2007). Electroporation is of special interest for some hard to transfect cells like endothelial cells (Hernández et al., 2004), neurons (Kitamura et al., 2007, Nevian and Helmchen, 2007), dendritic cells (van Driesche et al., 2005) and human embryonic stem cells (Costa et al., 2007; Mohr et al., 2006). The electroporation of dendritic cells and other antigen presenting cells in presence of mRNA in order to stimulate the immune system is regarded as a promising approach for cellular immunotherapy in various diseases (Minami et al., 2005; Schaft et al., 2006; van den Bosch et al., 2004). Also for the transfer of siRNA electroporation has been used (Matsuda and Cepko, 2003; Ovcharenko et al., 2005). The use of electroporation in drug delivery rapidly developed and nowadays provides a promising basis for electroporation-based therapies. The electroporation-mediated delivery of cytotoxic drugs, like bleomycin and cisplatinum (Belehradek et al., 1993; Mir et al., 1998; Sersa et al., 1998) is finding clinical application in the treatment of skin cancers and has potential to cure various other cancer types as well (Gothelf et al., 2003; Mir et al., 2006; Mlakar et al., 2009). Moreover, the electroporation-mediated delivery of drugs across diffusion barriers, like the skin (Prausnitz et al., 1999; Vanbever and Preat, 1999; Weaver et al., 1999; Jaroszeski et al., 2000b) or the intestinal epithelium (Ghartey-Tagoe et al., 2005) have been proposed.

Using *in vivo* electric transfer of DNA for gene therapy came in the focus of interest since viral methods failed due to safety problems and costs. Synthetic transfection strategies are still too inefficient (Gehl, 2003; Bloquel et al., 2004; Rols, 2006; Escoffre et al., 2009). The systematic electrotransfer of DNA into skeletal muscle or skin seems moreover promising for *in vivo* vaccination of mammalian organisms (Cristillo et al., 2008; Dobano et al., 2007; Chua et al., 2008).

Aside from nucleic acids, the potential of electroporation for the transfer of proteins has been recognized, since it directly transfers the protein into the cytoplasm of the cell in an efficient way. Proteins that were introduced by electroporation range from simple globular serum proteins like BSA (Prausnitz et al., 1994; Rols et al., 1998a) and lact- and ovalbumin (Prausnitz et al., 1993; Chen et al., 1993; Kim et al., 2003) to enzymes like ß-galactosidase (Rols et al., 1998), thymidin kinase (TK) (Dagher et al., 1992), caspases (Schimmer et al., 2003; Eksioglu-Demiralp et al., 2003) and various endonucleases (Morgan and Day, 1995; Winegar et al., 1989; Brennemann et al., 1995; Lips and Kaina, 2001) as well as other bioactive proteins participating in signal transduction and transcription, like cytochrome c (Garland and Rudin, 1998; Chertkova et al., 2008; Decrock et al., 2009) or the HIV transactivator protein TAT (Kasanchi et al., 1992; Verhoef et al., 1993). The electroporation of cells for loading with antibodies was used to inhibit the function of certain intracellular target proteins, which typically bear regulatory functions, like the cell cycle regulatory protein cyclin D1 (Lukas et al., 1994), the central metabolic enzyme asparagin synthase (Charakabarti et al., 1989), connexon subunits mediating cell-cell communication (Boitano et al., 1998) or the transcription activator ras-p21 (Berglund and Starkey, 1989, 1991).

1.2.2 Electrofusion: Merging of Membranes and Mixing of Cytoplasmic Content

The observation that electropermeabilized cells are associated with another property, its fusogenity, has led to further important biotechnical developments. If the destabilized membranes of two or more cells are in close apposition, lipids of adjacent membranes can intermix and after resealing build a continuous membrane that encloses a shared cytoplasm (cp. chapter 3.2.3). The cellular content of two or more cells of the same or different genomic and proteomic composition is combined. The most prominent application of cell fusion is the creation of hybridoma cells for the production of monoclonal antibodies (Kohler and Milstein, 1975). By fusion of the antibody producing but mortal B-cell with an immortalized myeloma cell, an immortalized antibody producing cell is generated. Cell fusion has been found to be a suitable tool to induce the reprogramming of somatic cells in order to identify the action of certain epigenetic factors that influence gene expression (Cowan et al., 2005; Silva et al., 2006). Cell fusion moreover became a tool for *in vitro* fertilization (Ogura and Yamagiachi, 1996). For purposes of drug delivery loaded erythrocyte ghosts, cells and vesicles can be exploited as material containers that are fused with target cells (Poste et al., 1976; Zimmermann et al., 1980; McElliot and Dice, 1984; Lee et al., 1993; Li et al., 1996). The

creation of giant cells by electrofusion of several cells has been proposed as a novel electrophysiological expression system for patch clamp studies on channel proteins (Zimmermann et al., 2006).

Naturally, membrane fusion takes place in fertilization, when a sperm cell fuses with an egg cell as well as in developmental and differentiation processes, like the establishment of the placenta or myocyte and bone marrow maturation. Also in the repair and regeneration of certain tissues, like liver, muscle, bone and cartilage fusion events play an essential role (Ogle et al., 2005). Intracellular vesicle transport relies on the fusion of internal membrane structures with one another. Similar mechanisms take place during infection with enveloped viruses, where the viral membrane fuses with the cell membrane or the endosomal membrane after endocytotic uptake in order to release its genome into the host cell (Hernandez et al., 1996; Dimitrov, 2004; Miyauchi et al., 2009). Certain types of viruses cause post-infectious agglutination and fusion of cells (Manservigi et al., 1977; Lifson et al., 1986; Bär et al., 2006; Duelli and Lazebnik, 2007). The role of cell fusion in the progression of cancer is discussed as well (Lu and Kang, 2009).

Biological fusion events are well-controlled and rely on specialized proteins that mediate specific, close membrane contact and induce a destabilization of the membrane lipid structure (Chen et al., 2005; Südhof and Rothman, 2009). Experimentally, cell-to-cell fusion can be induced using inactivated fusogenic viruses, e.g. sendai virus, (Scheid and Choppin, 1973; Cotton and Milstein, 1973) or isolated proteins like the influenza haemagglutinin (Sarkar et al., 1989). Alternatively, chemical or physical approaches can be exploited. The most prominent chemical agent used for cell fusion is polyethylene glycol (PEG) (Ahkong et al., 1975; Lane et al., 1984; Lentz, 2007). Whereas the use of PEG mediated fusion is limited by its toxicity and low efficiency, electric field induced fusion (electrofusion) is an extremely efficient method for the fusion of a wide variety of different cell types, yielding a high survival rate (Glassy, 1988; Zimmermann, 1982; Sukhorukov et al., 2006). In addition to the membrane destabilizing effect of electric pulsing, efficient electrofusion often requires the establishment of close cell-to-cell contacts by dielectrophoresis (Zimmermann and Vienken, 1982; Dimitrov, 1995) or other biological, chemical or mechanical methods (cp. chapter 3.2).

1.2.3 *In Situ* Approaches for Electroporation and Electrofusion

The classical electroporation and electrofusion protocols use cells in suspension. For this purpose anchorage-dependent cells have to be detached from their growth substrate by enzymatic treatment before they are placed between two plate electrodes in a cuvette or into an electrofusion chamber. The architecture and structure of polarized cell layers and tissues are disrupted by this detachment procedure. The enzymatically affected membrane proteins and the disintegrated cytoskeleton were shown to decrease the survival rate of cells and influence the electroporation efficiency (Müller et al., 2003; Zheng and Chang, 1991a). Moreover, significant metabolic alterations were found in anchorage-dependent cells after detachment from their growth substrate (Raptis and Firth, 2008). This makes the cells more

sensitive to further treatments which can essentially decrease their survival rate. Electroporation of suspended cells requires rather high voltage amplitudes, since a high fraction of the applied voltage drops across the bulk, leading to heating of the physiological buffer system, thereby affecting cell viability. This is the reason why electroporation and electrofusion in suspension typically require buffers with low ionic strength and lowered temperatures that, however, may create an additional trauma for the cells. After electric manipulation cells can be either analyzed directly in suspension or after they have been replated to a new culture substrate. The impact of a xenobiotic molecule introduced by electroporation on physiological processes has to be investigated after the cells have adhered and spread (Wegener et al., 2002).

An emerging interest to use the electroporation technique for basic cell biology and biomedical research as well as for *in vivo* electroporation of tissues, which all require high survival rates, led to the development of adequate devices for the electroporation of anchorage-dependent cells *in situ* (Raptis and Firth, 1990). During electric *in situ* manipulation anchorage dependent cells remain anchored to their growth substrate while the electric pulse is applied. The membrane proteins and the cytoskeleton are fully established and functional, which accelerates processes of membrane resealing and regeneration. The cell viability was found to be significantly increased after *in situ* electroporation compared to electroporation in suspension. *In situ* application of electric fields moreover allows for an immediate analysis of the manipulated cells.

1.2.3.1 Setups for *In Situ* Electroporation

Several setups for *in situ* electroporation have been described (Fig. 1.4). Cells can be cultivated on permeable filter substrates (Fig. 1.4 A), which are spanned between the electrodes of an electroporation cuvette (Yang et al., 1995; Kanthou et al., 2006) or they are placed into a specially designed electroporation chamber (Klenchin et al., 1991; Sukharev et al., 1992; Müller et al., 2003; Deora et al., 2007). By insertion of a PDMS mask stenciled with 3 x 3 arrays of holes with 0.1 – 0.6 mm in diameter to a filter setup allowed for spatially controllable loading of cells (Ishibashi et al., 2007).

Klenchin et al. (1991) placed the cell-covered filter substrate directly on the lower of two plate electrodes. Alternatively, cells can be directly cultivated on conducting substrates, which serve as electrodes for pulse application at the same time (Fig. 1.4 B – H). Thin-film electrodes of gold (Wegener et al., 2002; Ghosh et al., 1993; Jen et al., 2004) or ITO (*indium-tin oxide*) (Raptis, 1990; Raptis et al., 1994, 1995a, b, 2000) deposited on common culture substrates have been used. Whereas Raptis et al. first used a dipping counter electrode (Fig. 1.4 B), further developments made use of a coplanar electrode setup using two ITO electrodes (Anagnostopoulou et al., 2007) (Fig. 1.4 D). Further approaches for *in situ* electroporation with coplanar electrodes are based on interdigitated electrodes (Jen et al., 2004; Lin et al., 2003, 2004; Olbrich et al., 2008) (Fig. 1.4 F) or a small working electrode in combination with a large counter electrode (Wegener et al., 2002; Ghosh et al., 1993)

(Fig. 1.4 E). A similar coplanar electrode arrangement using a large counter electrode was chosen for electroporation electrode arrays, which were developed on the basis of silicon chip technology (Jain and Muthuswaja, 2007; Vassanelli et al., 2008). The most recent development are micro-structured needle electrodes, which can be integrated to the substrate of a silicon based micro chip for local electroporation of single cells (Sriperumbudur et al., 2009; Koester et al., 2010). However, these electrodes have not yet been used to load exogenous material into cells.

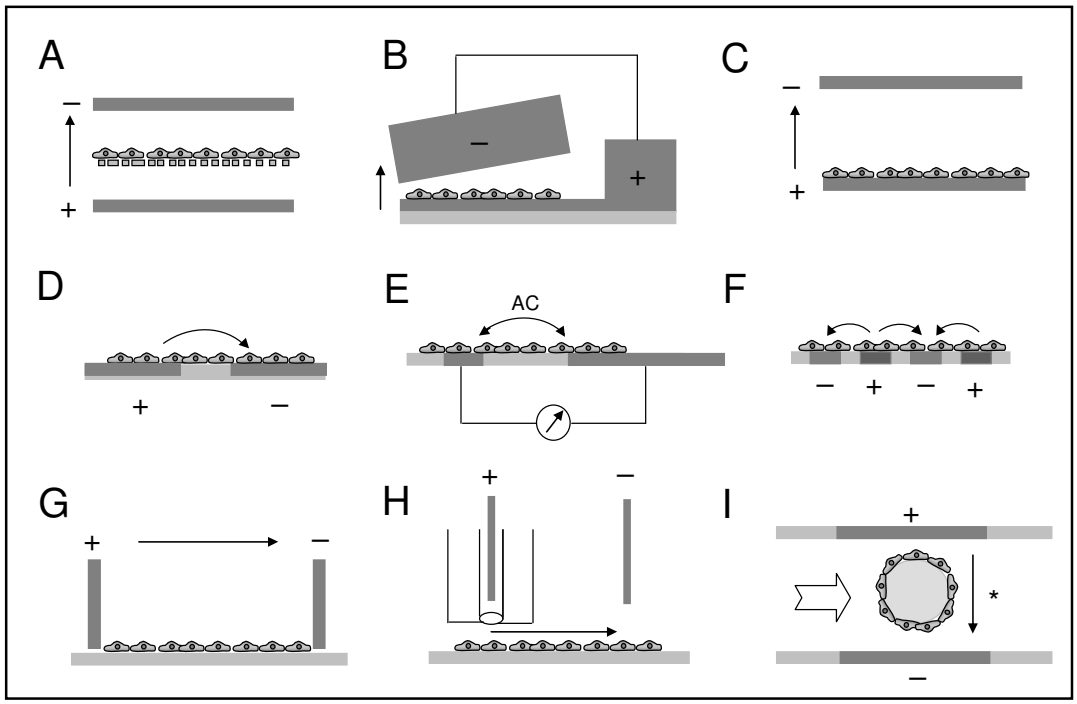

Fig. 1.4: Survey of different strategies for *in situ* electroporation and *in situ* fusion of anchorage-dependent cells. **A:** Cultivation of cells on porous membranes (e.g. Müller et al., 2003); **B:** Cultivation on conductive ITO (indium tin oxide) (Raptis and Firth., 1990); **C:** Cultivation on DNA coated gold electrodes (Yamauchi et al., 2004); **D, E:** Cultivation on coplanar ITO (Anagnostopoulou et al., 2007) or gold electrodes (Wegener et al., 2002; Ghosh et al., 1993); **F:** Cultivation on interdigitated electrode structures (IDES) of gold and titanium (Jen et al., 2004); **G:** Cultivation on glass substrates or culture dishes (e.g. Tereul et al., 1999); **H:** Scanning electrode (Oloffsson et al., 2005, 2007); **I:** Cultivation on beads under laminar flow (Teissié and Conte, 1988). Electrodes are illustrated by dark grey structures. The direction of the electric field (DC in most cases, AC in E) is indicated by an arrow and proceeds perpendicular (A – C), parallel (G, H) or in other form (D – F, I) with respect to the cell layer. The arrow marked with * indicates changes of field direction due to the use of rectangular bipolar pulses. Setups A – I were applied in electroporation experiments. Electrofusion was performed using setups A (Sukharev et al., 1990), G (Teissié et al., 1982; Blangero and Teissié, 1983; Blangero et al., 1989) and I (Teissié and Conte, 1988).

Whereas the electric field direction is usually applied perpendicular to the cell layers for pulsing (Fig. 1.4 A – C), the electric field has to be arranged in parallel to the cell layer, if cells are grown on non-conducting culture substrates (Fig. 1.4 G – I). Tereul et al. (1999) and Bright et al. (1996) cultivated cells on a common glass substrate, which was placed into a electroporation chamber with plate electrodes arranged perpendicular to the cell layer (Fig. 1.4 G). Alternatively, wire electrodes have been used for electric field application (Teissié et al., 1982; Kwee et al., 1990; Boitano et al., 1992). The company BTX Harvard Apparatus (http://www.btxonline.com) has developed electrodes for *in situ* electroporation in

a petri dish using 13 parallel plate electrodes covering the surface of an entire 35 mm dish. Commonly, the plates or wires are placed in direct contact with the bottom of the petri dish or are kept slightly above the cell layer. Potter and Cooke (1992) electroporated adherend cells cultured on Cytodex TM microcarrier beads that were suspended in a conventional electroporation cuvette. Since the method does not allow for microscopic examination, this setup did not achieve popularity.

Different approaches have been developed to reduce the required sample volume in electroporation experiments, which is especially crucial when introducing costly molecules. Oloffson et al. (2005, 2007) developed scanning capillaries for combined probe and electric field application at localized spots within a cell layer (Fig. 1.4 H). Tereul et al. (1999) used a microsyringe in a fixed electroporation chamber with plate electrodes to reduce the volume added to the cell layer down to 1 µl. De Vyst et al. (2008) used a system where two parallel wire electrodes can be automatically scanned sequentially over the adherent cell layer. The fluid for electroporation is only placed in the small space between the wires and is held by capillary forces. Raptis et al. (2003) have also developed a system to efficiently exploit the volume of material. A single narrow steel bar electrode (negatively charged) with a curved underside for uniform field direction is moved along the cell layer holding the fluid film, while the counductive ITO substrate is connected to a positive electrode.

Recent developments for the efficient transfer of DNA or RNA molecules rely on the pre-adsorbtion of the nucleic acids to the electrodes (Fujimoto et al., 2008; Koda et al., 2008). The immobilization of the genetic material is mediated by a carboxy functionalized self assembling monolayer (SAM) for contact with the gold electrode and a layer of cationic polymer for adsorbtion of the nucleic acids. Cells are finally cultivated on top of the transfectious layer.

Commonly, direct current pulses are used for electroporation of either cells in suspension or *in situ*. This bears, however, the risk of reactive and cytotoxic molecule production near the electrode surface, which is especially critical when using substrate integrated electrodes with a direct contact of cells to the electrode surface. Thus, the use of alternating current instead can significantly reduce the generation of harmful electrode products and thereby minimize invasiveness (Ghosh et al., 1993; Wegener et al., 2002). Due to the close contact to the electrode surface small voltages of only $2-5\,\mathrm{V}$ are sufficient to trigger membrane permeabilization, meaning that electroporations can be carried out in buffers with physiological ion content and in the cell incubator with a temperature of $37\,^{\circ}\mathrm{C}$ (Ghosh et al., 1993; Wegener et al., 2002).

1.2.3.2 Applications for *In Situ* Electroporation

Aside from loading cells with various reporter dyes for the evaluation of electroporation efficiency, *in situ* electroporation approaches have been used to deliver a wide variety of potentially therapeutic and genetically active agents into anchorage-dependent cells including

enzymes, antibodies, peptides, oligonucleotides, RNA and DNA (Rols, 2006) (see Appendix *A*3 Tab. A2).

In situ electroporation of adherent cells is of increasing interest in chip-based technologies. Several approaches have been developed that allow a spatially and temporally controlled transfer of genetic material in a selected population of cells (Olofsson et al., 2007; Koda et al., 2008) or even single cells (Vassanelli et al., 2008). Spatial control of transfection was achieved by either fabrication of multiple individually addressable electrodes or by pre-loading of the electrode substrate with different genetic material. Also the transfer of siRNA by *in situ* electroporation has already been used to demonstrate knock down of GFP expression in HEK-293 and NIH-3T3 cells, respectively (Fujimoto et al., 2008a, b; Jain and Mthuswami, 2007). The *in situ* delivery of mRNA into cultured neurons was shown by Tereul et al. (1999). Also proteins, peptides and antibodies have been transferred into anchorage-dependent cells by *in situ* electroporation. The *in situ* ITO-based electroporation setup developed by Raptis and Firth (1990) has for example been used to introduce several peptides containing protein-binding domains (e.g SH2, SH3) involved in certain protein-protein interactions in signal transduction cascades. The authors studied the growth factor-mediated activation of certain signaling cascades (Raptis et al., 2003; Anagnostopoulou et al., 2006; Boccaccio et al., 1998; Bardelli et al., 1998). The group of P.M. Comoglio loaded adherent cells with specific SH2-domain peptides in order to elucidate the participation of certain signaling pathways in HGF (hepatocyte growth factor)-mediated cytoskeletal reorganization, loss of intercellular junctions, cell migration and the formation of epithelial tubules in epithelial cells (Boccaccio et al., 1998). Nakashima et al. (1998) brought glutathione-S-transferase (GST) fusion proteins containing the SH2 or SH3 binding domains of the Crk protein into the cytoplasm of rat-1 fibroblasts in order to investigate the role of the c-Crk-II adaptor protein in growth factor-induced actin cytoskeleton organization. By isolating the GST fusion protein from the electroloaded cells the focal adhesion protein $p130^{cas}$ was found to bind to the Crk adaptor protein. Recently, Schönenberger et al. (2010) used *in situ* electroporation to load chondrocytes with the mechano growth factor (MGF) in order to demonstrate the biological activity of this peptide.

Antibodies have also been loaded into adherent cells by *in situ* electroporation, often using parallel plate electrodes (Bright et al., 1996) or the BTX *in situ* electroporation equipment (Schieffer et al., 1996; Ushio-Fukai et al., 1998; Lan et al., 2003; Rui et al., 2002). Frequently, antibodies addressing certain signaling proteins were used (Schieffer et al., 1996; Ushio-Fukai et al., 1998; Rui et al., 2002). Ushio-Fukai for example loaded vascular smooth muscle cells of rats with antibodies against different phospholipase C (PLC) subtypes (PLC-β1, PLC-δ1, PLC-γ1) and different subunits of heterotrimeric G-proteins ($G\alpha_{q/11}$, $G\alpha_{12}$ $G\alpha_{i}$, $G\alpha_{13}$, Gβ) in order to identify the AT_1 (angiotensin II type 1) receptor-mediated signaling pathway controlling the contraction and growth of these cells. Lan et al. (2003) loaded spinal neuronal rat cells *in situ* and *in vivo* with an antibody against the transcription factor c-Fos to evaluate its potential for the treatment of neuropathic pain.

The electroporation of adherent cells in presence of two different non-permeant [(alkylamino)methyl]acrylophenone derivatives was used to inhibit the EGF-mediated

activation of Erk1/2 signaling pathways activated via the EGF receptor, which is one of the most promising targets in cancer therapy (Brownell et al., 1998). This study demonstrates the potential of electroporation to assess the effectiveness of non-permeant drugs.
Yet, the use of ECIS electrodes to load cells with bioactive molecules is limited. Horseraddish peroxidase has been introduced to WI-38/VA13 cells grown on ECIS electrodes by Gosh et al. (1993). Albermann (2004) electroporated NRK cells in presence of TRITC-phalloidin, demonstrating specific staining of actin filaments. In addition, first approaches of an electroporation-assisted delivery of DNA and RNA for purpose of transfection have been pursued (Albermann, 2004).

1.2.3.3 Setups and Applications for *In Situ* Electrofusion

While the development and improvement of *in situ* electroporation approaches can still be found in the up-to-date literature, the electric field-induced fusion of cells *in situ* is rather limited to early studies. *In situ* electrofusion has been performed on non-conducting culture substrates using parallel plate (Teissié et al., 1982; Blangero and Teissié, 1983; Blangero et al., 1989) or wire (Teissié et al., 1982) electrodes. Electrofusion of cells grown on filters was performed using a sandwich setup. Sukharev et al. (1990) placed a membrane with adherent cells and an adlayer of suspended cells on the bottom electrode plate for fusion of the suspended cells with the bottom cell layer. Teissié and Conte (1988) used cells grown on beads that were subjected to rectangular pulses of changing direction applied by parallel plate electrodes in a flow channel (Fig. 1.4 H). The main application of *in situ* fusion has been the creation of heterokaryons and somatic cell hybrids. *In situ* electrofusion was used to create somatic cell hybrids of CHO cells with different mouse cell lines, which was shown to be a promising tool in somatic cell genetics (Finaz et al., 1984). However, many of these early studies were focussed on mechanistical studies rather than on their technical applicability.
Related to electric field-mediated fusion of cells *in situ* are certain forms of *in vivo* electrofusion. Grasso et al. (1989) fused different suspended cell types onto rabbit cornea *in vivo* in order to create tissue with novel membrane properties suitable for the investigation of receptor-mediated processes. Mekid and Mir (2000) demonstrated that the susceptibility of tumor tissue to *in vivo* fusion is dependent on the micro-environment in the respective tissue, like reduced amounts of extracellular matrix and increased concentrations of proteases. The authors assumed a link between metastatic potential and fusogenity. Because the formation of multinucleate cells induced cell death, a potential use of electrofusion in the treatment of cancer was proposed.

As all these examples demonstrate, many applications indicate the potential benefit of monitoring changes in cell morphology after *in situ* electroporation or electrofusion of adherent cells.

1.3 Combining *In Situ* Electromanipulation and Impedimetric Sensing

As presented above, electroporation allows for the direct transfer of a myriad of chemical and biological compounds into a broad variety of cells by simply optimizing the electric parameters. Since the survival rate can be enormously improved by *in situ* electroporation techniques, loading efficiencies of almost 100 % yielding high intracellular concentrations of the exogenous material can be achieved. After electroporation the transported molecule is directly exposed to the cytoplasm – the location of most targets of a xenomolecule – which is an essential benefit of the physical delivery technique.

Analysis of the cells after electroporation or cell fusion is frequently performed by optical methods using microscopy or flow cytometry. Alternatively, biochemical techniques are used for evaluation (cp. Appendix *A*3, Tab. A2), which often requires a large number of cells in order to obtain a measurable signal and / or the extraction of the analyte from the cell (Raptis and Firth, 2008). Many detection methods can only be performed once after harvesting or fixating the cells. The time point of analysis is often crucial, since the establishment of a detectable signal may be extremely variable. Therefore, online monitoring techniques are increasingly preferred for the analysis of cell responses. Since common light microscopic methods are often limited by their spatial resolution and quantitative character, other non-invasive electric sensing techniques are of growing interest.

Electric methods have already been used to assess the impact of electroporation on membrane integrity after manipulation of cells in culture or tissue. The invasiveness of electroporation pulses to cells in suspension has for example been investigated by conductance measurements (Kinosita and Tsong 1979; Pavlin et al., 2005) or impedance measurements (Glahder et al., 2005). Saulis et al. (2005, 2007) used a potassium selective microelectrode to measure the permeabilization in small volumes of cell suspensions, detecting the release of intracellular K^+ ions after electroporation. Microelectrode chips were constructed that monitor dynamic membrane permeabilization and resealing processes after electric pulsing of single suspended human HeLa cells by electrochemical impedance spectroscopy (EIS) (He et al., 2006, 2008). Changes in the transmembrane potential of single adherent cells after *in situ* electroporation were measured using substrate-integrated micro needle electrodes (MNEs) (Koester et al., 2010) or by manually controlled patch clamp pipettes (Vassanelli et al., 2008). Patch clamp techniques were also used to monitor cell fusion events (Leikina et al., 1992).

Deora et al. (2007) measured the resistance across confluent MDCKII cell layers grown on filters before as well as 1 h and 24 h after electroporation. Also Ghartey-Tagoe et al. (2005) electroporated confluent Caco-2 cell layers grown on filters and measured the transepithelial resistance of the monolayers in order to evaluate the epithelial barrier function after electroporation. Impedance measurements after electroporation of adherent cell layers have been reported by Müller et al. (2003), who monitored the complex impedance in order to determine the transepithelial resistance across confluent cell layers of L929 mouse fibroblasts cultivated on filter membranes before and after electroporation. Impedance analysis has

moreover been applied to examine the impact of electroporation on tissue (Grafström et al., 2006; Ivorra et al., 2007).

In situ electroporation of cells on gold-film electrodes usable for impedimetric analysis allows one to monitor the regeneration of cells after electric manipulation (Ghosh et al., 1993; Wegener et al., 2002). It was shown that the application of a well-defined, short invasive electric pulse led to a transient permeabilization of the membrane of anchorage dependent cells. The cellular response directly after electroporation was monitored in real time with high time resolution (Gosh et al., 1993). Monitoring of electroporated cell layers was used to evaluate the invasiveness and reversibility of the transient electric permeabilization of the cell membrane for efficient loading of the cells with impermeable dyes (Wegener et al., 2002).

Though electrical sensor techniques were applied to monitor the invasiveness of an electric pulse, most of them have not yet been exploited to analyze the impact of the molecule delivered into the cell. Only the ECIS technique was shown to be suitable to record the impact of bioactive molecules after *in situ* electroporation-mediated delivery[1]. Due to its high sensitivity to morphological changes – a typical reaction of cells on various kinds of external stimuli – ECIS can be used to directly monitor the impact of electroporation as well as the response to bioactive molecules after their cytoplasmic delivery by electroporation. The impact of the molecule under study on changes in cell morphology can be monitored in real time. Since cell fusion also causes drastic alterations in cell shape, ECIS is capable of detecting *in situ* cell fusion as well.

In this work the non-invasive impedimetric ECIS technique and invasive electric manipulations were performed in one setup combining the sensitive monitoring capabilities of ECIS and the action of defined electric field pulses for *in situ* electroporation and *in situ* electrofusion.

[1] The introduction of 8-OH-cAMP-a nonpermeable analogue of the second messenger cAMP into NRK cells grown on ECIS electrodes was shown to result in a typical transient impedance increase one hour after electroporation (information provided by J. Wegener).

2 Objectives

It was the aim of this thesis to use substrate-integrated planar gold-film electrodes for both, the electric manipulation and the impedimetric analysis of adherent mammalian cells *in situ* (Fig. 2.1). The electric manipulation of cells grown on gold-film electrodes using short invasive AC pulses intends to transiently permeabilize the cell membrane either for electroporation-mediated delivery of membrane-impermeable probes or for the initiation of cell fusion. The resulting cellular response to the electric manipulation should be monitored non-invasively using the well-established ECIS (electric cell-substrate impedance sensing) technique, which is highly sensitive to changes in cell morphology. Therefore, studies combining electric manipulation and analysis of adherent cells grown on gold-film electrodes should focus on the electroporation-mediated delivery of various bioactive probes including cytotoxic drugs, signaling molecules, enzymes, antibodies and nucleic acids, which can not enter the cell under normal conditions, but have the potential to affect cellular functions when brought inside the cell. Moreover, the potential of ECIS to detect the associated changes in cell morphology resulting from introduction of xenobiotics or cell fusion events, as induced by electric membrane permeabilization in presence of membrane agglutinating agents, should be evaluated.

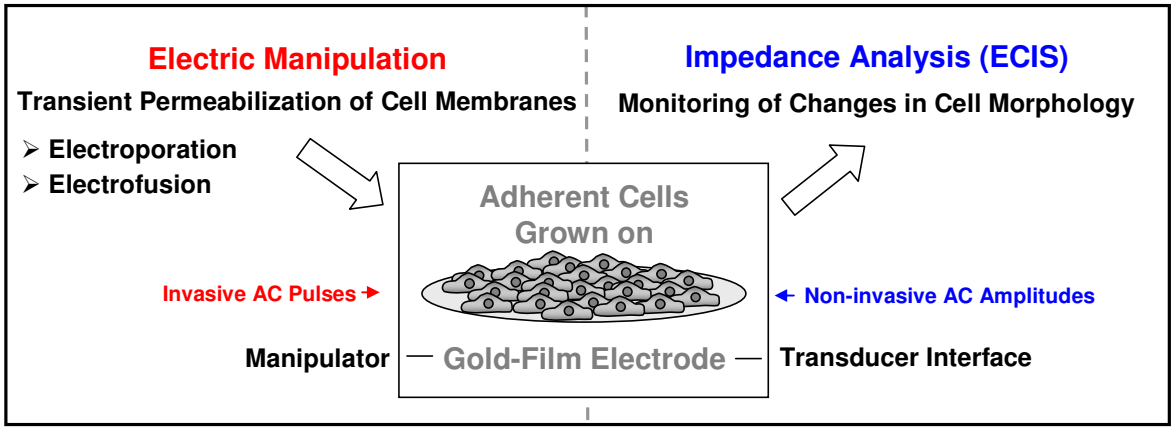

Fig. 2.1: Schematic illustration of the thesis's objective: Substrate-integrated gold-film electrodes are used for both, the electric manipulation (electroporation and electrofusion) and the impedance analysis (ECIS) of adherent mammalian cells.

3 Theoretical Background

3.1 Impedance Spectroscopy of Adherent Cells

Impedance spectroscopy (IS) is a versatile method to investigate and characterize intrinsic electric properties of a wide variety of materials and electrochemical systems (Ende and Mangold, 1993). The method is based on measuring the complex impedance Z of a system depending on the frequency of the AC (alternating current) signal that is used for excitation. Using small amplitudes of exciting sinusoidal current or voltage IS allows for a damage-free and non-invasive examination of a system and has therefore been increasingly applied to analyze also biological systems.

3.1.1 Physical Background of Impedance Spectroscopy

The complex impedance Z is a measure for the ability of an electric system to resist current flow in an AC circuit. According to Ohm's law the impedance is defined by the ratio of the applied voltage $U(t)$ to its resulting current $I(t)$ (eq. 3.1).

$$Z = \frac{U(t)}{I(t)} = \frac{U_0 \sin(\omega t)}{I_0 \sin(\omega t - \varphi)} \qquad \textbf{3.1}$$

with:
- $U(t)$: voltage at time t
- U_0: amplitude of voltage
- $I(t)$: current at time t
- I_0: amplitude of current
- ω: angular frequency
- t: time
- φ: phase shift between voltage $U(t)$ and current $I(t)$

Current and voltage of AC circuits are in phase only if the system is perfectly resistive. However, electric elements with capacitive and inductive properties cause a phase shift between voltage and current. Thus, the calculation of Z requires the division of sinusoidal functions of the same frequency ω but with different amplitudes and phases. Therefore, it is more convenient to regard $U(t)$ and $I(t)$ as complex quantities (eq. 3.2, 3.3). The complex impedance Z is defined by the exponential functions (eq. 3.4).

$$U(t) = U_0 \cdot e^{i\omega t} \qquad \textbf{3.2}$$

$$I(t) = I_0 \cdot e^{i(\omega t - \varphi)} \qquad \textbf{3.3}$$

$$Z = \frac{U(t)}{I(t)} = \frac{U_0 \cdot e^{i\omega t}}{I_0 \cdot e^{i(\omega t - \varphi)}} = \frac{U_0}{I_0} \cdot e^{i\varphi} = |Z| \cdot e^{i\varphi} \qquad \textbf{3.4}$$

$$\text{with } i =: \sqrt{-1} \text{ and } e^{i\alpha} = \cos\alpha + i\sin\alpha .$$

The complex impedance Z can be described by its magnitude |Z|, which is the ratio of the amplitudes U_0 and I_0 and the phase shift φ between voltage and current. Complex values can be graphically presented as a vector in a complex plane (Fig. 3.1). In this diagram the length of the impedance vector denotes its magnitude |Z| and the angle between the vector and the x-axis provides the phase shift φ.

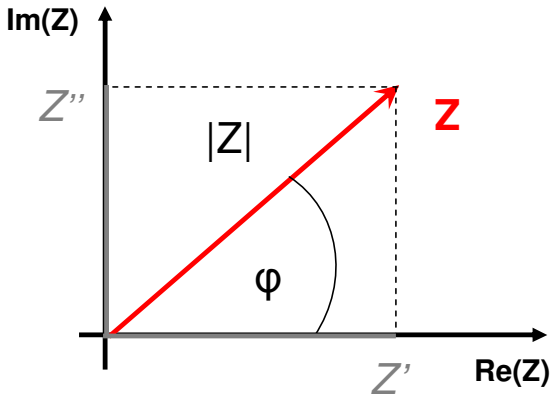

Fig. 3.1: Representation of the complex impedance Z as a vector in a Gaussian plane with a real (Re) and imaginary (Im) axis. The length of the vector of Z provides the magnitude of impedance |Z|. The angle between the impedance vector and the real axis corresponds to the phase shift φ between voltage and current. The complex impedance Z can be decomposed to a real and imaginary fraction as presented by the Cartesian coordinates, Z' (resistance) and Z'' (reactance) on the real and imaginary axis, respectively.

Expression of the complex impedance in Cartesian coordinates separates the values of the real and imaginary impedance components (eq. 3.5).

$$Z = Z' + iZ'' \qquad \textbf{3.5}$$

Real impedance contributions (Z') arising from current in-phase with the voltage are termed resistance. Imaginary components arising from 90° out-of-phase currents are termed reactance (Z'') and include impedances of capacitive (Z_C) and inductive elements (Z_L).
The Cartesian coordinates Z' and Z'' as well as the polar coordinates |Z| and φ are both used to describe and analyze the electric properties of a system and can easily be transformed into each other using equations 3.6 – 3.9.

$$Z' = \mathrm{Re}(Z) = |Z| \cdot \cos\varphi \qquad \textbf{3.6}$$

$$Z'' = \mathrm{Im}(Z) = |Z| \cdot \sin\varphi \qquad \textbf{3.7}$$

$$|Z| = \sqrt{Z'^2 + Z''^2} \qquad \textbf{3.8}$$

$$\varphi = \arctan\left(\frac{Z''}{Z'}\right) \qquad \textbf{3.9}$$

Since individual contributions of real and imaginary components within a complex system depend on the applied frequency, the complex impedance is described as a function of frequency (eq. 3.10; eq. 3.11).

$$Z(\omega) = |Z| \cdot e^{i\varphi(\omega)} \qquad \textbf{3.10}$$

$$Z(\omega) = Z'(\omega) + iZ''(\omega) \qquad \textbf{3.11}$$

The complex impedance can be plotted in several different types of diagrams for data illustration (MacDonald, 1992). A so-called Bode diagram plots the impedance magnitude $|Z|$ and phase shift φ versus the frequency of the excitation signal in double logarithmic or semi-logarithmic scales, respectively. The logarithmic representation allows for plotting of a wide range of frequencies and impedances with each decade given the same weight and is therefore advantageous for many applications.

Data obtained by impedance measurements always represent the response of the entire system. In order to unravel individual impedance contributions of the system under study, equivalent circuits with a similar electric frequency response have to be developed and compared to the experimental system. Equivalent circuits are composed of common electric circuit elements known from electronics that are arranged in a network such that the network mirrors the electric properties. The total impedance of an equivalent circuit is calculated using Ohm's and Kirchhoff's laws depending on the respective arrangement of individual model elements. A list of some common ideal and empirical circuit elements is presented in Tab. 3.1. Fitting the resulting transfer function of the equivalent circuit to the experimental data finally provides estimates for the individual impedance contributions of the system.

Tab. 3.1: Impedance contribution and phase shift of ideal and empirical equivalent circuit elements.

Equivalent Circuit Element	Parameter	Impedance $\|Z\|$	Phase Shift φ
Ohmic Resistor	R	R	0
Capacitor	C	$(i \cdot \omega \cdot C)^{-1}$	$-\pi/2$
Inductor	L	$i \cdot \omega \cdot L$	$+\pi/2$
Constant Phase Element (CPE)	A, n $(0 < n < 1)$	$(i \cdot \omega)^{-n} \cdot A^{-1}$	$-n \cdot \pi/2$

Ideal resistors are completely frequency independent and do not cause any phase shift. They only reduce the amplitude of the current upon voltage application. In contrast, impedance contributions of capacitors and inductors in AC circuits are frequency-dependent. The impedance of a capacitor decreases with increasing frequency, whereas impedance

contributions of an inductor increase if the frequency rises. With respect to the applied voltage the current through a capacitor is phase shifted by – 90° while inductors cause a phase shift of + 90°.
However, these ideal equivalent circuit elements (*R*, *C*, *L*) known from electronics are not always suitable to describe electrochemical or biological systems, where ions are involved as charge carriers. Since ions in electrolytes do not behave like electrons in standard electric elements, non-ideal empirical circuit elements have been introduced as they are often more suitable to describe the system.
The constant phase element (CPE) for example is a non-ideal circuit element, representing a non-ideal capacitor (McAdams et al., 1995). The exact physical basis of this empirical circuit element is still not fully understood. However, the electric properties of a CPE are characterized by the parameters *A* and *n*, which influence its impedance and phase shift contributions. The constant phase elements causes a frequency-dependent impedance contribution for values of *n* between 0 and 1 as well as a frequency independent phase shift ranging between 0 and $-\pi/2$. For $n = 0$ the resulting impedance is completely frequency independent with a constant value of $Z_{CPE} = A^{-1}$ and thus the CPE behaves like an ideal resistor ($R = 1/A$). For $n = 1$ the impedance of the CPE amounts to $(i\omega A)^{-1}$ and the phase shift is $-\pi/2$ describing an ideal capacitor with $C = A$. For values of *n* ranging between 0 and 1 the CPE shows resistive as well as capacitive behavior.

3.1.2 Electric Cell-Substrate Impedance Sensing (ECIS)

ECIS™ (electric cell-substrate impedance sensing) is a very versatile technique that allows quantitative non-invasive monitoring and analysis of adherent cells directly grown on a small planar electrode and it is capable of detecting cell morphological changes upon biological, chemical or physical stimuli (Giaever and Keese, 1984).
The ECIS technique is based on a two electrode setup, where the adherent cells are directly cultivated on thin coplanar gold-film electrodes deposited on a common cell culture substrate (Fig. 3.2). The electrical connection between the electrodes is provided by the cell culture medium above the cell layer serving as electrolyte. Electrodes are probed with a weak sinusoidal AC voltage at varying frequencies and the measured in-phase and out-of-phase current is converted to the real (Z') and imaginary (Z'') components of the complex impedance.
Since the working electrode (area: ~ 5×10^{-4} cm²) is significantly smaller (~ 500-fold) than the counter electrode, the voltage drop as well as the measured current density is much higher at the small working electrode. Thus, the total impedance of the system is clearly dominated by the impedance of the working electrode as this is acting as a bottleneck for current flow. The impedance contribution of the large counter electrode to the total impedance is below one percent and can therefore be neglected (Wegener, 2003). The difference in electrode size and the close proximity between adherent cells and the electrode surface provide the high sensitivity of this technique.

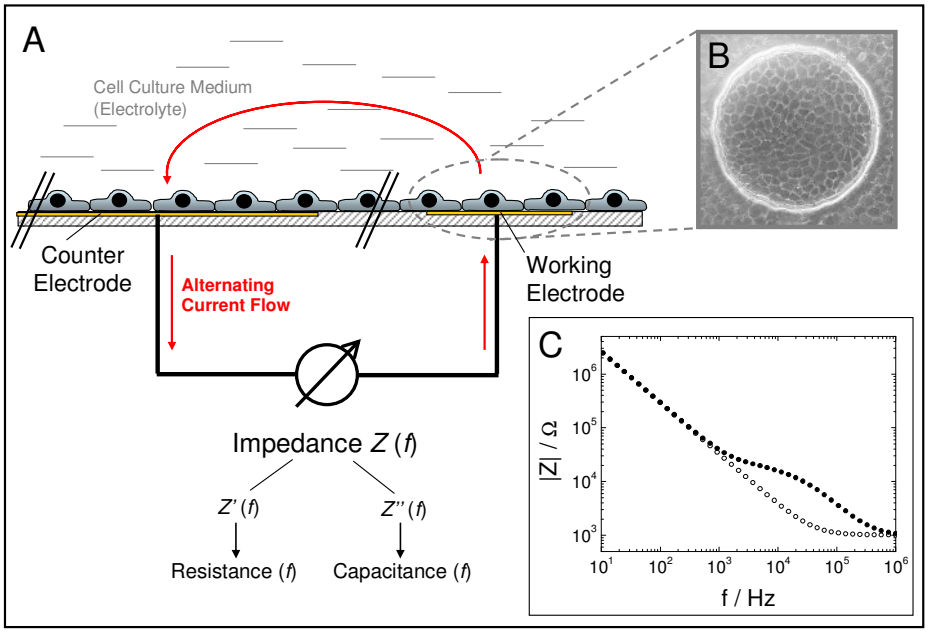

Fig. 3.2: A: Schematic presentation of the ECIS setup (side view) showing current flow across a cell-covered ECIS gold-film electrode. Electric connection between the small working electrode (~ 5×10^{-4} cm^2) and the significantly larger counter electrode is provided by a physiological electrolyte solution like common cell culture medium or buffer. Red arrows, drawn unidirectionally for clarity, indicate the alternating current flow. The frequency-dependent impedance of the system can be decomposed into its real (*Z'*) and imaginary (*Z''*) components representing the resistance and capacitance of the system, respectively. **B:** Phase contrast micrograph (top view) of a cell-covered ECIS electrode. **C:** Frequency-dependent impedance spectra of a cell-free (○) and a cell-covered (●) working electrode.

If adherent cells are cultivated on the electrode surface, their cellular bodies, due to the capacitive, non-conducting properties of the cell membrane, act as insulating particles. For a wide range of frequencies the current is forced to flow around the cellular bodies along the narrow clefts beneath and between neighboring cells. Only at higher frequencies the current can capacitively couple through the membrane. Due to this frequency-dependent behavior of the cell layer the total impedance of the cell-covered electrode is increased compared to a cell-free electrode within a certain frequency range (Fig. 3.2 C). Thus, frequency-dependent impedance contributions of the cell layer on the working electrode provide information about cell morphology as they allow to distinguish between impedance contributions from intercellular spaces, the cell-substrate contact area or certain membrane properties as described in more detail below (Keese and Giaever, 1994).

3.1.3 Modeling the Impedance of Cell-Covered Electrodes

A physical model to describe the various impedance contributions arising within a cell layer to the total impedance of the system has been developed by Giaever and Keese (Giaever and Keese, 1991). The constant part of the system which does not change is the cell-free electrode covered by the electrolyte, which can be described by a constant phase element (CPE) in series with an Ohmic resistor (Wegener et al., 2000a) (Fig. 3.3 A).

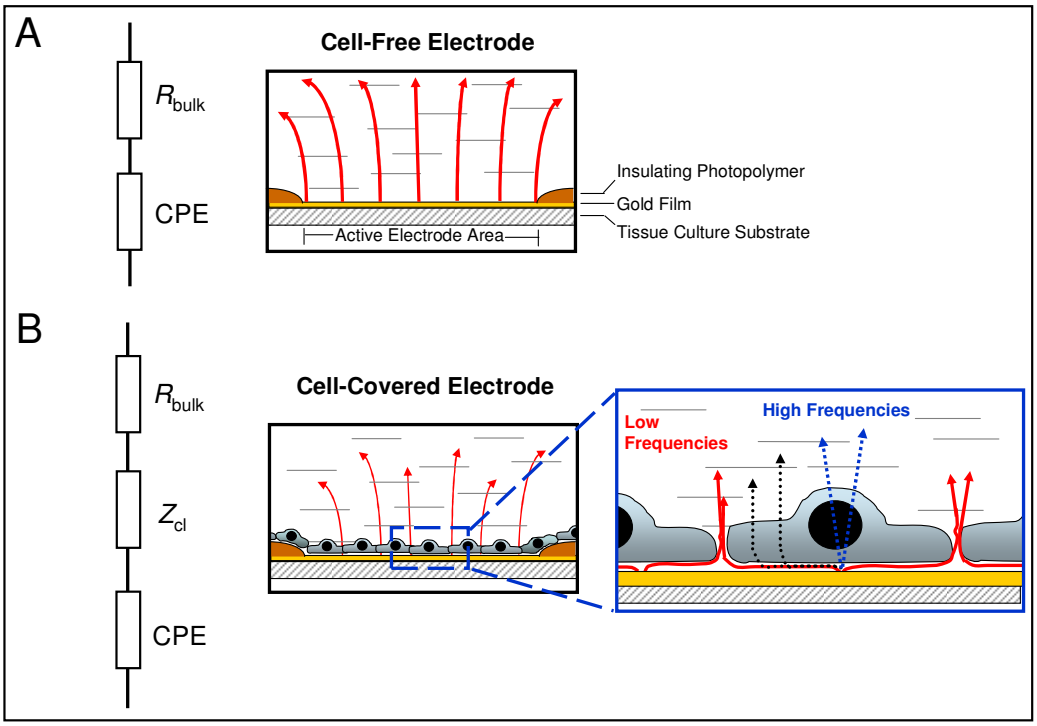

Fig. 3.3: Equivalent circuit models and corresponding schematic illustrations for a cell-free (**A**) and a cell-covered (**B**) gold-film electrode. The cell-free electrode is described by a serial combination of a constant phase element (CPE) representing the electrode-electrolyte interface and a resistor (R_{bulk}) including the resistance of the electrolyte as well as the constriction resistance due to electric field compression by the small surface area of the working electrode. Adherent cells on the electrode cause an additional frequency-dependent impedance contribution (Z_{cl}). At lower frequencies the current has to flow around the cellular bodies through the narrow subcellular and intercellular gaps (red arrows, →). At high frequencies the current couples across the membranes (blue arrows, ⇢). At intermediate frequencies (black arrows, ⇢) the current makes use of paracellular and transcellular pathways at varying ratios.

The CPE describes impedance contributions arising from the electrode-electrolyte interface of the almost ideally polarizable gold electrode (cp. 3.1.1, Tab. 3.1). The resistive impedance contribution of the bulk phase is represented by R_{bulk}, which includes the resistance of the electrolyte as well as the constriction resistance (Newman, 1966) arising from the electric field compression due to the small size of the electrode.

Cells adhering to the electrode surface increase the impedance of the system by an additional impedance contribution Z_{cl} that is connected in series to the circuit elements CPE and R_{bulk} (Fig. 3.3 B) (Wegener, 2003). In a first approximation the frequency-dependent impedance of the cell layer can be separated into two spatially different current pathways.

At lower frequencies (< 10 kHz) the current flows around the cell bodies (Fig. 3.3 B, red arrows) first passing through the narrow cleft (10 – 100 nm) between the basal membrane and the electrode surface underneath the cell bodies. Subsequently, the current flows through the intercellular spaces of adjacent cells. At higher frequencies (> 30 kHz) the current can couple capacitively through the cell membranes. The lipid bilayer membrane structure behaves like a capacitor with the hydrophobic membrane core acting as a dielectric resulting in the flow of a displacement current at sufficiently high frequencies (Fig. 3.3 B, blue arrows). Ohmic contributions by ion channels and ion leakage can be neglected.

Between these high and low frequency limiting cases the current can split up between both routes at varying ratios resulting in a complex network of possible pathways (Fig. 3.3 B, black arrows). As a consequence the ratio between paracellular and transcellular current and, thus, the particular impedance contributions arising from the subcellular cleft become frequency- and position-dependent. Because there is no lumped equivalent circuit element available reflecting the situation in the cell-electrode junction, the electric composition of the subcellular cleft can be described by a two-dimensional core-coat conductor composed of the electrolyte filled cleft and the plasma membrane and electrode surface as capacitive coats (Fig. 3.4 B) (Wegener, 2009).

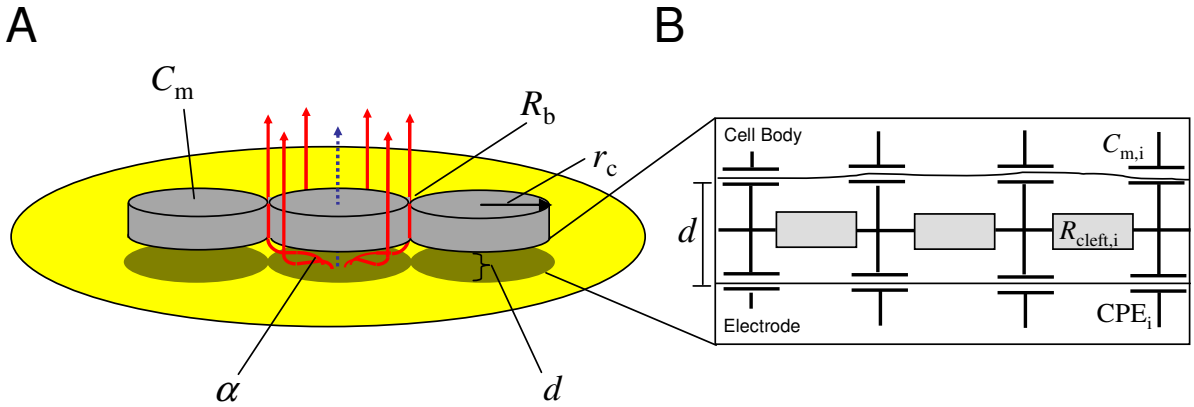

Fig. 3.4: A: Schematic representation of the model developed by Giaever und Keese (1991) for cell-covered electrodes. Cell bodies are regarded as circular disks with a radius r_c hovering at an average distance d above the electrode surface. Impedance contributions from the cell layer can be separated into three independent parameters R_b, α und C_m. $\boldsymbol{R_b}$ accounts for the impedance contribution arising from the intercellular pathway across the cell-cell contacts. $\boldsymbol{\alpha}$ quantifies the impedance portion resulting from the cell-electrode junction. $\boldsymbol{C_m}$ describes the capacitive contribution of the plasma membranes. AC current flow around or across the cell body is drawn unidirectional for clarity (arrows). **B:** Finite element model of the subcellular cleft. The subcellular cleft can be described as a two-dimensional electric system of finite and locally individual cleft resistance elements ($R_{cleft,i}$) within the electrolyte coated by the finite elements of local electrode and membrane capacitance (CPE_i, $C_{m,i}$). Depending on AC frequency and position on the electrode current flow individually collects local contributions of finite cleft resistance elements ($R_{cleft,i}$) before it passes the cell layer capacitatively via the cell membrane or paracellularly via the cell junctions. The figure was adapted from Wegener (2009).

In order to model the cell layer's impedance distinct current pathways were taken into account using differential equations to develop a transfer function that describes the frequency-dependent behavior of cell-covered gold-film electrodes. In this mathematical model cells in a confluent cell layer are assumed as circular disks with a radius r_c hovering at an average distance d above the electrode (Lo et al., 1995) (Fig. 3.4 A). Z_{total}, the specific impedance (per unit area) of the cell-covered electrode is then given by the transfer function 3.12.

$$Z_{total} = \left[\frac{1}{Z_{CPE}} \left(\frac{Z_{CPE}}{Z_{CPE}+Z_m} + \frac{\frac{Z_m}{Z_{CPE}+Z_m}}{\frac{1}{2}\gamma r_c \frac{I_0(\gamma r_c)}{I_1(\gamma r_c)} + R_b\left(\frac{1}{Z_{CPE}}+\frac{1}{Z_m}\right)} \right) \right]^{-1} + R_{bulk} \qquad \textbf{3.12}$$

with:

$$\gamma \cdot r_c = \sqrt{\frac{\rho}{d} \cdot \left(\frac{1}{Z_{CPE}} + \frac{1}{Z_m} \right)} \cdot r_c = \alpha \cdot \sqrt{\left(\frac{1}{Z_{CPE}} + \frac{1}{Z_m} \right)} \qquad \textbf{3.13}$$

I_0 and I_1 are modified Bessel functions of the first kind of the order zero and one. Z_{CPE} describes the specific impedance of the cell-free electrode modeled by a constant phase element (cp. 3.1.3) with:

$$Z_{CPE} = \frac{1}{(i\omega)^n A} \qquad \textbf{3.14}$$

Z_m represents the specific impedance across both, apical and basal, cell membranes of intact cells (eq. 3.15).

$$Z_m = \frac{1}{i\omega C_{cl}} \qquad \textbf{3.15}$$

C_{cl} is the capacitance of the cell layer – the apical and the basal cell membrane capacitance in series – providing an average capacitance for a single cell membrane according to:

$$C_m = 2 \cdot C_{cl} \qquad \textbf{3.16}$$

In fact, only the average capacitance of both membranes C_{cl} is experimentally accessible. To obtain a numerical value for C_m of one membrane equations 3.15 and 3.16 have to be combined. The model parameter C_m however does not consider that the properties of the apical and basal membrane can differ with respect to their surface area and capacitive behavior. The parameter C_m is determined by membrane properties and morphology, like undulations as it is typical for the apical membrane of epithelial cells (Wegener, 2003).
The parameter R_b is a measure for the constraint of the current flow in the intercellular clefts and is highly influenced by the tightness of cell-cell contacts. In addition, changes in the cell radius affect R_b since a reduction of the total sum of intercellular spaces increases the resistance across the cell layer. As derived from equation 3.13 the parameter α has been defined as:

$$\alpha = r_c \sqrt{\frac{\rho}{d}} \qquad \textbf{3.17}$$

The parameter α is a measure for the impedance of the subcellular cleft and its value depends on the cell radius r_c, the average distance d between electrode surface and the cell bodies as well as the specific resistivity ρ of the electrolyte in the subcellular space.
Although the subcellular impedance as well as the intercellular impedance contribution both describe the paracellular current pathway, their individual contributions can be separated. Electrically, impedance contributions occurring at the intercellular junctions are purely

resistive and thus frequency independent. The parameter α however has Ohmic as well as capacitive properties and its impedance contribution is therefore dependent on the frequency (cp. Fig. 3.6 A).

Tab. 3.2: Parameters used for modeling the electrical behavior of cell-covered electrodes according to Giaever and Keese.

Parameter	Unit	Description
R_b	$\Omega \cdot cm^2$	specific resistance of the cell-cell junctions
α	$\Omega^{1/2} \cdot cm$	impedance contribution of the subcellular cleft as a function of r_c, d and ρ
C_m	$\mu F \cdot cm^{-2}$	specific average capacitance of the cell membrane

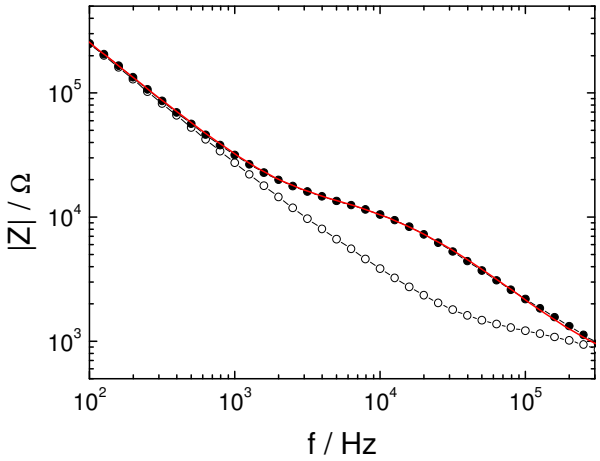

Fig. 3.5: Typical impedance spectra of a cell-free electrode (○) and an electrode covered with a confluent cell layer of NRK cells (●). The magnitude of the impedance |Z| is plotted versus the frequency f in double logarithmic scale. The solid red line represents the transfer function fitted to the experimental data with the parameters R_b (3.64 $\Omega \cdot cm^2$), α (4.04 $\Omega^{1/2} \cdot cm$) and C_m (2.73 $\mu F \cdot cm^{-2}$).

The values for the individual parameters (Tab. 3.2) are obtained by fitting the transfer function of the model to the experimental data following a method described by Wegener et al. (2000a) using least-square algorithm computations. A typical impedance spectrum presenting the impedance magnitude |Z| of a cell-free and a cell-covered electrode as a function of frequency is shown in Fig. 3.5.

At low frequencies (< 10^3 Hz) the electrode capacitance described by the CPE dominates both impedance spectra as indicated by a linear decrease with increasing frequencies. At high frequencies (> 10^5 Hz) the impedance of the cell-free electrode approaches a constant value, the electrolyte resistance (R_{bulk}). A cell layer grown on the electrode surface increases the electrode impedance in a characteristic way within a certain frequency range (here: ~ 10^3 – 3×10^5 Hz). The height, slope and width of the plateau in the impedance spectrum of

a cell-covered electrode within this characteristic frequency range depend on cell type specific morphological characteristics as described by the parameters α, R_b and C_m.

The impact of the individual parameters on the shape of the impedance spectrum of a cell-covered electrode is illustrated in Fig. 3.6. Discrete variation of the parameter α affects the slope within the plateau of the impedance spectrum of the cell-covered electrode, showing a stronger impedance increase towards lower frequencies (Fig. 3.6 A). An increase in R_b is indicated by an elevation of plateau values and a concomitant extension of the plateau region to lower frequencies (Fig. 3.6 B). If the values of C_m are increased the shoulder of the spectrum moves towards lower frequencies (Fig. 3.6 C).

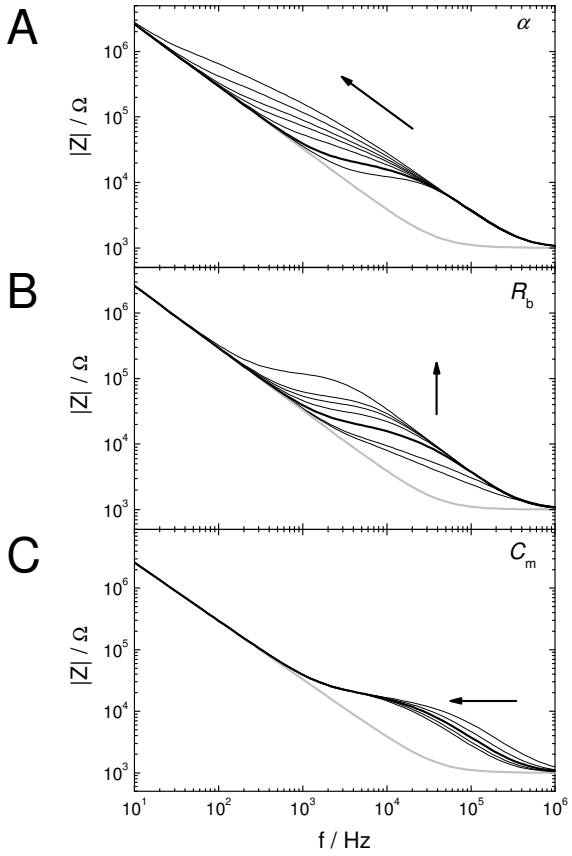

Fig. 3.6: Simulated impedance spectra for a cell-free (grey) and a cell-covered (black) electrode computed from the transfer function using a *LabView*-based software (written by J. Wegener, 2010). Parameters α (**A**), R_b (**B**) and C_m (**C**) were varied discretely, while the respective two other parameters were kept constant. For the standard curves (solid black line) parameter values were chosen on the basis of parameters found for NRK cells: $\alpha = 5\ \Omega^{1/2} \cdot cm$; $R_b = 5\ \Omega \cdot cm^2$; $C_m = 2\ \mu F \cdot cm^{-2}$. The bulk resistance R_{bulk} was set to $1000\ \Omega \cdot cm^2$, CPE parameters were $A = 1.5 \times 10^{-5}\ Fs^{n-1} \cdot cm^{-2}$, $n = 0.95$ for an electrode surface of $5 \times 10^{-4}\ cm^2$. Values were varied to: **A:** $\alpha = 0.1$, 5, 10, 15, 20, 30 and $50\ \Omega^{1/2} \cdot cm$; **B:** $R_b = 0.1$, 1, 5, 10, 15, 20 and $50\ \Omega \cdot cm^2$; **C:** $C_m = 1$, 1.5, 2, 2.5, $3\ \mu F \cdot cm^{-2}$. Arrows indicate the direction of increasing parameter values.

The complex impedance can be broken up in its real and imaginary components for each frequency (Fig. 3.2 A). The real part corresponds to the resistance of the cell-covered electrode ($R(\omega)$) (Fig. 3.7 A). Imaginary contributions are dominated by the capacitive behavior of the electrode and the cell membrane and are presented by the total capacitance ($C(\omega)$) (Fig. 3.7 B). Analysis of either resistance or capacitance can provide additional information about the cell layer on the electrode. Figure 3.7 shows how the variation of the

parameters α, R_b and C_m influence the total resistance (A) and capacitance (B) of a cell-covered electrode. The resistance ($R(\omega)$) reflects the influence of changes in parameters α and R_b, describing the paracellular pathway more clearly than the total impedance magnitude |Z| (Fig. 3.6). However, a crossover of resistance curves at intermediate frequencies has to be considered for increasing α and especially R_b values, which may artificially pretend a decrease of total resistance despite an actual increase of paracellular or subcellular resistance contributions (Fig. 3.7 A). Analyzing the capacitance at high frequencies (Fig. 3.7 B) can be useful to report on changes in membrane capacitance or cell coverage (chapter 3.1.4).

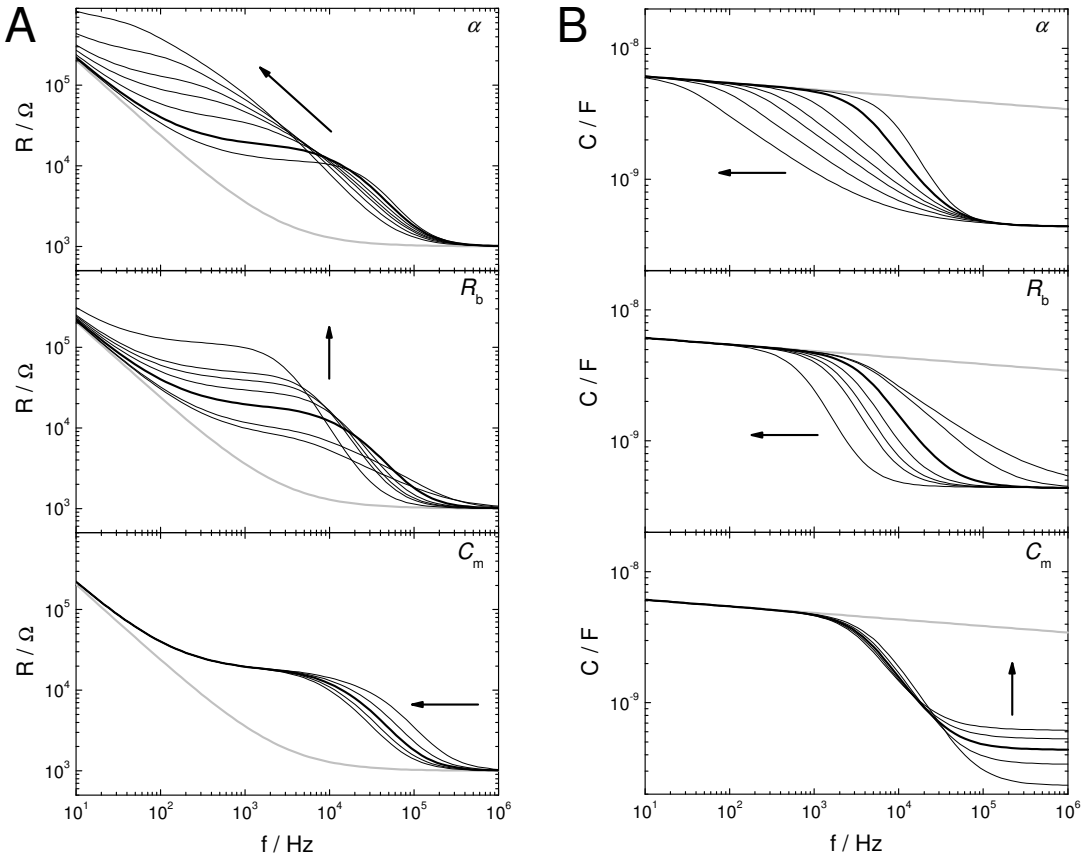

Fig. 3.7: Simulated resistance (**A**) and capacitance (**B**) spectra for a cell-free (grey) and a cell-covered (black) electrode computed from the transfer function using a *LabView*-based software (written by J. Wegener, 2010). Parameters α, R_b and C_m were discretely varied, while the other parameters were kept constant. For the standard curves (solid black line) parameter values were chosen on the basis of parameters found for NRK cells: $\alpha = 5\ \Omega^{1/2} \cdot cm$; $R_b = 5\ \Omega \cdot cm^2$; $C_m = 2\ \mu F \cdot cm^{-2}$. The bulk resistance R_{bulk} was set to $1000\ \Omega \cdot cm^2$, CPE parameters were $A = 1.5 \times 10^{-5}\ Fs^{n-1} \cdot cm^{-2}$, $n = 0.95$ for an electrode surface of $5 \times 10^{-4}\ cm^2$.Values were varied to: α = 0.1, 5, 10, 15, 20, 30 and 50 $\Omega^{1/2} \cdot cm$; R_b = 0.1, 1, 5, 10, 15, 20 and 50 $\Omega \cdot cm^2$; C_m = 1, 1.5, 2, 2.5, 3 $\mu F \cdot cm^{-2}$. Arrows indicate the direction of increasing parameter values.

3.1.4 Analysis of Experimental Data Using the Model of Giaever and Keese

The aim of a model is to find the best curve fit between experimental and calculated model data. Using an automated fitting algorithm based on least square analysis a best-fit combination of the three parameters α, R_b and C_m is determined. This parameter combination

is ideally found as the absolute minimum of the squared error function χ^2 = f (α, R_b, C_m) between simulated and experimental data (Bodmer et al., 2005).
Experiments provide 51 data points within the frequency spectrum of 10 – 10^6 Hz. Experimentally obtained impedance spectra were analyzed using a *LabView* based program (written by J. Wegener), which fits the transfer function (eq. 3.12) with the cell specific parameters α, R_b and C_m, to experimental data of a cell-covered electrode. The fitting routine uses the normalized impedance magnitude, i.e. the ratio of the impedance magnitude spectrum of a cell-covered electrode to that of a cell-free electrode for the least square optimization (cp. Fig. 3.9). This approach considers both, real and imaginary contributions of impedance data. The normalized presentation on a linear rather than a logarithmic scale reduces uneven weighting of the square error at different frequencies. A data proportional weighting of the square errors at different frequencies further reduces this problem. A specification of starting values for α, R_b and C_m determines the initial basis for parameter adjustment. Reasonable starting values close to correct experimental parameter combinations improve the stability of the fitting procedure and minimize errors. Starting from the local environment of starting values the algorithm searches for decreasing squared errors in the three dimensional (α, R_b and C_m) plane of possible parameter combinations. In several approximation rounds (number of iterations) an optimal parameter combination at the absolute minimum of squared errors is approached. The local environment (starting value ± ½ starting value for each parameter) can be subdivided into a defined number of increments, which defines the local accuracy of the parameter adjustment. Experimental data were fitted using 5 – 7 iterations and subdividing the local environment into 9 increments.
In addition to the cell-specific parameters α, R_b and C_m parameters of the CPE, A and n, can be fitted for a defined electrode area (5×10^{-4} cm^2) from the linear, low frequency end of the reactance. The bulk resistance is set to 1 kΩ and is majorly defined by the constriction resistance using a microelectrode with a surface area of 5×10^{-4} cm^2.

As presented in Fig. 3.8 impedance spectra generated on the basis of the model by Giaever and Keese (1991) (Fig. 3.8 A) and experimentally obtained impedance spectra (Fig. 3.8 B) deviate systematically from each other in the high frequency range. At frequencies above ~ 10^5 Hz simulated model spectra of cell-free electrodes level off to stable values of the bulk resistance (1 kΩ) (Fig. 3.8 A), whereas the impedance of the experimental system declines below 1 kΩ for frequencies above ~ 2×10^5 Hz (Fig. 3.8 B). This phenomenon can be explained by the existence of parasitic impedance contributions that arise from the electronic system and cables. These parasitic impedance contributions are not implemented in the basic model of Giaever and Keese.
Parasitic contributions are often complex in nature and may consist of capacitive, resistive and inductive parts. Since parasitic impedances depend on the load impedance of the system they are difficult to determine exactly for every individual system. Simple parasitic contributions often show a purely capacitive behavior (e.g. cable capacitance) and can therefore be modeled as parallel capacitances in the equivalent circuit.

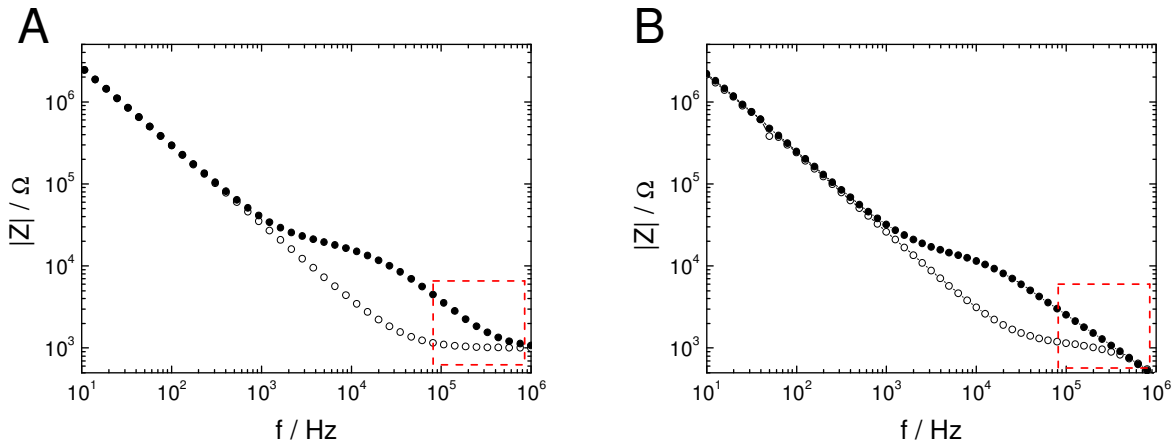

Fig. 3.8: Simulated (**A**) and experimental (**B**) impedance spectra for cell-free (○) and cell-covered (●) electrodes. In the high frequency range deviations occur between spectra simulated according to the model of Giaever and Keese (1991) and measured spectra (red box). In experimental measurements parasitic impedance contributions ($|Z|_{para}$) arising from the electronic equipment cause a decline of impedance below levels of R_{bulk} at frequencies above ~ 2×10^5 Hz .

Such parasitic contributions can influence the fitting procedure and the numerical results for the cell parameters α, R_b and C_m. Especially when the cell layer contributes considerably to the electrode impedance at high frequencies these elements have to be considered in order to allow for a correct determination of the cell parameters α, R_b and C_m.
Therefore, the parasitic contribution of the experimental setup used in this thesis was empirically approximated and implemented to all simulations as a CPE with the parameters $A_{para} = 1 \times 10^{-9}$ $Fs^{n-1} \cdot cm^{-2}$ and $n_{para} = 0.88$.

3.1.5 Presentation of Impedance Data

A continuous recording of impedance data with focus on one or a few characteristic sensitive frequencies enables real-time monitoring of cell-morphological changes upon different kinds of external stimuli over several days. The choice of the sampling frequency depends on the cell type as well as on the focus of analysis. Often the impedance magnitude |Z| is monitored, but for a detailed analysis real and imaginary components of the complex impedance data can also be plotted (cp. Fig. 3.7).
The sensitivity of a monitoring frequency recorded in the impedance, resistance or capacitance regime can be easily extracted from normalized presentations (Fig. 3.9) by plotting the ratio of the respective quantity for a cell-covered electrode to a cell-free electrode ($|Z|_{cell\text{-}covered}$ / $|Z|_{cell\text{-}free}$, $R_{cell\text{-}covered}$ / $R_{cell\text{-}free}$, $C_{cell\text{-}covered}$ / $C_{cell\text{-}free}$) as a function of frequency. The influence of changes in the model parameters α, R_b and C_m is shown below.

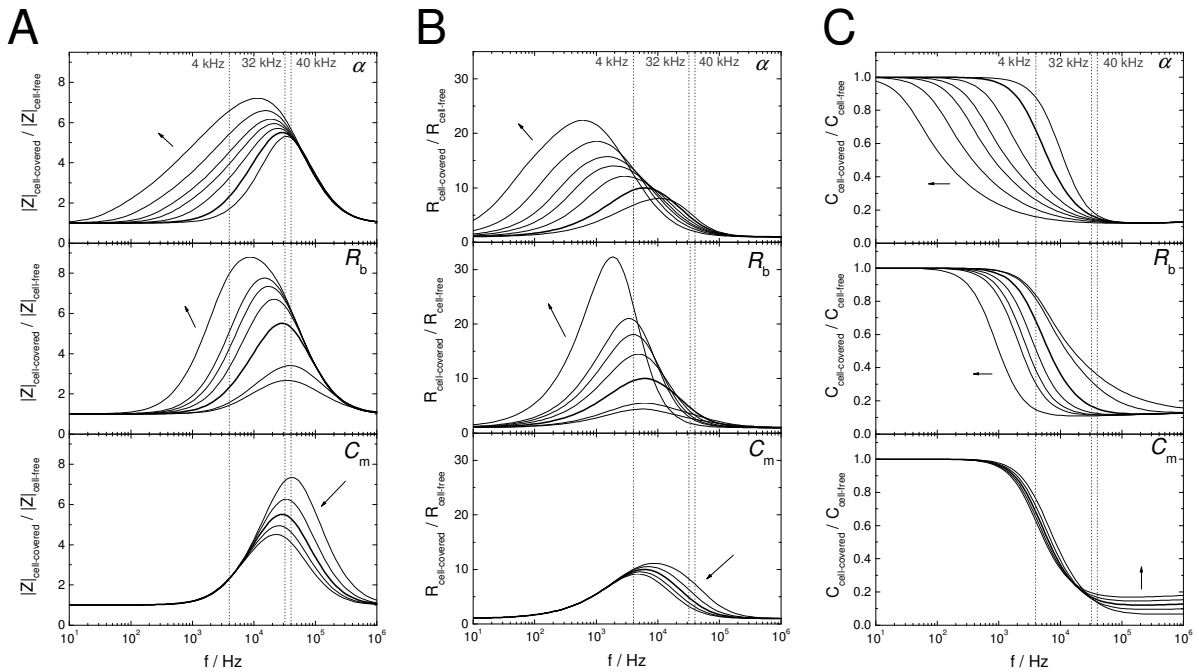

Fig. 3.9: Simulated frequency spectra of the normalized impedance $|Z|_{cell\text{-}covered}$ / $|Z|_{cell\text{-}free}$ (**A**), normalized resistance $R_{cell\text{-}covered}$ / $R_{cell\text{-}free}$ (**B**) and normalized capacitance $C_{cell\text{-}covered}$ / $C_{cell\text{-}free}$ (**C**). Parameters α, R_b and C_m were individually and discretely varied, while the other parameters were kept constant. For the standard curves (solid black line) parameter values were chosen as follows: $\alpha = 5\ \Omega^{1/2} \cdot cm$; $R_b = 5\ \Omega \cdot cm^2$; $C_m = 2\ \mu F \cdot cm^{-2}$. The bulk resistance R_{bulk} was set to $1000\ \Omega \cdot cm^2$, CPE parameters were $A = 1.5 \times 10^{-5}\ Fs^{n-1} \cdot cm^{-2}$, $n = 0.95$ for an electrode surface of $5 \times 10^{-4}\ cm^2$.Values were varied as follows : $\alpha = 0.1$, 5, 10, 15, 20, 30 and $50\ \Omega^{1/2} \cdot cm$; $R_b = 0.1$, 1, 5, 10, 15, 20 and $50\ \Omega \cdot cm^2$; C_m =, 1, 1.5, 2, 2.5, 3 $\mu F \cdot cm^{-2}$. Monitoring frequencies of 4 kHz as well as 32 kHz and 40 kHz used for data presentation are indicated by vertical lines. Arrows indicate the direction of increasing parameter values.

Using a monitoring frequency of 4 kHz the impedance (A) allows for sensitive measurement of morphological changes and cell motility (Keese and Giaever, 1994; Lo et al., 1993). Using standard electrodes with an active area of $5 \times 10^{-4}\ cm^2$ the normalized resistance exhibits a maximum close to 4 kHz for a wide variety of cell types (Fig. 3.9 B). Even slight morphological changes altering the tightness of the cell-cell contact area (R_b) and cell-substrate area (α) are detected at this frequency with high sensitivity (Fig. 3.9 A). Changes in the membrane capacitance (C_m) can not be recorded at 4 kHz (Fig. 3.9 A). For this reason, monitoring the impedance magnitude |Z| at 4 kHz essentially mirrors changes in the cell layer resistance that arise due to slight morphological alterations occurring in sub- and intercellular spaces.

At higher monitoring frequencies (40 or 32 kHz) resistive contributions from the intercellular (R_b) and especially the subcellular (α) spaces do not contribute as much to the impedance signal as compared to a lower monitoring frequency of 4 kHz (Fig. 3.9 A). In the higher frequency range, however, capacitive contributions arising from the cell membranes are detected with high sensitivity as a big fraction of the current can couple through the membranes as a displacement current (Fig. 3.9 A, C_m; Fig. 3.9 C). Cell membrane capacitances of the cell layer add to the electrode capacitance in a reciprocal manner following Kirchhoff's laws ($1/C_{total} = 1/C_{electrode/electrolyte} + 1/C_{cell\ layer}$) resulting in decreasing electrode capacitance values for increasing coverage with cells. The electrode capacitance

above a certain threshold frequency depends linearly on the fraction of electrode covered with cells (Wegener et al., 2000b). Thus, phenomena like cell attachment to or cell detachment from the electrode can be sensitively detected by measuring the impedance or capacitance at high frequencies (40 or 32 kHz).

In this work cell layer impedances |Z| were monitored at medium frequencies of 4 kHz when slight alterations within an intact cell layer were to be detected with high sensitivity. A monitoring frequency of 32 or 40 kHz was chosen in experiments where associated cell detachment or changes in cell coverage of the electrode were anticipated due to the onset of apoptosis or necrosis. The selection of 32 or 40 kHz was due to instrumental settings of different measuring setups (see Materials and Methods 4.3.1.1). Results were presented at both, medium (4 kHz) and high (32 or 40 kHz) frequencies if both processes – slight morphological changes as well as changes in electrode coverage with cells – occurred.

Time dependent ECIS measurements are commonly presented using normalized values of the absolute impedance magnitude |Z| in order to obtain a better inter-experimental comparability (Fig. 3.10 B). Absolute values of the impedance magnitudes (Fig. 3.10 A) that were used as the basis for normalization of absolute magnitudes (norm |Z| = 1) (Fig. 3.10 B) are given in the caption of each graph. These reference values were either taken from the first value at the beginning of the experiment, the last value before addition of a substance or the value directly before the application of an electric pulse. In some rare cases it was advantageous to use the absolute impedance magnitudes for analysis as shown in Fig. 3.10 A.

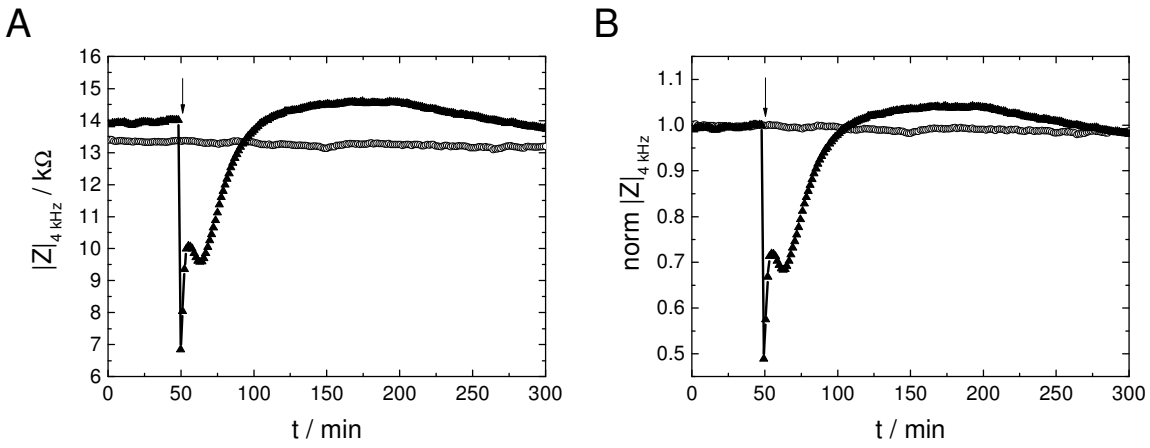

Fig. 3.10: Time course of absolute (**A**) and normalized (**B**) impedance magnitude (A: |Z| and B: norm |Z|) at a monitoring frequency of 4 kHz. In this example all absolute values were normalized to the last reading before the application of an electroporation pulse (arrow). In other measurements the basis for norm |Z| can also be the first value recorded at t_0 or the last value before the addition of a compound under test. The basis for normalization set to norm |Z| = 1 is given in the figure captions. Absolute impedance values in the example presented here were normalized to: ○: 13.37 kΩ; ▲: 14.01 kΩ.

3.2 Electroporation and Electrofusion of Mammalian Cells

Electroporation and electrofusion of cells are interrelated phenomena which occur when cells are subjected to external electric fields with amplitudes high enough for transient membrane destabilization (Fig. 3.11). Reversible perturbation of membrane integrity allows a free diffusion of membrane impermeable substances across the permeabilized membrane for a limited period of time. As a result, these substances remain entrapped within the cytoplasm after membrane resealing. Loading of cells with membrane impermeable exogenous molecules like drugs or nucleic acids is commonly referred to as electroporation (Neumann et al., 1982). If destabilized membranes of neighboring cells are in close contact during the resealing process, membrane lipids can rearrange in such a way that cell fusion occurs. The cell membranes of two or more individual cells merge and cytoplasmic contents including solutes and organelles are intermixed (Senda et al., 1979).

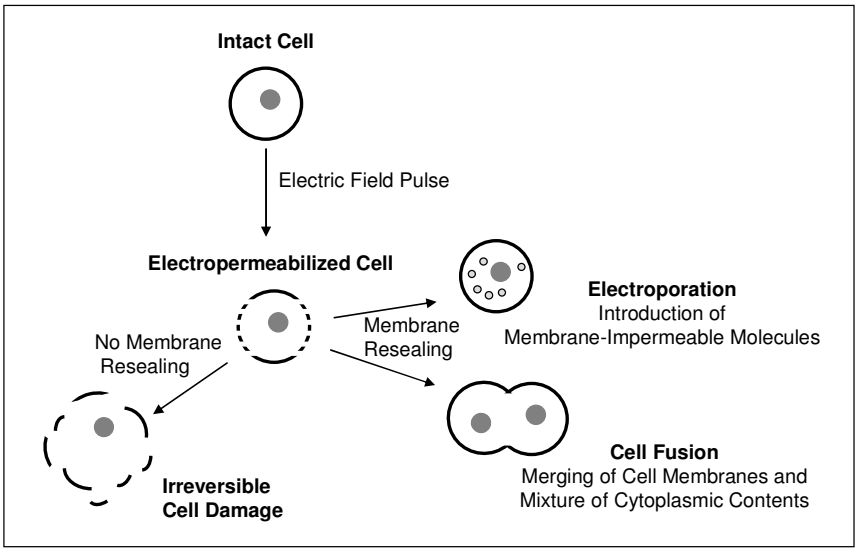

Fig. 3.11: Schematic illustration of processes occurring upon exposure of a cell to an invasive electric field pulse (adapted from Puc et al., 2004). Reversible electropermeabilization of cells using well-defined electric pulse conditions can be applied to introduce exogenous, membrane impermeable molecules as well as to induce cell fusion. Electric pulses which prevent membrane resealing lead to irreversible cell damage.

Most experimental and theoretical studies leading to a better understanding of the physical background of electric field effects on cells are based on cell suspensions, regarding the cell body as a spherical electrolyte-filled dielectric shell. This model system is much simpler than a cell layer or tissue, where complex cell morphologies and electric field distributions occur. Additional studies on lipid bilayer model membranes offer further valuable contributions to the understanding of the basic behavior of membranes in electric fields (Abidor et al., 1979; Chernomordik and Chizmadzhev, 1989).

3.2.1 Biophysical Behavior of Cells in Electric Fields

The behavior of cells in electric fields can be ascribed to polarization effects that occur at the surface of the cell membrane. The lipid membrane essentially acts as a dielectric separating the conducting cytoplasm from the surrounding electrolyte (Dimitrov, 1995; Ramos and Teissié, 2000). Due to the selective permeability of the cell membrane to certain ions (Na^+, K^+, Cl^-) a natural resting potential difference ($\Delta\Psi_0 = \Psi_{in} - \Psi_{out}$) of about – 40 to – 70 mV prevails between the interior of the cell and the surrounding medium with $\Psi_{out} = 0$ taken as the reference (Barrau et al., 2004). This natural membrane potential difference ($\Delta\Psi_0$) finally originates from an electrochemical ion gradient, which is metabolically maintained by active membrane transport in many cells (Tinoco et al., 2002). Additionally, an asymmetric distribution of charged lipids and glycoproteins contributes to the natural transmembrane potential difference (Neumann, 1989).

The local breakdown of the lipid bilayer structure as observed in electroporation and electrofusion can be explained by electric forces which essentially rely on transversal field effects (Teissié, 2007). Application of an external electric field (E_i) across the dielectric membrane induces an ion accumulation at the interfaces between the membrane surfaces and the aqueous media on either side. This membrane polarization establishes the potential difference $\Delta\Psi_i$ across the membrane, which is superimposed to the natural resting potential difference $\Delta\Psi_0$ (3.18) (Gabriel and Teissié, 1997; Rols, 2006).

$$\Delta\Psi_{total} = \Delta\Psi_0 + \Delta\Psi_i \qquad \textbf{3.18}$$

The induced membrane potential difference $\Delta\Psi_i$ depends on the relative orientation of the membrane surface with respect to the electric field direction. When regarding a spherical cell of radius r in a homogenous electric field E_i (Fig. 3.12), the local value of the induced membrane potential difference $\Delta\Psi_i$ on the cell surface is described by the angle Φ between the direction of the electric field E_i and the normal to the membrane surface at the position M (eq. 3.19) (Kinosita and Tsong, 1977; Neumann et al., 1999; Ramos and Teissié, 2000).

$$\Delta\Psi_i = f \cdot g(\lambda) \cdot r \cdot E_i \cdot \cos \Phi(M) \qquad \textbf{3.19}$$

The individual shape of a cell influences the electric field distribution, which is considered by the shape factor f. For a sphere the shape factor f has the value of 1.5 (Berhardt and Pauly, 1973). The factor $g(\lambda)$ takes into account that the membrane is not a perfect dielectric but slightly permeable to selected ions. It depends on the specific conductivity of the cell membrane (λ_m), the cytoplasm (λ_c) and the extracellular fluid (λ_i) (Neumann, 1989; Teissié and Rols, 1993; Kotnik et al., 1997, 1998).

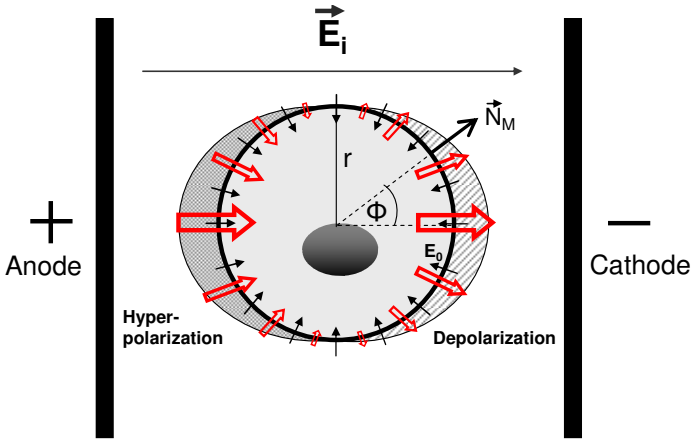

Fig. 3.12: Schematic illustration of the membrane potential difference modulation of a spherical cell in a homogenous electric field E_i between two equally sized plate electrodes. The parameters are defined as follows: r: Cell radius; Φ: Angle between the membrane normal N_M at the position M and the direction of the electric field E_i; E_0: Endogenous electric field within the cell membrane according to the natural membrane potential difference $\Delta\psi_0$. Arrows indicate the electric potential gradient and direction of the resting potential (closed, black arrows) or the electric field induced potential (open arrows). The length and thickness of the arrows represent the magnitude of induced potential difference $\Delta\psi_i$, which is maximal at the cell poles facing the electrodes ($\Phi = \pi$ and $\Phi = 2\pi$) and close to zero for $\Phi = \pi/2$ and $\Phi = 3\pi/2$. The induced membrane potential difference is superimposed on the native resting potential of the cell resulting in hyperpolarization of the membrane area facing the anode and depolarization of the membrane part at the cathode (shaded areas) (adapted from Rols et al., 2000).

According to the angular factor (cos Φ(M)) in equation 3.19 the induced potential difference is position dependent. At the cell poles facing the electrodes the induced membrane potential difference attains its maximal value. Since the induced potential difference is added to the resting potential (eq. 3.18) the cathodal side of the cell is depolarized while the anodal side is hyperpolarized. No change in membrane potential is observed at the equator where $\Phi = 90°$ (Ramos and Teissié, 2000). These physical predictions of position-dependent and asymmetrical membrane potential modulation were experimentally validated by the use of voltage sensitive dyes and fast digital videomicroscopy at the single cell level (Hibino et al., 1991, 1993; Gross et al., 1986).

The maximal value of the induced membrane potential difference $\Delta\Psi_i$ is reached after a very short charging time $t = \tau$, which is in the range of ~ 1 µs for a conventional cell membrane (Bernhard and Pauly, 1973; Kinosita and Tsong, 1977).

$$\Delta\Psi(t) = \Delta\Psi_i \cdot [1 - e^{-t/\tau}] \qquad \textbf{3.20}$$

This characteristic charging time τ is a function of the dielectric membrane properties as well as the conductivity of the cytoplasm and external medium (Kotnik et al., 1998; Pauly and Schwann, 1959).

Most studies described in the literature use exponential decay pulses or direct current (DC) pulses which can be controlled more easily with respect to amplitude and pulse duration and for which the above described theories are valid. Only few theoretical descriptions for the influence of alternating electric fields on the transmembrane potential difference of spherical cells are available. The transmembrane potential difference $\Delta\Psi_i$ induced by an AC pulse can

be essentially described by equation 3.21, which includes a frequency-dependent term compared to equation 3.19 (Marszalek et al., 1990).

$$\Delta\Psi_i = 1.5 \cdot \frac{g(\lambda) \cdot E_i \cdot r \cdot \cos\Phi(M)}{\sqrt{1+(\omega\tau)^2}} \quad \textbf{3.21}$$

$$E_i = E_0 \cdot \sin\omega t \quad \textbf{3.22}$$

When applying an AC field pulse its AC frequency in relation to the charging time τ of the membrane has an essential influence. The induced membrane potential difference will be smaller than for a DC field of the same strength, if the period of the applied AC voltage is shorter than the charging time of the membrane. Only for frequencies smaller than ~ 100 kHz AC pulses induce the same transmembrane potential differences as a DC pulse of the same strength (Neumann, 1989; Tsong, 1991). Due to the oscillating field direction, membrane polarization was observed to be symmetrical on both cell poles (Marszalek et al., 1990).

Many phenomena observed for suspended cells in electric fields are based on the above described polarization effect. Subcritical polarization of the cell body leads to phenomena like electrodeformation (Riske and Dimova, 2005) and dielectrophoresis, the movement of particles in a non-uniform electric field (Voldmann, 2006). If an overcritical potential difference is generated, insulator properties of the membrane get lost (Neumann and Rosenheck, 1979). A transient dielectric breakdown of the membrane is the basis for electroporation and electrofusion.

3.2.2 Electroporation

Electroporation is defined as the transient permeabilization of the membrane lipid bilayer caused by the application of short, well-defined electric pulses of micro- to millisecond time duration and sufficiently high amplitude (Zimmermann et al., 1974; Neumann et al., 1982). Due to the temporarily permeabilized membrane of electroporated mammalian cells hydrophilic molecules from the extracellular fluid are able to enter the cytoplasm and remain entrapped in there after membrane resealing (Gehl, 2003; Rols, 2006).
According to Teissié et al. (2005) the entire process of electroporation can be subdivided into five subsequent steps (Tab. 3.3). The following chapters discuss (i) the essential steps of the electroporation process, (ii) the most widely accepted structural model of the permeabilized state and (iii) transmembrane transport mechanisms of exogenous molecules across these permeable structures.

Tab. 3.3: Electropermeabilization of cells by electric fields occurs in five steps according to Teissié et al. (2005).

Step	Process	Time Scale
Initiation	field induced increase of transmembrane potential up to the permeabilizing threshold value.	µs
Expansion	expansion of membrane defects as long as supercritical field strength is maintained.	ms
Stabilization	reorganization of membrane structure as soon as the field is subcritical again. A stable permeabilized state for the diffusion of small molecules is established.	ms
Resealing	reclosure of transient permeabilization structures.	s
Memory	continuous recovery of the membrane structure and their physiological properties.	h

3.2.2.1 Initiation of Membrane Permeabilization

Only if the overall membrane potential difference $\Delta\Psi_{total}$ (eq. 3.18) exceeds a certain critical potential difference ($\Delta\Psi_{total} \geq \Delta\Psi_{perm}$) a field induced reorganization of membrane structure takes place. This critical transmembrane potential difference has been estimated to be in the range of 0.2 – 1 V (Chen et al., 2006). In order to achieve the critical membrane potential, the applied electric field has to exceed the threshold field strength E_{perm} (Teissié et al., 2005).

$$\Delta\Psi_{perm} = f \cdot g(\lambda) \cdot r \cdot E_{perm} \qquad \textbf{3.23}$$

Critical electric potentials at lowest field intensities (E_{perm}) are reached first at the cell pole facing the positively charged electrode (anode). Here, the electric field vectors E_0 of the endogenous membrane potential $\Delta\Psi_0$ as well as the induced potential difference $\Delta\Psi_i$ have the same orientation (eq. 3.19; Fig. 3.12). For permeabilization of the cell pole facing the cathode higher field strengths are required, since the conversely orientated field vectors of the endogenous membrane potential and induced potential are substracted.
The critical threshold field strength is influenced by the cell radius. Thus, larger mammalian cells are permeabilized at lower electric field values (~ 200 V/cm) than small cells like bacteria (~ 1 – 2 kV/cm) (Teissié and Rols, 1993) or intracellular organelle membranes (Deng et al., 2003).
Above the critical transmembrane potential difference the permeabilized area of the cell surface increases with growing field strength due to the angular dependency of membrane polarization (eq. 3.24) (Teissié et al., 2005).

$$A_{perm} = A_{tot} (1 - E_{perm} / E) / 2 \qquad \textbf{3.24}$$

Using conventional electroporation protocols permeabilization remains restricted to localized areas on the pole caps of the cell surface (Fig. 3.13).

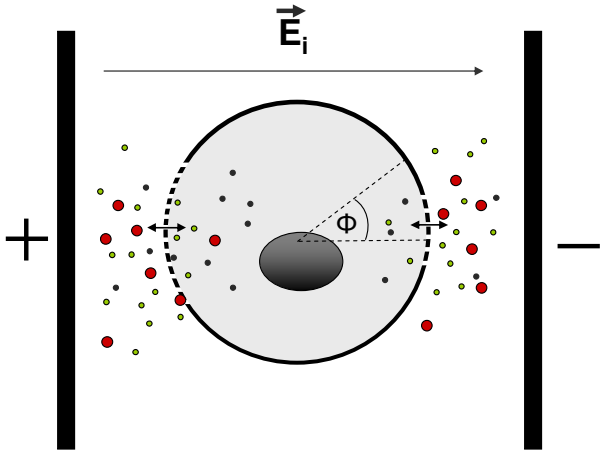

Fig. 3.13: Schematic illustration of a cell during electroporation with a supercritical electric field pulse. The overall fraction of the affected membrane area is controlled by the field strength. The density and size of permeable structures within this defined area is controlled by pulse duration and pulse number. The permeabilized membrane area allows for the exchange of membrane impermeable molecules between the cytoplasm and the extracellular fluid (grey: cytoplasmic molecules; green: small extracellular molecules; red: extracellular macromolecules).

3.2.2.2 Expansion and Stabilization of the Permeabilized State

In a subsequent expansion step the local density and size of membrane defects increase as long as the electric field prevails above the threshold field strength. Whereas the field strength defines the geometry of the permeabilized cell surface (eq. 3.24), the local density of leaky structures within these defined destabilized areas is influenced by the pulse duration (T) as well as by the number (N) of pulses (Kinosita and Tsong, 1977; Rols and Teissié, 1990a; Gabriel and Teissié, 1997). Most studies described in the literature illustrating the effect of T and N make use of DC pulses. Dye loading studies revealed that the degree of membrane permeabilization depends on the pulse duration (T) describing a sigmoidal curve shape (Rols and Teissié, 1998; Neumann et al., 2000). Above the critical pulse duration in the range of the membrane charging time τ (eq. 3.20) the dye loading efficiency increases with pulse duration (T) until saturation can be measured for too extended pulse durations that cause irreversible cell damage. If more than one pulse is used for electroporation, the degree of cell permeabilization, as has been revealed by dye uptake (Rols and Teissié, 1998) or metabolite release (Rols and Teissié, 1990a) studies, rises linearly with increasing pulse number (N). Above a critical number of pulses irreversible permeabilization finally causes cell death. Using a train of pulses, the repetition frequency as well as alterations of the electric field direction can influence the loading efficiency during electroporation (Rols and Teissié, 1998; Tekle et al., 1991). When AC pulses are used for electroporation, pulse durations are typically longer as compared to DC pulses, since the field strength of an AC pulse only exceeds the specific threshold field strength (eq. 3.23) for a small fraction of the entire pulse duration (Wegener et al., 2002).

Permeable structures induced within a defined membrane area (eq. 3.24) in the period of pulse application do not spread over the surface with time, which suggests that membrane proteins

and the underlying cytoskeleton interacting with lipids may be involved in the stabilization of these structures (Rols and Teissié, 1990a).
As soon as the electric field drops below the threshold field strength the degree of membrane perforation decreases (Gabriel and Teissié, 1999). However, the membrane remains in a transient state which is permeable to polar molecules beyond the time frame of electric pulse application (Teissié et al., 2005). This post pulse state of the permeabilized membrane is suggested to be relevant for the considerably delayed exchange of metabolites and extracellular molecules across the membrane.

3.2.2.3 Structural Description of the Permeabilized State

Several theoretical approaches on the basis of model lipid bilayer membranes try to explain the molecular structure and mechanism behind the electric field induced membrane permeabilization. A model most widely accepted and capable of explaining most of the experimental observations and key features of electroporation claims the formation of transient hydrophilic pores (Abidor et al., 1979; Weaver and Powell, 1989; Chen et al., 2006). The external electric field provides the energy to support the formation of initially hydrophobic pores emerging from thermally induced lipid fluctuations. With increasing radii these hydrophobic pores transform to hydrophilic pores which are lined by the polar headgroups of membrane lipids (Fig. 3.14) (Chernomordik and Chizmadzhev, 1989; Weaver and Chizmadzhev, 1996; Neumann et al., 1999).

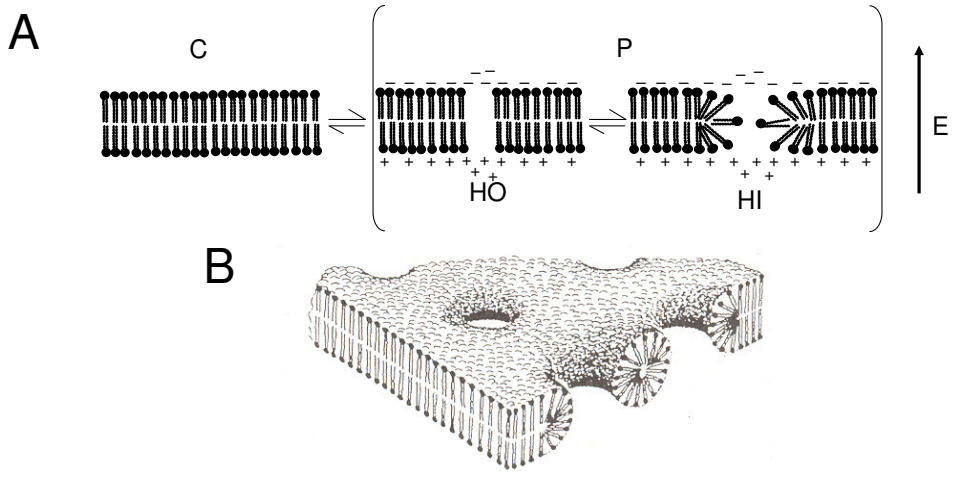

Fig. 3.14: Schematic illustration of a permeabilized membrane according to the hydrophilic pore model**. A:** Molecular transitions of a membrane in a pulsed electric field. Upon exposure to a supercritical permeabilizing electric field (*E*) interfacial polarization of the membrane (+, –) induces a change from its closed impermeable state (C) to a permeabilized state (P). Initially hydrophobic membrane defects (HO) rearrange their lipid structure forming hydrophilic pores (HI) to minimize contact of hydrophobic lipid tails with water (adapted from Neumann et al., 1999). **B:** Schematic view of a lipid bilayer membrane with several hydrophilic pores (Weaver and Powell, 1989).

As long as an external electric field is present pore formation and expansion is favored (Weaver and Powell, 1989). However, pore expansion is slowed down as soon as a conduction of ions across pores takes place as this lowers the transmembrane potential difference. The membrane stabilizes to an equilibrium state with a certain pore density and

size distribution when the external field is turned off (Joshi et al., 2002). The size of the cylindrical water filled pores is linked to the superimposed membrane potential as well as to the balance between the line tension of the pores and the membrane surface tension. Pore diameters were calculated to be in the range of ~ 0.39 – 5.8 nm and associated pore densities accounted for 0.01 – 2 % with respect to the total membrane area (Rols et al., 2000).

Supporting the pore theory, several molecular dynamics simulations were able to show the formation of pores in ideal model membranes exposed to electric fields (Tarek, 2005; Tielemann, 2004). In these theoretical simulations, which needed a significantly higher field strength for electroporation than experimentally required (Teissié et al., 2005), pore formation was initiated by a finger-like penetration of the hydrophobic membrane interior by water molecules.

To date, the existence of electropores could not be proved experimentally (Teissié et al., 2005) and the explicit molecular ultrastructure of membrane transitions remains unclear. There are only a few structural studies on membranes in electric fields which do not necessarily support the pore theory (Teissié et al., 2005). Existing electron microscopic images of electropermeabilized erythrocyte membranes showing crater-like structures (Chang and Reese, 1990) are critically discussed because these results were obtained under strong hypoosmotic conditions (Weaver and Chidzmadzhev, 1996; Teissié et al., 2005; Rols, 2008). P^{31}-NMR studies (Stulen, 1981; Lopez et al., 1988) revealed significant field induced reorientation of the membrane lipid polar headgroups that caused a perturbation in the membrane-solution interfacial region (Teissié, 2007). However, no alterations in the structure of the fatty acid hydrophobic core, as claimed by the hydrophilic pore theory, could be detected (Stulen, 1981).

Various alternative approaches exist trying to explain the enhanced membrane permeability independently from hydrophilic pore formation (Teissié et al., 2005; Chen et al., 2006). An electromechanical approach predicts the electric field induced compression of the membrane till dielectric breakdown (Crowely, 1973). This theory is, however, in conflict with essential experimental findings like the stochastic, reversible character of membrane breakdown in electric fields and its dependence on pulse duration (Weaver and Chizmadzhev, 1996). Other authors proposed that dynamic membrane properties and mismatches between different lipid domains or between lipids and transmembrane proteins might support the formation of leaky defect sites (Teissié et al., 2005; Teissié, 2007). Enhanced mobility of lipids and flip flops in electropermeabilized membranes was indeed found to resemble the phenomena occurring at thermal phase transitions of membranes, which were described to increase their permeability towards hydrophilic molecules (Haest et al., 1997; Teissié et al., 2005).

Besides the common opinion that permeabilization is initiated in the lipid matrix, prevailing models do only insufficiently consider the influence of membrane proteins or the submembraneous cytoskeletal network on formation and stabilization of the permeable state (Sung and Park, 1997). The high complexity of biological membranes is one reason why current models cannot explain all experimental results. Since the exact molecular structure of the permeabilized membrane is still unclear, the term electropermeabilization instead of electroporation is preferred by many researches of this field (Teissié et al., 2005; Rols, 2006).

3.2.2.4 Exchange of Hydrophilic Compounds across the Permeabilized Membrane

The electroporated membrane is permeable for exogenous molecules in the time frame ranging from dielectric membrane breakdown till complete membrane resealing (chapter 3.2.2.5) (Gehl, 2003). The total time frame in which the membrane is open to polar molecules is discussed to be in the range of minutes (Rols and Teissié, 1990a; Gabriel and Tessié, 1997, 99; Bier et al., 1999) or just a few seconds (Hartmann, 2003; Ghosh et al., 1993).

The entire time frame of the permeable state can be subdivided into two phases (Puc et al., 2003). The first phase is limited to the time frame of pulse application, where the pores reach their maximal size and density. During the application of the pulse an exchange of molecules across the membrane takes place via diffusion, electrophoresis or electroosmosis, with their individual contributions depending on pulse length and amplitude as well as on the properties of the permeating molecule (Puc et al., 2003).

As soon as the electric field drops below the threshold field strength the degree of membrane perforation decreases (Gabriel and Teissié, 1999). In this second post-pulse phase of multistep stabilization and resealing an exchange of molecules is reported to be only possible by diffusion (Rols and Teissié, 1998).

Based on these observations two kinds of permeable states can be distinguished allowing individual transfer mechanisms for small molecules or macromolecules (Zaharoff et al., 2008).

Small Molecules

As long as the membrane is in the permeabilized state, it allows diffusion of small molecules and ions up to a molecular weight of about 4 kDa independent of their chemical nature. Small molecules and ions permeate across the cell membrane for a time much longer than the electric pulse itself and are able to enter the cell even when they are added after electric pulse application (Golzio et al., 2004; Rols et al., 2000). Exchange of small molecules across the membrane governed by their concentration gradient can be quantified by Fick's law for free diffusion in the time frame immediately after electropermeabilization (eq. 3.25). The flow F_S at time t of a diffusing molecule S across the permeabilized membrane is dependent on the critical field strength (E_{perm}), the pulse duration (T) and the pulse number (N) (Rols and Teissié, 1990a).

$$F_S(t) = \frac{P_s \cdot x(N,T) \cdot A}{2} \cdot (1 - E_{perm}) \cdot \Delta S \cdot e^{-k(N,T)t} \qquad \textbf{3.25}$$

P_s is the permeability coefficient of the molecule S across the membrane. The function x represents the probability of permeabilization ($0 < x < 1$) and depends on the pulse number N and pulse duration T. The concentration gradient across the permeabilized membrane with the surface area A is described by ΔS. Diffusion of molecules across the membrane is influenced by the resealing process, which is characterized by the time constant k, also depending on N

and *T*. Equation 3.25 is only valid under the assumption that the resting potential difference is zero and the molecular species *S* is uncharged. In principle, small molecules can enter a cell at both permeabilized cell poles, but depending on a molecule's charge and electric field direction, uptake has also been observed to occur only at one side of the cell (Gabriel and Teissié, 1999). Electrophoretic forces and charge repulsion effects of charged molecules can be considered by additional implementation of electrodynamic terms into the above mentioned equation (Rols et al., 2000). Due to the interactions of the permeating molecule with membrane lipids the diffusion coefficient across the membrane might be lower than observed for the free molecule in solution, such that rather facilitated than free diffusion occurs (Neumann et al., 1998). Increasing molecule size and interactions with the perforated membrane will hamper free diffusion.

Macromolecules

In contrast to small molecules, macromolecules are transferred to the cytoplasm only if they are present during electropulsing (Rols and Teissié, 1998). FITC-dextrans and proteins for example, added within minutes following the electropermeabilizing pulse, did not exist freely in the cytoplasm but were incorporated into intracellular vesicles which might indicate an endocytotic mechanism (Glogauer et al., 1993; Rols et al., 1995). In analogy, efficient gene transfer can only be detected when electropermeabilization takes place in presence of nucleic acids (Wolf et al., 1994; Golzio et al., 2002; Rols, 2008).

An introduction of larger molecules is therefore thought to happen through other mechanisms than free diffusion. However, efficient membrane permeabilization is still an essential prerequisite. A sufficiently long pulse duration at moderate field strengths was reported to be a crucial parameter for efficient transfer of macromolecules across a permeabilized membrane (Rols and Teissié, 1998; Zaharoff et al., 2008). As an estimated pore size of maximal 5.8 nm for an individual pore does not allow the transfer of macromolecules via single membrane defects, Sugar et al. (1987) proposed that electric pulses with appropriate pulse duration may enable the coalescence and fusion of individual pores to form membrane defects large enough for the passage of macromolecules.

Uptake of high molecular FITC-dextran (2 MDa, Ø 52 nm) via membrane pores was suggested to be mediated by convection occurring due to colloid- and electroosmotic cell swelling or electrodeformation (Zaharoff et al., 2008). Whereas the mechanism of protein transfer remains quite unclear (Morgan and Day, 1995), the mechanism behind electric field mediated uptake of nucleic acids into cells has been under intense investigation. DNA molecules seem to enter the cell via a multistep mechanism including electrophoretic accumulation on the cell surface and subsequent direct interactions with the destabilized membrane before the molecule is finally released to the cytoplasm with a considerable delay (Faurie et al., 2010). Direct interactions of accumulating DNA on the permeabilized membrane lead to the formation of stable, long-lived membrane complexes that aggregate to microdomains with a size ranging from 0.1 – 0.5 µm (Golzio et al., 2002, 2004; Phez et al., 2005; Rols, 2006). Using an unipolar DC pulse the DNA accumulates only at the permeable cell poles facing the cathode, whereas bipolar pulses lead to interactions with both cell poles.

Efficient gene transfer is generally obtained using millisecond pulses, ensuring efficient electrophoretic DNA accumulation and insertion (Rols, 2008; Escoffre et al., 2009). During the electric pulse DNA is trapped at the plasma membrane, whereas the final DNA uptake into the cytoplasm occurs in the minutes subsequent to the pulse (Golzio et al., 2002).
Although the translocation mechanism is not fully elucidated yet, DNA transfer across membrane defects is suggested to be driven by entropic and diffusion forces (de Gennes, 1999; Golzio et al., 2002) or an uptake process similar to electrostimulated endocytosis (Angelova et al., 1999; Satkauskas et al., 2001). The mechanism of further intracellular migration of DNA and its passage across the nuclear pore complex into the nucleus, where transcription and insertion into the genome take place, remain insufficiently understood (Rols, 2008).

3.2.2.5 Membrane Resealing and Memory Effects

Using well-defined electropermeabilization conditions, membrane integrity fully recovers after pulsing. The lifetime of membrane permeability is influenced by electric pulse parameters as pulse duration and pulse number but is independent from field strength (Rols and Teissié, 1990a, 1998).
In planar lipid membranes electric field induced pores or defects are resealed within 2 – 20 µs (Benz and Zimmermann, 1981) whereas resealing of cell membranes is observed to take several seconds to minutes (Sowers and Lieber 1986; Rols and Teissié, 1990a; Bier et al., 1999) up to 1 h (Zimmermann and Vienken, 1982). Dye loading experiments, where the dye (Serva blue G, M_w = 854 g/mol) was added to a cell suspension at different time points after pulsation, revealed the presence of at least two different recovery processes with individual time constants (Neumann et al., 1998). During the initial, fast resealing process the permeability for the dye decreased about 50 % within one minute. Only after a second, slower resealing process (~ 15 min) cells were impermeable to the probe under study.
Membrane resealing is dependent on temperature as well as on lipid composition of the membrane (Benz and Zimmermann, 1981). In addition, ion strength and osmotic pressure affect resealing (Rols and Teissié, 1989, 1990b). The closure process of membrane defects was shown to be controlled by protein reorganizations (Golzio et al., 2004) where especially the functionality of cytoskeletal proteins seems to play an essential role (Rols and Teissié, 1992; Teissié and Rols, 1994). The nutritional state of cells is regarded as another factor controlling resealing behavior (Rols et al., 1998b).

After resealing the cell re-attains its impermeability towards hydrophilic molecules what preserves the cell from lysis (Kinosita and Tsong, 1977; Zimmermann et al., 1981). However, the cell may be affected to such an extent that some cellular alterations can not be repaired, leading to cell death on the long term (Gabriel and Teissié, 1995; Förster and Neumann, 1989). Loss of membrane lipid bilayer asymmetry (Haest et al., 1997) or altered protein activities induced by electroconformational changes (Chen and Lee, 1994 a, b) may influence

cell survival as well. It has been observed that it takes several hours till the original, asymmetrical lipid distribution is re-attained (Dressler et al., 1983; Haest et al., 1997). After electro-permeabilization cells were observed to show enhanced endocytosis and macropinocytosis activities (Rols et al., 1995; Glogauer et al., 1993). During the resealing process reactive oxygen species (ROS) are produced in the permeabilized part of the membrane which are known to trigger these kinds of long-term effects (Gabriel and Teissié, 1994; Escande-Geraud et al., 1988). In total, cells were reported to be quite vulnerable in the first minutes (~ 15 min) after electropulsation (Gehl et al., 1998).
Too invasive pulses will dramatically affect cell viability and integrity due to excessive leakage of cytoplasmic contents (Neumann and Rosenheck, 1972) or irreversible membrane rupture (Golzio et al., 1998).

3.2.3 Electrofusion

The electropermeabilized cell membrane has another unique property: its fusogenity (Zimmermann, 1982). If the membranes of two or more cells in close contact are destabilized by an electric pulse, their adjacent membranes do not reseal independently in the zone of contact but tend to intermix lipids. Thereby hybrid or giant cells are created which share a common cytoplasm (Senda et al., 1979; Teissié et al., 1982). Using finely tuned pulse parameters electric field induced cell fusion can be achieved with a multitude of cell species including bacteria, fungi, plant and animal cells (Chang et al., 1992).

3.2.3.1 Experimental Strategies to Induce Cell Fusion

Cell fusion is a rare event since Brownian motion, the negative membrane surface charge and hydration forces make adjacent membranes to repel each other. A basic requirement for cell fusion is, however, a close contact between the plasma membranes. Chemical and biological fusion methods use the agglutinating properties of fusogenic chemicals like PEG or inactivated viruses (Dimitrov, 1995). These agents simultaneously mediate cell contact and disturb the membrane structure in a way that fusion is triggered.
Electric field mediated fusion of cells, commonly termed electrofusion (Teissié, 1988), is one of the most versatile methods to trigger intermembrane mixing. While an electric field pulse induces membrane destabilization, the necessary close membrane contact has to be achieved by various biological, chemical, mechanical or physical methods (Tab. 3.4). A prominent, non-invasive and easy to perform method in combination with electric field induced fusion of suspended cells is dielectrophoresis, the alignment of cells in a non-invasive inhomogeneous alternating electric field (Pohl and Crane, 1971). Electrofusion of adherent cells without adding agglutinating agents mostly relies on naturally occurring contact inhibition within a cell layer (Blangero et al., 1989).
Like electroporation efficiency also the yield of cell fusion was found to be dependent on pulse strength and duration. Similar pulsing parameters as required for electroporation are

necessary to induce cell fusion (Dimitrov, 1995). According to the classical protocol cells are first brought in close contact and secondly subjected to a destabilizing electric pulse, which is referred to as the "contact first" approach (Fig. 3.15 A). The "pulse first" concept (Fig. 3.15 B) is based on the existence of long-lived fusogenic states and transient permeable structures in the cell membrane after electroporation (Sowers and Lieber, 1986; Teissié and Rols, 1986; Teissié and Ramos, 1998).

Tab. 3.4: Methods to create close membrane contact for electrofusion of cells.

Biological	natural contact of adherent cells	Blangero and Teissié, 1983 ; Blangero et al., 1989 Teissié et al., 1982
	agglutinating proteins and viruses	Xiao et al., 1996 Yu and Berg, 1998
	specific interaction	Lo et al., 1984 Wojchowski and Sytkowski, 1986
Chemical	agglutinating agents	Stoicheva and Hui, 1994 Zhang, 1994
Mechanical	centrifugation	Teissié and Rols, 1986
	micromanipulation	Senda et al., 1979 Strömberg et al., 2000
Physical	dielectrophoresis	Crane and Pohl, 1971 Zimmermann and Vienken, 1982
	sonic field	Vienken et al., 1983
	magnetic field	Kramer et al., 1984

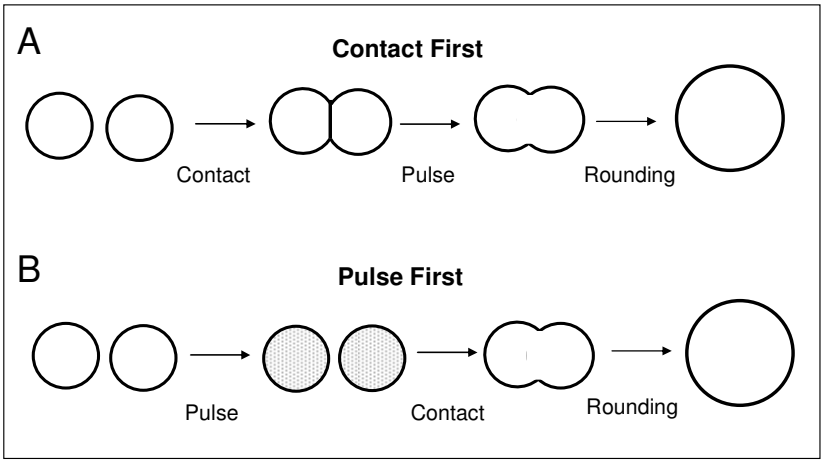

Fig. 3.15: Contact first (**A**) and pulse first (**B**) approach of electrofusion (adapted from Ramos and Teissié, 2000).

Several groups have shown that it is possible to fuse cells after electropermeabilization, if close cell contacts were created by mild mechanical conditions like gentle centrifugation (Sowers, 1984; Sowers and Lieber, 1986; Teissié and Rols, 1986). However, for the pulse first approach fusion efficiency was found to be lower as compared to the contact first protocol and multiple pulses were required (Sowers and Lieber, 1986; Teissié and Rols, 1986). The lifetime of the fusogenic state is assumed to be in the range of seconds to minutes, but its nature is still unclear (Ramos and Teissié, 2000; Dimitrov, 1995).

3.2.3.2 Proposed Mechanism for Electrofusion of Cells

Electrofusion is considered to follow a multi-step mechanism: (1) formation of tight membrane contact, (2) electropermeabilization of the membrane and (3) formation of a series of fusion stages (Sugar et al., 1987).

Cells are first brought in contact by any of the above mentioned techniques like dielectrophoresis of suspended cells (Tab. 3.4). Membrane defects are generated in the two adjacent cell membranes by electroporation (Zimmermann and Vienken, 1982). Electric field induced dielectric and ionic-electric polarization effects at the cell membrane are moreover thought to enforce an approximation of the adjoining membranes from initially ~ 25 nm to ~ 5 nm (Stenger and Hui, 1989). The additional attractive forces between opposing membranes are suggested to compensate for the electrostatic repulsion of the usually negatively charged membrane surfaces. Actually, weakened membrane hydration forces were identified in electrically permeabilized membranes by P^{31}-NMR studies (Ramos and Teissié, 2000). On the basis of electron microscopic images it was proposed that these small patches of tight membrane contact without repulsive hydration boundaries are preferentially established in protein-free lipid domains in the cell-cell contact zone (Stenger and Hui, 1989).

The structural molecular organization within the electrically perturbed membranes remains unclear. In a model provided by Zimmermann and Vienken (1982) lipids within electrically induced defect sites are thought to be randomly orientated (Fig. 3.16 A). Other models, however, suggested a pair of interacting hydrophilic pores (Dimitrov and Jain, 1984) or pore independent mechanisms (Melikyan and Chernomordik, 1989). With high probability double membrane defect sites occur at the same spot as they are assumed to be energetically favourable compared to two individual single membrane defects (Sugar et al., 1987). For fusion to take place both membranes have to be permeabilized and a critical density of defect sites is necessary (Teissié and Ramos, 1998). During the post pulse resealing process lipids tend to reorient and form bridges between adjacent membranes (Fig. 3.16 B) (Zimmermann and Vienken, 1982). If a bridging process dominates over normal resealing of individual membranes, open pores between neighboring cells are created establishing first intercytoplasmic contact between cells (Fig. 3.16 C).

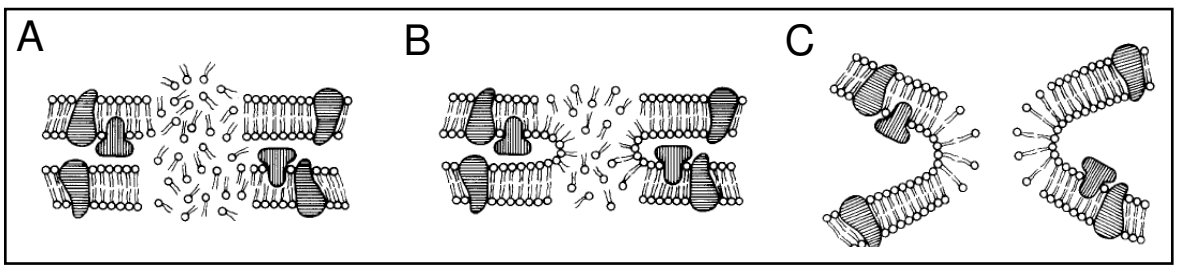

Fig. 3.16: Schematic model for electric field induced membrane fusion (Zimmermann and Vienken, 1982). Electric breakdown of two membranes in close proximity leads to a local disturbance of the lipid bilayer structure (**A**). During the resealing process contact between both membranes may be formed when lipids reorganize in a way that the outer membrane leaflets are connected (**B**). Membrane tension and post-pulse water backflow favor the formation of a hydrophilic fusion pore and lateral expansion of the cytoplasma bridge (**C**).

The membrane tension within the strong membrane curvature at fusion sites is energetically unfavorable and drives pore expansion to complete fusion. However, it is not clarified if single pore fusion is sufficient to cause complete cell fusion. Electron microscopy of freeze-fracture membranes revealed macroscopic cracks and loops at the cell surface (Escande-Geraud et al., 1988; Stenger and Hui, 1986, 1989).
Sugar et al. (1987) proposed that these macroscopic membrane defects are the actual origin of membrane fusion. Due to lateral diffusion of lipids, initial microscopic membrane defect sites (Fig. 3.17 A, a) might migrate within the plane of the membrane contact area and coalesce to form small cracks and loops (Fig. 3.17 A, b). Above a supercritical pore density long-range coalescence of interacting defect sites of both membranes is supposed to result in a closed chain of fused pores, termed the percolation line (Fig. 3.17 A, c). Double membrane cracks finally create a hole in the membrane contact area (Fig. 3.17 B). If membrane areas are surrounded by a continuous percolation line membrane patches may even detach from the system and form inside-out vesicles leaving a macroscopic hole (Sowers, 1983).

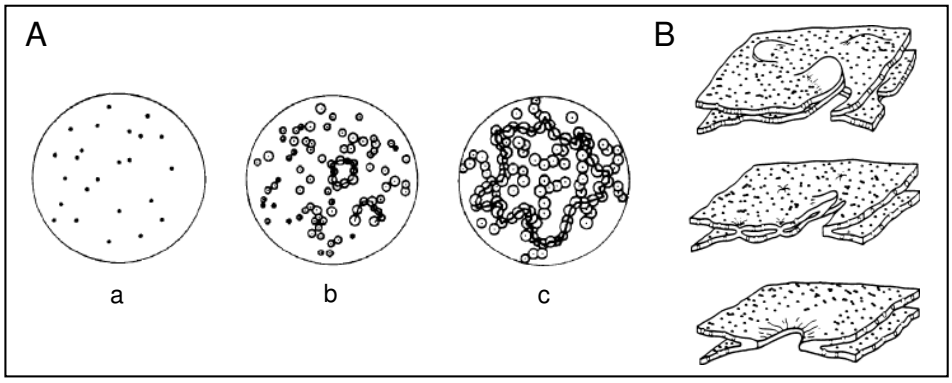

Fig. 3.17: Schematic model for lateral pore-pore interactions of electroporated double membranes leading to macroscopic cracks and loops. **A:** Pore-pore interactions as a function of pore density in a permeabilized membrane area (Sugar et al., 1987): a: non-interacting pores (dots) at low pore density in the beginning of electric field application; b: short-range pore coalescence forming small loops at a subcritical pore density with increasing pore number and pore size; c: long-range pore interactions (percolation) at a supercritical pore density, forming macroscopic loops that might detach from the system. **B:** Ultrastructural model where cracks and loops lead to membrane fusion (Stenger and Hui, 1986).

After the electric field has been turned off small defect sites, pores and loops reseal. Water can flow back to the intermembrane space, what increases the membrane tension and forces membrane-membrane separation in the contact zone. Consequently, the edges of larger cracks and holes round up and merge, forming an intercellular cytoplasm bridge (Zimmermann and Vienken, 1982; Stenger and Hui, 1986; Sowers, 1985).
A delay between the electric pulse and the beginning of the fusion process has been observed (Dimitrov and Sowers, 1990), leading to the assumption of a two step process for membrane fusion (Ramos and Teissié, 2000). The first and significantly faster step including initial membrane merging within seconds to minutes (Stenger and Hui, 1989; 10 – 60 s) is followed by a slow extension step of the cytoplasmic bridge in the time regime of an hour. The second step including cytoskeletal reorganization and a clustering of nuclei only takes place when cell viability is preserved (Blangero et al., 1989).

4 Materials and Methods

4.1 Cell Culture Techniques

4.1.1 Cell Lines

This work includes experiments with the adherently growing epithelial-like cell line NRK-52E (normal rat kidney, strain 52E), Hep G2, a human hepatocellular carcinoma cell line, and CHO (chinese hamster ovary) cells as well as the fibroblastoid cell lines HEK-293 (human embryonic kidney) and NIH-3T3 embryonic cells. All wild type cell lines listed in Tab. 4.1 were obtained from the *Deutsche Sammlung von Mikroorganismen und Zellkulturen* (DSMZ, Braunschweig).

Tab. 4.1: Anchorage-dependent cell lines used in this work. Information about origin and morphology was adopted from the DSMZ (http://www.dsmz.de).

Cell Line	Origin	DSMZ No.	Morphology	Literature
NRK-52E	normal rat kidney clone 52E	ACC 199	epithelial-like	De Larco and Todaro, 1978
HEK-293	human embryonic kidney	ACC 305	fibroblastoid	Graham et al., 1977
Hep G2	human hepatocellular carcinoma	ACC 180	epithelial-like	Aden et al., 1979
CHO-dhfr [–]	chinese hamster ovary dehydrofolate reductase negative	ACC 126	epithelial-like	Puck, 1957 Urlaub and Chasin, 1980
NIH-3T3	mouse embryo	ACC 59	fibroblastoid	Jainchill et al., 1969

4.1.2 General Culture Conditions

All cell culture work was performed under sterile conditions in a flow hood (*LaminAir*®, Holten, Gydevang, Denmark or *HERAsafe*®, Thermo Scientific, Munich) following common cell culture procedures (Freshney, 2005). Buffers and solutions were autoclaved at 120 °C for 20 min (DX-45, Systec, Wettenberg) or passed through a sterile filter with a pore diameter of 0.2 µm, if not already purchased as sterile liquid. Glassware, pipette tips as well as 0.5, 1.5 and 2 ml tubes were autoclaved or sterilized. For routine culture cell lines were grown on the bottom of sterile polystyrene culture flasks with a growth area of 12.5 or 25 cm^2 in 2 or 4 ml of culture medium (Biochrom, Berlin), respectively. Cells were kept in an ordinary cell

culture incubator (Heraeus BB15 function line, Thermo Scientific, Munich) at 37 °C in an atmosphere with 5 % CO_2 and 95 % relative humidity.

NRK-52E culture medium	Dulbecco's Modified Eagle's Medium (DMEM) with 3.7 g/l $NaHCO_3$ and 4.5 g/l D-glucose + 10 % (v/v) fetal calf serum (FCS) + 100 µg/ml penicillin + 100 µg/ml streptomycin + 2 mM L-glutamine
HEK-293 culture medium	DMEM with 3.7 g/l $NaHCO_3$ and 4.5 g/l D-glucose + 10 % (v/v) FCS + 100 µg/ml penicillin + 100 µg/ml streptomycin + 2 mM L-glutamine
Hep G2 culture medium	RPMI 1640 with 2 g/l $NaHCO_3$ + 10 % (v/v) FCS + 100 µg/ml penicillin + 100 µg/ml streptomycin + 2 mM L-glutamine
CHO-dhfr [–] culture medium	Alpha Medium with 1.176 g/l $NaHCO_3$ + 10 % (v/v) FCS + 100 µg/ml penicillin + 100 µg/ml streptomycin + 2 mM L-glutamine
NIH-3T3 culture medium	DMEM with 3.7 g/l $NaHCO_3$ and 4.5 g/l D-glucose + 10 % (v/v) FCS + 100 µg/ml penicillin + 100 µg/ml streptomycin + 4 mM L-glutamine

4.1.3 Subculturing

As soon as cell layers reached a certain degree of confluence (HEK-293, NIH-3T3: ~ 70 %; CHO, Hep G2: ~ 80 %; NRK: 100 %) cells were transferred to new culture flasks following a similar subculturing protocol (Freshney, 2005) (Tab. 4.2).
All media and buffer solutions were pre-warmed in a water bath (GFL, Julabo, Seelbach) to 37 °C prior to use. First, cell layers were washed twice with phosphate buffered saline (PBS^{--} without Ca^{2+} and Mg^{2+}). Cell lines with strong cell-cell and cell-substrate contacts were subsequently incubated with a 1 mM EDTA (ethylenediaminetetraacetic acid) solution in PBS^{--} for 5 – 10 min at 37 °C (NRK, Hep G2, CHO). Cells were detached from the substrate by incubation in a 0.25 % (w/v) solution of trypsin in PBS^{--} supplemented with 1 mM EDTA for 1 – 10 min at 37 °C (Tab. 4.2). Cell detachment was assisted by gentle tapping of the culture flasks to a solid surface. In order to inactivate trypsin activity after cell detachment, an excess of the respective cell culture medium was added to the cell suspension. Cells were collected by centrifugation at 110 × g for 10 min at room temperature (RT) and resuspended in an appropriate amount of pre-warmed cell culture medium. A dilution ratio of 1:20 with respect to the surface area of the former culture substrate was chosen for seeding cells to new culture flasks. Subculturing was performed once or twice a week depending on the cell type (Tab. 4.2). The culture medium was exchanged every 3 – 4 days or 24 h before starting an experiment. Cells were subcultured up to passage numbers of ~ 50.
For experiments cells were seeded upon appropriate substrates (ECIS electrode arrays, well-plates, glass slides) and maintained in the incubator until use. If defined cell numbers were necessary, the cells were counted by using an ordinary haemacytometer (*Bürker*) and the suspension was diluted to the required concentration before seeding the cells to the respective substrate.

Tab. 4.2: Subculturing data for adherent cell lines used in this study.

Cell Line	Incubation Time with EDTA [min]	Incubation Time with Trypsin [min]	Time Span between Consecutive Subculturing [d]
NRK-52E	8 – 10	8 – 10	7
HEK-293	–	1	3 – 4
Hep G2	3 – 5	3 – 5	5 – 6
CHO	3 – 5	3 – 5	4 – 5
NIH-3T3	–	1 – 2	3 – 4

PBS^{--} 140 mM NaCl
2.7 mM KCl
8.1 mM Na_2HPO_4
1.5 mM KH_2PO_4
in deionized water

EDTA solution	1 mM EDTA in PBS^{--}
Trypsin / EDTA	0.25 % (w/v) trypsin 1 mM EDTA in PBS^{--}

4.1.4 Cryopreservation

For cryopreservation of adherently growing cell lines (Freshney, 2005), cells were detached from the bottom of the culture flask following standard subculturing protocols (chapter 4.1.3). After collection by centrifugation cells were suspended in a cryoprotective solution consisting of FCS and 10 % (v/v) DMSO (dimethylsulfoxide). Aliquots of about 1.5 ml cell suspension were frozen in cryovials using a standard two-step process with a first phase of slow cooling at a rate of 1 °C/min in an isopropanol bath down to – 70 °C and a subsequent transfer to liquid nitrogen for final storage.
For recultivation of frozen cells the cryovials were first kept at – 20 °C for about 1 h and subsequently the cells were thawn rapidly in a water bath at 37 °C. As soon as only a small ice core was left, the cell suspension was transferred to a sterile centrifugation tube and diluted by dropwise addition of 10 ml of pre-warmed culture medium. Cells were collected by centrifugation at 110 × g for 10 min at RT. Afterwards, the DMSO containing medium was discarded and cells were resuspended in fresh culture medium. Cells were seeded to culture flasks at different ratios with respect to their former growth area (1:2, 1:4, 1:8). Cell culture medium was exchanged 24 h after thawing. Cells were further cultivated by following the subculturing protocol described above (chapter 4.1.3).

Cryoprotective solution	90 % (v/v) FCS 10 % (v/v) DMSO

4.1.5 Coating of Culture Substrates

HEK-293 cells do not form strong cell-substrate contacts. With an increasing degree of confluence, cell layers become even more susceptible to mechanical stress or temperature fluctuations. Thus, to improve the attachment, spreading and growth of this cell type on ECIS electrode arrays (chapter 4.3), the gold-film electrodes were pre-coated with cross-linked gelatin (Ai et al., 2002).
For this purpose all wells of the ECIS electrode array were incubated with 300 µl of a sterile solution of 0.5 % (w/v) gelatin in water for 1.5 – 2 h at RT. After removal of the gelatin solution the gelatin layer was cross-linked by incubation with 2.5 % (v/v) glutaraldehyde for 10 min at RT in order to provide a mechanically stable protein layer on the substrate surface. Excess of cytotoxic glutaraldehyde was removed by washing the substrates thoroughly ~ 10 × with deionized water. The coated substrates were kept under deionized water until use.

4.1.6 Determination of Solution Osmolality

The osmolality in mOsmol/kg is a measure for the amount of osmotically active solutes in an aqueous solution. A defined osmolality of solutions used in cell culture is important since notable osmotic imbalance between the cytosol of a cell and the surrounding medium causes unphysiological cell swelling or shrinkage (Macknight, 1991; McManus et al., 1995). Osmolalities between 260 and 320 mOsmol/kg are acceptable for most cells (Freshney, 2005). Osmolalities of various buffer solutions supplemented with bioactive compounds or other solutes were measured using the cryoscopic osmometer *Osmomat* 030 (Gonotech, Berlin). It determines the osmolality of a solution by measuring the depression of the freezing point of the sample compared to the freezing point of pure water.

4.2 Molecular Biological Techniques

Applied molecular biological methods were based on standard procedures and protocols described in *"Der Experimentator Molekularbiologie / Genomics"* (Mülhardt, 2006) and *"Gentechnische Methoden"* (Schrimpf, 2002).

4.2.1 Cultivation of *E. coli*

Escherichia coli (*E. coli*) strains *ElectroMAX™ DH10B™* (Durfee et al., 2008) (Invitrogen, Darmstadt) and *One Shot® TOP10F'* (Invitrogen, Darmstadt) were used for amplification of plasmid DNA such as pCH1 and pEYFP-Actin (Appendix *A*4) which were further used for mammalian cell transfection (chapter 4.2.9) or in electroporation experiments (chapter 4.3.3.4). *E. coli* stocks carrying the corresponding plasmid (Tab. 4.3) were stored at – 70 °C in 30 % glycerine in LB-medium (lysogeny broth) (Bertani, 1951). For recultivation about 10 – 20 µl of the thawn *E. coli* suspension were transferred to 3 ml LB-medium.

LB-medium	1 % (w/v) peptone
	0.5 % (w/v) yeast extract
	1 % (w/v) NaCl
	pH 7.0

For selective growth of *E. coli*, sterile LB-medium was supplemented with a specific antibiotic depending on the resistance mediating gene provided on the plasmid (Tab. 4.3, Appendix *A*4). After the first recultivation step at 180 rpm and 37 °C for 5 – 8 h, 100 – 500 µl of the pre-culture suspension were used to inoculate 100 ml of antibiotic supplemented LB-medium for a second amplification step. The bacterial culture was incubated over night at 180 rpm and 37 °C.
Bacterial growth was quantified by determining the optical density of the culture broth at 600 nm (OD_{600}). For plasmid isolation *E. coli* cultures with an OD_{600} of ~ 1 were used.

Tab. 4.3: Antibiotics for selective growth of *E. coli* strains carrying the plasmid indicated in the table. The plasmids pEGFP-N1 and pECFP-N1 were amplified and kindly provided by S. Arndt and T. Schmedt, respectively.

***E. coli* Strain**	**Antibiotic**	**Plasmid**	**Applied Concentration [µg/ml]**
E. coli DH10B / pCH1	Ampicillin	pCH1	50
E. coli DH10B / pEGFP-N1	Kanamycin	pEGFP-N1	50
E. coli TOP10F' / pEYFP-Actin	Kanamycin	pEYFP-Actin	50
E. coli TOP10F' / pECFP-N1	Kanamycin	pECFP-N1	50

4.2.2 Plasmid Isolation from *E. coli*

Isolation of plasmid DNA from *E. coli* was carried out using the *QIAGEN Plasmid Maxi Kit* (QIAGEN, Hilden) following the manufacturer's instructions. Different to the supplier's protocol the co-precipitate of SDS (sodium dodecyl sulfate), proteins and cell debris was removed by filtration through a paper filter (MN 640 w, 110 mm pore diameter, Macherey-Nagel) before adding the plasmid solution to the anion exchange column (*QIAGEN Tip*)[1]. After elution from the column DNA was precipitated by addition of 10.5 ml isopropyl alcohol and subsequent gentle mixing. The DNA was pelleted by centrifugation (15 000 × g, 4 °C, 30 min), washed with 70 % (v/v) ethanol and, after an additional centrifugation step (15 000 × g, 4 °C, 30 min), DNA was air dried to remove excess ethanol. Finally, plasmid DNA was dissolved in 200 – 500 µl ddH_2O (double deionized water), its concentration was determined photometrically (chapter 4.2.3) and the plasmid solution was stored at – 20 °C.

4.2.3 Determination of DNA Concentration

Determination of plasmid DNA concentration was carried out by UV/VIS-absorbance measurement at a wavelength of 260 nm (E_{260}), where purin- and pyrimidin-bases of nucleic acids absorb. DNA solutions were diluted in destilled water by a factor of 1:100 – 1:400 in order to ensure that absorbance values fall in the linear range between 0.1 and 1.0. Diluted samples were measured in a quartz cuvette with a chamber thickness of 1 cm. The DNA concentration can be calculated from the absorption of the solution according to the Beer-Lambert law (Tinoco et al., 2002). Additionally, the absorbance at a wavelength of 280 nm (E_{280}) was measured, which is the characteristic absorbance maximum of proteins. The ratio E_{260}/E_{280} provides the purity of the DNA sample. The ratio of sufficiently pure DNA samples should be in the range of 1.8 – 2.0. If this was not the case, the DNA was purified by phenol-chloroform extraction (chapter 4.2.7).

[1] Simple centrifugation is often not sufficient for complete removal of solid components. However, *QIA*filter pores are easily blocked by cell debris so that the DNA solution can not be filtered completely.

4.2.4 DNA Fragmentation by Restriction Enzyme Digestion

Restriction enzymes were applied to obtain a linear DNA fragment encoding EGFP from the plasmid DNA pCH1. By digestion of the plasmid pCH1 (Appendix *A*4) with the restriction endonucleases *Bgl*II and *Dra*III a 2278 bp EGFP fragment was generated. In Tab. 4.4 the composition of a reaction batch for digestion of pCH1 is presented.

Tab. 4.4: Composition of the reaction mixture to obtain the 2278 bp EGFP fragment from pCH1. Restriction endonucleases and reaction buffer were purchased from *New England Biolabs* (NEB, Beverly / MA, USA).

Component	Volume [µl]
pCH1 (~ 1 µg/µl)	5
10 × buffer	3
*Bgl*II (10 000 U/ml)	3
*Dra*III (20 000 U/ml)	1.5
ddH_2O	ad 30

Restriction batches were incubated for at least 2 h at 37 °C. Afterwards, the EGFP fragment was isolated from remaining fragments by gel electrophoresis (chapter 4.2.5) and subsequent gel extraction (chapter 4.2.6).

4.2.5 Agarose Gel Electrophoresis

DNA fragments were separated by electrophoresis in agarose gels of 1 % (w/v) agarose in 1 × TAE (Tris-acetate-EDTA) buffer before the fragment of interest was isolated by gel extraction. Agarose was dissolved in 1 × TAE-buffer by warming up the suspension in a microwave. The agarose solution was poured into a gel chamber after being cooled down to about 60 °C. The gel chamber was equipped with a comb creating one broad sample pocket for loading with ~ 15 µg of the DNA sample and one small pocket for loading with a DNA size marker. After complete gelation of the agarose the gel chamber was flooded with 1 × TAE buffer.

DNA samples were mixed with loading dye (2 µl 6 × Loading Dye (Fermentas, St. Leon-Rot, Germany) per 10 µl DNA solution) and were injected into the pockets of the gel. The DNA size marker, a 1 kb ladder (GIBCO®, Invitrogen, Darmstadt), was diluted by a factor of 1:18 with ddH_2O and mixed with 1 µl Loading Dye before adding into the respective pocket.

Two or three *Bgl*II/*Dra*III restriction batches were pooled and loaded into the agarose gel. By applying a direct voltage of 70 V DNA fragments were separated for 30 – 45 min. Afterwards, the DNA was stained by bathing the agarose gel in 0.5 µl/ml ethidium bromide in 1 × TAE-buffer for 5 – 10 min. Separated DNA bands were visualized using UV light.

50 × TAE-buffer	2 M Tris/HCl 2 M NaAc 0.5 M EDTA pH 7.4 – 7.8

4.2.6 Isolation of DNA Fragments from Agarose Gels

For isolation and purification of DNA fragments from agarose gels, the gel piece with the DNA fragment of interest was cut out under UV illumination. UV exposition was kept as short as possible in order to prevent thymine dimer formation within the DNA strands. Excised agarose pieces were transferred to reaction tubes. DNA extraction was performed using the *QIAquick Gel Extraction Kit* (QIAGEN, Hilden) following the supplier's protocol.

4.2.7 Purification of DNA by Phenol-Chloroform Extraction

DNA preparations with a E_{260}/E_{280} ratio smaller than 1.8 were purified from protein contaminants by a phenol-chloroform extraction. DNA solutions were gently mixed in a ratio of 1:1 with phenol-chloroform-isoamylalcohol (25:24:1). After a 5 min incubation at RT, phase separation was supported by centrifugation at 4 °C (13 000 × g) for 5 min. The upper DNA containing water phase was carefully collected and remaining contaminants of organic solvents were allowed to evaporate for about 30 min. Finally, the purified DNA was precipitated by addition of ethanol (chapter 4.2.8.1).

4.2.8 Concentrating DNA Solutions

4.2.8.1 Precipitation with Ethanol

Isolated plasmid DNA from *E. coli* showed a final concentration of about 1 µg/µl. This was not high enough for electroporation experiments requiring concentrations of 8 – 9 µg/µl. For precipitation the DNA solution was gently mixed with 3 M sodium acetate (pH 5.2) to a final concentration of 10 % (v/v). A 2.5-fold volume of ice-cold ethanol (96 % p. a.) was added. After incubation for 1 h at – 70 °C, DNA was pelleted by centrifugation (13 000 × g, 4 °C, 15 min). The resulting DNA pellet was rinsed with 70 % (v/v) ethanol. Residual ethanol was allowed to evaporate for several minutes and the DNA was resuspended in an appropriate volume of ddH_2O. DNA concentration was determined photometrically (chapter 4.2.3) and the solution was stored at – 20 °C.

4.2.8.2 Solvent Evaporation

The EGFP fragment obtained after enzyme digestion of pCH1 with *Bgl*II and *Dra*III and subsequent gel electrophoresis showed rather low concentrations of about 150 – 300 ng/µl.

Additionally, the total amount of DNA obtained from experiments was low (~ 18 µg). For this reason the EGFP fragment was not concentrated by ethanol precipitation because of the technique's low efficiency for small DNA amounts. Instead, the EGFP fragment solution was concentrated by evaporation of excess solvent (ddH_2O) in a thermoheater at 50 °C (Eppendorf, Hamburg) or under sterile air flow in a flow hood for 5 h down to about 1/20 of the original volume.

4.2.9 Chemical Transfection and Establishment of Recombinant Cell Lines

HEK-293 cells were transfected with various plasmid DNA vectors (Tab.4.5), each carrying a gene for a fluorescent protein (EGFP: enhanced green fluorescent protein; ECFP: enhanced cyan fluorescent protein; EYFP: enhanced yellow fluorescent protein). These protein variants, originally isolated from *Aequorea victoria*, are heterologously expressed in the cytoplasm of mammalian cells (EGFP, ECFP). If the gene is linked to the DNA of another protein, the respective chimeric proteins are expressed (e.g. EYFP-actin).

Tab. 4.5: Eukaryotic expression vectors used for chemical transfection of HEK-293 cells. Vectors were purchased from Clontech, Mountain View / CA, USA or provided by C. Hartmann (Appendix *A*4).

DNA	Description of Eukaryotic Gene	Encoded Protein
pCH1 (Hartmann, 2003)	EGFP	EGFP
pEYFP-Actin (Clontech)	EYFP-Actin	fusion protein of EYFP and ß-actin
pECFP-N1 (Clontech)	ECFP	ECFP
pEGFP-N1 (Clontech)	EGFP	EGFP

4.2.9.1 Transfection of HEK-293 Cells by Lipofection

Transfections of mammalian cell lines with DNA were carried out using *Lipofectamine™ 2000* (Invitrogen, Darmstadt). The cationic lipid vesicle reagent forms complexes with DNA that adhere to the plasma membrane and induce endocytotic uptake (Ciccarone et al., 1999).
HEK-293 cells were transfected with plasmid DNA following the supplier's information. For transfection, HEK cells were grown to ~ 80 % confluence in 48-well plates with a growth area of 0.75 cm^2 per well. About 2 h before transfection, the cell culture medium was exchanged by serum free culture medium (SFM, with L-glutamine and antibiotics). Individual mixtures of 0.4 µg plasmid DNA and 1 µl *Lipofectamine™* in 25 µl SFM, respectively, were prepared. Both solutions were incubated for 5 min at RT, mixed afterwards and incubated for further 20 min. After addition of 100 µl SFM the resulting transfection solution was applied to the cells. After 4 – 6 h of incubation the medium was exchanged again to serum containing medium. The yield of transfection was evaluated by epifluorescence microscopy after 24 h.

4.2.9.2 Establishment of Stable Cell Clones

After transfection the majority of the cells exhibits transient expression of the extra gene, since they loose the incorporated genetic material due to cell divisions and degradation. Only a small percentage of transfected cells inserts the genetic information from the plasmid DNA into the genomic DNA inside the nucleus, which ensures the continuous propagation and stable expression of the recombinant gene. The plasmid DNA includes a gene that confers resistance to a specific antibiotic which can then be used for selection of stable cell clones. In order to obtain stably transfected HEK-EGFP and HEK-ECFP clones, cells were cultured in presence of the selection antibiotic geneticin (G418) (Tab. 4.6) for several weeks after transfection (chapter 4.2.9.1).

Tab. 4.6: Stably transfected HEK cell lines and antibiotics used for selection. HEK-EYFP/pAbcg2 cells were kindly provided by M. Seidl.

Recombinant Cell Line	Wild Type Cell Line	Plasmid	Antibiotic	Antibiotic Concentration [µg/ml]
HEK-EGFP	HEK-293	pEGPF-N1 (Clontech)	G418	750
HEK-ECFP	HEK-293	pECFP-N1 (Clontech)	G418	750
HEK-EYFP/pAbcg2	HEK-293	pEYFP-C1-pAbcg2 (Seidl, 2008)	G418	750

After a few consecutive subculturing cycles under antibiotic selection colonies positive for the respective fluorescent proteins were obtained. Stably transfected HEK clones were separated by the method of limited dilution (Freshney, 2005). Transfected cells showing fluorescence were seeded to 96-well plates in a density of one cell per well in order to obtain single colonies. This process was repeated three times with one or two cell populations that showed the highest fraction of fluorescence positive cells. Following this protocol the recombinant cell lines HEK-EGFP and HEK-ECFP expressing cytoplasmic EGFP or ECFP were created. Stable positive clones were expanded on culture flasks and aliquots were stored in liquid nitrogen (chapter 4.1.4) until use.

Clones stably expressing HEK-EYFP/pAbcg2 were kindly provided by M. Seidl (Seidl, 2008). This cell line expresses a fusion protein of the porcine (p) transmembrane multidrug resistance protein Abcg2 and EYFP. Vector information and the pAbcg2 sequence can be found in the appendix (Appendix *A*4).

4.3 Electric Cell-Substrate Impedance Sensing and Application of Electric Fields to Manipulate Cells

Electric monitoring of mammalian cell layers is based on the well-established Electric Cell-Substrate Impedance Sensing (ECIS) technique (Giaever and Keese, 1993) presented in chapter 3.1. The basic setup uses two coplanar gold-film electrodes that serve as a substrate for adherently growing cells as well as electrodes for non-invasive sensing and application of invasive electric fields. For impedance measurements a non-invasive low amplitude sinusoidal AC voltage signal of varying frequency is applied to the electrodes and the complex impedance of the system is recorded. Pulses of invasive electric fields were applied to the cells using the same setup. Reversible membrane permeabilization (electroporation, electrofusion) or irreversible cell membrane damage (electric wounding) was achieved by application of invasive AC pulses of well-defined frequency, amplitude and duration.
Electric manipulation of adherent cells was always accompanied by non-invasive ECIS monitoring before and after electric pulsing in order to elucidate the impact of electric manipulations on cell viability and morphology.

4.3.1 Experimental Setup

4.3.1.1 Basic Measurement Setup

The basic measurement setup for non-invasive impedimetric monitoring and electric manipulation of adherent cell layers is depicted in Fig. 4.1.

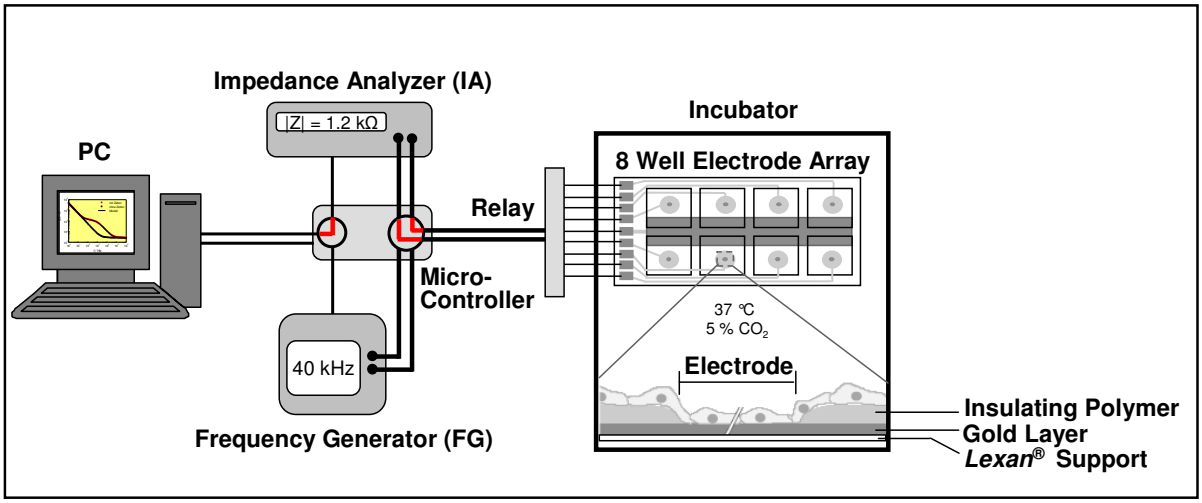

Fig. 4.1: Schematic illustration of the experimental setup for ECIS measurements and electric manipulations of cells. Switching between the impedance analyzer (IA) and frequency generator (FG) is performed by a micro-controller and allows for pre- and post-pulse ECIS measurements. The software controlled relay enables to switch between the working electrodes. The magnified inset shows a side view of a cell-covered working electrode.

An electrode array containing eight individual measuring chambers (chapter 4.3.1.3) was placed in a humidified cell culture incubator at 37 °C with 5 % CO_2. Electrodes were interfaced to the electronic equipment located outside the incubator by a clamp manufactured by Applied BioPhysics (Troy / NY, USA). A relay enabled switching between the different working electrodes. Relay, impedance analyzer (IA) (SI 1260, Solartron Instruments, Farnborough, UK) and frequency generator (FG) (type 33120A, Hewlett Packard, Böblingen) for pulse application were connected via a micro-controller to an ordinary PC.
To acquire ECIS data the oscillator of the impedance analyzer applied an AC voltage of a preset frequency and amplitude of 70 mV to the electrodes. Data were recorded at 51 individual frequencies equally spaced on a logarithmic scale within a frequency range of 10^1 – 10^6 Hz. Continuous, sequential acquisition of impedance spectra of eight electrodes provided a time resolution of about 5.5 min. The measurement was controlled by a personal computer using a *LabView* based software (written by J. Wegener, Regensburg).
Alternatively to this home-made setup (Fig. 4.1), the commercially available ECIS 1600R device (Applied BioPhysics, Troy / NY, USA) was used. The ECIS 1600R setup matches the basic functions of all individual hardware components like IA, FG, micro-controller and relay of the home-made device. The ECIS 1600R applied an AC signal with frequency-dependent amplitudes. For time-dependent measurements with a similar time resolution of 5 – 6 min, data were acquired in 3f-ECIS mode at three different frequencies (400, 4000, 40 000 Hz). A set of 11 different frequencies ranging from 62.5 to 64 000 Hz (62.5, 125, 250, 500, 1000, 2000, 4000, 8000, 16 000, 32 000, 64 000 Hz) was applied in MFT- (multi frequency / time-) mode using an revised software version adapted to ECIS 1600R. The time resolution of the MFT-mode was ~ 1.5 min for a sequential measurement of eight electrodes.
For electric manipulation of cell layers (chapters 4.3.2 – 4.3.4) single invasive AC pulses with a frequency of 40 kHz, voltage amplitudes[2] between 1 V and 7 V and pulse durations of 50 ms – 30 s were applied to the electrodes.

4.3.1.2 Impedance Measurements with High Time Resolution

For impedance recordings with a time resolution of about 600 ms, a slightly modified setup was used (Fig. 4.2). The impedance was recorded at one single frequency of 4 kHz using 2000 cycles for integration. For electric pulse application the setup was modified in a way that the frequency generator was connected to the relay by a manual switch instead of using the micro-controller. The manual switch turned out to operate faster than the software-controlled micro-controller interfaced via the RS232 port.
Since the frequency generator (FG) for electric pulse application was not controlled by the computer in this setup, the desired parameters for pulsing had to be adjusted manually. Thus, the pulse was triggered by the FG front panel. Immediately afterwards electric connection to the impedance analyzer was reestablished by the manual switch. Pulses provided by the FG were monitored by an oscilloscope.

[2] Amplitudes are given as root mean square (rms) values.

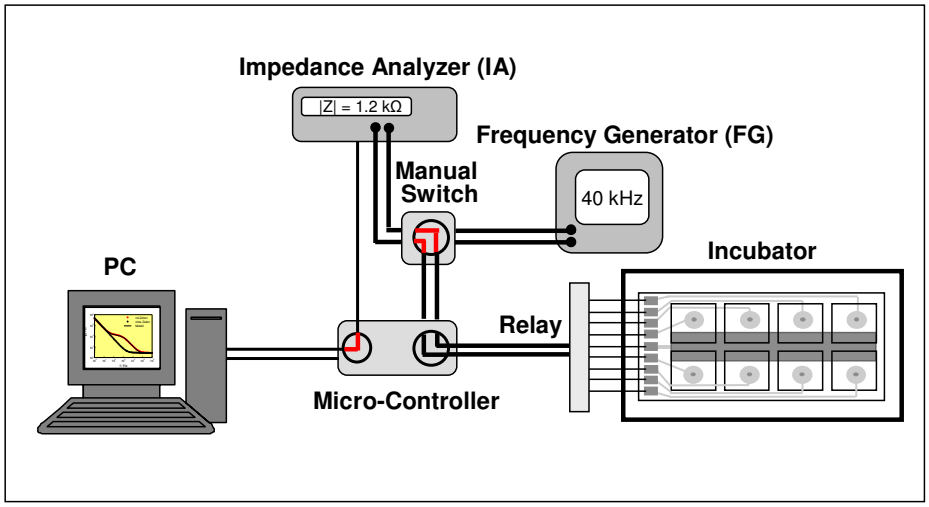

Fig. 4.2: Schematic illustration of the experimental setup for impedance monitoring with high time resolution after electric pulse application. A manual switch was inserted between impedance analyzer and micro-controller. This switch allows for disconnecting impedance measurements for pulse application using the manually controlled frequency generator.

4.3.1.3 Electrode Arrays

Electrode arrays used for ECIS measurements (Applied BioPhysics, Troy / NY, USA) are made from a polycarbonate (*Lexan*®) base substrate covered with a gold electrode layout generated by sputter deposition of gold and subsequent photolithographic techniques (http://www.biophysics.com). A polystyrene chamber defines the eight individual measuring chambers with a growth area of 0.75 cm^2 each. Different electrode layouts were applied depending on the experimental requirements. The commercially available arrays of the type *8W1E* (Fig. 4.3) as well as the modified custom-made double-electrode arrays (Fig. 4.4) are described in more detail below.

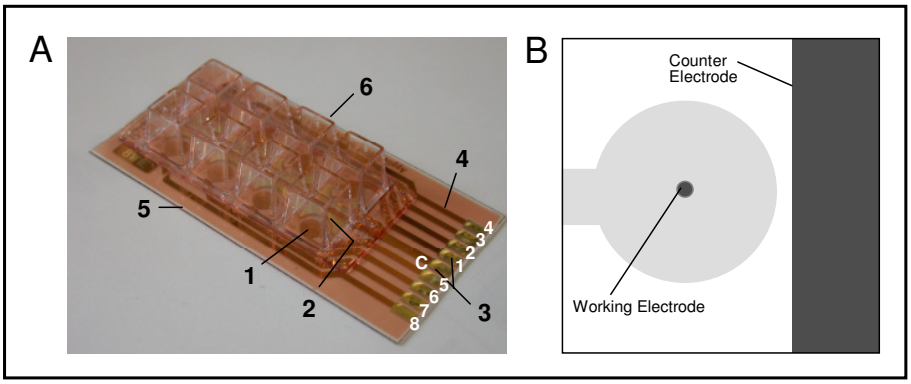

Fig. 4.3: A: Photograph of an electrode array of the type *8W1E* with one working electrode per well (electrode area: 5×10^{-4} cm^2). **1:** Working electrode; **2:** Counter electrode; **3:** Contact area for connection to the electric devices: C: contact with common counter electrode, 1 – 8: contact to electrodes 1 – 8; **4:** Photopolymer insulated gold layout for electric connection between electrodes and contact areas, **5:** Polycarbonate (*Lexan*®) substrate covered with photopolymer, **6:** 8-well *LabTek*®-chamber sealed with silicone glue. The 8-well chamber is capped with a polystyrene lid (not shown) to maintain sterile conditions and reduce fluid evaporation. **B:** Schematic top view of one well of the *8W1E* electrode array.

For most experiments well-established electrode arrays of the type *8W1E* were used (Fig. 4.3 A). Each well of the electrode array contains a small working electrode (area: 5×10^{-4} cm^2) and an about 500 times larger counter electrode (area: ~ 0.25 cm^2). The active electrode area is delineated by openings in a photoresist overlayer that insulates the rest of the deposited gold from the bulk electrolyte (Fig. 4.3 B). The underlying gold layout connects the active electrode area to contact areas outside the measuring chambers. When clamped to the array holder these contact areas provide the electric connection to the electric devices for ECIS measurements and invasive electric field application.

Some experimental concepts required to work in small sample volumes (chapters 4.3.3.2 – 4.3.3.5). For loading of cells with costly molecules like enzymes, antibodies or nucleic acids by electroporation, special custom-made electrode arrays (Applied BioPhysics, Troy / NY, USA) (Fig. 4.4) were used that have been further modified for this purpose (chapter 4.3.1.5).

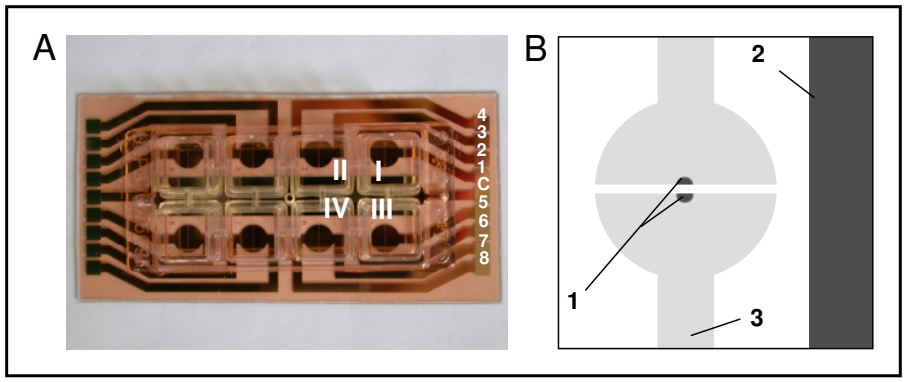

Fig. 4.4: A: Photograph of a custom-made double-electrode array. Contact areas of the 16 electrodes are distributed at both sides of the array. Via the relay eight working electrodes (1 – 8) and the common counter electrode (C) are connected in a way that data from four wells (I – IV) can be collected in a single experiment. **B:** Schematic top view of one well. **1:** Half-circle shaped electrodes with a surface area of about 2.5×10^{-4} cm^2 separated by a 100 µm wide gap; **2:** Counter electrode; **3:** Photopolymer insulated gold areas for electric connection between electrodes and contact areas.

These electrode arrays contained two half-circle shaped electrodes per well, each with a surface area of about 2.5×10^{-4} cm^2, which were separated by a gap of either 100 or 200 µm. Each of the 16 working electrodes were connected to a contact area at the periphery of the *Lexan*® substrate. One common counter electrode was contacted via a central contact area at each side of the array. Contact sites of the 16 electrodes were equally split to the two opposing sides of the array, meaning that only data of four wells could be collected during a single experiment.

The special electrode arrangement of two small electrodes in one well offered the possibility to electrically connect these electrodes in series so that one of them becomes formally the counter electrode even though the electrodes have the same size. Further modification enabled to significantly reduce the required working volume which is described in the following chapters (4.3.1.4 and 4.3.1.5).

4.3.1.4 Electric Connection of Microelectrodes

Measurements with microelectrodes were carried out using the custom-made ECIS equipment (chapter 4.3.1.1) controlled by a tailor-made *LabView* software (written by J. Wegener, Regensburg) for data acquisition and analysis. Figure 4.5 illustrates the two options of electrode connection to the relay. The basic setup sequentially connects each working electrode (1 – 8) and the common counter electrode to the impedance analyzer (IA) (Fig. 4.5 A) as performed for *8W1E* arrays.

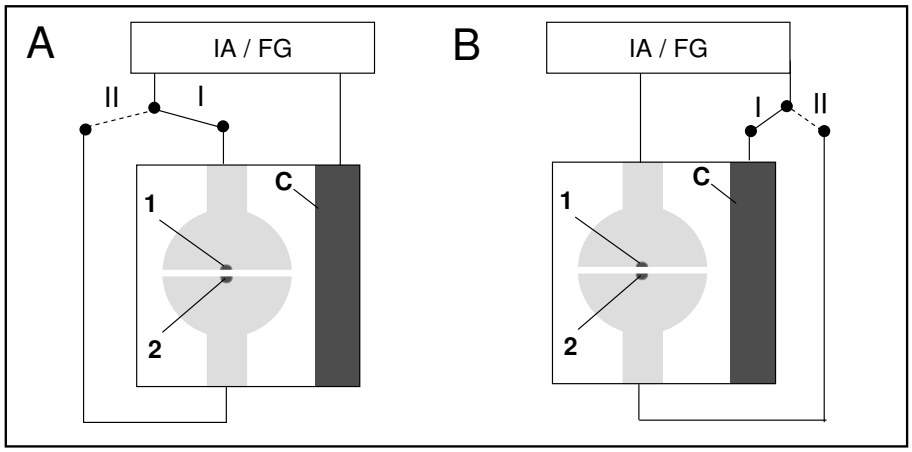

Fig. 4.5: Schematic illustration of possible electric circuit setups for impedance readings with microelectrodes. **A:** Regular connection (I, II) of each working electrode (1, 2) and the common counter electrode (C) to the IA. **B:** Modified contacting setup for microelectrodes which connects the first working electrode and the counter electrode to the IA (I) and allows a connection of the second and the first working electrode to the IA (II). Electrodes are connected to the impedance analyzer (IA) for impedance measurements or to the frequency generator (FG) for electric pulse application.

A modified connection to the relay enabled the situation illustrated in Fig. 4.5 B. Selecting electrodes with an odd number (1, 3, 5, 7) connects these electrodes and the common counter electrode to the IA (Fig. 4.5 B, I). Electrodes with an even number (2, 4, 6, 8) are connected to the IA in combination with their odd-numbered partner electrode (1, 3, 5, 7) in the same well (Fig. 4.5 B, II). As described above, the selected electrodes can be connected to the impedance analyzer (IA) or the frequency generator (FG) (Fig. 4.1).
Due to the same size of the two working electrodes, the readout for their combination (Fig. 4.5 B, II) provides an impedance value of both cell-covered electrodes. A differentiation between individual contributions of each half-circle electrode to the overall impedance signal is not possible. Nevertheless, the use of two small electrodes provides a crucial benefit, which is explained in chapter 4.3.1.5.

4.3.1.5 Array Modifications for Small Volume Applications

The use of two small adjacent electrodes allows for a significant reduction of the required sample volumes, since impedimetric monitoring and electroporation can be performed independent of the large counter electrode residing at the periphery of the well (Fig. 4.5 B, II; Fig. 4.6). Electric connection between the two adjacent electrodes is provided by the

conducting cell culture medium. For complete coverage of the adjacent electrodes with bulk electrolyte the surrounding surface area was reduced to a small fraction of the total chamber area, thereby reducing the required sample volume. Volume reduction was achieved by inserting a silicone ring with an inner diameter of 4 mm and a height of about 3 mm (Fig. 4.6 B; Fig. 4.7).

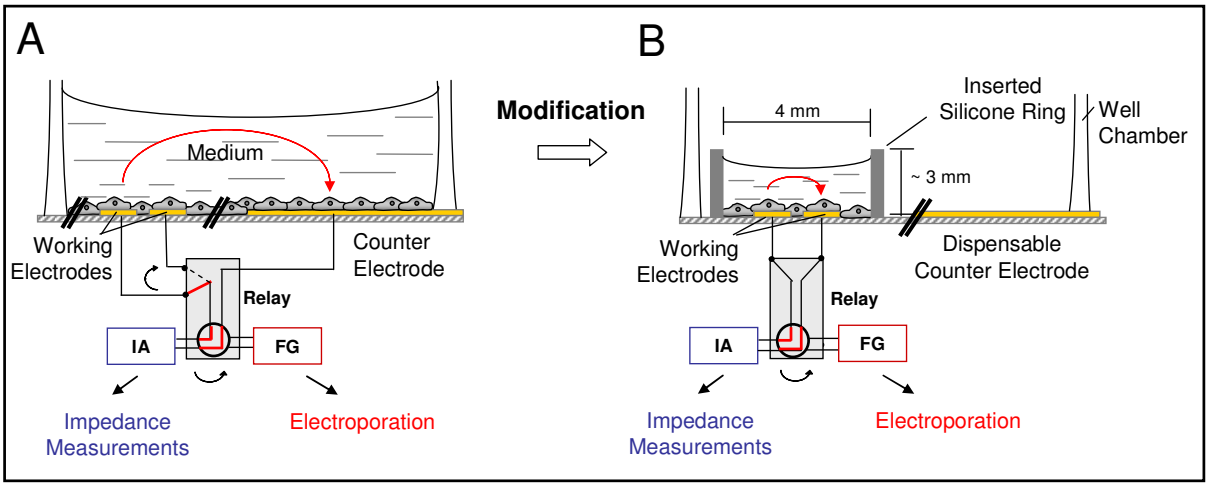

Fig. 4.6: Schematic side view of one well comparing an unmodified (**A**) and a modified (**B**) custom-made double-electrode array. Using an inserted silicone ring with an inner diameter of 4 mm (**B**) the minimum sample volume is reduced from ~ 150 µl to ~ 30 µl. The two half-circle shaped electrodes are connected to the relay, which can switch between the impedance analyzer (IA) for impedance measurements and the frequency generator (FG) for electric field applications. AC current flow in the electrolyte is indicated by the red arrow.

The silicone ring was prepared by cutting ~ 3 mm slices of common meter ware silicone tubes. The silicone ring was fixed and sealed using non-toxic silicone glue suitable for application in aquaria or kitchen (*Master fix Aquarium Silikon*, Warenimport und Handels GmbH, Vienna). After 24 h the silicone had solidified and arrays were sterilized by argon plasma treatment for 15 s or were exposed to UV light for 30 min. These modified arrays allowed the reduction of the volume required for complete electrode coverage from ~ 150 µl to ~ 30 µl.

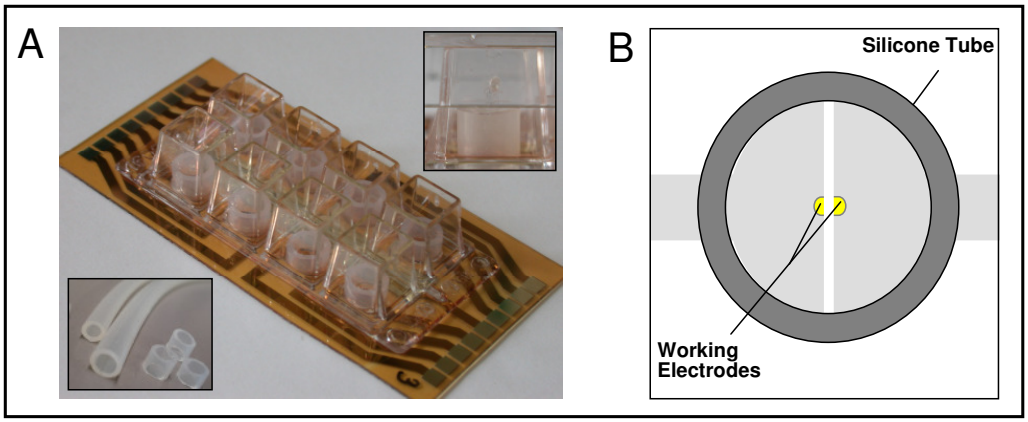

Fig. 4.7: A: Photograph of a modified custom-made double-electrode array. **B:** Schematic top view of one well of a modified array. The half-circle shaped electrodes in the center with a surface area of about 2.5×10^{-4} cm^2 are separated by a 100 µm wide gap and chambered by a silicone ring with an inner diameter of 4 mm (A, picture left bottom). The 8-well chamber is capped with a polystyrene lid (A, picture right top) to maintain sterile conditions and prevent fluid evaporation.

4.3.1.6 Experimental Application of Small Volume Arrays

Small volume arrays were used to load cells with costly molecules like antibodies, enzymes, nucleic acids and quantum dots which is described in more detail in chapters 4.3.3.2 – 4.3.3.5. Prior to an experiment cells were seeded to modified microelectrode arrays in a volume of 400 µl culture medium. Thereby, the inner silicone chamber as well as the outer *LabTek*® chamber were flooded (Fig. 4.8 A).

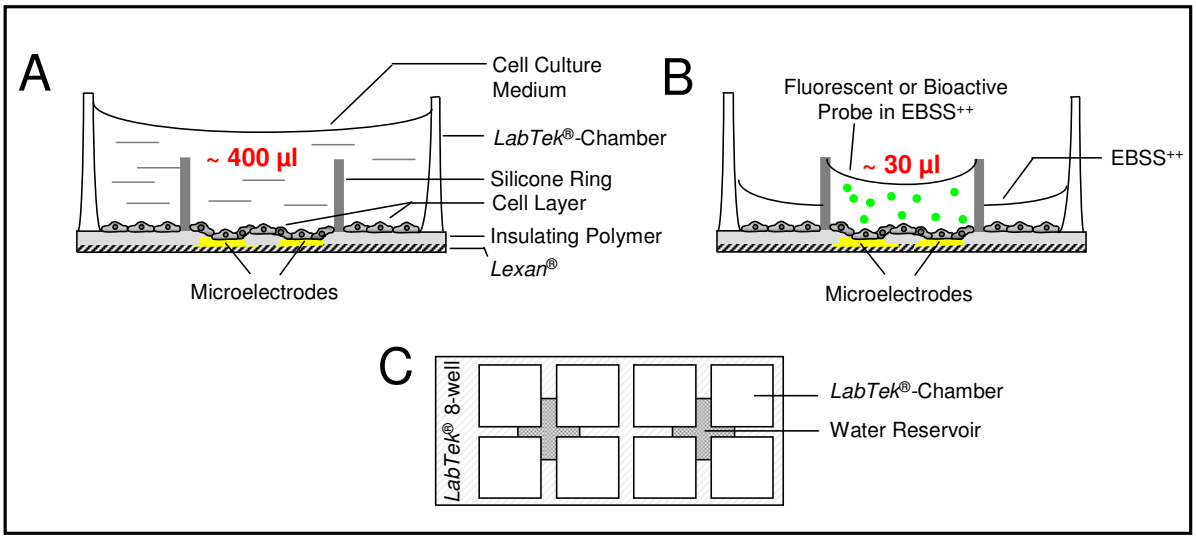

Fig. 4.8: Application of small volume microelectrode arrays in electroporation experiments. Cells were seeded to the entire *LabTek*® well (**A**). For ECIS based electroporation ~ 30 µl of the probe solution in $EBSS^{++}$ was added to the cell population inside the silicone tube (**B**). In order to reduce evaporation from the inner probe solution a small volume of $EBSS^{++}$ (~ 100 µl) was added to the outer *LabTek*® chamber just covering the cell layer. Water reservoirs of the *LabTek*® 8-well (**C**) were filled with 100 µl ddH_2O for the same reason.

For the electroporation experiment itself cell culture medium was removed and the probe solutions were only added to the cell population inside the silicone chamber holding a volume of ~ 30 µl (Fig. 4.8 B). In order to prevent critical solvent evaporation from these small fluid volumes buffer was added to the area surrounding the inner chamber. For the same reason each of the water reservoirs in between the *LabTek*® chambers were filled with 100 µl ddH_2O. The chambers were capped with a polystyrene lid during the course of an experiment.

4.3.1.7 Electrode Array Modifications for Combined ECIS and Microscopy

For combined ECIS and confocal microscopy (chapter 4.4.3.1) special requirements needed to be considered. Due to the limited optical transparency of the gold-film electrodes, electrically manipulated and stained cell layers had to be approached from the top for imaging by an upright confocal microscope (chapter 4.4.1). Commonly used objectives with small working distance, however, could not be used for chambered electrode arrays. Therefore, custom-made electrode arrays of the type *8W1E* without mounted 8-well frame (Applied BioPhysics, Troy / NY, USA) (Fig. 4.9 A) were equipped with a flat measuring chamber fabricated from polydimethylsiloxane (PDMS).

About 25 ml of PDMS base polymer (*Sylgard® 184* silicone elastomer, Dow Corning, Michigan / MI, USA) were mixed in a ratio of 10:1 with *Sylgard® 184* curing agent (Dow Corning, Michigan / MI, USA) and poured into a petri dish to a height of about 5 mm. The polymer was incubated at 37 °C for about 12 – 24 h until polymerization was complete. A chamber-like piece of about 2.5 cm × 5 cm with a wall thickness of about 4 – 5 mm was cut out of the polymer (Fig. 4.9 A). The chamber was fixed and sealed on the array substrate using silicone glue. Individual wells were built using PDMS pieces sealed with silicone glue (Fig. 4.9 B). These sub-chambers were only necessary if different solutions needed to be applied to individual electrodes. Arrays were sterilized by argon plasma treatment for 15 s and were covered with a sterile petri dish for cell culture use.

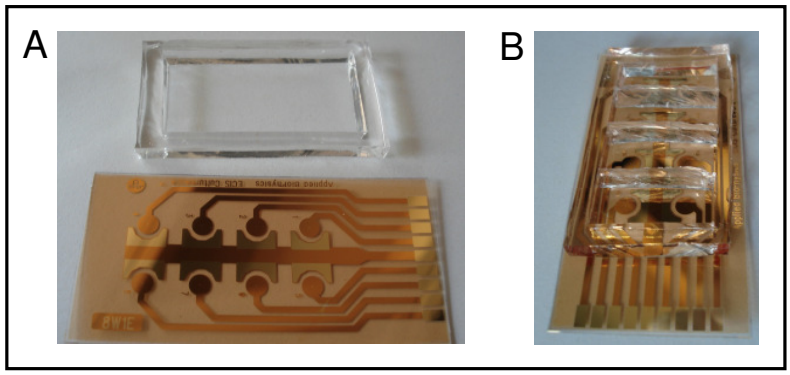

Fig. 4.9: Modified ECIS array for combined ECIS and confocal microscopy applications. *8W1E* ECIS arrays without 8-well top frames (**A**) were equipped with flat chambers made from PDMS (**B**).

The array was warmed to 37 °C by a brazen water-jacketed array holder placed on the microscope stage and connected to a temperature controlled water bath (Fig. 4.10). Electric connection to the measurement device was ensured by short and flexible copper wires fixed to the array contact areas using silver conductive adhesive. Using these copper wires the respective electrodes were manually selected and connected to the electronic system.

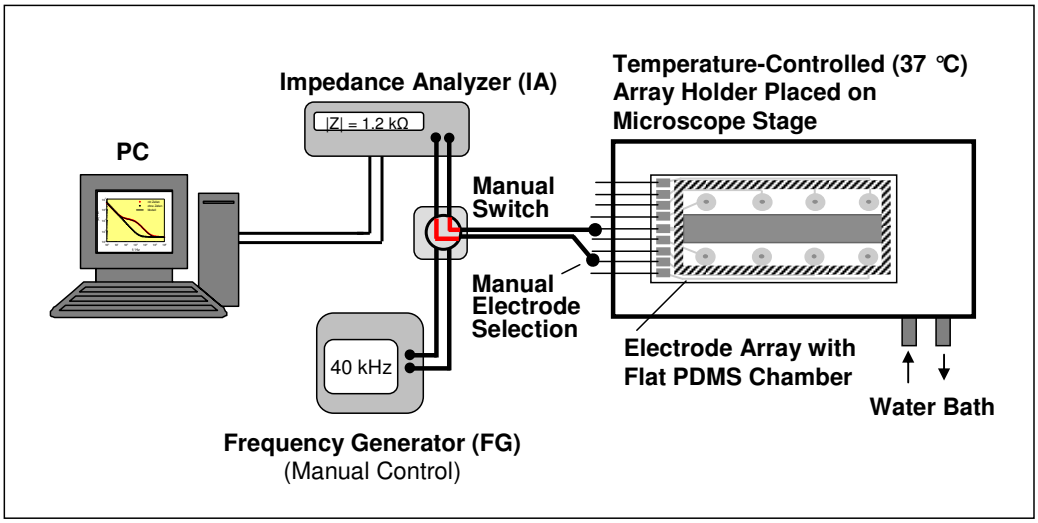

Fig. 4.10: Schematic illustration of the measuring setup for combined online microscopy and impedance measurements on the stage of an upright confocal microscope. Impedance measurements were controlled by a PC using a *LabView* based software. Impedance analyzer (IA) and frequency generator (FG) were connected to a manual switch connecting either the IA or the FG to the electrodes. The individual electrodes were connected manually to the IA / FG switch. The array holder was heated by a water bath to ~ 37 °C.

4.3.2 Basic Experimental Procedure

The basic experimental procedure for combined impedance measurements with integrated electric pulse application is illustrated in Fig. 4.11.

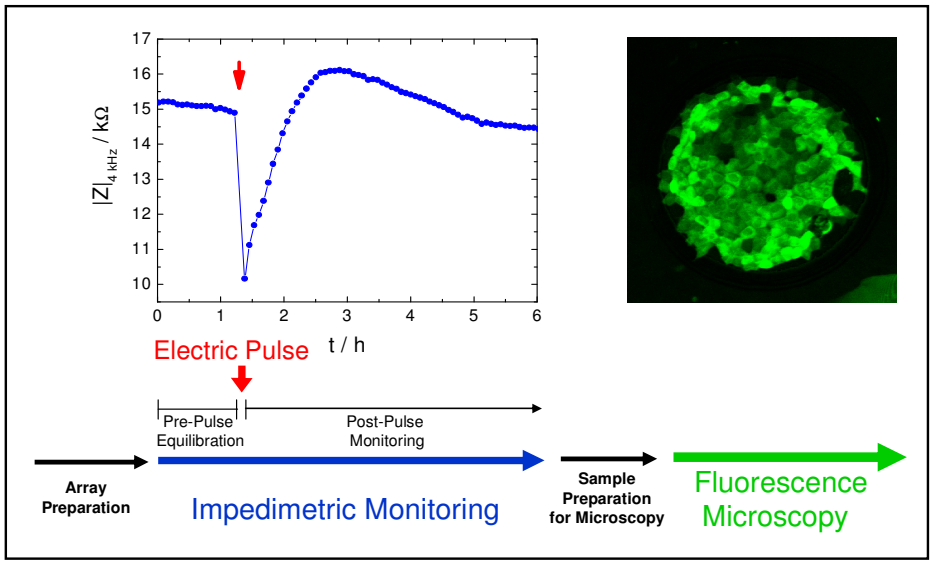

Fig. 4.11: Basic experimental procedure for monitoring of cell layers manipulated by an electric field pulse. The impedance of the cell layer was followed at a single sensitive frequency of 4 kHz over time. After a preceeding equilibration phase of several minutes to a few hours data acquisition was paused and a transient invasive electric field of well-defined frequency, amplitude and duration was applied. The cell layer response was monitored for at least 20 min after pulse application. The impact of cell layer manipulation was often inspected by subsequent fluorescence microscopy. Depending on the type of experiment an individual sample preparation was required (chapters 4.4.2 and 4.4.3).

Array Preparation

Cells were seeded into the wells of electrode arrays (*8W1E* and microelectrode arrays) in standardized densities using a volume of 400 µl cell culture medium and were cultivated for defined periods of time prior to an experiment (Tab. 4.7).

Tab. 4.7: Standardized cultivation protocols for confluent layers of different cell types on gold-film electrodes. Cell suspensions of defined cell density were seeded in a volume of 400 µl into each chamber of an electrode array and cultivated for 1 – 3 days, depending on the cell type.

Cell Type	Seeded Cell Density [cells / cm^2]	Days of Cultivation	Pre-Coating of Electrode
NRK-52E	250 000	2.5 – 3	–
HEK-293	375 000	1 – 1.5	cross-linked gelatin
Hep G2	250 000	2	–
CHO	180 000	1.5 – 2	gelatin (on micro-arrays)
NIH-3T3	250 000	1.5 – 2	–

Before seeding HEK-293 cells electrode surfaces had to be pre-coated with cross-linked gelatin (chapter 4.1.5). Pre-coating with gelatin was applied to stabilize adherent layers of

CHO cells when cultivated on micro-arrays. One day before starting an experiment cell culture medium was exchanged. Several minutes before starting an impedance measurement the cell culture medium was exchanged for pre-warmed $EBSS^{++}$ buffer or cell culture medium, which contained the respective probe (chapters 4.3.3 and 4.3.4).

Impedimetric Monitoring

In order to monitor the morphological response of the cell layer upon electric manipulation as a function of time, the impedance was recorded at one sampling frequency of 4 kHz which proved to be the most sensitive frequency for detecting changes in confluent layers (chapter 3.1.5). A custom-made software switching between impedimetric monitoring and electric field application allowed for a comfortable integration of electric pulses within an ECIS experiment (Fig. 4.1).

The time course of an impedance measurement can be divided into two phases: (i) a period of pre-pulse monitoring, i.e. before application of the electric pulse in order to guarantee equilibrated cell layers and (ii) a post-pulse monitoring period to document the cell layer's response upon the electric pulse and the introduced bioactive probes (Fig. 4.11). To apply an electric pulse at a given time, the non-invasive ECIS data acquisition was paused and the electrodes were switched to the external frequency generator by computer controlled relays. Subsequently, sinusoidal AC voltages of defined amplitude and duration were applied to the selected electrodes. The frequency of the applied voltage pulse was always set to 40 kHz as this has been reported to be the most efficient frequency in more recent studies (Wegener et al., 2002). Depending on the invasiveness of the electric pulse and the resulting cellular response, three types of electric manipulation of adherent cells on ECIS electrodes can be distinguished: **(i) electroporation**, **(ii) electrofusion** and **(iii) electric wounding**.

(i) Well-defined transient cell permeabilization, termed electroporation, was performed in order to load cells with membrane-impermeable substances like large dye molecules, toxic agents, nucleic acids and bioactive proteins. The basic concept of electroporation is explained in more detail in chapter 3.2. Confluent cell layers grown on the gold-film sensor surface were subjected to sinusoidal AC voltages of 40 kHz and 3 – 7 V amplitude for 200 or 500 ms.

(ii) Transient permeabilization of cells within a cell layer with closely adjacent cell membranes may lead to a phenomenon called cell fusion. Electric membrane destabilization is followed by lipid reorganization forming merged membranes and shared cytoplasms of adjacent cells. In this work a significantly enhanced degree of fusion was observed for HEK cells when a common electroporation protocol was applied to the cell layer that was pre-incubated with certain functionalized nanoparticles or polymers.

(iii) By application of a strong invasive electric field of 40 kHz, 5 – 7 V for 15 – 60 s cells can be irreversibly damaged. Cell death is restricted to the electrode area and occurs as a consequence of excessive irreversible membrane pore formation and joule heating. This electrically induced cell damage is termed electric wounding in the following chapters.

After electric pulsing data acquisition was continued and the response of the cell layer after electric manipulation was recorded. In physiological fluid the detected cellular response can be assigned to the electric pulse alone. If bioactive substances were added to the extracellular fluid morphological changes of the cells are due to a combination of both, the electric pulse application and the introduction of certain probes.
Detailed experimental protocols for loading of adherent cells with various membrane-impermeable and bioactive probes by electroporation are given in the following chapter (4.3.3). A more detailed description of procedures used for impedimetric investigation of the fusogenic effect of electric fields and membrane fusion mediating substances is given in chapter 4.3.4.

Fluorescence Microscopy

For further analysis of the experimental results cell layers were inspected by fluorescence microscopy (chapter 4.4). Depending on experimental needs, samples were prepared following cell staining (chapter 4.4.4) and array preparation protocols (chapter 4.4.2). Time-lapse fluorescence microscopy was performed immediately before and after electric manipulation in order to visualize the time course of electroporation and fusion processes (chapter 4.4.3.1).

4.3.3 Electroporation Protocols

The general electroporation protocol follows the basic experimental procedure described above including array preparation, impedimetric monitoring with integrated pulse application and, if required, final microscopic inspection. All electroporation experiments were performed in $EBSS^{++}$ buffer. To achieve a maximal loading efficiency with minimum invasiveness, the different cell types were exposed to individually optimized pulse conditions. These were previously determined by systematic variation of electric pulse parameters in presence of fluorescent reporter dyes (chapter 4.3.3.1). Optimized electric pulse conditions for efficient loading of different cell types with membrane-impermeable probes are summarized in Tab. 4.8.

Tab. 4.8: Electric pulse conditions for maximal loading efficiency of different cell types with membrane-impermeable extracellular probes using *in situ* electroporation (n.d.: not determined). The frequency of the electroporation pulse was set to 40 kHz.

Cell Type	*8W1E*	Microelectrodes
NRK-52E	4 V, 200 ms	5 V, 200 ms
HEK-293	4 V, 200 ms	7 V, 200 ms
Hep G2	4 V, 200 ms	5 V, 200 ms
CHO	3 V, 500 ms	3 V, 500 ms
NIH-3T3	4 V, 200 ms	n.d.

4.3.3.1 Electroporation of Adherent Cells in Presence of FITC-Dextran

Electroporation experiments using fluorescein isothiocyanate (FITC) labeled dextran with a molecular weight of 250 000 g/mol as a fluorescent membrane-impermeable probe were carried out in order to find suitable electroporation conditions for further experiments with other molecules. These basic experiments were performed with various cell types (NRK, HEK-293, Hep G2, CHO and NIH-3T3) on *8W1E* ECIS arrays as well as on small volume arrays. The uptake of fluorescent probes into the cytoplasm was evaluated by subsequent fluorescence microscopy. FITC-dextran was applied in a final concentration of 2 mg/ml in $EBSS^{++}$. The establishment of a confluent cell layer before an electroporation experiment was routinely monitored by ECIS measurements and further verified by phase contrast microscopy. After addition of the probe solution cells were re-equilibrated to incubator conditions for at least 15 min until stable impedance values were recorded. To load cells with the fluorescent probe, defined voltage pulses were applied to confluent cell layers in presence of the dye. Amplitudes were varied between 1 V and 7 V in 1 V steps. Pulse durations were usually chosen to be 200 ms or 500 ms. After electroporation cells were left in the incubator for additional 15 – 30 min. Post-pulse time frames of data recordings were kept as short as possible to restrict unspecific adsorption of FITC-dextran to the cell surface or vesicle mediated dye uptake by endocytosis. However, post-pulse recovery of the cell layer impedance after electroporation with the least invasive conditions should be completed. Finally, cell layers were carefully rinsed three times with $EBSS^{++}$ and the array was prepared for microscopic inspection (chapter 4.4.2).

4.3.3.2 Electroporation of Adherent Cells in Presence of Bioactive Compounds

Bioactive substances (sodium azide, bleomycin, cytochrome c, RNase, DNase) were dissolved in 200 µl (*8W1E*) or 30 µl (modified small volume array) $EBSS^{++}$ depending on the array type. Cells were equilibrated for about 30 min till an electroporation pulse of 40 kHz was applied. Suitable combinations of amplitude and pulse duration were taken from dye loading experiments as well as impedance readings and are listed in Tab. 4.8. After electroporation manipulated cell layers were further monitored by non-invasive ECIS measurements for several hours. Probe specific concentrations are given below.

Sodium Azide

Working concentrations of sodium azide used in electroporation experiments with NRK cells on *8W1E* arrays were 0.1, 0.5, 1.5, 5, 15, 50 and 150 mM in $EBSS^{++}$. Dilutions were made from a 1 M stock solution in ddH_2O stored at – 20 °C.

Bleomycin

NRK cells on *8W1E* arrays were loaded with bleomycin. Applied concentrations of bleomycin were 1, 3, 10, 30 and 100 µM prepared from a 5 mg/ml stock solution in $EBSS^{++}$ stored at – 20 °C.

Cytochrome c

Cytochrome c experiments were carried out using standard *8W1E* electrode arrays as well as modified small volume arrays. Cytochrome c from equine heart (Sigma-Aldrich) was used at concentrations of 0.1 – 10 mg/ml in $EBSS^{++}$. Solutions were freshly prepared from a lyophilized cytochrome c formulation. For co-electroporation with the caspase inhibitor (Acetyl-Asp-Glu-Val-Asp-Aldehyde; Sigma-Aldrich) 10 mg/ml cytochrome c and 20 µM caspase inhibitor were used.

RNase

For experiments with RNase (Roche, Basel, Switzerland) electrode arrays fabricated for low volume applications with a working volume of 30 µl were used. Applied RNase concentrations were 0.1, 0.25 and 0.5 mg/ml. Heat inactivation of RNAse was performed by boiling the enzyme at 100 °C for 30 min. Heat inactivated RNase served as a control for unspecific effects of the enzyme.

DNase

To load NRK cells on small volume micro-arrays with DNase (Roche, Basel, Switzerland), cell layers were exposed to 0.5, 1 and 2 U/µl DNase. Heat inactivation of the enzyme was performed by boiling the solution at 100 °C for 30 minutes.

Bovine Serum Albumin

Bovine serum albumin (BSA) served as a globular control protein since it exhibits no enzymatic or acute cytotoxic activity within the cell. BSA was applied at concentrations of 0.1, 0.25 and 0.5 mg/ml.

Cytochalasin D

In some experiments the ability of cells to re-populate a cell-free electrode after killing the original cells by electroporation with the cytotoxic substance bleomycin (see above) or electric wounding (chapter 4.3.3.6), was inhibited by incubation with 0.5 µM cytochalasin D (Sigma-Aldrich). Cytochalasin D is a membrane-permeable fungal toxin which shifts the equilibrium of filamentous and globular actin towards the monomers, thereby inhibiting actin polymerization and consequently cell movement. Cytochalasin D solutions in $EBSS^{++}$ were prepared from a 2 mg/ml stock solution in DMSO stored at – 20 °C. In order to determine the lowest effective dose, concentrations were varied from 0.1 to 5 µM. For microscopic documentation the actin structures were stained using TRITC-phalloidin (chapter 4.4.4.3).

4.3.3.3 Electroporation of Adherent Cells in Presence of Antibodies

For electroporation of antibodies into NRK and Hep G2 cells small volume electrode arrays were used (Fig. 4.7). By electroporation cells were either loaded with unlabeled antigen-specific primary antibodies or fluorophore-labeled secondary antibodies (Tab. 4.9).
Prior to the addition of antibody containing fluid cell layers were washed once with 1 % (w/v) BSA in $EBSS^{++}$ and incubated in 1 % (w/v) BSA for 15 min. All antibodies were dissolved in 0.5 % (w/v) BSA in $EBSS^{++}$ at concentrations given in Tab. 4.9.

Tab. 4.9: Antibodies used for electroporation experiments of NRK and Hep G2 cells.

Antibody	Type	Immunized Species	Supplier	Concentration
Anti-ß-Catenin	primary, unlabeled	rabbit	Sigma-Aldrich	2.8 mg/ml
Anti-ZO-1	primary, unlabeled	rabbit	Zymed Laboratories	125 µg/ml
Anti-Occludin	primary, unlabeled	rabbit	Zymed Laboratories	125 µg/ml
Anti-F_c Mouse	secondary, *Alexa Fluor*® 568	goat	Molecular Probes	1 mg/ml

Cell layers were incubated with the antibody containing solutions for 10 – 15 min before electroporation in order to equilibrate them. Electroporation parameters used for NRK and Hep G2 cells correspond to the ones listed in Tab. 4.8. The cell layer impedance was monitored before and after electric pulse application. About 30 min after electroporation, data acquisition was stopped and wells were flooded with 1 % (w/v) BSA in $EBSS^{++}$ in order to dilute the antibody solution, thereby minimizing unspecific post-pulse uptake of antibody by endocytosis.

Subsequently, cells were thoroughly washed with 1 % BSA solution and finally fixed with 4 % (w/v) PFA in PBS^{++} (phosphate buffered saline supplemented with Ca^{2+} and Mg^{2+}, chapter 4.4.4.1) for 10 min at RT. Cell layers were washed with PBS^{++} three times and – depending on the electroporated antibody type (primary or secondary) – were either directly prepared for microscopy or subjected to an extended immunostaining protocol (see below).

Electroporation in Presence of Fluorescently Labeled Secondary Antibodies

An *Alexa Fluor*® 568 labeled anti-F_c mouse antibody (Tab. 4.9) was used to load the cytoplasm of NRK and Hep G2 cells in electroporation experiments. After post-pulse monitoring cell layers were washed and preserved by PFA fixation (chapter 4.4.4.1). Electroporative loading of cell layers with the fluorescently labeled antibody was documented by fluorescence microscopy using the Leica TCS SL confocal laser scanning microscope (chapter 4.4.1).

Electroporation in Presence of Antigen Specific Primary Antibodies

For electroporation of NRK cells with primary antibodies a rabbit anti-ß-catenin, a rabbit anti-ZO-1 or a rabbit anti-occludin antibody were used (Tab. 4.9). After finishing the electroporation experiment cell layers were fixed with PFA and permeabilized with 0.2 % (v/v) Triton-X 100 following the protocol in chapter 4.4.4.1. Fixed and permeabilized cell layers were incubated with 3 % (w/v) BSA in PBS^{++} for 15 min. The cell layers were washed three times with 0.5 % BSA in PBS^{++} and stained afterwards for 1 h at 37 °C with an *Alexa Fluor*® 488 labeled goat anti-rabbit secondary antibody (1:1000 in 0.5 % BSA), binding to the electroporated primary antibodies inside the cell (cp. chapter 4.4.4.7). Stained cell layers were washed three times with PBS^{++}. Antibody uptake was finally documented by fluorescence microscopy using the Leica TCS SL confocal laser scanning microscope (chapter 4.4.1).

4.3.3.4 Electrotransfection of Adherent Cells with DNA

For transfection of cells by *in situ* electroporation the plasmid pCH1 (Tab. 4.5, Appendix *A*4) was used. The EGFP containing linear fragment (2278 bp) was obtained by digestion of the plasmid with *Bgl*II and *Dra*III (chapter 4.2.4, Appendix *A*4). The fragment of interest was isolated by electrophoresis and gel extraction (chapters 4.2.5 and 4.2.6). For electroporation 0.5 – 10 µg DNA in a total volume of 30 µl was used, resulting in final concentrations of 17 – 333 µg/ml. Therefore, DNA stock solutions of 6 – 9 mg/ml in ddH_2O were diluted in $EBSS^{++}$. Since DNA molecules of different sizes were used, the copy number of the reporter gene was adjusted to 8×10^{11}. At standard conditions this resulted in a plasmid DNA concentration of around 180 µg/ml. Amounts of plasmids and DNA fragments are listed in Tab. 4.10.

Tab. 4.10: DNA amounts for electroporation of adherent cells on microelectrodes, each corresponding to 8×10^{11} reporter gene replicates in a sample volume of 30 µl per well.

DNA	Size [bp]	Amount per Well [µg]
pCH1	6191	5.43
pEYFP-Actin	5820	5.11
EGFP Fragment	2278	2

Electrotransfection experiments with nucleic acids were carried out using the modified small volume electrode arrays. The culture medium was removed from the cell layer and DNA solution in $EBSS^{++}$ was added to the cells in the area confined by the silicone ring. About 15 – 30 min after electric pulse application (Tab. 4.8), the complete chamber was flooded using 200 µl culture medium supplying the cells with nutrients. Cells were allowed to synthesize EGFP from the DNA template for 24 h before the transfection efficiency was evaluated by confocal fluorescence microscopy (chapter 4.4, Leica TCS SL).

4.3.3.5 Electroporation of Adherent Cells in Presence of Quantum Dot Nanoparticles

For the electroporation of NRK cell layers with quantum dot nanoparticles cells were cultured on small volume microelectrodes requiring working volumes of only ~ 30 µl. PEGylated *QTracker* quantum dots (Q21031MP, Invitrogen, Darmstadt) (ex. / em.: 405 – 525 nm / 565 nm), were diluted in $EBSS^{++}$ buffer to a final concentration of 0.4 µM. The quantum dot suspension was given on top of the cell layer inside the area of the microelectrode array being confined by the silicone ring. After a short equilibration of the cell layers (~ 20 – 30 min) electroporation pulses of 40 kHz, 4 V and 200 ms were applied. About 20 – 30 min after electroporation, cell layers were carefully washed three times with $EBSS^{++}$ buffer and were subsequently prepared for epi-fluorescence microscopic documentation using the Nikon Diaphot or Leica TCS SL microscope (chapter 4.4.1). Samples were illuminated with UV

light (ex.: 330 – 380 nm, dicroic mirror: 400 nm) and fluorescence was detected via a 420 nm longpass emission filter. Despite the specifications of *QTracker* quantum dots provided by invitrogen the quantum dots could be excited using the indicated optical filter system. According to the literature quantum dots also absorb light in the UV within a range of 300 – 400 nm (Dabbousi et al., 1997; Bruchez et al., 1998).

4.3.3.6 Electric Wounding of NRK Cells

In order to differentiate between chemically induced cell death due to loading of the cytoplasm with cytotoxic substances by electroporation and electrically induced cell death, electric wounding of cells was additionally performed in some assays as a control experiment. The respective NRK cell layers were subjected to a strong invasive pulse of 5 V with a frequency of 40 kHz for a duration of 30 s.

4.3.4 Electrofusion of HEK Cells

The phenomenon of electric pulse-induced cell fusion dependent on membrane-contact mediating substances has been first investigated using *PolyMAG* nanoparticles (Chemicell, Berlin). These are superparamagnetic iron oxide (Fe_3O_4) nanoparticles with an average size of about 200 nm and they are coated with polyethyleneimine (PEI). The particles were originally designed to mediate gene transfer in adherent cells since their PEI coat mediates complexation of nucleic acids as well as endocytotic uptake by cells (Scherer et al., 2002; Huth et al., 2004). The application of magnetic fields supports the gravimetric force in accelerating the nucleic acid loaded particles towards the cell surface and thereby enhances the local concentration of the transfection complex at the cell membrane (Fig. 4.12). The experimental protocol for this method of gene transfer is called magnetofection. Details can be taken from the supplier's product information (Chemicell, Berlin).

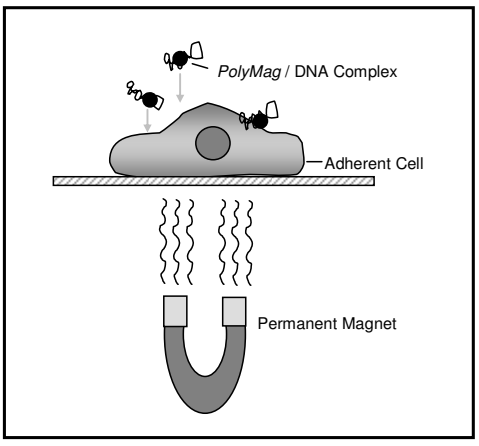

Fig. 4.12: Schematic illustration of the magnetofection principle. Paramagnetic, PEI-coated *PolyMAG* nanoparticles form a complex with DNA due to electrostatic forces. A magnetic force draws DNA loaded particles towards the cell surface, leading to a fast accumulation of genetic material for endocytotic uptake.

Magnetofection of HEK-293 cells was combined with the ECIS-based electroporation method, which led to the observed phenomenon of *in situ* cell fusion (cp. chapter 6). The corresponding experimental procedure is described in the following chapter (4.3.4.1). In

addition to PEI-coated *PolyMAG* nanoparticles, polystyrene nanoparticles with different surface modifications (amine, carboxy, non-modified) as well as various polymers carrying different surface charges (polycationic, polyanionic, uncharged) were applied in order to elucidate the fusogenic effect of *PolyMAG* particles on cell membranes (chapter 4.3.4.2) (Tab. 4.11; Tab. 4.12).

4.3.4.1 Electrofusion of HEK Cells Mediated by *PolyMAG* Nanoparticles

HEK-293 wild type cells or the genetically modified clones HEK-EYFP/pAbcg2, HEK-EGFP and HEK-ECFP were used in these experiments. Cells were seeded in a density of 350 000 cells/cm^2 about 24 – 36 h before starting any fusion experiment allowing them to form a confluent monolayer. Cells were seeded on ECIS electrode arrays of the type *8W1E* that have been pre-coated with cross-linked gelatin (chapter 4.1.5).

The three basic experimental setups are illustrated in Fig. 4.13. In most experiments *PolyMAG* nanoparticles were added before starting an ECIS measurement (Fig. 4.13, 1). In a minor number of experiments particles were added while already recording impedance data (Fig. 4.13, 2). A special self-constructed setup was used to simultaneously monitor the time-resolved process of cell fusion microscopically and impedimetrically (chapters 4.3.1.5 and 4.4.3.1) (Fig. 4.13, 3).

For standard application DNA-free *PolyMAG* nanoparticles were used in a concentration of roughly 9 pM in 200 µl of serum-free culture medium, which corresponds to a particle density of ~ 1.4 × 10^9 particles/cm^2.

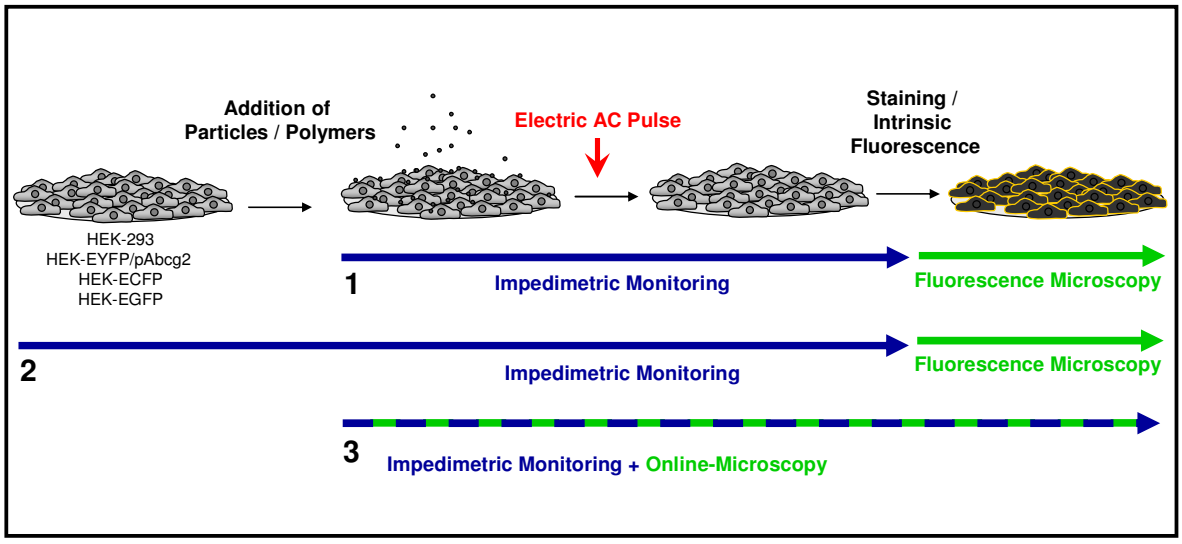

Fig. 4.13: Schematic illustration of the three different basic experimental setups used for cell fusion experiments with HEK cells. Particles or polymers were added before (1) or during (2) impedimetric monitoring. Cell layers were equilibrated for ~ 1 h before electric pulse application. After a post-pulse incubation time of about 2 h the cells were stained and evaluated by fluorescence microscopy. Recombinant cell lines with intrinsic fluorescence (HEK-EYFP/pAbcg2, HEK-ECFP, HEK-EGFP) allowed for a microscopic inspection without previous staining. In a third experimental setup (3) impedimetric monitoring and confocal microscopy were performed simultaneously.

PolyMAG / DNA complexes were prepared following the supplier's protocol (Chemicell, Berlin) in serum-free medium and were applied to the cell layer in a final concentration of 9 pM. In concentration dependent studies, particle concentrations of 0.15 pM up to 36 pM were used. Sedimentation of the particles could be supported by incubation on a permanent magnet plate (MagnetoFACTOR plate 96, Chemicell, Berlin) for 15 min at 37 °C.
Cell layers were usually incubated with the particle suspension for ~ 1 h while monitoring the equilibration phase by ECIS readings. When the influence of the pre-incubation time, i.e. the time of particle exposure before pulse application, should be analyzed, the incubation time was varied between 5 min and 24 h.
Standard AC pulse conditions to induce electrofusion were 40 kHz, a 4 V amplitude and a pulse duration of 200 ms. In parameter studies different amplitudes between 1 V – 4 V or a varying pulse duration of 50, 100, 200 or 500 ms were applied in separate experiments. In order to document the cellular response to the physicochemical and electric manipulation by particle exposure and electric field application non-invasive ECIS readings were continued following the electrofusion pulse for 2 – 3 h. Subsequently, cell layers were inspected by fluorescence microscopy. For studies without any microscopic analysis post-pulse monitoring of manipulated cell layers was performed for several hours up to one day.

4.3.4.2 Electrofusion of HEK Cells Mediated by Polystyrene Nanoparticles or Soluble Polymers

PolyMAG particles are described to have an average diameter of ~ 200 nm (Scherer et al., 2002). The polymer coating with polyethyleneimine (PEI, 800 kDa) provides a positive net charge to the particle surface. In order to elucidate the fusogenic property of the *PolyMAG* particles in comparison to other materials, electrofusion experiments as described above (chapter 4.3.4.1) were carried out using various polystyrene particles and soluble polymers.

Tab. 4.11: Properties of polystyrene nanoparticles applied in HEK electrofusion experiments.

Particle	Average Diameter (supplier's information)	Surface Modification
FluoSpheres®, amine (Invitrogen, Darmstadt)	200 nm	amine red fluorescent (ex. / em.: 580 nm / 605 nm)
FluoSpheres®, carboxylate (Invitrogen, Darmstadt)	200 nm	carboxylate red fluorescent (ex. / em.: 580 nm / 605 nm)
Polybead® Microspheres (Polysciences, Warrington / PA, USA)	200 nm	no modification non-fluorescent

Polystyrene particles with a size of 200 nm and different surface modifications were applied (Tab. 4.11) in order to investigate the impact of a particle's surface charge on fusion

efficiency. According to the experimental procedure established for *PolyMAG* particles, polystyrene particles were applied in a concentration of 9 pM in SFM.
Soluble polymers that were applied in electrofusion experiments are listed in Tab. 4.12 (Appendix *A*5). The fusogenic effect of two PEI types differing in their molecular weight (1.3 and 750 kDa) was compared to the fusogenity of (1) poly-L-lysine, also presenting amine functionalities, (2) uncharged polyethyleneglycol and (3) negatively charged poly-L-glutamic acid. The amount of polymer was adjusted to match the weight per volume amount of *PolyMAG* particles, which was 3 µg/ml in the standard protocol.

Tab. 4.12: Soluble polymers applied in HEK electrofusion experiments.

Polymer	Molecular Weight [kDa]	Geometry of Polymer	Functional Groups
Polyethyleneimine (PEI 1.3)	1.3	branched	primary, secondary, tertiary amines
Polyethyleneimine (PEI 750)	750	branched	primary, secondary, tertiary amines
Poly-L-Lysine (PLL)	30 – 70	linear	primary amines
Polyethyleneglycol (PEG)	1.3 – 1.6	linear	hydroxyl
Poly-L-glutamic acid (PGA)	2 – 15	linear	carboxyl

4.3.4.3 Biophysical Characterization of Nanoparticles

Size and Topography

PolyMAG nanoparticles were imaged by scanning electron microscopy (SEM) (Goodhew et al., 2000). This electron microscopic method uses a cathodic electron beam, which is focussed by magnetic lenses to the conducting surface of the object. Backscattered secondary electrons released from the probe under study are detected. The obtained information can finally be reconstructed to create a three-dimensional topographic image of the sample. SEM images were kindly recorded by the nanoAnalytics GmbH (Münster) using a LEO 1530VP electron microscope. For electron microscopic inspection *PolyMAG* nanoparticles were washed with deionized water and centrifuged at 9079 × g for 10 min three times in order to remove salt residues from the storage buffer. A drop of the nanoparticle suspension in deionized water was deposited and dried on a silicon substrate.

Hydrodynamic Radius and Zeta Potential

PolyMAG nanoparticles and polystyrene nanoparticles were characterized with respect to their hydrodynamic diameter and their zeta potential.
The hydrodynamic diameter was measured by means of dynamic light scattering (DLS) (Pecora, 1985). Size distribution determination by dynamic light scattering, also known as photon correlation spectroscopy, is based on the interaction of monochromatic light with particles in Brownian motion. Time-dependent fluctuations in the intensity of 90° scattered

light can be related to the hydrodynamic radius of the particle via their respective size dependent diffusion coefficient.
The zeta (ζ-) potential, a measure for the particle's surface charge, was determined by a DLS based method termed laser Doppler electrophoresis (Uzgiris, 1980). Charges attached to the particle surface give rise to an electric double layer built of a tightly adsorbed as well as a loosely associated, diffuse layer of ions. Ions within the diffuse layer held together by weak attractive coulomb forces still undergo thermal motion. When the particle moves with respect to the fluid phase, the ions of the diffusive layer are sheared off to a certain fraction. The zeta potential is a measure for the electric potential within the shear plane at the boundary between the compact layer of immobile ions and the diffusive layer. When a voltage is applied across the particle suspension, charged particles move towards the electrode due to electrophoretic forces. The resulting migration velocity is proportional to the zeta potential. The laser Doppler electrophoresis technique determines the electrophoretic mobility by reading the particle velocity dependent frequency shift of scattered laser light. Analysis of these Doppler shifts finally provides an average value for the ζ-potential of a particle species.
Hydrodynamic diameter and zeta potential were measured using the Malvern Zetasizer Nano ZS (Malvern Instruments, Malvern, UK). Polystyrene particles were diluted in water to a concentration of $\sim 2 \times 10^{10}$ – 3.5×10^{12} particles per ml. Suspensions were filled into disposable capillary cuvettes (Malvern Instruments, Malvern, UK) for determination of the zeta potential or into PMMA cuvettes for size determination. All measurements were carried out at 25 °C. The intensity of scattered light was measured at 90° with respect to the incident He-Ne laser beam (633 nm). The number of runs was set to 12 for zeta potential measurements and chosen to be variable (10 – 20) for size determination.

4.3.4.4 Staining of DNA-Loaded *PolyMAG* Nanoparticles

For fluorescence microscopic visualization of DNA-loaded *PolyMAG* particles they were stained with the DNA intercalating dye ethidium homodimer-1 (EthD-1) (Invitrogen, Darmstadt; ex. / em.: 528 nm / 617 nm). According to the supplier's instructions (Chemicell, Berlin) *PolyMAG* particles were loaded with pCH1 plasmid DNA. The particle bound DNA was stained with EthD-1 by adding 4 µM EthD to the particle solution in SFM. After incubation at RT for 30 min in the dark stained particles were washed three times with PBS^{++} by performing repeated centrifugation and resuspension steps. Centrifugation was performed at $9079 \times g$ for 10 min. Finally, stained particles were resuspended in SFM and were dispersed by incubation in an ultrasonic bath (*Sonorex Digitech*, Bandelin, Berlin) for 10 min.

4.4 Microscopy

Phase contrast microscopy was performed in order to confirm cell layer confluence before starting and after finishing an ECIS experiment. Fluorescence microscopy was used to evaluate electroporation efficiency (chapter 4.3.3) as well as to prove and characterize electrofusion events (chapter 4.3.4). Electromanipulated cell layers could be inspected directly if they were electroporatively loaded with fluorescent probes (chapters 4.3.3.1, 4.3.3.3 and 4.3.3.5) or expressed recombinant fluorescent proteins (chapters 4.2.9 and 4.3.3.4). Non-fluorescent cells were selectively labeled using cytochemical staining protocols (chapter 4.4.4).

4.4.1 Applied Microscopes

Phase contrast images were taken using the inverted microscopes Leica DM IRB (Leica, Wetzlar) or Nikon Diaphot (Nikon, Tokio, Japan). For cell layer inspection objectives with 10 × and 20 × magnification were usually applied.
For fluorescence microscopy inverted microscopes (Leica DM IRB / Nikon Diaphot) with oil immersion objectives (63 ×) or upright microscopes (Leica TCS SL / Nikon Eclipse 90i) with water objectives (10 ×, 60 × / 63 ×) were used. Epifluorescence from either inverted or upright microscopes was documented by digital cameras using memory cards or a standard PC for data storage. Confocal laser scanning microscopic (CLSM) images were digitized by photomultipliers and saved on a computer. All microscopes and objectives are listed in Tab. 4.13. Specifications of the excitation and emission filters can be found in the Appendix *A*3 Tab. A1.

Tab. 4.13: Microscopes, specifications and objectives.

Microscope	Modes of Microscopy	Setup	Objectives (type, magnification, aperture, immersion)
Leica DM IRB	Phase contrast Epifluorescence	inverted	N PLAN L 10 × / 0.25 N PLAN 20 × / 0.4 HCX PL FLUOTAR 63 × / 1.25 Oil
Nikon Diaphot	Phase contrast Epifluorescence	inverted	PLAN 10 × / 0.25 PLAN 20 × / 0.4 PLAN APO 60 × / 1.40 Oil
Leica TCS SL	Phase contrast Epifluorescence CLSM	upright	HCX APO L 10 × / 0.30 W HCX APO L 63 × / 0.90 W HCX PL APO CS 63 × / 1.32 Oil
Nikon Eclipse 90i	Phase contrast Epifluorescence CLSM	upright	NIR Apo 60 × / 1.0 W

4.4.2 Sample Preparation for Fluorescence Microscopy on ECIS Arrays

Since the extremely low transmission of the ECIS gold-film electrodes for fluorescence light prevents a microscopic observation of cells from the back of the ECIS electrodes, arrays had to be prepared in a certain way to get access to the cell layer from the top. Thus, for microscopic inspection of the cell-covered electrodes, the polystyrene chamber on the electrode array had to be removed. In case of modified arrays for electroporation in small volumes the inserted silicone chamber was also removed. Cells were inspected using inverted epifluorescence microscopes, for which the sample however has to be inverted (Tab. 4.13), or an upright confocal laser scanning microscope with water dipping objectives (Leica TCS SL or Nikon Eclipse 90i). Both microscope types required an individual sample preparation: *AquaPolymount* embedding (chapter 4.4.2.1) or coverage with PBS^{++} as immersion fluid (chapter 4.4.2.2).

4.4.2.1 *AquaPolymount* Embedding for Inverted Microscopes

When using inverted epifluorescent microscopes to evaluate cell-covered thin-film gold electrodes, cells were embedded in *AquaPolymount* (Polysciences, Warrington / PA, USA) and sandwiched between the polycarbonate array support and a coverglass prior to documentation. Polystyrene chambers had been removed carefully while avoiding disruption of the cell layer or damage of the gold layout. Silicone glue that remained on the array after removal of the chamber was carefully peeled off. During the entire process the cell layer was kept under a thin layer of PBS^{++}. After removal of PBS^{++} a small droplet of *AquaPolymount* was deposited next to each cell layer and a coverglass (24 × 50 mm, # 1) was used to cover the electrode area. The embedded sample was allowed to solidify for about 24 h in the dark before microscopic examination.

4.4.2.2 Sample Preparation for Upright Microscopes

For upright laser scanning microscopy the chamber was removed and the *Lexan*® support was fixed by teflon weights in a petri dish (Fig. 4.14). Silicone residues were not removed as they would not interfere with the following protocol. The array was carefully flooded with ~ 20 ml pre-warmed PBS^{++} and the cells on the gold-film electrodes were analyzed using water dipping objectives (magnification: 10 ×, 63 × / 60 ×).

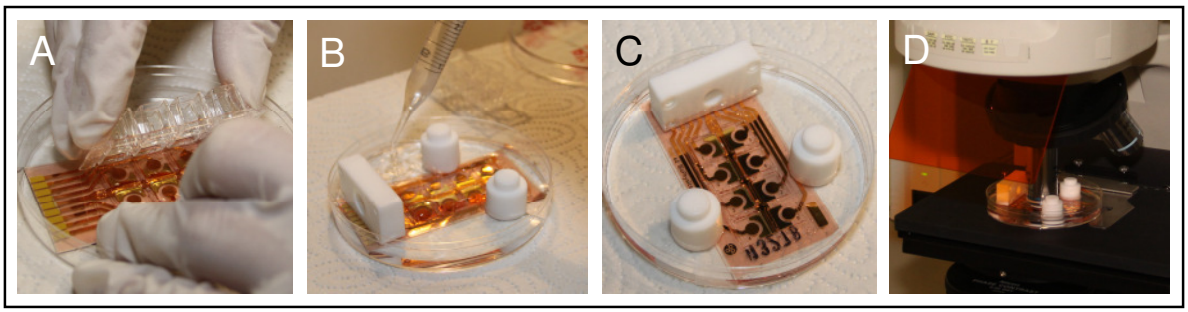

Fig. 4.14: Array preparation for upright fluorescence microscopy with water dipping objectives (**D**). The 8-well chamber is removed (**A**) and the *Lexan*® substrate carrying the electrode layout is fixed to the bottom of the petri dish by teflon weights (**B**). For water immersion microscopy the array is flooded with 20 – 30 ml pre-warmed PBS^{++} (**B**, **C**).

4.4.3 Confocal Laser Scanning Microscopy

Confocal laser scanning microscopy (CLSM) provides particularly sharp images of an object by collecting light (fluorescence or reflected light) from only one focal plane and excluding out of focus scattered light. Thus, fine details within a thin cross-section of the sample can be recorded while reducing the background haze typical for conventional wide-field fluorescence microscopes (Semwogere and Weeks, 2005). The basic concept of a CLSM combines pinhole apertures with sequential point-by-point illumination (Minsky et al., 1988). A two-dimensional picture is generated by scanning the sample within the specified xy-plane and collecting digitized fluorescence information from each point via a photomultiplier tube (PMT). Acquiring a series of optical sections from different positions along the optical z-axis allows a three-dimensional reconstruction of the object. Appropriate software can reconstruct the optical information in several ways providing zx- and zy-views of the object or even a three-dimensional image.
Here, the CLSM technique was applied in order to generate simple optical xy-sections of electromanipulated cell layers on ECIS electrodes as well as side views on the cells under study. Time-resolved series of xy-sections were recorded to visualize the time course of electroporation and fusion processes.

4.4.3.1 Time-Resolved Series of xy-Sections

Time-resolved microscopic experiments were performed on a home-made, temperature-controlled array holder placed on the stage of the Leica TCS SL confocal microscope using a 63 × water dipping objective. Optical xy-sections were recorded at a fixed z-position[3] of the cell layer during electric manipulation and simultaneous ECIS readings using the modified measuring setup as described in chapter 4.3.1.7. For this purpose tailor-made electrode arrays were applied (Fig. 4.9).

[3] The position of the microscope stage was set manually to a suitable position. However, the position of the stage was not automatically controlled and could undergo thermally induced minor drifts in z-direction.

Online-Electroporation of NRK Cells in Presence of FITC-Dextran

Cell layers were covered with 2 mg/ml 250 kDa FITC-dextran in PBS^{++} and electroporated using a 40 kHz pulse of 4 V and 200 ms. Scans of predefined xy-sections with fixed z-position were recorded at 3 s intervals directly before and after application of the electroporation pulse.

Online-Electrofusion of HEK-EYFP/pAbcg2 Cells

A combined ECIS/CLSM experiment allowed time-resolved documentation of cell fusion of HEK-EYFP/pAbcg2 cells on ECIS electrodes. Cell layers were covered with cell culture medium containing 9 pM *PolyMAG* particles. Pictures were taken manually before and after electric pulsing (40 kHz, 4 V, 200 ms) at irregular time frames of 1 min to 30 min over a period of ~ 3 h.

4.4.3.2 Z-Stacks

Three-dimensional data sets of electrically manipulated cells on gold-film electrodes were recorded in order to either visualize electroporative loading of the cells with fluorescent molecules or to image the merging of cell membranes and mixing of cytoplasms of individual cells upon electrofusion. Cell-covered ECIS electrodes were analyzed using an upright confocal laser scanning microscope (Leica, Tab. 4.13) and a 63 × water objective.

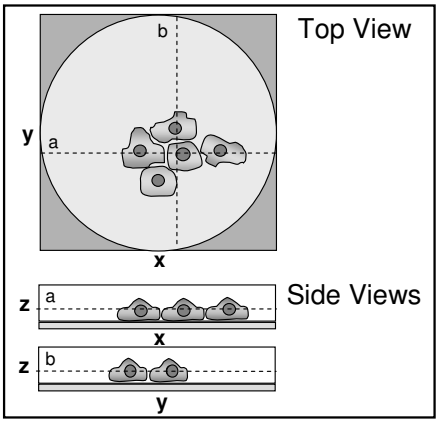

Fig. 4.15: Schematic illustration of CLSM data presentation. The upper picture shows a top view of a cell-covered gold-film electrode, presenting one confocal xy-section from within the cell layer. The z-position of this slice is illustrated by the vertical line in the respective xz- or yz-presentation. The z-presentation of stacked xy-sections provides a vertical side view on the cell layer. Stacks were sliced in x- or y-direction at the position marked by the lines within the xy-presentation.

Array preparation for microscopy was described in chapter 4.4.2.2. Z-stacks were recorded along the height of the cell in steps of 0.1 to 0.5 µm. Every xy-section was generated by a single xy-scan or by averaging over two or three scans per section. Micrographs are presented as illustrated in Fig. 4.15. The top view shows one selected confocal xy-section within the cell layer above the electrode. Z-stacks are presented as zx- or zy-side views of the cell layer being sliced at the position indicated by dotted lines within the top view picture of the xy-plane.

4.4.4 Cytochemical Stainings

4.4.4.1 Fixation and Permeabilization

For staining of intracellular structures with membrane impermeable dyes or antibodies, cell layers had to be fixed and permeabilized. PBS^{++} buffer used in several staining protocols was always freshly prepared from PBS^{--} and a stock solution of $MgCl_2$ and $CaCl_2$. Final concentrations are as follows:

PBS^{++}	PBS^{--}
	0.5 mM $MgCl_2$
	0.9 mM $CaCl_2$

Before staining, cell layers were washed twice with PBS^{++}. Subsequently, cell layers were fixed by incubation with 4 % (w/v) paraformaldehyde (PFA) in PBS^{++} for 10 min at RT. After washing the cell layers twice with PBS^{++}, cells were permeabilized with 0.1 % (v/v) Triton-X-100 in PBS^{++} for 10 min at RT. After removal of the detergent cell layers were washed twice with PBS^{++} to eliminate excess Triton-X-100.

4.4.4.2 Live/Dead Staining with CalceinAM and Ethidium Homodimer

The *LIVE/DEAD*® viability/cytotoxicity kit (Molecular Probes, Göttingen) relies on a combination of calcein acetoxymethylester (CaAM) and ethidium homodimer-1 (EthD-1) (Appendix *A*5) allowing for simultaneous staining of viable and dead cells within a given cell population. The membrane-permeable probe CaAM addresses the intracellular cytoplasmic esterase activity as well as the membrane integrity of living cells. After diffusion of CaAM across the cell membrane, intracellular esterases of living cells hydrolyze ester groups within the non-fluorescent CaAM, thereby generating the polyanionic, membrane-impermeable calcein (ex. / em.: 494 nm / 517 nm) which is retained inside the cytoplasm. EthD-1 is a membrane-impermeable DNA intercalating dye, that selectively stains nuclei of dead cells with compromised membrane integrity (ex. / em.: 528 nm / 617 nm). Thus, combining both dyes, viable and dead cells can be easily distinguished by their green or red fluorescence, respectively.
In order to perform live/dead staining, cell layers were carefully washed with PBS^{++} once and incubated in a freshly prepared staining solution in PBS^{++}, containing 2 µM CaAM and 4 µM EthD-1. After incubation for 30 min at 37 °C in the dark, the staining solution was removed and cells were carefully washed with PBS^{++} before microscopic documentation.

4.4.4.3 Staining of the Actin Cytoskeleton with TRITC-Phalloidin

Staining of the actin cytoskeleton was performed using fluorescently labeled phalloidin (Appendix *A*5). The staining method utilizes the strong and selective affinity of the fungal

(*Amanita phalloides*) phallotoxin to filamentous actin. Phalloidin stabilizes filamentous actin structures and thereby disturbs essential dynamic assembly and disassembly of filaments in the cell.
For staining of mammalian cells with TRITC (tetramethylrhodaminisothiocyanate; ex. / em.: 550 nm / 570 nm) labeled phalloidin cell layers were first fixed and permeabilized following the protocol described in chapter 4.4.4.1. Cell layers were then incubated with a solution of 3 µg/ml TRITC-phalloidin in PBS^{++} for 45 min at RT in the dark. TRITC-phalloidin staining solutions were freshly prepared from a stock solution (0.3 mg/ml) in ethanol which can be stored at – 20 °C. Afterwards, unbound TRITC-phalloidin was removed by washing the sample four times with PBS^{++}.

4.4.4.4 Membrane Staining with DiI

The lipid soluble stain 1,1'-dioctadecyl-3,3,3',3'-tetramethylindocarbocyanine (DiI) was used for staining of cell membranes (ex. / em.: 549 nm / 565 nm). The two C_{18} hydrocarbon chains being attached to the indocarbocyanine dye scaffold intercalate into the lipid bilayer structure and thereby selectively labels membranes (Appendix *A*5).
A stock solution of DiI in dimethylformamide (DMF) (3 mg/ml) was diluted by a factor of 1:1000 in fresh PBS^{++}. After removal of the culture medium, cells were covered with the DiI solution and incubated at 37 °C for 30 min while shaking the sample gently (30 rpm; Shake 4450-1CE, Thermo Scientific) in the dark. Afterwards, cell layers were washed three times with PBS^{++} followed by microscopic documentation.

4.4.4.5 DAPI Staining of Cellular DNA

In order to visualize the nuclei of cells, the DNA-binding dye 4',6-diamidino-2-phenylindole (DAPI) was used (Appendix *A*5). Bound to the minor groove of AT-rich sequences in double stranded DNA, its blue fluorescence is enhanced about 20-fold (ex. / em.: 358 nm / 461 nm).
A stock solution with a concentration of 100 ng/ml was prepared in deionized water. For staining of cell layers, a 1:10 dilution in PBS^{++} was used (10 ng/ml). DAPI staining of fixed and permeabilized cells required an incubation time of only 1 min. If nuclei of non-permeabilized cells were stained, cell layers were incubated with the DAPI solution for 10 – 15 min, since DAPI only passes the intact plasma membrane with low efficiency. Afterwards, cell layers were rinsed three times with PBS^{++} to remove unbound DAPI.

4.4.4.6 Staining of Mitochondria with *MitoTracker*® Red

Mitochondria of adherent cells were stained using the mitochondria-selective dye *MitoTracker*® Red CHXRos (ex. / em.: 579 nm / 599 nm) (Invitrogen, Darmstadt). The *MitoTracker*® probe (Appendix *A*5) passively diffuses across the plasma membrane and is

accumulated in active mitochondria by a membrane potential driven uptake mechanism (Plasek and Sigler, 1996).
MitoTracker® Red CHXRos was added to viable cell layers in a concentration of 200 nM in cell culture medium. After incubation for 45 min at 37 °C in the incubator cells were rinsed once with PBS^{++}. Cell layers were subsequently fixed (chapter 4.4.4.1) in order to retain the *MitoTracker*® probe inside the mitochondria.

4.4.4.7 Immunostaining

Classical immunostainings were performed in order to check the binding capacity and specificity of antibodies before using them in electroporation experiments. Following an indirect immune fluorescence protocol (Bratke et al., 2006), fixed and permeabilized cell layers were incubated with an antigen specific primary antibody followed by staining with a fluorophore-labeled secondary antibody, which recognizes the F_c-region of the primary antibody.
NRK cells were seeded to *LabTek No.1* chambered coverglasses with a growth area of ~ 0.8 cm^2 (NUNC, Wiesbaden) in a density of 670 000 cells/cm^2 one day before staining. Cells were fixed and permeabilized following the protocol described above (chapter 4.4.4.1). After removal of excess PFA and Triton, cell layers were incubated with 3 % (w/v) BSA in PBS^{++} for 20 min at RT to block unspecific binding sites. After a subsequent additional washing step, cells were incubated with a solution of primary antibody in 0.5 % (w/v) BSA in PBS^{++} for 90 min at 37 °C. Individual concentrations of the different antibodies are listed in Tab. 4.14.

Tab. 4.14: Antibodies used for immunostaining protocols.

Antibody	Type	Species	Supplier	Dilution / Final Concentration
Anti-ß-Catenin	primary, unlabeled	rabbit	Sigma-Aldrich	1:500 / 112 µg/ml
Anti-ZO-1	primary, unlabeled	rabbit	Zymed Laboratories	1:50 / 20 µg/ml
Anti-Occludin	primary, unlabeled	rabbit	Zymed Laboratories	1:50 / 20 µg/ml
Anti-F_c Rabbit	secondary, *Alexa Fluor*® 488	goat	Molecular Probes	1:1000 / 2 µg/ml

Afterwards, cells were washed four times with 0.5 % BSA in PBS^{++} and incubated with *Alexa Fluor*® 488 labeled secondary antibody in 0.5 % (w/v) BSA in PBS^{++} for 1 h at 37 °C. Samples were washed three times with PBS^{++} and finally fixed with 4 % PFA for 10 min. Microscopic documentation was performed with an inverted microscope using an 63 × oil immersion objective (Leica DM IRB, Tab. 4.13).

5 *In Situ* Electroporation of Adherent Cells on Gold-Film Electrodes

Electric cell-substrate impedance sensing (ECIS) as well as electroporation of cells are both well-established and versatile techniques with wide applicability in cell biology, biotechnology and biomedical research. Wegener et al. (2002) combined impedimetric sensing and *in situ* electroporation using planar gold-film electrodes that serve for both, cell manipulation and analysis. *In situ* electroporation enables the transfer of membrane-impermeable molecules into the cytoplasm of adherent cells. By non-invasive impedance sensing the cell response resulting from the electric pulse can be monitored with high sensitivity and time resolution, since the electroporation event can be integrated into the ECIS experiment.

This work is focused on the transfer of bioactive molecules into anchorage-dependent mammalian cells by electroporation. The individual action of these substances inside the cell provokes cell shape changes, which can be monitored using the ECIS technique. The studies presented here intend to give a proof of principle for loading adherent cells with different classes of molecules and membrane-impermeable probes, ranging from small inorganic ions over fluorescent dyes, antibiotics, proteins, enzymes and antibodies up to high molecular weight DNA and nanoparticles. Bioactive probes with high intracellular cytotoxicity or degrading activity were chosen, since the resulting cell responses are dramatic and easy to detect. Especially the introduction of antibodies and nucleic acids into cells grown on the impedimetric sensor have an enormous potential for future research, since these molecules open up versatile strategies for specific target blocking and genetic manipulation, respectively. Therefore, the efficiency of loading antibodies and DNA into adherent cells on ECIS electrodes by electroporation was evaluated by fluorescence microscopy, the first step on the way to a reliable impedimetric detection of cell responses induced by these versatile biomolecules in future applications.

For economic use of these bioactive macromolecules, which are in part very expensive and laborious to prepare, an electroporation system was developed that allows to work with small sample volumes.

5.1 Optimization of Electroporation Parameters

For loading extracellular probes into the cytoplasm of adherent cells, ECIS gold-film electrodes that serve as growth substrate for the cells and transducer element for impedimetric

sensing can be used to apply a well-defined membrane permeabilizing electric pulse to the cell layer.

Alternating current instead of direct current was chosen for electric pulsing in order to prevent the creation of electrochemically reactive products or electrode impairments (Wegener et al., 2002). Using AC electric fields for membrane permeabilization, the parameters of the applied electric field can be varied with respect to frequency, amplitude and pulse duration. For successful electroporation of cells it is important that these pulse parameters are optimized in a way that high loading efficiencies as well as a high survival rates are ensured. Most notably, the major fraction of the applied voltage has to drop across the cells and not across the electrode or bulk electrolyte in order to achieve efficient membrane permeabilization (cp. chapter 3.2.1).

The cell-covered electrode immersed in cell culture medium can be regarded as a system of three individual electrochemical impedances in series, the impedance arising from (1) the electrode/electrolyte interface, (2) the cell layer and (3) the bulk electrolyte (chapter 3.1.3). The fraction of the applied voltage that drops across the cell layer – not the electrode or the electrolyte – is decisive for efficient cell membrane permeabilization. The fractional voltage drop across each part of the system primarily depends on the frequency of the applied electric field. In order to determine the frequency at which the major fraction of the applied voltage drops across the cell layer, the specific frequency range where the cell layer impedance contributes the most has to be determined. The reason for this is that the fraction of voltage that drops across the cells is directly dependent on the fractional impedance contribution of the cells to the entire impedance. Thus, the normalized impedance spectrum received by dividing the impedance of a cell-covered electrode by the one of a cell-free electrode ($|Z|_{\text{cell-covered}} / |Z|_{\text{cell-free}}$) for each frequency reveals the relevant frequency range (cp. Fig. 5.1). When the cell layer provides the major contribution to the overall impedance of the system in a certain frequency range, the applied voltage mainly drops across the cell layer. At the maximum of the normalized impedance the voltage drop across the cell layer is thus maximal. The frequency of maximal voltage drop is cell type dependent, since differences in the tightness of cell-cell contacts, indicated by the parameter R_b, in membrane capacitance (C_m), or values for α, describing the cell-electrode junction determine the passive electric properties of the cell layer. How the individual parameters α , R_b and C_m influence the optimal frequency of the voltage used for electroporation was computed by C. Hartmann (Hartmann, 2003) and is shown in Fig. 5.1.

Frequencies for a maximum voltage drop across the cell layer range between 1 kHz and 100 kHz (Fig. 5.1 A – C). Below or above this frequency range only a minor fraction of the applied voltage is delivered to the cells on the electrode. Increasing values for α or R_b and a small membrane capacitance C_m broaden the frequency range of efficient voltage delivery to the cell layer. From such simulations the optimum of frequency of the electroporation pulse can be estimated for each cell type. Since a frequency of 40 kHz has proved to be appropriate for electroporation and wounding of various different cell types grown on ECIS electrodes, this frequency was chosen for all experiments presented in this thesis.

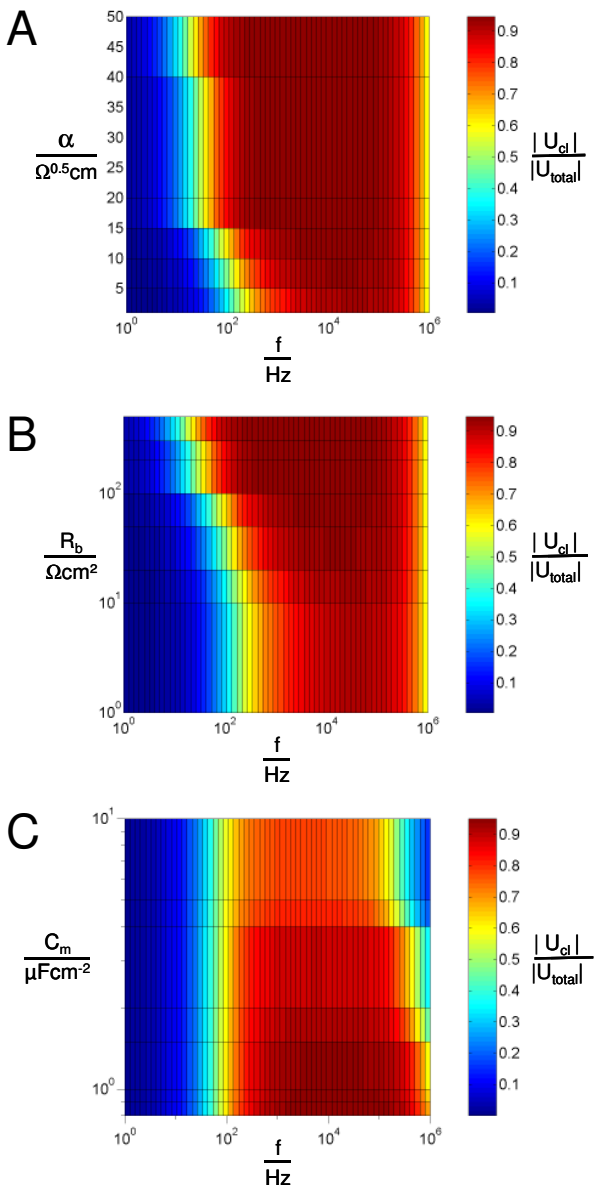

Fig. 5.1: Fractional voltage drop across the cell layer ($|U|_{cl}$ / $|U|_{total}$) for discrete variations of the model parameters α (**A**), R_b (**B**) and C_m (**C**) as a function of frequency (Hartmann, 2003). For calculations each parameter was discretely varied, while the remaining were kept constant (α = 20 $\Omega^{1/2} \cdot$ cm, R_b = 100 $\Omega \cdot cm^2$, C_m = 1 µF/cm^2). $|U|_{total}$ describes the voltage drop across the entire system, while the quotient $|U|_{cl}$ / $|U|_{total}$ describes the fractional voltage drop across the cell layer. If $|U|_{cl}$ / $|U|_{total}$ = 1, the total voltage drops across the cell layer. A high fractional voltage drop across the cell layer is color-coded dark red.

For membrane permeabilization the voltage of the electroporation pulse has to be strong enough to raise the membrane potential difference above a critical value (cp. Theoretical Background, chapter 3.2.2, eq. 3.23), but too high amplitudes will irreversibly destroy membrane integrity. As the impedance of the working electrode dominates the total impedance of the system, the voltage applied for electroporation drops almost exclusively across the working electrode. Applied voltages (~ 3 – 5 V_{rms}) are quite small in comparison to amplitudes needed for electroporation of cell suspensions. Nevertheless, the resulting electric field strength (2.5 – 7.5 kV/cm) across the cell layer is similar to field strengths used for electroporation of cells in suspension (Wegener et al., 2002). The degree of permeabilization is also affected by pulse duration which influences the number and size of membrane defects

(cp. chapter 3.2.2.2). Since AC pulses are used instead of direct current pulses, the electric field strength fluctuates with time. Thus, the effective time with field strengths above threshold values is much shorter for a given AC pulse length than for a DC pulse with the same duration. A suitable combination of pulse amplitude and duration has to be found for each cell type to enable efficient transfer of extracellular membrane impermeable probes across the permeabilized membrane on the one hand and to guarantee a maximal survival rate of electropermeabilized cells on the other hand.
Besides reversible electropermeabilization for loading of cells with extracellular probes the electric field can also be used to irreversibly damage the cell population on the electrode. An ECIS-based wound healing assay uses strong invasive electric pulses for wounding the cell layer on the active electrode (Keese et al., 2004). Thereby, a defined microlesion is introduced to the cell layer and intact cells in the periphery, not affected by the invasive electric field, can move into the wounded area and thereby reseal the cell-free space on the electrode. This type of experiment allows to determine the migration potential of cells under different conditions.

5.1.1 *In Situ* Electroporation and Electric Wounding of NRK Cells Grown on ECIS Electrodes

In this work NRK cells were the predominant cell type which was loaded with various classes of bioactive membrane-impermeable probes by electroporation. A proper choice of electroporation parameters was a prerequisite for a successful electric manipulation of NRK cell layers. Electric parameters for electroporation or electric wounding of confluent cell layers can be found in the literature (Wegener et al., 2002; Keese et al., 2004). Here, the two types of electric manipulation are compared for confluent layers of NRK cells with respect to the time course of the impedance as well as the microscopic characteristics of the cell layer after electroporation or wounding. Moreover, the electroporation efficiency of established NRK cell layers was evaluated by means of dye loading studies and impedance monitoring.

5.1.1.1 Electroporation versus Electric Wounding

Figure 5.2 shows the time course of impedance magnitude before and after electric manipulation (arrow) of established NRK cell layers recorded at frequencies of 4 kHz and 40 kHz. One cell layer was reversibly electroporated with a pulse of 4 V and 200 ms at a frequency of 40 kHz (black curve). The other was electrically wounded by a 5 V pulse for 30 s at 40 kHz (red).

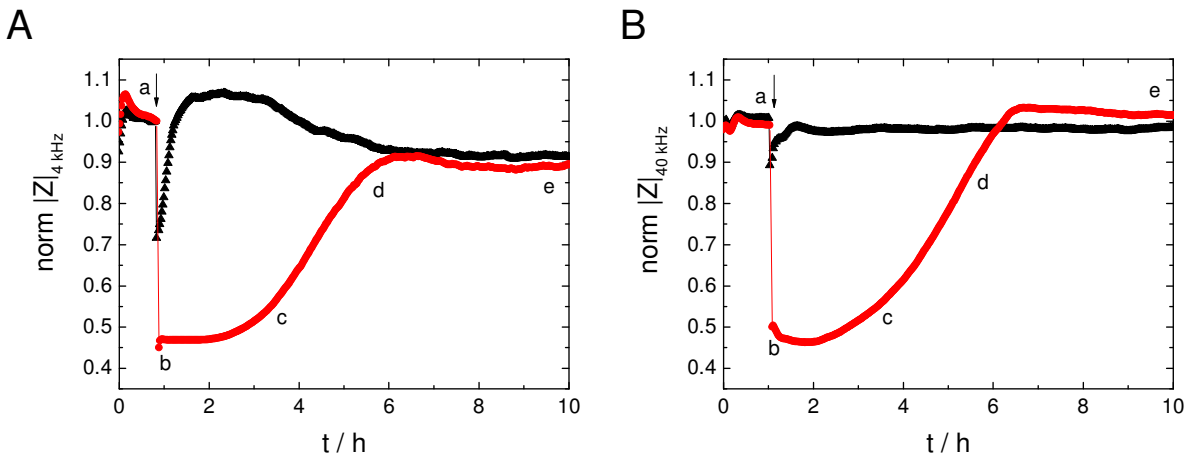

Fig. 5.2: Time course of the normalized impedance magnitude at 4 kHz (**A**) and 40 kHz (**B**) before and after electric wounding (●) or electroporation (▲) of NRK cell layers. The time point of wounding (40 kHz, 5V, 30 s) and electroporation (40 kHz, 4 V, 200 ms) is indicated by an arrow. Letters a – e mark time points of the cell layer before (a) and after electric wounding (b – e) indicating b: 0 %, c: ~ 45 %, d: ~ 95 % and e: 100 % electrode surface coverage with cells as estimated from capacitances at 40 kHz. Absolute impedance magnitudes were normalized to the last value before electric pulse application (A: electroporation: 15.26 kΩ, wounding: 14.28 kΩ; B: electroporation: 4.04 kΩ, wounding: 3.93 kΩ). T = 37 °C.

For a monitoring frequency of 4 kHz the cell layer impedance drops to about 0.7 after electroporation and recovers above initial base line values within one hour (Fig. 5.2 A). The impedance increase of 0.08 above pre-pulse impedance values subsequently settles down to stable values of around 0.92 within 5 h after electroporation. These impedance overshoots above base line values about one hour after electroporation before final re-equilibration are frequently, but not always, observed after electroporation of NRK cells. They may be ascribed to calcium influx across the permeabilized membrane, transient ionic or osmotic imbalance and the resulting cell-morphological responses. The same measurement monitored at 40 kHz only reveals a slight impedance drop to about 0.9 immediately after pulsing, and pre-pulse values are almost re-attained 40 min after electroporation (Fig. 5.2 B). Beside the small transient maximum 40 min after electroporation, the impedance level remains quite constant at values around 0.98. Since a monitoring frequency of 4 kHz is sensitive towards changes in the cell layer resistance arising from the cell-cell contacts or the cell-substrate contact area, the electroporated cell layer is assumed to respond by morphological changes. Instead, a monitoring frequency of 40 kHz predominantly mirrors electrode surface coverage with cells and should only reveal minor changes when most cells are supposed to survive the electroporation pulse. Consequently, a monitoring frequency of 4 kHz is suitable to follow the cell layer response after electroporation events.

Electric wounding of the initially intact cell layer (time point a) by an invasive electric pulse results in a rapid impedance drop to values corresponding to a cell-free electrode (time point b). This indicates that all cells attached to the active electrode area are irreversibly perforated. During the following 5 h the impedance increases (~ time points b – d), finally reaching pre-pulse values (time point e). This response can be monitored at both frequencies. The time frame of wound healing can be determined more exactly from impedance recordings at 40 kHz than at 4 kHz. Normalized values at 40 kHz clearly recover above pre-pulse levels

and settle at 1.01 in the end of the experiment (Fig. 5.2 B), whereas impedance values remain 0.12 below base line values at a monitoring frequency of 4 kHz (Fig. 5.2 A).

Electric wounding of cells on an ECIS electrode and the process of wound healing can be visualized by live/dead staining and fluorescence microscopy. Using this staining method the cytoplasm of vital cells is stained green, whereas the nuclei of dead cells are stained red (cp. chapter 4.4.4.2). Fluorescence microscopic images of individual NRK cell layers before, immediately after and at different time points after wounding are shown in Fig. 5.3. The fraction of electrode surface coverage is indicated and can be correlated to the letters a – e in the ECIS measurement shown in Fig. 5.2. Before pulse application all cells on the electrode are vital (Fig. 5.3 A). Immediately after pulsing nuclei of cells on the electrode are stained red, while cells protected from the electric field by the insulating polymer remain vital (green) (Fig. 5.3 B). Consecutive images show different post-pulse stages of the cell layer during the wound healing process (Fig. 5.3 C – E), indicating that increasing fractions of the electrode are re-populated with time.

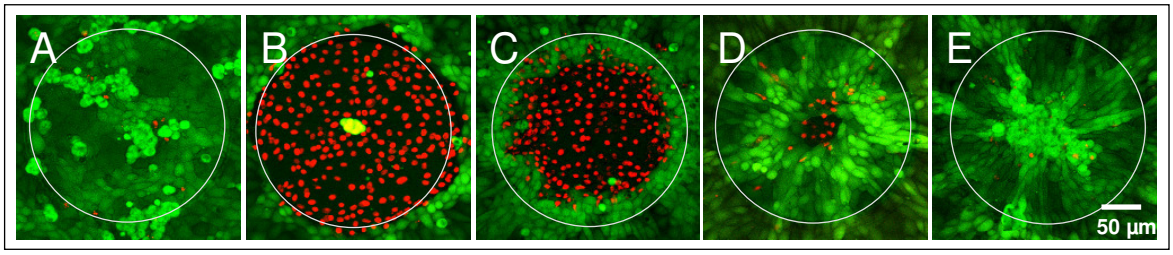

Fig. 5.3: Confocal fluorescence micrographs of live/dead stained NRK cell layers grown on ECIS gold-film electrodes before (**A**), immediately after (**B**) and at different time points after electric wounding (**C** – **E**). Vital cells were stained by calcein-AM (green), the nuclei of dead cells were stained with EthD-1 (red). Active electrode areas are delineated by grey circles. The fraction of electrode coverage with vital cells was calculated by image analysis (*Image J*) and is **A:** 100 %; **B:** 0 %; **C:** ~ 45 %; **D:** ~ 95 %; **E:** 100 %. The figure was adopted from Heitmann, 2008.

During the migration of vital cells from the perimeter of the active electrode to the center, dead cell bodies on the electrode are removed in a snowplow like manner. Due to concentrical movement of the cell sheet, converging in the center of the electrode, a star-like scar is left on the electrode after wound healing has been completed (Fig. 5.3 E).

When cell layers are electroporated with an electric pulse of low invasiveness, the cell membranes are only permeabilized for a short period of time. Thus, the main fraction of cells on the electrode remains vital (Fig 5.4 A). This could be demonstrated by live/dead stainings of NRK cells about 1.5 h after electroporation, indicating living cells by green cytoplasmic fluorescence. Even 20 h after pulsing (Fig 5.4 C) the cell layer is vital. Its structure appears homogeneous without scar-like structures (C), which is in contrast to cell layers observed after electric wounding (cp. Fig. 5.3 E). This indicates that well-controlled electroporation does not induce cell damage, even on the long term. If electroporation conditions are not chosen properly, however, an increasing fraction of cells can be irreversibly damaged by the

electric field (Fig 5.4 B). Irreversible permeabilization of the membrane is indicated by red stained nuclei of dead cells within the electroporated cell layer (B).

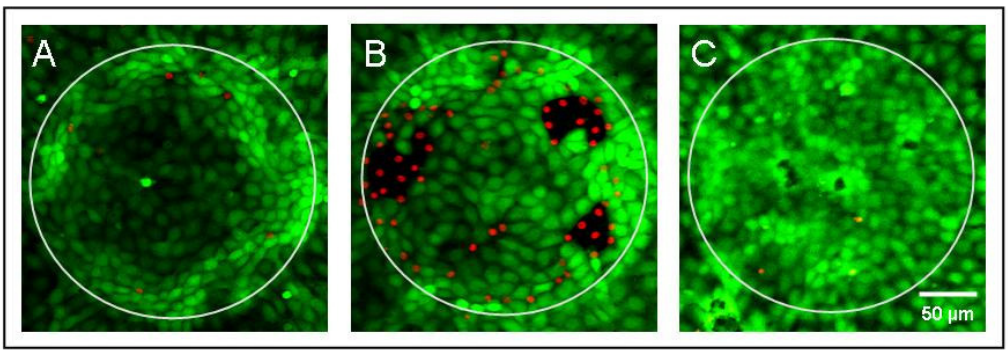

Fig. 5.4: Confocal fluorescence micrographs of live/dead stained NRK cell layers grown on *8W1E* ECIS electrodes 1.5 h (**A**, **B**) or 20 h after (**C**) electroporation. Cell layers were subjected to well-adjusted (**A:** 3 V, **C:** 4 V) or too invasive (**B:** 4.5 V) electroporation conditions. Vital cells are stained by calcein-AM (green), dead cells are stained with EthD-1 (red). Areas of the active electrode surface are illustrated by white circles.

5.1.1.2 Evaluation of Electroporation Efficiency

In order to guarantee optimal pulsing conditions for reversible membrane permeabilization and loading of cells with membrane-impermeable probes, microscopic dye uptake studies were combined with impedimetric monitoring. Electroporation efficiency was evaluated by cellular uptake of membrane-impermeable FITC-dextran (250 kDa) after electric pulse application. Pulse durations of 200 ms and 500 ms as well as amplitudes between 1 V and 6 V were chosen for the experiments similar to pulse parameters presented for NRK cells and the fluorescent probe Lucifer Yellow (Wegener et al., 2002). The fluorescence micrographs of dye loaded cell layers were supported by impedance measurements. The impedance magnitude at 4 kHz of the cell-covered electrode was recorded several minutes before pulse application, providing base-line values of the established cell layer under steady state conditions. Immediately after electroporation the impedance was further monitored in order to detect the cell layer response to the manipulating field. In dye loading experiments pre- and post-pulse incubation times were kept short in order to limit unspecific adsorption of FITC-dextran to the cell surface or vesicle-mediated dye uptake by endocytosis. In most cases independent impedance measurements were repeated in the same buffer but without the fluorescent probe to provide impedance data for these experiments over an extended time range.

Evaluation of Electric Pulse Parameters for Efficient Electroporation of NRK Cell Layers: Dye Uptake Studies

Electroporation parameters suitable for electroporation of NRK cells with the small dye Lucifer Yellow were found to be 40 kHz, 4 V and 200 ms (Wegener et al., 2002). The electroporation parameters for the NRK cells used in this thesis were evaluated using the fluorophore 250 kDa FITC-dextran.

Figure 5.5 shows confocal fluorescence micrographs of confluent layers of NRK cells grown on ECIS electrodes after electroporation in the presence of FITC-dextran dissolved in the extracellular buffer ($EBSS^{++}$). At optimal electric pulse parameters of 40 kHz, 4 V and 200 ms about 90 % of the cells on the electrode surface are loaded with the fluorescent dye (Fig. 5.5 B). The entire cytoplasm of the cells is filled with the fluorescent probe, whereas the dye remains excluded from the nucleus (E, F). Choosing non-optimal combinations of amplitude and pulse duration, as exemplarily presented for a 3 V and 200 ms pulse (A) or a 4.5 V and 200 ms pulse (C), loading efficiencies decrease[1] or the cells get killed. When no electroporation pulse is applied the dye can not enter the cell and the cell layer remains non-fluorescent (D).

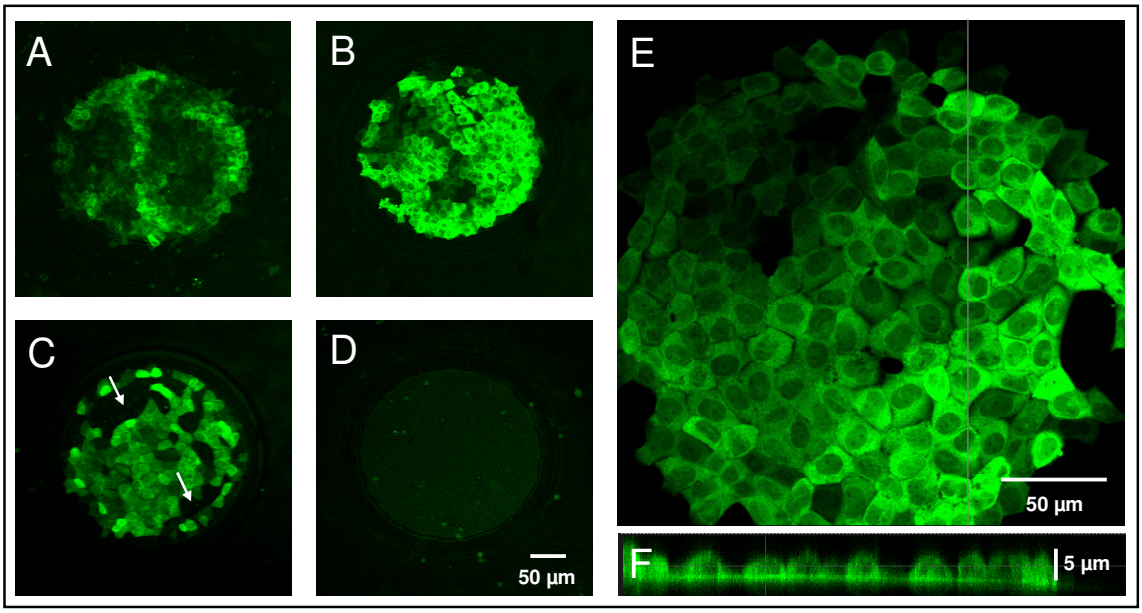

Fig. 5.5: Confocal fluorescence micrographs of NRK cell layers grown on *8W1E* ECIS electrodes after electroporation in presence of FITC-dextran (250 kDa) in $EBSS^{++}$ (2 mg/ml). Cell layers were pulsed at 40 kHz for 200 ms with different pulse amplitudes: **A:** 3 V; **B:** 4 V; **C:** 4.5 V and compared to a control cell layer with no electroporation pulse in FITC-dextran containing buffer (**D**). **E:** Magnified confocal fluorescence micrograph of a FITC-dextran loaded cell layer and **F:** Optical yz-section of the cell layer at the position indicated by the grey line in E.

As apparent from Fig. 5.5 A, the cells pulsed with 3 V for 200 ms show only a weak cytoplasmic fluorescence compared to an efficiently loaded cell layer (B). Electroporation using a pulse of 4.5 V for 200 ms results in a high loading efficiency of single cells (C). However, the micrograph reveals non-fluorescent sites within the cell layer compared to electroporation at optimized conditions. These dark areas might occur due to inefficient loading with fluorescent dye or they mirror irreversible membrane damage and cell lysis.
In order to elucidate the origin of non-fluorescent areas within the cell layer after electroporation (Fig. 5.5 C) CLSM images taken after electroporation of NRK cells with

[1] The sensitivity of NRK cells towards electric pulses significantly depends on the age of the cell culture (passage number), the time of cultivation of the cell layer on the electrodes as well as the nutritive status. Thus, the optimum loading efficiency with certain pulse parameter combinations might vary within a certain range. Therefore electroporation parameters should be re-evaluated for NRK cells and each other cell line under laboratory conditions.

overly invasive electric pulses can be compared to their corresponding reflection images and live/dead stained cell layers (Fig. 5.6). Two individual cell layers were pulsed at 4.5 V for 200 ms either in presence of extracellular FITC-dextran (A) or in dye-free buffer. The latter was stained afterwards for vital and dead cells using the live/dead assay (C).

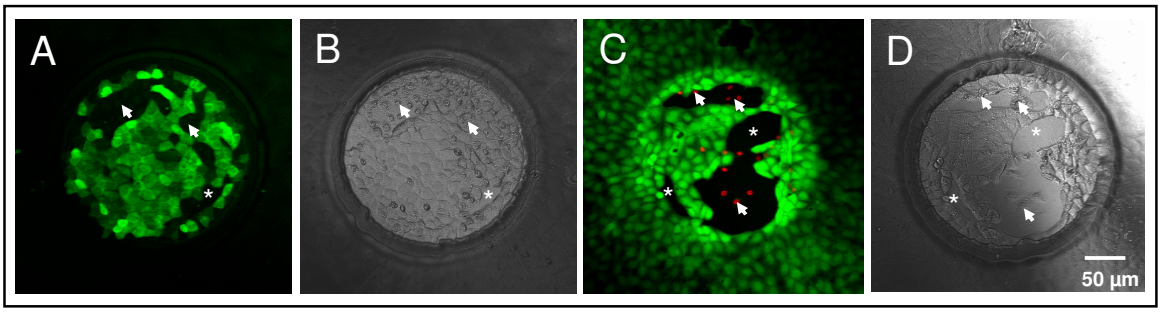

Fig. 5.6: Confocal fluorescence micrographs (**A**, **C**) and corresponding reflection images (**B**, **D**) of confluent layers of NRK cells grown on *8W1E* ECIS electrodes after electroporation at 40 kHz, 200 ms and 4.5 V. **A**, **B:** Cells were pulsed in EBSS^{++} buffer containing FITC-dextran (250 kDa, 2 mg/ml); **C**, **D:** After electroporation in dye-free EBSS^{++} buffer cells were probed with the live/dead assay. Arrows exemplarily indicate areas on the electrode surface that are covered by damaged cells. Asterisks (*) in A and B indicate cell-free areas, which are also visible in C and D.

Both fluorescence micrographs reveal dark areas on the electrode surface (A, C). These dark areas are covered with cells of unusual morphology (arrows) or they are cell-free as becomes obvious from corresponding reflection images (B, D). In fluorescence micrographs irreversibly permeabilized cells fluoresce red due to nuclei staining with EthD-1 (C) or have detached from the substrate leaving behind cell-free areas (B, D). In summary, the observed defects in cell layer fluorescence after electroporation with overly invasive electric pulses can be assigned to irreversible cell membrane damage and cell detachment.
Thus, dye loading studies are suitable to evaluate both, dye uptake efficiency of reversibly permeabilized cells and irreversible cell damage. In systematic dye loading studies, the pulse duration and / or amplitude are discretely varied while keeping the other parameter constant. The resulting dye uptake is quantified by fluorescence microscopy (Wegener et al., 2002).

Evaluation of Electric Pulse Parameters for Efficient Electroporation of NRK Cell Layers: Impedimetric Monitoring

In addition to dye loading studies time-resolved, continuous impedance measurements were performed to identify the optimal electroporation conditions with respect to a minimum of cell damage. Recovery of the impedance to pre-pulse base line values after electric manipulation within a certain time frame is a prerequisite to guarantee the reversibility of membrane permeabilization. The cell response before and after electric pulsing was followed by ECIS measurements at a monitoring frequency of 4 kHz, which is sensitive even to small morphological changes. NRK cell layers equilibrated in EBSS^{++} buffer were pulsed at 40 kHz for 200 ms or 500 ms at 2, 3, 4 and 5 V, respectively. The resulting time course of the normalized impedance at 4 kHz is presented in Fig. 5.7. Figure 5.7 A presents the results for

electroporation with a pulse duration of 200 ms and varying amplitudes, whereas Fig. 5.7 B shows the respective results for a 500 ms pulse.

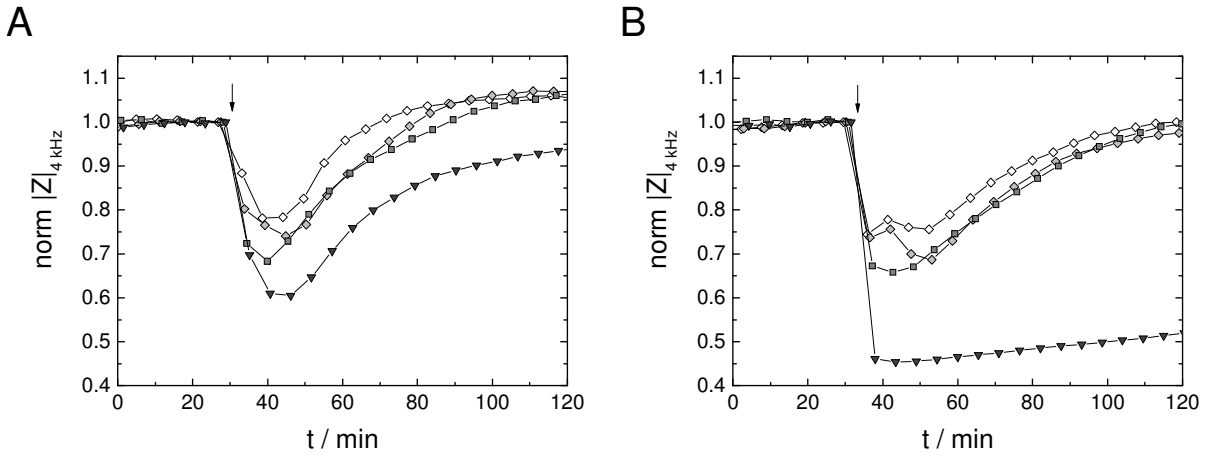

Fig. 5.7: Typical time course of the normalized impedance magnitude at 4 kHz before and after electroporation (arrow) of NRK cells grown on *8W1E* ECIS electrodes in $EBSS^{++}$ with 250 kDa FITC-dextran (2 mg/ml)[2]. Cell layers were electroporated using an AC pulse at 40 kHz for 200 (**A**) or 500 ms (**B**) with different pulse amplitudes: ◇: 2 V; ◈: 3 V; ■: 4 V; ▼: 5 V. Absolute impedance magnitudes were normalized to the last value before electroporation (A: 2 V: 17.02 kΩ; 3 V: 16.88 kΩ; 4 V: 17.18 kΩ; 5 V: 17.72 kΩ; B: 2 V: 16.53 kΩ; 3 V: 16.76 kΩ; 4 V: 15.76; 5 V: 16.29 kΩ). T = 37 °C.

The immediate impedance drop after a permeabilizing electric pulse was applied is characteristic for electroporated NRK cells. The extent of the impedance drop as well as the times needed to recover to pre-pulse impedance magnitudes obviously depend on both, the applied voltage and the pulse duration. For a pulse duration of 200 ms and an amplitude of 2 V (◇) the normalized impedance drops to 0.78 and fully recovers within 40 min (A). Application of an electroporation pulse of 200 ms and a voltage of 3 V (◈) or 4 V (■) causes an impedance drop to roughly 0.75 (3 V) or 0.7 (4 V). The cell layer impedance recovers within 50 – 60 min to pre-pulse values. If the cell layer is pulsed with an amplitude of 5 V, the impedance drops to 0.6. Within the observed time frame the impedance does not reach initial impedance values. For the same voltage of 5 V (▼) applied for 500 ms the electrode impedance even decreases below 0.5 (B). Only a slow increase of norm |*Z*| is recorded and values remain below 0.55 even 90 min after pulsing. Amplitudes of 2 – 4 V applied for 500 ms result in complete impedance recovery within 80 – 90 min after electroporation (B). However, recovery times are retarded when a pulse duration of 500 ms is chosen (B) compared to a shorter pulse duration of 200 ms (A).

For further experiments implementing *in situ* electroporation of NRK cells grown on gold-film electrodes of the type *8W1E*, electric pulse parameters of f **= 40 kHz,** U **= 4 V and** τ **= 200 ms** were chosen on the basis of dye loading experiments with 250 kDa FITC-dextran and impedance measurements of cell layer recovery as presented above.

[2] Confocal fluorescence micrographs can be found in the Appendix *A*3 Fig. *A*1

5.1.2 *In Situ* Electroporation of Different Anchorage-Dependent Cell Types

Among the multitude of anchorage-dependent cell lines available there are a few prominent ones, which are often used in fundamental cell biological and physiological research. Here, the epithelial-like cell lines NRK, Hep G2 and CHO as well as the fibroblastoid cell lines HEK-293 and NIH-3T3 were selected. Optimal parameters for *in situ* electroporation on ECIS electrodes were determined for these cell lines in the course of this work. These adherent cell lines can be readily cultured on ECIS gold-film electrodes and form dense cell layers if cultivated to confluence (Fig. 5.8).

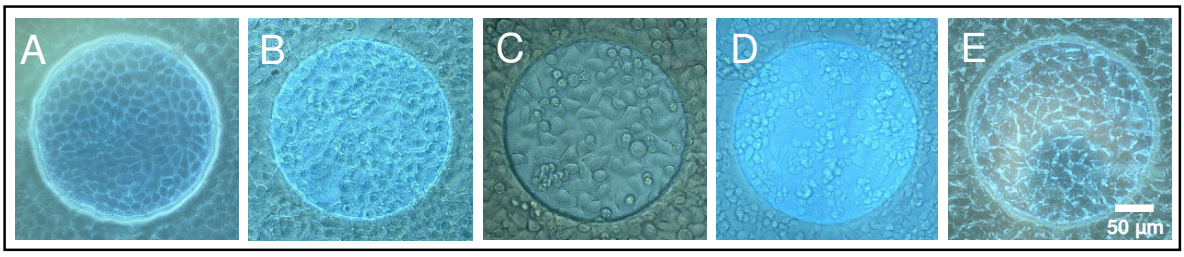

Fig. 5.8: Phase contrast micrographs of confluent cell layers of different anchorage-dependent cell lines grown on *8W1E* ECIS electrodes. **A:** NRK; **B:** HEK-293; **C:** Hep G2; **D:** CHO; **E:** NIH-3T3.

The individual cell layers show differences in their passive electric behavior as apparent from their impedance spectra and the corresponding values for the model parameters α, R_b and C_m (Fig. 5.9; Tab. 5.1).

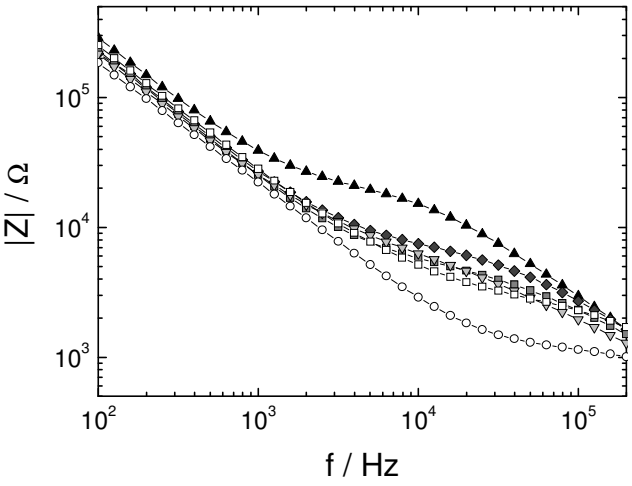

Fig. 5.9: Impedance spectra of various cell types: ▲: NRK; ◆: HEK-293; ▽: NIH-3T3; ●: CHO; □: Hep G2 compared to a cell-free electrode (○). T = 37 °C.

Tab. 5.1: Values of the ECIS parameters α, R_b and C_m given as mean value with standard deviation of the mean ($\mu \pm SD$) (NRK: N = 20; HEK-293: N = 20; CHO: N = 15; Hep G2: N = 15; NIH-3T3: N = 8).

Cell Line	α [$\Omega^{1/2} \cdot$ cm]	R_b [$\Omega \cdot$ cm^2]	C_m [µF/cm^2]
NRK	3.8 ± 0.5	5.7 ± 0.6	2.4 ± 0.4
HEK-293	3.1 ± 0.7	2.0 ± 0.6	2.3 ± 0.3
Hep G2	2.8 ± 0.4	1.1 ± 0.2	1.9 ± 0.3
CHO	3.9 ± 0.5	0.9 ± 0.3	1.5 ± 0.5
NIH-3T3	2.3 ± 0.5	1.0 ± 0.2	0.9 ± 0.2

Cell coverage changes the impedance of the initially cell-free electrode (○) in the frequency range between roughly 5×10^2 Hz and 5×10^5 Hz for all cell types under investigation. The difference in impedance spectra between the cell-free and the cell-covered electrode essentially depends on the individual cell layer characteristics, such as tightness of cell-cell contacts, the cell-electrode junction as well as the membrane capacitance. These cell type

dependent cell layer properties can be quantified by the three model parameters α, R_b and C_m within the transfer function that was established to analyze impedance spectra of cell-covered electrodes (Giaever and Keese, 1991) (cp. chapter 3.1.3).
Among all investigated cell lines the epithelial-like NRK cells provide the most pronounced impedance increase relative to a cell-free electrode. This is also reflected by the ECIS parameters α (~ 4 $\Omega^{1/2} \cdot$ cm) and R_b (~ 5 – 6 $\Omega \cdot cm^2$) (Tab. 5.1). For electrodes covered with HEK-293 cells the impedance rises relative to a cell-free electrode in a frequency range between 1 kHz and 200 kHz. This is also mirrored by the lower values for α (~ 3 $\Omega^{1/2} \cdot$ cm) and especially R_b (~ 2 $\Omega \cdot cm^2$) (Tab. 5.1). Rather flat impedance spectra are obtained for Hep G2, CHO and NIH-3T3 cells, characterized by low values for the paracellular resistance R_b of around 1 $\Omega \cdot cm^2$. For NIH-3T3 cells a quite low value for the membrane capacitance C_m of 0.9 µF/cm^2 is obtained (Tab. 5.1).
Despite significant morphological and electric differences within cell layers of different cell types, their susceptibility towards loading with membrane-impermeable probes by electroporation was evaluated on the basis of electric pulse parameters found to be suitable for NRK cells using a pulse with a frequency of 40 kHz. An optimal combination of the electric pulse parameters amplitude and duration was determined for the electroporation of HEK-293, Hep G2, CHO and NIH-3T3 cells by dye loading studies and supporting impedimetric monitoring (cp. chapter 5.1.1.2).

5.1.2.1 *In Situ* Electroporation of HEK-293 Cells

Figure 5.10 presents the dye loading efficiency for established HEK-293 cell layers after electroporation with a pulse of 200 ms duration and varying amplitudes ranging from 1 V to 5 V in presence of 250 kDa FITC-dextran. For electroporation of HEK cells with a pulse of 1 V only a weak and irregular green fluorescence restricted to the electrode area can be detected. Following the fluorescent micrographs of HEK cell layers pulsed with increasing amplitudes up to 4 V (Fig. 5.10 A – D) the fluorescence intensity of the cells on the electrode increases. The green cytoplasmic fluorescence is homogeneously distributed across the very dense cell layers. Almost 100 % of the cells on the electrode are loaded with the dye when using pulses of 3 V or 4 V (C, D). Dye loading is not only restricted to those cells on the active gold electrode, since a few cells at the edge of the electrode being attached to the insulating polymer are stained as well (B – E).
When electroporating HEK-293 cells with a voltage of 5 V (Fig. 5.10 E) the fraction of dye-loaded cells is similar to the fraction after electroporation with an amplitude of 4 V. Only the number of dye-loaded cells beyond the edge of the electrode (grey circle) is slightly increased. However, the fluorescence intensity of dye loaded cells on the electrode is slightly decreased. As revealed by a magnified image of cells in the center of the electrode, areas of decreased fluorescence intensity show vesicle like structures within the cell layer, which are an indication for cell damage (F).

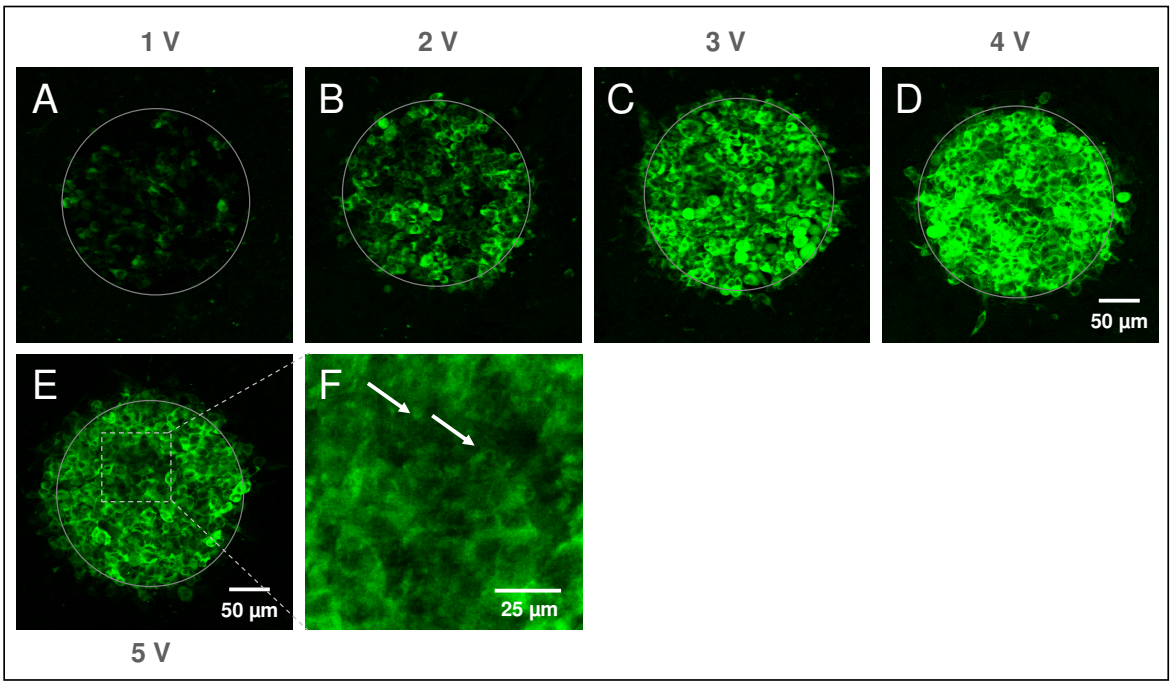

Fig. 5.10: Confocal fluorescence micrographs of confluent **HEK-293** cell layers grown on *8W1E* ECIS electrodes after electroporation in EBSS^{++} with 250 kDa FITC-dextran (2 mg/ml). Cells were electroporated using an AC pulse at 40 kHz for 200 ms and different amplitudes: **A:** 1 V; **B:** 2 V; **C:** 3 V; **D:** 4 V; **E:** 5 V. **F:** 4-fold digital magnification of the area indicated by the dotted rectangle in E. Active electrode areas are delineated by grey circles.

Since pulsing parameters of 200 ms and 4 V were sufficient to load HEK-293 cells with FITC-dextran with high efficiency, no further dye loading experiments were performed. However, more conditions were investigated impedimetrically.

Impedance measurements before and after electroporation of HEK-293 cell layers in EBSS^{++} are presented in Fig. 5.11. Pulse durations were varied between 200 ms and 500 ms and amplitudes of 2, 3, 4 and 5 V were applied. A voltage of 1 V was omitted in impedance monitoring, since this condition revealed only marginal dye loading (Fig. 5.10 A).

When confluent cell layers of HEK-293 cells grown on ECIS gold-film electrodes are subjected to an electroporation pulse the cell layer impedance response at 4 kHz is amplitude-dependent for both pulse durations of 200 ms (A) and 500 ms (B) (Fig. 5.11). Immediately after electric pulsing using a pulse duration of 200 ms the cell layer's normalized impedance decreases to 0.9 for a 2 V (◇) and to about 0.95 for a 3 V (◈) pulse. It re-equilibrates to slightly above base line values within ~ 10 min (Fig. 5.11 A). Applying amplitudes of 4 V (■) and 5 V (▼) the impedance shows an immediate increase above base line values, reaching a transient maximum of 1.25 for 4 V and 1.45 for 5 V within 40 min after electroporation. Subsequently, impedance values decrease but remain above base line values within the time frame of the experiment. Values level out between about 1.15 and 1.2 after electroporation with 4 V or 5 V.

Results for electroporations with a longer pulse duration of 500 ms (Fig. 5.11 B) are very similar to those observed for a pulse duration of 200 ms. However, cell layer responses are slightly shifted towards higher transient impedance maxima after pulsing, except for 5 V. After electroporation with amplitudes of 2 V and 3 V the cell layer recovers to base line

values within 10 min (2 V) or 70 min (3 V) after electroporation. For amplitudes of 4 V and 5 V the normalized impedance increases up to 1.4 and decreases again to about 1.2 (4 V) and 1.35 (5 V) within the time frame of the experiment. Initial values are not re-attained within the time frame of observation.

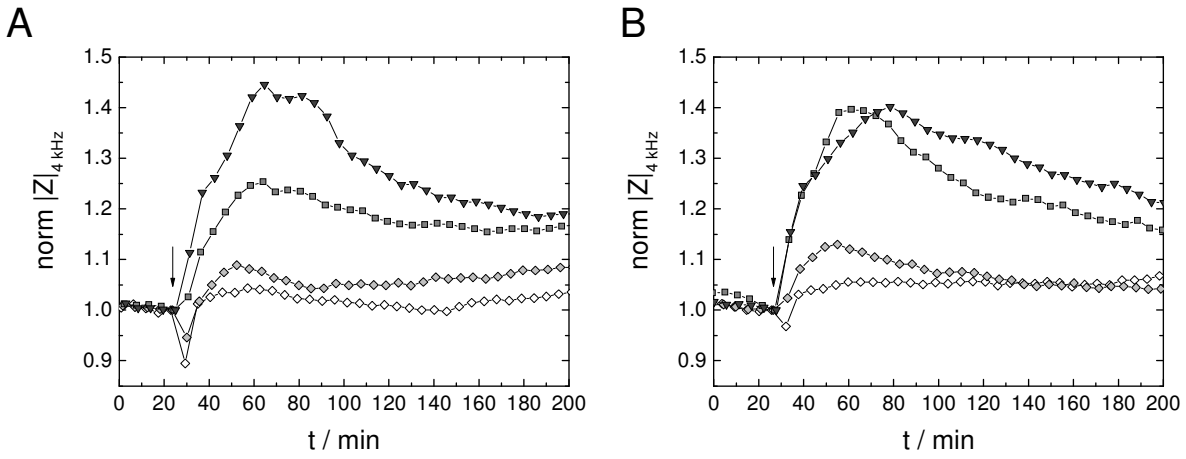

Fig. 5.11: Typical time course of the normalized impedance magnitude at 4 kHz before and after electroporation (arrow) of **HEK-293** cells grown on *8W1E* ECIS electrodes in EBSS^{++}. Cell layers were electroporated using an AC pulse at 40 kHz for 200 ms (**A**) or 500 ms (**B**) with different pulse amplitudes: ◇: 2 V; ◈: 3 V; ■: 4 V; ▼: 5 V. Absolute impedance magnitudes were normalized to the last value before electroporation (A: 2 V: 8.34 kΩ; 3 V: 7.77 kΩ; 4 V: 7.71 kΩ; 5 V: 8.97 kΩ; B: 2 V: 7.89 kΩ; 3 V: 7.73 kΩ; 4 V: 8.25 kΩ; 5 V: 7.85 kΩ). T = 37 °C.

Since a good dye loading efficiency was obtained for the electric pulse parameter combination **f = 40 kHz, U = 4 V and τ = 200 ms**, these conditions were applied in all further experiments to electroporate confluent layers of HEK-293 cells grown on *8W1E* electrodes. Supporting impedimetric data of the electroporated cell layers did not reveal any severe cell layer damage after electroporation with these settings.

5.1.2.2 *In Situ* Electroporation of Hep G2 Cells

The microscopic results of a dye loading experiment for confluent layers of Hep G2 cells are presented in Fig. 5.12. Cells were pulsed at amplitudes of either 3 V or 4 V for a duration of 50 ms, 100 ms, 200 ms or 500 ms. As a control, one cell layer was only incubated with the extracellular dye, but not pulsed. Here, no significant dye uptake by cells can be observed (A). Following electroporations at 3 V in the upper panel, dye uptake is enhanced for pulse durations of 200 ms and 500 ms when compared to 100 ms. Almost all cells on the electrode surface exhibit a green cytoplasmic fluorescence due to dye uptake. There is only a small fraction of stained cells beyond the electrode borders. The lower panel of the figure presents fluorescent micrographs after electroporation of Hep G2 cells with an amplitude of 4 V and increasing pulse durations (E – H). The fluorescence intensity within the cytoplasm of cells attached to the electrode surface reaches a maximum for a pulse duration of 200 ms. Electroporation with lower pulse durations shows similar results as obtained for electroporations at 3 V, 200 ms and 3 V, 500 ms.

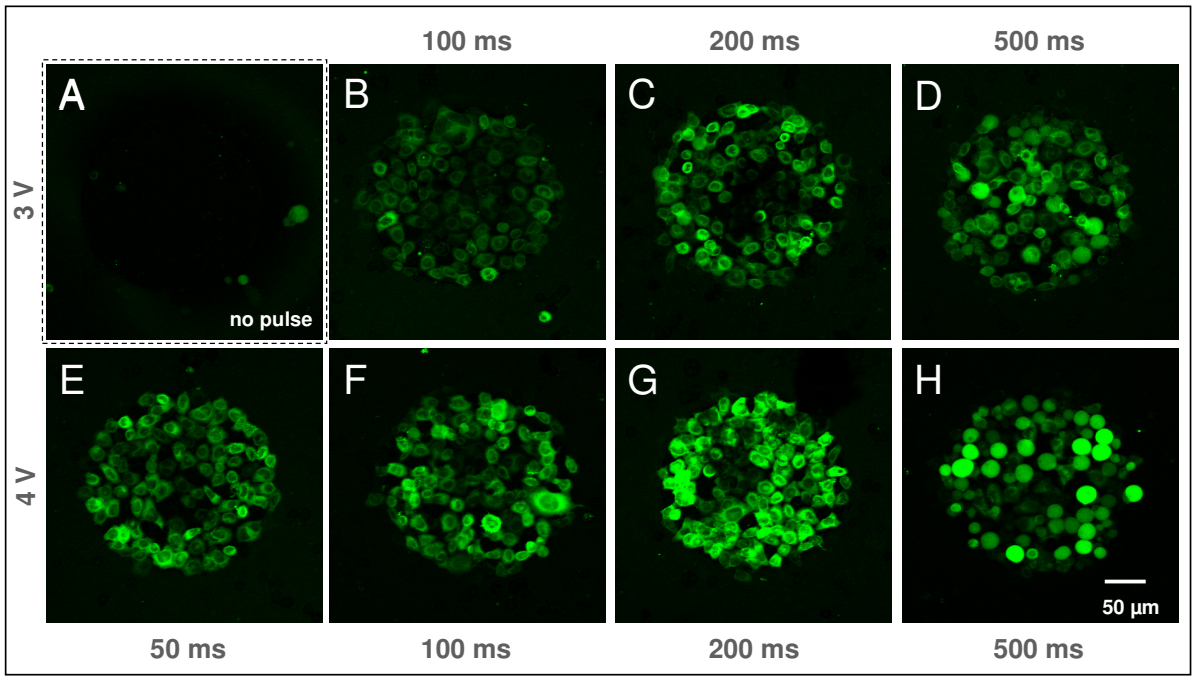

Fig. 5.12: Confocal fluorescence micrographs of **Hep G2** cells grown on *8W1E* ECIS electrodes after electroporation in EBSS^{++} with 250 kDa FITC-dextran (2 mg/ml). All cell layers, except **A:** No pulsing, were electroporated with an AC pulse of 40 kHz and discrete combinations of pulse parameters: **B:** 3 V, 100 ms; **C:** 3 V, 200 ms; **D:** 3V, 500 ms; **E:** 4 V, 50 ms; **F:** 4 V, 100 ms; **G:** 4 V, 200 ms; **H:** 4 V, 500 ms.

A pulse duration of 500 ms (H) for a 4 V pulse caused the cell morphology to change drastically. A high fraction of cells shows a spherical morphology without a distinct nucleus, though being loaded with the fluorescent probe, indicating severe damage of the cells.

Impedance data recorded during dye uptake experiments (Fig. 5.12) are shown in Fig. 5.13. The general response of Hep G2 cells after electroporation again differs from those observed for NRK and HEK-293 cells, but has in common that it depends on the pulse strength.

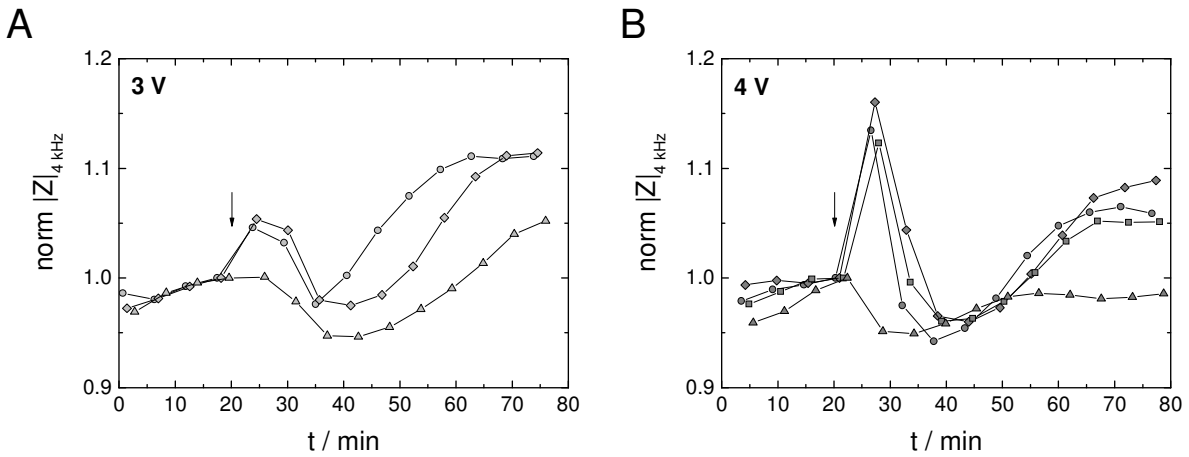

Fig. 5.13: Typical time course of the normalized impedance magnitude before and after electroporation (arrow) of **Hep G2** cells grown on *8W1E* ECIS electrodes in EBSS^{++} with 250 kDa FITC-dextran (2 mg/ml). Cells were electroporated using an AC pulse at 40 kHz with amplitudes of 3 V (**A**) or 4 V (**B**) and varying pulse durations: **A: 3 V:** ○: 100 ms; ◇: 200 ms; △: 500 ms; **B: 4 V:** ●: 50 ms; ◆: 100 ms; ■: 200 ms; ▲: 500 ms. Absolute impedance magnitudes were normalized to the last value before electroporation (A: 100 ms: 8.48 kΩ; 200 ms: 8.15 kΩ; 500 ms: 9.06 kΩ; B: 50 ms: 8.48 kΩ; 100 ms: 8.81 kΩ; 200 ms: 8.61 kΩ; 500 ms: 8.77 kΩ). T = 37 °C.

For electric pulses of 3 V amplitude (Fig. 5.13 A) the time course of the cell layer impedance varies with increasing pulse duration. At shorter pulse durations of 100 ms (○) and 200 ms (◇) the cell layer impedance first increases after pulsing and shows a decrease within 10 minutes. Finally, normalized impedance values rise to 1.1 within roughly one hour after electroporation. If pulse durations of 500 ms (△) were applied using the same amplitude of 3 V, the cell layer impedance does not show a transient increase as observed for shorter pulse durations. After the normalized impedance decreases about 0.05 below initial values within 20 min, the cell layer finally recovers. About one hour after electroporation values of about 1.05 are reached.[3]

For electroporation pulses at 4 V (Fig. 5.13 B) similar results are observed as for the lower amplitude of 3 V (Fig. 5.13 A). However, the initial impedance increase after pulsing with pulse durations of 50 ms – 200 ms (●, ◆, ■) is more pronounced for 4 V than for 3 V amplitudes. Impedance values roughly increase to 1.15 within the first 5 min under these conditions. The further time course reveals a transient decrease of the normalized impedance below base line values and a final settlement at about 1.05 – 1.1, very similar to the time course observed for electroporations at 3 V. The cell layer response after pulsing for 500 ms with 3 V (△) and 4 V (▲) amplitudes is also similar, since there is no initial impedance increase and the impedance values recover to a lower extend compared to initial values.

Most experiments addressing electric pulse conditions for the various individual cell lines were performed by varying the pulse duration between 200 ms and 500 ms. Additional impedance measurements in dye-free EBSS^{++} were performed, addressing the response of Hep G2 cells after electroporation with 2, 3, 4 and 5 V pulses at 200 ms and 3, 4 and 5 V pulses at 500 ms (Fig. 5.14).

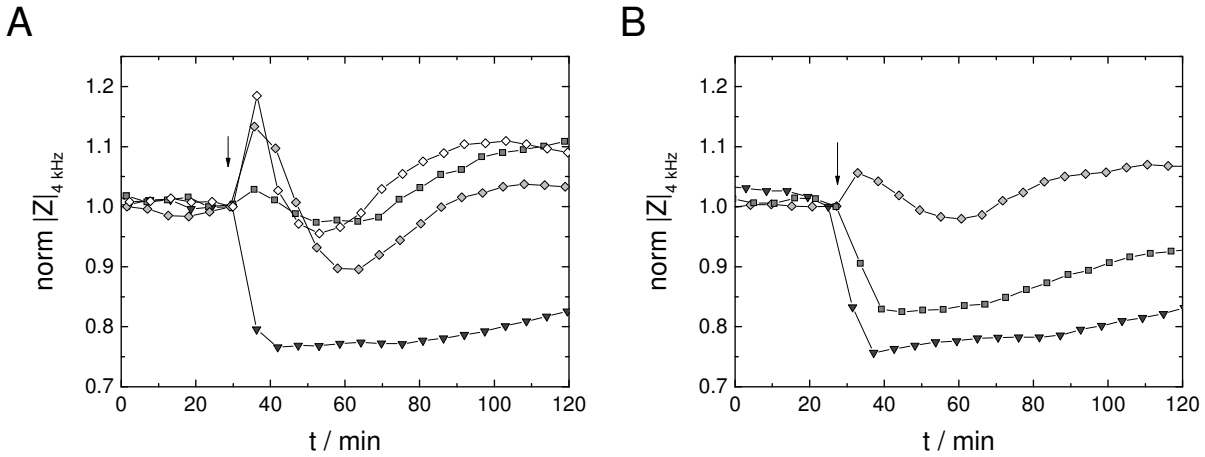

Fig. 5.14: Typical time course of the normalized impedance magnitude at 4 kHz before and after electroporation (arrow) of **Hep G2** cells grown on *8W1E* ECIS electrodes in EBSS^{++}. Cell layers were electroporated using an AC pulse at 40 kHz for 200 ms (**A**) or 500 ms (**B**) with different pulse amplitudes: ◇: 2 V; ◇: 3 V; ■: 4 V; ▼: 5 V. Absolute impedance magnitudes were normalized to the last value before electroporation (A: 2 V: 10.78 kΩ; 3 V: 12.66 kΩ; 4 V: 10.12 kΩ; 5 V: 11.48 kΩ; B: 3 V: 10.15 kΩ; 4 V: 11.01 kΩ; 5 V: 11.30 kΩ). T = 37 °C.

[3] In order to prevent possible endocytotic dye uptake, the further development of the cell layer impedance was not monitored.

The results of this experiment are in accordance with previous observations. For electroporations applying pulse durations of 200 ms (Fig. 5.14 A) cell layer recovery is completed within roughly 1 h after pulsing for amplitudes of 2 – 4 V (◇, ◈, ■). The extent of the initial impedance increase after pulsing is amplitude dependent and more pronounced for lower amplitudes. After electric pulsing with an amplitude of 5 V (▼) for 200 ms no considerable recovery of the cell layer impedance is observed within the time of observation. Using pulse durations of 500 ms (Fig. 5.14 B), cell layer recovery is significantly retarded for amplitudes higher than 3 V (■ , ▼). 90 min after pulsing cell layer impedances remain below initial values (4 V: 0.93; 5 V: 0.84).

Taking into account dye loading as well as the impedimetric monitoring experiments, electric pulse parameters of $f = 40$ **kHz,** $U = 4$ **V and** $\tau = 200$ **ms** are found to be most suitable for efficient transfer of membrane-impermeable probes from the extracellular fluid into the cytoplasm of **Hep G2** cells grown on *8W1E* ECIS electrodes.

5.1.2.3 *In Situ* Electroporation of CHO Cells

Established cell layers of CHO cells grown on ECIS electrodes were pulsed for 200 ms and 500 ms with varying amplitudes between 1 V and 4 V in EBSS^{++} buffer supplemented with 250 kDa FITC-dextran (2 mg/ml) as the fluorescent probe. Corresponding confocal fluorescence micrographs of CHO cell layers after electroporation are presented in Fig. 5.15.

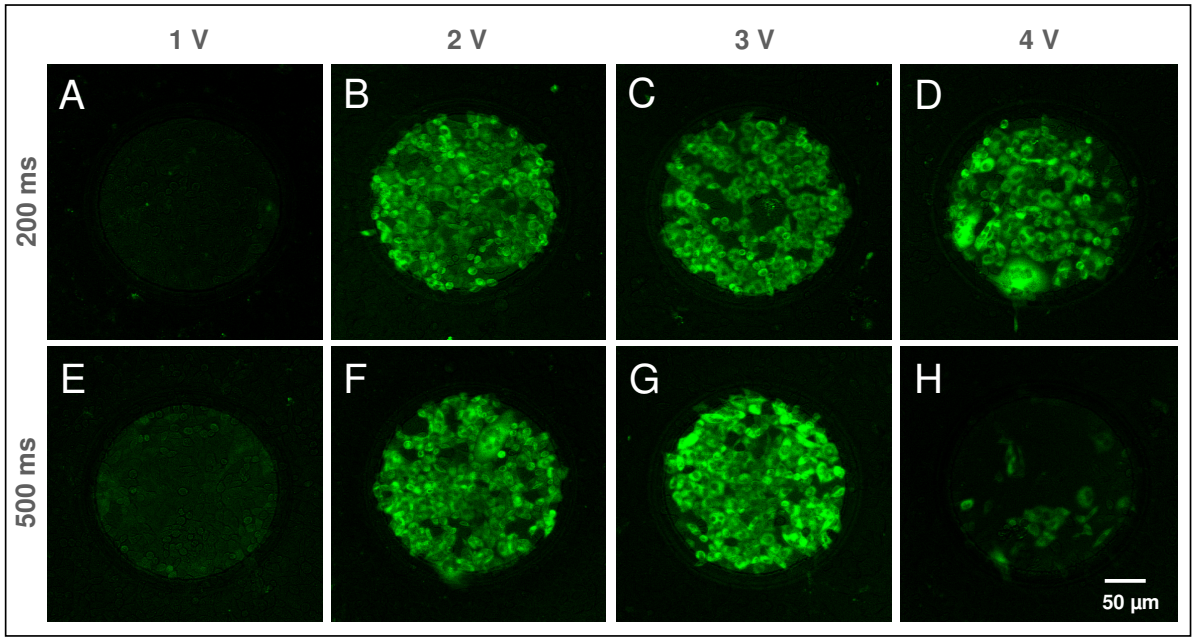

Fig. 5.15: Confocal fluorescence micrographs of **CHO** cells grown on *8W1E* ECIS electrodes after electroporation in EBSS^{++} with 250 kDa FITC-dextran (2 mg/ml). All cell layers were electroporated using an AC pulse of 40 kHz and discrete combinations of pulse parameters. **A:** 200 ms, 1 V; **B:** 200 ms, 2 V; **C:** 200 ms, 3 V; **D:** 200 ms, 4 V; **E:** 500 ms, 1 V; **F:** 500 ms, 2 V; **G:** 500 ms, 3 V; **H:** 500 ms, 4 V.

Whereas for amplitudes of 1 V hardly any cells on the electrode surface are stained using either pulse durations of 200 or 500 ms (A, E), cell layers pulsed with an amplitude of 2 V show reasonable dye uptake for almost all cells attached to the electrode surface (B, F). Dye loading is restricted to cells directly attached to the electrode surface. The number of cell layer defects is slightly increased for the longer pulse duration of 500 ms (F).
Similar dye uptake was observed after electroporation at 3 V and 4 V amplitudes for 200 ms duration (C, D). However, amplitudes of 4 V induced morphological alterations (D). Some cells near the rim of the electrode show an increased cell size with an enhanced number of nuclei, which remain dark due to dye exclusion by the nuclear envelope. Electroporation of CHO cells using a pulse duration of 500 ms shows similar results compared to using a 200 ms pulse duration when amplitudes of 1 V or 2 V are chosen (E, F). No cells are loaded with the FITC-dextran when using a 1 V pulse. A considerable dye loading is achieved for a 2 V pulse of 500 ms. Maximum dye loading efficiency is observed for the electric pulse parameter combination of 3 V and 500 ms (G). Higher amplitudes using the same pulse duration of 500 ms caused irreversible cell damage (H). Fluorescence images of CHO cell layers electroprated with pulse amplitudes of 5 V and 6 V are not presented, since dye loading efficiency was significantly reduced for these conditions. Nevertheless, these high pulse amplitudes are implemented in the following impedance measurements (Fig. 5.16).

The time course of the normalized impedance of ECIS gold-film electrodes covered with a monolayer of CHO cells before and after electroporation using pulses with amplitudes of 1 V – 6 V for 200 ms (A) and 500 ms (B) is presented in Fig. 5.16.

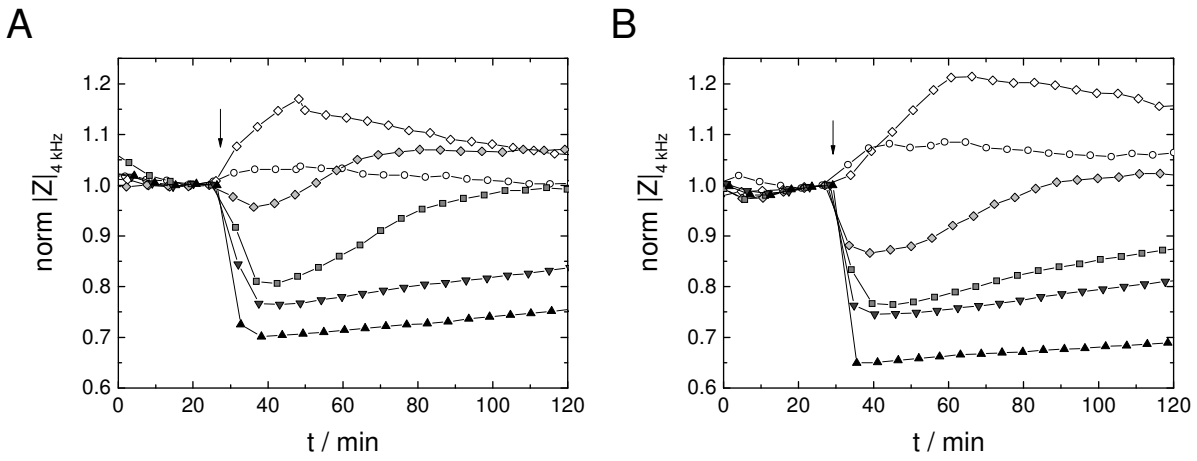

Fig. 5.16: Typical time course of the normalized impedance magnitude at 4 kHz before and after electroporation (arrow) of **CHO** cells grown on *8W1E* ECIS electrodes in EBSS^{++} with 250 kDa FITC-dextran (2 mg/ml). Cell layers were electroporated using an AC pulse at 40 kHz for 200 ms (**A**) or 500 ms (**B**) with different pulse amplitudes: ○: 1 V; ◇: 2 V; ◈: 3 V; ■: 4 V; ▼: 5 V; ▲: 6 V. Absolute impedance magnitudes were normalized to the last value before electroporation (A: 1 V: 8.33 kΩ, 2 V: 8.15 kΩ, 3 V: 9.30 kΩ, 4 V: 11.01 kΩ, 5 V: 11.20 kΩ, 6 V: 12.50 kΩ; B: 1 V: 7.98 kΩ, 2 V: 8.16 kΩ, 3 V: 10.36 kΩ, 4 V: 10.29 kΩ, 5 V: 11.23 kΩ, 6 V: 12.7 kΩ). T = 37 °C.

The impedimetric response of CHO cells after electric pulsing is strongly influenced by the pulse amplitude. Electroporations with pulse durations of 200 ms (A) provoke a significant

cellular response for amplitudes above 1 V. After a pulse with 2 V amplitude (◇) a transient impedance increase to 1.2 can be observed, whereas higher amplitudes cause a voltage dependent decrease of the cell layer impedance. After electroporations with 2 V (◇), 3 V (◇) or 4 V (■) the cell layer impedance recovers to or slightly above starting values within 40 – 90 min. For higher pulse amplitudes impedance magnitudes do not reach initial values within the time of observation, but remain on the level of 0.85 (5 V,▼) or 0.75 (6 V, ▲).
The time course of the normalized impedance after electroporation pulses of 500 ms duration shows parallels to the results presented for 200 ms pulses. However, using 500 ms pulses the extent of the immediate impedance changes after the electroporation pulse is more pronounced when comparing to pulses of the same amplitude, but a shorter pulse duration of 200 ms (A). The time required for complete cell layer recovery is longer when using pulses of 500 ms than for 200 ms. After electroporation with 3 V for 500 ms the cell layer impedance attains starting values within ~ 1 h. Again, impedance profiles for 5 V and 6 V pulses indicate cell death.

Best electroporation results for **CHO** cells on *8W1E* ECIS electrodes evaluated by dye loading efficiency and cell layer impedance recovery are obtained for electric pulse parameter combinations of f **= 40 kHz,** U **= 3 V and** τ **= 500 ms**. Satisfying results are also obtained for the three other combinations of 2 V and 200 ms, 2 V and 500 ms as well as 3 V and 200 ms.

5.1.2.4 *In Situ* Electroporation of NIH-3T3 Cells

Figure 5.17 shows dye loading experiments for established cell layers of NIH-3T3 fibroblasts grown on *8W1E* electrodes. Parameters for the electric pulses applied to load cells with 250 kDa FITC-dextran varied between amplitudes of 3 – 6 V and pulse durations of 200 ms (A – D) and 500 ms (E – H).
For pulses of 3 V and 200 ms almost all cells on the electrode surface are loaded with low concentrations of the fluorescent dye. The fluorescence intensity further increases when using amplitudes up to 6 V. Cells pulsed with amplitudes of 4 V exhibit their normal cell morphology, whereas for electroporation at 5 V polynucleated cells are observed (Fig. 5.17 I, J). Using a pulse amplitude of 6 V the major portion of cells on the electrode appears severely damaged (Fig. 5.17 D). Cell damage at higher amplitudes was even more pronounced using longer pulse durations of 500 ms (E – H). For low amplitudes cell layers show a typical cell morphology and appropriate loading with fluorescent dye, whereas for amplitudes of 5 V and 6 V severe cell damage occurs with increasing amplitudes (G, H). Several cells reveal a spherical morphology and a homogeneous distribution of the dye within the cytoplasm, showing no exclusion of the dye from the nucleus. Loading of NIH-3T3 cells with FITC-dextran is not restricted exactly to the area of the active electrode. Cells residing within a few micrometer beyond the electrode edge are loaded with the fluorescent probe as well (C, D, G, H). The amount of stained cells beyond the electrode border increases with increasing pulse amplitude (C → D; F → H).

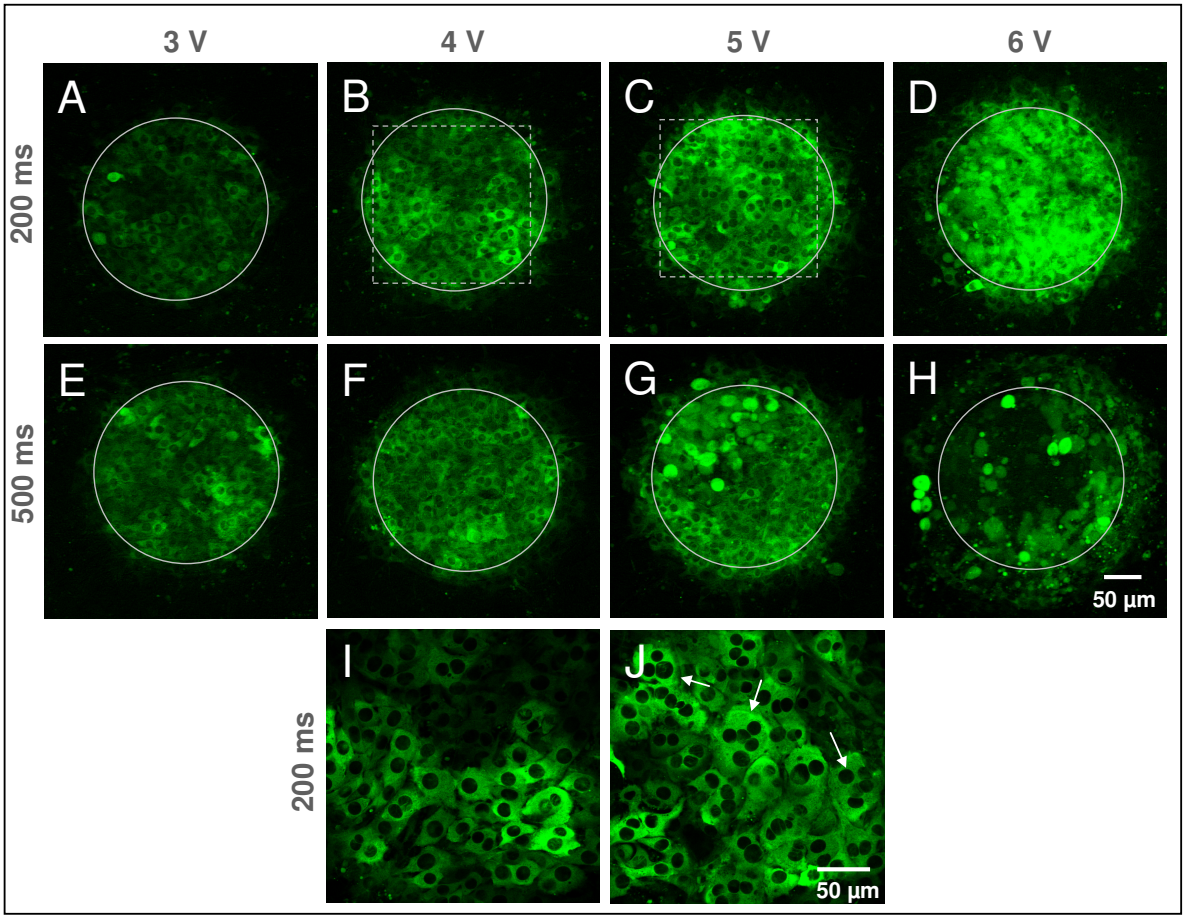

Fig. 5.17: Confocal fluorescence micrographs of **NIH-3T3** cells grown on *8W1E* ECIS electrodes after electroporation with 250 kDa FITC-dextran (2 mg/ml) in EBSS^{++}. Cell layers were electroporated using an AC pulse at 40 kHz for 200 or 500 ms and different pulse amplitudes: **A:** 200 ms, 3 V; **B:** 200 ms, 4 V; **C:** 200 ms, 5 V; **D:** 200 ms, 6 V; **E:** 500 ms, 3 V; **F:** 500 ms, 4 V; **G:** 500 ms, 5 V; **H:** 500 ms, 6 V. Electrode areas are delineated by white circles. **I** and **J** show magnifications of those areas indicated by dashed boxes in B and C, taken with a 63 × water objective.

Figure 5.18 presents the time course of the normalized impedance magnitude for established NIH-3T3 cell layers before and after electroporation in EBSS^{++} with FITC-dextran. The cell layer response after electroporation with pulses of 3 – 6 V amplitude and 200 ms or 500 ms durations was investigated.

Instantaneously after application of an electric pulse of any parameter combination the cell layer impedance of NIH-3T3 cells drops below initial base line values. For pulse durations of 200 ms the magnitude of impedance decrease is basically dependent on the amplitude (Fig. 5.18 A). With increasing pulse amplitudes the normalized impedance initially drops to values of 0.9 (3 V, ◇), 0.8 (4 V, ■), 0.85 (5 V, ▼) or 0.65 (6 V, ▲). Also the time required for cell layer recovery to pre-pulse values rises with increasing pulse amplitudes. For amplitudes of 3 V and 4 V initial impedance values are attained within roughly 40 min. After electroporation with an amplitude of 5 V the impedance increases even above base line values and settles at about 1.2. After pulsing a NIH-3T3 cell layer with 6 V the impedance does not fully recover within the observation time. This incomplete cell layer recovery measured impedimetrically corresponds to the microscopic observations (Fig. 5.17 D).

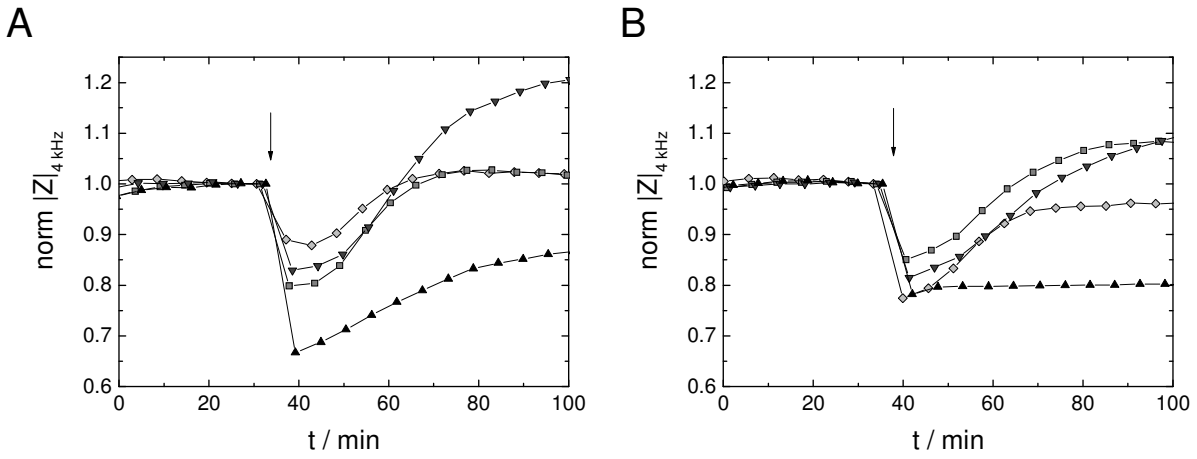

Fig. 5.18: Typical time course of the normalized impedance magnitude at 4 kHz before and after electroporation (arrow) of **NIH-3T3** cells grown on *8W1E* ECIS electrodes in EBSS^{++} with 250 kDa FITC-dextran (2 mg/ml). Cell layers were electroporated using an AC pulse at 40 kHz for 200 ms (**A**) or 500 ms (**B**) with different pulse amplitudes: ◇: 3 V; □: 4 V; ▼: 5 V; ▲: 6 V. Absolute impedance magnitudes were normalized to the last value before electroporation (A: 3 V: 9.5 kΩ; 4 V: 10.8 Ω; 5 V: 9.6 kΩ; 6 V: 11.5 kΩ; B: 3 V: 7.5 kΩ; 4 V: 8.9 kΩ; 5 V: 9.2 kΩ; 6 V: 9.7 kΩ). T = 37 °C.

Using a higher pulse duration of 500 ms (Fig. 5.18 B), the relation between the applied pulse amplitude and the extent of the subsequent impedance drop is not as pronounced as for 200 ms pulses. However, the time courses of cell layer recovery show similar results as those reported for 200 ms pulses. Recovery of cell layer impedance almost reaching initial base line values is obtained after electroporation with 3 V. For 4 V and 5 V pulses impedance values slightly rise above starting values, whereas for an amplitude of 6 V no impedance increase can be detected after pulse application, as also confirmed by corresponding fluorescent micrographs (cp. Fig. 5.17 E – H). This impedance profile (▲) indicates cell death.

Subsuming the results from dye loading and impedimetric studies pulse parameters of **f = 40 kHz, U = 4 V and τ = 200 ms** provide an optimal transfer of membrane-impermeable probes from the extracellular fluid into the cytoplasm of NIH-3T3 cells grown on *8W1E* ECIS electrodes. A similar loading efficiency is obtained using the parameter combination 500 ms and 3 V.

5.1.2.5 Survey of Electroporation Parameter Combinations for Different Cell Types

Survey of optimal electric pulse parameter combinations for the electroporation of NRK, HEK-293, Hep G2, CHO and NIH-3T3 cells grown on *8W1E* ECIS electrodes is shown in Fig. 5.19. Results are presented by fluorescent micrographs documenting dye loading efficiency as well as the corresponding impedance measurements monitoring the cell layer response and recovery after electroporation using these optimized pulse parameter combinations. This comprehensive presentation points out cell type specific differences in cell layer response after electric pulsing as is mirrored by impedance monitoring. The cell layer impedance after electroporation either transiently (1) decreases (NRK, CHO, NIH-3T3),

(2) increases (HEK-293) or (3) first increases and subsequently decreases (Hep G2), before pre-pulse values are reached. For all cell types considerable dye uptake could be achieved when using the proper electroporation conditions. Optimal parameter combinations of pulse amplitude and duration are found to be similar for different cell lines. Using an AC frequency of 40 kHz, best loading results were obtained for 4 V and 200 ms (NRK, HEK-293, Hep-G2, NIH-3T3) or 3 V and 500 ms (CHO).

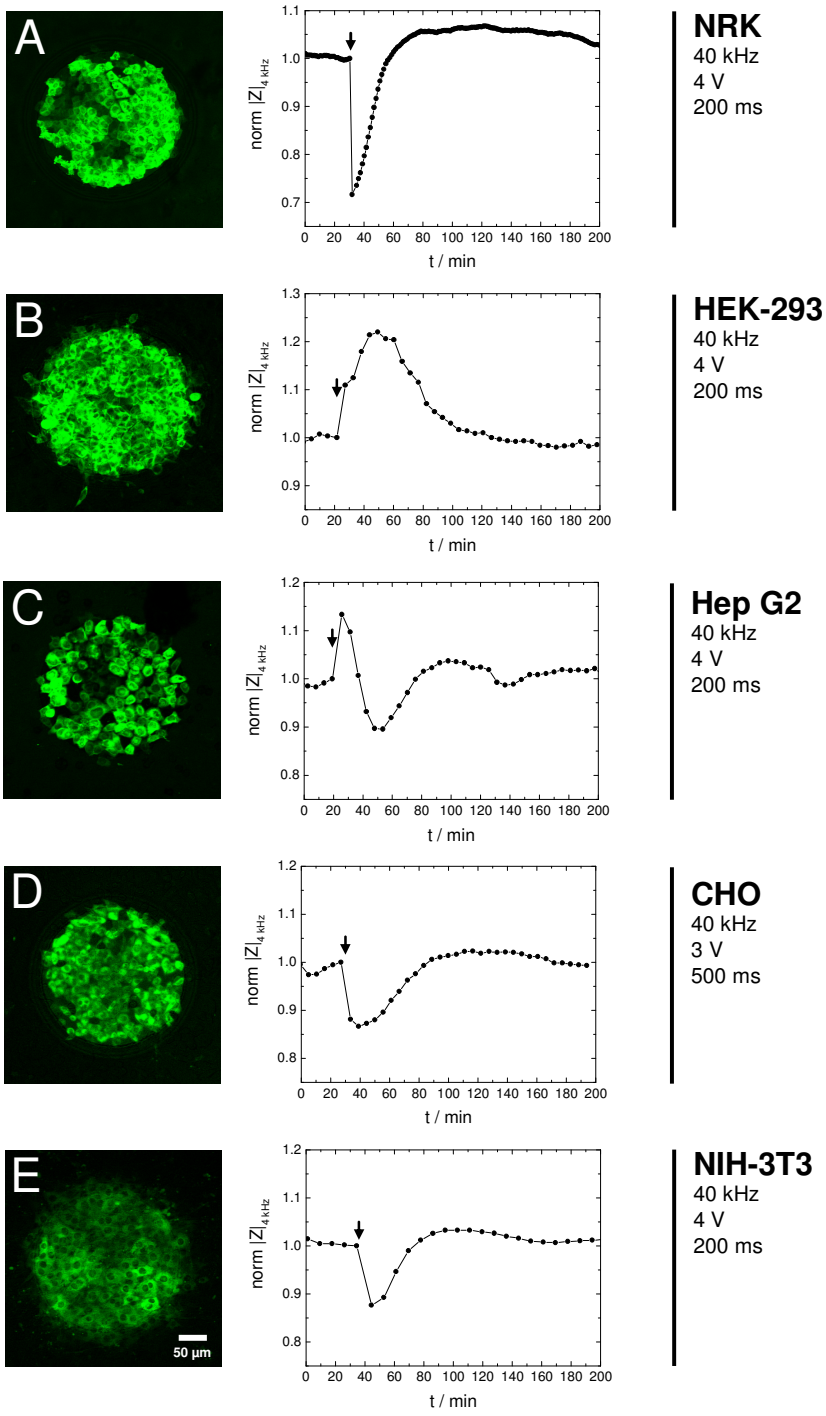

Fig. 5.19: Survey of optimized electric pulse parameter combinations for efficient electroporation of different cell types grown on *8W1E* ECIS electrodes presented by confocal fluorescence micrographs after electroporation in presence of 250 kDa FITC-dextran (left) and the time courses of the normalized impedance magnitude before and after electroporation (right). All cell layers were pulsed (arrow) at 40 kHz using the optimized combination of pulse amplitude and duration. **A: NRK;** 4 V, 200 ms; **B: HEK-293;** 4 V, 200 ms; **C: Hep G2;** 4 V, 200 ms; **D: CHO;** 3 V, 500 ms; **E: NIH-3T3;** 4 V, 200 ms.

5.1.3 Kinetics of Electroporation-Mediated Uptake of High Molecular Mass Probes

The way of electroporation-mediated uptake of high molecular, membrane-impermeable probes by mammalian cells is still discussed in the literature. Whereas for low molecular probes of a few kDa facilitated diffusion across membrane defects is assumed, the mechanism for the transfer of high molecular probes is not clear yet. Rather indirect uptake mechanisms like electrostimulated endocytosis are considered for the field-mediated uptake of macromolecules instead of direct diffusive transfer. Critical parameters being discussed in this context are the size of electroporation induced membrane defects available for diffusion and the time required for membrane resealing, which is supposed to take place within several seconds.
Thus, the dye loading process and the time course of impedance readings during the first seconds immediately after electroporation were investigated using experimental approaches providing a high time resolution in the order of seconds (cp. chapter 4.3.1.2; 4.4.3.1).

5.1.3.1 Dye Uptake Kinetics

Dye uptake kinetics during *in situ* electroporation were studied by time-lapse confocal microscopy. Using a self-developed setup that allows to combine electric pulse application and time-resolved fluorescence microscopy (cp. chapter 4.4.3.1), a confluent NRK cell layer was electroporated at standard conditions (40 kHz, 4 V, 200 ms) in presence of 250 kDa FITC-dextran in the extracellular fluid. A sequence of confocal xy-sections was recorded from the center of the cell bodies every three seconds (Fig. 5.20).
Before pulse application the membrane-impermeable fluorescent dye fills the extracellular spaces, but the cell interior remains unlabeled (Fig. 5.20 A). Within three seconds after an electric pulse of 40 kHz, 4 V and 200 ms, the dye enters the cytoplasm of the cells (B). During the following 9 s no further dye uptake, as it would be indicated by increasing fluorescence intensity, is observed (C, D). Due to its molecular size the FITC-dextran remains excluded from the cell nuclei. The intracellular dye is not in a concentration-equilibrium with the dye in the extracellular spaces, which is indicated by the lower fluorescence intensity of the cellular interior compared to that of the extracellular spaces. This observation supports complete membrane resealing for the 250 kDa probe within a few seconds after pulse application.

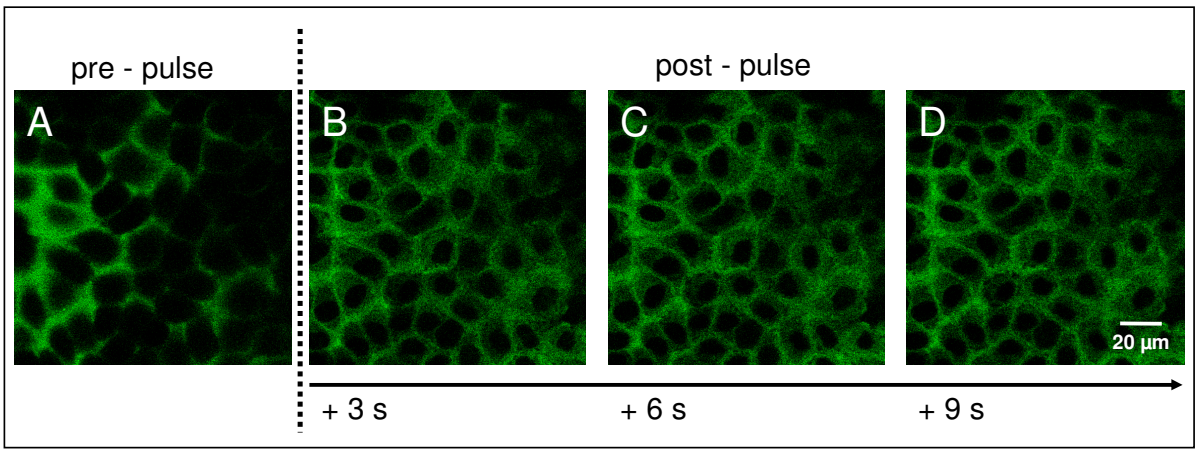

Fig. 5.20: Confocal fluorescence microscopic xy-sections from within an NRK cell layer grown on a *8W1E* ECIS gold-film electrode before (**A**) and after (**B – D**) a membrane permeabilizing pulse of 200 ms and 4 V at 40 kHz. Images are taken 3 s (**B**), 6 s (**C**) and 9 s (**D**) after electroporation. Cells are incubated with an extracellular dye solution of 2 mg/ml FITC-dextran (250 kDa) in $EBSS^{++}$ buffer.

5.1.3.2 Impedimetric Monitoring of the Morphological Cell Response with High Time Resolution

ECIS recordings with high time resolution enable a more detailed look into the kinetics of the impedance time course, which mirrors the cell layer morphological response induced by a transient membrane permeabilizing pulse plus the membrane permeabilization itself. A confluent NRK cell layer was electroporated at 40 kHz, 4 V for 200 ms. Before and after application of the electric pulse the cell layer impedance at 4 kHz was recorded with a time resolution of approximately 500 ms (Fig. 5.21). The time of the last data point before electric pulsing was set to zero. For application of the electroporation pulse electrodes were connected to the frequency generator (FG) by a manual switch (cp. chapter 4.3.1.2). Since the impedance measurement was continued during pulse application without contact to the cell-covered electrode, this resulted in an immediate impedance increase to infinite values for a period of roughly 2 seconds (asterisks and grey shaded box in C). Data acquisition of the cell layer was resumed immediately after electroporation by switching back to the impedance analyzer (IA). Measurements without pulse application proved that manual switching between the IA and the FG does not affect cell layer impedance measurements (not shown).

Figure 5.21 A presents the characteristic response of an NRK cell layer after electroporation at 4 V for 200 ms with improved time resolution. The curve shows an immediate impedance drop, a subsequent steep increase to a transient plateau, followed by a second but much longer lasting decrease and a final recovery of pre-pulse values with a lower time constant, indicating a multistep process.

Zooming in on the first 10 min of post-pulse response provides a more detailed look to the first minutes of the overall cellular response. Immediately after electric pulsing the normalized impedance drops to 0.55 and recovers to about 0.9 within a few seconds. This process is followed by a second, much slower impedance decrease to 0.7. About 10 min after electroporation the impedance then increases again (A).

The first 10 s of the cell layer response are illustrated in Fig. 5.21 C. However, technical limitations leave a gap (shaded box) of data recording of maximal 2 s representing the time necessary for switching between IA, FG and back, as required for pulse application. The exact onset of the 200 ms pulse resides in the middle of the data gap.

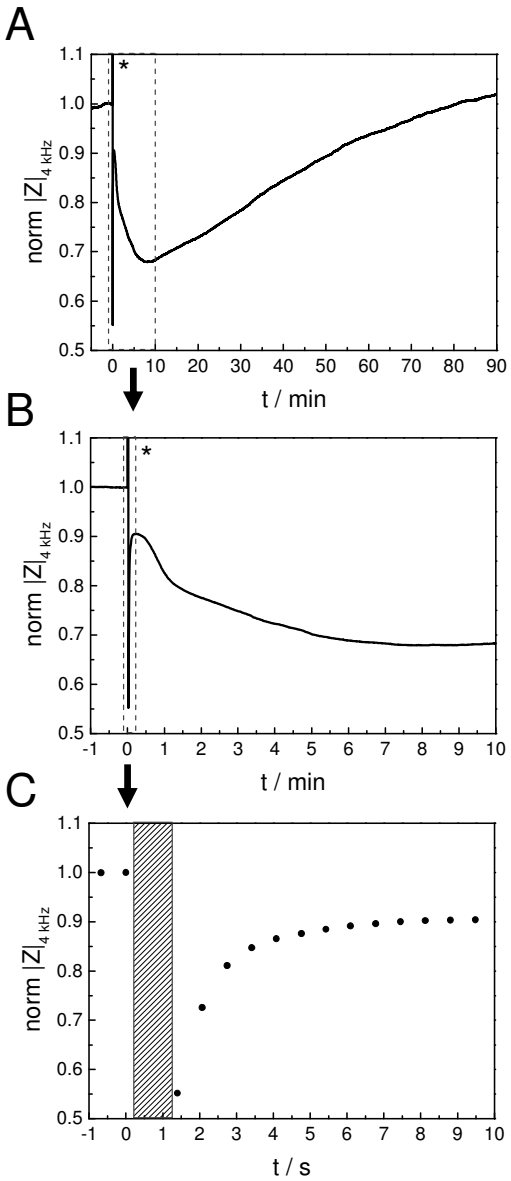

Fig. 5.21: Time course of the normalized impedance magnitude at 4 kHz recorded with high time resolution for an NRK cell layer grown on an *8W1E* ECIS electrode before and after electroporation at 40 kHz with 4 V for 200 ms in different magnifications: **A:** 90 min; **B:** 10 min; **C:** 10 s. The time immediately before pulse application was set to zero (t = 0). Absolute impedance magnitudes were normalized to the last value before electroporation (15.70 kΩ). Data acquisition was disconnected for pulse application (*, ▨). T = 37 °C.

The multiphasic time course suggests that several overlapping processes take place. The response on the longer time scale lasting roughly one hour till pre-pulse impedance recovery can be ascribed to major morphological alterations in the cell layer (Fig. 5.21 A). In contrast, the initial impedance drop and fast increase in the first seconds might be interpreted as (i) the permeabilization of the membrane enabling increased current flow directly across the cell bodies followed by (ii) the resealing of the membrane towards ion flow (Fig. 5.21 C).

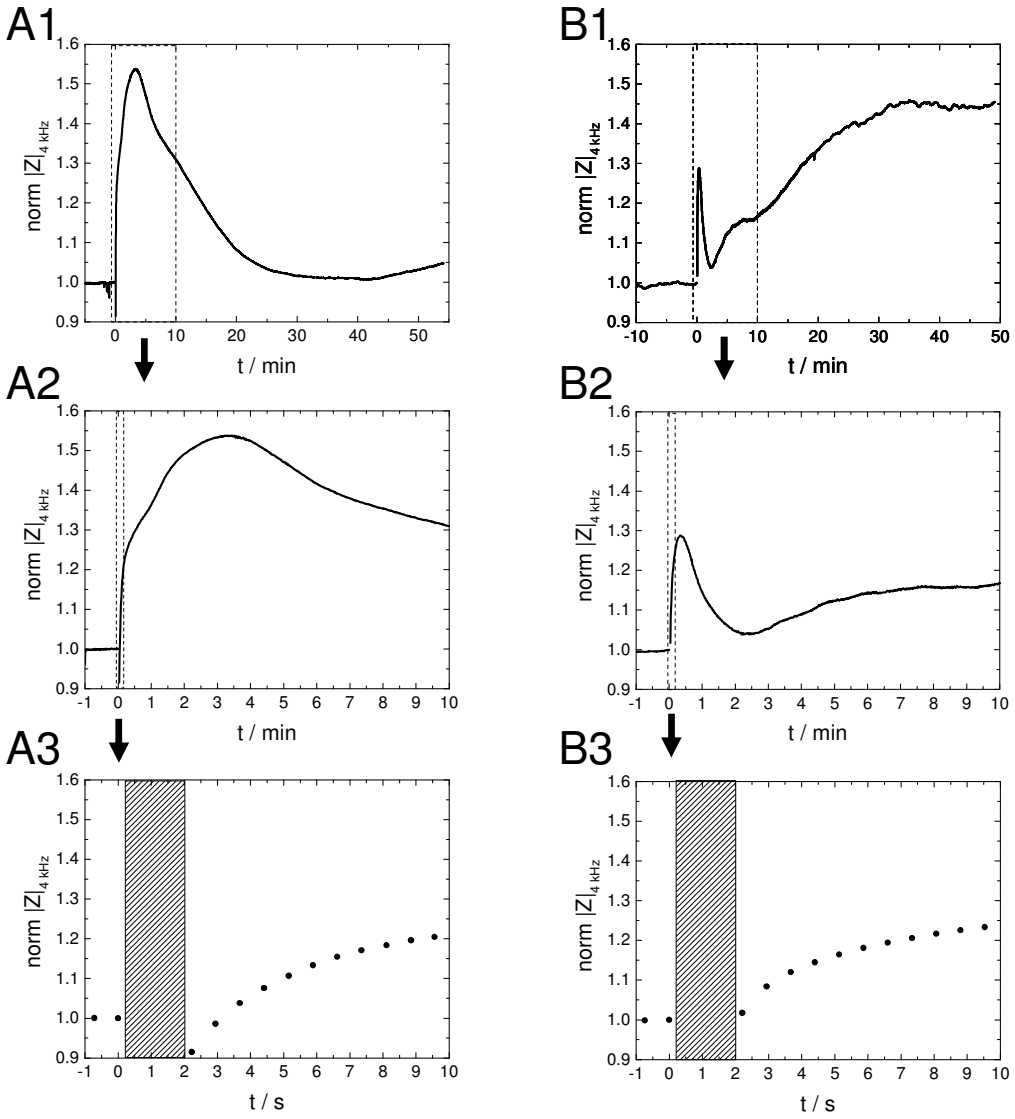

Fig. 5.22: Time course of the normalized impedance magnitude at 4 kHz with high time resolution for **Hep G2** (**A**) and **HEK-293** (**B**) cells grown on *8W1E* electrodes before and after electroporation at 40 kHz with 4 V in different magnifications: **1:** ~ 50 min; **2:** 10 min; **3:** 10 s. The time immediately before pulse application was set to zero (t = 0). Absolute impedance magnitudes were normalized to the last value before electroporation (Hep G2: 10.20 kΩ; HEK-293: 9.83 kΩ). Data acquisition was disconnected for pulse application (▨). T = 37 °C.

However, this initial impedance drop after pulse application could not be detected for all cell lines. The initial drop was less pronounced after electroporation of Hep G2 cells (Fig. 5.22 A1 – 3) and no impedance decrease was detected after electroporation of HEK-293 cells (Fig. 5.22 B1 – 3). Again, the cell type specific morphological responses within the cell layer after electroporation become apparent in this time-resolved measurements, also revealing multistep responses for these cell types (Fig. 5.22 A1, A2; B1, B2).

In the following experiments only the secondary morphological response is considered and how this is changed when selected extracellular molecules are introduced into the cytoplasm.

5.1.4 Electroporation of Subconfluent Cell Layers

To date, only confluent cell layers grown on ECIS electrodes have been loaded with membrane impermeable probes by electroporation. Since it might be favorable for certain applications, e.g. transfection, to use subconfluent cell layers the question arose, if it is possible to permeabilize and load non-confluent cell patches or cell islets by ECIS-based *in situ* electroporation as well.

Therefore cells were seeded at various densities ranging from 100 000 to 425 000 cells/cm^2 about 15 h before electroporation corresponding to ~ 20 % – 80 % of confluence when an electroporation experiment was started (Fig. 5.23). The electrode coverage was roughly estimated by phase contrast microscopy and electrode capacitance measurements at 40 kHz, since the capacitance is linearily correlated with electrode surface coverage (cp. chapter 5.1, Wegener et al., 2000a). $C_{40\,\mathrm{kHz}}$ ranges from ~ 4.5 – 5 nF for cell-free ECIS electrodes to slightly below 1 nF for NRK cell-covered electrodes. Estimates for electrode coverage and capacitance values at 40 kHz before electroporation are given in the figure caption. The cells were pulsed with standard conditions of 40 kHz, 4 V and 200 ms in presence of 250 kDa FITC-dextran. The impedance before and immediately after pulse application was monitored at 4 kHz and compared to the response of a fully established cell layer (Fig. 5.23).

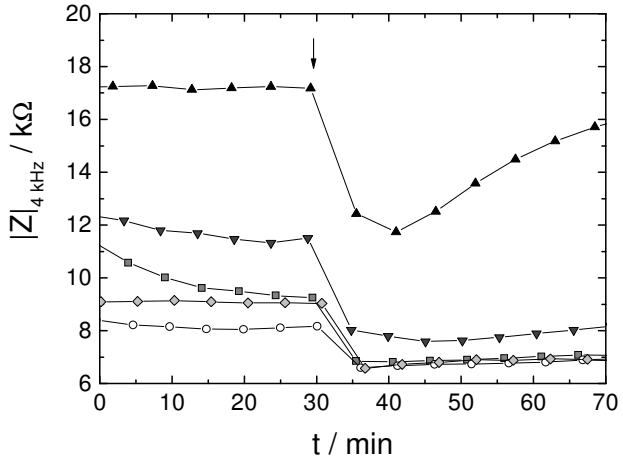

Fig. 5.23: Time course of the impedance magnitude at 4 kHz before and after electroporation of subconfluent NRK cell layers seeded at different cell densities and cultivated for 15 h on *8W1E* ECIS electrodes. Cells were pulsed at 40 kHz and 4 V for 200 ms (arrow). The time course of impedance before and after electroporation of a confluent cell layer seeded at a density of 250 000 cells/cm^2 and cultivated for 60 h is added to the graph for comparison (▲). Cell densities and the resulting electrode coverage, roughly estimated from electrode capacitances at 40 kHz were: ○: 100 000 cells/cm^2, ~ 50 % ($C_{40\,\mathrm{kHz}}$ = 2.99 nF); ◇: 200 000 cells/cm^2, ~ 70 % ($C_{40\,\mathrm{kHz}}$ = 2.36 nF); □: 250 000 cells/cm^2, ~ 75 % ($C_{40\,\mathrm{Hz}}$ = 2.16 nF); ▼: 425 000 cells/cm^2, ~ 90 % ($C_{40\,\mathrm{kHz}}$ = 1.43 nF); ▲: 250 000 cells/cm^2, 100 % ($C_{40\,\mathrm{kHz}}$ = 0.89 nF).

Whereas the confluent cell layer recovers from the electroporation pulse at 4 V and 200 ms as indicated by an impedance increase towards pre-pulse values (▲), for non-confluent cell layers no significant impedance increase after electric pulse application can be detected (○, ◇, □, ▼). Phase contrast micrographs reveal severe damage of cells on the electrode as well as and altered cell morphology (Fig. 5.24 A1 – D1). Only few cells, which are often found at the rim of the electrode, are able to retain the fluorescent dye within their cytoplasm (A2, B2, C2, arrows →). Cells adhering to the insulating polymer beyond the active electrode area

show a slight fluorescence in the cytoplsm, which might be attributed to background auto-fluorescence or unspecific endocytotic uptake (D2, ····►).

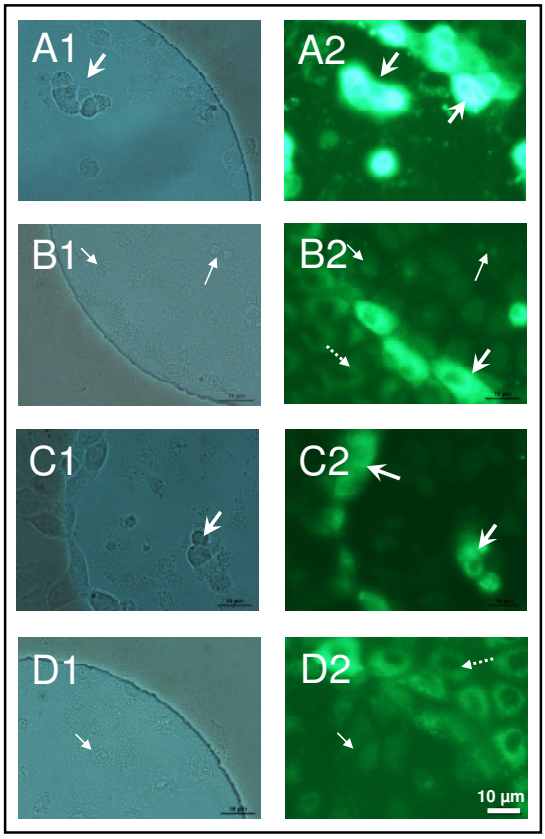

Fig. 5.24: Phase contrast (**1**) and epifluorescent (**2**) micrographs of subconfluent NRK cell layers after electroporation. NRK cells were seeded at different densities 15 h before electroporation, resulting in an electrode coverage, roughly estimated from electrode capacitances at 40 kHz: **A:** 425 000 cells/cm^2, ~ 90 %; **B:** 250 000 cells/cm^2, ~ 75 %; **C:** 200 000 cells/cm^2, ~ 70 %; **D:** 100 000 cells/cm^2, ~ 50 %;. Cells were electroporated using an AC pulse at 40 kHz and 4 V for 200 ms in EBSS^{++} with 250 kDa FITC-dextran (2 mg/ml). Images present only parts of the electrode surface and the adjoining insulating polymer. Arrows indicate dye loaded cells (⟶) or dead cells (⟶) on the electrode or autofluorescence of cells on the photopolymer (····►). Micrographs were taken using the Nikon Eclipse 90i epi-fluorescence equipment and a 60 × water immersion objective.

Obviously, pulse conditions optimized for fully established cell layers are too invasive for subconfluent cell layers. Therefore, suitable electroporation parameters for subconfluent cells needed to be determined in a first approach, monitoring the impedance at 4 kHz for varying amplitudes (Fig. 5.25). Amplitudes ranging from 0.5 V to 3 V were applied at a pulse duration of 200 ms and a frequency of 40 kHz.

After electroporation with an amplitude of only 0.5 V (○) no impedance decrease can be detected, whereas electroporation voltages of 1 and 2 V (◇, ◆) result in an impedance drop to 0.94 and 0.79, respectively. Afterwards, the normalized impedance increases and reaches almost pre-pulse values. If a voltage of 3 V (●) is chosen to permeabilize subconfluent cells, no significant impedance recovery is detected after an initial impedance drop to below 0.7. Since subconfluent cell layers completely recovered from electroporations with voltages of 1 V or 2 V (Fig. 5.25), dye loading experiments were carried out using these amplitudes. Cells

were seeded in densities varying from ~ 100 000 to 500 000 cells/cm^2 15 h before starting the experiment. Resulting confocal fluorescence images are presented in Fig. 5.26.

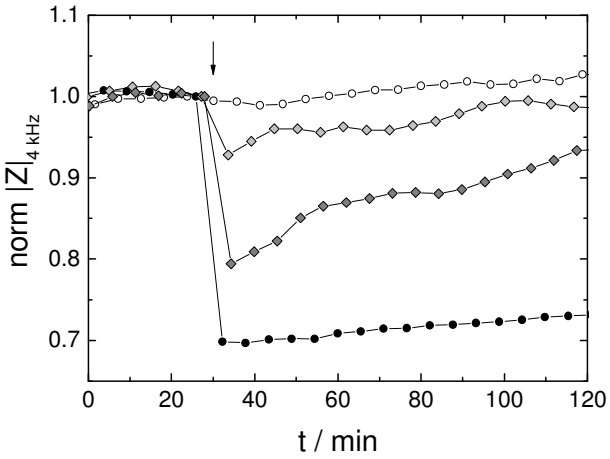

Fig. 5.25: Time course of the normalized impedance magnitude at 4 kHz for subconfluent NRK cell layers before and after electroporation. Cells were seeded in a density of 100 000 cells/cm^2 and cultivated on *8W1E* ECIS electrodes for 15 h resulting in an electrode coverage of ~ 35 – 60 % at the time point of the experiment. Cells were electroporated (arrow) using an AC pulse at 40 kHz for 200 ms with varying amplitudes: ○: 0.5 V; ◇: 1 V; ◈: 2 V; ●: 3 V. Absolute impedance magnitudes were normalized to the last value before electroporation (0.5 V: 9.11 kΩ; 1 V: 11.81 kΩ; 2 V: 10.35 kΩ; 3 V: 9.72 kΩ). T = 37 °C.

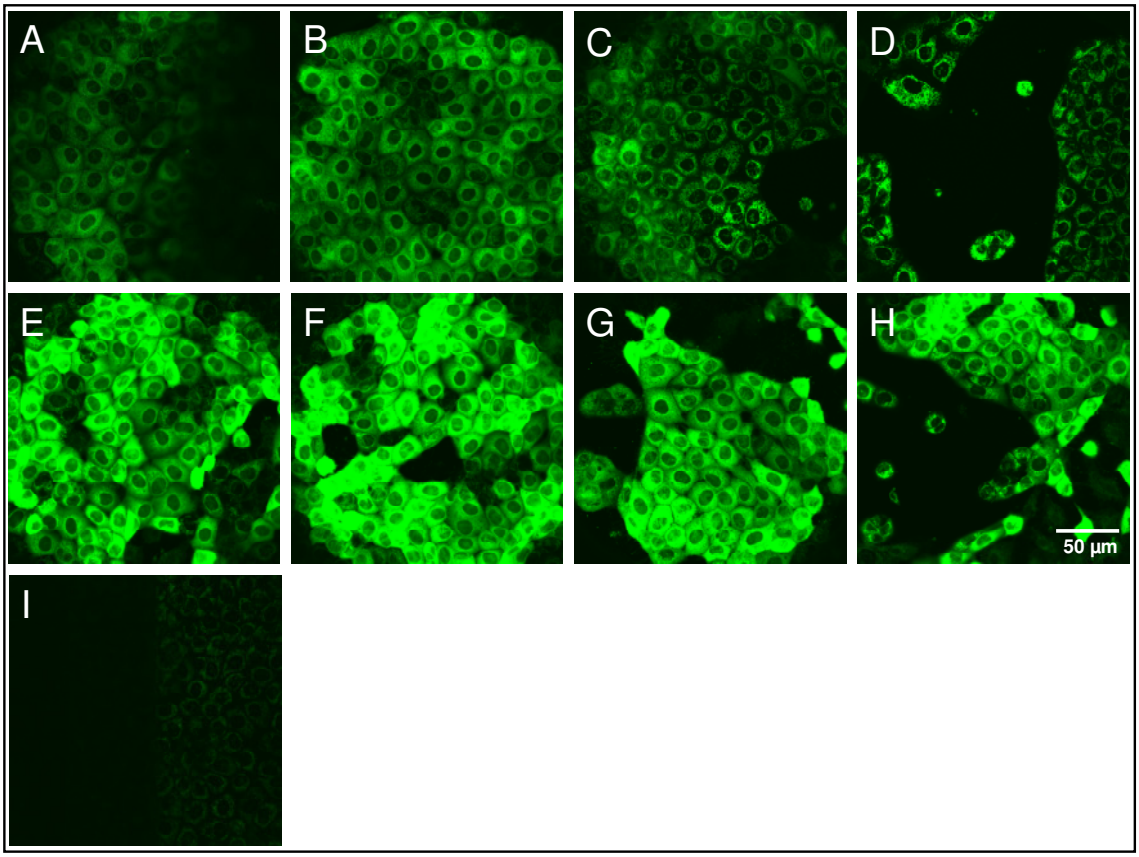

Fig. 5.26: Confocal fluorescence micrographs of subconfluent NRK cell layers grown on *8W1E* ECIS electrodes after electroporation at 40 kHz for 200 ms and 1 V (**A** – **D**) or 2 V (**E** – **H**) in the presence of 250 kDa FITC-dextran in EBSS^{++} (2 mg/ml). Cells were seeded at various densities and cultivated for 15 h before electroporation: **A**, **E:** 500 000 cells/cm^2; **B**, **F:** 250 000 cells/cm^2; **C**, **G:** 200 000 cells/cm^2; **D**, **H:** 100 000 cells/cm^2. **I:** Control cells (left: cells on insulating polymer, right: cells on counter electrode) were incubated in presence of FITC-dextran but were not electroporated.

Cell layers of decreasing seeding intensity (from left to right) shown in the upper panel were pulsed with 1 V (A – D). Compared to the non-electroporated control cell layer (I) cells on the electrode can be loaded with the fluorescent probe. However, the fluorescence intensity is not as high as observed for cell layers electroporated with a pulse amplitude of 2 V (E – H). Within the cell layer established from the lowest seeding density some cells seem to be damaged (H). Despite varying cell densities on the electrode surface before electroporation, dye loading efficiencies are similar. Differences in cell density can be verified by phase contrast microscopy (not shown) or impedance measurements (Fig. 5.27). Moreover, impedance measurements assured complete cell recovery for most cell layers after electroporation.

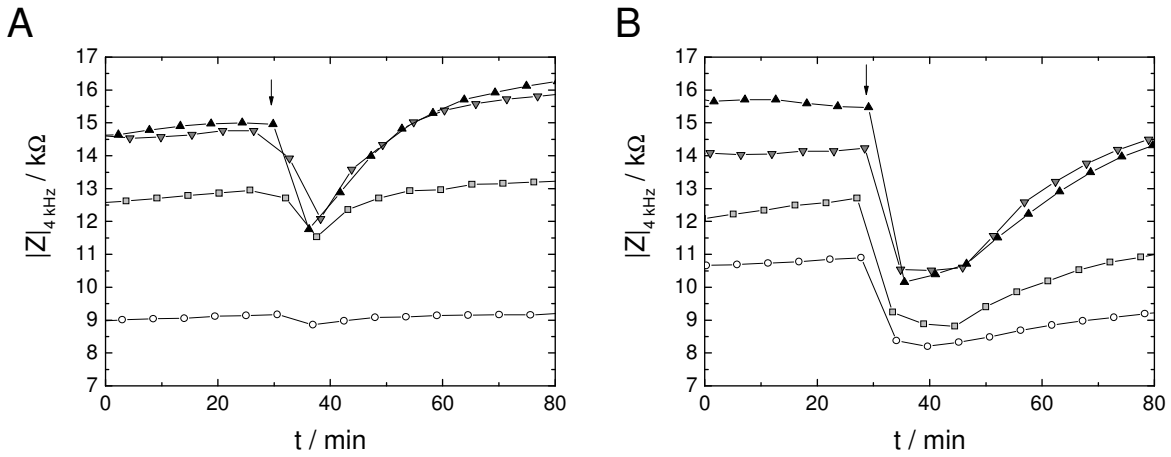

Fig. 5.27: Time course of the impedance magnitude at 4 kHz for subconfluent NRK cell layers grown on *8W1E* ECIS electrodes before and after electroporation (arrow) at 40 kHz for 200 ms and **A: 1 V** or **B: 2 V**. Cells were seeded at different densities and were cultivated for 15 h before electroporation. Electrode capacitances at 40 kHz give an estimate for electrode surface coverage after 15 h of cultivation. ○: 100 000 cells/cm^2, A: 3 nF, ~ 35 %; B: 2.2 nF, ~ 60 %; ■: 200 000 cells/cm^2, A: 1.5 nF, ~ 80 %, B: 1.5 nF, ~ 80 %; ▼: 250 000 cells/cm^2, A: 0.94 nF, ~ 95 %, B: 0.93 nF, ~ 95 %; ▲: 500 000 cells/cm^2, A: 0.86 nF, ~ 100 %; B: 0.87 nF, ~ 100 %.

After electroporation with 1 V the impedance recovers to initial values within 30 min for all cell densities (Fig. 5.27 A). The impedance drop observed immediately after pulsing as well as the time needed for complete recovery is dependent on the pre-pulse impedance magnitude. The higher the initial impedance of the cell layer , the more pronounced is the impedance drop after electroporation. The impedance dropped by ~ 2.5 kΩ for cell layers with ~ 95 % (▼) and 100 % (▲) electrode coverage but only by ~ 1.5 kΩ for the electrode covered by ~ 80 % (■) with cells. Cell layers showing ~ 95 – 100 % electrode coverage (▼, ▲) take about 50 min for complete impedance recovery to pre-pulse values. Only 20 min recovery time are required when cells cover ~ 80 % (■) of the surface at the time of pulse application. The impedance drop for the cell layer of lowest electrode coverage is negligible (○).

Subconfluent cell layers electroporated with a voltage of 2 V (Fig. 5.27 B) recover from the electric pulse almost to pre-pulse values when seeded at densities of 250 000 and 500 000 cells/cm^2 (▼, ▲). For lower cell densities the degree of impedance recovery is decreased (○, ■). The impedance of the cell layer electroporated at ~ 80 % cell coverage (■) remains ~ 1 kΩ below pre-pulse values 50 min after electroporation, while the impedance for the cell density of 100 000 cells/cm^2 (~ 60 %) is ~ 1.5 kΩ below pre-pulse values.

These results present that it is possible to load subconfluent cell layers with extracellular probes, although the optimal electroporation parameters change. Subconfluent NRK layers covering more than ~ 60 % of the *8W1E* ECIS electrode surface area can be loaded with FITC-dextran using a pulse of f = **40 kHz,** U = **2 V and** τ = **200 ms**. However, all experiments with NRK cells presented in the following chapters use confluent cell layers, which require pulses of f **= 40 kHz,** U **= 4 V and** τ **= 200 ms**.

5.2 Electroporation-Mediated Loading of Adherent Cells with Cytotoxic Substances and Monitoring of their Cell Death Response

Since the substrate-integrated electrodes can be easily used for both – loading of cells by electroporation and analysis of cellular responses by impedance monitoring – it should be possible to detect cell responses which are induced by electroporation-mediated uptake of bioactive substances.

Binding and inhibition of certain functions or structures inside the cell is an essential approach in fundamental research and applied medicine. A biochemical or medical application of many bioactive compounds is, however, often limited by their inability to cross the cell membrane. Thus, there is still a strong driving force to find efficient methods for the transfer of bioactive compounds across the membrane.

This section demonstrates the transfer of bioactive, cytotoxic probes across the cell membrane by *in situ* electroporation and the impedimetric detection of cell death induced by their intracellular activity. Three compounds with intracellular cytotoxic activity from different chemical classes were chosen: the very small inorganic azide ion, bleomycin, a complex glycopeptide antibiotic isolated from *Streptomyces verticillus*, and the small mammalian intracellular protein cytochrome c.

5.2.1 Loading of NRK Cells with Azide

The azide ion is known to inhibit the mitochondrial cytochrome oxidase of the respiratory chain complex IV, resulting in energy depletion of the cells (Keilin, 1936; Eytan et al., 1975). The toxic effect of NaN_3 on different cells has been reported by various authors (Sato et al., 2008) and is described to induce necrosis (Bal-Price et al., 1999; Frankfurt and Krishan, 2001) or apoptosis (Chen et al., 1998; Wang et al., 2004). Azide itself has a quite low intrinsic membrane permeability and it has been shown that the toxicity of azide can be significantly enhanced when the plasma membrane barrier is bypassed using experimental methods (Raicu and Mixich, 1992).

Figure 5.28 shows the response of NRK cells to the incubation with different concentrations of sodium azide (A) and after cytoplasm delivery by *in situ* electroporation (B). The cell response is monitored by time-resolved impedance readings at 4 kHz.

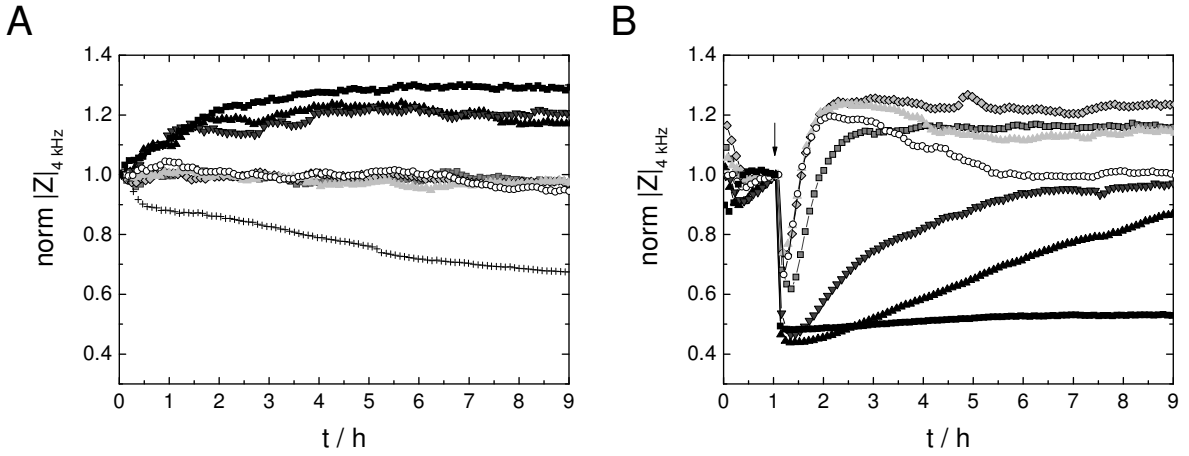

Fig. 5.28: Time course of the normalized impedance magnitude at 4 kHz upon incubation (**A**) or before and after electroporation (40 kHz, 4 V, 200 ms; arrow) (**B**) of NRK cells grown on *8W1E* ECIS electrodes in presence of different concentrations of sodium azide (NaN_3) in $EBSS^{++}$: ○: 0 mM; ▲: 0.1 mM; ◇: 0.5 mM; □: 1.5 mM; ▼: 5 mM; ▲: 15 mM; ■: 50 mM; +: 150 mM. Absolute impedance magnitudes were normalized to the first value of the measurement at t_0 in A (0 mM: 16.3 kΩ; 0.1 mM: 17.15 kΩ; 0.5 mM: 17.52 kΩ; 1.5 mM: 17.79 kΩ; 5 mM: 15.49 kΩ; 15 mM: 15.93 kΩ; 50 m: 14.09 kΩ; 150 mM: 10.71 kΩ) or to the last value before electroporation in B (0 mM: 19.45 kΩ; 0.1 mM: 16.52 kΩ; 0.5 mM: 18.72 kΩ; 1.5 mM: 16.69 kΩ; 5 mM: 17.68 kΩ; 15 mM: 16.2 kΩ; 50 mM: 14.33 kΩ). T = 37 °C.

The very small azide anion does not significantly alter cell layer impedance when cells are merely incubated with the respiratory chain inhibitor present in a physiological medium in concentrations up to 1.5 mM (▲, ◇, □) (Fig. 5.28 A). For higher concentrations of 5 mM to 50 mM azide (▼, ▲, ■), the normalized cell layer impedance increases to about 1.2 – 1.3 within the first two hours of incubation and remains at this level for the time of observation. Exposure to 150 mM azide (+) results in a constant decrease of the cell layer impedance below 0.7 within 9 h.

If the azide ion is provided free access to the cytoplasm after transient electroporation for a short period of time (Fig. 5.28 B), a concentration-dependent cell response can be monitored. In a concentration range of 1.5 to 50 mM (□, ▼, ▲, ■) the post-pulse recovery of the impedance to pre-pulse values is retarded in comparison to the azide-free control (○) in a concentration dependent fashion. For concentrations of 0.1 mM (▲) and 0.5 mM (◇) the same post-pulse recovery kinetics as observed for the control cell layer are recorded. But even for these low concentrations minor deviations from the control cell layer are obvious. Whereas the control cell layer without azide shows a typical impedance overshoot about 1 h after electroporation, which levels off to baseline values within about 5 h, this time course is less pronounced with azide concentrations of 0.1 mM (▲) and 0.5 mM (◇). The normalized impedance level after electroporation remains about 0.2 above starting values. Electroporation with 1.5 mM azide (□) results in a retarded recovery of cell layer impedance. Stable values for the normalized impedance around 1.18 are reached ~ 1.5 h after pulse application. For higher concentrations of 5 mM (▼) and 15 mM (▲) initial impedance values are not fully re-attained

within the observed time frame. The cell layer, which had been electroporated in presence of 50 mM azide (■), does not reveal any cell recovery.

In order to sort out effects arising from increased osmolalities of the applied NaN_3 solutions, osmotic effects of a non-toxic solute with similar concentrations were checked. Assuming an ideal solution, 150 mM sodium azide dissociates to 300 mM osmotically active ions. Thus, cell responses upon electroporations in sucrose solutions with sucrose concentrations up to 300 mM were recorded (Fig. 5.29). Absolute impedance values are presented instead of normalized values in order to reveal osmotic effects already occurring during pre-pulse equilibration.

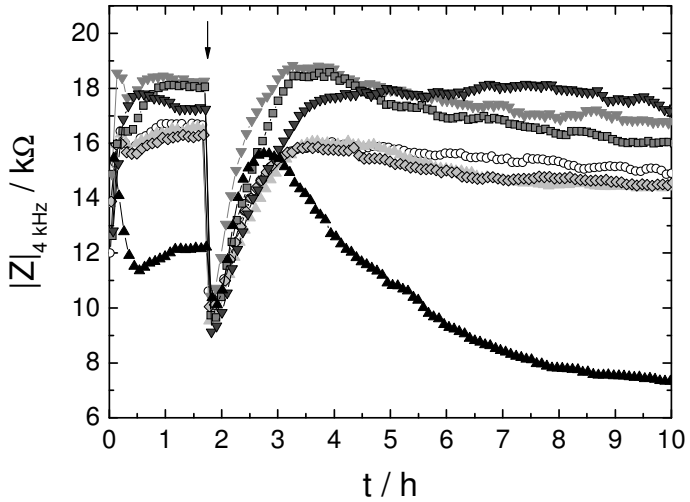

Fig. 5.29: Time course of the impedance magnitude at 4 kHz before and after electroporation (arrow) of NRK cells grown on *8W1E* ECIS electrodes in presence of different concentrations of sucrose in $EBSS^{++}$: ○: 0 mM; △: 1 mM; ◇: 3 mM; ▽: 10 mM; □: 30 mM; ▼: 100 mM ▲: 300 mM. T = 37 °C.

Addition of 300 mM (▲) sucrose causes an immediate drop of impedance to ~ 12 kΩ. After electroporation the impedance decreases below 8 kΩ. For sucrose concentrations from 1 mM up to 100 mM impedance values remain constant during the initial equilibration and no significant differences in post-pulse cell recovery can be observed. Thus, severe osmotic effects after electroporation with 50 mM sodium azide can be ignored. Nevertheless, increased impedance values for sucrose concentrations of 10 – 100 mM compared to lower sucrose concentrations (1 mM, 3 mM) are obvious. Osmolalities of azide and sucrose solutions were measured by a cryoscopic osmometer (chapter 4.1.6) and are given in Tab. 5.2.

Tab. 5.2: Osmolalities of sodium azide and sucrose solutions in $EBSS^{++}$ with different solute concentrations.

Sodium Azide Solutions		**Sucrose Solutions**	
Concentration [mM]	Osmolality [mOsm/kg]	Concentration [mM]	Osmolality [mOsm/kg]
0	268	0	268
0.5	270	1	272
1.5	270	3	273
5	276	10	278
15	283	30	294
50	315	100	357
150	408	300	556

An osmolality around 270 – 300 mOsm/kg is regarded to be physiological (O'Connor et al., 1993; Golzio et al., 1998; Müller et al., 2003). The solvent $EBSS^{++}$ itself has an osmolality of 268 mOsm/kg. Sodium azide and sucrose solutions in $EBSS^{++}$ exhibit osmolalities below 300 mOsm/kg for concentrations up to 15 mM and 30 mM, respectively. A slightly higher osmolality of 315 mOsm/kg was measured for 50 mM sodium azide in $EBSS^{++}$, while 100 mM sucrose accounted for 357 mOsm/kg. Higher azide (150 mM) and sucrose (300 mM) concentrations show unphysiological osmolalities above 400 and 550 mOsm/kg, respectively. Since an osmotic effect of azide solutions up to 50 mM on post-pulse recovery kinetics is unlikely, the retarding effect on cell layer impedance recovery after electroporation with azide can be ascribed predominantly to its intracellular cytotoxic activity.

5.2.2 Loading of NRK Cells with Bleomycin

One of the most often applied cytotoxic drugs with a low transmembrane permeability but a high intracellular toxicity is bleomycin. Inside the cell bleomycin induces DNA single and double strand breaks and thereby triggers the cellular apoptotic cascade leading to cell death. If the cell membranes were permeabilized by electroporation, the toxic concentration of bleomycin was found to increase about 100 – 5000 fold (Jaroszeski et al., 2000; Gehl et al., 1998; Orlowski et al., 1988). Based on these observations therapeutic approaches were developed for electroporation of cancer tissues with poorly membrane permeable cytotoxic drugs, nowadays referred to as electrochemotherapy.
In the scope of this work, the effect of electroporation of bleomycin into epithelial cells was experimentally demonstrated using the ECIS-based electroporation and sensing system. By *in situ* electroporation an adherent cell population residing on the active electrode area was permeabilized to allow free diffusion of bleomycin into the cytoplasm of the cells. The bleomycin loaded cells were subsequently monitored by impedance readings in order to follow morphological alterations within the cell layer in response to the introduced cytotoxic drug.

5.2.2.1 Monitoring the Cell Layer Response after Bleomycin Uptake

Figure 5.30 shows the response of a fully established NRK cell layer upon electroporation in presence of 100 µM bleomycin in comparison to control cell layers. Cell layer integrity and the cellular response were continuously followed via impedance measurements at 4 kHz and 32 kHz.
For a cell layer exposed to 100 µM bleomycin over 40 h without electroporation, a slight increase of the normalized impedance at 4 kHz to 1.1 can be detected (Fig. 5.30 A, curve c). In comparison, an untreated cell layer remains fluctuating among its base line level over the time of observation (curve a). If the membrane is permeabilized by an electric pulse two hours after starting the experiment, bleomycin and other substances within the extracellular fluid get access to the cytoplasm. The control cell layer electroporated only in $EBSS^{++}$ buffer without

bleomycin shows the characteristic response of a NRK cell layer after a membrane permeabilizing pulse (cp. chapter 5.1.1.1). The cell layer electroporated in presence of bleomycin shows a retardation for the initial impedance recovery compared to the impedance profile after electroporation in vehicle buffer alone. About 4 h after pulsing ($t_{|Z|max}$) a transient maximum of the normalized impedance at 0.92 is reached. Afterwards, the impedance decreases to a transient minimum of about 0.85 approximately 13 h after loading with bleomycin ($t_{|Z|min}$). Within the following 10 h the impedance increases again and reaches a plateau near base line values roughly 25 h after electroporation.

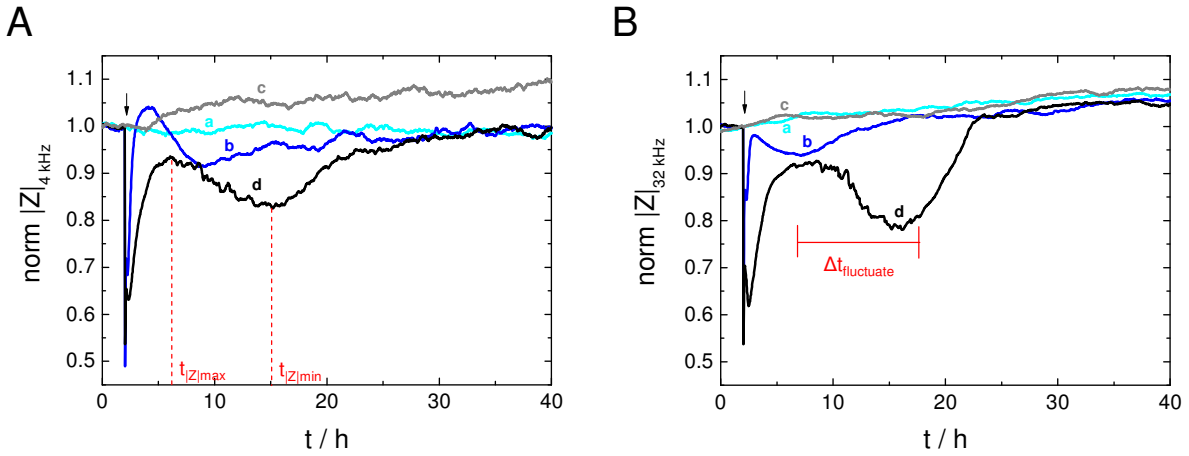

Fig. 5.30: Time course of the normalized impedance magnitude for NRK cells grown on *8W1E* ECIS electrodes before and after electroporation in presence of 100 µM bleomycin (d, ▬) compared to control cell layers. Data are presented for the frequencies **A:** 4 kHz and **B:** 32 kHz. Control cell layers remained either untreated in EBSS^{++} buffer (a, ▬), were electroporated at standard conditions (b, ▬) (40 kHz, 4 V, 200 ms) or were incubated in presence of 100 µM bleomycin without electroporation (c, ▬). The arrow marks the time point of electric pulse application. Absolute impedance magnitudes were normalized to the last value before electroporation (A: a: 13.37 kΩ; b: 14.01 kΩ; c: 12.11 kΩ; d: 13.02 kΩ; B: a: 3.77 kΩ; b: 3.89 kΩ, c: 4.04 kΩ; d: 4.13 kΩ). T = 37 °C.

Using a monitoring frequency of 32 kHz the impedance curves for the three control cell layers are smoother compared to the time courses recorded at 4 kHz (Fig. 5.30 B). Simple incubation of NRK cells with bleomycin does not reveal any effect and the impedance overshoot observed at 4 kHz is diminished at this higher observation frequency. By contrast, the cell layer response after electroporation in pesence of bleomycin is more pronounced at 32 kHz than at 4 kHz, showing an impedance drop below 0.8 about 13 h after pulsing.

The impedance data recorded at 32 kHz reveal another remarkable characteristic. About 6.5 h after electroporation in presence of bleomycin the impedance signal begins to fluctuate while it decreases to the transient minimum (B, curve d). This time frame showing increased impedance fluctuations is indicated by $\Delta t_{fluctuate}$. In contrast, the curves of the control cell layers remain smooth (curves a – c). These fluctuations are also observed in the 4 kHz data (A), but they are less prominent and not as clearly distinguishable from normal fluctuations of a healthy control cell layer at this lower frequency.

Phase contrast images of ECIS electrodes covered with NRK cells 40 h after electroporation in presence of bleomycin and corresponding controls obtained from a comparable experiment are shown in Fig. 5.31. The cell layer, which has been electroporated in presence of

bleomycin (D), is covered with a patch of highly contrasted and spherical cells, a characteristic feature of aggregated dead cells, on top of a confluent monolayer in the center of the electrode. Control cell layers, which were either only incubated with bleomycin (C), remained completely untreated (A) or were electroporated in $EBSS^{++}$ buffer without bleomycin (B), all reveal smooth cell layers with only a few spherical, dead cells randomly distributed on the entire cell sheet.

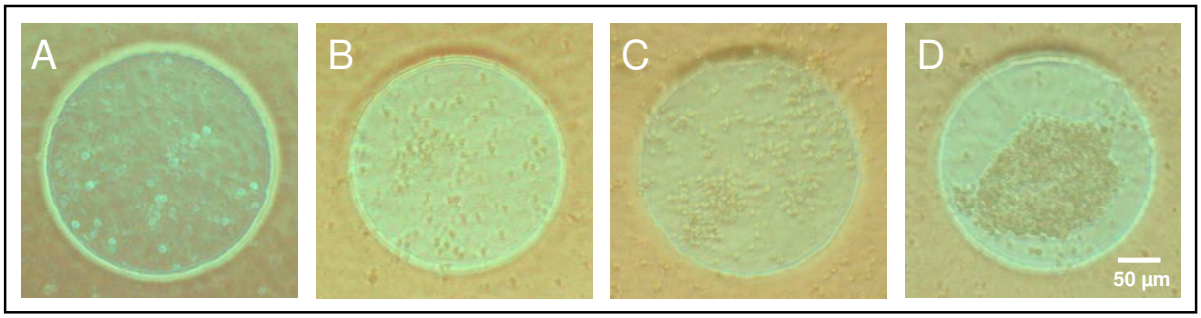

Fig. 5.31: Phase contrast micrographs of NRK cell layers grown on *8W1E* ECIS electrodes 40 h after electroporation in presence of 100 µM bleomycin (**D**) and control cell layers: **A:** Incubation in $EBSS^{++}$, no electroporation; **B:** Electroporation in $EBSS^{++}$; **C:** Incubation with 100 µM bleomycin, no electroporation.

Whereas the cell layers showed very reproducible results under control conditions when repeated in different experiments, cellular responses after electroporation in presence of bleomycin varied significantly. Impedance measurements revealed weak, moderate or strong responses after loading the cells with bleomycin (Fig. 5.32). Figure 5.30 represents a good example for a moderate response after electroporation of NRK cells in presence of bleomycin. In order to illustrate the range of cellular reactions upon the same kind of manipulation, examples for a weak and strong response are given in Fig 5.32.

A weak response is represented in Fig. 5.32 A, B, showing only slight differences between those cells that have been electroporated in presence of bleomycin and those electroporated without. At 4 kHz only a slight impedance decrease to about 0.8 after electroporation-mediated loading with bleomycin can be detected (A). At a monitoring frequency of 32 kHz the characteristic impedance fluctuations can be detected, which only occur after electroporation with bleomycin (B, curve d) but not in control curves (curves a – c). An experiment with a strong cellular response after electroporation with bleomycin is shown in Fig. 5.32 C, D. Impedance values significantly decrease below 0.6 at 4 kHz or even below 0.5 at 32 kHz within 12 h. At 32 kHz characteristic impedance fluctuations are only observed within the first 1 – 7 h after electroporation and are reduced in the course of the subsequent strong impedance drop. Beginning cell layer recovery is indicated by an only slight increase of the normalized impedance values in the last period of the experiment.[4]

[4] The impedimetric response of NRK cells after electroporation in presence of 100 µM bleomycin was found to be strongly dependent on the status of the cell layer. The number of passages, the time of cultivation before seeding on ECIS electrodes, the cultivation time on the electrodes itself as well as the nutritive status influence the cellular reaction. NRK cell layers of low passage number and low pre-cultivation time before seeding on electrodes lower the impedance decrease after loading with bleomycin by electroporation and promote fast regeneration to pre-pulse values. NRK cells used in these experiments were commonly cultivated for 2.5 – 3.5 d on ECIS electrodes and supplied with fresh medium 0.5 – 1 d before starting an experiment.

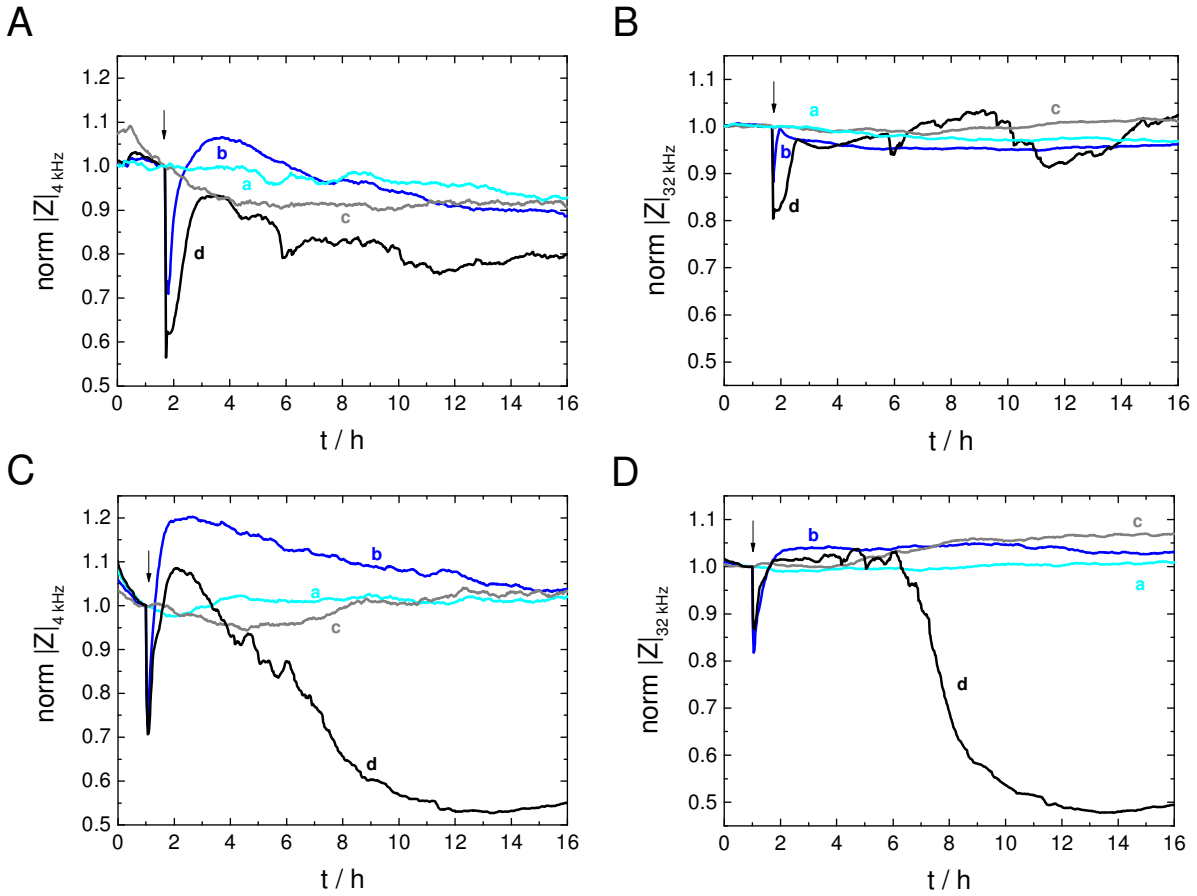

Fig. 5.32: Time course of the normalized impedance magnitude for NRK cells grown on *8W1E* ECIS electrodes before and after electroporation in presence of 100 µM bleomycin (d, ▬) showing a weak (**A**, **B**) or strong (**C**, **D**) response upon bleomycin uptake compared to control cell layers. Data are presented for 4 kHz (**A**, **C**) and 32 kHz (**B**, **D**). Control cell layers remained either untreated in $EBSS^{++}$ buffer (a, ▬), were electroporated at standard conditions (b, ▬) (40 kHz, 4 V, 200 ms) or were incubated in presence of 100 µM bleomycin without electroporation (c, ▬). The arrow marks the time point of electric pulse application. Absolute impedance magnitudes were normalized to the last value before electroporation (A: a: 16.49 kΩ; b: 16.49 kΩ; c: 15.67 kΩ; d: 16.45 kΩ; B: a: 4.13 kΩ; b: 3.93 kΩ; c: 4.19 kΩ; d: 4.02 kΩ; C: a: 13.39 kΩ; b: 13.87 kΩ; c: 14.35 kΩ; d: 13.77 kΩ; D: a: 4.06 kΩ; b: 4.28 kΩ; c: 4.28 kΩ; d: 4.17 kΩ). T = 37 °C.

For ten individual experiments the time points of reaching the transient impedance maximum ($t_{|Z|max}$) and minimum ($t_{|Z|min}$) (cp. Fig. 5.30) measured at a frequency of 4 kHz after electroporation of NRK cells in presence of 100 µM bleomycin are listed in Tab. 5.3. Additionally, the time frame showing characteristic impedance fluctuations at a monitoring frequency of 32 kHz ($\Delta t_{fluctuate\ (|Z|32\ kHz)}$) is provided for each measurement (Tab. 5.3).

In all experiments the cell layer impedance initially increased to a transient maximum shortly after, which was reached 2.2 ± 1.1 h after pulsing on average. A second minimum of impedance was reached 12.5 ± 3.5 h after bleomycin had been introduced to the cytoplasm of the cells. The impedance at a frequency of 32 kHz always revealed characteristic fluctuations, mostly occuring in a time frame roughly between 3.5 and 12 h after electroporation.

Severe impedance drops indicate rounding and detachment of dying cells from the electrode surface. Thus, bleomycin electroporated cell layers were inspected microscopically at the end of an ECIS experiment to evaluate electrode surface coverage. Phase contrast images of cell layers revealing weak and strong cellular responses after bleomycin electroporation are shown in Fig. 5.33.

Tab. 5.3: Characteristic time points and time frames in the impedance time course of 10 different experiments after electroporation of NRK cells in presence of bleomycin. Given are the time points of the transient impedance maximum $t_{|Z|max}$ and impedance minimum $t_{|Z|min}$ at 4 kHz after electroporation as well as the individual time frames revealing strong impedance fluctuations at 32 kHz ($\Delta t_{fluctuate\ (32\ kHz)}$).

Experiment	$t_{\|Z\|max}$ [h]	$t_{\|Z\|min}$ [h]	$\Delta t_{fluctuate\ (\|Z\|32\ kHz)}$ [h]
1	1.5	16	–
2	2	10	4.5 – 14.5
3	4	13	4 – 12
4	3.2	13.3	5.5 – 17.5
5	1	10	4 – 10
6	1.15	12	2.5 – 7
7	0.7	9	3 – 12
8	2	9	2.5 – 12.5
9	3.3	20	3.5 – 14
10	3	13	3 – 10
mean ± SD	**2.2 ± 1.1 h**	**12.5 ± 3.5 h**	**(~ 3.5 – 12 h)**

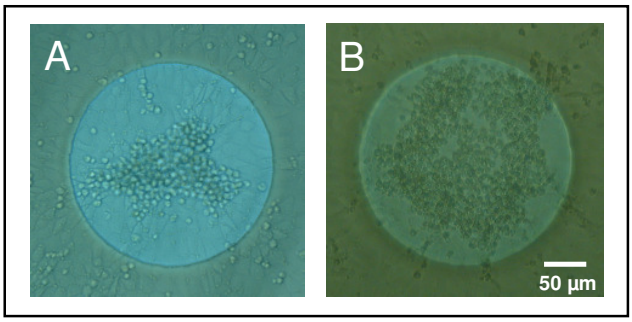

Fig. 5.33: Phase contrast micrographs of NRK cell layers grown on *8W1E* ECIS electrodes about 18 h after electroporation in presence of 100 µM bleomycin obtained from experiments with different cellular responses showing a fast (**A**) or a slow (**B**) regeneration of the cell layer impedance.

Both cell layers show agglomerates of spherical cells in the center of the electrode, which indicates that cell detachment took place. However, these images differ with respect to the fraction of electrode area that is covered by these presumably dead cells. In the end of an experiment with a weak impedance response (cp. Fig. 5.32 A, B) a high fraction of the electrode surface is covered by intact cells and a dense agglomeration of dead cells covers only about 30 % of the central electrode surface area, presumably lying on top of the intact cells (Fig. 5.33 A). Dead cells, however, almost cover 85 % of the electrode surface area for cell layers with a strong impedimetric response (Fig. 5.33 B, cp. Fig. 5.32 C, D). Only the rim area of the electrode is covered with intact cells.

These phase contrast micrographs confirm the impedance data of Fig. 5.32. For a weak cell layer response after electroporation in presence of bleomycin the impedance values are on the level of the confluent control cell layers at the end of the measurement, meaning a fast regeneration of the cell layer (cp. Fig. 5.32 A, B). This matches to the corresponding phase contrast image, which does not reveal any cell-free sections on the electrode surface (Fig. 5.33 A). Impedance measurements which suggest incomplete electrode coverage with cells due to slow regeneration (cp. Fig. 5.32 C, D) are mirrored by phase contrast micrographs showing an extended area with dead cells as well as single small openings in the cell layer at the center of the electrode (Fig. 5.33 B).

5.2.2.2 Concentration-Response Studies

Exposure of NRK cells to different concentrations of bleomycin and subsequent electroporation results in a dose-dependent time course of the impedance at 4 kHz (Fig. 5.34).

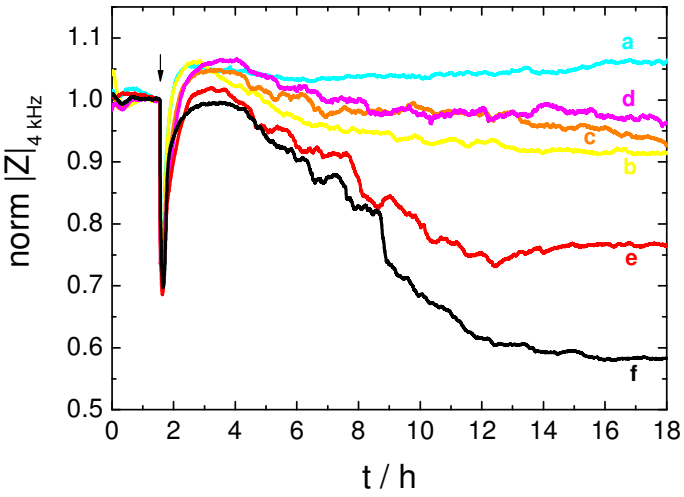

Fig. 5.34: Time course of the normalized impedance magnitude at 4 kHz for NRK cells grown on *8W1E* ECIS electrodes before and after electroporation in presence of different concentrations of bleomycin. Concentrations of bleomycin were: a, : 0 µM; b, : 1 µM; c, : 3 µM; d, : 10 µM; e, : 30 µM; f, : 100 µM. Cell layers were pulsed at 40 kHz, 4 V and 200 ms at the time point marked by the arrow. Absolute impedance magnitudes were normalized to the last value before electroporation (a: 13.45 kΩ; b: 14.13 kΩ; c: 13.49 kΩ; d: 13.21 kΩ; e: 13.51 kΩ; f: 13.98 kΩ). T = 37 °C.

The cellular response can be categorized as strong (cp. Fig. 5.32 C), since the normalized impedance drops below 0.6 after electric pulsing in presence of 100 µM bleomycin (curve f). The lower the applied bleomycin concentration, the less pronounced is the post-pulse response compared to the control, which was electroporated without bleomycin (curve a). When cells are electroporated in presence of 30 µM bleomycin the normalized impedance decreases to a minimum of 0.75 about 11 h after electroporation and then levels off (curve e). Electroporation in presence of 1, 3 or 10 µM bleomycin results in an impedance decrease to 0.91 – 0.96 within 16 h after pulse application (curves b – d). For these lower concentrations no clear concentration dependence exists.

Although changes in the electrode impedance for low concentrations of bleomycin are not very pronounced compared to electroporation without bleomycin, phase contrast micrographs taken at the end of the experiment reveal the characteristic agglomeration of dead cells in the center of the electrode, except for the bleomycin-free control (Fig. 5.35). Clusters of spherical, contrast rich cells lie in the center of all cell layers that have been electroporated in presence of bleomycin (Fig. 5.35 B – F). However, the fraction of electrode area covered with dead cell bodies is significantly enlarged after electroporation in presence of 30 or 100 µM bleomycin (E, F) compared to concentrations of 1, 3 and 10 µM (B – D).

When the cells only show a weak response after electroporation in presence of bleomycin, a concentration dependence is difficult to detect (Fig. 5.36). At a monitoring frequency of 4 kHz almost no concentration dependence can be observed (Fig. 5.36 A), while monitoring

the impedance at a higher frequency of 32 kHz reveals concentration dependent intensity fluctuations (Fig. 5.36 B).

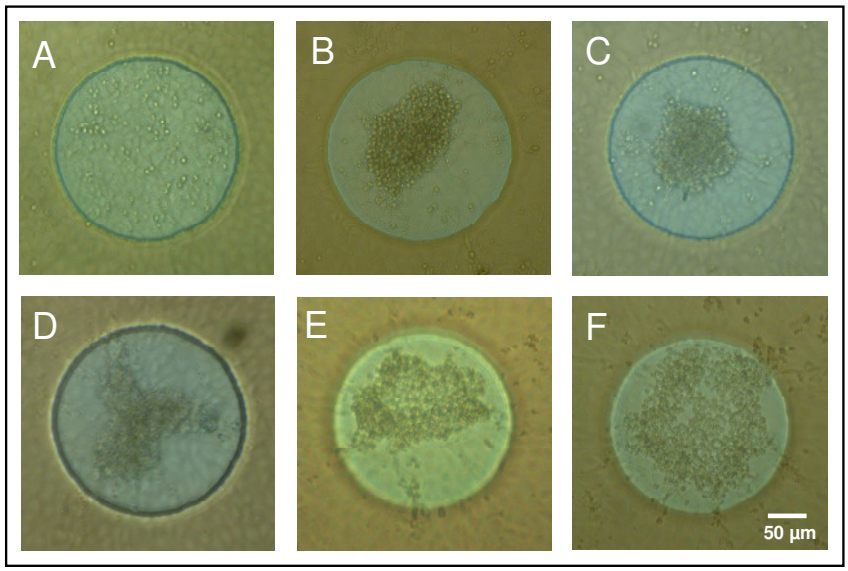

Fig. 5.35: Phase contrast micrographs of NRK cell layers grown on *8W1E* ECIS electrodes 17 h after electroporation in presence of different concentrations of bleomycin. **A:** 0 µM; **B:** 1 µM; **C:** 3 µM; **D:** 10 µM; **E:** 30 µM; **F:** 100 µM.

For the highest concentration of bleomycin (100 µM) the impedance fluctuations are most prominent (B, curve f). For decreasing concentrations (30 µM → 1 µM) the curves become smoother (B, curves b – e). In addition, the height of the impedance maximum, which is observed about 8 h after electroporation with 100 µM bleomycin, is reduced with decreasing concentration and shifts along the time axis to shorter times. The control cell layer remains smooth and almost at a constant level of the normalized impedance.

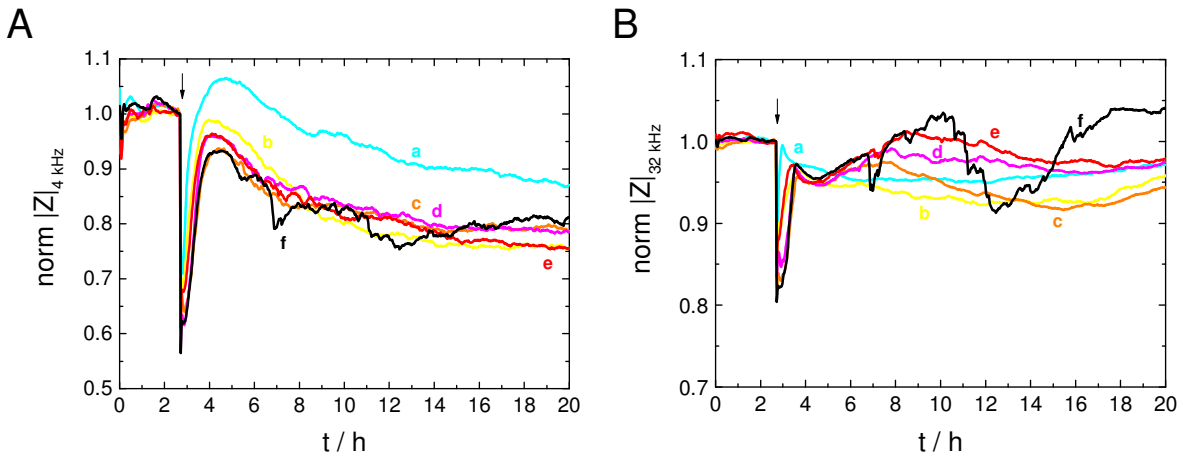

Fig. 5.36: Time course of the normalized impedance magnitude for NRK cells grown on *8W1E* ECIS electrodes before and after electroporation in presence of different concentrations of bleomycin. Data are presented at frequencies **A:** 4 kHz and **B:** 32 kHz. Cell layers were pulsed at 40 kHz, 4 V, 200 ms (arrow). Concentrations of bleomycin were: a, ——: 0 µM; b, ——: 1 µM; c, ——: 3 µM; d, ——: 10 µM; e, ——: 30 µM; f, ——: 100 µM. Absolute impedance magnitudes were normalized to the last value before electroporation (A: a: 12.17 kΩ; b: 11.75 kΩ; c: 11.40 kΩ; d: 10.57 kΩ; e: 11.17 kΩ; f: 10.22 kΩ; and B: a: 3.93 kΩ; b: 3.98 kΩ; c: 4.02 kΩ; d: 4.02 kΩ e: 3.99 kΩ; f: 4.02 kΩ). T = 37 °C.

5.2.2.3 Microscopic Evidence for the Cytotoxic Effect of Bleomycin

The major toxic effect of bleomycin is ascribed to the generation of DNA single-strand and double-strand breaks. Irreversible DNA damage is a typical intracellular stress signal which triggers apoptosis. In the course of the complex multistep apoptotic mechanism specialized enzymes lead to degradation of cellular components. In contrast to accidental necrosis, membrane integrity is maintained for a prolonged period of time and various other characteristic molecular and morphological changes occur in apoptotic cells. Typical cellular alterations are cell shrinkage, chromatin condensation, nuclear fragmentation, membrane blebbing and shedding of apoptotic bodies filled with enzymatically degraded material. Though various biochemical assays are available to detect apoptosis, they are not suitable for detection of apoptosis within a small fraction of the entire cell layer. Therefore, apoptosis restricted to the area of the working electrode was verified microscopically.

Cell Vesiculation and Loss of Membrane Integrity

About 20 h after electroporation of NRK cells in presence of 100 µM bleomycin the cell layers were stained for viable and dead cells using the live/dead staining assay based on two specific fluorescent probes (Fig. 5.37) (cp. chapter 4.4.4.2). The DNA-intercalating red fluorescent dye Ethidium homodimer-1 (EthD-1) is a marker for the loss of membrane integrity as observed for dead cells. In contrast, viable cells are stained green due to the hydrolysis of a calcein acetoxymethylester by intracellular esterases.

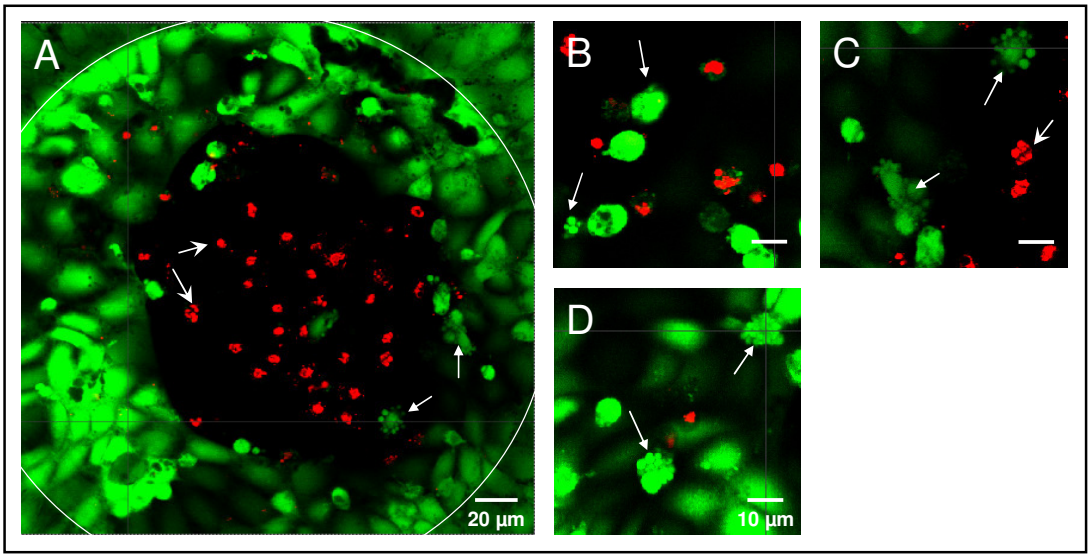

Fig. 5.37: Confocal fluorescence micrographs of live/dead stained NRK cells grown on a *8W1E* ECIS electrode (white circle) 20 h after electroporation in presence of bleomycin. **A:** Cell-covered electrode after electroporation in presence of 100 µM bleomycin **B**, **C:** Magnified presentations of selected areas within the cell layer depicted in A. **D**: Magnified presentation of a selected area within a cell layer electroporated with 30 µM bleomycin. Green fluorescence indicates esterase activity of vital cells, red fluorescence of nuclei the loss of membrane integrity of dead cells. Arrows mark vesicular bodies (→) or fragmented nuclei (→).

In the center of the electrode red stained cell nuclei of dead cells are found (Fig. 5.37 A). Cell nuclei appear shrinked and fragmented, which is not typical for intact nuclei (Fig. 5.37 B) or necrotic nuclei (cp. chapter 5.1.1.1). The periphery of the electrode surface is covered with

calcein stained cells having a flat morphology of irregular shape typical for viable cells (A). However, some vital cells, especially near the center of the electrode, exhibit a spherical morphology which is more typical for dying cells (A, B). A closer look reveals vesicle-like compartments which surround these cellular bodies (B – D). Some cells completely converted to apoptotic bodies and appear as clusters of vesicle-like structures (D, →). In close approximity to these blebbing cells some fragmented nuclei of dead cells (red) are found (B, C, →).

Chromatin Condensation and Nuclear Fragmentation

The nuclei of cell layers on gold-film electrodes were stained with the DNA binding dye 4',6-diamidino-2-phenylindole (DAPI) after cell layer fixation and membrane permeabilization (cp. chapter 4.4.4.5). In Fig. 5.38 a DAPI stained cell layer about 20 h after electroporation in presence of 100 µM bleomycin is presented.

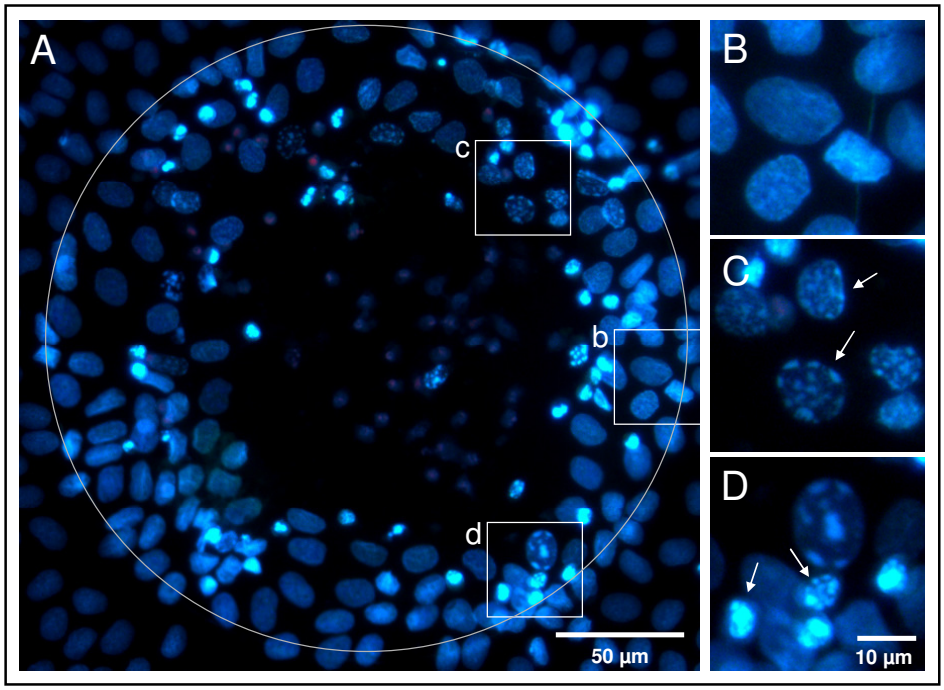

Fig. 5.38: Epifluorescence micrograph of a DAPI stained NRK cell layer grown on a *8W1E* ECIS electrode (grey circle) 20 h after electroporation in presence of 100 µM bleomycin. Regions b, c and d marked by white boxes in **A** are presented with 2.25-fold magnification in **B**, **C** and **D**. Arrows indicate nuclei with condensed DNA.

Three types of stained nuclear structures on the electrode can be distinguished. Different stages of DNA condensation and cell nucleus decomposition can be observed ranging between healthy appearing nuclei and strongly condensed and fragmented structures.

A normal morphology of the nuclei, also found beyond the active electrode, is only observed at the border of the active electrode (B). In the center of the electrode there are no healthy nuclei but only poorly stained DNA clusters, which correspond to the EthD-1 stained fragments in Fig. 5.37. These structures are similar to the bright fluorescent nuclear bodies which are irregularly distributed over the electrode surface (Fig. 5.38 A). The bright fluorescent, condensed DNA clusters are significantly smaller than normal nuclei and at a

closer look reveal a punctuated composition, typical for fragmented nuclei (D, arrows). The characteristic dotted staining structure is also apparent in some nuclei with normal outer morphology and indicates early stages of chromatin condensation in these cells (C, arrows).

Cell layers that were loaded with lower concentrations of bleomycin (1 – 10 µM) showed this characteristic DAPI staining pattern as well. Nuclei with apparent DNA condensation and fragmentation could mainly be found within the cell aggregates in the center of the electrode (Fig. 5.39). In most cases condensation and fragmentation was already advanced in these cells.

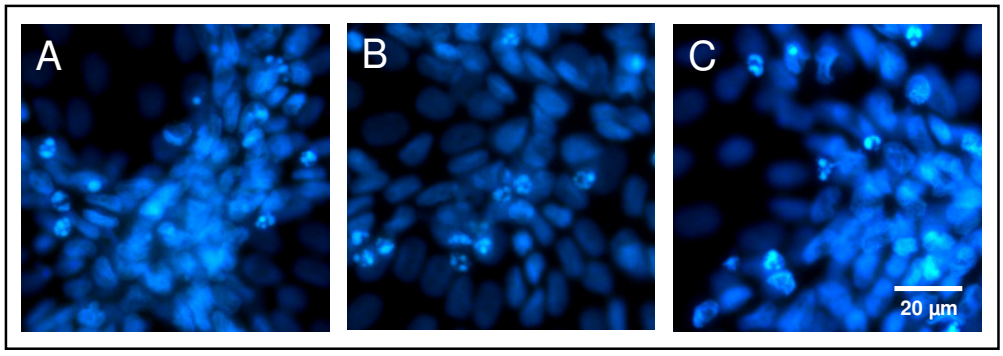

Fig. 5.39: Epifluorescence micrographs of DAPI stained NRK cell layers grown on *8W1E* ECIS electrodes 20 h after electroporation in presence of **A:** 1 µM; **B:** 3 µM; **C:** 10 µM bleomycin. The central area of the electrode, where apoptotic cells are collected after recovery from bleomycin electroporation, is shown.

5.2.2.4 Electric Wounding versus Loading with Bleomycin

When cells grown on ECIS gold-film electrodes are loaded with bleomycin by means of *in situ* electroporation, apoptosis is thought to be induced (cp. chapter 5.2.2.3). This genetically encoded cell death mechanism upon DNA fragmentation by bleomycin is only restricted to the cell population on the active electrode, since the membrane-impermeable drug has no access to the interior of cells, which are beyond the perimeter of the electrode. These cells remain viable and have the potential to migrate towards free spaces resulting from the detachment of apoptotic cells.

Another method to induce death of cells clearly restricted to the electrode area is electric wounding (cp. chapter 5.1.1.1). By applying a strong electric pulse, much more invasive than used for electroporation, cells on the electrode are irreversibly damaged by membrane rupture, loss of essential molecules and joule heating. If this electric wounding is integrated into an ECIS experiment, the impedance values at 32 kHz immediately decrease to those of a cell-free electrode (cp. Fig. 5.2 and Fig. 5.3). Intact cells from the electrode periphery can migrate inwards and repopulate the electrode. Repopulation of the electrode by NRK cells is measured as a slow impedance increase after a lag time of about 1 h. Within roughly 6 – 8 h initial impedance values of a fully established cell layer are re-attained. The time required for complete pre-pulse impedance re-establishment indicates cell migratory activity and wound healing potential. After repopulation of the electrode, cell layers that have been wounded can be distinguished microscopically from cell layers that have not been wounded by a scarred

structure and aggregates of dead cells covering the cell layer in the center of the electrode (cp. Fig. 5.3; Fig. 5.40 B). After electric wounding viable cells migrating inward remove dead cell bodies from the electrode and replace them. To a certain extent these dead cell bodies accumulate in the center of the electrode and lie on the newly established cell layer till detachment from the agglomerate or degradation by extracellular enzymes.
The impedimetric response of cells electroporated in presence of bleomycin has been described for several examples in chapter 5.2.2.1. Although the impedimetric response may vary among different experiments, phase contrast micrographs always look very similar when cell layers are inspected several hours after electroporation (cp. Fig. 5.33; Fig. 5.35; Fig. 5.40 C). On the other hand a replacement of apoptotic cells and their accumulation on the re-established cell layer is not present when cells remain untreated or are only electroporated without additives (Fig. 5.40 A, D).

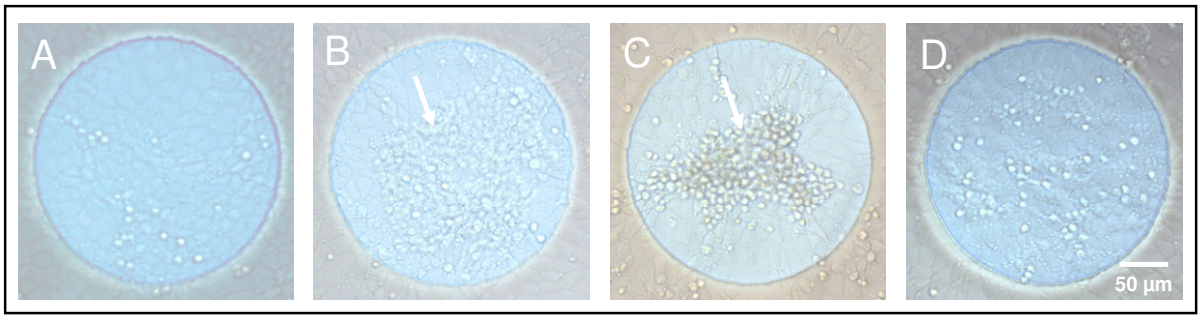

Fig. 5.40: Phase contrast micrographs of NRK cell layers grown on *8W1E* ECIS electrodes **A:** untreated **B:** ~ 20 h after electric wounding, **C:** ~ 20 h after electroporation in presence of 100 µM bleomycin, **D:** ~ 20 h after electroporation without bleomycin. Arrows indicate dead cells, which have accumulated in the center of the electrode.

In the following, NRK cell layers are directly compared with respect to the time course of impedance as well as their staining behavior with live/dead and DAPI after electric wounding and electroporation in presence of bleomycin (Fig. 5.41).
Cell layers were stained by the live/dead assay and with DAPI directly (A) or 21 h (B) after electric wounding and 21 h after electroporation in presence of 100 µM (C) or 1 µM (D) bleomycin (Fig. 5.41). Whilst already dead cells with a defect membrane were stained easily by EthD-1, DNA of cells with intact membranes could only be stained by DAPI after permeabilization with Triton-X.
Immediately after electric wounding the nuclei of all cells on the electrode surface are stained red, indicating loss of membrane integrity, whereas cells beyond the active electrode are stained by the green fluorescent vitality marker calcein (A1). This microscopic finding is associated with a drop of the normalized impedance at 40 kHz to 0.4 in the end of the experiment (Fig. 5.41 E, curve a, arrow 2). After membrane permeabilization nuclear DNA of vital cells can be stained blue by DAPI (A2). The nuclei on the electrode appear violet due to color mixing of DAPI and EthD-1. About 21 h after electric wounding a vital cell layer has repopulated the electrode (B1) but still a few nuclei of dead cells are residing on the re-established cell layer. Vital cells within the cell layer exhibit a centripetal orientation as a relict of their inward migration. After permeabilization and DAPI staining all nuclei on the

electrode appear blue and show a typical healthy morphology (B2). Corresponding impedance measurements support the complete re-establishment of the cell layer on the electrode surface (E, curve b).

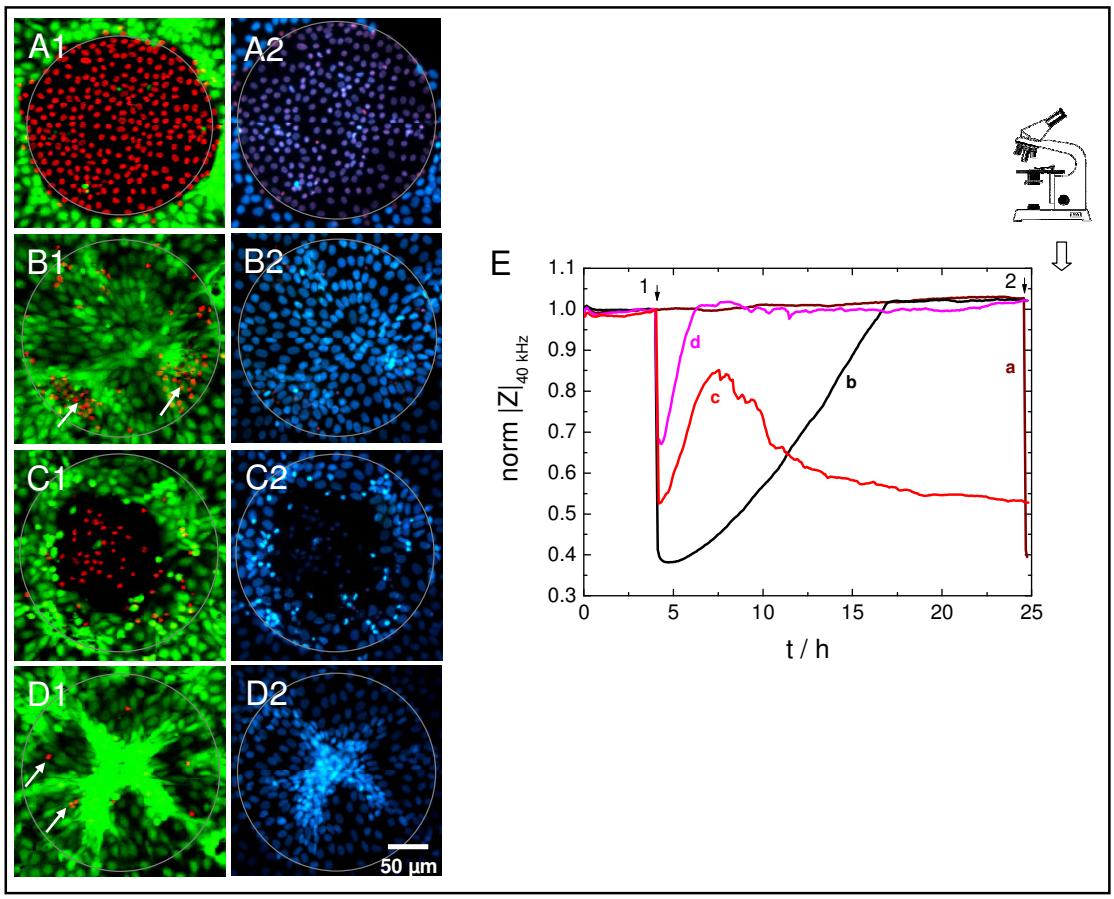

Fig. 5.41: Confocal fluorescent micrographs (**1**) and corresponding epifluorescent micrographs (**2**) of NRK cell layers grown on *8W1E* ECIS electrodes **A:** immediately after electric wounding, **B:** 21 h after electric wounding, **C:** 21 h after electroporation in presence of 100 µM bleomycin, **D:** 21 h after electroporation in presence of 1 µM bleomycin. Cell layers were live/dead stained by EthD-1 for nuclei of permeabilized cells (red) and by calcein-AM for esterase activity of viable cells (green) (**1**). Permeabilized cell layers were stained with DAPI for nuclei of all cells (**2**). Cell layers were stained in the end of the measurement shown in **E:** Time course of the normalized impedance magnitude at 40 kHz: **a, b:** Cell layers were wounded (40 kHz, 5 V, 30 s) at time points marked by arrows 1 (b), 2 (a); **c, d:** Cell layers were electroporated (40 kHz, 4 V, 200 ms, arrow 1) in presence of 1 µM (d) or 100 µM (c) bleomycin. Absolute impedance magnitudes were normalized to the last value before pulse application (a: 4.42 kΩ; b: 4.52 kΩ; c: 4.76 kΩ; d: 4.77 kΩ).

After electroporation of NRK cells in presence of 100 µM bleomycin the impedance shows a first transient increase and a subsequent significant decrease (E, curve c). In the end of the measurement the normalized electrode impedance remains below 0.55, slightly above values of a cell-free electrode (~ 0.4). No indication for cell layer recovery can be observed. The incomplete electrode coverage is also mirrored by cytological stainings (C1, C2). The center of the electrode is covered with EthD-1 positive nuclei indicating dead cells (C1). As already mentioned before (cp. Fig. 5.37, 5.38) these nuclei show a fragmented morphology, which is typical for apoptotic cells. Vital cells are found along the electrode perimeter (indicated by the white line) and cover roughly 50 % of the electrode surface (C1). Although cells in the border area show esterase activity and membrane integrity, DAPI staining reveals many nuclei with

condensed chromatin as well as already fragmented nuclei (C2). If a cell population has been electroporated in presence of 1 µM bleomycin, significant centripetal cell orientation and scar-like aggregation of cells in the center of the electrode is observed (D). Live/dead staining does not show many cells with defect membranes or significantly reduced esterase activity (D1). In contrast, cells within the star-like cell aggregate reveal bright calcein fluorescence as well as enhanced DAPI fluorescence, indicating condensed chromatin structures (D2). Though the texture of the cell layer resembles to some extend an electrically wounded cell layer after wound re-closure (cp. B1), the time course of impedance is completely different (Fig. 5.41 E, curve d). Normalized impedance values never drop below 0.65 and indicate full electrode coverage already within two hours after electroporation.

5.2.2.5 Loading of NRK Cells with Bleomycin after Inhibition of Cell Motility

The experiments presented above revealed parallels between wound healing after physical damage by strong electric pulsing and cell layer recovery after loading with bleomycin by electroporation. The question arose, if inhibition of cell motility and, thus, the ability to repopulate cell-free spaces after detachment of apoptotic cells by lateral cell migration has an effect on cell layer recovery on the electrode surface. It was the aim to clarify if wound healing masks the effect of apoptosis, induced in the cell population on the electrode by bleomycin electroporation. Wound healing of cells can be inhibited by addition of cytochalasin D, an actin binding drug which inhibits actin polymerization and associated functions like cell motility. In order to determine the lowest effective dose to inhibit cell motility, NRK cell layers were incubated with different concentrations of cytochalasin D and analyzed (i) microscopically (Fig. 5.42) and (ii) impedimetrically (Fig. 5.43).

After 3 h of incubation with the membrane-permeable cytochalasin D the actin cytoskeleton of the cell layers was stained with TRITC-phalloidin and compared to an untreated cell layer (Fig. 5.42). The actin cytoskeleton of intact cells reveals characteristic thin filaments, forming a network through the cell body, and a strong accumulation of actin at the cell borders, forming the so-called actin belt (A). Incubation of the cells with cytochalasin D causes the thin filament network to disappear and instead point-like structures occur (B – G). Whereas at low concentrations of 0.1 to 0.5 µM cytochalasin D some fine filament structures can still be observed (B – D), they entirely disappear at higher concentrations above 1 µM (E – G). The actin belt remains prominent even at higher concentrations but initial defects are induced at concentrations of 2 µM and 5 µM cytochalasin D (F, G, arrows).

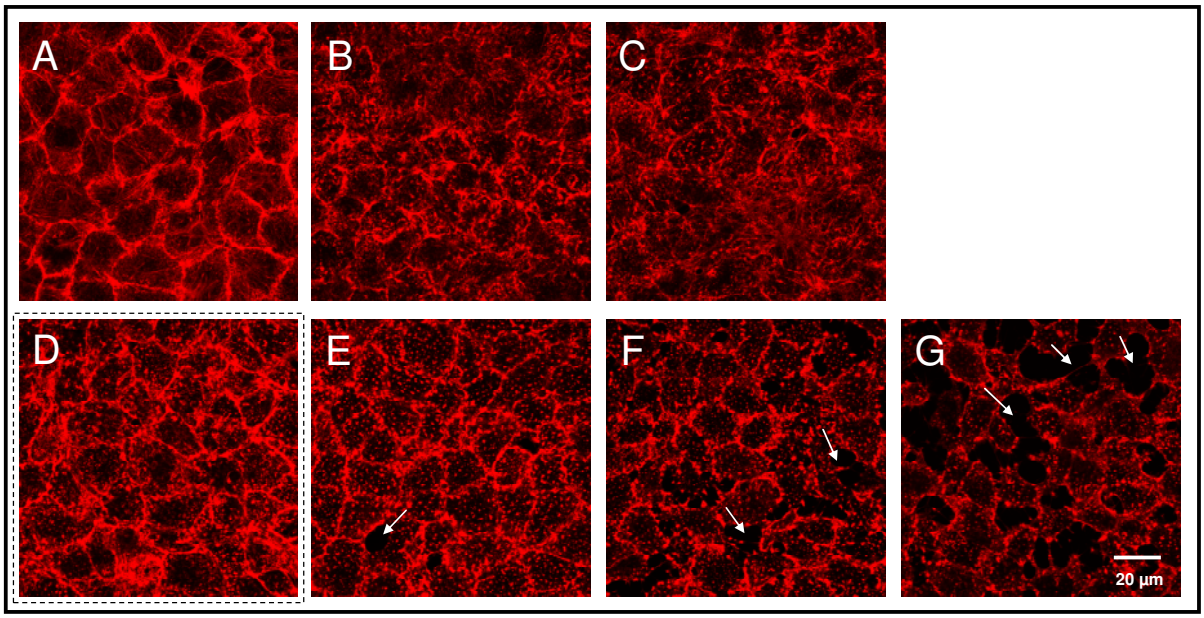

Fig. 5.42: Confocal fluorescence micrographs of the TRITC-phalloidin stained actin cytoskeleton of NRK cell layers after 3 h of incubation with different concentrations of cytochalasin D: **A:** control; **B:** 0.1 µM; **C:** 0.25 µM; **D:** 0.5 µM; **E:** 1 µM; **F:** 2 µM; **G:** 5 µM. The dotted box frames the image of a cell layer treated with 0.5 µM cytochalasin D, which was used in later experiments. Arrows indicate defect sites in the actin belt.

In the experiment shown in Fig. 5.43 the effect of different cytochalasin D concentrations on the migratory and wound healing capacity of NRK cells was analyzed impedimetrically. In the course of this experiment NRK cells grown on ECIS electrodes were incubated for 3 h with different concentrations of cytochalasin D before cell layers were wounded by a strong invasive electric pulse of 5 V for 30 s at 40 kHz. Subsequent repopulation of the electrode by migration of non-wounded, cytochalasin D pre-treated cells from the electrode periphery was monitored by recording the impedance at 32 kHz.

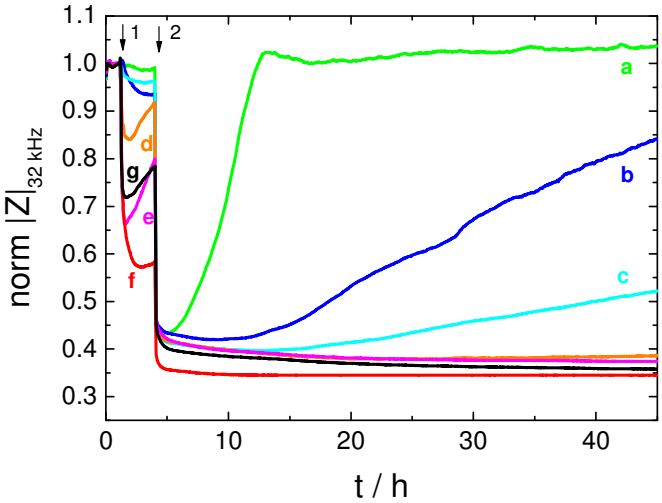

Fig. 5.43: Time course of the normalized impedance magnitude at 32 kHz for NRK cell layers grown on *8W1E* ECIS electrodes in presence of different concentrations of cytochalasin D in EBSS^{++} (arrow 1) and subsequent electric wounding (arrow 2) using an AC pulse of 40 kHz with 5 V for 30 s. Concentrations of cytochalasin D were: a, ▬: 0 µM; b, ▬: 0.1 µM; c, ▬: 0.25 µM; d, ▬: 0.5 µM; e, ▬: 1 µM; f, ▬: 2 µM; g, ▬: 5 µM. Absolute impedance values were normalized to the value before cytochalasin D addition (a: 4.05 kΩ; b: 4.11 kΩ; c: 4.07 kΩ; d: 3.98 kΩ; e: 3.92 kΩ; f: 4.16 kΩ; g: 3.99 kΩ). T = 37 °C.

In the beginning of the experiment the impedance base line of untreated cell layers was recorded. After 1 h different amounts of cytochalasin D were added resulting in final concentrations ranging from 0.1 µM to 5 µM (arrow 1). The control cell layer was incubated with cytochalasin D-free $EBSS^{++}$ buffer (curve a). Depending on the cytochalasin D concentration a decrease of normalized impedance values can be observed even without wounding. At higher concentrations of 1 – 5 µM an instantaneous drop down to 0.72 or lower can be measured (curves e – g). When using 0.5 µM cytochalasin D only a moderate decrease to 0.85 is detected (curve d). For the lowest concentrations of 0.1 and 0.25 µM cytochalasin D the normalized impedance declines to less than 0.95 (curves b and c). Addition of cytochalasin D-free fluid does not significantly change impedance values (arrow 1, curve a).
During the incubation time of 3 h cell layers exposed to cytochalasin D concentrations between 0.5 and 5 µM slightly recover before they are wounded by an electric pulse (5 V for 30 s at 40 kHz, indicated by arrow 2). Normalized impedance values of all cell layers immediately drop to values of roughly 0.4. Whereas the cell layer impedance regains starting values within 8.5 h after pulse application in absence of cytochalasin D (curve a), cells wounded in presence of cytochalasin D do not fully recover in the observation time of the experiment (curves b – g). About 40 h after wounding only cell layers incubated with 0.1 and 0.25 µM cytochalasin D show an impedance increase back to 0.84 and 0.52, respectively (curves b and c). The impedance for cell layers that were wounded in presence of 0.5 µM cytochalasin D or higher concentrations remains below 0.4 and does not show any indication of electrode re-population (curves d – g).
Since a concentration of 0.5 µM cytochalasin D was discovered to be the lowest effective concentration for the complete inhibition of wound healing for at least 40 h upon pulse application (Fig. 5.42 D and Fig. 5.43, curve d), this concentration was applied in further ECIS experiments.
In order to demonstrate that the recovery of cell layer impedance after electroporation with bleomycin can be inhibited if the process of wound healing is prevented, cell layers were pre-incubated with 0.5 µM cytochalasin D for 3 h. Figure 5.44 presents an ECIS experiment where cell layers were kept in absence of cytochalasin D (Fig. 5.44 A) or were pre-incubated with 0.5 µM cytochalasin D (Fig. 5.44 B) for 3 h before electroporation in presence of bleomycin (curves d). In both cases control cell layers were either simply incubated with bleomycin (curves a) or electroporated without bleomycin (curves b) in order to exclude possible adverse effects of cytochalasin D. To visualize the pure wound healing prohibiting effect of cytochalasin D cell layers were wounded in bleomycin-free buffer (curves c).
As already presented in experiments before, NRK cell layers electroporated in presence of bleomycin give rise to a slight initial increase and a subsequent decrease of the normalized impedance about 10 h after electroporation (Fig. 5.44 A, curve d). In the time frame of 5 – 10 h after electric pulsing in presence of bleomycin typical impedance fluctuations are observed. The initial impedance level is re-attained roughly 16 h after electroporation. In contrast, if cell layers have been pre-incubated with cytochalasin D before electroporation of bleomycin, the impedance values continuously decrease below 0.4 within about 10 h

(Fig. 5.44 B, curve d). There is no indication of cell layer impedance recovery for the recorded time frame of 24 h.

After addition of cytochalasin D to the cell layer impedance values decrease to a value of 0.9 within 3 h of incubation (B, arrow 1), whereas buffer addition in the control experiment does not have a significant effect (A, arrow 1). Exposure to bleomycin only causes minor changes of the cell layer impedance even when cytochalasin D is also present (B, curve a). Simple electroporation of NRK cells in cytochalasin D containing buffer does not affect the ability of the cell layer to recover from electric pulsing (B, curve b). Wound healing of cells in presence of cytochalasin D (B, curve c) is clearly inhibited when compared to wounding without cytochalasin D (A, curve c). Even though, a slight recovery of the cell layer is observed after wounding in presence of 0.5 µM cytochalasin D.

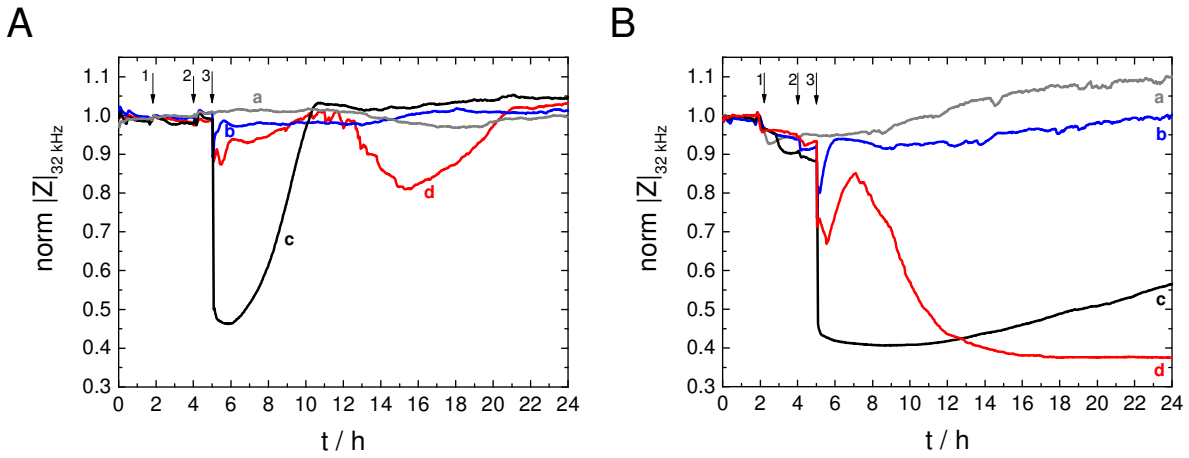

Fig. 5.44: Time course of the normalized impedance magnitude at 32 kHz for NRK cell layers grown on *8W1E* ECIS electrodes before and after electroporation in presence of bleomycin without (**A**) or with (**B**) pre-incubation with cytochalasin D. Cytochalasin D in a final concentration of 0.5 µM (**B**) or EBSS^{++} buffer alone (**A**) was added after 1 h of equilibration (arrow 1). Bleomycin was added in a final concentration of 100 µM to the cell layers (arrow 2) a: and d: after 4 h. Cell layers were either electroporated at 40 kHz, 4 V for 200 ms or wounded at 40 kHz, 5 V for 30 s (arrow 3). a,: 100 µM bleomycin, no electric pulsing; b,: no bleomycin, electroporation; c,: no bleomycin, electric wounding; d,: 100 µM bleomycin, electroporation. Absolute impedance magnitudes were normalized to value before cytochalasin D or buffer addition (arrow 1) (A: a: 4.00 kΩ; b: 4.01 kΩ; c: 3.96 kΩ; d: 4.18 kΩ; B: a: 3.90 kΩ; b: 4.12 kΩ; c: 4.25 kΩ; d: 4.20 kΩ). T = 37 °C.

In order to demonstrate the potential of even lower bleomycin concentrations to efficiently induce apoptosis, cytochalasin D pre-incubated cell layers were electroporated in presence of 1 µM, 10 µM and 100 µM bleomycin (Fig. 5.45 B).

Whereas under cytochalasin D-free conditions (Fig. 5.45 A) no significant effect can be monitored for 1 µM (A, curve c) and 10 µM (A, curve d) bleomycin compared to control cell layers (A, curve a), a significant decrease to values of a cell-free electrode is observed when these concentrations were used after pre-incubation with 0.5 µM cytochalasin D (Fig. 5.45 B). The ability to regenerate from the electric pulse to initial impedance values is delayed but not significantly affected by cytochalasin D (curve a).

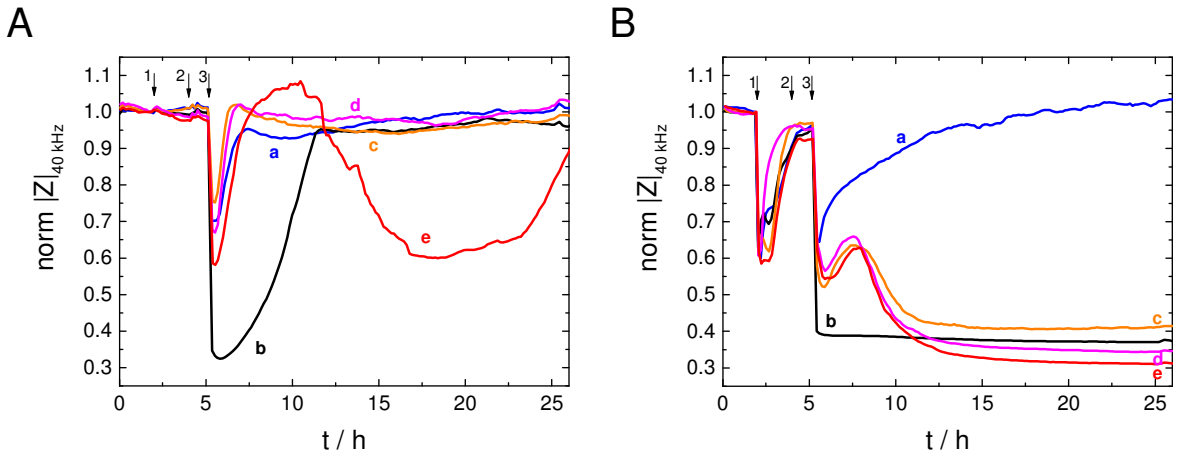

Fig. 5.45: Time course of the normalized impedance magnitude at 40 kHz for NRK cell layers grown on *8W1E* ECIS electrodes before and after electroporation in presence of different concentrations of bleomycin without (**A**) or with (**B**) pre-incubation with cytochalasin D. Cytochalasin D in a final concentration of 0.5 µM (**B**) or EBSS^{++} buffer (**A**) was added after 2 h of equilibration (arrow 1). Bleomycin in different final concentrations was added to cell layers c, d and e (arrow 2) after 4 h. Cell layers were electroporated at 40 kHz and 4 V for 200 ms or wounded at 40 kHz and 5 V for 30 s (arrow 3): a, ▬: no bleomycin, electroporation; b, ▬: no bleomycin, electric wounding; c, ▬: 1 µM bleomycin, electroporation; d, ▬: 10 µM bleomycin, electroporation; e, ▬: 100 µM bleomycin, electroporation. Absolute impedance magnitudes were normalized to the value before fluid addition (arrow 1) (A: a: 4.76 kΩ; b: 5.45 kΩ; c: 4.77 kΩ; d: 5.19 kΩ; e: 4.97 kΩ; B: a: 4.34 kΩ; b: 4.62 kΩ; c: 4.69 kΩ; d: 4.65 kΩ; e: 4.74 kΩ). T = 37 °C.

Cytochalasin D pre-incubated cell layers from parallel experiments electroporated in presence of low (1 µM), medium (10 µM) or high (100 µM) concentrations of bleomycin were stained with DAPI in order to visualize their nuclear structure (Fig. 5.46). In all cases typical chromatin condensation and nuclear fragmentation (Fig. 5.46 D, arrows) is observed for nuclei residing on the active electrode area. At highest bleomycin concentrations apoptotic nuclei were obviously removed from the major part of the electrode in the course of the staining and washing processes (C).

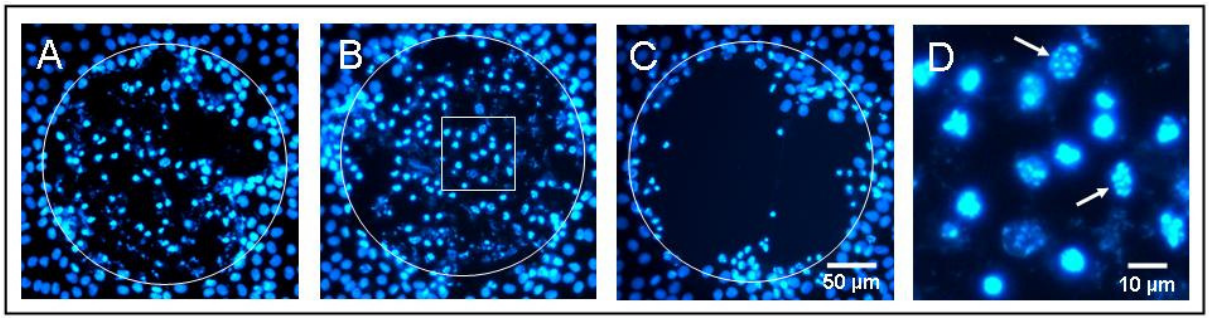

Fig. 5.46: Epifluorescence micrographs of DAPI stained NRK cell layers grown on *8W1E* ECIS electrodes pre-treated with 0.5 µM cytochalasin D documented 25 h (A, B) or 16 h (C)* after electroporation in presence of **A:** 1 µM, **B:** 10 µM, **C:** 100 µM bleomycin. *: The cell layer in C was obtained from another experiment than cell layers in A and B. **D:** Digitally magnified area selected from B. Arrows indicate cell nuclei with fragmented and condensed DNA.

Cell layers pre-treated with or without cytochalasin D after electroporation were subjected to live/dead staining (Fig. 5.47) and subsequent DAPI staining in presence of different bleomycin concentrations as well as all necessary controls (Fig. 5.48).

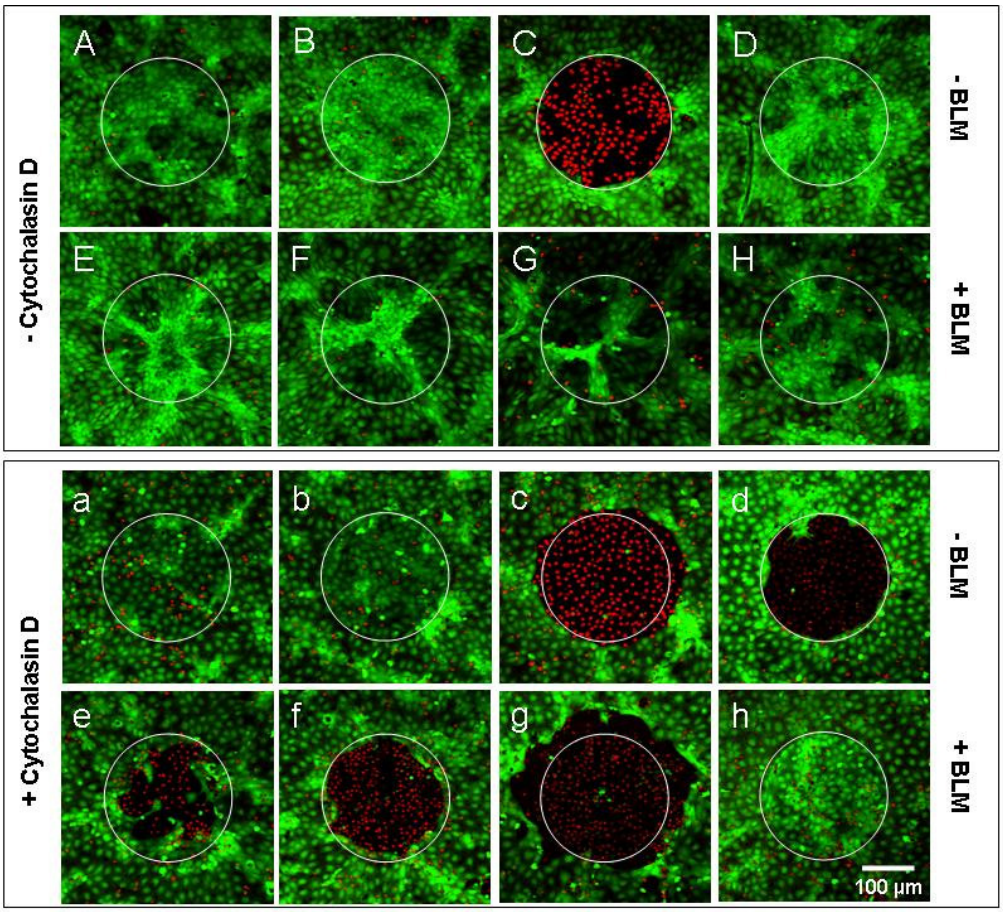

Fig. 5.47: Confocal fluorescence micrographs of NRK cell layers grown on *8W1E* ECIS electrodes after staining with the live/dead assay. Cell layers **A – H** were kept **without cytochalasin D.** Cell layers **a – h** were pre-incubated for 3 h **with 0.5 µM cytochalasin D**. The cells were electroporated in presence of different concentrations of bleomycin (+ BLM) and compared to wounded cell layers and control cell layers (– BLM), respectively. **A**, **a:** Untreated cell layer; **B**, **b:** Electroporation in $EBSS^{++}$; **C**, **c:** Electric wounding at 40 kHz, 5 V, 30 s 10 min before staining; **D**, **d:** Electric wounding at 40 kHz, 5 V, 30 s ~ 20 h before staining; **E**, **e:** Electroporation (40 kHz, 4 V, 200 ms) in presence of 1 µM bleomycin; **F**, **f:** Electroporation in presence of 10 µM bleomycin; **G**, **g:** Electroporation in presence of 100 µM bleomycin; **H**, **h:** Incubation with 100 µM bleomycin but no electroporation.

What becomes apparent from these staining experiments is that microlesions resulting from electric field-induced necrosis (C, D) or bleomycin-induced apoptosis (E – G) are efficiently resealed by inward migration of vital cells from the electrode periphery. If cell migration is inhibited by cytochalasin D, cell layer defects due to electric wounding (c, d) or apoptosis (e – g) can not be resealed. Mere incubation with bleomycin or simple electroporation without a cytotoxic probe present in the extracellular fluid yields mainly unaffected cell layers (B, H, b, h). It has to be considered, that cytochalasin D, due to its disrupting effect on the actin cytoskeleton (cp. Fig. 5.42), impairs cell morphology and cell layer structure. Nevertheless, it does not influence membrane resealing and recovery from electric pulsing (Fig. 5.47 h and Fig. 5.48 b).

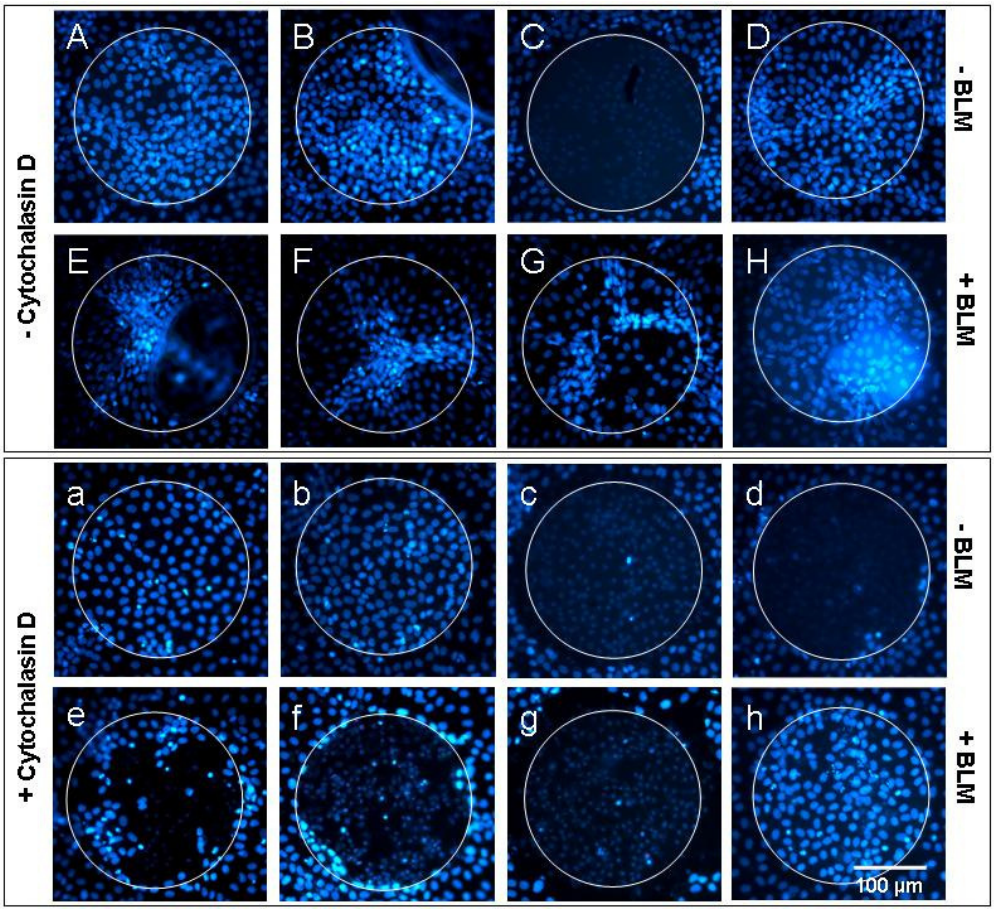

Fig. 5.48: Epifluorescence micrographs of NRK cell layers grown on *8W1E* ECIS electrodes after staining of nuclei with DAPI. Cell layers **A** – **H** were kept **without cytochalasin D.** Cell layers **a** – **h** were pre-incubated for 3 h **with 0.5 µM cytochalasin D**. The cells were electroporated in presence of different concentrations of bleomycin (+ BLM) and compared to wounded cell layers and control cell layers (– BLM), respectively. **A**, **a:** Untreated cell layer; **B**, **b:** Electroporation in $EBSS^{++}$; **C**, **c:** Electric wounding at 40 kHz, 5 V, 30 s 10 min before staining; **D**, **d:** Electric wounding at 40 Hz, 5 V, 30 s ~ 20 h before staining; **E**, **e:** Electroporation (40 kHz, 4 V, 200 ms) in presence of 1 µM bleomycin; **F**, **f:** Electroporation in presence of 10 µM bleomycin; **G**, **g:** Electroporation in presence of 100 µM bleomycin; **H**, **h:** Incubation with 100 µM bleomycin but no electroporation.

In summary, these experiments demonstrate that *in situ* electroporation-mediated cytoplasmic delivery of bleomycin into NRK cells induces apoptosis. The apoptosis associated morphological changes can be detected with a high time resolution by continuous monitoring of the cell layer impedance. However, recovery mechanisms like wound healing can mask cell death induced impedance decreases.

5.2.3 Loading of NRK Cells with Cytochrome c

Cytochrome c induces apoptosis in mammalian cells when it gets access to the cytoplasm. Cytochrome c is primarily known for its function as one of the essential electron carriers in the mitochondrial respiratory chain. Under physiological conditions the small heme protein is attached to the inner mitochondrial membrane and it is located in the inter-membrane space. Upon certain pro-apoptotic signals cytochrome c is released from the mitochondria and triggers and amplifies programmed cell death by activation of the apoptosome and subsequent

downstream effector caspases (Ow et al. 2008). Introducing cytochrome c into the cytoplasm of healthy cells by means of electroporation should activate the apoptotic cascade with all its consequences.

In the experiment presented in Fig. 5.49 a confluent layer of NRK cells grown on a *8W1E* ECIS electrode was electroporated in presence of cytochrome c applied to the extracellular buffer and the impedance was monitored at a frequency of 4 kHz (A) and 32 kHz (B). When cytochrome c is electroporated into NRK cells at a concentration of 10 mg/ml (curve d) cell recovery after the electric pulse (arrow) is significantly retarded compared to electroporation under cytochrome c-free conditions (curve b). Control cell layers electroporated in $EBSS^{++}$ completely recover from the electric pulse within about 1 h after an initial drop of the normalized impedance to 0.6. In presence of 10 mg/ml cytochrome c the impedance drops almost to 0.4 and it takes more than 3 h before the cell layer impedance reaches a constant value. Initial pre-pulse impedance values are not attained but values remain well below pre-pulse values within the observed time frame of 8 h (Fig. 5.49 A). Cell layers that were incubated with 10 mg/ml cytochrome c but not subjected to electroporation, show an impedance decrease from 1.1 at the beginning of the experiment down to 0.9 within the first 3 h.

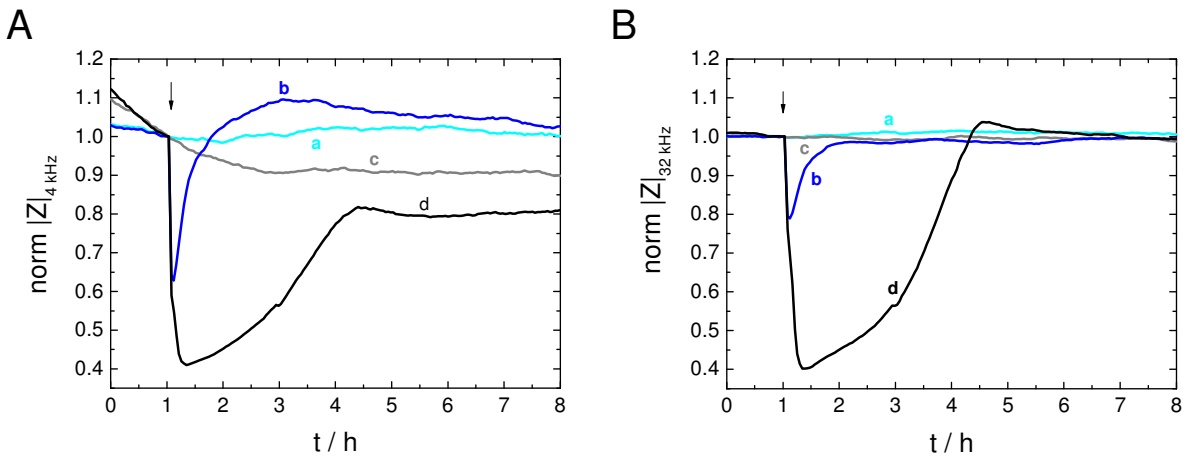

Fig. 5.49: Time course of the normalized impedance magnitude at 4 kHz (**A**) and 32 kHz (**B**) for NRK cells grown on *8W1E* ECIS electrodes before and after electroporation in presence of 10 mg/ml cytochrome c in $EBSS^{++}$ (d, ▬) compared to control cell layers: a, ▬: $EBSS^{++}$, no electroporation; b, ▬: $EBSS^{++}$, electroporation; c, ▬: 10 mg/ml cytochrome c, no electroporation. Cell layers were electroporated at 40 kHz, 4 V for 200 ms at the time point marked by the arrow. Absolute impedance values were normalized to the last value before electroporation (A: a: 15.8 kΩ; b: 16.31 kΩ; c: 15.89 kΩ; d: 17.9 kΩ; B: a: 4.154 kΩ; b: 4.21 kΩ; c: 4.48 kΩ; d: 4.30 kΩ). T = 37 °C.

These offsets in the time course of impedance after electroporation with cytochrome c compared to control cell layers without cytochrome c are not observed at a monitoring frequency of 32 kHz, where all cell layers reach pre-pulse impedances in the end of the experiment (Fig. 5.49 B).

Cell layers from a parallel experiment were stained for their nuclei using DAPI. Figure 5.50 presents central parts of the cell layer on the ECIS electrode after electroporation in presence of 10 mg/ml cytochrome c (D) compared to control cell layers treated as in the ECIS

experiment (A – C). Control cell layers all show normal morphology of their nuclei. No significant amount of apoptotic nuclei, characterized by fragmented and condensed chromosomes, can be observed for the control cell layers (A – C). On top of cytochrome c electroporated cell layers a cluster of fragmented nuclei with condensed chromatin can be observed, indicating apoptotic cells that have detached from the cell layer (D).

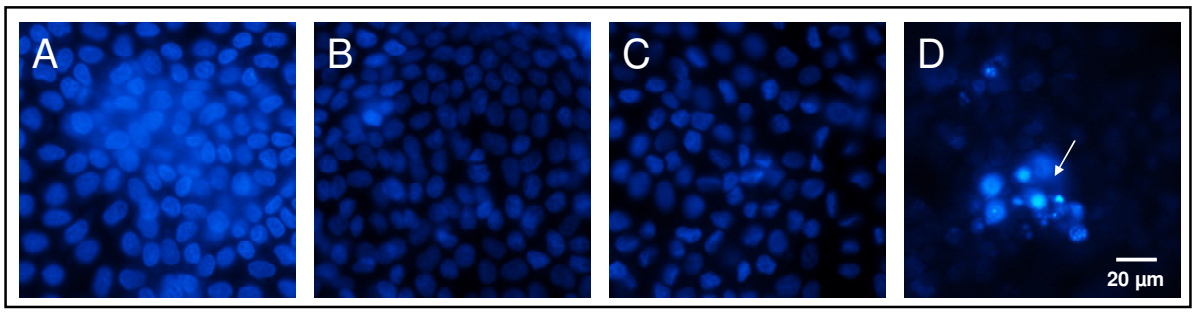

Fig. 5.50: Epifluorescence micrographs of DAPI stained NRK cells grown on gold-film electrodes 20 h after electroporation in presence of 10 mg/ml cytochrome c in EBSS^{++} (**D**) compared to control cell layers: **A:** EBSS^{++}, no electroporation; **B:** EBSS^{++}, electroporation (40 kHz, 4 V, 200 ms); **C:** 10 mg/ml cytochrome c, no electroporation. The arrow indicates a cluster of nuclei from apoptotic cells that have detached from the cell layer. T = 37 °C.

Figure 5.51 shows the concentration dependent cell response after electroporation-mediated loading with cytochrome c as monitored by the normalized impedance at 4 kHz (A) and 32 kHz (B).

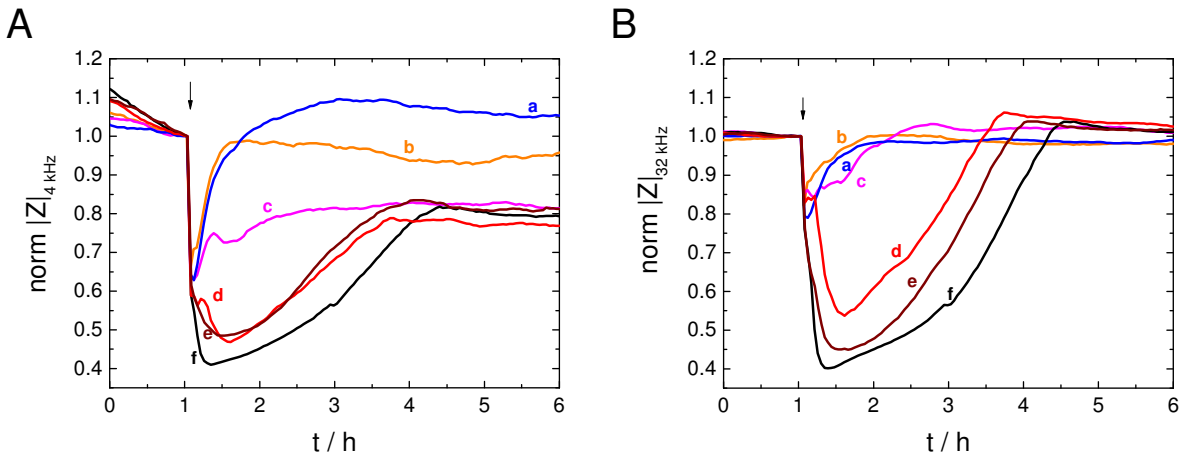

Fig. 5.51: Time course of the normalized impedance magnitude at 4 kHz (**A**) and 32 kHz (**B**) for NRK cells before and after electroporation in presence of different concentrations of cytochrome c in EBSS^{++}: a, ▬: 0 mg/ml, b, ▬: 0.1 mg/ml; c, ▬: 0.3 mg/ml; d, ▬: 1 mg/ml; e, ▬: 3 mg/ml; f, ▬: 10 mg/ml. Cell layers were electroporated at 40 kHz, 4 V for 200 ms at the time point marked by the arrow. Absolute impedance magnitudes were normalized to the last value before electroporation (**A:** a: 16.31 kΩ; b: 16.02 kΩ; c: 17.49 kΩ; d: 18.82 kΩ; e: 15.8 kΩ; f: 17.9 kΩ; **B:** a: 4.21 Ω; b: 4.43 Ω; c: 4.22 Ω; d: 4.19 Ω; e: 4.27 Ω; f: 4.30 Ω). T = 37 °C.

When cell layers get pulsed in presence of 0.1 mg/ml cytochrome c (curve b) the time course of the normalized impedance is very similar to that observed for a control cell layer electroporated in EBSS^{++} without cytochrome c (curve a). The cell layer recovers from electric pulsing in the same time range of about 1 h (Fig. 5.51, curve b). While at 4 kHz after cell layer recovery a small offset of impedance level for the cell layer electroporated in

presence of 0.1 mg/ml cytochrome c is observed compared to the control cells (A), this difference disappears at 32 kHz (B). At this higher frequency even the presence of 0.3 mg/ml cytochrome c does not provide significantly different impedance profiles compared to control cells, despite small irregularities in the response profile and a delay of roughly 30 min occur before the plateau phase is reached (B, curve c). At a monitoring frequency of 4 kHz, however, electroporation in presence of the same concentration of 0.3 mg/ml causes a considerable difference compared to the control (A, curve c). After a transient maximum ~ 25 min after electroporation, the impedance first slightly decreases and finally increases towards 0.82 approximately 7 h after pulsing. For concentrations of 1, 3 and 10 mg/ml cytochrome c a significant impedance drop directly after electroporation can be observed (A, curves d – f). A slight shoulder as observed for 0.3 mg/ml cytochrome c is present in the curve for 1 mg/ml using a monitoring frequency of 4 kHz. For these higher concentrations final impedance values settle below pre-pulse impedance values at ~ 0.8 (A, curves d – f). The time required for cell layer recovery to a stable impedance level of an established cell layer is extended with increasing concentrations, taking ~ 2.5, 3 and 3.5 h after electroporation (B, curves d – f).

In order to exclude unspecific cytochrome c effects due to high protein concentrations in the cells after electroporation, NRK cells were loaded with similar concentrations of BSA, a small globular serum protein without known enzymatic or bioactive effect. Figure 5.52 A presents the impedimetric response of NRK cells upon electroporation in presence of 1, 3 and 10 mg/ml BSA in EBSS^{++}.

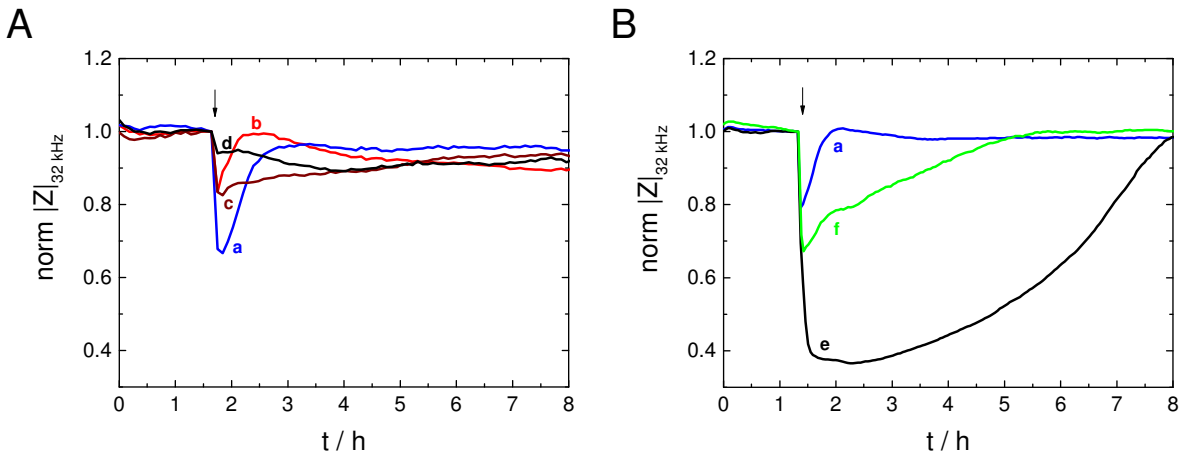

Fig. 5.52: Time course of the normalized impedance magnitude at 32 kHz for NRK cell layers grown on *8W1E* ECIS electrodes before and after **A:** electroporation in presence of different concentrations of BSA in EBSS^{++}: a, ▬: 0 mg/ml; b, ▬: 1 mg/ml; c, ▬: 3 mg/ml; d, ▬: 10 mg/ml or **B:** electroporation in presence of 10 mg/ml cytochrome c with or without caspase inhibitor: a, ▬: EBSS^{++}; e, ▬: 10 mg/ml cytochrome c; f, ▬: 10 mg/ml cytochrome c and 20 µM caspase inhibitor. Cell layers were electroporated at 40 kHz, 4 V for 200 ms at the time point marked by the arrow. Absolute impedance magnitudes were normalized to the last value before electroporation (**A:** a: 5.53 kΩ; b: 5.30 kΩ; c: 6.51 kΩ; d: 7.09 kΩ; **B:** a: 4.19 kΩ; e: 4.42 kΩ; f: 4.36 kΩ). T = 37 °C.

With respect to electroporation in protein-free EBSS^{++} buffer loading the cells with high concentrations of the biologically inactive BSA protein has only a minor effect on cell layer impedance or recovery kinetics as compared to electroporation in presence of 10 mg/ml

cytochrome c. With increasing concentrations of BSA the impedance drop after pulse application decreases. It was moreover observed that high BSA concentrations also notably increase the viscosity of the solutions what may lead to the deviations in resealing kinetics as well as to the elevated levels of absolute impedance magnitudes (see figure caption Fig. 5.52). An apoptosis inducing effect of BSA can be excluded.
In order to evaluate the specifity of the intracellular cytochrome c reaction, NRK cells were co-electroporated with the caspase inhibitor peptide DEVD (Fig. 5.52 B). In presence of the inhibitor peptide (curve f) the impedance recovery after cytochrome c electro-loading is slightly faster than without inhibitor peptide (curve e). Compared to control cells electroporated in buffer (curve a), there is still a considerable retardation of impedance recovery.

Thus, by means of *in situ* electroporation cytochrome c could be efficiently introduced into the cytoplasm of NRK cells. The specific activation of apoptosis in affected cells could be demonstrated by continuous impedance measurements being sensitive for cell morphological alterations occurring during apoptosis and cell death.

5.3 *In Situ* Electroporation Using Small Sample Volumes for the Efficient Transfer of Enzymes, Antibodies, DNA and Nanoparticles

As most of the bioactive molecules like enzymes, antibodies or nucleic acids are usually quite expensive and not always available in high amounts, a reduction of the sample volume during electroporation is inevitable for economic electroporation experiments with these kinds of molecules.

For typically used *8W1E* ECIS arrays the ratio between the surface area of the working electrode (Fig. 5.53 A) and the total well surface is less than 0.1 %. This is to a certain extend due to the 500 times bigger counter electrode, that covers up to 30 % of the total well area (cp. chapter 4.3.1.3, Fig. 4.3). These dimensions limit the minimum sample volume to ~ 150 µl, ensuring complete coverage of the well surface (Fig. 5.53 C; chapter 4.3.1.5, Fig. 4.6).

Here, an electroporation setup was established, which uses two small working electrodes of the same geometry separated by just 100 µm (Fig. 5.53 B). Connecting these two electrodes in series to the impedance analyzer for impedance measurements or to the frequency generator for electric pulse application (chapter 4.3.1.4, Fig. 4.5) allows to work in small volume chambers, thereby reducing the required sample volume to ~ 30 µl (chapter 4.3.1.5, Fig. 4.6).

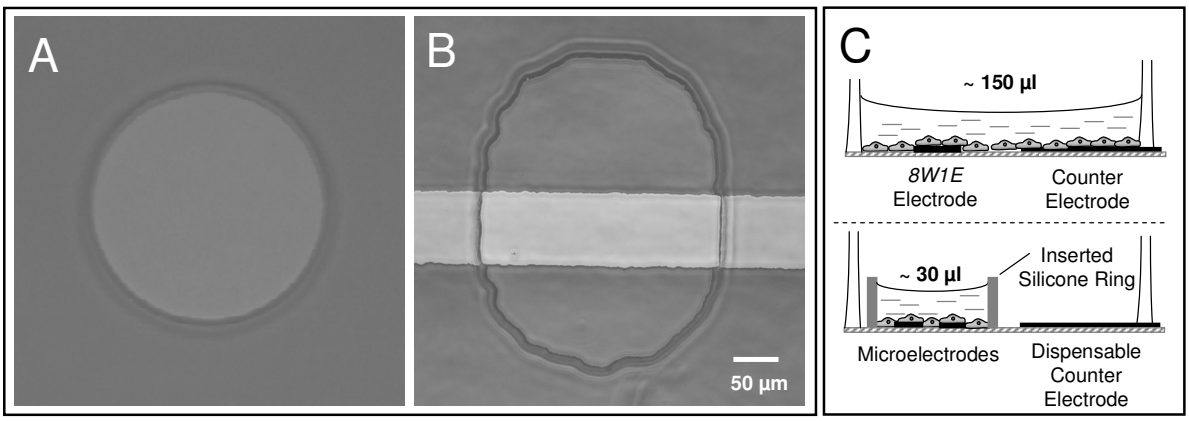

Fig. 5.53: Phase contrast micrographs of gold-film electrodes presented as greyscale images. **A:** Circular working electrode of the type *8W1E* with a surface area of ~ 5×10^{-4} cm^2; **B:** Microelectrodes for small volume applications consisting of two half-circle electrodes with a surface area of about 2.5×10^{-4} cm^2 each and a distance of 100 µm. **C:** Schematic illustration of *8W1E* (upper image) and microelectrode (lower image) setup as presented in detail in Materials and Methods.

5.3.1 Characterization of the Miniaturized Electrode Layout

The custom-made microelectrode arrays contain two small adjacent half-circle shaped gold-film working electrodes and one additional ~ 500 times larger counter electrode per well. The small working electrodes can be connected to the electronic equipment either (i) in combination with the second same-sized partner electrode or (ii and iii) each one individually in combination with the larger counter electrode (cp. chapter 4.3.1.4, Fig. 4.5). The three

different electrode interfacing modes provide different information of the system, collecting either (i) an integrated signal over both electrodes or (ii and iii) individual signals for each of the two half electrodes (cp. Fig. 5.54).

Figure 5.54 presents the three different sets of impedance spectra that were recorded from cell-free and NRK-covered microelectrodes, respectively. When one of the two half-circle shaped electrodes is measured against the larger counter electrode, the overall impedance of the system is dominated by the impedance contribution of the small working electrode. For the two microelectrodes individually interfaced to the impedance analyzer in combination with the large counter electrode two sets of impedance spectra, one for the cell-free (ii: ○, iii: ○) and one for the cell-covered (ii: ●, iii: ●) electrode, respectively, are obtained. The shift of the impedance spectra for the two cell-free working electrodes (○, ○), which is most prominent in the low frequency range of the CPE, can be attributed to minor differences in electrode surface area (cp. Fig. 5.53 B), mainly due to the fabrication processes. The offset in the spectra almost disappears for frequencies higher than 10^5 Hz, where the constriction resistance and parasitic impedances dominate the total impedance (cp. chapter 3.1.4, Fig. 3.8). In the frequency range between 10^3 – 5×10^5 Hz the NRK cell layer dominates the impedance spectrum (●, ●). While a distinct offset between both individual working electrodes is obvious in the low frequency range due to the dominating influence of the CPE, the spectra approach each other for frequencies above 10^4 Hz. The membrane capacitance as well as the constriction resistance and parasitic impedances arising from the electronics are quite similar for both electrodes and dominate the overall impedance in the high frequency regime.

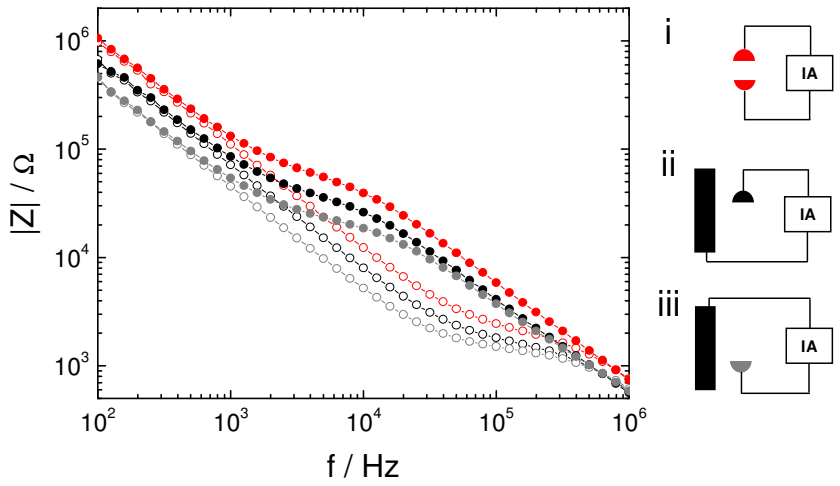

Fig. 5.54: Impedance spectra for cell-free (open symbols) and cell-covered (filled symbols) microelectrodes. They where measured individually either in combination with the large counter electrode (ii: ○, ● and iii: ○, ●) or in series to each other (i: ○, ●). Illustrations (i, ii and iii) at the right demonstrate the respective connection of the electrodes to the impedance analyzer (IA). The electrodes were covered with confluent layers of NRK cells. T = 37 °C.

If both adjacent working electrodes are connected in series to the impedance analyzer (cp. chapter 4.3.1.4, Fig. 4.5 B II), the total impedance is influenced by both electrodes. Spectra for cell-free and cell-covered electrodes recorded in this mode (i: ○, ●) show a course,

which is quite similar to the spectra recorded from one of the individual electrodes measured against the larger counter electrode (○, ●). The increase in impedance can be attributed to the reduced electrode area of the second working electrode compared to the large counter electrode. A reduction of the total electrode area causes a shift of the CPE to higher frequencies. Additionally, a second source of constriction resistance arises, which elevates the impedance level in the high frequency range. Since interfacing two working electrodes creates an impedance that is determined by both working electrodes, individual contributions arising from either half-electrode can not be distinguished. As the small surface area of both electrodes as well as their close proximity allows to restrict the volume of the sample fluid to ~ 30 µl (cp. 4.3.1.5), using two adjacent working electrodes connected in series to the IA (i: ○, ●) is the small volume experimental mode used here (cp. chapter 4.3.1.4 – 4.3.1.6).
In the following, impedance spectra of cell-free and cell-covered microelectrodes in the small volume arrangement (○, ●) are compared to spectra of the typical *8W1E* electrode setup (○, ◍) in the frequency range from 10^2 – 10^6 Hz (Fig. 5.55 A). Normalized impedance values ($|Z|_{\text{cell-covered}} / |Z|_{\text{cell-free}}$) are given in Fig. 5.55 B.

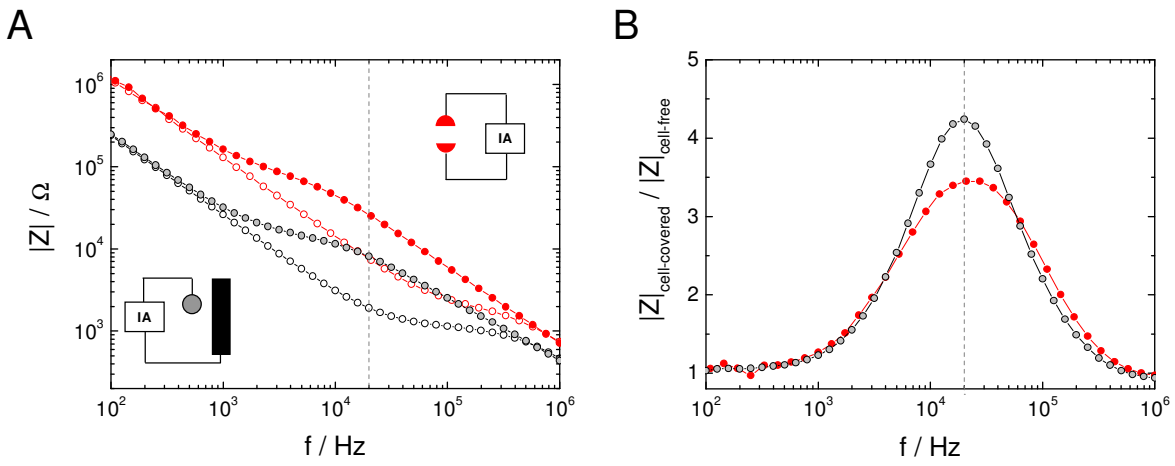

Fig. 5.55: A: Impedance spectra for cell-free (open symbols) and NRK cell-covered (filled symbols) microelectrodes (○, ●) compared to spectra for *8W1E* electrodes (○, ◍). **B:** Normalized impedance spectra ($|Z|_{\text{cell-covered}} / |Z|_{\text{cell-free}}$). T = 37 °C.

At low frequencies the impedance |Z| is dominated by the CPE of the electrodes. Due to the reduced electrode area of microelectrodes compared to *8W1E* electrodes, impedance spectra of microelectrodes are clearly shifted to higher impedance values (Fig. 5.55 A). The influence of the cell layer is obvious in a frequency range between 10^3 Hz – 5×10^5 Hz for both electrode types. The ratio of the spectra for the cell-covered and cell-free electrodes also termed the normalized impedance ($|Z|_{\text{cell-covered}} / |Z|_{\text{cell-free}}$) is illustrated in Fig. 5.55 B. The normalized impedance spectra for both electrode types overlap for a wide range of frequencies and both peak at about 20 kHz. The maximum value of the normalized impedance spectrum is only slightly higher for the *8W1E* electrode (4.2) when compared to the microelectrodes (3.4). Only in the high frequency regime above 5×10^4 Hz the normalized impedance is slightly shifted to higher frequencies for microelectrodes compared to an *8W1E* electrode.

Since microelectrodes show a similar peak sensitivity and frequency dependence for |Z|, the same monitoring frequency as for *8W1E* electrodes was selected for time-dependent impedance measurements using microelectrodes. To observe changes in cell morphology that affect the cell-substrate and cell-cell contact a monitoring frequency of 4 kHz was chosen (cp. Theoretical Background 3.1.5).

The working volume required for the microelectrode arrangement was reduced by inserting a small silicone ring around the microelectrodes (cp. chapter 4.3.1.5). In order to exclude an influence of the silicone insert on the electric measurement, impedance spectra of microelectrodes were recorded before and after introduction of the ring, as presented in Fig. 5.56. Impedance spectra of cell-free as well as cell-covered electrodes before and after modification correlate well, indicating no influence of the silicone chamber on the measurement.

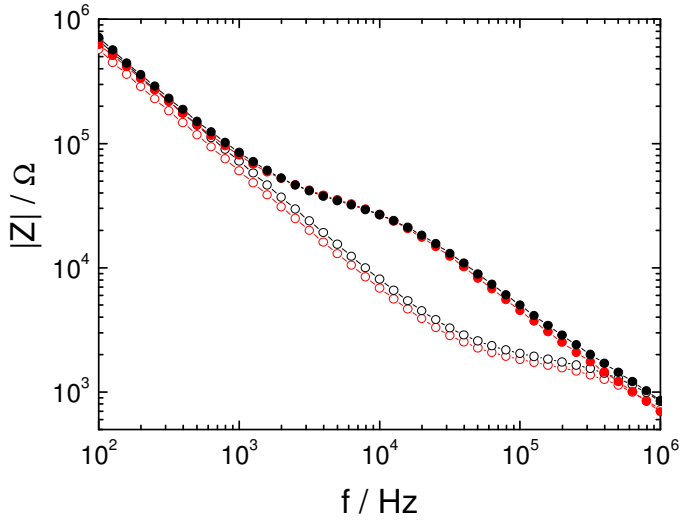

Fig. 5.56: Impedance spectra for cell-free (open symbols) and NRK cell-covered (filled symbols) microelectrodes before (○, ●) and after (○, ●) introducing a volume reducing silicone ring into each well of the array. T = 37 °C.

A major concern when working with small volumes is to prevent fluid evaporation. Water evaporation from the cell culture medium will result in elevated ion concentrations, which influence the ionic and osmotic balance of the cells. Therefore, certain precautions were taken to limit evaporation from the small working volume (cp. chapter 4.3.1.6). In order to evaluate the impact of volume reduction on cell layer integrity the cell layer impedance of NRK cells grown on small volume microelectrodes was recorded over several days (Fig. 5.57).
The cell layer impedance at 4 kHz remains stable over ~ 70 h in sample volumes of 10 – 30 µl (Fig. 5.57). With decreasing culture volume (30 µl → 20 µl → 10 µl) the cell layer impedance decreases to values of cell-free electrodes after roughly 75, 80 or 85 h, respectively. Keeping cells in a volume of 400 µl, as usually performed for *8W1E* electrode arrays, maintains a stable cell layer impedance over at least 120 h. In conclusion, microelectrodes proved to be well-suited for long-term measurements over at least ~ 70 h without affecting the cells by evaporation effects. Although a sample volume of 10 µl turned out to be sufficient for long-

term experiments, a sample volume of 30 µl was used in most experiments presented in this work.

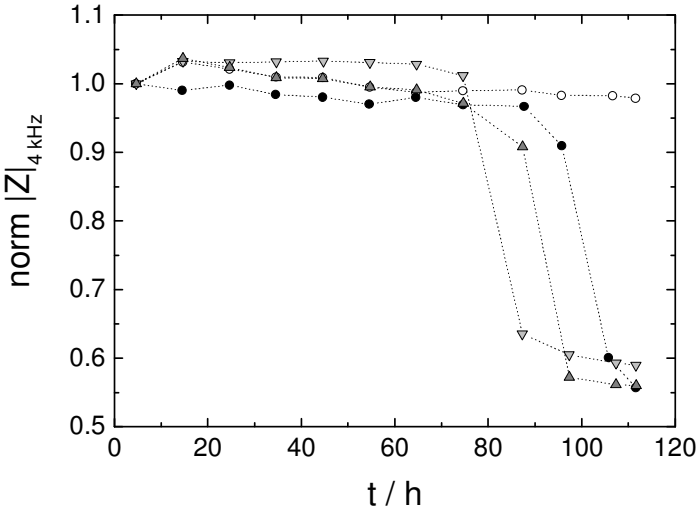

Fig. 5.57: Time course of the normalized impedance magnitude for NRK cell layers grown on microelectrodes loaded with different volumes of $EBSS^{++}$ buffer, using 10 (▽), 20 (△) or 30 µl (●) compared to a control volume of 400 µl (○). The effect of volume reduction on the cell layer impedance was measured discontinuously (dotted line) over several days. Absolute impedance magnitudes were normalized to the first value presented (t = 4.7 h) (10 µl: 33.53 kΩ; 20 µl: 34.81 kΩ; 30 µl: 39.82 kΩ; 400 µl: 37.83 kΩ). T = 37 °C.

5.3.2 Electroporation of Anchorage-Dependent Cell Lines on Microelectrodes: Dye Loading Studies

In contrast to the regular *8W1E* electrode setup, in which the total impedance of the system is dominated by the impedance of the considerably smaller working electrode, the impedance of the double electrode arrangement is determined by both electrodes. When applying an electroporation pulse, the voltage splits up between the two same-sized working electrodes of the same size instead of dropping across a single working electrode as it is the case when using a *8W1E* electrode setup. Thus, optimal electroporation parameters will be different for the modified microelectrodes, what makes it necessary to determine the best pulsing conditions for each cell line under study using this setup.

Electroporation parameters using the small volume microelectrode arrangement have been evaluated for NRK, HEK-293, Hep G2 and CHO cells. In dye uptake studies confluent cell layers were pulsed at a frequency of 40 kHz and varying pulse amplitudes and durations (2 – 7 V and 200 ms or 500 ms) in $EBSS^{++}$ supplemented with 250 kDa FITC-dextran as the fluorescent probe. The time course of cell layer impedance was monitored for several minutes before and after electric pulse application.

5.3.2.1 Micro-Electroporation of NRK Cells

Dye uptake studies for NRK cell layers grown on microelectrodes are presented in Fig. 5.58. The cell layers were pulsed for 200 ms with amplitudes of 4, 5, 6 and 7 V (A – D) or for 500 ms with amplitudes of 3, 4, 5 and 6 V (E – H).

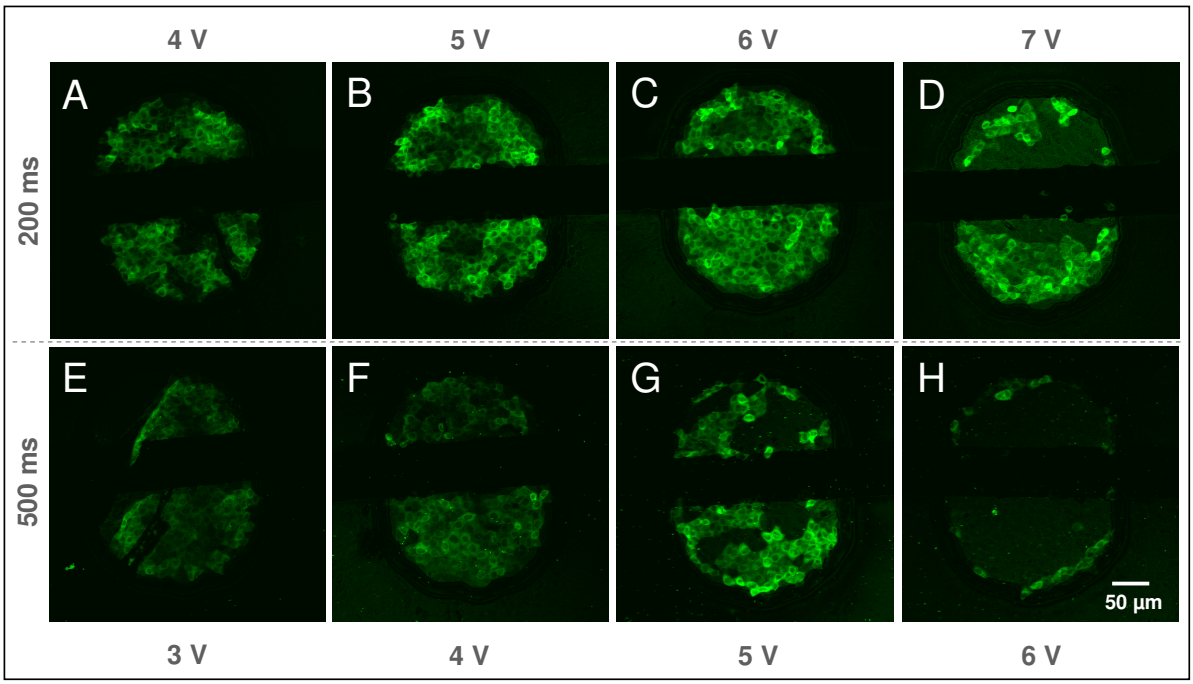

Fig. 5.58: Confocal fluorescence micrographs of confluent **NRK** cell layers grown on microelectrodes after electroporation in presence of 250 kDa FITC-dextran (2 mg/ml) in EBSS^{++} using an AC pulse of 40 kHz while pulse amplitude and duration were varied: **A:** 200 ms, 4 V; **B:** 200 ms, 5 V; **C:** 200 ms, 6 V; **D:** 200 ms, 7 V; **E:** 500 ms, 3 V; **F:** 500 ms, 4 V; **G:** 500 ms, 5 V; **H:** 500 ms, 6 V.

The population of cells showing dye uptake after *in situ* electroporation is restricted to the area of the active half-circle shaped microelectrodes. Using electroporation pulses of 200 ms duration (A – D), the intensity of cytoplasmic fluorescence increases for increasing pulse amplitudes ranging from 4 V to 6 V (A – C). Almost all cells on the electrode are loaded with the membrane-impermeable dye when pulse amplitudes of 4 V to 6 V are used (A – C). After electroporation with a 4 V pulse the major fraction of cells on the electrodes shows only a weak cytoplasmic fluorescence, whereas amplitudes of 5 V and 6 V yield cells, which are homogeneously filled with FITC-dextran and exhibit enhanced fluorescence intensity. Using a pulse amplitude of 7 V, however, only yields about 50 % of fluorescent cells. The remaining fraction of cells obviously could not hold the dye due to irreversible membrane damage (D).
Going to a pulse duration of 500 ms (E – H) the fluorescence intensity of dye loaded cells increases from 3 V to 5 V (E – G). However, after pulsing with a 5 V amplitude the fraction of fluorescent cells on the active electrode is significantly reduced to about 60 %, while the other fraction of the cells is presumably irreversibly damaged by the pulse (G) (cp. Fig. 5.6). Electroporation with a 6 V pulse applied for 500 ms results in a very low dye loading efficiency as only few cells at the rim of the electrode could hold the fluorescent dye within the cytoplasm (H).

Figure 5.59 shows time courses of the normalized impedance of NRK cells grown on microelectrodes after electroporation with pulse parameter combinations as used for dye loading experiments. NRK cell layers grown on microelectrodes show their cell type specific impedimetric response after an electroporation pulse: An immediate impedance drop is followed by an impedance increase to pre-pulse values (Fig. 5.59 A, B) (cp. chapter 5.1.1.2; Fig. 5.7).

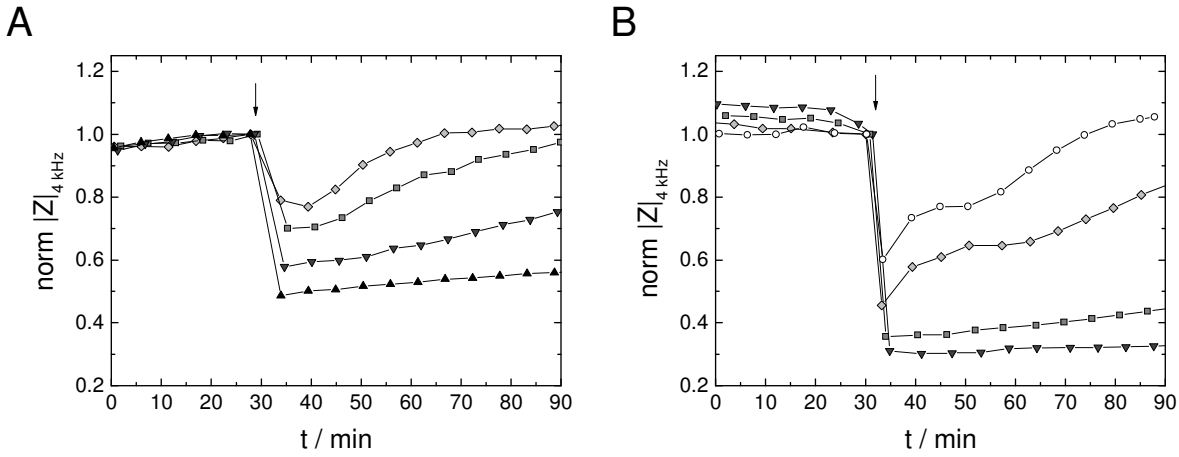

Fig. 5.59: Time course of the normalized impedance magnitude at 4 kHz before and after electroporation of **NRK** cells grown on microelectrodes in EBSS^{++} with 250 kDa FITC-dextran (2 mg/ml). Cell layers were electroporated using an AC pulse at 40 kHz for 200 ms (**A**) or 500 ms (**B**) and different pulse amplitudes: ○: 3 V; ◇: 4 V; □: 5 V; ▽: 6 V; ▲: 7 V. Absolute impedance magnitudes were normalized to the last value before electroporation (200 ms: 4 V: 49.24 kΩ; 5 V: 50.55 kΩ; 6 V: 46.49 kΩ; 7 V: 47.45 kΩ; 500 ms: 3 V: 57.98 kΩ; 4 V: 51.28 kΩ; 5 V: 47.68 kΩ; 6 V: 47.95 kΩ). T = 37 °C.

The capability to recover from the electroporation pulse is increasingly affected when elevated amplitudes and pulse durations are chosen for the electroporation pulse. Full recovery of the cell layer within ~ 1 h is achieved for pulses of 200 ms and amplitudes of 4 V (◇) and 5 V (□). For a pulse duration of 500 ms cell layers recover within this time frame only for a pulse amplitude of 3 V[5] (○).

As determined by dye uptake studies (Fig. 5.58) and impedimetric cell layer recovery studies (Fig. 5.59) electroporative loading of NRK cells on microelectrodes with membrane-impermeable probes is most efficiently performed by applying an electric AC pulse of: ***f* = 40 kHz, *U* = 5 V and *τ* = 200 ms.** Other suitable parameter combinations, which are, however, associated with lower loading efficiencies, are found to be 40 kHz, 4 V and 200 ms as well as 40 kHz, 4 V and 500 ms (cp. Fig. 5.58 A and F).

[5] Exact voltage drops and recovery times recorded for NRK cell layers after electric pulses of different amplitude and duration combinations vary significantly with the age of the cell culture (passage number), the time of the cell layer on the electrodes and the nutritional status. Electroporation parameters should be re-evaluated for each cell line under respective laboratory conditions.

5.3.2.2 Micro-Electroporation of HEK-293 Cells

Figure 5.60 presents confocal fluorescence micrographs of HEK-293 cell layers grown on microelectrodes after electroporation using varying combinations of pulse duration (200 ms, 500 ms) and amplitude (3 – 7 V). In the extracellular EBSS^{++} buffer 250 kDa FITC-dextran was offered as the membrane-impermeable fluorescent probe.

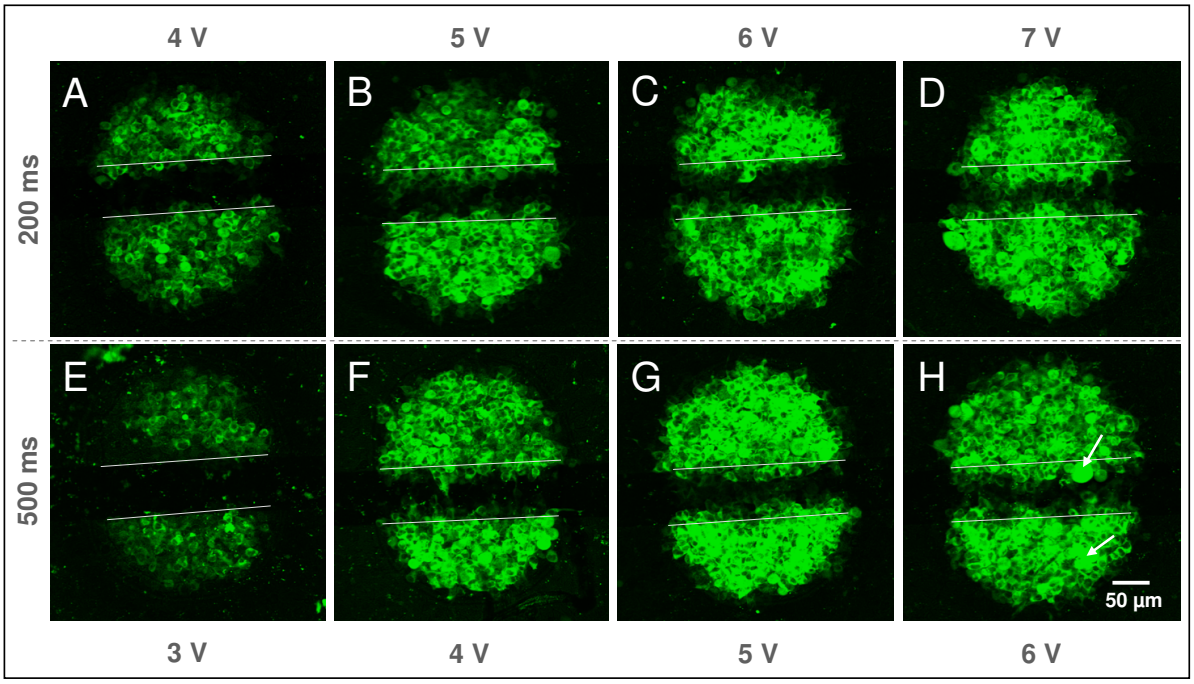

Fig. 5.60: Confocal fluorescence micrographs of confluent **HEK-293** cell layers grown on microelectrodes after electroporation in presence of 250 kDa FITC-dextran (2 mg/ml) in EBSS^{++} using an AC pulse of 40 kHz while pulse amplitude and duration were varied: **A:** 200 ms, 4 V; **B:** 200 ms, 5 V; **C:** 200 ms, 6 V; **D:** 200 ms, 7 V; **E:** 500 ms, 3 V; **F:** 500 ms, 4 V; **G:** 500 ms, 5 V; **H:** 500 ms, 6 V. Grey lines delineate the border of the active electrode surface towards the ~ 100 µm wide, non-conducting gap. Arrows indicate cells with altered cell morphology.

For both pulse durations of 200 and 500 ms the dye loading efficiency increases with increasing pulse amplitudes (A – D, E – H). Using a pulse duration of 500 ms ~ 1 V lower amplitudes compared to 200 ms pulses are required to obtain similar loading efficiencies, i.e. 200 ms, 5 V and 500 ms, 4 V. With increasing pulse amplitudes the extent of cell loading beyond the active electrode area increases, as indicated by the grey line marking the border of the active electrode towards the electrode-separating gap. Although no severe cell damage is observed at any of the tested parameter combinations, some dye loaded cells show an altered, rounded cell morphology when a pulse of 6 V is applied for 500 ms (H, arrows).

Impedance measurements obtained from a parallel experiment as described above are shown in Fig. 5.61. The overall impact of an electric pulse on the cell layer impedance is quite moderate as known from electroporation experiments of HEK-293 cells on *8W1E* electrodes (cp. chapter 5.1.2 1). HEK cell layers respond either by a slight decrease or increase of the impedance (Fig. 5.61 A, B). Choosing a moderate pulse amplitude of 4 V or 5 V for 200 ms results in a slight transient impedance decrease (4 V, ◇) or increase of the normalized

impedance to 1.08 (5 V, ■) (Fig. 5.61 A). With increasing amplitudes of 6 V and 7 V (▽, ▲) the cells respond with a transient impedance drop to about 0.8, which recovers to pre-pulse values within about 40 min. In the experiment shown in Fig. 5.61 B using a pulse duration of 500 ms to electroporate HEK-293 cells, a similar time course of the post-pulse impedance for all pulse amplitudes (3 – 6 V) is obtained. With increasing pulse amplitudes a slightly increasing impedance decrease down to ~ 0.9 can be detected. Within 20 min after electroporation pre-pulse values are attained for all pulse amplitudes. Repeating experiments, however, revealed that no clear dependence of the impedance time course with respect to the selected pulse parameters can be deduced. But for all measurements using the different pulse parameter combinations presented here, the normalized impedance directly after electroporation yielded values between about 0.8 and 1.2 and pre-pulse values were attained within maximal 1h.

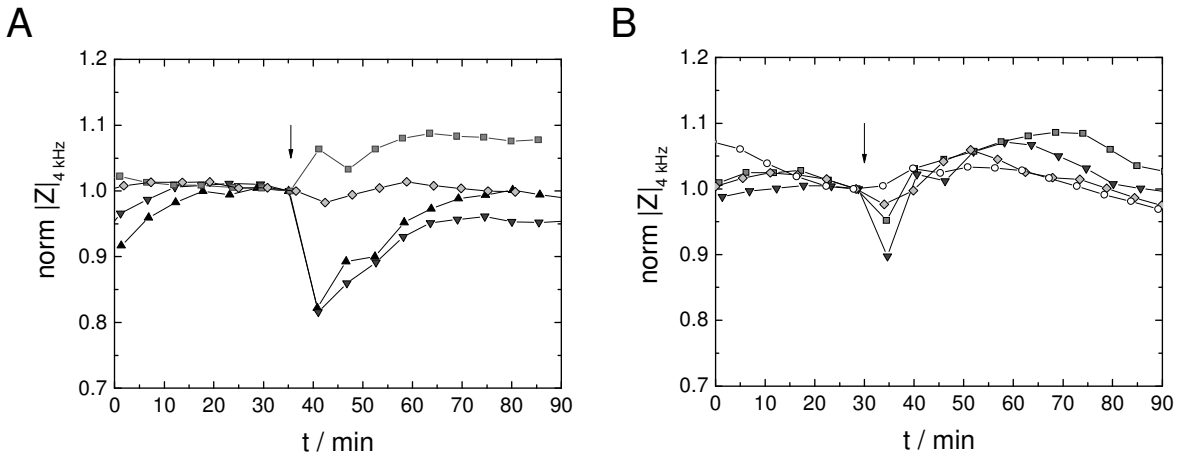

Fig. 5.61: Time course of the normalized impedance magnitude at 4 kHz before and after electroporation of **HEK-293** cells grown on microelectrodes in EBSS^{++} with 250 kDa FITC-dextran (2 mg/ml). Cell layers were electroporated using an AC pulse at 40 kHz for 200 ms (**A**) or 500 ms (**B**) and different pulse amplitudes: ○: 3 V; ◇: 4 V; ■: 5 V;▽: 6 V; ▲: 7 V. Absolute impedance magnitudes were normalized to the last value before electroporation (200 ms: 4 V: 46.33 kΩ; 5 V: 42.79 kΩ; 6 V: 35.7 kΩ; 7 V: 36.62 kΩ; 500 ms: 3 V: 30.73 kΩ; 4 V: 33.56 kΩ; 5 V: 39.02 kΩ; 6 V: 33.44 kΩ). T = 37 °C.

As revealed by dye loading experiments and impedance measurements, HEK-293 cells can be easily loaded with FITC-dextran without severe damage using pulses up to 7 V applied for 200 ms. A similar loading efficiency and a reduced impedimetric response can be achieved by using electroporation pulses of 6 V and 200 ms or 5 V and 500 ms. In further experiments **HEK-293** cells on microelectrodes were electroporated using pulses of f **= 40 kHz,** U **= 7 V and** τ **= 200 ms**.

5.3.2.3 Micro-Electroporation of Hep G2 Cells

Figure 5.62 presents dye loading studies for Hep G2 cell layers grown on microelectrodes. Pulse parameters for electroporation were varied between 200 ms and 500 ms choosing amplitudes between 4 V and 7 V or 3 V and 6 V, respectively.

Most FITC-dextran molecules are entrapped inside the Hep G2 cells when using an amplitude of 5 V for 200 ms or 500 ms (B, G). Below 5 V dye uptake is clearly reduced for both pulse durations (A, E, F). Using pulses with amplitudes above 5 V, however, results in a reduced cell layer fluorescence intensity and an increasing amount of cells with an untypical, mostly spherical morphology, showing cytoplasmic fluorescence without a distinguishable nucleus inside (C, D, H).

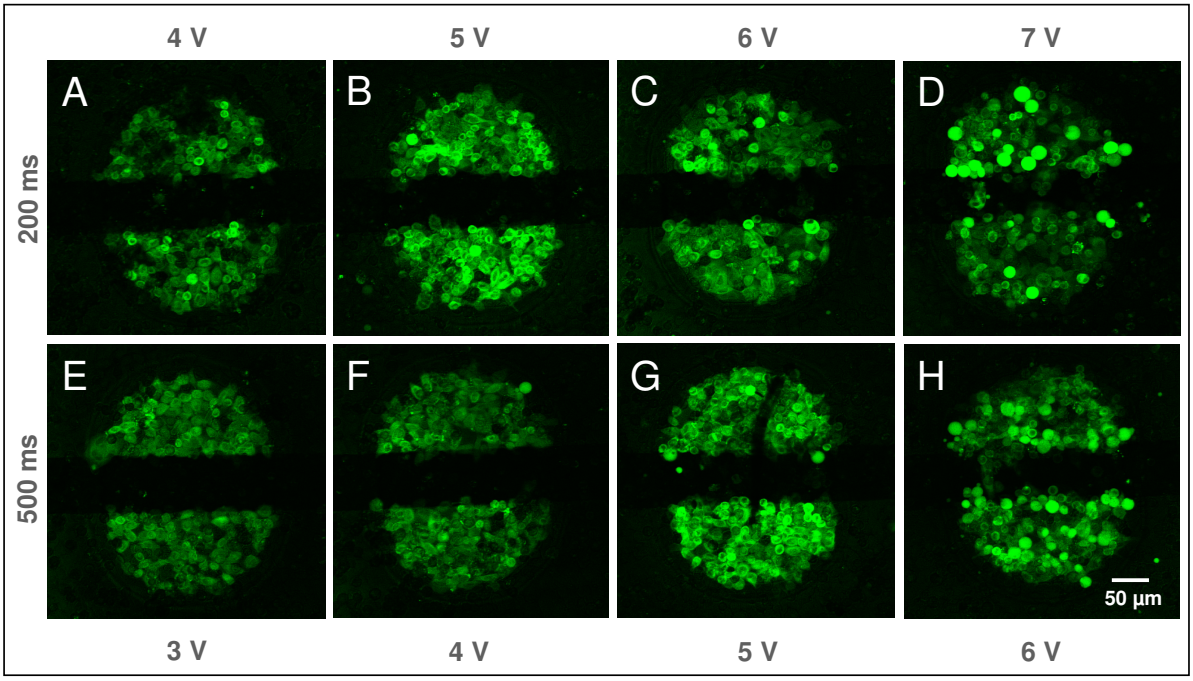

Fig. 5.62: Confocal fluorescence micrographs of confluent **Hep G2** cell layers grown on microelectrodes after electroporation in presence of 250 kDa FITC-dextran (2 mg/ml) in $EBSS^{++}$ using an AC pulse at 40 kHz while pulse amplitude and duration were varied: **A:** 200 ms, 4 V; **B:** 200 ms, 5 V; **C:** 200 ms, 6 V; **D:** 200 ms, 7 V; **E:** 500 ms, 3 V; **F:** 500 ms, 4 V; **G:** 500 ms, 5 V; **H:** 500 ms, 6 V.

Corresponding impedance measurements before and after electroporation of Hep G2 cells grown on microelectrodes using varying pulse durations and field strengths are presented in Fig. 5.63.

The characteristic cell layer response of Hep G2 cells after electroporation pulses is mirrored in a first, rapid impedance increase followed by a transient decrease before returning to pre-pulse values. For all pulse parameter combinations, a similar impedance time course is observed. Only for the highest pulse amplitude (7 V for 200 ms, 6 V for 500 ms) the initial impedance peak is reduced in height (A) or completely omitted (B).

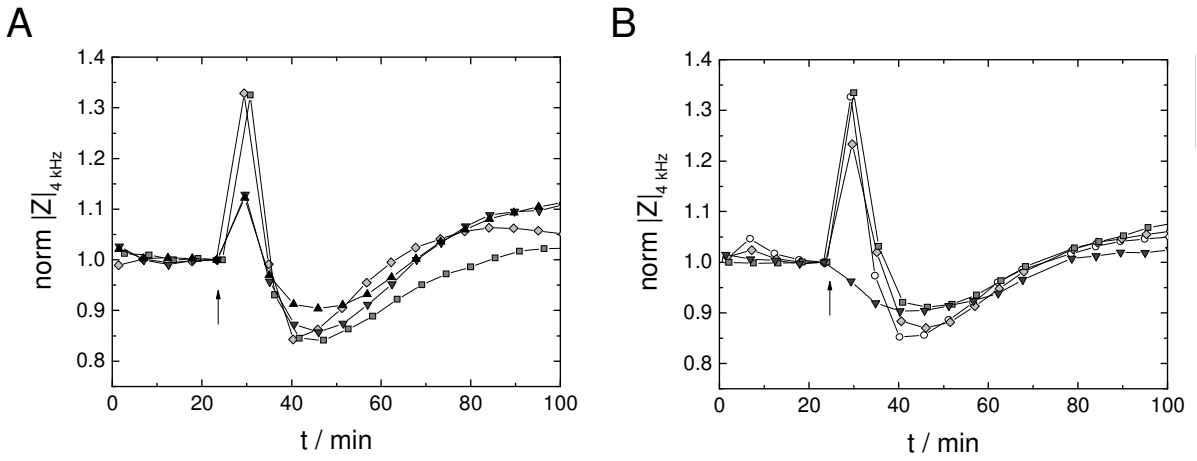

Fig. 5.63: Time course of the normalized impedance magnitude at 4 kHz before and after electroporation of **Hep G2** cells grown on microelectrodes in EBSS^{++} with 250 kDa FITC-dextran (2 mg/ml). Cell layers were electroporated using an AC pulse at 40 kHz for 200 ms (**A**) or 500 ms (**B**) and different pulse amplitudes: ○: 3 V; ◇: 4 V; □: 5 V;▽: 6 V; ▲: 7 V. Absolute impedance magnitudes were normalized to the last value before electroporation (200 ms: 4 V: 34.89 kΩ; 5 V: 36.41 kΩ; 6 V: 38.96 kΩ; 7 V: 35.00 kΩ; 500 ms: 3 V: 36.80 kΩ; 4 V: 36.91 kΩ; 5 V: 34.83 kΩ; 6 V: 37.57 kΩ). T = 37 °C.

In further experiments Hep G2 cells grown on microelectrodes were loaded with membrane impermeable probes using an electroporation pulse of f **= 40 kHz,** U **= 5 V and** τ **= 200 ms**, as probed by dye loading experiments and impedance monitoring.

5.3.2.4 Micro-Electroporation of CHO Cells

To determine suitable pulse parameter combinations for the electroporation of CHO cells grown on microelectrodes amplitudes were varied between 2 V and 5 V using pulse durations of 200 or 500 ms (Fig. 5.64).

For a pulse duration of 200 ms the best dye loading efficiency is obtained for amplitudes of 2 and 3 V (Fig. 5.64 A, B). Higher amplitudes of 4 and 5 V result in a slightly reduced and inhomogeneous loading, indicating cell layer defects (C, D). Using pulses of 500 ms duration uniform and efficient loading of CHO cells with the fluorescent probe is obtained after electroporation with 3 V amplitude (F). Other amplitudes show a reduced loading efficiency (E, G) or induced changes in cell morphology, like enlarged, multinucleate cells (H). However, severe cell damage is not detected for any of the chosen parameter combinations.

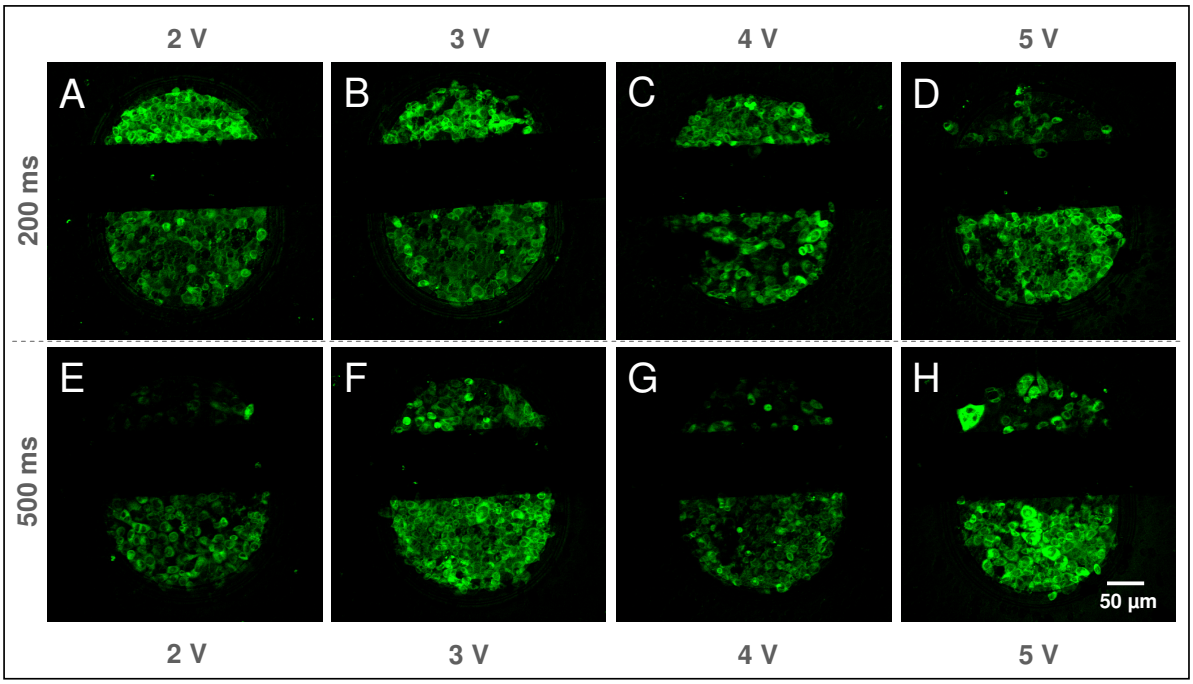

Fig. 5.64: Confocal fluorescence micrographs of confluent **CHO** cell layers grown on microelectrodes after electroporation in presence of 250 kDa FITC-dextran (2 mg/ml) in EBSS^{++} using an AC pulse at 40 kHz while pulse amplitude and duration were varied: **A:** 200 ms, 2 V; **B:** 200 ms, 3 V; **C:** 200 ms, 4 V; **D:** 200 ms, 5 V; **E:** 500 ms, 2 V; **F:** 500 ms, 3 V; **G:** 500 ms, 4 V; **H:** 500 ms, 5 V.

Time courses of normalized impedance values recorded at 4 kHz before and after electroporation of CHO cells in EBSS^{++} buffer without any fluorescent probe are shown in Fig. 5.65.

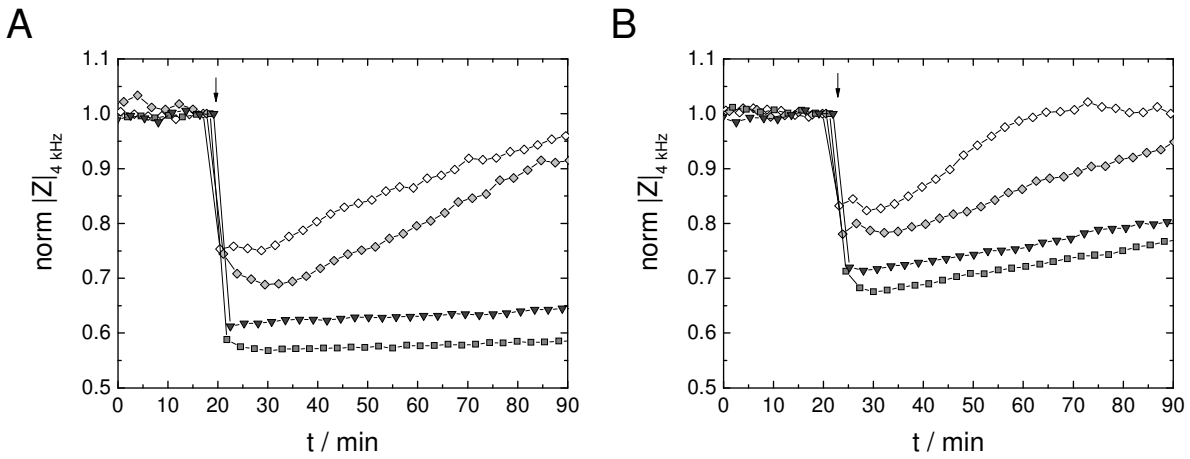

Fig. 5.65: Time course of the normalized impedance magnitude at 4 kHz before and after electroporation of **CHO** cells grown on microelectrodes in EBSS^{++}. Cell layers were electroporated using an AC pulse at 40 kHz for 200 ms (**A**) or 500 ms (**B**) and different pulse amplitudes: ◇: 2 V; ◈: 3 V; ▣: 4 V;▼: 5 V. Absolute impedance magnitudes were normalized to the last value before electroporation (200 ms: 2 V: 52.64 kΩ; 3 V: 52.23 kΩ; 4 V: 56.12 kΩ; 5 V: 50.82 kΩ; 500 ms: 2 V: 46.08 kΩ; 3 V: 42.58 kΩ; 4 V: 48.96 kΩ; 5 V: 43.63 kΩ). T = 37 °C.

CHO cell layers subjected to an electroporation pulse for either 200 ms (A) or 500 ms (B) show an amplitude dependent initial impedance drop. The cell layers electroporated with a

4 V (■) or 5 V (▼) pulse seem to be an exception. But due to normalization of absolute impedance magnitudes to the last value before electroporation the post-pulse impedance time courses for these cell layers are interchanged in order (see caption Fig. 5.65). Cell layers electroporated with amplitudes of 2 V (◇) and 3 V (◈) for 200 ms drop to 0.75 and 0.7, respectively. The impedance almost recovers to pre-pulse values of 0.96 (2 V) and 0.91 (3 V) within about 50 – 70 min. Cell layers respond with an impedance drop to ~ 0.6 after electroporation with amplitudes of 4 V and 5 V and do not recover to initial impedance values within the observed time frame.
A similar result is obtained for electroporations carried out with pulses of 500 ms duration (B). While the cell layer impedance increases back to pre-pulse values within ~ 50 min after pulsing at 2 V (◇), the impedance recovery is slightly retarded after pulsing at 3 V (◈). When amplitudes of 4 V (■) or 5 V (▼) are used, the impedance remains below ~ 0.8 within the observed post-pulse time frame of roughly one hour.
Comparing the impedance time courses after 200 ms and 500 ms pulses, the post-pulse impedance drop and time requirements for cell layer recovery are slightly more pronounced using a pulse duration of 200 ms instead of 500 ms. However, higher absolute impedance values before electroporation of these cell layers with 200 ms pulses may explain an increased voltage drop across these cell layers and, thus, the stronger drop of post-pulse impedance.

Based on the dye loading experiments and impedance measurements the best combination of pulse parameters for the electroporation of CHO cells grown on microelectrodes were found to be **f = 40 kHz, U = 3 V and τ = 500 ms**.

An overview of the best parameters used for electroporation of the investigated cell lines NRK, HEK-293, Hep G2 and CHO grown on microelectrodes is presented in Fig. 5.66. These combinations of pulse parameters were used in all further experiments, performed to load cells with various bioactive molecules as presented in the following chapters.

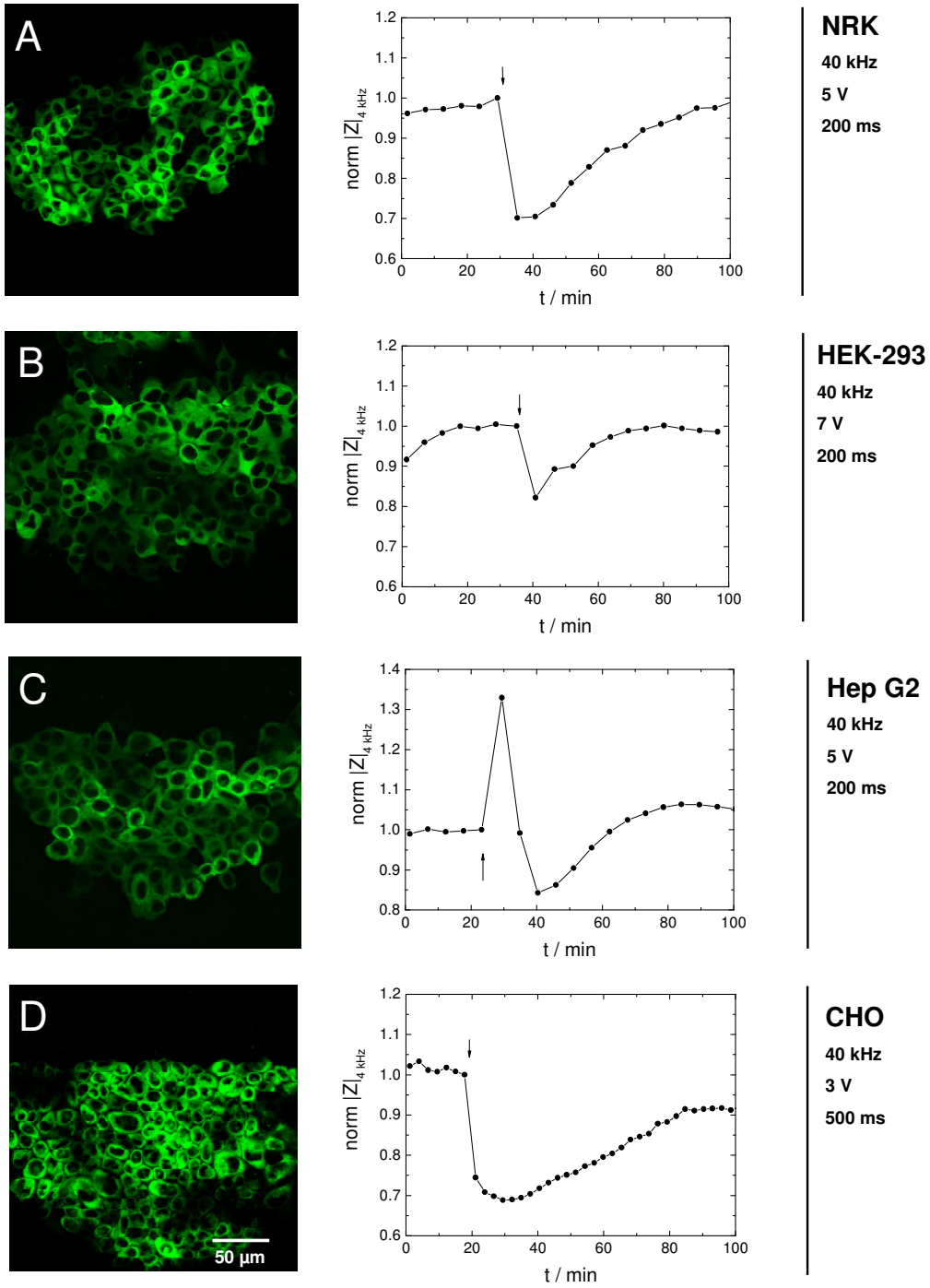

Fig. 5.66: Optimal electroporation conditions for different anchorage-dependent cell types grown on microelectrodes as determined by loading with 250 kDa FITC-dextran (2 mg/ml) and impedance monitoring at 4 kHz. **A: NRK:** 200 ms, 5 V, **B: HEK-293:** 200 ms, 7 V; **C: Hep G2:** 200 ms, 5 V; **D: CHO:** 500 ms, 3 V. CLSM micrographs show dye loaded cell layers on one half-circle shaped electrode. Impedance measurements show the time course of normalized impedance recorded before and after electroporation (arrow).

5.3.3 Micro-Electroporation of Anchorage-Dependent Cells: Delivery of Bioactive Molecules and Probes to the Cytoplasm

The investigation and specific manipulation of cell function is still a major goal of basic and applied research. Thus, cytoplasmic delivery of selected bioactive molecules by electroporation and concomitant impedance monitoring of the morphological changes by ECIS may provide a novel technique in the field of cell function analysis. The potential of transmembrane transport of bioactive molecules by electroporation coupled to an impedimetric readout has been shown in chapter 5.2. But many bioactive molecules are not available in high amounts or cause immense costs leading to experimental limitations of the conventional ECIS electrode setups. Therefore, the established small volume microelectrode arrangement provides a useful tool to efficiently probe the intracellular activity of selected biomolecules and probes. Chemically very different bioactive molecules were introduced into the cytoplasm of anchorage-dependent cell lines using the microelectrode setup: the apoptosis triggering protein cytochrome c, nucleic acid degrading enzymes, antibodies and DNA. Moreover, quantum dot nanoparticles were delivered into the cytoplasm of anchorage-dependent cells. The electroporation-mediated introduction of the respective molecule or probe into the cells was either verified impedimetrically monitoring the cell morphological response (cytochrome c, endonucleases) or microscopically detecting the intracellular localization of the probe itself (antibodies, quantum dots) or its products after transcription (DNA).

5.3.3.1 Loading of NRK Cells with Cytochrome c by Micro-Electroporation

NRK cells were loaded with extracellularly applied cytochrome c using a modified microelectrode arrangement with a working volume of only 30 µl, in order to validate the suitability and sensitivity of the microelectrode setup in comparison to *8W1E* electrodes. The impedimetric response of NRK cell layers upon electroporation in presence of 10 mg/ml cytochrome c in the extracellular fluid is presented in Fig. 5.67.

Cytoplasmic cytochrome c introduced into NRK cells by electroporation (▲) induces a significant delay of cell layer recovery from the electroporation pulse when compared to a control cell layer which was electroporated in cytochrome c-free $EBSS^{++}$ buffer (●) (Fig. 5.67 A). DAPI stainings of NRK cells after micro-electroporation in presence of 10 mg/ml cytochrome c clearly reveal a high amount of apoptotic cells, which are characterized by chromatin condensation and nuclear fragmentation (C, arrows). No effect on the nuclear structure is observed after electroporation in cytochrome c-free buffer, revealing nuclei with their typical round morphology and homogeneous chromatin distribution (B).

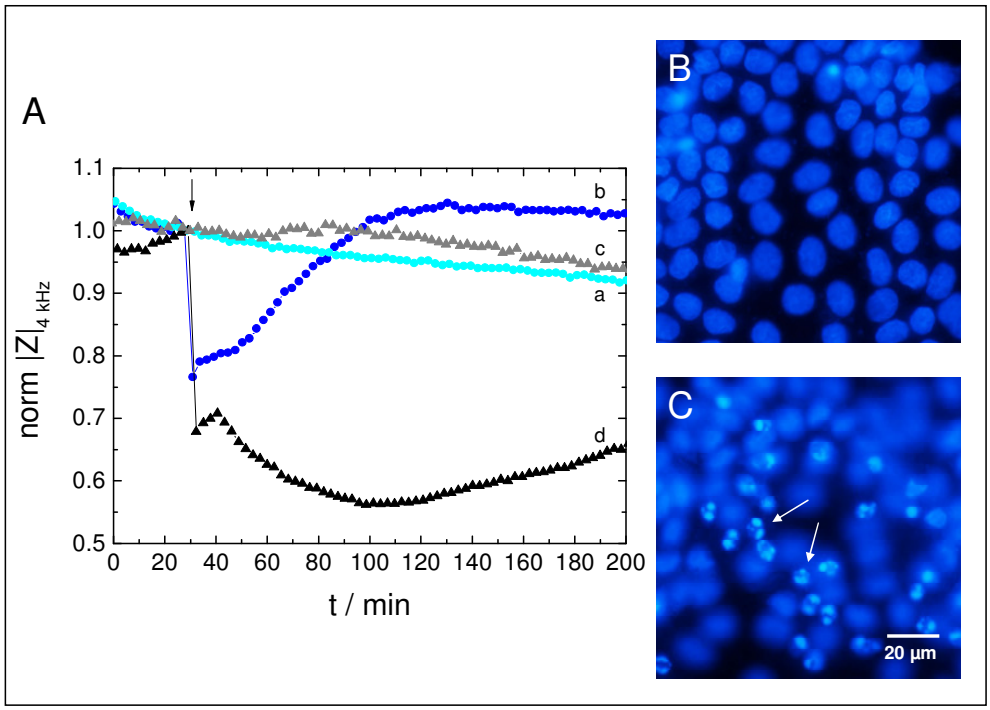

Fig. 5.67: A: Time course of the normalized impedance magnitude at 4 kHz for NRK cell layers grown on microelectrodes before and after electroporation in presence of 10 mg/ml cytochrome c (d, ▲) compared to control cell layers: a, ●: $EBSS^{++}$ without cytochrome c, no electroporation; b, ●: electroporation in $EBSS^{++}$ without cytochrome c; c, ▲: 10 mg/ml cytochrome c, no electroporation. Cell layers were electroporated using an AC pulse of 40 kHz, 5 V and 200 ms at the time point marked by the arrow. Absolute impedance magnitudes were normalized to the last value before electroporation (a: 59.51 kΩ; b: 29.28 kΩ; c: 63.81 kΩ; d: 60.20 kΩ). **B**, **C:** Epifluorescent micrographs of DAPI stained NRK cell layers grown on microelectrodes ~ 3 h after electroporation without (**B**) or in presence of (**C**) 10 mg/ml cytochrome c. T = 37 °C.

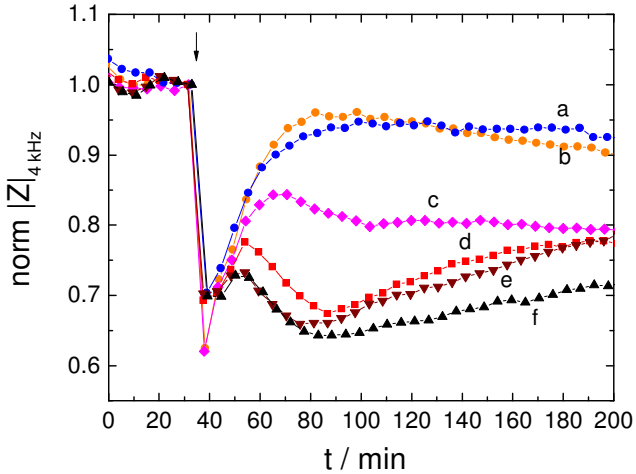

Fig. 5.68: A: Time course of the normalized impedance magnitude for NRK cell layers grown on microelectrodes monitored at 4 kHz before and after electroporation with different concentrations of cytochrome c in $EBSS^{++}$: a, ●: 0 mg/ml, b, ●: 0.1 mg/ml; c, ◆: 0.3 mg/ml; d, ■: 1 mg/ml; e,▼: 3 mg/ml; f, ▲: 10 mg/ml. Cell layers were electroporated at 40 kHz, 4 V for 200 ms at the time point marked by the arrow. Absolute impedance magnitudes were normalized to the last value before electroporation (a: 35.91 kΩ; b: 32.83 kΩ; c: 34.01 kΩ; d: 35.67 kΩ; e: 35.96 kΩ; f: 36.97 kΩ). T = 37 °C.

A limitation of the microelectrode setup in this work is that only four microelectrode pairs can be measured in parallel. Therefore, after initial characterization of the microelectrodes and approval of their use for electroporations in small volumes, a new modified design of

electrodes was developed in cooperation with Applied BioPhysics Inc. (Troy / NY, USA). To investigate the concentration dependent response of NRK cells to the introduction of cytochrome c, a new modified design of electrodes was used enabling parallel measurement of up to eight samples almost simultaneously[6] (Applied BioPhysics Inc., Troy / NY, USA) (Fig. 5.68).
With increasing cytochrome c concentrations the impedance recovery upon electric pulse application is significantly retarded for concentrations of 0.3 mg/ml and above. The cell layer behavior measured on small volume microelectrodes correlates well to results recorded for conventional *8W1E* electrode arrays (cp. chapter 5.2.3, Fig. 5.49).

5.3.3.2 Loading of NRK Cells with Endonucleases

NRK cells were electroporated with two different nucleic acid degrading enzymes, that are reported to have a considerable intracellular effect when being introduced into the cytoplasm: RNase A and DNase I.
RNase A is a riboendonuclease, an enzyme that is secreted by bovine pancreatic cells and decomposes RNA (Raines, 1998; Kartha, 1967). It recognizes the pyrimidine bases uracil and cytosin and cleaves the sugar backbone of the RNA.
DNase I is a secretory glycoprotein which cleaves DNA double strands. It was first isolated from bovine pancreas in the 1950's (Kunitz, 1950). DNase was additionally identified to efficiently bind globular actin (Lazarides and Lindberg, 1974), to act as inhibitor for g-actin polymerization (Eulitz and Mannerz, 2007) and to depolymerize f-actin (Hitchcock et al., 1976).

Electroporation of NRK Cells in presence of RNase A

Figure 5.69 A presents the response of NRK cells upon electroporation in presence of different concentrations of RNase A. While the incorporation of lower RNase concentrations (0.1 mg/ml, ◇) has a negligible effect on cell recovery after electroporation, already 0.25 mg/ml RNase (▽) disclose a reduced recovery potential of the cells after pulsing. After the typical impedance drop to 0.8 after electroporation the impedance further declines to a minimum of 0.67 within 20 min after pulse application. Although the impedance increases again in the following minutes, the initial value of the normalized impedance is not fully restored but settles down at 0.85. The post-pulse impedance decline and cell recovery delay after pulsing are even more pronounced at a RNase concentration of 0.5 mg/ml (▲). If heat inactivated RNase is applied to NRK cells (○) (Fig. 5.69 B), the kinetics of impedance recovery after electroporation are indistinguishable from control cells. The effect of active RNase is no longer visible.

[6] Microelectrodes used in this experiment have a somewhat different design (Applied BioPhysics Inc., Troy, NY) with an active electrode area of each microelectrode of 5×10^{-4} cm^2 instead of 2.5×10^{-4} cm^2. The electrode distance is about 1 mm. Despite the size difference they proved to be as suitable as the smaller electrodes used in all other experiments.

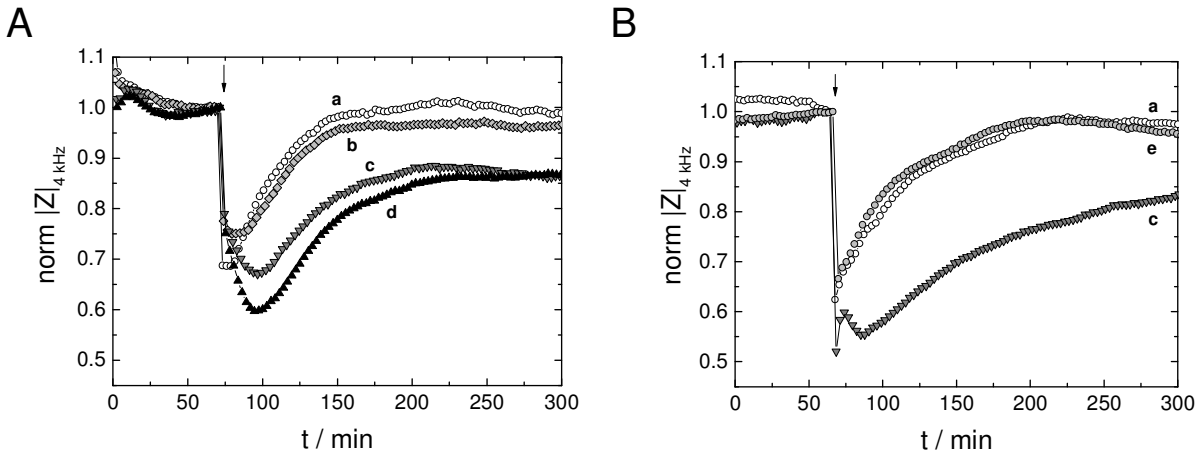

Fig. 5.69: Time course of the normalized impedance magnitude at 4 kHz before and after electroporation of NRK cells grown on microelectrodes in presence of RNase A. **A:** Electroporation with different concentrations of RNase in EBSS^{++}: ○ (a): 0 mg/ml; ◇ (b): 0.1 mg/ml; ▽ (c): 0.25 mg/ml; ▲ (d): 0.5 mg/ml; **B:** Electroporation with heat inactivated RNase (◍, e) in comparison to a control cell layer electroporated with EBSS^{++} (○) and active RNase (▽: 0.25 mg/ml). The activity of RNase is reported to be in the range of about 50 U/mg. Absolute impedance magnitudes were normalized to the last value before electroporation (A: a: 41.6 kΩ; b: 38.38 kΩ; c: 39.35 kΩ; d: 40.9 kΩ; B: a: 42.46 kΩ; c: 45.74 kΩ; e: 43.36 kΩ). T = 37 °C.

Electroporation of NRK Cells in presence of DNase I

After electroporative loading of the cellular cytoplasm with various concentrations of DNase I, a retarding effect on cell layer recovery can be detected for concentrations of 1 U/µl (▽) and above (Fig. 5.70 A).

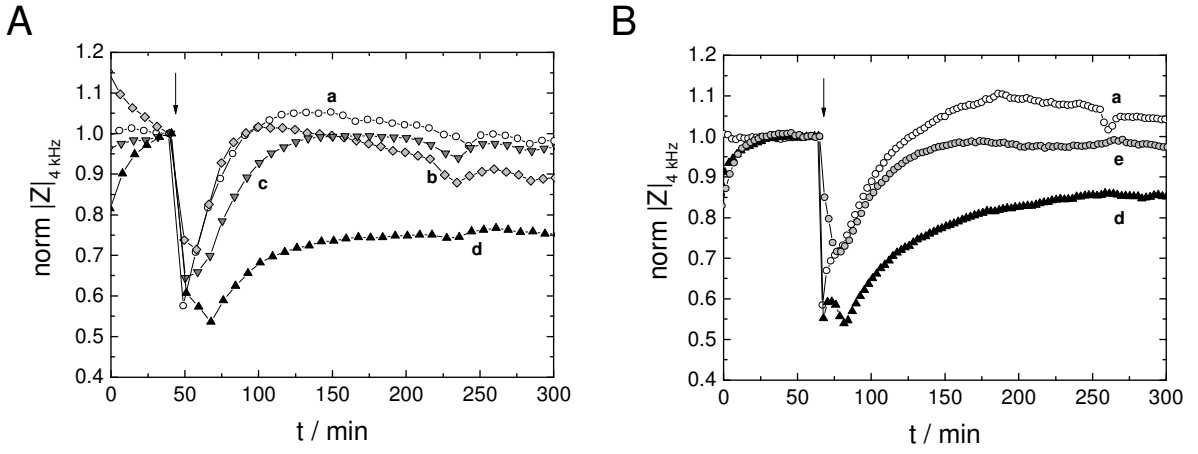

Fig. 5.70: Time course of the normalized impedance magnitude at 4 kHz before and after electroporation of NRK cells grown on microelectrodes in presence of DNase I. **A:** Electroporation with different concentrations of DNase I in EBSS^{++}: ○ (a): 0 U/µl; ◇ (b): 0.5 U/µl; ▽ (c): 1 U/µl; ▲ (d): 2 U/µl; **B:** Electroporation with heat inactivated DNase I (◍, e) in comparison to a control cell layer electroporated in EBSS^{++} (○) or with active DNase (▲: 2 U/µl). Absolute impedance magnitudes were normalized to the last value before electroporation (A: a: 43.39 kΩ; b: 40.69 kΩ; c: 41.12 kΩ; d: 47.14 kΩ; B: a: 35.29 kΩ; c: 45.27 kΩ; e: 43.54 kΩ). T = 37 °C.

After electroporation of NRK cells in presence of 2 U/µl DNase I the initial drop of the normalized impedance in response to electric pulsing (~ 0.6) is followed by a further decrease over ~ 10 min to a minimum of 0.54 (▲). Afterwards, the impedance increases again but remains below base line values settling at ~ 0.75 at the end of the measurement. Heat inactivation eliminates enzyme activity, as elucidated by an impedance time course similar to the control cell layer (B, ◍).

For appropriate concentrations of RNase A and DNase I the intracellular activity of these nucleic acid degrading enzymes is mirrored by a post-pulse impedance decrease (10 – 20 min) and by a delayed and incomplete cell layer impedance recovery. Moreover, enzyme activity is efficiently eliminated by heat inactivation.

5.3.3.3 Loading of Adherent Cells with Antibodies

Electroporation-mediated loading of viable cells with antibodies promises a very versatile spectrum of applications. Antibodies combine a consistent basic structure with a high variability in the amino acid sequence of the antigen binding sites. The enormous variability in target recognition can be utilized to block specific functionalities within the cell. A combination of *in situ* electroporation with the ECIS technique would enable to introduce the selected antibody into the cells by electroporation and to monitor the morphological changes within a cell layer in real time. In a first proof of principle experimental antibody delivery was documented by fluorescence microscopy. In a first approach a fluorophore-labeled antibody being non-specific to any intracellular target was electroporatively loaded into the cytoplasm of NRK and Hep G2 cells. In further experiments target specific antibodies were chosen that bind intracellular epitopes of proteins which are associated with cell-cell contacts.

Electroporation of Cells in Presence of Fluorescently Labeled Unspecific Antibodies

Figure 5.71 presents NRK and Hep G2 cell layers after electroporation in presence of an *AlexaFluor*®568-labeled secondary antibody added to the extracellular fluid. As can be seen in Fig. 5.71 A and D, almost all cells have been loaded with the fluorescent antibody. Fluorescent cells can only be found on the electrode surface. The entire cytoplasm is loaded with the fluorescent antibody, whereas the nucleus remains dark. Since the antibody does not bind to a specific epitope in the NRK cells, the fluorescence intensity inside the cytoplasm is homogeneously distributed. This is also true for Hep G2 cells, which show some additional punctuate structures. If cells are incubated with the fluorescently labeled antibody without applying an electroporation pulse only some unspecific fluorescence, not attached to any cellular structures, can be detected (B, E). Electroporation in absence of any fluorophore-linked antibody does not yield fluorescent cells (C, F).

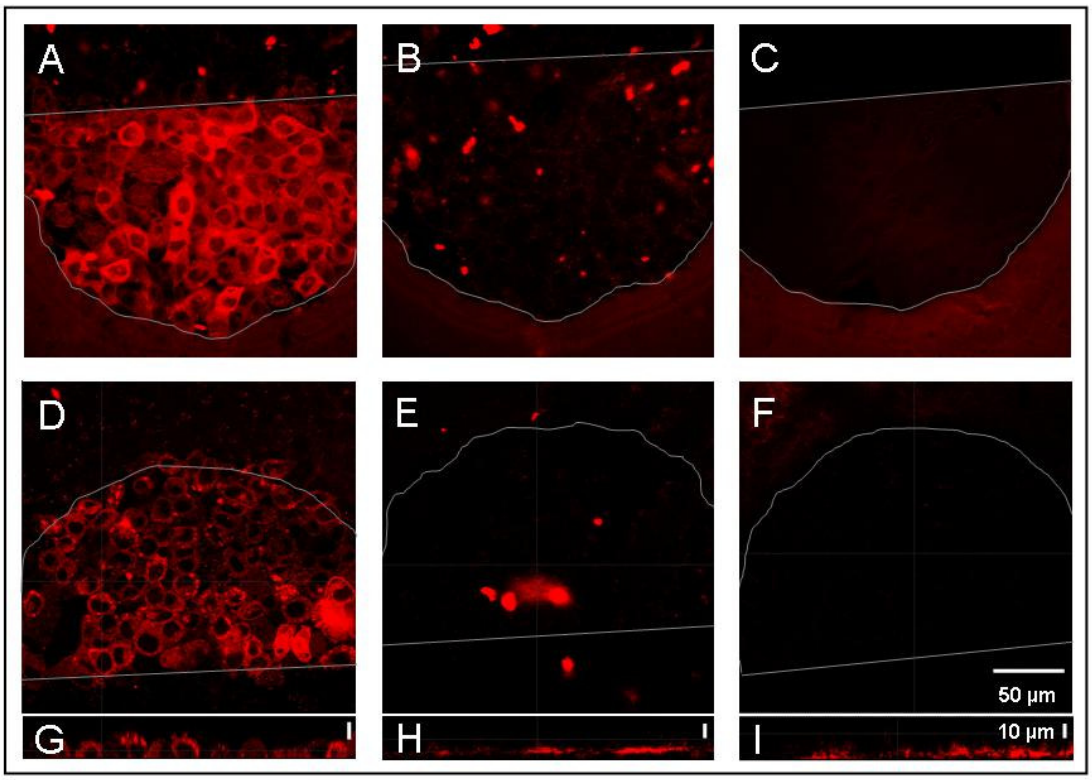

Fig. 5.71: Confocal fluorescence micrographs of adherent cell layers grown on microelectrodes after loading with an *AlexaFluor*®568 labeled non-specific antibody (anti-Fc-mouse) by electroporation **A – C: NRK** cells; **D – I: Hep G2** cells. **A**, **D:** Electroporation in antibody containing $EBSS^{++}$; **B**, **E:** Incubation in antibody containing $EBSS^{++}$ without electroporation; **C**, **F:** Electroporation without antibody. Images show one of the two half-circle shaped microelectrodes. Grey lines illustrate borders of the active electrode. **G – I:** Optical xz-sections of the images D – E.

Electroporation of NRK Cells in Presence of Antigen Specific Antibodies

For electroporative introduction of target specific antibodies into viable cells primary antibodies were chosen, each recognizing an intracellular epitope of membrane-associated proteins. Anti-ß-catenin specifically binds to ß-catenin, which connects the cadherin transmembrane protein to the actin cytoskeleton. Anti-occludin recognizes the intracellular N-terminus of occludin, a transmembrane protein involved in tight junction formation. ZO-1 is a cytoplasmic cell-junction associated protein anchoring transmembrane junction proteins to the actin cytoskeleton.

First, the specifity of the chosen antibodies was investigated by common immuno-cytochemical staining using Triton-X permeabilization to introduce the epitope specific antibody into the cells (Fig. 5.72). The localization of the primary antibody is verified by using a fluorophore-labeled secondary antibody (cp. chapter 4.4.4.7). For all selected antibodies specific binding of their epitope in NRK cells could be proven (Fig. 5.72). Immunostainings for occludin and ZO-1 show distinct labeling of the cell borders (B, C), whereas some cell-cell contact obscuring haze is revealed for the anti-ß-catenin antibody (A).

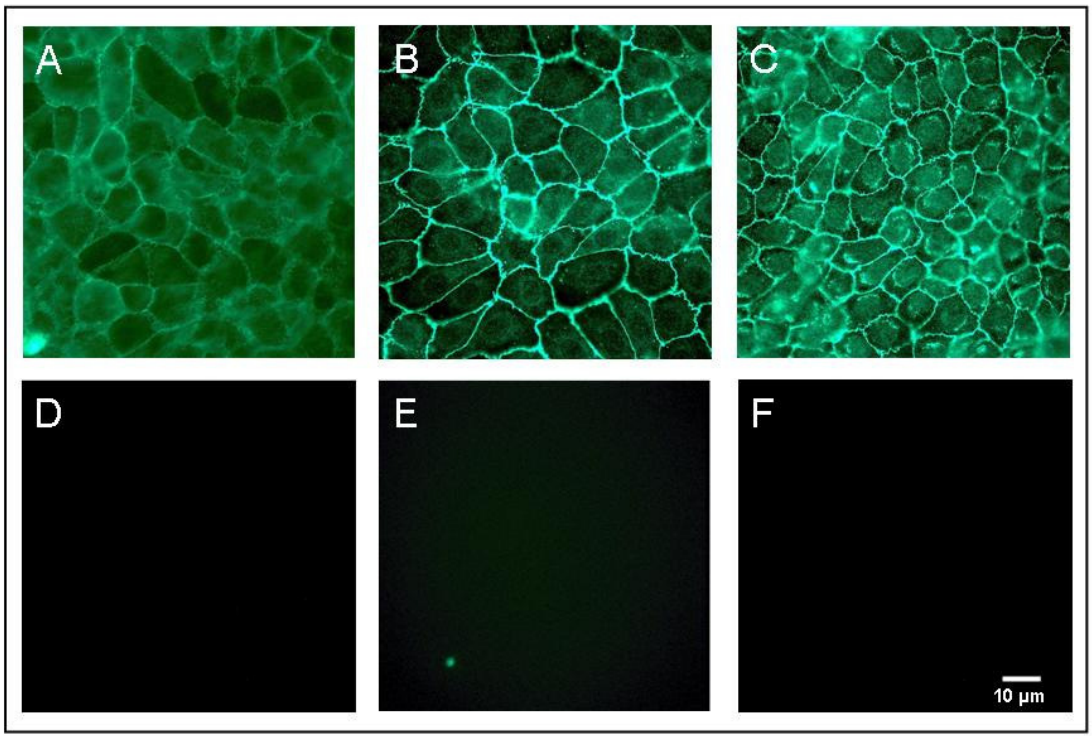

Fig. 5.72: Epifluorescence micrographs of immunostained NRK cell layers using antibodies specific for intracellular, membrane-associated epitopes. **A:** Anti-ß-catenin; **B:** Anti-occludin; **C:** Anti-ZO-1. **D – E:** Secondary antibody controls.

NRK cells were loaded with each of these antibodies by electroporation (Fig. 5.73). Entrapped antibodies after post-pulse membrane resealing were visualized by subsequent immunostaining using a fluorescence-labeled secondary antibody (cp. chapter 4.3.3.4).
As can be deduced from Fig. 5.73 NRK cells adhering to the electrode surface are efficiently loaded with all three different primary antibodies: anti-ß-catenin (A), anti-occludin (B) and anti-ZO-1 (C). For anti-occludin (B) and anti-ZO-1 (C) specific intracellular binding of their membrane-associated target proteins at the cell borders can be detected (E, F, G) as well as an unspecific cytoplasmic fluorescence. For ß-catenin, however, specific and unspecific bound antibodies can not be discriminated due to the strong overall cytoplasmic fluorescence (A). The fluorescence is homogeneously distributed throughout the cytoplasm, indicating that it is completely filled with antibody, whereas the nucleus remains dark.
Antibodies are not incorporated by processes other than electroporation as can be seen from the control cell layer, which has been incubated with the anti-ß-catenin primary antibody without electroporation (D).

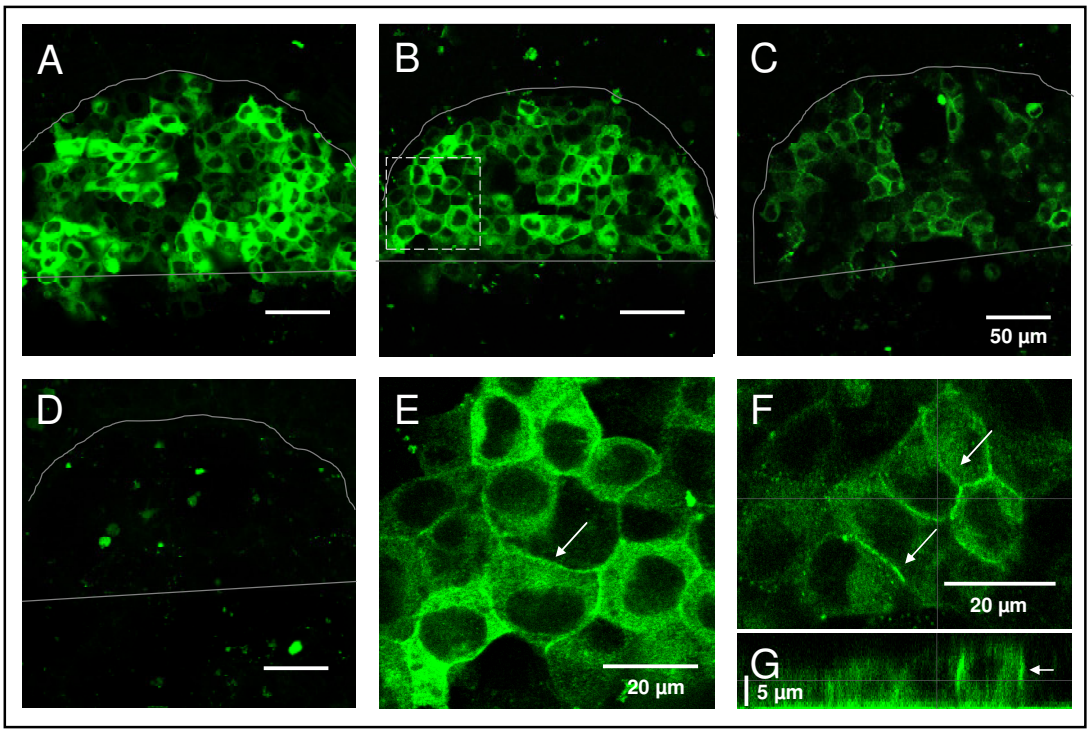

Fig. 5.73: Confocal fluorescence micrographs of NRK cells grown on microelectrodes after electroporation in presence of antibodies binding intracellular membrane-associated targets. **A:** Anti-ß-catenin, **B:** Anti-occludin and **C:** Anti-ZO-1. After electroporation the intracellular antibodies were detected by immunostaining with an *Alexa*® 488-labeled secondary antibody. The control cell layer (**D**) was held in anti-ß-catenin containing solution without electroporation. **E** and **F** show magnified areas of cell layers loaded with anti-occludin (**E**, magnification of area marked in B), or anti-ZO-1 (**F**, other cell layer). In **G** a side view to a z-stack of a confocal xy-series across the anti-ZO-1 loaded cells (see F) is shown. Arrows indicate increased antibody concentrations at the cell borders. Grey lines in A – D illustrate the borders of the active electrode.

5.3.3.4 Loading of Adherent Cells with DNA: *In Situ* Electrotransfection

Another important class of biomolecules are nucleic acids. Similar to antibodies their consistent structure differing only in the base sequence and size provides an enormous versatility. Only limited by the size of the respective genes, genetic information for various proteins can be transferred into living cells by experimental methods like electroporation. Heterologous expression of these recombinant genes brings about an important tool in functional genomics and proteomics. Again, combining the capability of electroporative transfer of exogenous DNA into anchorage-dependent cells with impedimetric sensing allows for online monitoring of changes in cell morphology induced by expression of the recombinant gene.

Thus, the applicability of DNA transfer into the cytoplasm of adherent cells by ECIS based *in situ* electroporation was investigated using the small volume microelectrode arrangement tailored for low volume applications.

NRK, HEK-293 and Hep G2 cells were loaded with the pCH1 plasmid encoding the green fluorescent protein (GFP) by electroporation. Figure 5.74 shows confocal fluorescence micrographs of different cell layers 24 h after electrotransfection. Depending on the cell type individual numbers of fluorescing cells can be detected in the cell layers on the electrodes.

HEK-293 as well as Hep G2 cells show good transfection efficiencies of about 70 – 80 % and 50 – 60 %, respectively (B, C). NRK cells, however, were not very susceptible to electroporation-assisted transfection as revealed by a low amount of EGFP-positive cells resulting in a transfection efficiency of only ~ 10 % (A). Transfected cells are not exclusively residing on the microelectrode surface but can also be found in the non-conducting cleft between the electrodes (A – C).

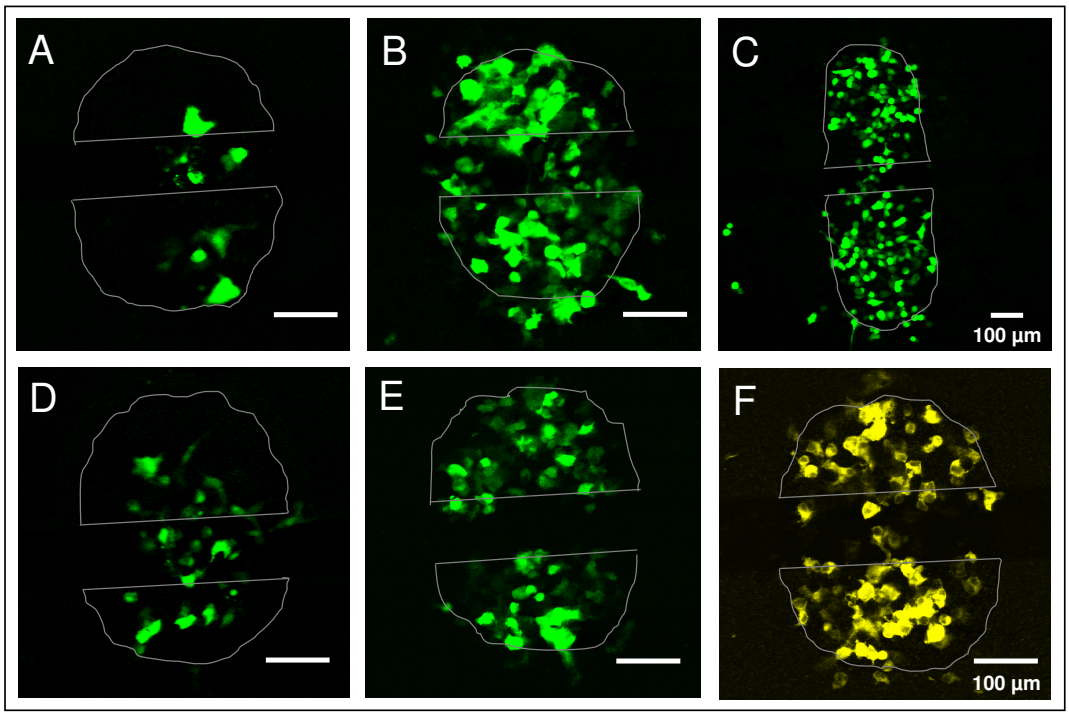

Fig. 5.74: Confocal fluorescence micrographs of *in situ* electrotransfected cells. Different cell types grown on micro- electrodes were electroporated in presence of plasmid DNA (pCH1, pEYFP-actin) carrying the EGFP or EYFP-actin gene or a linear 2278 bp DNA fragment isolated from pCH1 (6191 bp) encoding EGFP (EGFP-fragment). **A:** NRK, pCH1; **B:** HEK-293, pCH1; **C**[7]**:** Hep G2, pCH1; **D:** NRK, EGFP-fragment; **E:** HEK-293, EGFP-fragment; **F:** HEK-293, pEYFP-actin. Grey lines outline the border of the active electrodes.

Alternatively to the quite large pCH1 plasmid, a linear DNA molecule, the 2278 bp fragment of pCH1 containing the EGFP gene and all regulatory sequences, was used for electrotransfection (D, E) in order to evaluate the influence of DNA size and structure. In NRK cells the EGFP fragment, which was applied with the same number of copies as the plasmid DNA, results in a slightly improved transfection efficiency of almost 20 % (D) compared to plasmid DNA (A). HEK-293 cells show similar transfection efficiencies for both DNA types (70 – 80 %) (B, E). Electrotransfection of Hep G2 cells with the EGFP fragment DNA was not evaluated.

Since HEK-293 cells show a quite high transfection efficiency, they were additionally electroporated with pEYFP-actin, a plasmid encoding a fusion protein between globular (g) actin and fluorescent EYFP (F). A transfection efficiency of ~ 70 % is achieved and the g-

[7] Electrodes used for electrotransfection of Hep G2 cells slightly differed in size and shape compared to those used in experiments with NRK and HEK-293 cells.

actin is predominantly located in the cytoplasm. Due to over-expression of the fusion protein distinct actin structures can not be visualized.

5.3.3.5 Loading of NRK Cells with Quantum Dot Nanoparticles

Fluorescent nanoparticles in the nanometer range have gained increasing interest for biological applications in visualizing cellular structures or processes. Among all types of nanoparticles available, quantum dots are most suitable for highly resolved localization studies within cells due to their small dimensions and extraordinary photophysical properties. Quantum dots are inorganic crystals of semiconductor material with a diameter of only a few nanometers (1 – 10 nm). Their optical supremacy compared to most organic dyes is manifested by a high quantum yield and photostability combined with a broad excitation spectrum, a large Stokes shift and a narrow, symmetric emission peak, which is tunable by the nanocrystal size (Bruchez et al., 1998; Delehanty et al., 2009). Several coating strategies exist, rendering quantum dots water-soluble and biocompatible, as necessary for their use in biological systems. The transfer of tailor-made quantum dots into viable cells has become a major issue for specific labeling and tracking purposes. Most delivery approaches rely on inherent cellular uptake mechanisms resulting in quantum dot sequestration within endocytotic vesicles. Only direct physical manipulation using techniques like electroporation or microinjection enable an efficient delivery of quantum dots into the cytoplasm of adherent cells where they can interact with different intracellular structures and target molecules.
PEG-coated CdSe/ZnS core-shell quantum dot nanoparticles were transferred into the cytoplasm of NRK cells by ECIS based *in situ* electroporation. Figure 5.75 shows epifluorescent micrographs of NRK cells grown on microelectrodes after electroporation in presence of PEG-coated quantum dots in a concentration of 0.4 µM (A, C). The PEG coat inhibits rapid adsorption of the particles to the cell membrane and reduces unspecific endocytotic uptake. As illustrated by cell layers which were only incubated with the nanocrystals without electroporation (B, D) no considerable unspecific particle uptake takes place in the time frame of the experiment (~ 30 min). Thus, loading of the cytoplasm of NRK cells on the microelectrodes can be exclusively assigned to electroporation-mediated membrane permeabilization. Quantum dot particles fill the entire cytoplasm but remain excluded from the nucleus (C). The bluish and reddish background result from autofluorescence of the lexan substrate (blue), the cells on the electrode (blue) or the insulating photopolymer (red), respectively.

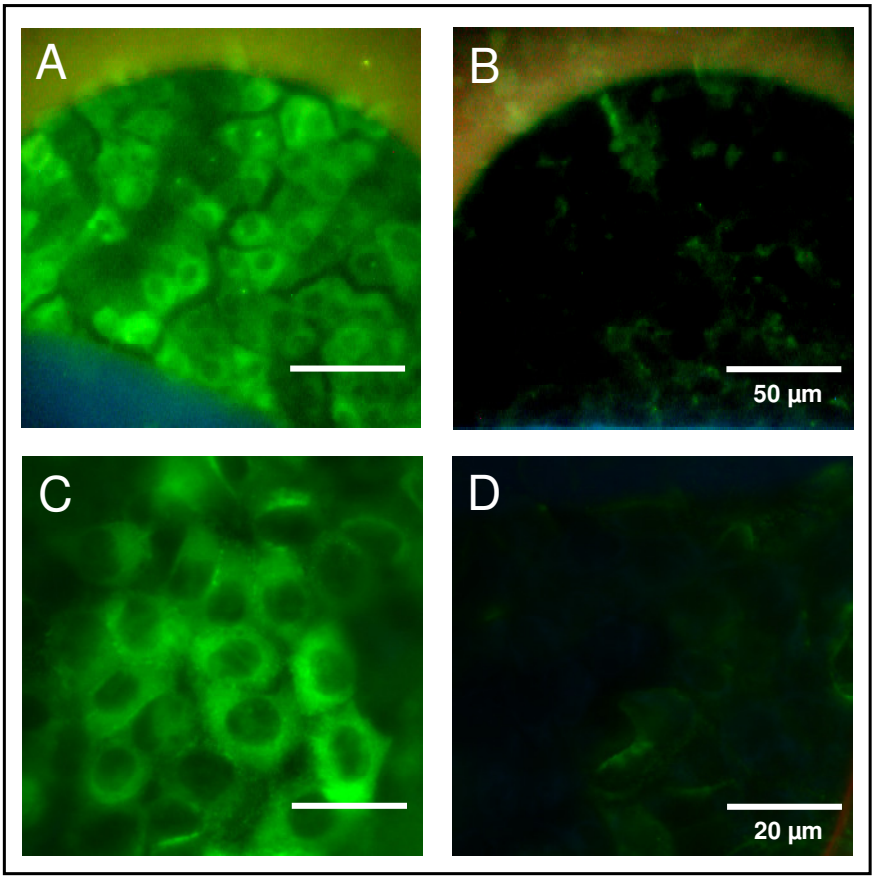

Fig. 5.75: Epifluorescence micrographs of NRK cells grown on microelectrodes after electroporation (40 kHz, 4 V and 200 ms) in presence of PEG-coated quantum dots (**A**, **C**). Control cell layers were subjected to the quantum dot solution (0.4 µM in $EBSS^{++}$) but were not permeabilized by electric pulsing (**B**, **D**). A, B show one cell-covered half-circle shaped microelectrode. C, D present magnified areas of cells in the center of a microelectrode. Micrographs were taken with the Nikon Diaphot (A, B) or Leica TCS SL (C, D).

5.4 Discussion

The ultimate goal of this work was to transfer biologically active molecules directly into the cytoplasm of anchorage-dependent cells by *in situ* electroporation using ECIS gold-film electrodes for pulse delivery. Combining this versatile technique for xenomolecule delivery with the analytical capabilities of the Electric Cell-Substrate Impedance Sensing (ECIS) technique creates a novel experimental setup for the study of cell function and drug delivery (Wegener et al., 2002). Some of the most interesting classes of biomolecules with the potency for molecular recognition inside the cell capable of modulating cellular properties are bioactive substances, like antibiotics and cytokines, as well as biomacromolecules like proteins (enzymes, antibodies) and nucleic acids. ECIS allows to monitor the specific impact of these kinds of intracellularly delivered molecules on cell morphology more precisely than optical microscopy with respect to spatial and temporal resolution. Keeping the cells grown on the electrode in their adherent state – *in situ* – during impedimetric analysis as well as during electroporation and cytoplasmic delivery of exogenous molecules, the presented *in situ* approach has great advantages over systems working with cells in suspension or other *in situ* setups with biochemical or microscopic detection. Cells can be electroporated in medium or physiological buffer without need for cooling or low ionic strength media in standard cell incubators at 37 °C (Wegener et al., 2002).

5.4.1 *In Situ* Electroporation of Adherent Cells on ECIS Electrodes

As a prerequisite for the use of ECIS electrodes for *in situ* electroporation-mediated loading of anchorage-dependent cells with bioactive molecules optimal electroporation conditions and pulse parameters have to be determined.

In the scope of this work most of the bioactive molecules were loaded into NRK cells. Electroporation of NRK cells on ECIS electrodes has already been studied by Wegener et al. (2002), using Lucifer Yellow (457 kDa) as fluorescent dye uptake probe. These studies provide a profound overview over the individual influence of pulse frequency, pulse amplitude and pulse duration on the loading efficiency. Therefore, the typical behavior of NRK cells after electroporation and loading with 250 kDa FITC-dextran was presented in this work without systematically showing complete dye loading studies (chapter 5.1.1.2). NRK cells were used to study the mechanism of electroporation-mediated dye uptake (chapter 5.1.3.1), the kinetics of impedance recovery after electropermeabilization (chapter 5.1.3.2) and the influence of subconfluent cell layers on loading efficiency (chapter 5.1.4). Optimal electroporation parameters for HEK, CHO, Hep G2 and NIH-3T3 cells were determined by systematic dye loading studies using 250 kDa FITC-dextran as well as impedance readings before and after electric pulse application for monitoring of cell layer recovery kinetics

(chapter 5.1.2). The results obtained from these studies are summarized below and are discussed in the following chapters.

- ***The anchorage-dependent cell lines NRK, HEK-293, Hep G2, CHO and NIH-3T3 can be efficiently loaded with membrane-impermeable FITC-dextran by in situ electroporation using ECIS electrodes in physiological buffer at 37 °C.***
- ***Maximum dye loading efficiencies are obtained using the following pulse parameter combinations: 40 kHz, 200 ms and 4 V (NRK, HEK-293, Hep G2 and NIH-3T3) or 40 kHz, 500 ms and 3 V (CHO).***
- ***Different cell types show a cell type specific time course of the normalized impedance after exposure to an electroporation pulse before cell layers recover to pre-pulse impedance values within ~ 40 – 80 min.***
- ***Dye loading efficiency and the time required for cell layer impedance recovery depend on pulse amplitude and duration.***
- ***The impedimetric response of the cell layer is a multi-phasic process and can be roughly subdivided into a fast response in the first ~ 10 s after electroporation and subsequent slow cell morphological changes till complete cell layer recovery after ~ 1 h.***
- ***Dye uptake takes place within the first 3 s upon electroporation with a 200 ms pulse.***
- ***Electroporation of subconfluent NRK cell layers using standard pulse parameters (40 kHz, 4 V, 200 ms) results in irreversible cell damage, while efficient dye loading is achieved using pulses of 40 kHz, 200 ms and 2 V.***

5.4.1.1 Optimization of Electroporation Parameters

The loading efficiency of cells with exogenous molecules essentially depends on the degree of permeabilization of their cell membrane. The extent of membrane permeabilization in turn is influenced by the electric pulse parameters used for electroporation. The fraction of voltage of the applied electric pulse that drops across the cell layer determines the degree of membrane polarization and, thus, the degree of permeabilization (cp. chapter 3.2). The frequency of the AC pulse was set to 40 kHz for all cell types. The frequency range suitable for efficient electroporation is generally rather wide (cp. Fig. 5.1). Simulations calculated by Hartmann (2003) predict that a high fraction of the applied voltage drops across the cell layer between ~ 5 kHz – 100 kHz (Hartmann, 2003; Albermann, 2004). Above this frequency range the major fraction of the applied voltage is lost in the electrolyte leading to joule heating of the ionic medium, while below 5 kHz a voltage drop across the electrode-electrolyte interface causes severe electrode damage (Wegener et al., 2002). As illustrated in Fig 5.1 the model parameters α, R_b and C_m (cp. chapter 3.1.3) influence the fractional voltage that drops across the cell layer at a selected frequency (Fig. 5.1).

The cellular parameters α, R_b and C_m were determined for the five different cell types under study (Tab. 5.1). For all cell types R_b values range from $2.3\,\Omega \cdot \mathrm{cm}^2$ for NIH-3T3 to

5.7 $\Omega \cdot cm^2$ for NRK cells. For R_b values between 1 and 10 $\Omega \cdot cm^2$ about 85 – 90 % of the applied voltage are assumed to drop across the cell layer at the frequency of 40 kHz (Fig. 5.1). For all selected cell lines values for α are between 2 and 4 $\Omega^{1/2} \cdot cm$, for which the simulated fractional voltage drop across the cell layer indicates 85 – 90 % (Fig. 5.1). At 40 kHz the fractional voltage drop across the cell layer decreases from ~ 90 % to slightly above 80 % when the cell membrane capacitance (C_m) increases from 1 $\mu F/cm^2$ to 2 $\mu F/cm^2$. C_m values for the different cell types range from 0.9 – 2.4 $\mu F/cm^2$ (Tab. 5.1). Thus, it can be assumed that for all cell lines under study the applied frequency of 40 kHz is suitable to yield efficient electroporation, as shown by successful loading of cells with membrane-impermeable 250 kDa FITC-dextran (Fig. 5.19). However, it has to be considered, that the respective fixed parameter pairs used for simulations differed from the parameter values obtained for the cell types under study (Fig. 5.1 A, B, C). Therefore, simulations shown in Fig. 5.1 only provide approximate estimates for the fractional voltage drop across layers of cells under study.
Further optimization of electroporation conditions was carried out with respect to pulse amplitude and duration choosing the parameter values in accordance to Wegener et al. (2002) (1 V – 6 V; 50, 100, 200 and 500 ms). On the basis of both, dye loading efficiency and cell layer impedance recovery kinetics optimal electric parameter combinations for the different cell types were determined.

Dye Loading Efficiency

Dye loading studies are among the most often used methods to evaluate electroporation efficiency (Neumann et al., 1999; Rols and Teissié, 1990a; Raptis et al., 1994; Ishibashi et al., 2007). Loading efficiency and viability are commonly determined microscopically or by flow cytometry. Frequently used dyes to determine dye loading efficiency are trypan blue (Teissié et al., 1999; Wolf et al., 1994), propidium iodide (PI) (Gabriel and Teissié, 1998; Golzio et al., 2002), Lucifer Yellow (LY) (Mir et al., 1998; Glogauer et al., 1993; Bright et al., 1996), and FITC-dextrans (FDs) with different molecular weights. In most cases FDs below 70 kDa have been used (Prausnitz et al., 1993; Rols and Teissié, 1998; De Vyst et al., 2008). Only in a few cases FDs with higher molecular weights, available up to 2 MDa, have been used in dye loading studies (Zaharoff et al., 2008).
To date, *in situ* electroporation studies on ECIS electrodes have been performed using Lucifer Yellow (Wegener et al., 2002) or FITC-dextrans of different molecular weights up to 2 MDa (Albermann, 2004) (Tab. 5.4). With the help of these dyes suitable electric parameters for efficient *in situ* electroporation of anchorage-dependent cells grown on ECIS electrodes have been determined for NRK, MDCK-I, MDCK-II and BSC-1 cells (Tab. 5.4).
While in most cases a direct approach with fluorophores or fluorophore-labeled molecules was pursued, WI-38/VA13 cells grown on ECIS electrodes have been loaded with the enzyme HRP (horse radish peroxidase). The loading efficiency was then determined by an indirect colorimetric peroxidase assay based on the conversion of a colorless substrate to a blue precipitate by the HRP enzyme in presence of hydrogenperoxide (Ghosh et al., 1993). These published studies used pulses of 40 kHz, 4 V and 200 ms (Wegener et al., 2002) or 100 kHz,

3 V and 200 ms for electroporation of NRK cells. Ghosh et al. (1993) used a pulse of 4 kHz, 5 V and 200 ms for successful electroporation of WI-38/VA13 cells.

Tab. 5.4: Electroporation parameters for different anchorage-dependent cell lines grown on *8W1E* ECIS electrodes as determined with various hydrophilic dye molecules. (LY: Lucifer Yellow; FD: FITC-dextran; HRP = Horse Radish Peroxidase, *: non fluorescent; d_h: hydrodynamic diameter). Molecules in brackets indicate fluorescent probes that have been loaded into the cells using optimal electroporation parameters but were not used for systematic uptake studies.

Cell Line	Electroporation Parameters	Dye / M_w [kDa] / d_h [nm]	Literature
BSC-1	40 kHz, 4 V, 200 ms	LY / 0.5 / 1.6	Wegener et al., 2002
CHO	40 kHz, 3 V, 500 ms	FD / 250 / 18	this work
HEK-293	40 kHz, 4 V, 200 ms	FD / 250/ 18	this work
Hep G2	40 kHz, 4 V, 200 ms	FD / 250 / 18	this work
MDCK-I	40 kHz, 3 V, 200 ms	LY / 0.5 / 1.6	Wegener et al., 2002
MDCK-II	40 kHz, 3 V, 200 ms	LY / 0.5 / 1.6	Wegener et al., 2002
NIH-3T3	40 kHz, 4 V, 200 ms	FD / 250 / 18	this work
NRK	40 kHz, 4 V, 200 ms	LY / 0.5 / 1.6 (FD / 250 / 18)	Wegener et al., 2002
NRK	100 kHz, 3 V, 200 ms	LY / 0.5 / 1.6 (FD / 4 / 3) (FD / 20 / 6.5) (FD / 40 / 7.5) (FD / 70 / 12) (FD / 150 / 13) (FD / 250 / 18) (FD / 500 / 30) (FD / 2000 / 40) (FITC-BSA / 67)	Albermann, 2004
NRK	40 kHz, 4 V, 200 ms	FD / 250 / 18	this work
WI-38/VA13	4 kHz, 5 V, 200 ms	HRP* / ~ 44 / 5.34	Gosh et al., 1993

For most cell types under investigation the optimal parameter combination was found to be 4 V and 200 ms (Fig. 5.19). Only for CHO cells a lower pulse amplitude of 3 V and longer pulse duration of 500 ms was preferred. The loading efficiency, mirrored by the fluorescence intensity of the cellular cytoplasm, typically increased with increasing pulse amplitude, until a critical, irreversibly permeabilizing voltage was reached. Below a critical voltage no loading of the cytoplasm with FITC-dextran was detected (Fig. 5.15 A, E). This critical voltage is assumed to be about 1 V, since CHO cells could not be loaded with pulses of this amplitude (Fig. 5.15 A, E) and HEK-293 cells only showed weak fluorescence after electroporation with an amplitude of 1 V (Fig. 5.10 A). For other cell lines this condition was not tested. For successful permeabilization and loading with the extracellular probe it is decisive that a critical transmembrane potential difference is induced by the applied electric field, i.e. a critical fraction of the applied voltage has to drop across the cell membranes. As estimated from experimental data (cp. chapter 5.4.3.1, Tab. 5.8) about 69 – 79 % of the applied voltage drop across the cell layer grown on ECIS electrodes. Applying an external voltage of 1 V this corresponds to an induced transmembrane potential of 345 – 395 mV in a monolyer. As

described in the literature the critical transmembrane potential difference was determined to be in the range of ~ 200 mV – 1 V (Chen et al., 2006). Thus, above the critical voltage leading to membrane perforation the fluorescent dye can be incorporated into the cells. Already at low amplitudes (2 V, 3 V) of a 200 ms pulse almost all cells showed cytoplasmic fluorescence of low fluorescence intensity (NRK: 3 V; HEK-293: 2 V; CHO: 2 V; NIH-3T3: 3 V). With increasing pulse amplitude the intensity of intracellular fluorescence due to dye uptake gradually increased, while the number of fluorescing cells did not significantly change. A gradual increase in fluorescence was observed for HEK-293 cells using a pulse with 200 ms duration and amplitudes between 1 V and 4 V (Fig. 5.10), for Hep G2 cells between 3 V and 4 V (Fig. 5.12), for CHO cells between 2 V and 3 V (Fig. 5.15) as well as for NIH-3T3 cells between 3 V and 5 V. This observation fits to the commonly accepted theory of electroporation. With increasing voltage of the applied pulse the number and density of pores increases (Chernomordik and Chizmadzhev, 1989; Weaver and Chizmadzhev, 1996). For spherical cells also the area of permeabilization increases (Teissié et al., 2005) (cp. chapter 3.2.2.1). Above a certain voltage, irreversible cell damage was mirrored in cell morphology or unefficient dye loading. Severely damaged cells with defect membranes can not hold cytoplasmic dyes like FITC-dextran inside the cytoplasm. In contrast, the nuclei of irreversibly permeabilized cells can be stained by EthD-1 and cells may even detach from the substrate (Fig. 5.6). Cell morphology changes like rounding of cells (Hep G2: Fig. 5.12 H; NIH-3T3: Fig. 5.17 G, H) can result from secondary effects after electroporation including excessive loss or irreversible damage of essential cytoplasmic molecules and structures (cp. chapter 3.2.2.5) as is also discussed below. In addition, cell fusion (cp. chapter 3.2.3) may occur due to merging of adjacent membranes in the course of the resealing process (NIH-3T3: Fig. 5.17 C).

The pulse duration influences the pore size and density meaning that the probability of pore nucleation is enhanced during a long pulse and pores can grow in size as long as the external electric field is present (Rols and Teissié, 1998; Weaver and Powell, 1989). A dependence of electroporation efficiency on pulse duration could also be found for *in situ* electroporation of the different cell types grown on ECIS electrodes. The effect of increasing pulse durations on loading efficiency for NRK cells has been nicely illustrated by Wegener et al. (2002). Using pulses at 40 kHz with 4 V and 50 ms, 100 ms, 200 ms or 500 ms pulse duration for electroporation of NRK cells in presence of Lucifer Yellow revealed that with increasing pulse duration the number and fluorescence intensity of loaded cells increased. This behavior could also be observed for Hep G2 cells which were loaded with FITC-dextran using the same electroporation pulses as described in Wegener et al. (2002). While the fraction of cells that have incorporated the dye did not change, the fluorescence intensity within the cytoplasm increased from 50 ms to 200 ms (Fig. 5.12). A pulse duration of 500 ms, however, caused severe cell morphology changes in the loaded cells (Fig. 5.12 H). For optimal loading of most cell types (NRK, HEK, Hep G2 and NIH-3T3) a pulse duration of 200 ms was chosen. However, similar loading results were also obtained for a pulse duration of 500 ms when the amplitude was lowered by 1 V compared to a pulse with a duration of 200 ms. Increasing the pulse duration to 500 ms while keeping the amplitude constant at 4 V often resulted in

morphological changes and irreversible cell damage (Fig. 5.10 E; Fig. 5.15 H; Fig. 5.17 H) as discussed in more detail below.

Since excessive permeabilization by both, too high amplitudes and too long pulse durations, leads to irreversible cell damage (cp. chapter 5.1.1.1, Keese et al., 2004), often a trade-off has to be made between either the fraction of the permeabilized membrane area or the size and density of pores to guarantee a fully reversible process. In total, pulses of short duration and high amplitude can result in the same degree of permeabilization as pulses of long duration and low amplitude (Rols and Teissié, 1998). Thus, similar dye uptake can be achieved for different electric pulse parameter combinations and there is not always strictly one optimal electroporation condition. Although the mode of permeabilization is not assumed to be decisive when the molecule is small enough to efficiently pass also smaller pores (< 4 kDa), several authors claimed that for uptake of macromolecules the pulse duration is a more crucial factor due to it's influence on the average pore size distribution (Rols and Teissié, 1998; Zaharoff, 2008). However, on the basis of experiments shown in this work no clear preference for the longer pulse duration of 500 ms could be identified. On the contrary, electroporations with a duration of 200 ms often resulted in similar or slightly better dye uptake than for 500 ms pulses (Fig. 5.12; Fig. 5.17).

A schematic model for *in situ* electroporation using ECIS electrodes can be established on the basis of the common electroporation theory (cp. chapter 3.2.2; Fig. 3.13). Cells organized in a confluent monolayer are anchored to the extracellular matrix on the electrode surface and, depending on the cell type, are in contact to neighboring cells via more or less pronounced cell-cell contacts. As direct consequence of using a small working electrode relative to the growth area in a given well, the cell fraction which is loaded with the extracellular dye is naturally restricted to the cells residing on the active electrode area. During an electric pulse the electric AC field is applied perpendicular to the cell layer via the substrate-integrated electrode (Fig. 5.76). Thus, the apical and basal membrane of the cells on the electrode will be permeabilzed and an exchange of molecules will occur via the apical membrane. Depending on the cell type, only cells residing on the electrode are loaded with the electroporation marker (NRK, Hep G2 and CHO) or cells attached to the photoresist in vicinity of the electrode are also loaded (NIH-3T3 and HEK-293).

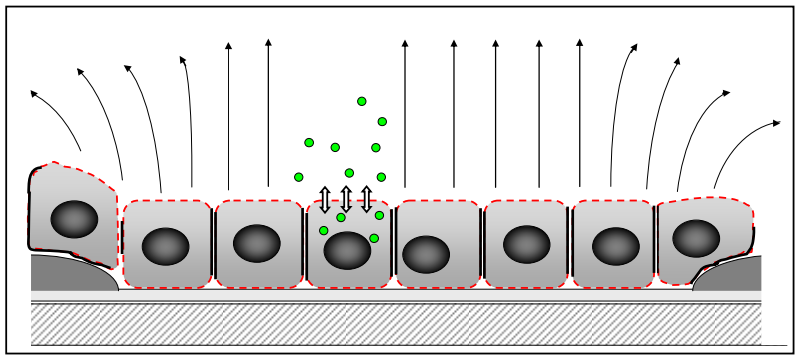

Fig. 5.76: Schematic illustration of *in situ* electroporation of anchorage-dependent cells grown on ECIS electrodes. The membranes perpendicular to the electric field are permeabilized by the electroporation pulse (red). Intact membranes are black. The extent of lateral permeabilization increases with growing field strength (pulse amplitude).

For the fibroblastoid cell types NIH-3T3 and HEK-293 for example dye loading was also observed for cells that reside up to ~ 30 µm beyond the active electrode area, depending on the pulse amplitude.

Due to the constriction effect of the small electrode on the electric field lines, a certain portion of voltage might also strike cells at the rim of the electrode and electroporate them (Fig. 5.76). This diverging electric field distribution at the electrode borders may explain the occurrence of dye loading also beyond the active electrode area. Moreover, cells that adhere to the active electrode area only with a certain fraction of the cell body may be permeabilized to such an extent that uptake of the fluorescent probe diffusing into the entire cell body can take place. To date, no theoretical models for *in situ* electroporation are available in the literature.

Although most of the cell types under study show optimal dye uptake after electroporation with a pulse of 40 kHz, 4 V and 200 ms, the different cell types revealed a specific loading behavior, which might be explained by individual cell morphologies. CHO cells were the only cell type with optimal electroporation pulse parameters of 40 kHz, 3 V and 500 ms. The pulse amplitude determines the size and geometry of the permeabilized area in spherical cells (cp. chapter 3.2.2.1). The geometry of the permeabilized membrane area can easily be calculated for spherical cells in suspension, but is difficult to estimate for the complex cell geometries as of adherent cells (Bernhardt and Pauly, 1973). Thus, the geometry of the adherent cell on the electrode might considerably influence the degree of permeabilization. For large and flat cells it can be assumed that a high fraction of the apical cell membrane is electroporated even at relative low field strength, because a large fraction of the membrane is perpendicular to the field direction (Fig. 5.77 A). Contrary, in epithelia with a more cuboidal (Fig. 5.77 B) or columnar (Fig. 5.77 C) cell geometry the area of molecule exchange across the membrane might be reduced. However, all cell types used in this study have similar cell radii with the largest radius for NIH-3T3 cells (Fig. 5.77 D).

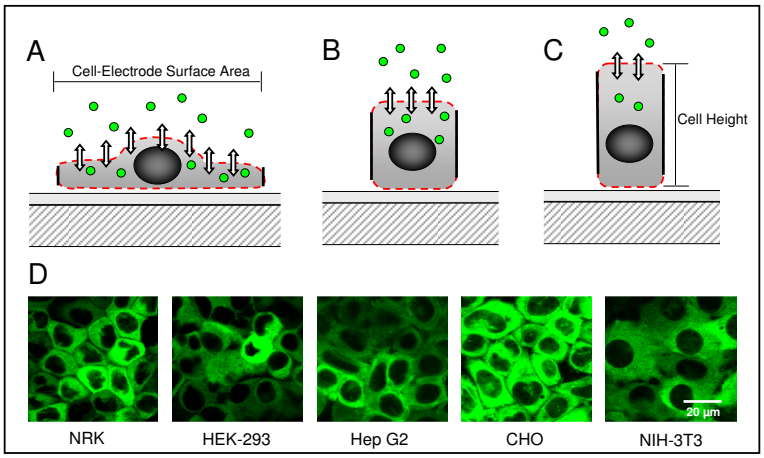

Fig. 5.77: Schematic illustration of *in situ* electroporation of adherent cells with different geometries. A: Large and flat cell geometry; **B:** Cuboidal cell geometry; **C:** Columnar cell geometry; **D:** Confocal fluorescence micrographs of cell lines used in this study to illustrate their cell radius.

An additional aspect to be considered is cell height. Due to the close proximity of the cells to the electrode surface the applied field strength in kV/cm relevant for cell permeabilization is determined by the cell height. As determined from confocal micrographs after loading with

FITC-dextran NRK cells exhibit a cell height of about 4 – 6 µm (Fig. 5.5 F). According to Breitenstein et al. (2008) NRK cells exhibit a height of 6 – 8 µm. Applying a voltage of 4 V at 40 kHz to the electrode corresponds to a voltage drop across the cell layer of about 3 V (cp. chapter 5.4.3.1), which can be translated to a field strength across an NRK cell layer with a thickness of 6 µm of ~ 5 kV/cm. Also the height of Hep G2 cells was reported to be in the range of 4 µm (Okajima et al., 2007) and the cell height found in literature for NIH-3T3 was 9.6 µm (Boudreault and Grygorczyk, 2004). The height of HEK-293 cell layers was determined from confocal fluorescent images presented in chapter 6 (Fig. 6.10; 6.13; 6.14). Confluent layers of HEK-293 cells typically revealed a height of about 20 µm. However, HEK-293 cells typically form multi-layers of 1 – 3 cells and the applied voltage is distributed along the cells that arrange perpendicular to the electrode. With increasing cell height the field strength along the cell layer decreases. Assuming a cell height of 10 µm (NIH-3T3, HEK-293), for example, results in a field strength of 3 kV/cm for a 3 V drop across the cell layer. This field strength is about half as high as calculated for NRK cells. This means that for cell types forming rather thick cell layers higher pulse amplitudes for efficient dye uptake can be expected. Actually, HEK-293 and NIH-3T3 cells tolerated pulse amplitudes of 5 V (Fig. 5.10; Fig. 5.17), whereas other cell types did not (Fig. 5.5; Fig. 5.15).
Significantly smaller cell heights can be found for CHO cells. The group of Takagi reported cell heights of around 2 µm (Takagi et al., 2000; Ito and Takagi, 2009), meaning that a field strength of roughly 15 kV/cm is established across a CHO cell layer when 3 V are assumed to drop across the cell layer. This is three times more than calculated for NRK cells, explaining the reduced tolerance of CHO cells toward pulse amplitudes above 3 V.

Impedance Monitoring of Cell Layer Recovery

ECIS measuremets are highly sensitive to cell morphology changes. Monitoring the cell layer impedance at a sensitive frequency (4 kHz) mirrors alterations that occur in the cell-cell and cell-substrate contact area with a resolution much below that of optical microscopes (Giaever and Keese, 1993). As the same electrodes are used for cell manipulation and analysis, electroporation is fully integrated into an ECIS measurement monitoring cell layer impedance before and immediately after application of the permeabilizing pulse.
The time course of impedance measured at 4 kHz after electroporation was found to be cell type specific (cp. Fig. 5.19). NRK, CHO and NIH-3T3 cells showed an initial impedance drop after pulsing, which was follwed by a slow increase back to pre-pulse values within a period of 50 – 70 min (Fig. 5.19). After pulse application to HEK-293 cells the normalized impedance increased by about 0.2 – 0.25 within ~ 30 – 40 min and afterwards slowly decreased again, stabilizing to or slightly above pre-pulse values (Fig. 5.11). Hep G2 cells responded with a first immediate increase above, a subsequent decrease below pre-pulse values and final recovery back to pre-pulse values within 1 h (Fig. 5.13).
A dependence of the impedance response on the cell type has already been described by Ghosh et al. (1994). The initial impedance response at 4 kHz directly after pulsing at 4 kHz, 5 V for 1 s as well as the time required for recovery to pre-pulse values differed for WI-38/VA13, B3B5 and MDCK-II cells. The changes in pre-pulse impedance and cell type

specific differences after electroporation were, however, not understood. Impedance changes are assumed to result from certain alterations in cell morphology which recover within roughly 1 h. Morphological responses that cause an impedance decrease can result from loosening of cell-cell contacts or cell-substrate contacts as induced either by a transient volume reduction or alterations in cell mechanics (Fig. 5.78).

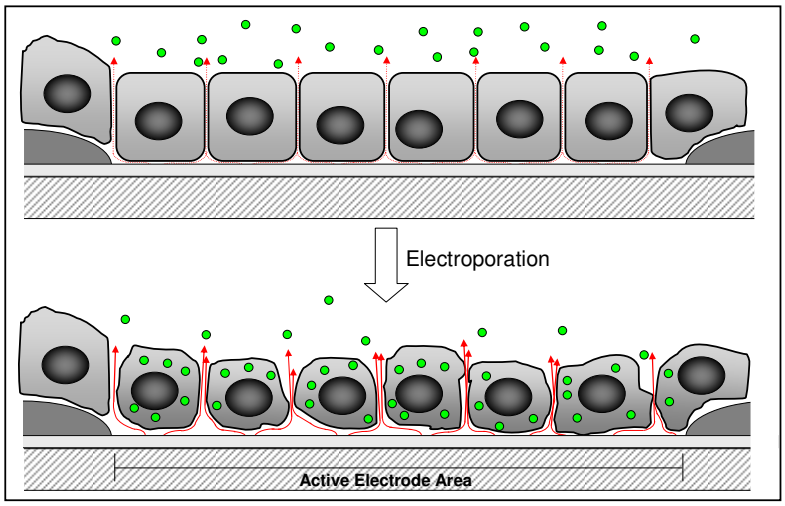

Fig. 5.78: Schematic illustration of cell morphology changes after *in situ* electroporation of anchorage-dependent cells grown on ECIS electrodes. Presented is an example where electroporation leads to a reduced cell layer impedance. Arrows indicate non-invasive AC current flow for impedance measurements.

Analysis of impedance spectra before and after electroporation of NRK cells, which respond with an immediate impedance decrease, showed that after pulsing with 100 kHz, 3 V and 200 ms the parameter R_b describing the tightness of cell-cell contacts dropped from 5 $\Omega \cdot cm^2$ to ~ 3.8 $\Omega \cdot cm^2$ (Albermann, 2004). Also the parameter α characterizing the cell-substrate contact changed from 5.2 $\Omega^{1/2} \cdot cm$ to ~ 4.6 $\Omega^{1/2} \cdot cm$, while the membrane capacitance remained roughly at the same level of about 2 $\mu F/cm^2$.

In order to illustrate the morphological changes of different anchorage-dependent cell types after electroporation in this work, the time courses of the normalized ECIS parameters norm α, norm R_b and norm C_m for different cell types are shown in Fig. 5.79. For most cell types the changes in impedance can be ascribed to alterations in R_b as well as in α. Values for R_b typically decreased, while the parameter α either transiently increased for NRK and HEK-293 cells (Fig. 5.79 A, B) or decreased for Hep G2 and CHO cells (Fig. 5.79 C, D). The cell membrane capacitance is not significantly affected.

An increase of impedance as a reaction to electroporation may result from a cell volume increase or other cellular processes which lead to a tightening of the intercellular and subcellular clefts as the essential pathways for current flow. Volume alterations, for example, can result from osmotic imbalances created by molecule exchange (influx or efflux) across the permeabilized membrane during electroporation. A volume increase as response to an electric pulse was for example observed by Golzio et al. (1998), who observed swelling of CHO cells after electroporation in suspension.

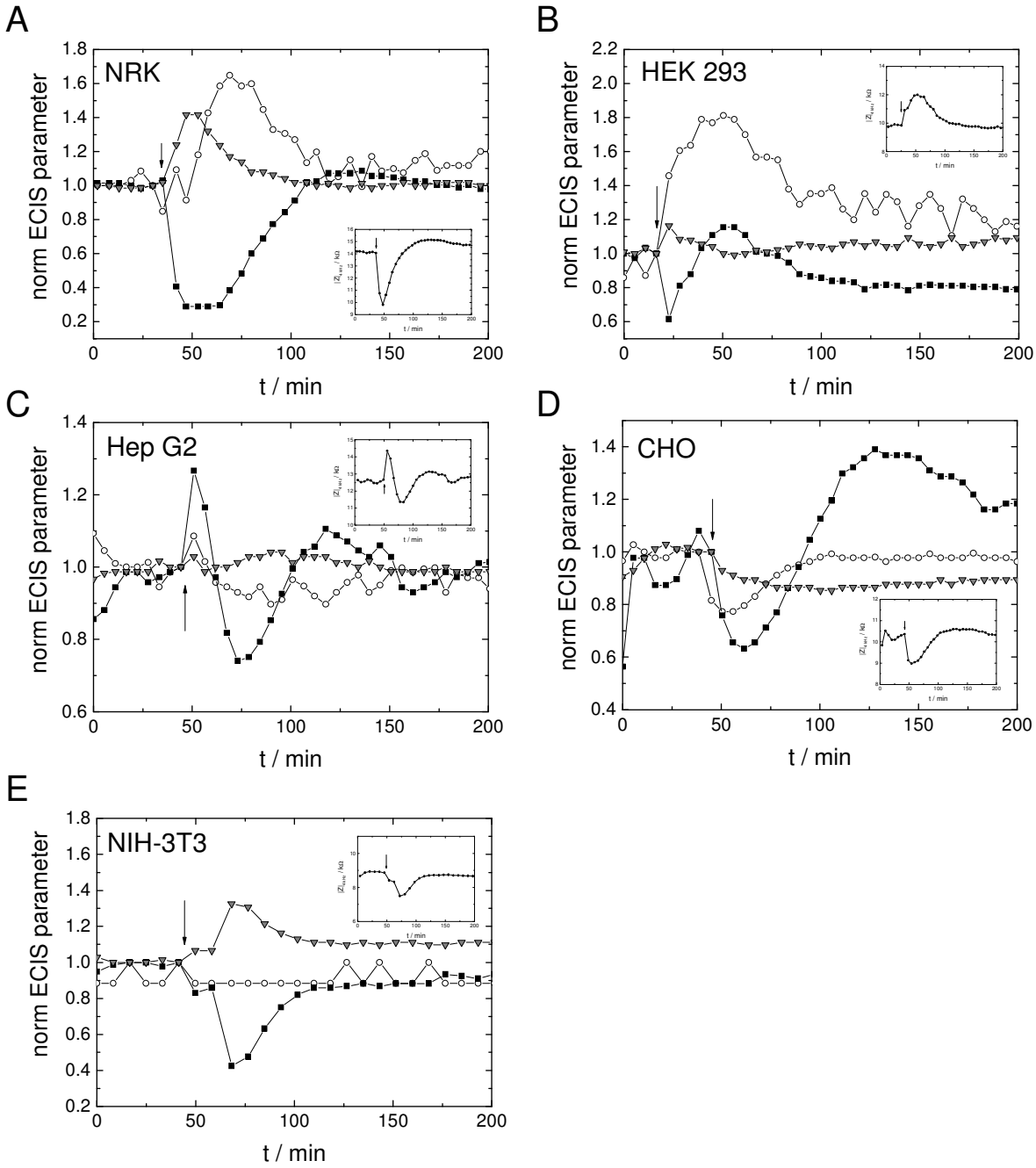

Fig. 5.79: Time course of normalized ECIS parameters α (○), R_b (■) and C_m (▽) before and after electroporation (arrow) of different cell types. **A:** NRK; **B:** HEK-293; **C:** Hep G2; **D:** CHO; **E:** NIH-3T3. The parameters were extracted from repeatedly recorded impedance spectra providing the time course of impedance |*Z*| at 4 kHz shown in the inserts. The absolute parameter values were normalized to the last values before electroporation (**NRK:** α: 2.58 $\Omega^{1/2} \cdot$ cm, R_b: 4.35 $\Omega \cdot cm^2$, C_m: 2.93 µF/cm^2; **HEK 293:** α: 2.56 $\Omega^{1/2} \cdot$ cm, R_b: 1.48 $\Omega \cdot cm^2$, C_m: 2.14 µF/cm^2; **Hep G2:** α: 3.98 $\Omega^{1/2} \cdot$ cm, R_b: 2.85 $\Omega \cdot cm^2$, C_m: 2.4 µF/cm^2; **CHO:** α: 4.06 $\Omega^{1/2} \cdot$ cm, R_b: 0.87 $\Omega \cdot cm^2$, C_m: 1.71 µF/cm^2; **NIH-3T3:** α: 1.38 $\Omega^{1/2} \cdot$ cm, R_b: 2.12 $\Omega \cdot cm^2$, C_m: 2.15 µF/cm^2).

According to Kinosita and Tsong (1977) as well as Abidor et al. (1993b, 1994), who also observed osmotic swelling of cells after electroporation in isotonic buffer, the main reason for such volume alterations after transient permeabilization is ascribed to the colloid osmotic effect. Due to the high intracellular concentration of macromolecules under isoosmotic conditions the intracellular ionic concentration is low compared to that of the extracellular fluid (Donnan potential). During electric permeabilization uptake of small ions driven by their concentration gradient can not be balanced osmotically by export of cellular macromolecules,

because these are too large in size to pass the membrane. In order to balance tonicity ion movement is followed by water flow resulting in cell swelling (Hui and Lee, 2000). Pavlin et al. (2005) measured a reduction of bulk conductivity in a dense cell suspension after electroporation which was due to colloid osmotic swelling.

No impedance increase after pulsing was detected for NRK, CHO and NIH-3T3 cells. In contrast to other cell types HEK-293 cells form multilayers, which might create a similar situation as observed for very dense cell suspensions. Indeed, for HEK-293 cells transient impedance increases were observed as a response to electroporation. A cell volume increase in a multilayer can easily be assumed to cause a narrowing of the current pathways. Actually, ECIS measurements could demonstrate that exposure of HEK-293 cell layers to hypoosmotic media resulted in a significant impedance increase at 4 kHz from 15 kΩ for isotonic media to 19 kΩ for hypotonic media, indicating cell swelling (Stolwijk, 2006).

Extensive water inflow, however, can result in rounding of cells, loosening of cell-cell and cell-substrate contacts and finally lysis of cells (Kinosita and Tsong, 1977). Such effects might thus be responsible for observations made for Hep G2 and NIH-3T3 cells (Fig 5.12 H; Fig 5.17 H). After electroporation with too invasive pulses cells swell and may detach from the substrate.

As a response to osmotic imbalance volume regulatory mechanisms are activated in many cell types. During regulatory volume decrease (RVD) for example the osmotically swollen cell actively exports ions and organic osmolytes like amino acids and sugars out of the cell in order to balance the osmotic pressure (McCharty and O'Neil, 1992). Often an overshoot of regulatory volume decrease can be observed, meaning that cells may even shrink as a response to transient hypotonic exposure. Since a transient osmotic imbalance is induced by transient membrane permeabilization, such osmotic regulatory mechanisms may induce a volume reduction as a response to electroporation. Volume regulation mechanisms upon osmotic imbalance are typically reported to be in the time scale of a few minutes (Montrose-Rafizadeh and Guggino, 1990; Golzio et al., 1998) or may even take as long as ~ 30 – 60 min (O'Connor et al., 1993; Desmet et al., 1995, Smets et al., 2002), depending on the cell type and osmotic conditions. Such effects might thus be responsible for at least some of the impedimetrically detected cell morphology changes after electroporation taking place also on the time scale of minutes.

In addition, the typical ion gradients, which are carefully maintained by transport mechanisms under normal conditions, are short-cut by electroporation. After resealing, an activation of ion pumps and channels has to counteract ion mixing and reconstitute the natural membrane potential. Initial ion imbalance may induce changes in cell morphology by changed enzyme activities as well as binding affinities between structural proteins.

Direct effects of electric fields on protein structures like the cytoskeleton, which essentially determines cell morphology, may also contribute to morphological changes (Teissie and Ramos, 1994). Kanthou et al. (2006) studied the impact of *in situ* electroporation on the cytoskeleton of HUVEC cells by immunocytochemical stainings and Western Blot analysis. They found that electroporation of the endothelial cells resulted in a profound disruption of the microfilament and microtubule filamentous network and a loss of the cell-cell contact

associated protein VE-cadherin. A loss of contractility moreover indicated impairment of cytoskeletal functions. The observed effects were voltage dependent and reversible, recovering within 60 min. Without any significant loss of cell viability, the permeability of the epithelial barrier was increased immediately after electroporation, as was detected by enhanced passage of FITC-dextran tracer molecules across the epithelium. Since disruption of the cytoskeleton and a loss of cell-cell contact proteins lead to a compromised barrier function, these kinds of electric pulse effects can easily explain the measured impedance decrease after electroporation of anchorage-dependent cells grown on ECIS electrodes. Morphological alterations due to changes in cytoskeletal proteins of cells electroporated *in situ* have also been reported by Escande-Geraud et al. (1988). They electroporated monolayers of CHO cells on petri dishes by inserting parallel plate electrodes in the fluid above the cell layer. SEM and TEM microscopy of cells immediately fixed after electroporation revealed an increased density of actin filled microvilli on the cell surface as well as an assembly of small vesicles within the cells.

Changes in the structure of the cytoskeleton may be either caused by direct effects of the electric field on the proteins itself or by indirect effects. Leakage of essential molecules like ATP, GTP, cAMP or uptake of calcium, important for controlling polymerization and structural organization, can lead to cell morphological alterations (Rols and Teissié, 1992).

Morphological changes can moreover occur as a result of activation of cell signaling processes, as for example induced by changes of the intracellular calcium concentration. The cytoplasmic calcium concentration (~ 100 nM) is typically several orders of magnitude lower (~ 20 000-fold) than in the external medium (Clapham, 2007). An increase of intracellular Ca^{2+} levels is known to cause activation of signaling cascades that can evoke a multitude of cellular responses (Clapham, 2007). Thus, elevating the intracellular calcium concentration by electroporation might trigger various calcium controlled processes. High intracellular calcium concentrations were reported to lead to an activation of a regulatory volume decrease (RVD) in many cell types (Tinel et al., 2000). Thus, the frequently observed impedance drop after pulsing might be induced by calcium activated volume decreases, leading to an opening of cell-cell contacts. Direct regulatory mechanisms of cell-cell contacts and cell-substrate contacts as well as the cytoskeleton are also known to intersect with calcium signaling cascades (Sjaastad et al., 1996; Clapham, 2007). Ca^{2+}/Calmodulin, for example, controls the interaction of myosin and actin and thereby regulates rearrangements of the cytoskeleton and, thus, cell shape. An activation of certain signaling cascades may also be the reason why after electroporation the cell layer impedance does not always exactly return to pre-pulse conditions. For NRK cells an impedance overshoot was often observed, which either leveled off exactly to, slightly below or above pre-pulse values afterwards (Fig. 5.2; Fig. 5.19 A). Such kind of transient impedance overshoot could also be observed by Ghosh et al. (1994), who electroporated WI-38/VA13 cells on ECIS electrodes. Although the cells reached pre-pulse impedance values 10 min after electric pulsing, the cell layer impedance further increased within the following minutes and finally returned to the base line impedance. That electroporation of signaling molecules can induce such an impedance overshoot was shown by Wegener et al. (unpublished data), who loaded NRK cells by electroporation with a

membrane-impermeable cAMP analog. After electroporation with 8-OH-cAMP the impedance first dropped as a typical reaction on electric pulsing and subsequently increased about 15 % above pre-pulse values within 1 h after electroporation before settling down to initial values after ~ 3 h again (information provided by J. Wegener; Fig. 5.80). The control layer, in contrast, simply recovers to pre-pulse values within ~ 1 h without showing a considerable impedance overshoot. It has been shown that intracellular cAMP can modulate the cytoskeleton and cell-cell contacts in certain cell types, leading to an increased cell layer impedance (Wegener et al., 2000a). The level of cAMP is intracellularly regulated by the activity of adenylate cyclases and phosphodiesterases that are under control of other signaling pathways like calcium signaling, subunits of G proteins, inositol lipids and receptor tyrosine kinases (Fimia and Sassone-Corsi, 2001). Elevated cAMP levels activate the protein kinase A (PKA), which has a central role in the regulation of various cellular mechanisms via PKA anchoring proteins (AKAPs) and is amongst others connected to components of the cytoskeleton for regulation of its structural and functional organization.

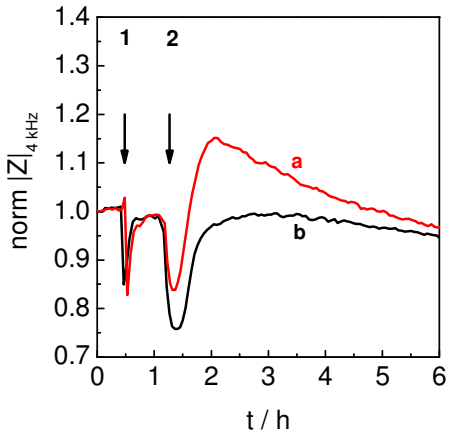

Fig. 5.80: Time courses of the normalized impedance magnitude at 4 kHz for NRK cells after addition (arrow 1) and subsequent electroporation (arrow 2) in presence of 100 µM membrane-impermeable 8-OH-cAMP (▬, curve a) compared to control cells (▬, curve b) electroporated without 8-OH-cAMP. (Data were provided by J. Wegener).

Cell type specific differences in the time course of impedance after electroporation are presumably due to individual sensitivities of cell morphology for electric pulsing. These can result from differences in cell size or shape as well as the membrane composition, i.e. the lipid composition (Benz and Zimmermann, 1981) and the fraction of membrane proteins (Schwister and Deuticke, 1985; Tsong et al., 1991). The conductivity of the membrane can influence the efficiency of membrane permeabilization as well (eq. 3.19) (Kotnik et al., 1997). The lipid composition and protein content are moreover thought to affect pore stabilization and resealing rate (Kanduser et al., 2006; Glaser et al., 1988; Saulis et al., 1991). The period of membrane permeabilization determines uptake of extracellular molecules as well as a potential loss of essential intracellular metabolites and enzymes. Thus, the susceptibility of a cell towards loss of crucial intracellular content into the bulk might influence the survival rate and time required for regeneration. Differences in volume regulatory mechanisms after pulse induced osmotic imbalance may also contribute to the cell type specific cell shape alterations. Moreover, the mechanical stabilization within the cell layer due to the cytoskeleton and

associated cell-cell as well as cell-substrate contacts might influence the impedimetric response.

Variations in pulse amplitude and duration not only influence the efficiency of dye uptake but also have a clear effect on the recovery behavior of the cell layer after electric pulsing. This phenomenon has already been described by Ghosh et al. (1994) and Wegener et al. (2002) for layers of WI-38/VA13 and NRK cells, respectively. The depth of impedance drop and the time required for recovery to pre-pulse values was found to increase with increasing pulse amplitude for both cell types (Ghosh et al., 1994; Wegener et al., 2002). Ghosh et al. (1994) additionally observed a multi-phasic impedance time course when pulses within a certain range were applied (transcellular voltage: 0.732 V – 1.76 V). This behavior was missing after pulses with lower or higher transcellular voltages. Also in the studies presented in this work an effect of pulse amplitude on the impedance time course is obvious for all cell types.[8] Not all cell types showed a successive decrease of the transient impedance drop for increasing pulse amplitudes. HEK-293 cells, for example, responded to increasing amplitudes with an increase of impedance (Fig. 5.11).
Increasing pulse amplitudes enhance the invasiveness of a pulse. A strong influence of high pulse amplitudes ($\geq$ 4 V) on the cell layer recovery is measured for NRK, Hep G2 and CHO cells. The impedance shows a strong impedance drop after electroporation and the cell layer recovery is significantly retarded after application of voltages above the optimum amplitude. NIH-3T3 cells were severely damaged above 5 V as already indicated by dye loading studies.
Increasing pulse durations enhance the invasiveness of a pulse of given amplitude. Using a pulse with a duration of 500 ms instead of 200 ms leads to a stronger impedance drop after pulsing and a more retarded recovery to pre-pulse values (eg.: NRK, 5 V: 200 ms or 500 ms; Hep G2, 4 V: 200 ms or 500 ms). The effect of pulse duration is not as clear for HEK-293 and NIH-3T3 cells, where very similar impedance profiles and recovery times are obtained for most amplitudes at both pulse durations. Since pulse amplitude and duration both increase the degree of membrane permeabilization and influence the time required for membrane resealing (Rols et al., 1990), it can easily be imagined that the extent and duration of membrane permeabilization scales the effect of osmotic imbalance, the extend of disturbance of cytoskeletal and cell-cell contact structures as well as the extent of calcium inflow and, thus, affects the impedimetric response in a certain cell type in an amplitude and duration dependent manner. As shown for NRK cells pulses of 5 V and 30 s lead to complete irreversible damage of the cells on the electrode (Fig. 5.2, Fig. 5.3).

[8] Normalizing absolute impedance values in some cases leads to interchanged dependencies of the impedance time course on amplitude and duration. As an example, the initial normalized impedance drop immediately after electroporation of NIH-3T3 cells with 6 V for 500 ms was less than after a pulse with same amplitude for 200 ms. The cell layer pulsed for 500 ms had lower absolute initial impedance magnitudes than the cell layer pulsed for 200 ms. The more invasive character of a 500 ms versus a 200 ms pulse became obvious in the impedance time courses during the NIH-3T3 regeneration phase. Cell layers recovered above 0.85 within 60 min when pulsed with 6 V for 200 ms, but the normalized impedance remained constant below 0.8 when a pulse of 6 V and 500 ms was applied.

5.4.1.2 Morphological Changes versus Membrane Permeabilization

The basic experimental setup used for a typical measurement only has a time resolution of about 5 min (cp. Materials and Methods, chapter 4.3.1.1). At a first glance the impedance time course after electroporation of NRK cells exhibits a significant dip of the normalized impedance, reaching a transient minimum roughly 10 min after the pulse before the impedance recovers to pre-pulse values again within ~ 60 min. Since membrane permeabilization increases current flow directly through the cell bodies, an impedance drop and recovery to pre-pulse values might be ascribed to membrane permeabilization and subsequent membrane resealing. The gross impedance alterations occurring several minutes after electroporation are, however, not assumed to be due to membrane permeabilization, but due to changes in cell morphology (chapter 5.4.1.1).

The time scale of membrane permeabilization, roughly defined by the time between the onset of the electroporation pulse and complete post-pulse membrane resealing, is typically reported to be in the range of seconds (Gabriel and Teissié, 1995; Rols and Teissié, 1998) or a few minutes (Escanade-Geraud et al., 1988; Neumann et al., 1998) in the case of mammalian cells. The cytoskeleton is assumed to be responsible for the considerably longer time scale of membrane resealing in mammalian cells as compared to pure lipid vesicles, which is below 1 s (Rols and Teissié, 1992; Benz and Zimmermann, 1980). Particularly in adherent cells during *in situ* electroporation the cytoskeleton is fully established. Escande-Geraud et al. (1988) *in situ* electroporated CHO cells on petri dishes and evaluated the time of the permeabilized state of the cells by adding trypan blue after pulsing. At 37 °C cells lost their permeability towards trypan blue within less than 10 min after electric pulsing. TEM analysis of CHO cells after post-pulse addition of ruthenium red moreover revealed that no dye was incorporated 5 min after electroporation. Even after electroporation of cells in muscle tissue *in vivo* as well as *ex vivo*, the time required for resealing was reported to be in the range of ~ 10 min (Gehl et al., 2002; Bier et al., 1999) However, it was shown by some groups that the resealing process can even take more than 1 h when electroporation is performed at room temperature (Escande-Geraud et al., 1988; Rols and Teissié, 1989) or even lower temperatures (Lopez et al., 1988). Since electroporation of cells grown on ECIS electrodes was performed at 37 °C membrane resealing is considered to be completed within several minutes. Actually, Hartmann (2003) found that Lucifer Yellow is not incorporated into NRK cells when the dye is added to the cell layer 1 min after electroporation. A further study supporting a fast membrane permeabilization and resealing within a few seconds is provided by Ghosh et al. (1993) who electroporated mouse fibroblasts grown on ECIS electrodes. After electroporation the normalized resistance immediately dropped and recovered to pre-pulse values within a few seconds. The fast impedance drop and recovery to pre-pulse values were ascribed to membrane permeabilization and subsequent membrane resealing (Ghosh et al., 1993). Subsequent secondary effects like changes in cell morphology on the longer time scale were, however, not recorded in the same measurement (Ghosh et al., 1993). An impedance decrease after electroporation of anchorage-dependent cells was also measured by Müller et al. (2003), who electroporated L929 cells grown on filters and measured the transepithelial resistance

(TER) before and after electroporation. After electroporation a drop of the TER was measured which restored to pre-pulse values within several minutes (2 – 8 min). Although the authors ascribed the measured impedance and subsequent recovery exclusively to membrane permeabilization and resealing effects, it is not clear if morphological alterations have also contributed to the signal. A similar study has been performed by Abidor et al. (1994) electroporating pellets of suspended rabbit erythrocytes and measuring the resistance before and after pulsing. They found that within a few microseconds after pulsing the resistance of the cell pellet decreased by almost 90 % and afterwards restored within a few seconds. A few minutes later the resistance even exceeded the initial value by about 4 times due to osmotically induced cell swelling (Abidor et al., 1994).

Measurements performed in this work allowed to clearly distinguish initial membrane resealing from secondary cell morphology responses. A measuring setup with high time resolution and fast switch between the impedance analyzer and the frequency generator was constructed in order to document immediate responses as well as long-term impedance changes (cp. chapter 4.3.1.2). The measurements with enhanced time resolution revealed a fast process taking place immediately after pulse application to NRK cells within the first few minutes (Fig. 5.21). After an immediate drop of the normalized impedance to 0.55 of initial values, the normalized impedance increased almost back to pre-pulse values (~ 0.9) within 10 s. This first part of the response is very similar to that observed by Gosh et al. (1993), who measured an immediate drop of normalized resistance to ~ 0.6 after a pulse of 4 kHz, 4 V and 200 ms. The pulse was applied within a period of ~ 0.5 s during which the measurement had to be paused for pulse application. The resistance recovered to pre-pulse values within less than 5 s, indicating membrane permeabilization and resealing (Ghosh et al., 1993).

Simulations based on the ECIS model (Giaever and Keese, 1991) by Hartmann (2003) showed that membrane permeabilization significantly reduces the NRK cell layer impedance at 4 kHz. Assuming more than 100 pores per cell with a diameter of 40 nm, which is the diameter of the largest FITC-dextran introduced into the cells, reduces the membrane resistance to zero, resulting in an impedance drop to values of a cell-free electrode (Hartmann, 2003). Impedances at 4 kHz of cell-free *8W1E* ECIS electrodes were typically measured to be in the range of 6 – 8 kΩ. Indeed, a relative impedance drop to ~ 0.55 as measured for NRK cell layers with an impedance of initially 15.7 kΩ corresponds to an absolute impedance drop down to 8.64 kΩ, almost reaching values for a cell-free electrode. Since the time frame during which such low impedances occurred after electroporation was extremely short (~ 5 s) (Fig. 5.21), transient changes in the membrane resistance are very likely responsible for the observations, instead of irreversible damage or morphological changes. Thus, supported by the literature discussed above, the initial impedance drop and subsequent fast increase in the first seconds after pulse application can be interpreted as the permeabilization of the membrane and the subsequent fast resealing. After cell membrane permeabilization has reached its maximum during application of the pulse (Gehl, 2003) pores begin to close following a yet unknown mechanism taking place in the range of seconds to minutes (Teissié et al., 2005). Since the pulse duration of 200 ms is short compared to the time required for switching between frequency generator and impedance analyzer (1 – 2 s) (Fig. 5.21; 5.22), not

the complete phase of initial impedance response could be monitored. Therefore, the impedance during electroporation may even be lower than detected here. Especially for the cell lines Hep G2 and HEK-293, where switching took almost 2 s, the magnitude of the actual impedance drop is inaccurate (Fig. 5.22).
Another explanation for the weak impedance drop recorded for Hep G2 and HEK-293 cells compared to NRK cells may be based on the nature of the impedance readout. The passive electric properties of a cell layer influence the impedance signal and the sensitiviy for changes in certain current pathways. Cells that form tight epithelia, for example, have a high paracellular resistance, which can be as high as the resistance of the membrane. The membrane resistance is short-cut when it is perforated by electroporation and the current will predominantly flow across the perforated membrane for the short period of permeabilization. Thus, rather tight epithelia as formed by NRK cells allow for a sensitive measurement of membrane permeabilization and resealing, while during the permeabilized state morphological changes are hard to detect. Cells with low barrier properties, in contrast, provide sufficient space for current flow around the cell bodies. The paracellular resistance is low compared to the membrane resistance. Therefore, changes in the transmembrane resistance as they are induced during electroporation are hardly detected, because the main fraction of the current will still flow along the paracellular pathway.
However, a similar time course following saturation kinetics is observed for all three cell lines that were investigated with this measurement setup. It indicates that similar processes with similar kinetics, i.e. membrane resealing, are recorded. Pore formation and resealing are rather fundamental processes that are thought to proceed via similar mechanisms in all biological membranes (Dimitrov, 1995). After the initial fast response the impedance of the NRK cell layer drops again within about 5 – 10 min. The regular measuring setup with a time resolution of only ~ 5.5 min (cp. chapter 4.3.1.1) does not detect such initial fast responses. Since after the first few seconds the following time course of impedance is very complex and cell type specific, less fundamental processes than simple membrane permeabilization and resealing are assumed to take place. Therefore, these complex multi-phasic impedance alterations taking ~ 1 h are assigned to changes in cell shape as discussed in chapter 5.4.1.1.

5.4.1.3 Size Limit of Molecules Crossing the Permeabilized Membrane

Because most interesting bioactive molecules are complex macromolecules with high molecular weights, FITC-dextran with a molecular weight of 250 kDa was chosen instead of small dyes like Lucifer Yellow or propidium iodide to determine optimal electroporation parameters. Most bioactive molecules used in this work have a molecular weight below 250 kDa and can be assumed to readily cross the membrane using pulse conditions determined for the 250 kDa FITC-dextran (Tab. 5.5). Albermann (2004) even loaded NRK cells with FITC-dextrans up to 2 MDa and although it is unclear if molecules of even higher molecular weights can pass the electropermeabilized membrane, there is no reason to assume that this is the natural limit. Due to the size exclusion of the nuclear envelope of ~ 20 –

50 kDa (~ 9 nm) for passive diffusion across the nuclear pore complex (Fried and Kutay, 2003; Lechardeur and Lucas, 2006), molecules bigger than this remain excluded from the nucleus, which thus appears as a black dot within the fluorescent cytoplasm. Obviously, for NRK cells the nuclear pore exclusion limit is between 20 and 70 kDa (cp. Fig. 5.81).

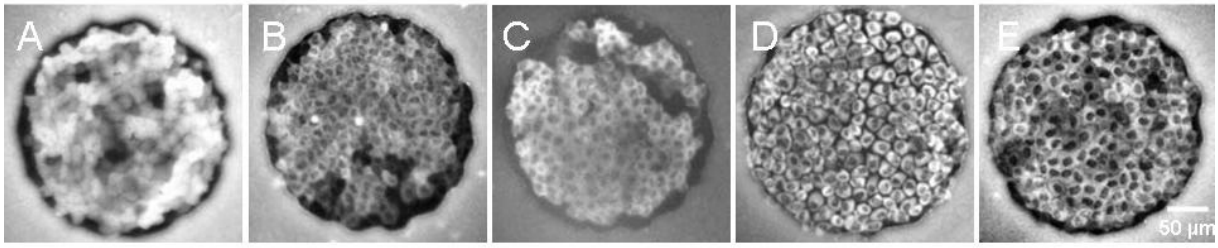

Fig. 5.81: Fluorescent micrographs of NRK cells grown on *8W1E* ECIS electrodes after electroporation in presence of FITC-Dextranes of different molecular weights. **A:** 20 kDa; **B:** 70 kDa, **C:** 250 kDa; **D:** 500 kDa, **E:** 2 MDa. Micrographs were taken from Albermann (2004).

Since the 2 MDa FITC-dextran probe with a hydrodynamic radius between 15 and 20 nm (Erikson et al., 2008; Weiss et al., 2004) can be transferred into the cytoplasm of cells, it is likely that most drugs as well as proteins and peptides with significantly smaller hydrodynamic radii can be readily introduced (Tab. 5.5). For instance, the radius of antibodies of the IgG type is approximately 5.3 nm (Armstrong et al., 2004), horse heart cytochrome c is in the order of 1.8 nm (Wilkins et al., 1999) and enzymes like RNase A and DNase I are reported to have radii in the range of 1.9 nm and 4.75 nm, respectively (Kim et al., 2006; Adel et al., 2007).

Tab. 5.5: Molecular weight (M_w) and hydrodynamic radius (r_h) of molecules used for loading of anchorage-dependent cells grown on ECIS electrodes by *in situ* electroporation. The molecular weight of DNA molecules was calculated by the number of base pairs (pCH1: 6191 bp; pEYFP-Actin: 5800 bp; EGFP-fragment: 2278 bp) multiplied with the average molecular weight of a base pair (660 Da). (– : no information available).

Molecule	M_w [kDa]	r_h [nm]	Literature
FITC-dextran 250	250	9	Toprak et al., 2007
FITC-dextran 2000	2000	15 – 20	Weiss et al., 2004
Sodium Azide	0.065	–	Fluka
Bleomycin	~ 1.4	–	Sigma Aldrich
cytochrome c	12.4	1.78	Beavis and Chait, 1990; Wilkins et al., 1999
RNase A	13.7	1.9	Kim et al., 2006
DNase I	39	2.64	Kunitz, 1950; Adel et al., 2008
BSA	68	4.75	Prausnitz et al., 1993; Adel et al., 2008
IgG	150	5.29	Armstrong et al., 2004
pCH1	~ 4000	–	–
pEYFP-Actin	~ 3800	~ 90 – 130	Sebestyen et al., 1998
EGFP-fragment	~ 1400	–	–
Quantum Dots	–	~ 23	Keren et al., 2009

However, nucleic acids are often far beyond this size. A circular DNA molecule of 4 kbp, for example, has got a diameter of about 90 – 130 nm (Sebestyen et al., 1998), while 12.5 kbp already correspond to a hydrodynamic diameter of about 520 nm (Sato, 2005). Nevertheless,

DNA molecules in the range of 4.7 – 7.1 kbp were reported to be readily electroporated into cells (Faurie et al., 2010; Wu et al., 2001; Golzio et al., 2002; Klenchin et al., 1991). Except the linear EGFP-fragment (~ 1400 kDa) the DNA molecules used in this work have a molecular weight above 2 MDa. However, it has been demonstrated that due to the unique shape and charge of nucleic acids, the mechanism of DNA uptake is not based on simple diffusion through electropores but includes complex interactions of the polyanionic molecule with the plasma membrane triggering an active uptake mechanism that takes much longer than the field is applied (Golzio et al., 2002) (chapter 3.2.2.4).

Also the uptake mechanism for many other macromolecules is not fully understood, since only molecules with a molecular weight up to 4 kDa are reported to pass the membrane via diffusion after electroporation (Rols et al., 2000). If the uptake mechanism for macromolecules with a molecular weight up to 250 kDa does indeed rely on pore formation and not on stimulated endocytosis, the electropores introduced into the membrane of NRK cells by the electric field must have diameters of at least 18 nm (Tab. 5.5). This is a lot bigger than found by other groups (Ghosh et al., 1993; Neumann et al., 1998; Rosemberg and Korenstein, 1990). In order to address this question, uptake kinetics for 250 kDa FITC-dextran were studied during *in situ* electroporation of NRK cells by time lapse confocal fluorescence microscopy (Fig. 5.20). As became evident from the experiment, the cytoplasms of almost all cells were homogeneously loaded with the extracellular probe within 3 s after pulse application. There was no change in probe distribution or concentration as the time progressed and no change in the fraction of cells showing dye uptake. Thus, an immediate diffusive mechanism can be assumed rather than an indirect endocytotic one. No punctuate structures were detectable, which would indicate endocytotic uptake (Zha et al., 1998).

As indicated by the higher fluorescence of the intercellular spaces compared to the cytoplasm, no equilibrium of dye concentration is reached between the cytoplasm and the extracellular fluid (Fig. 5.20). This phenomenon has been described in the literature. Zaharoff et al. (2008) who electroporated FITC-dextran with molecular weights of 4 kDa and 2 MDa into murine mammary carcinoma cells found that, depending on the molecular weight of the dye, the intracellular concentration remained below ~ 7 % (FD-4) or ~ 3 % (FD-2000) of that in the pulsing medium, respectively. Also Prausnitz et al. (1994) reported an intracellular FITC-BSA concentration of ~ 2.8 µM which was ~ 30 % lower as compared to the extracellular concentration of 10 µM. Zaharoff et al. (2008) calculated that the pores, which are large enough to allow uptake of 4 kDa FITC-dextran, are open for less than 10 ms after pulsing. They concluded that most of the dye is transferred into the cell during pulse application. Only when small molecules (LY, ions) were electroporated, the intracellular concentration was found to reach Donnan equilibrium with the extracellular fluid (Mir et al., 1988; Schwister and Deuticke, 1985; Prausnitz et al., 1994). In some cases even an intracellular accumulation of electrotransferred molecules was found, presumably because the probes have bound to intracellular molecules (Glogauer and McChulloch, 1992; Prausnitz et al., 1994).

As reported by many authors, macromolecules have to be present before the electroporation pulse is applied, which is in contrast to a possible post-pulse uptake of small molecules (chapter 3.2.2.4). Thus, in case of *in situ* electroporation of cells grown on ECIS electrodes

studies by Hartmann (2003) addressed the question whether probes have to be present in the extracellular fluid while the field is applied or whether the electric field renders the membrane permeable for some time beyond the actual pulse. Confluent layers of NRK cells have been either electroporated in presence of the fluorescent dye or it was added 1 – 3 min after the electric field was turned off. Probes could only enter the cells, if they were present during field application but not if they were added 1 min or later after the pulse (Hartmann, 2003).

5.4.1.4 Electroporation of Subconfluent Cell Layers

Electroporation of subconfluent cells is advantageous in cases where the macromolecule introduced by electroporation has to enter the nucleus in order to be functional, e.g. DNA. The limiting size for free diffusion through the nuclear pore complex is, however, about 40 kDa (Fried and Kutay, 2003; Lechardeur and Lucas, 2006). For molecules above this limit either active transport has to take place or the nuclear envelope has to decompose, as it is the case during cell division. Many *in situ* electroporation protocols reported in literature therefore use subconfluent cell layers of about 50 – 80 % confluency (Klenchin et al., 1991; Koda et al., 2008; Yamauchi et al., 2004; Yang et al., 1995).

To date, electroporation of cells grown on ECIS electrodes has exclusively been carried out using confluent cell layers. The reason is primarily based on the following theoretical consideration: When the entire electrode is covered with cells, the impedance contribution of the cell layer to the overall impedance at 40 kHz, the frequency of the pulse used for electroporation, is high. This means that a large fraction of the applied voltage for electroporation drops across the cell layer. If, however, cell-free areas exist on the electrode, part of the current from the electroporation pulse can bypass the cell bodies and is lost for cell permeabilization, generating a situation similar to cells in suspension. For electroporation in suspension typically pulses with high amplitudes have to be applied, because a high fraction of the applied voltage drops across the buffer solution instead of across the cells. According to this phenomenon, electroporation efficiency should also be lower for non-confluent cell layers electroporated on ECIS electrodes when the same pulse parameters are chosen. Using a pulse of 40 kHz, 4 V and 200 ms for electroporation of subconfluent NRK cells should then result in a reduced dye uptake and concomitantly a reduced impact on cell integrity. The latter should be detected by a reduced post-pulse impedance decrease and faster impedance recovery as compared to confluent NRK cell layers.

But as shown by dye loading experiments (Fig. 5.24) a high fraction of the cells was irreversibly damaged, while only a few cells were stained by dye uptake. This unexpected invasive effect was also confirmed by impedance measurements (Fig. 5.23) showing an impedance drop to values of cell-free electrodes and poor or no cell layer impedance recovery. Apparently, a high percentage of the applied voltage has actually dropped across the cells and led to irreversible cell damage instead of reversible permeabilization.

Subconfluent cell layers were, however, reversilbly electroporated using lower amplitudes of 1 V or 2 V. The impedance increased to pre-pulse values again within 60 – 80 min (Fig. 5.25;

Fig. 5.27) and pulses of 2 V were high enough to result in considerable dye loading (Fig. 5.26).
These observations suggest that the direct contact between the cell and the electrode might prevent excessive current losses due to paracellular flow. Instead, an increasing contact area of spread cells in subconfluent layers might enhance the degree of permeabilization and, thus, the sensitivity to a pulse amplitude of 4 V (cp. Fig. 5.77).

Outlook: Electroporation of Adherent Cells Grown on ECIS Electrodes

Dye loading studies using an appropriate model dye and supporting impedance measurements have proven to be reliable tools to establish suitable electroporation conditions for various types of anchorage-dependent cells. Since all cell types under study could be readily loaded with the extracellular probe, it can be assumed that also many other anchorage-dependent cell lines will be amenable to *in situ* electroporation on ECIS electrodes.
All molecules to be loaded into cells should be administered to the cell layer before electroporation, since especially macromolecules are essentially incorporated during or immediately following the pulse presumably by a diffusive process. Following electroporation, a cell type specific cell morphology response can be measured by impedance monitoring. When measuring the specific impact of a bioactive probe after loading into the cytoplasm by *in situ* electroporation using impedance monitoring, it has to be considered that a cell type specific change in the time course of impedance will automatically occur due to the electroporation pulse itself. The effects of the electric pulse on cell layer impedance may mask the influence of electroloaded molecules or may even be changed by them.
Using ECIS based *in situ* electroporation as a research tool to study cell functions after cytoplasmic delivery of bioactive molecules, a substantiated knowledge of the cellular processes induced by the electric pulse itself is a prerequisite. This includes, for example, a better understanding of electric pulse effects on cell morphology. Investigations addressing changes in the cytoskeletal structure as well as the distribution of proteins normally associated with cell-cell contact and cell-substrate contact formation will be of interest in this context. Although cell morphological alterations seem to be restored within 60 min after electroporation, it will be important to elucidate the molecular basis for electric field induced cellular alterations. Future experiments could, for example, include systematic cytological stainings of cellular components being associated with cell morphology and correlating these to the measured impedance signals. Since the status of the cell layer was shown to have an influence on cell layer recovery kinetics, a systematic study of the influence of cell density, age of cells and nutritive status could help to elucidate critical parameters and to improve electroporation protocols.
Also the size limit and kinetics of molecule uptake still provide an open field for basic investigations. Still the size limit for xenomolecule delivery by electroporation is unresolved. Since the 2 MDa FITC-dextran was the biggest fluorescently labeled dextran molecule commercially available, use of other fluorescent probes like nanoparticles, i.e. quantum dots (cp. chapter 5.3.3.5) could be advantageous to systematically enhance the probe diameter beyond the hydrodynamic diameter of 2 MDa FITC-dextran (40 nm). Since the surface of

nanoparticles can be easily modified, also the influence of surface charge on electrotransfer may be investigated by this means. Moreover, it is not clear if such nanoparticles and other macromolecules are incorporated into the cytoplasm by diffusion across the permeabilized membrane or by other mechansisms like endocytosis. The online confocal microscopy technique presented in this work to illustrate delivery of 250 kDa FITC-dextran applied to even larger probes may shed light on the uptake mechanisms for different types of macromolecules. Also the proposed role of pulse duration on delivery of macromolecules may be elucidated by these kinds of studies. A change in dye loading efficiency dependence on pulse parameters might differ for increasing molecular weights.

5.4.2 Electroporation in Presence of Cytotoxic Molecules

It was the major aim to deliver bioactive substances into the cytoplasm of anchorage-dependent cells grown on impedimetric sensor electrodes. Bioactive probes that have already been loaded into cells grown on ECIS electrodes are the HRP enzyme (Ghosh et al., 1993) and the TRITC-labeled bicyclic heptapeptide phalloidin (Albermann, 2004) (Tab. 5.6).

Tab. 5.6: Bioactive molecules that have been transferred into the cytoplasm of anchorage-dependent cells grown on ECIS electrodes by *in situ* electroporation.

Cell Line	Electroporation Parameters	Molecule	Literature
NRK	100 kHz, 3 V, 200 ms	TRITC-Phalloidin	Albermann, 2004
NRK	40 kHz, 4 V, 200 ms	8-OH-cAMP	Wegener, unpublished
NRK	40 kHz, 4 V, 200 ms	Bleomycin	Hartmann, unpublished
NRK	40 kHz, 4 V, 200 ms	Cytochrome c	Balani, unpublished
WI-38/VA 13	4 kHz, 5 V, 200 ms	HRP	Gosh et al., 1993

These molecules were shown to maintain their capability of molecular recognition and biological specifity after electroporation by colorimetric or microscopic analysis of the cell layer. To date, however, no experiments have been published that analyze the cellular response to bioactive probes after intracellular delivery by electroporation with impedance readings. Only a few preliminary studies performed in the Wegener group have addressed the influence of electroloading of NRK cells with 8-OH-cAMP, bleomycin and cytochrome c.

Electroporation of cell membranes provides the cytotoxic molecule free access to the cytoplasm, where essential cellular reactions take place. This can be a decisive advantage in certain biochemical experiments and therapeutical approaches aiming for a controlled and direct cytoplasmic administration of the biochemical probe or drug. Under normal conditions the cell membrane protects the intracellular environment from free entry of harmful polar compounds. The intrinsic cytotoxicity of a substance is attenuated by a limited diffusion across the membrane or an enclosure in endocytotic vesicles and degradation in lysosomes. Following intrinsic cellular uptake routes the amount of cytotoxic molecules, which actually

reach the cytoplasm, is commonly unknown. By electroporation in contrast, specific blockage of crucial cellular functions and a targeted stimulation of cellular death programs can be accomplished in a well-controlled and very efficient way.

Typically, cytotoxic substances lead to cell death, which generally proceeds via either necrosis or apoptosis (Potten and Wilson, 2004; Majno and Joris, 1995). Necrosis is provoked by acute injury, severe alterations of physiological conditions or strong metabolic poisons. Cells undergoing necrosis are characterized by a failure in cell homeostasis and ceased cell metabolism. The cell rapidly swells due to inflow of sodium ions and water. Cell organelles like mitochondria swell and rupture and DNA and other cellular constituents disintegrate in a random and uncontrolled fashion. Due to cell swelling the cell membrane becomes permeable to cell debris and enzymes, leaking into the extracellular fluid and affecting surrounding tissue.

Apoptosis, in contrast, is a cell death mechanism which is actively controlled by the cell itself and requires the initiation and propagation of specific well-orchestrated processes in order to cleanly delete the cell. Apoptosis occurs under physiological conditions during embryonic development and in order to control cell turnover and tissue homeostasis in mature organisms (Vaux, 1993). Apoptosis can be triggered by extracellular signals like growth factor deprivation and binding of specific death signal molecules (Vaux, 1993; Lawen, 2003) or by intracellular signals as they are triggered upon severe damage or dysfunction of vital cellular structures (DNA, proteins, membranes) or processes (Norbury and Zhivotovsky, 2004; Gourlay and Ayscough, 2005; Croons et al., 2009; Leist et al., 1997).

Cells undergoing apoptosis are characterized by several morphological changes, like cell shrinkage, breaking contact with neighbors and rounding of the cell body, membrane blebbing, chromatin condensation, nuclear fragmentation and the creation of so-called apoptotic bodies (Kerr et al., 1972). Typical biochemical events associated with apoptosis are the activation of specialized proteases, the caspases (Thornberry and Lazebnik, 1998), a release of cytochrome c from mitochondria (Desagher and Martinou, 2000; Tait and Green, 2010), fragmentation of nucleosomal DNA (Zhang and Xu, 2000) and loss of membrane asymmetry by externalization of phosphatidylserine (Lawen, 2003). Whereas in the organism apoptotic bodies are engulfed by macrophages or adjacent cells, *in vitro* phagocytotic cells are missing and, thus, cells may eventually swell and finally lyse during their terminal phase of apoptosis (Potten and Wilson, 2004). The decision if apoptosis or necrosis is induced is not only determined by the sort of drug or cytotoxic stimulus, but is also often dependent on the cell type as well as on the concentration of the drug or intensity of the stimulus (Kanduc et al., 2002; Sunquist et al., 2006). The action of cytotoxic molecules on adherent cells can be easily detected by impedimetric monitoring, since cell death-associated cell permeabilization, rounding and detachment typically lead to a significant reduction of cell layer impedance (Arndt et al., 2004; Xiao and Luong, 2005).

In the scope of this work different cytotoxic substances with low intrinsic membrane permeability, ranging from the small anionic sodium azide over the glycopeptide antibiotic bleomycin to the small protein cytochrome c, have been loaded into NRK cells grown on

ECIS electrodes by electroporation. Findings from these experiments can be summarized as follows:

- ***Cytoplasmic delivery of cytotoxic molecules with only minor extracellular effect to anchorage-dependent cells grown on ECIS electrodes by in situ electroporation results in a concentration dependent retardation of cell layer impedance recovery from electroporation following a similar but drug specific time course (Fig. 5.82).***

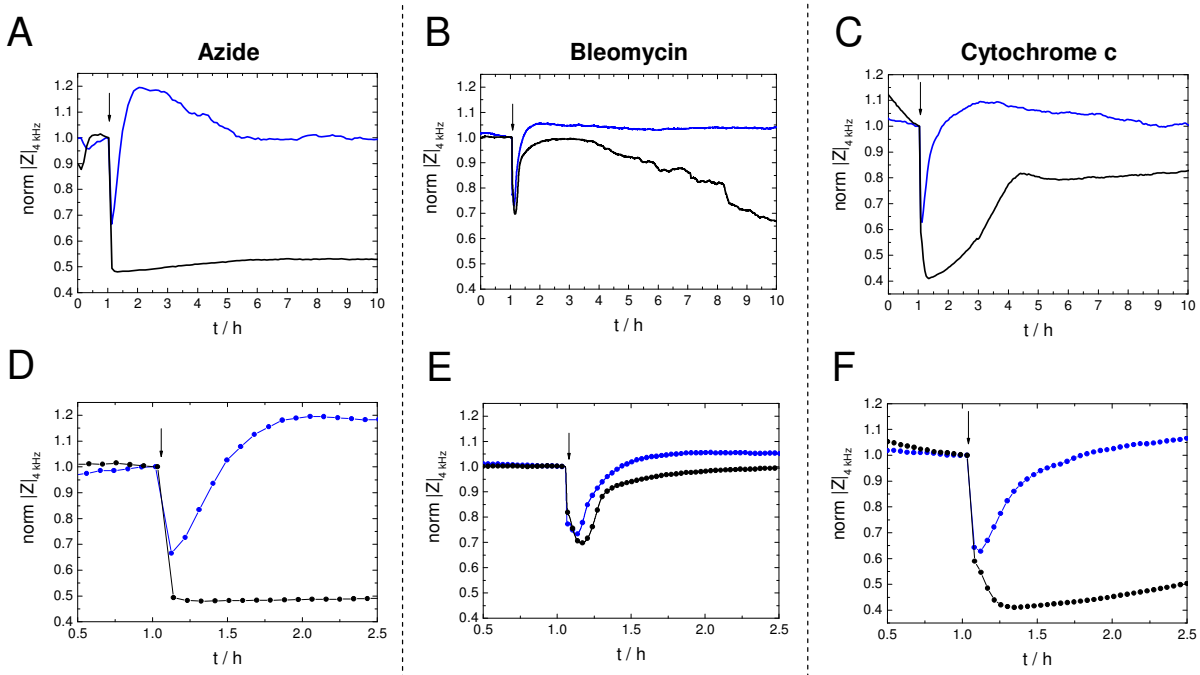

Fig. 5.82: Individual time courses of the normalized impedance magnitude at 4 kHz before and after electroporation (40 kHz, 4 V, 200 ms, arrow) of NRK cells grown on *8W1E* ECIS electrodes in presence of different cytotoxic substances. **A**, **D:** Azide; **B**, **E:** Bleomycin; **C**, **F:** Cytochrome c. A – C show time courses of the impedance on a 10 h scale, while D – F show the same measurements along a 2.5 h time scale. ▬, ●: Control: Electroporation in $EBSS^{++}$; ▬, ●: Electroporation in presence of the cytotoxic drug: 50 mM azide (A, D); 100 µM bleomycin (B, E); 10 mg/ml cytochrome c (C, F).

The individual results obtained for electroporation of NRK cells with azide, bleomycin and cytochrome c will be summarized and discussed separately.

5.4.2.1 Electroporation in Presence of Sodium Azide

The toxicity of azide arises from its action on the mitochondrial cytochrome oxidase and concomitant inhibition of respiration (Eytan et al., 1975). Energy depletion causes the cell to undergo necrosis (Bal-Price et al., 1999; Frankfurt and Krishan, 2001) or apoptosis (Chen et al., 1998; Wang et al., 2004) apparently strongly depending on cell type (Ishikawa et al., 2006; Chen et al., 1998) and azide concentration (Inomata and Tanaka, 2003; Wilhelm et al., 1997; Sato et al., 2008). In diverse studies toxic concentrations (EC_{50}) between 2 mM and 10 mM have been reported. However, the experiments were conducted with strong differences in incubation time between 3 h and 72 h (Bal-Price et al., 1999; Sato et al., 2008; Wang et al., 2004).

In this work simple incubation of NRK cells with increasing concentrations of sodium azide (0.1 – 150 mM) only revealed an acute decrease of cell layer impedance for a concentration of 150 mM. Incubation with sodium azide in concentrations ranging from 5 – 50 mM in contrast induced a slow increase of the normalized impedance of about 20 – 30 %, while for concentrations of 1.5 mM azide and below no influence was detected compared to an untreated control. As already discussed earlier, an impedance increase can be due to an increase in the cell volume (chapter 5.4.1.1). Cell swelling as a consequence of cytotoxicity is very typical for necrosis but might also occur in the end of the apoptosis process.

Addition of surplus ions, i.e. the azide and sodium ions, to an osmotically balanced buffer, however, might additionally provoke osmotic effects. Addition of sucrose to $EBSS^{++}$ buffer in the same concentrations as expected for completely dissociated NaN_3 in ideal solution should elicit this potential osmotic effect. A doubled concentration of sucrose as used for NaN_3 created solutions of similar osmolalities (Tab. 5.2). Non-ideal behavior at high NaN_3 concentrations might, however, explain the rather low osmolality of 150 mM sodium azide (408 mOsm/kg) in $EBSS^{++}$ when compared to 300 mM sucrose (556 mOsm/kg). Typically, osmolalities of about 270 – 300 mOsm/kg are regarded to be isotonic and physiological (Golzio et al., 1998; O'Connor et al., 1993; Müller et al., 2003). For $EBSS^{++}$ buffer alone an osmolality of 298 mOsm/kg is measured (Tab. 5.2).

Cell layers were incubated in solutions with different sucrose concentrations for 2 h before an electroporation pulse was applied. Although the exposure profiles are different compared to the prolonged exposure to sodium azide, the experiment provides a reasonable estimate for the osmotic effect of different hypertonic solutions on the cell layer impedance when extracellularily applied (Fig. 5.29). Indeed, 300 mM sucrose in $EBSS^{++}$ resulted in an impedance drop of about 4 kΩ within 2 h (Fig. 5.29), which can be explained by the osmotic effect of high extracellular solute concentrations. High osmolalities cause the cells to shrink and to widen the cell-cell contact area, thereby inducing an impedance decrease. O'Connor et al. (1993) used the ECIS technique to measure the influence of hypo- and hypertonic media on astrocytes and detected a considerable decrease of normalized resistance for osmolalities of 343 – 493 mOsm/kg, while hypotonic media caused an increase of resistance. Thus, the impedance drop observed for NRK cells in a solution of 150 mM azide in $EBSS^{++}$ with an osmolality of 408 mOsm/kg might not be ascribed exclusively to a toxic effect.

Cell layers incubated with 10 – 100 mM sucrose, osmotically similar to 5 – 50 mM sodium azide solutions, revealed slightly (~ 1 – 2 kΩ) elevated impedances when compared to the control cell layer. As a reduced impedance is expected for cells shrinking in hypertonic media, an increase of cell layer impedance might indicate that a volume regulatory response might be activated by the cells upon exposure to hypertonic media, which in turn creates an increase of cell volume.

It is known that epithelial cells of the kidney are well adapted to hypertonic stress dealing with osmolalities up to ~ 500 mOsm/kg (Capasso et al., 2001). Activation of a regulatory volume increase (RVI) mechanism in cells of the nephron induces uptake of osmolytes and water to restore cell volume (Wehner et al., 2003). The genetically programmed RVI is also accompanied by remodeling of the actin cytoskeleton in these cells leading to

depolymerization of the actin cortical ring and remodeling of a dense, diffuse actin network (Bustamante et al., 2003), which may additionally influence cell morphology and, thus, the cell layer impedance.

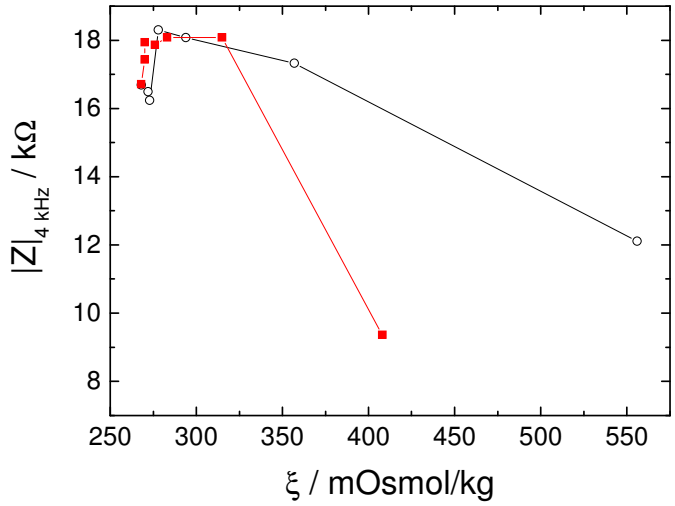

Fig. 5.83: Impedance magnitude at 4 kHz for NRK cell layers grown on *8W1E* ECIS electrodes after exposure to sucrose and sodium azide solutions with different osmolalities (ξ) for 60 – 110 min. ○: Sucrose (0, 1, 3, 10, 30, 100, 300 mM); ■: Sodium azide (0, 0.5, 1.5, 5, 15, 50, 150 mM). T = 37 °C

Since the elevation of impedance above the level of control cells is overestimated due to normalizing absolute impedance values in the beginning of the measurement where azide solutions of 5 – 50 mM have induced an initial impedance decrease, NRK cells might have restored to normal impedance levels by volume regulatory mechanisms. Comparing absolute impedance values of NRK cell layers about 2 h after incubation in solutions with different sucrose or sodium azide concentrations (Fig. 5.83) shows that only for the 150 mM solution a significant deviation from normal osmotic behavior is detected.

No acute cytotoxic effect was detected for azide concentrations up to 50 mM upon extracellular exposure over 9 h by impedance monitoring. However, this study could not clarify if slightly elevated impedances rising over several hours can be an indication of successive colloid osmotic swelling occurring as a response to accumulating energy depletion and ceasing ion homeostasis that will result in cell death on the long term. Sato et al. (2008) studied the effect of different sodium azide concentrations on rat squamous carcinoma cells (SCC131). They found that the SCC131 cells died by necrosis 48 – 72 h after treatment with azide concentrations greater than 5 mM in cell culture medium. A cytotoxicity of 65 % within a time frame of 10 h, similar to the time recorded in this work, was achieved for 100 mM sodium azide. However, the solution was not balanced for osmolality and no control for the osmotic effect was provided. In order to induce considerable cell death within a short period of time (3 h), high azide concentrations (500 mM) are often required (Frankfurt and Krishan, 2001).

When azide got free access to the cytoplasm by electroporation, a drastic effect on the cells was observed for concentrations of 5 mM and above. With increasing concentration the recovery of cell layer impedance after electroporation was significantly retarded (5 mM,

15 mM) or completely blocked (50 mM) when compared to the control (Fig. 5.28 B). Because omolalities up to ~ 350 mOsm/kg (obtained by 100 mM sucrose in $EBSS^{++}$) have only a minor effect on cell recovery from electroporation (Fig. 5.29), an unspecific effect of the solutions can be excluded.

For concentrations of 0.1 – 1.5 mM azide retardation of cell layer recovery was negligible. However, even these low concentrations caused elevated impedance levels above pre-pulse values compared to the control layer. An osmotic effect could be excluded for these concentrations, as shown by the electroporation experiment in sucrose solutions up to 3 mM (Fig. 5.29). However, these low azide concentrations, when brought in direct contact with the cytoplasm during electroporation, may have a similar effect as observed for azide applied extracellularly in concentrations of 5 – 50 mM azide. The elevation of cell layer impedance by about 20 % compared to control cell layers may eventually indicate an energy depletion induced volume increase that might result in necrosis or apoptosis on the long term. Then, the acute toxicity of azide would be enhanced by a factor of 10 – 30 upon transfer across the membrane by electroporation. Also Raicu and Mixich (1992) reported that the toxicity of azide could be considerably enhanced when the plasma membrane barrier is bypassed by delivering azide via multilammelar vesicles.

After electroporation the cell layers recovered to pre-pulse values for concentrations of 15 mM and below. Cells on the electrode loaded with azide and brought to necrosis or apoptosis are not expected to recover from the treatment. Since cells beyond the electrode are not loaded with azide, it is likely that these cells repopulate the electrode. The capability of several epithelial cells to repopulate the ECIS electrode after selective killing of the population on the electrode leads to a recovery of the impedance to values of a fully cell-covered electrode (Keese et al., 2004). However, cell migration driven by the actin cytoskeleton engine is energy-dependent (Mitchison and Cramer, 1996; Buss et al., 2002). For high azide concentrations of 50 mM, constant extracellular exposure of the cells to the azide solution might have depleted the cells surrounding the electrode, since these cells were not able to re-establish a confluent cell layer (Fig. 5.28 B).

Only cells exposed to 0.1 – 15 mM azide maintained the capability to recover to pre-pulse impedance values. For azide concentrations of 5 and 15 mM the impedance reached values for a cell-free electrode after electroporation, indicating cell death of the population on the electrode. The impedance reached values of a confluent monolayer after 6 h or 9 h, respectively. The time typically required for NRK cells to repopulate the ECIS electrode is in the range of 5 h – 8 h (Fig. 5.2; Fig. 5.43). This indicates that the extracellular azide (15 mM) might affect the migration of cells from the periphery to the center of the electrode by energy depletion, leading to a concentration-dependent retardation of electrode recovery (Fig. 5.28 B). Although no acute toxicity could be detected for an azide concentration of 5 mM (Fig. 5.28 A), cells may nevertheless suffer from energy depletion affecting their mobility. This assumption can be supported by the findings of Sato et al. (2008) who showed that 5 mM azide has a cytotoxic effect on SCC131 cells, finally leading to 50 % cell death after 72 h. In glucose-free buffer 50 % of a rat kidney proximal tubular cell population exhibited apoptosis after 3 h incubation in presence of 10 mM azide (Wang et al., 2004). In

this study, the glucose deprivation might have accelerated the energy depletion. Bal-Price et al. (1999) could show that a 24 h incubation with 2 mM azide led to 97 % of necrotic cells in glucose-free medium, but only 15 % in glucose-containing medium.

5.4.2.2 Electroporation in Presence of Bleomycin

One of the most often applied cytotoxic drugs with a low transmembrane permeability but a high intracellular toxicity is bleomycin (Mir et al., 1996; Sersa et al., 2009; Miklavcic et al., 2010). The very hydrophilic and charged glycopeptide antibiotic isolated from *Streptomyces verticillus* (Umezawa et al., 1966) became prominent because of its very efficient clinical use in electrochemotherapy (ECT) in the treatment of various cancer types (Gothelf et al., 2003). In ECT the membrane-impermeable cytotoxic drugs are administered systemically at a weak dose, but electric field mediated membrane permeabilization is only applied locally at the site of the tumor (Campana et al., 2009).
By electroporation the cytotoxicity of bleomycin is increased 300 – 5000-fold (Orlowski et al., 1988; Gehl et al., 1998; Jaroszeski et al., 2000). With free access to the cytoplasm by electroporation, the small molecule (~ 1.4 kDa) easily enters the nucleus and creates DNA defects. Its high cytotoxicity can be ascribed to its enzyme-like action, since each bleomycin molecule can induce several DNA single strand and double strand breaks (SSB and DSB) with a ratio of 1:6 (Cullinan et al., 1991; Tounekti et al., 1993). These DNA defects activate the apoptosis cascade essentially by an ATM-p53-induced signaling pathway, which triggers cytochrome c release from mitochondria (Chen and Stubbe, 2005; Roos and Kaina, 2006). Cytoplasmic cytochrome c triggers activation of caspase proteases and finally apoptotic cell death.

The combined *in situ* electroporation and impedimetric sensing approach was used to study the effect of bleomycin on cell morphology after electroporation of confluent NRK cells (chapter 5.2.2). The most important experimental findings can be summarized as follows:

- ***1 – 2 h after electroporation of NRK cells with 100 mM bleomycin the impedance at 4 kHz drops below control values and typically recovers to pre-pulse values again.***
- ***At a monitoring frequency of 32 / 40 kHz characteristic fluctuations are detected for cell layers electroporated in presence of bleomycin.***
- ***The cellular response quantified by the magnitude of impedance drop and time required for cell layer recovery is strongly dependent on the status of the cell layer.***
- ***Concentration dependence can only be detected impedimetrically when cells show a strong response to electroporation in presence of bleomycin.***
- ***Bleomycin loaded cells show morphological properties that are typical for apoptosis.***
- ***Recovery of cell layers from bleomycin electroporation shows wound healing characteristics.***

- ***Cell layer recovery after bleomycin electroporation can be impeded by the actin inhibitor cytochalasin D, effectively inhibiting wound healing by cell migration.***

Bleomycin was applied to confluent layers of NRK cells grown on ECIS electrodes in concentrations of 1 – 100 µM. The cytotoxic effect of bleomycin before and after cytoplasmic delivery by electroporation was recorded by time-resolved impedance measurements at a monitoring frequency of 4 kHz as well as 32 or 40 kHz[9]. While a monitoring frequency of 4 kHz is more sensitive for even slight changes in the cell-cell and cell-substrate contacts, the higher monitoring frequency is more useful to observe gross changes of electrode coverage with cells (cp. chapter 3.1.5). Measurements at both frequencies essentially showed the same results: Simple incubation with 100 µM bleomycin did not influence the cell layer impedance even over a period of ~ 40 h, whereas a significant impedance decrease could be detected after electroporation-mediated transmembrane delivery of bleomycin (Fig. 5.30). About 1 – 2 h after electroporation the impedance started to decline below impedance values of control cell layers and after (12.5 ± 3.5) h a minimum of the impedance was reached (Tab. 5.3). The absolute impedance drop at 4 kHz varied between 2 kΩ and 7 kΩ. In principle a monitoring frequency of 4 kHz is sufficient to present the essential apoptosis inducing effect on cell impedance behavior. Nevertheless, higher monitoring frequencies revealed an additional interesting behavior. Noticable fluctuations of cell layer impedance at 32 or 40 kHz only occurred for bleomycin electroporated cells while the signal of the controls remained smooth. These typical impedance fluctuations were not present over the entire observation period, but occurred after a delay of about 2.5 – 5 h after electroporation and ceased again ~ 5 – 10 h later (Tab. 5.3).

As a final consequence of bleomycin uptake cells die in the course of their genetically programmed apoptotic cascade, which is activated upon severe DNA damage. In principle all cells that reside on the electrode during electric pulse application are exposed to bleomycin molecules that get free access to their cytoplasm. If enough bleomycin molecules enter the cells to induce apoptosis all electroporated cells will experience cell death. Tounekti et al. (1993) discussed that an intracellular concentration of 1 nM bleomycin has the potency to induce ~ 500 double strand breaks per cell. However, only above a yet unknown critical number of double strand breaks apoptosis is induced.

According to Goldstein et al. (2000) the time required to initiate the apoptosis cascade in HeLa cells after inducing severe DNA damage by UV exposure as measured by cytochrome c release is in the range of ~ 4 – 8 h. About 1 – 2 h after cytochrome c release they could detect phosphatidylserine on the outer membrane and loss of plasma membrane integrity after 3 – 9 h. Similar results were obtained by Bossy-Wetzel et al. (1998) who studied apoptosis induced by UVB radiation on HeLa and CEM cells. Cytochrome c release was detected 1 h after radiation in HeLa cells and in CEM cells after 2 h reaching a maximum after 5 h. Caspase activity was detected after 3 h with a maximum after 6 h in CEM cells.

[9] The exact monitoring frequency (32 or 40 kHz) depended on the ECIS setup (chapter 4.3.1.1) used for the measurement.

Tounekti et al. (1993) electroporated DC-3F cells with 10 µM bleomycin in suspension and detected the highest amount of apoptotic cells showing membrane blebbing, shrinkage and chromatin condensation 6 h after electroporation.

This typical delay between exposure to an apoptotic stimulus and the first detectable morphological changes explains why NRK cells electroporated in presence of bleomycin on ECIS electrodes electrically behave similar to control cell layers in the first minutes after pulse application (Fig. 5.82 E). Like controls the cell layers electroporated in presence of bleomycin recover almost to pre-pulse values within ~ 1 h. Roughly 10 – 20 h after electroporation a minimum of impedance at 4 kHz is reached for bleomycin loaded cell layers. This time frame indicates the period where the rate of cell death is maximal and correlates well with the time scales reported for apoptosis induced by DNA damage as described by other authors (Goldstein et al., 2000; Bossy-Wetzel et al., 1998; Tounekti et al., 1993).

Unfortunately, the time courses of impedance diverged a lot between individual experiments (Fig. 5.30; Fig. 5.32; Tab. 5.3), which is most likely due to differences in the status of the cell layer at the time point of treatment. Even though the cultivation time on the electrodes itself was kept constant, especially passage number and the time of pre-cultivation before seeding on electrodes turned out to have a considerable effect on the susceptibility of the cells to bleomycin electroporation. Although not investigated systematically, the status of the cell layer especially affected the recovery kinetics. Preferently, lower passage numbers, short pre-culturing times before performing ECIS experiments and good nutritive status seemed to promote reconstitution of cell layer impedance. In cases where older cells were used, the cell layer impedance strongly decreased almost to values of a cell-free electrode. No or only minor impedance recovery was detected within the time frame of observation. Because in very vital cell layers it was difficult to detect an impedance change even upon loading with high concentrations of bleomycin, a concentration-dependent effect could only be observed when older cells were used. Although this “age effect” is not clarified yet, the observations give first indications for the reason of the strong differences in cell layer recovery, as will be discussed in a section further below.

However, this behavior makes it difficult to quantify the cytotoxic potential of the drug. Only above 30 µM a clear cytotoxicity of bleomycin upon electroporation could be measured. The literature provides diverse information on the cytotoxic potential of bleomycin. Electroporation experiments with bleomycin using suspended cells typically revealed EC_{50} values in the range of 0.01 µM to 10 µM, strongly depending on the cell type (Jaroszeski et al., 2000; Orlowski et al., 1988; Tounekti et al., 2001). This is 3 – 300 times lower than detected by ECIS measurements presented here. In clinical studies of electrochemotherapy bleomycin is applied in concentrations between 7 and 350 µM (Horiuchi et al., 2000; Kambe et al., 1996; Ueki et al., 2008), which covers the range of bleomycin concentrations used in this work.

Actually, all phase contrast micrographs of cell layers that have been exposed to an electric pulse and bleomycin, even at rather low concentrations like 1 µM, revealed accumulations of dead cells on the electrode surface (Fig. 5.35). Depending on the degree of cell layer recovery

at the time point of microscopic inspection these dead cells still covered a large fraction of the electrode surface or were found as aggregates in the center of the electrode. Also in cases where impedance measurements could hardly detect changes in the cell layer impedance, accumulations of dead cells were found on top of an intact cell layer in the center of the electrode (Fig. 5.33; Fig. 5.35).

Cytological stainings revealed that NRK cells loaded with bleomycin by electroporation showed typical morphological characteristics of apoptotic cells (chapter 5.2.2.3). Membrane blebbing, nuclear fragmentation, formation of apoptotic bodies and a final loss of membrane integrity were detected by live/dead staining ~ 20 h after electroporation with 100 µM bleomycin (Fig. 5.37). Different stages of chromatin condensation and nuclear fragmentation became evident by DAPI stainings due to the enhanced staining susceptibility of condensed chromatin to certain DNA binding dyes (Darzynkiewicz, 2001) (Fig. 5.38). In early stages of DNA condensation the morphology of the nucleus is maintained but dotted staining patterns occur. In proceeding apoptosis the nucleus disintegrates. DNA is fragmented and packed in vesicle-like structures. All stages of chromatin organization during the process of apoptosis could be detected within one NRK cell population after electroporation in presence of bleomycin. Obviously, the individual time scales along which single cells undergo these processes differed a lot. The heterogenity of morphologies typical for apoptosis in a cell population indicates that after electroporation in presence of bleomycin the process of apoptosis is not triggered simultaneously in all cells.

Tounekti et al. (1993, 2001) showed that the mechanism of cell death is closely related to the number of bleomycin molecules introduced to the cytoplasm. When only a few thousand molecules enter the cell (5000 – 50 000 per cell), cells are arrested in the G2/M phase of the cell cycle, become enlarged and polynucleated and finally die, very similar to mitotic cell death seen with ionic radiations. When several million molecules enter the cell, morphological changes identical to those usually associated with apoptosis are observed. A rapid DNA fragmentation into oligonucleosomal fragments occurs within a few seconds and leads to a direct internucleosomal cleavage of chromatin by bleomycin instead of cleavage by downstream caspases. It was moreover found that actively transcribed DNA is more susceptible to bleomycin cleavage (Kuo et al., 1981) and that bleomycin-induced DNA damage is cell cycle-dependent (Olive and Banath, 1993). In synchronized CHO cells bleomycin induced 2 – 3 times more double strand strand breaks (DSB) in the G_1 or G_2/M phase than in the S phase, where DNA replication takes place (Olive and Banath, 1993). The execution of apoptosis after DNA damage depends on the status of checkpoint proteins, like p53 as well as the cell's DNA repair capacity (Roos and Kaina, 2006). It is believed that at low levels DNA double strand breaks induce cell cycle arrest, whereas at high levels pro-apoptotic genes are directly activated. A retardation of apoptosis induction by initial cell cycle arrest and late induction of apoptosis can lead to a further deferment of apoptosis in some cells.

In many cases the cell layer fully recovered after electroporation with bleomycin (chapter 5.2.2.1). This could be verified by impedance measurements as well as by phase contrast microscopy. A typical feature of re-established cell layers after electroporation in presence of

bleomycin was a scar-like texture of the new cell layer, which was covered with dead cells in the central area of the electrode (Fig. 5.31; Fig. 5.35). Since the cell layers strongly resembled cell layers after performing the ECIS based electric wound healing assay with this cell type, a similar mechanism of cell layer reconstitution was considered (Fig. 5.40; Fig. 5.41). Electric wounding creates a necrotic microlesion in the cell layer residing on the active electrode area by application of a strong invasive pulse (Fig. 5.41 A1, A2). In contrast, loading of cells with bleomycin by electroporation induces apoptosis. Each cell follows its individual apoptosis program, which may be influenced by the number of bleomycin molecules introduced as well as individual cellular properties as described above. Thus, in contrast to electric wounding apoptosis is not triggered simultaneously.
Immediately after electrically induced wounding the electrode area is covered by dead cells. The electrode can be repopulated by the surrounding unaffected cells (Keese et al., 2004). This is nicely illustrated by the continuous impedance increase due to inward migration of vital cells on the cell-free electrode after pulsing (Fig. 5.41 E). A similar process may take place after electroporation with bleomycin, considering, however, that cell death and recovery are asynchronous. The processes of apoptosis and cell detachment overlap with cell layer reconstitution processes replacing dead cells within the affected cell layer. Replacement of single apoptotic cells within a cell layer is thought to occur in an actin-dependent ring closure mechanism (Florian et al., 2002).
Above considerations might explain the fluctuations which were measured at a monitoring frequency of 32 / 40 kHz after the cell layer was loaded with bleomycin (Fig. 5.30 B; Fig. 5.32 B; Fig. 36 B). Since especially higher frequencies are sensitive to changes in electrode coverage with cells, these fluctuations might reflect continuous, dynamic cell death and recovery processes in the cell layer. The time required to induce and execute apoptosis after electroporation in presence of bleomycin may depend on the vitality of the cell layer. In a similar way cell vitalilty will influence the velocity of cell layer recovery by replacement of dead cells by motile cells. These considerations might explain the strong variations in the impedance time course measured after electroporation in presence of bleomycin as well as its dependence on cell culture age.

In order to prove the assumption that cell migration of vital cells from the periphery of the active electrode, not subjected to membrane permeabilization and bleomycin loading, is responsible for cell layer recovery, cell migration was inhibited by pre-incubation of the cell layer with cytochalasin D (chapter 5.2.2.5). Cytochalasin D is an actin binding drug which inhibits actin polymerization and associated functions like cell motility (White et al., 2001).
Indeed, a suitable concentration of 0.5 µM cytochalasin D can effectively block wound healing within an NRK cell layer (Fig. 5.43). After electroporation of a cytochalasin D pre-incubated cell layer in presence of bleomycin no cell layer recovery took place, whereas cell layers electroporated without cytochalasin D revealed cell layer recovery within ~ 20 h (Fig. 5.44). The cytotoxic effect of bleomycin even in low concentrations of 1 µM could be easily detected impedimetrically (Fig. 5.45). DAPI stainings as well as live/dead stainings nicely illustrated that after bleomycin electroporation in presence of cytochalasin D the

electrode remained covered by apoptotic, dead cells spread over the entire area of the active electrode surface (Fig. 5.46; Fig. 5.47). Dead cells could not be replaced by vital cells from the periphery as observed when no cytochalasin D was present (Fig. 5.47; Fig. 5.48). After electroporation with 1 – 100 µM bleomycin similar impedance signals were recorded. In all cases values of a cell-free or almost cell-free electrode were reached (Fig. 5.45). The small concentration-dependent gradation in impedance at 40 kHz at the end of the measurement mirrors that by lowering the bleomycin concentration from 100 µM over 10 µM to 1 µM the fraction of surviving cells on the electrode slightly increases. This was also proven by live/dead staining (Fig. 5.47; Fig. 5.48). To verify this tendency, lower concentrations should be tested enabling to define an EC_{50} value where half of the cell population has detached from the electrode due to apoptosis. Nevertheless, it has to be considered that cytochalasin D treatment means an additional manipulation of natural cell physiology. It was reported that cytochalasin D itself can induce apoptosis when applied in concentrations between 0.1 and 1 µM (Rubstova et al., 1998; White et al., 2001) and might therefore have a promoting effect on bleomycin cytotoxicity (Malecki et al., 2010). However, no acute cytotoxicity of cytochalasin D could be detected for NRK cells in this work. Only a few apoptotic nuclei in cell layers incubated with cytochalasin D might indicate that an apoptosis promoting effect has to be considered as well (Fig. 4.9 h).

Although the time course of the apoptosis inducing effect of bleomycin on NRK cells grown on gold-film electrodes after *in situ* electroporation can be detected with high temporal resolution by continuous monitoring of the cell layer impedance, it has to be considered that in motile cell layers asynchronously induced apoptosis is superimposed by cell layer reconstruction mechanisms, hiding cell death induced impedance decreases.

5.4.2.3 Electroporation in Presence of Cytochrome c

Release of cytochrome c from mitochondria is a key signal in the initiation of apoptosis. Cytochrome c accumulating in the cytoplasm triggers the assembly of the apoptosome, which subsequently activates essential apoptosis executing caspases (Liu et al., 1996). Cytochrome c release from the inner mitochondrial membrane is essentially triggered by intracellular apoptotic stimuli, like DNA damage, metabolic stress or the presence of unfolded proteins via the intrinsic apoptotic pathway (Ow et al., 2008). In addition, cytochrome c release is used to amplify signals generated by other apoptotic pathways.
Due to the central role of cytochrome c in apoptosis, the active manipulation of its cytoplasmic concentration is of immense biochemical interest. Therefore, the spatially and temporally controlled delivery of cytochrome c by electroporation became a popular technique to investigate the apoptotic cascade (Vier et al., 1999; Tsoneva et al., 2005; Chertkova et al., 2008; Eksioglu-Demiralp et al., 2003).
The impact of *in situ* electroporation of NRK cells in presence of cytochrome c on the cell layer impedance was studied in the scope of this work allowing for a label-free and time-

resolved analysis by impedance measurements (chapter 5.2.3). Essential results can be summarized as follows:

- ***Electroporation of NRK cells in presence of cytochrome c led to a concentration-dependent retardation of cell layer impedance recovery for extracellular concentrations between 0.3 – 10 mg/ml.***
- ***DAPI staining of cytochrome c electroloaded cells revealed nuclear fragmentation and chromatin condensation – a typical characteristic for apoptosis.***
- ***The specific apoptosis inducing effect of cytochrome c was attenuated by co-electroporation in presence of the caspase inhibitor peptide DEVD, while the biologically inactive BSA had no cytotoxic effect.***

Direct cytoplasmic delivery of cytochrome c (10 mg/ml) by electroporation into NRK cells resulted in an immediate impedance drop to impedances near values of a cell-free electrode and a retarded recovery of cell layer impedance to base line values when compared to electroporation under cytochrome c-free conditions (Fig. 5.49). Cell layer impedance recovery took more than 3 h (Fig. 5.49 B; Fig. 5.51 B), which is much longer than observed for simple electroporation in buffer. The time course of impedance is, however, very similar to that observed for an electrically wounded NRK cell layer (cp. Fig. 5.2), which is characterized by an impedance drop to values of a cell-free electrode and a retarded cell layer recovery taking about 5 – 8 h (cp. Fig. 5.2). Values of a cell-free electrode are achieved when all cells on the electrode that have been loaded with cytochrome c follow the apoptosis programm leading to cell death. As already discussed in the context of bleomycin-induced apoptosis, the synchrony of apoptosis induction and wound healing capacity of cells beyond the active electrode will influence the recorded impedance profile. As a synchronously induced death of the cell population on the electrode creates a cell-free electrode, which then can be repopulated by the intact cells from the periphery, the measured impedance profile is supposed to be similar to an electrically induced cell death. The time between exposure of the cytoplasm to cytochrome c and onset of apoptosis is a crucial aspect. In the literature this time frame was studied by microinjection of defined cytochrome c concentrations into the cytoplasm of cells and was reported to be in the range of ~ 2 h (Li et al., 1997; Juin et al., 1999; Johnson et al., 2007a). After microinjection of 3 mg/ml cytochrome c into HEK-293 cells significant caspase activity could already be detected after 1 h. After 2 h 50 % of the cells showed caspase activity (Li et al., 1997). Also Juin et al. (1999) measured considerable cell death 2 h after 25 µM cytochrome c injection. Johnson et al. (2007a) used 10 mg/ml cytochrome c for microinjection and measured an onset of caspase activity already after 10 min and maximal caspase activity after ~ 80 min. Also cytochrome c introduced by electroporation was reported to induce apoptosis within ~ 2 h, as indicated by DNA fragmentation (Garland and Rudin, 1998; Garland et al., 2000). The susceptibility to cytochrome c injection was found to depend on the cell type (Li et al., 1997) and the cell cycle status (Garland and Rudin, 1998). Li et al. (1997) moreover studied the dependence of apoptosis on the cytocrome c concentration. With

decreasing cytochrome c concentrations down to 0.1 mg/ml the time required to measure significant apoptosis increased and the number of cells that underwent apoptosis decreased.
Also in this work a delay of a few minutes between the transfer of cytochrome c into the cytoplasms of NRK cells by *in situ* electroporation and onset of cell death was detected by impedance measurements. After electroporation of NRK cells in presence of 10 mg/ml cytochrome c the initial electrically induced drop of the normalized impedance to about 0.6 – 0.7, starting to recover within ~ 5 min in control cells, was followed by a second phase of impedance decrease, reaching an impedance minimum ~ 10 – 15 min after cytochrome c uptake (Fig. 5.51; Fig. 5.82). After electroloading in presence of different cytochrome c concentrations (0.1 – 10 mg/ml) the magnitude of impedance drop as well as the time required for recovery back to stable impedance values increased with rising cytochrome c concentration (Fig. 5.51). The pro-apoptotic effect down to concentrations of 0.3 mg/ml was reliably detectable. Garland and Rudin (1998) detected cytochrome c-induced apoptosis after electroporation in presence of concentrations as low as 8 µg/ml by flow cytometry. In most other applications of electroporation-assisted cytochrome c transfer into cells concentrations ranged between 10 µg/ml (Eksioglu-Demiralp et al., 2003) and 1.25 mg/ml (Decrock et al., 2009). As reported in this study, apoptosis was induced in NRK cells with considerable efficiency using 1 mg/ml cytochrome c, which was also the concentration used in most electroporation studies reported in literature (Vier et al., 1999; Schimmer et al., 2003; Tsoneva et al., 2005).

After recovery from electroporation in presence of cytochrome c the initial impedance at 4 kHz was not completely re-attained, whereas at a monitoring frequency of 32 kHz impedances rose back to pre-pulse values within 3.5 – 6.5 h (Fig. 5.51). The time span needed for full recovery after cytochrome c electroporation was therefore more easily quantified using the monitoring frequency of 32 kHz. Since this deflection of impedance at 4 kHz was observed in several experiments and also for low concentrations, it might be assumed that cytochrome c influences the cell morphology. These sub-microscopical changes in the cell layer are detected with high sensitivity at a frequency of 4 kHz, while they are almost negligible when monitoring cell layer impedance at 32 kHz. At a frequency of 32 kHz in turn the electrode coverage with cells is efficiently detected. A slight reduction of cell layer impedance at 4 kHz over time was also observed when NRK cells were simply incubated in the 10 mg/ml cytochrome c solution. This supports the theory of a moderate extracellular effect of the protein. Due to its large positive charge under physiological pH (Ow et al., 2008) cytochrome c has low membrane permeability and is presumably only incorporated into cells by an endocytotic pathway and intracellular release from the endosome (Hiraoka et al., 2004; Gilmore et al., 2001). Potential toxicity of extracellularly applied cytochrome c to certain cells has yet only been reported by a few authors. Extracellular cytochrome c was shown to induce apoptosis in neuronal cells at concentrations as low as 25 ng/ml (Ahlenmeyer et al., 2002) as well as in J774 cells at concentrations above 100 µg/ml (Hiraoka et al., 2004). Also Codina et al. (2010) reportet that cytochrome c, released into the extracellular fluid by dying cells, is cytotoxic to lymphocytes. In most experimental electroporation studies described in literature

the extracellular cytochrome c was removed after the electroporation step and, thus, after a short incubation time. Thus, cytochrome c in concentrations up to 500 mg/ml had no cytotoxic effect on cells as the exposure was limited to 2 h (Garland and Rudin, 1998). Although in this work no acute cytotoxicity of extracellular cytochrome c was detected along the observation time of 8 h, a considerably prolonged incubation with the highest concentration of 10 mg/ml for ~ 25 h revealed a significant impedance drop to values of a cell-free electrode, indicating cell death (data not shown). Using lower concentrations the cell layer impedance remained unaffected over 25 h.

Microscopic analysis of NRK cell layers several hours after electroloading with cytochrome c showed typical characteristics of apoptotic cells that have been collected on top of the newly established cell layer after inward migration of vital cells from the periphery onto the active electrode (Fig. 5.50). The DAPI stained cluster of apoptotic cells in the center of the electrode revealed advanced chromatin condensation and nuclear fragmentation. The specifity of the intracellular cytochrome c effect was tested by electroporation of NRK cells in presence of similar concentrations of the biologically inert protein bovine serum albumin (BSA), for which no cytotoxic effect was detected (Fig. 5.52 A). In order to verify that the delayed impedance recovery is coupled to the onset of apoptosis after electroporation-assisted cytochrome c delivery, a caspase inhibitor was co-electroporated into NRK cells (Fig. 5.52 B). Cytoplasmic cytochrome c initiates assembly of the apoptosome, which activates executioner caspases, essentially caspase-3 and caspase-7 that perform specific proteolysis (Tait and Green, 2010). Most caspase inhibitors contain the typical recognition and cleavage sequence DEVD (Asp-Glu-Val-Asp) of caspases (Nicholson et al., 1996; Kumar and Dorstyn, 2009) as well as an aldehyde group, which reversibly inactivates caspase activity (Garcia-Calvo et al. 1998). The caspase inhibitor applied in a concentration of 20 µM led to a significant reduction, but not complete blockage, of apoptosis (Fig. 5.52 B). Likely, incomplete inhibition of the downstream caspases can be ascribed to an insufficient inhibitor concentration. In a preliminary study performed by P. Balani (unpublished data) caspase activity after electroporation in presence of 10 mg/ml cytochrome c could be efficiently blocked by using 250 µM of the inhibitor peptide Acetyl-Asp-Glu-Val-Asp-aldehyde in a co-electroporation experiment. Nevertheless, specific blockage of caspase activity demonstrates apoptosis specific action of cytochrome c.

In conclusion, morphological changes as a result of apoptosis, specifically induced by caspase activating cytochrome c, brought into the cytoplasm of NRK cells by *in situ* electroporation, can be monitored impedimetrically with high time resolution.

Synopsis - *In situ* Electroporation with Azide, Bleomycin and Cytochrome c

Azide, bleomycin and cytochrome c induce cell death when efficiently transferred into the cytoplasm of adherent cells by electroporation. The mechanisms by which they induce cell death is of fundamental difference (Fig. 5.84). Azide creates energy depletion and presumably induces a necrotic cell death, since apoptosis is energy-dependent, requiring ATP consuming processes. Azide-induced cell death is quite immediate upon cytoplasmic contact as revealed by the instantaneous impedance drop (Fig. 5.82 A).

Although bleomycin and cytochrome c both induce apoptosis, signal transduction within the cell differs. Therefore, bleomycin and cytochrome c cause drug typical impedance time courses reflecting these individual processes (Fig. 5.82 B, C). In the intrinsic apoptotic pathway, cytochrome c release is the central signal, which integrates intracellular pro-apoptotic stimuli, like DNA damage. Cytochrome c alone can induce apoptosis via direct activation of executioner caspases, while DNA damage induced by bleomycin, for example, acts as an intrinsic upstream signal which is dependent on further complicated regulation mechanisms. Signaling cascades, cell cycle arrest and DNA repair programs can be activated before the final decision guides the cell to apoptosis. Thus, the apoptosis pathway induced by cytochrome c is more direct than the cellular response induced by the action of bleomycin. Since cytocrome c-dependent apoptosis is almost immediately activated, cells start to die several minutes after introduction. The impedance signal is very similar to that obtained by azide electroporation (Fig. 5.82 A, D) or electrically induced cell death as known from the electric wound healing assay (Keese et al., 2004).

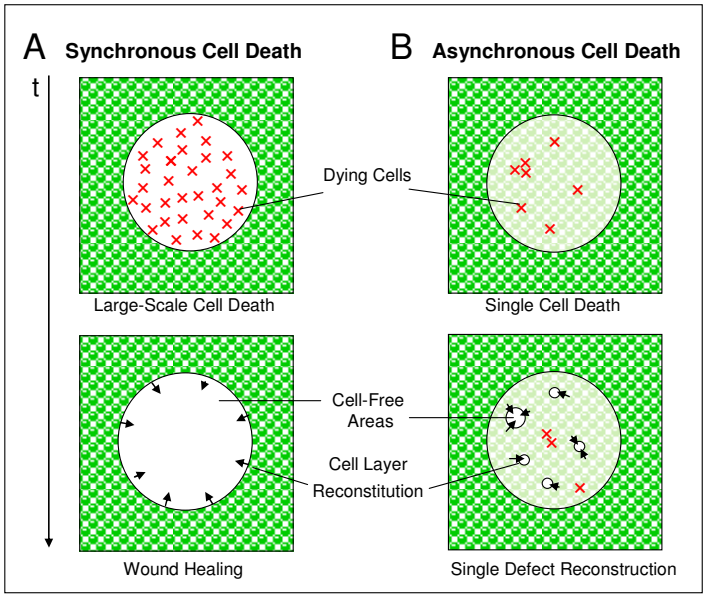

Fig. 5.84: Schematic illustration of two scenarios after induction of cell death in the population residing on the gold-film electrode (circle). Two types of cell death can be distinguished according to their chronology: **A:** Synchronous cell death: all cells die at the same time (e.g. induced by electric wounding), the electrode surface is covered by dead cells instantaneously and after a short delay intact cells from the periphery of the active electrode start to repopulate the empty space; **B:** Asynchronous cell death: cell death proceeds individually and asynchronous in each single cell (e.g. induced by electroporation of cytotoxic substances inducing apoptosis), small cell-free areas are created on the electrode where cells disintegrate from the cell layer and detach. These small defect sites are occupied by vital neighboring cells, while new defects are created at other sites within the drug loaded population. (Green dots: vital cell layer; light green dots: cells loaded with pro-apoptotic drug; red crosses: dying cells; white circles: cell-free areas; arrows: direction of cell movement for cell layer reconstitution).

The onset of apoptosis is highly asynchronous in cells that have been loaded with bleomycin. Individual defects in the cell layer are continuously repaired, as seen by impedance fluctuations at 32 / 40 kHz. Due to the higher synchrony of apoptosis after electroporation in presence of cytochrome c, these impedance fluctuations are missing. Results obtained for cytochrome c and bleomycin have in common that apoptosis-induced cell death and

detachment is masked by cell layer reconstitution processes in which vital cells from the periphery of the active electrode replace dead cells.
Time-resolved impedance monitoring of the manipulated cell layers allowed to reveal mechanistic differences of their cytotoxic action due to drug specific time courses, although on first sight electroporation of any cytotoxic molecule just led to a retardation of cell layer recovery from the electroporation pulse.

Outlook: *In situ* Electroporation in presence of Cytotoxic Substances

To date the analysis of the intracellular effect of cytotoxic substances has been performed by microscopy, flow cytometry or biomolecular methods. Using conventional biochemical endpoint assays the main challenge is often to figure out the optimal time point to detect specific hallmarks of apotosis. Since not all biochemical events are only specific to apoptosis, do not occur in all cell types, at all stages of apoptosis or upon all kinds of pro-apoptotic stimuli (Sunquist et al., 2006), this kind of assays have their limitations. Even cell population heterogeneity and differences in cell cycle as well as drug concentration influence the time course of apoptosis and, thus, the quality of their detection in cell ensembles (Goldstein et al., 2000). In contrast, continuous impedance measurements allow label-free monitoring with high time resolution before and immediately after electroporation-assisted loading of anchorage-dependent cells with substances inducing apoptosis (bleomycin) or necrosis (azid) or even cellular signaling molecules that contribute to the regulation of these processes (cytochrome c).
Since the coordination of cell growth, cell division and cell death is essential for development, tissue homeostasis and disease, elucidating the mechanisms of apoptosis is still a major aspect in current research. Therefore, impedance analysis of cell layers after induction of apoptosis by electroporation in presence of cytotoxic agents may find many interesting applications. There is, for example, a strong interest in the development of simplified, miniaturized multi-well assay devices for electrochemotherapeutic testing (Choi et al., 2009; Neumann et al., 2000). Thus, *in situ* electroporation in combination with ECIS monitoring provides a useful tool to study the intracellular effects of membrane-impermeable exogenous molecules. The ECIS technique is especially interesting, since it is able to reveal mechanistic differences of the drug specific cytotoxic action by measurements with high time resolution. These properties might be useful in revealing the contribution of different signaling and cytotoxic pathways.
However, cell layer recovery processes like wound healing competing with cell death in a small population of the cell layer can hide apoptotic effects and have to be considered in this kind of studies. Because the surrounding cells are able to re-establish the cell layer at sites of bleomycin induced apoptosis on the electrode area, the surrounding cell layer is obviously not influenced by bleomycin in the extracellular fluid. Drug screening campaigns searching for new candidates in electrochemotherapy might use this property of wound healing to probe drugs that have no extracellular cytotoxic effect, but are exclusively toxic when introduced into the cytoplasm by electroporation. Actually, the process taking place on the electrode resembles the situation in living tissue when a locally confined tumor site is treated by

electrochemotherapy and the healthy tissue around the lesion recovers the wound. If on the other hand only the mere cytotoxic potential of a drug has to be studied, it is favorable to eliminate the masking effect of cell layer recovery mechanisms. Because chemicals like cytochalasin D also have adverse side effects that might influence the impact of a drug under study, other approaches have to be developed. A synchronization of the NRK cell layer may already reduce part of the strong asynchrony. However, wound healing processes will nevertheless occur. Only if the area surrounding the active electrode area remains cell-free, no vital cells are available to restore cell layer impedance, masking the apoptosis inducing effect of cytotoxic drugs. This setup could be created using non-adhesive material surrounding the electrode area, so that cells can only grow on the electrode but do not adhere to the surrounding polymer.

Interesting ECIS applications might moreover arise from highly time-resolved measurements at high frequencies (32 / 40 kHz), that reflect dynamic changes in the electrode coverage with cells. Similar to micromotion analysis, which detects small shape fluctuations within the cell layer at lower frequencies (4 kHz) sensitive to changes in cell-cell and cell-substrate contacts, analysis of fluctuations at higher frequencies may be used to detect single cell detachment and recovery events. For example, cell layers with pathologically enhanced apoptosis rates can be studied. Enhanced single cell apoptosis in epithelial cell layers is the basis for several diseases (Chron's disease, lung fibrosis) causing a constant damage of the epithelium's barrier function. Thus, a high frequency micromotion ECIS mode may be useful to analyze processes directed by the balance between apoptosis and regeneration.

5.4.3 Electroporation of Adherent Cells Using A Miniaturized Electrode Layout

In situ electroporation of adherent cells grown on ECIS electrodes enables the efficient loading of cells with membrane-impermeable molecules. In contrast to other methods for the delivery of membrane-impermeable molecules into mammalian cells, electroporation essentially relies on passive uptake of molecules. The exogenous molecule can not accumulate intracellularly over time. In contrast, the cells are only open for macromolecule uptake during and shortly after the electroporation pulse (cp. chapter 3.2.2). During this period of time only a limited amount of the extracellularly applied substance can diffuse across the permeabilized membrane or is facilitated to interact with the membrane for later uptake by non-diffusive mechanisms (cp. chapter 3.2.2.4). A concentration equilibrium between the cellular interior and the extracellular fluid is typically not achieved, so that the efficient delivery of molecules requires rather high extracellular concentrations. Many bioactive molecules like antibodies, enzymes and nucleic acids, however, are not always available in large amounts. Thus, for the use of costly samples in electroporation experiments common *8W1E* ECIS electrodes are not very economic. The total well area of the *8W1E* arrays (0.75 cm^2) limits the minimum sample volume to about 150 µl. This rather large well area is based on the concept of using the small working electrode (5×10^{-4} cm^2) in

combination with a large counter electrode (~ 0.25 cm^2). In contrast, an electrode layout consisting of two microelectrodes of the same size (cp. chapters 4.3.1.4 – 4.3.1.6) allows to reduce the minimal sample volume considerably (Fig. 5.53).

5.4.3.1 Characterization of a Miniaturized Electrode Layout for *In Situ* Electroporation and Impedance Monitoring of Adherent Cells

The development of a modified electroporation and measuring setup for electroporation of cells in small sample volumes provided the following results:

- ***The miniaturized electrode layout enables the electroporation and impedance monitoring of adherent cells in a sample volume of only 10 – 30 µl with similar electroporation efficiency and quality of the measurement when compared to commercial 8W1E electrodes.***
- ***Optimal electroporation of NRK, HEK-293 and Hep G2 cells on microelectrodes require enhanced pulse amplitudes that were increased by 1 – 3 V compared to electroporation on 8W1E electrodes.***

Impedance Measurements Using the Miniaturized Electrode Layout

The sensitivity of the basic ECIS setup is based on its electrode geometry using a small working electrode and a significantly larger counter electrode (Fig. 5.85 A). In a system with two electrodes of large surface area the impedance created by the electrode-solution interface is normally small compared to the solution resistance. The total impedance of the system is dominated by the solution resistance (R_s) which increases with increasing electrode distance l and decreasing cross sectional area A ($R_s = \rho \cdot l/A$). In such a system the electrode impedance can only dominate the total impedance, if the solution resistance is kept small, which is the reason for the small electrode distances (10 µm – 60 µm) used in interdigitated electrode layouts (Moore et al., 2009; Ceriotti et al., 2007; Alexander et al., 2010). When one of the electrodes becomes small, the compression of electric field lines to the small area of the electrode surface, also referred to as constriction resistance, determines the total bulk resistance R_{bulk}. For a circular electrode the constriction resistance varies with ρ/r, where r is the radius of the electrode and ρ the specific resistance of the bulk solution (Giaever and Keese, 1991). This is the reason why R_{bulk} for a conventional *8W1E* electrode with an electrode radius of 125 µm is ~ 1 kΩ, although the resistance of the bulk solution itself is small in comparison (~ 68 Ω)[10].

[10] $EBSS^{++}$ buffer has a specific resistance of ρ = 72.5 Ω · cm (specific conductivity: 13.8 mS/cm) and the solution resistance R_s can be calculated when certain assumptions are made. The maximal cross section (A) for current flow between the two electrodes is considered as the liquid cross section in an *8W1E* ECIS well, which is filled with 400 µl buffer (0.38 cm^2). The length of the current pathway (l) is approximated as the distance between the center of the circular working electrode and the edge of the large counter electrode, which is 0.35 cm. The solution resistance between the electrodes then corresponds to 67.7 Ω.

The impedance contribution of the electrode with or without cells depends on the area and increases with $1/r^2$ (Ghosh et al., 1994). Since these contributions of the bulk and the electrode are connected in series, the impedance of the cell layer dominates the overall impedance when the radius of the electrode is small (Fig. 5.86). Thus, using the conventional *8W1E* electrodes, the major fraction of the total impedance is created at the small working electrode that serves as a bottleneck for current flow. Because the impedance contribution of the counter electrode can be ignored due to its much bigger surface area, the measured impedance signal is dominated by the impedance of the working electrode.

When the microelectrodes are used individually in combination with the large counter electrode residing at the periphery of the well the electric situation is similar to that in *8W1E* arrays (Fig. 5.85 B).

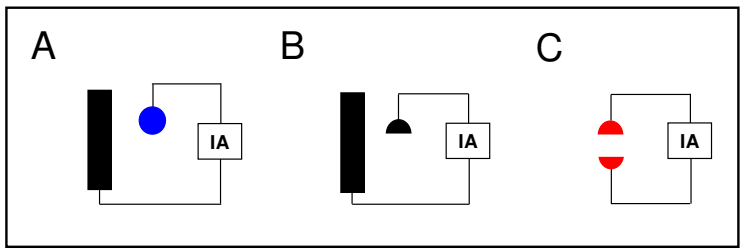

Fig. 5.85: Schematic illustration of different electrode arrangements used in this work: **A:** *8W1E*: Small working electrode (5×10^{-4} cm^2) and large counter electrode (~ 0.25 cm^2); **B:** One microelectrode (2.5×10^{-4} cm^2) in combination with the large counter electrode; **C:** Miniaturized Electrode arrangement: Two microelectrodes in series.

However, the surface area of a microelectrode (2.5×10^{-4} cm^2) is smaller compared to the *8W1E* electrodes (5×10^{-4} cm^2). In general, the impedance increases for decreasing size of the working electrode, as illustrated by simulated impedance spectra in Fig. 5.86 A.

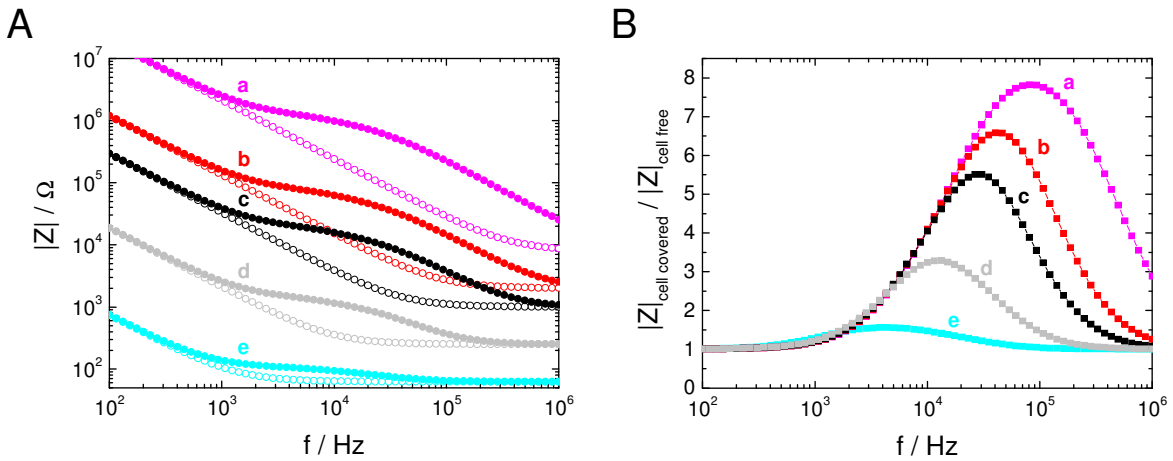

Fig. 5.86: A: Simulated impedance spectra of cell-free (open symbols) and cell-covered (filled symbols) circular electrodes with different radius: ○, ● (a): 1.5×10^{-3} cm; ○, ● (b): 6.25×10^{-3} cm; ○, ● (c): 1.25×10^{-2} cm; ○, ● (d): 5×10^{-2} cm; ○, ● (e): 0.2 cm. Changes in the electrode radius influence the CPE by $1/r^2$ and the bulk resistance by $R_{bulk} = f \cdot 1/r$ ($f = 12.5$) due to the constriction of current to the small electrode. Parameters for the cell layer were: $\alpha = 5\ \Omega^{1/2} \cdot$ cm; $R_b = 5\ \Omega \cdot$ cm^2; $C_m = 2\ \mu$F/cm^2; n_{CPE}: 0.95; A_{CPE}: 1.5×10^{-5} Fs^{n-1}cm^{-2}. **B:** Normalized impedance spectra ($|Z|_{cell\text{-}covered}$ / $|Z|_{cell\text{-}free}$) for different electrode radii (see code in A).

Because the microelectrodes do not have perfectly the same size due to slight variances in the fabrication process, the impedance spectra of the two microelectrodes measured in connection with the counter electrode can be slightly shifted (Fig. 5.54).

Theoretically, the sensitivity of the measurement increases with decreasing electrode radius, since the electrode impedance increasingly dominates the total impedance over the bulk resistance and the influence of the cell layer becomes more and more pronounced (Fig. 5.86 A). This is reflected by an increase in the normalized impedance ($|Z|_{cell\text{-}covered}$ / $|Z|_{cell\text{-}free}$) at all frequencies (Fig. 5.86 B). For discussion of the experimental data the results of Fig. 5.54 and Fig. 5.55 were combined and are presented here in Fig. 5.87 C and D. Theoretical simulations that match the geometries of the electrodes under study are provided in Fig. 5.87 A and B.

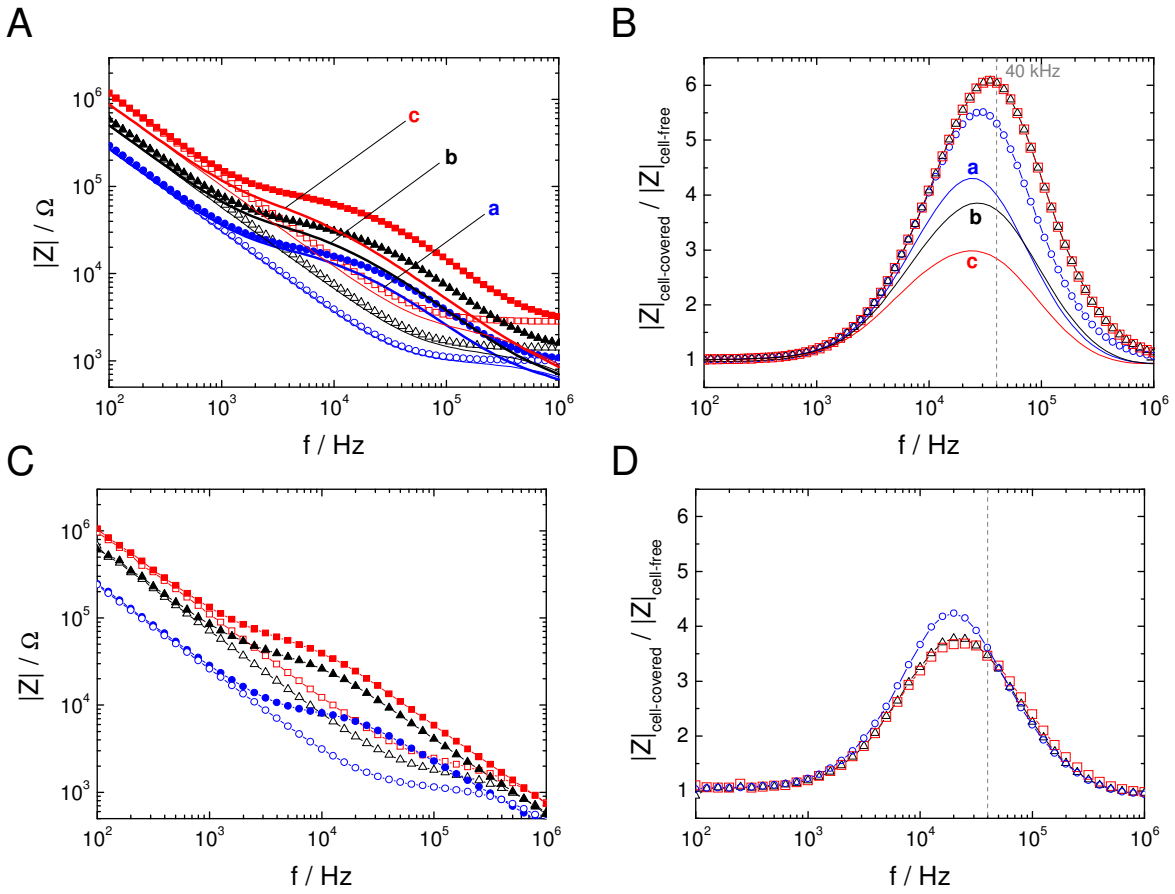

Fig. 5.87: Comparison of simulated (**A**, **B**) and experimental (**C**, **D**) spectra for microelectrodes and *8W1E* electrodes. **A:** Simulated impedance spectra of cell-free (open symbols) and cell-covered (filled symbols) circular electrodes with different surface areas corresponding to either *8W1E* electrodes or microelectrodes: ○, ●: 5×10^{-4} cm^2 (*8W1E*); △, ▲: 2.5×10^{-4} cm^2 (microelectrode); □, ■: 1.25×10^{-4} cm^2 (two microelectrodes in series). Parameters for the cell layer were: α = 5 $\Omega^{1/2} \cdot$ cm; R_b = 5 $\Omega \cdot$ cm^2; C_m = 2 µF/cm^2; n_{CPE}: 0.95; A_{CPE}: 1.5×10^{-5} Fs^{n-1}cm^{-2}. Spectra for cell-free and cell-covered electrodes presented by solid lines consider parasitic impedance contributions: curve a, ▬: *8W1E*; curve b, ▬: microelectrode; curve c, ▬: two microelectrodes in series. **B:** Normalized impedance ($|Z|_{cell\text{-}covered}$ / $|Z|_{cell\text{-}free}$) for spectra in A (See code in A). **C:** Experimental impedance spectra shown in Fig. 5.54, Fig. 5.55. ○, ●: *8W1E*; △, ▲ : One half-circle shaped microelectrode measured individually against the large counter electrode; □, ■: microelectrodes in series. **D:** Normalized impedance ($|Z|_{cell\text{-}covered}$ / $|Z|_{cell\text{-}free}$) for spectra in C (See code in C).

One microelectrode measured individually in combination with the significantly larger counter electrode (▲, △) revealed higher absolute impedance magnitudes compared to the *8W1E* electrode (Fig. 5.87 C). The normalized impedance for the microelectrode measured against the counter electrode (△) is lower compared to the *8W1E* electrode (○) (Fig. 5.87 D), although an increase of sensitivity was expected due to its obviously smaller surface area (Fig. 5.87 B). Also the shift of the normalized impedance to higher frequencies is less pronounced than in simulated spectra for these electrodes (Fig. 5.87 D, B).
The impedance spectrum further changes when the counter electrode becomes also small. Then, the impedance contribution of the second electrode can not be ignored anymore. When two small microelectrodes of the same size are electrically combined in series (Fig. 5.85 C), both electrodes equally contribute to the total impedance in an additive way following Kirchoff's law (Fig. 5.88).

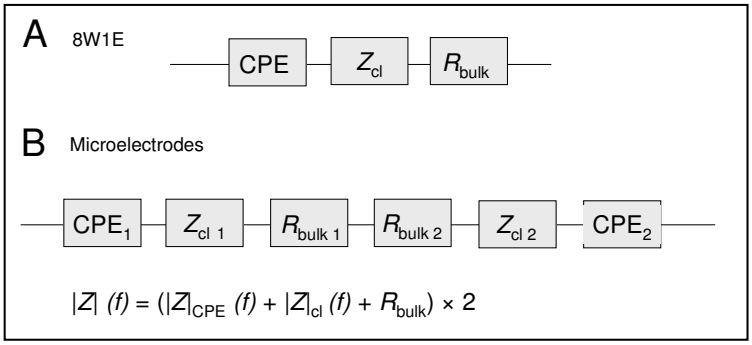

Fig. 5.88: Equivalent circuits for **A:** *8W1E* and **B:** Microelectrodes combined in series. Subscripts (1, 2) indicate the contributions from either half-circle shaped electrode.

As a result, the total impedance of the system is shifted to higher impedances (□, ■) (Fig. 5.87 A, C). The normalized impedance is similar for the microelectrodes in series (□) and a microelectrode in combination with the large counter electrode (△) (Fig. 5.87 B, C). In the experimental system the normalized impedance for microelectrodes in series (□) was smaller compared to the *8W1E* electrode (○) (Fig. 5.55 B; Fig. 5.87 C).
Simulations considering parasitic impedance contributions (cp. chapter 3.1.4, Fig. 3.8) revealed that the impedance of the cell-covered electrodes is significantly shifted towards lower frequencies in the high frequency regime of the spectrum (Fig. 5.87 A). The influence of parasitic impedances increases when the electrode size decreases (Fig. 5.87 A, curves a, b) and is moreover enhanced when two small electrodes are measured in series (Fig. 5.87 A, curve c). These parasitic impedance elements considerably affect the peak of the normalized impedance, which mirrors the sensitivity of a system. The maximum of the normalized impedance of a *8W1E* electrode simulated with and without a parasitic impedance, for example, is significantly reduced when parasitic impedances contribute (Fig. 5.87 B, curves a – c). The parasitic impedance moreover leads to a shift of the normalized impedance spectrum to lower frequencies, which was also observed for experimental data (Fig. 5.87 D).
Cho and Thieleke (2010) studied the influence of parasitic impedances when decreasing the electrode size. A maximum of normalized impedance, meaning a maximum sensitivity was

found for an electrode radius of 200 µm. An electrode radius above 630 µm and below 90 µm resulted in a reduced normalized impedance. Also Rahman et al. (2007) investigated the effect of electrode geometry on bio-impedance measurements and found that below 50 – 100 µm in electrode diameter non-uniform current distribution effects occur.

In conclusion, parasitic impedance contributions are probably responsible for the reduced maxima of the normalized impedance in the experimental system. For *8W1E* electrodes (○) as well as one of the two microelectrodes (△) measured individually against the large counter electrode theoretical predictions including parasitic impedances correlate well with data of the experimental systems. The normalized impedance of two microelectrodes in series including parasitic impedances is predicted to be smaller than experimentally observed (Fig. 5.87 B, ▬ Fig. 5.87 D, □). This shift might be explained by a size difference between the two half electrodes.

The use of both microelectrodes in series allows reduction of the sample volume in electroporation experiments with costly probes (Fig. 5.53). The small size of both electrodes and their close spatial arrangement on the array substrate are the decisive properties. It was the aim to create a measuring chamber that allows a stable measurement in a volume below 50 µl over a period of at least 2 days. A silicon ring with an inner diameter of 4 mm was placed around the electrodes without influencing the measurement (Fig. 5.56). Although chambers with an even smaller diameter of 3 mm can also be used, the risk of electrode inactivation by the silicone grease and of problems with air bubbles captured above the cell layer increases with decreasing chamber diameter. With a chamber height of ~ 3 – 4 mm the sample volume is limited to 37 – 50 µl. In order to evaluate the lowest possible sample volume that guarantees stable cell layer impedance over several hours, the fluid volume was distinctly reduced down to 10 µl (Fig. 5.57). In such small volumes even slight fluid evaporation can easily lead to considerable changes in ionic strength and osmolality of the solution, which can severely affect cell layer homeostasis (Heo et al., 2007; Bertier et al., 2008). As demonstrated in Fig. 5.57 the impedance of an NRK cell layer remained stable over ~ 70 h when using a volume of 10 µl, while filling chambers with a volume of 30 µl even allowed to measure the cell layer impedance over ~ 90 h.

Setups for *in situ* electroporation with reduced sample volumes for efficient delivery of valuable molecules into cells have also been developed by other groups (cp. Introduction, chapter 1.2.3.1). The smallest volume reported in literature to be used for *in situ* electroporation of cells grown on an area of 3 mm^2 is 1 µl (Tereul et al., 1999). Olofsson et al. (2005, 2007) used capillaries for storage of the electroporation solution (~ 80 µl) typically ejecting 2 µl of the solution during an experiment (Fig. 1.4 H). In that setup the number of cells subjected to electroporation is determined by the capillary wall thickness of 400 µm or 2600 µm, creating a ring pattern in the cell layer. The electroporation setup used by deVyst et al. (2007) consists of two parallel wire electrodes that hold a volume of 10 µl above the cell layer for loading of an area of ~ 2 mm^2. Raptis and Firth (2008) cultured cells on a conductive ITO substrate and used a conical counter electrode which is lowered to the cell surface from the top, holding a volume of 30 µl by surface tension. The electrode can be slided over the cell layer grown on a substrate with an area size of 32 × 10 mm. Other *in situ* electroporation

setups using a coplanar arrangement of substrate integrated electrodes typically require sample volumes of 50 – 300 µl (Lin et al., 2003; Olbrich et al., 2008; Jain and Muthusjawa, 2007; Vassanelli et al., 2008). However, in all cases the analysis of cells loaded with membrane impermeable probes by electroporation was performed by biochemical and microscopical means, instead of using electrical measurements.

In Situ Electroporation of Cells Grown on Microelectrodes

When using microelectrodes for electroporation two important phenomena have to be considered. (i) The voltage applied for electroporation drops equally across both electrodes as long they are of the same size; not only across one single working electrode as is the case when using *8W1E* electrodes. Because the two cell layers on the microelectrodes share the applied voltage, it can be expected that the pulse amplitude required for efficient membrane permeabilization might be twice as high as needed for electroporation on *8W1E* electrodes. (ii) The microelectrodes are smaller in size. This theoretically results in an increased fractional voltage drop across the cell layer due to an increased normalized impedance at 40 kHz. This means that smaller voltages are required to perform electroporation with microelectrodes compared to an *8W1E* electrode. As discussed above the maximum of the normalized impedance is however decreased instead of increased for microelectrodes.
Thus, the expected voltage needed for efficient electroporation of cells grown on microelectrodes might be almost twice as high as required for electroporation on *8W1E* electrodes.

Optimal combinations of pulse amplitude and duration were established for NRK, HEK-293, Hep G2 and CHO cells by dye loading studies as well as impedance measurements before and after electroporation. Because the spectra of the normalized impedance of *8W1E* and microelectrodes in series show the same frequency dependence (Fig. 5.55; Fig. 5.87 D), the electroporation frequency was kept constant at 40 kHz.
Indeed, the optimal electroporation of these cell lines required enhanced pulse amplitudes compared to optimal *8W1E* electroporation conditions for most cell types (Tab. 5.7). The optimal pulse amplitude increased by 1 V for NRK and Hep G2 cells from 4 V on *8W1E* to 5 V on microelectrodes. For HEK-293 cells the amplitude optimum even rose from 4 V to 7 V. Only for CHO cells the electroporation conditions remained the same for both electrode types (3 V and 500 ms).

Tab. 5.7: Electroporation conditions for different cell types using *8W1E* electrodes or microelectrodes.

Cell Type	**Electrode Type**	
	8W1E	Microelectrodes
NRK	4 V, 200 ms	5 V, 200 ms
HEK-293	4 V, 200 ms	7 V, 200 ms
Hep G2	4 V, 200 ms	5 V, 200 ms
CHO	3 V, 500 ms	3 V, 500 ms

Because the voltages required for efficient electroporation of cells on microelectrodes were lower than expected for most cell types, the fractional voltage drop across the cell layers during electroporation with a pulse at 40 kHz was analyzed in more detail. The fractional voltage drop F across a cell layer can be calculated in a first approximation from the relative impedance magnitudes of a cell-free and a cell-covered cell layer at the electroporation frequency.

$$F = 1 - (|Z|_{\text{cell-free}} / |Z|_{\text{cell-covered}}) \times 100\ [\%].$$

In Tab. 5.8 F-values calculated from experimental data are compared to theoretical values obtained by model simulations using cell type specific model parameters α, R_b and C_m that were provided in Tab. 5.1.

Tab. 5.8: Comparison of the expected fractional voltage drop across cell-covered electrodes after electroporation for *8W1E* and microelectrodes calculated from the impedance magnitudes |*Z*| at 40 kHz for experimental ($n \geq 5$) and theoretical data (based on average α, R_b and C_m values cp. Tab. 5.1) of cell-free and cell-covered electrodes (n.d.: not determined). The calculation for microelectrodes provides values for the total fractional voltage drop across the cells grown on both microelectrodes.

Cell Type	**Electrode Type**	**$\|Z\|_{40\ kHz}$ [kΩ]**		**fractional voltage drop across the cell layer [%]**	
		theoretical	experimental	theoretical	experimental
cell-free	*8W1E*	1.45	1	–	–
	microelectrodes	4.99	4	–	–
NRK	*8W1E*	7.06	4.7	79	79
	microelectrodes	27.68	13.5	82	70
HEK-293	*8W1E*	5.46	3.3	73	70
	microelectrodes	20.99	12.2	76	67
Hep G2	*8W1E*	4.5	3.5	68	71
	microelectrodes	17.02	11.0	71	63
CHO	*8W1E*	4.73	3.2	69	69
	microelectrodes	17.97	10.5	72	62
NIH-3T3	*8W1E*	4.30	4.0	66	75
	microelectrodes	16.14	n.d.	69	n.d.

As discussed above, the theoretical fractional voltage drop across the cell layer is increased for the microelectrodes compared to *8W1E* electrodes. Experimental data however revealed, that the fractional voltage drop across the cell layer is lower than the theory predicts. This means that 3.16 V (79 %) of an electroporation pulse of 4 V will drop across an NRK cell layer grown on *8W1E* electrodes for example. Only 2.8 V (70 %), however, would drop across NRK cells grown on microelectrodes, instead of 3.28 V as theoretically predicted. This voltage drops, however, across both cell layers on the two half electrodes, instead of only one electrode, as it is the case for *8W1E* electrodes. When a pulse of 5 V is chosen instead, the voltage drop across the NRK cells grown on microelectrodes is 3.5 V, which explains the slightly higher voltages required for electroporation using microelectrodes.
For the different cell types under study the experimental values for the fractional voltage drop are quite similar ranging between 62 and 70 % for microelectrodes and between 69 % and 79 % for *8W1E* electrodes. However, the voltage required for efficient electroporation of

CHO cells grown on microelectrodes was not enhanced compared to electroporation of cells grown on *8W1E* electrodes, although the fractional voltage drop across an CHO cell layer is quite low (62 %). In contrast, the voltage drop across an HEK-293 cell layer grown on microelectrodes is 67 %, which is only slightly different from the voltage drop across HEK-293 cells on *8W1E* electrodes. Nevertheless, the voltage required for successful electroporation on microelectrodes (7 V) is considerably higher than used for electroporation on *8W1E* electrodes (4 V).
As already mentioned above the voltage dividing effect due to the voltage drop across both microelectrodes in series has to be considered. When an electroporation pulse at 40 kHz with an amplitude of 4 V is for example applied to HEK-293 cells the calculation predicts a voltage drop of 2.76 V across the cell layer grown on microelectrodes compared to 2.80 V across the cell layer grown on *8W1E* electrodes. The voltage drops across a single cell layer (height ~ 20 µm) in the case of *8W1E* electrodes, but across two cell layers in case of microelectrodes. This results in field strengths of ~ 1.4 kV/cm across cells grown on *8W1E* and ~ 0.7 kV/cm across cells on microelectrodes. Application of a 7 V amplitude pulse in contrast results in a field strength of ~ 1.2 kV/cm across a HEK-293 cell layer grown on microelectrodes, which is similar to the field strength obtained for HEK-293 cells grown on an *8W1E* electrode using a 4 V pulse. But also for the other cell lines the field strength across the cell layer is reduced by a factor two, due to the fact that two small electrodes are arranged in series. However, other cells do not require as high voltages for electroporation when grown on microelecrodes. Finally, the cell type specific differences between the optimal electroporation voltages required for efficient loading with FITC-dextran using microelectrodes can not be fully explained.

For most cell types impedance measurements after electroporation showed the same cell type specific impedance responses as measured for cells grown on *8W1E* electrodes (Fig. 5.66). Only one exception was observed. While on *8W1E* electrodes HEK-293 cells responded to an electoporation pulse with an initial impedance increase, impedance measurements with microelectrodes revealed an impedance drop as a response to electroporation. For most cell types a similar dependence of cell layer recovery kinetics on pulse amplitude and duration was observed as previously discussed for cells on *8W1E* electrodes, showing increased post-pulse recovery times for increasing pulse amplitudes and durations.
Whereas the location of the stained cells was restricted to the active electrode surface areas for NRK, and CHO, the electroporation of HEK-293 cells in presence of 250 kDa FITC-dextran resulted in loading of cells beyond the active electrode area. The area of cell permeabilization for dye uptake beyond the electrode border increased with increasing pulse amplitude and duration (Fig. 5.60). Also for Hep G2 cells dye loading of cells within the insulating gap between the electrodes could be observed at high pulse amplitudes of 7 V (Fig. 5.62). A similar observation was reported by the group of L. Raptis, who developed a coplanar *in situ* electroporation setup to study gap junctional communication (Anagnostopoulou et al., 2007). The aim was to create clearly defined areas of dye loaded cells by restricting areas of cell permeabilization by means of electrode geometry. They

designed a coplanar electrode setup with an electrode distance of a few millimeter. When loading A549 cells with Lucifer Yellow they observed, that also cells beyond the electrode borders were loaded with the fluorescent dye. Fractions of the electric field striking the cell surface in this region presumably led to this effect. Because loading of cells beyond the border was not desired, they introduced a barrier for current flow close to the cell surface, limiting cell permeabilization to the cells residing on the active electrode surface area. In the work presented here, electroporation beyond the electrode border does not limit the applicability of the microelectrodes for electroporation experiments.

5.4.3.2 Electroporation-Mediated Delivery of Bioactive Proteins - Impedimetric Detection of the Cell Response

Direct delivery of bioactive proteins into the cytoplasm is one of the most direct methods of manipulating cell function. Protein transfection sometimes is even the only way to alter protein content when transfection strategies with nucleic acids fail. Electroporation of proteins into the cytoplasm of cells has been used to study signal transduction cascades by introducing signal molecules and enzymes (Decrock et al., 2009; Carney and Morgan, 1999). Instead of analyzing the effect of the introduced protein by biochemical means ECIS based *in situ* electroporation allows to measure cell morphology responses electrically. The miniaturized ECIS microelectrode setup was used to measure the impact of cytochrome c, RNase A and DNase I on the target cells. The reasoning for electroporation of cells in presence of cytochrome c has already been discussed above. Moreover, RNase A and DNase I, enzymes that induce cuts in either RNA or DNA strands, were loaded into NRK cells by *in situ* electroporation. The results of these electroporation experiments can be summarized as follows and are discussed below:

- ***The use of the miniaturized electrode layout for electroporation-assisted loading of NRK cells with cytochrome c and subsequent impedance monitoring showed the same characteristic post-pulse impedance drop and retardation of impedance recovery as was measured by using 8W1E electrodes.***
- ***Electroporation of NRK cells in presence of RNAse A or DNase I led to a retarded cell layer impedance recovery in a concentration dependent manner, unless the enzymes were inactivated by heat prior to electroporation.***

Cytochrome c

The experiments using the miniaturized electrode layout instead of conventional *8W1E* electrodes for electroporation of NRK cells in presence of cytochrome c and subsequent impedance monitoring, demonstrate that microelectrodes provide a similar sensitivity as conventional *8W1E* electrodes. Thus the miniaturized electrode layout is well-suited for combined *in situ* electroporation and impedance monitoring.

RNase A

RNases cleave cellular mRNA and tRNA molecules which are essential molecular species in protein synthesis. Actually, microinjection of RNase A to xenopus oocytes was shown to abolish protein synthesis at concentrations of only 0.03 nM (Saxena et al., 1991). Inhibition of protein synthesis is a typical intracellular stress signal that might induce apoptosis by yet unknown pathways (Trisciuoglio et al., 2008). RNase A led to a concentration dependent impedance drop within the first 30 min after electroporation and a subsequent retardation of cell layer recovery by at least 4 h when concentrations of 0.25 or 0.5 mg/ml were used (Fig. 5.69 A). This response of the cell layer was abolished (Fig. 5.69 B) when enzymatic activity of RNase was eliminated by heat treatment (Fujita and Noda, 1984; Zale and Klibanov, 1986). Since the profile of the impedance response after electroporation with active RNase is similar to those observed for cytochrome c and azide (Fig. 5.82), measurements indicate that cell death is induced in RNase loaded cells on the electrode. The impedance increase back to pre-pulse values can be ascribed to migration of vital cells from the periphery to the center of the electrode (Fig. 5.69 A). This indicates that extracellular RNase has no effect on the cell layer. Actually, extracellular application of RNase A was found to be non toxic to K-562 cells within a 44 h incubation in concentrations up to 100 µM (Leland et al., 1998), which is ~ 3 times higher than the concentration used in this work (0.5 mg/ml: ~ 36 µM). Whereas bovine pancreatic RNase A itself was not found to be cytotoxic when extracellularly applied, an homologous variant, the enzyme ranpirnase (onconase) from *Rana pipiens*, was shown to efficiently induce cell death by apoptosis (Iordanov et al., 2000; Grabarek et al., 2002) or autophagy (Michaelis et al., 2007). Due to their cytotoxic potential ribonucleases are proposed as new candidates in chemotherapy (Lee and Raines, 2008). The RNase A homologue ranpirnase, for example, has already been used in clinical trials on chemotherapy (Pavlakis and Vogelzang, 2006).

However, in most studies presented to date RNases have exclusively been administered extracellularly and, thus, their intracellular activity was dependent on cellular uptake mechanisms like endocytosis (Haigis and Raines, 2003; Rodriguez et al., 2007). The low cytotoxicity of normal RNase A is ascribed to its intracellular inhibition by a natural RNase inhibitor that is ubiquitous in the cytoplasm. Well-regulated specific types of RNase, help to keep intracellular RNA concentrations in balance (Cheng and Deutscher, 2005) or participate in host immune defence (Nadal et al., 2002; Rosenberg, 2008). Certain members of the RNase A family are bound and inactivated with femtomolar affinity (Johnson et al., 2007). The natural intracellular concentration of RNase inhibitor (RI) was estimated to be in the range of 1 – 4 µM which is sufficient to efficiently block RNases introduced in this concentration range. In the lowest RNase concentration applied in this work (0.1 mg/ml = ~ 7.2 µM) intracellular RI in a concentration of 4 µM could potentially block about 50 % of the RNase. Since typically no concentration equilibrium between extracellular and intracellular molecules is achieved during electroporation (Zaharoff et al., 2008; Prausnitz et al., 1994), the intracellular concentration may even be considerably lower than 7.2 µM. Then, no residual intracellular activity of RNase may be expected, which could actually be confirmed by impedance measurements after *in situ* electroporation of NRK cells in presence

of 0.1 mg/ml RNase, showing no retardation of impedance recovery compared to the control (Fig., 5.69 A). In contrast, 0.25 mg/ml and 0.5 mg/ml RNase A resulted in an impedance decrease and retardation of cell layer recovery after electroporation. These higher concentrations may therefore be high enough to exceed intracellular RNase inhibitor concentration and cause severe damage on intracellular RNAs.

To date, applications of RNases as potential anticancer drugs are focussed on extracellular administration. Improved delivery by electroporation has yet not been described. In total, experiments performing electroporation of cells with ribonucleases are not frequently reported in the literature. Glogauer and McCulloch electroporated fibroblasts and loaded them in presence of bovine pancreatic RNase A. They detected a reduction of cytoplasmatic RNA by Pyronin Y staining of RNA and subsequent flow cytometry analysis but they did not report on any cytotoxic effect (Glogauer and McCulloch, 1992). Electroporation of RNase A may however provide an interesting novel option for use in electrochemotherapy.

DNase I

When DNase I was electroporated into NRK cells a significatnt inhibition of cell layer recovery was detected for a concentration of 1 U/ml and above. After the initial post-pulse impedance drop, a further slight impedance decrease was measured taking 10 – 15 min (Fig. 5.70). The cell layer impedance was not fully re-established within the following 4 h of observation. A cytotoxic activity of DNase I can be ascribed to the catalytic and binding properties of the enzyme. DNase I binds to the minor groove of DNA and leads to double strand breaks with different base overhangs (Obe and Johannes, 1993). Although this primary target molecule is located in the nucleus, the small DNase I molecule (~ 39 kDa) with a hydrodynamic radius of 2.64 nm (Kunitz, 1950) can easily pass the nuclear envelope (Rogagoku et al., 2000). Another cytotoxic effect might be ascribed to its action on the cytoskeleton. DNase I binds to globular actin monomers and depolymerises F-actin (Hitchcock, 1980; Nehmhauser and Goldberg, 1985). Actin is regarded as a natural inhibitor of DNase, although its role in the organism is not fully elucidated yet (Kayalar et al., 1996; Rao et al., 1999). Alterations in the dynamic equilibrium of actin polymerization and depolymerisation are capable of activating apoptosis as became evident from the action of various actin modulating drugs (Gourlay et al., 2005; Odaka et al., 2002; Kruidering et al., 1998). The action of DNase I on the actin cytoskeleton may explain the fast apoptosis response of NRK cells after electroporation (Fig. 5.70). As shown by the bleomycin experiments and the literature discussed in this context (5.4.2.2), DNA damages normally cause time consuming regulation mechanisms before apoptosis is induced.

As described in the literature an introduction of DNA cleaving enzymes can be performed by different methods using osmolytic shock, inactivated viruses, liposomes, glycerol, sorbitol or streptolysin or microinjection (Obe and Johannes, 1993; Nakagawa et al., 1999). Due to its high efficiency electroporation became the method of choice to introduce several different restrictionendonucleases into mammalian cells (Winegar et al., 1989; Yorifuji and Mikawa et al., 1990; Rogaku et al., 2000). Electroporation of cells in presence of nucleases has been used to study homologous recombination (Brenneman et al., 1996), the role of double strand breaks

in apoptosis (Rokagou et al., 2000; Lips and Kaina, 2001) as well as to elucidate DNA repair mechanisms (Bryant and Johnston, 1993; Chang et al., 1993, Philips and Morgan, 1994).
Lips and Kaina (2001), for example, electroporated BK4 mouse cells in presence of the restriction endonuclease *Pvu*II (500 U/ml) in order to clarify if double strand breaks can act as a primary trigger for apoptosis. They found that enzymatically induced double strand breaks induced apoptosis, whereas ionizing radiation which also leads to DNA base modifications and other side effects provokes apoptosis as well as necrosis (Lips and Kaina, 2001). No double strand breaks were observed and no apoptosis was induced when the enzyme was inactivated by heat. Also in experiments presented here, DNase activity could be abolished by heat denaturation (Fig. 5.70 B). For active *Pvu*II Lips and Kaina (2001) measured a maximum of double strand breaks about 6 h after electroporation. In contrast, Ager et al. (1991) electroporated CHO cells in presence of the restriction endonucleases *Pvu*II or *Pst*I and found that these enzymes induced excessive DNA cleavage within 20 min, which corresponds more to the time frame observed in experiments presented here. Due to their exclusively hydrolytic action the introduction of restriction enzymes into the cytoplasm of mammalian cells has been proven to be a valuable tool to investigate the biological consequences of double strand breaks in the genome (Carney and Morgan, 1999). Yet, only cells in suspension have been loaded with endonucleases. However, *in situ* electroporation of cells on ECIS electrodes with specific restriction endonucleases might be interesting to study the effect of double strand breaks on apoptosis. Since also other groups used *in situ* electroporation for loading of cells with different bioactive proteins and peptides (Boccaccio et al., 1998; Raptis et al., 2003; Nakashima et al., 1999) ECIS based *in situ* electroporation may also find interesting applications using a variety of other enzymes, peptides and therapeutic ptoteins.

5.4.3.3 *In Situ* Electroporation of Cells with Antibodies, DNA and Nanoparticles - Detection of Uptake by Fluorescence Microscopy

Antibodies and nucleic acids are two of the most interesting bio-macromolecules which allow versatile manipulation and analysis of biological processes. The exchange of a few amino acids in the antigen binding region of an antibody considerably determines its potential function in the cell, though its gross structural properties are highly conserved. In analogy, most typical DNA vectors have a similar basal structure, only varying in size and base sequence. Especially, strategies to transport DNA across the cell membrane with the aim of transfection have been a central issue since decades.
Nanoparticles made of organic or inorganic material are normally biologically inactive itself. But by linking specific biological functions to the particle scaffold they can be used as carriers for a wide variety of cargo molecules. Since nanoparticles are proposed to serve as carrier structures in diverse biomedical and biotechnological applications, the biological transfer into mammalian cells is a crucial aspect.
The efficiency of electroporation-based delivery of these three types of macromolecular probes into anchorage-dependent cells grown on ECIS electrodes has been evaluated using

fluorescence microscopy. The results are listed below and are discussed individually in the following sections.

- ***Using the miniaturized electrode layout NRK and Hep G2 cells were efficiently loaded with a dye labelled unspecific secondary antibody as well as different target specific primary antibodies.***
- ***Electrotransfection of HEK-293 and NRK cells using plasmid and linear DNA encoding fluorescent GFP variants resulted in cell type specific transfection efficiencies of 10 – 70 %.***
- ***NRK cells were efficiently loaded with PEG-coated quantum dot nanoparticles.***

(i) Antibodies

The transfer of antibodies into the cytoplasm of living cells allows to perform functional studies by the specific binding of target protein structures and blocking their function in the cell (Morgan and Roth, 1988; Perez-Martinez et al., 2010). Like other proteins antibodies can be brought across the plasma membrane by methods like osmotic lysis of pinocytotic vesicles or membrane fusion with antibody loaded vesicles (Charakabarti et al., 1989). Also chemichal transfection reagents based on cationic or amphiphatic liposome formulations, polymers or peptides are available for protein transfection (Plank et al., 1998; Zelphati et al., 2001; Weill et al., 2008). In the scope of this work antibodies were brought into cells by *in situ* electroporation using ECIS electrodes.

One of the first authors who described the electroporation of mammalian cells in presence of antibodies were Chakarabarti et al. (1989), loading HeLa cells in suspension with a monoclonal antibody against asparagine synthase. Actually, after electroporation with the antibody cells showed an increased dependence on an exogenous source of asparagine in the culture medium (Chakarabarti et al., 1989). Many electroporations for loading with antibodies have been performed using suspended cells (Berglund and Starkey, 1989; Gloghauer and McCulloch, 1992; Boitano et al., 1998; Baron et al., 2000). *In situ* electroporation of cells in presence of antibodies was often carried out using selfmade electroporation chambers with coverglass inserts (Bright et al., 1996) or the commercial BTX pulser system for electroporation of cells grown on petri dishes (Marrero et al., 1995; Schieffer et al., 1996; Ushio-Fukai et al., 1998).

The basic applicability of *in situ* electroporation of cells grown on ECIS electrodes was demonstrated by loading a dye labeled antibody into the cytoplasm of NRK and Hep G2 cells with an efficiency of almost 100 % (Fig. 5.71). Since an antibody of the IgG type is too large to pass the nuclear pore complex, the nucleus remains dark (Raptis and Firth, 1990). NRK cells have moreover been loaded with different target specific antibodies recognizing intracellular epitopes of the proteins ß-catenin (Pokutta and Weis, 2007), occludin (Feldman et al., 2005) and ZO-1 (Van Itallie et al., 2010) (Fig. 5.73). These proteins are components of the adherens junctions or tight junctions and are therefore associated to the cell borders (Niessen, 2007; Hartsock and Nelson, 2008). Due to the distinct localization of these target

proteins the specifitiy of the intracellular recognition by the respective antibodies was detected by immunofluorescence techniques (Fig. 5.72).

After electroporation of target specific antibodies into NRK cells the antibodies were not exclusively found at the cell borders but were also detected in the entire cytoplasm (Fig. 5.73). This does not necessarily indicate a reduced specifity of the antibody. Inactivation of the antibodies due to the electroporation process is unlikely, since most studies reported in the literature could not reveal adverse effects of the electroporation pulse on antibody function (Charakabarti et al., 1989; Rui et al., 2001). The high background fluorescence presumably has rather mechanistic reasons. During electroporation the antibodies can enter the cell, but after membrane resealing they remain entrapped in the cytoplasm where they can bind their specific target protein. However, the antibodies were administered to the extracellular fluid in rather high concentrations, leading to an excess of antibody compared to the amount of available epitopes in a cell. By subsequent secondary antibody staining all intracellular antibodies – bound to their antigen or not – are labeled fluorescently. This is in contrast to a conventional immunostaining protocol, where unbound primary antibodies are removed from the permeabilized cells by washing cycles. Since especially the ß-catenin antibody was used in a high concentration of 2.8 mg/ml, background fluorescence of unbound antibodies masks the actual structures of interest (Fig. 5.73 A). However, a reduction of the ß-catenin antibody concentration did not result in a more distinct staining pattern (data not shown). As mirrored by the immunofluorescence image, the ß-catenin structures in NRK cells are rather weak and diffuse (Fig. 5.72 A). The ß-catenin protein is not exclusively bound to the adherens junctions, since due to its role in signal transduction it can also be found in the cytoplasm and nucleus (Moon et al., 2004). Therefore, a distinct staining of the cell borders will be difficult to achieve for this target protein. In contrast, immunostainings of occludin and ZO-1 showed very sharp labeling (Fig. 5.72 B, C). The electroporation-mediated delivery of these antibodies provided a predominant localization of the antibody at the cell borders. However, also for these antibodies used in a concentration of 125 µg/ml unspecific staining of the cytoplasm was found (Fig. 5.73 E, F). As described in the literature, for *in situ* electroporations antibodies were typically applied in concentrations between 5 µg/ml and 3 mg/ml (Schieffer et al., 1996; Ushio-Fukai et al., 1998; Rui et al., 2002, Lan et al., 2003; Bright et al., 1996; Raptis and Firth, 1990).

In situ electroporation approaches for loading cells with antibodies that have been described in the literature require sample volumes between 0.5 and 3 ml and typically load large numbers of cells with the antibody (Marrero et al. 1995; Schieffer et al., 1996; Ushio-Fukai et al., 1998; Rui et al., 2002, Lan et al., 2003). Rather large amounts of loaded cells are typically required for detection of the incorporated antibody and analysis of its intracellular function by flow cytometry or biochemical methods (Western Blot, immunopreciptation, ELISA) (Raptis et al., 2003). Loading of adherent cells grown on gold-film electrodes with antibodies by *in situ* electroporation, in contrast, offers a new versatile method of analyzing protein function. Detecting changes in cell morphology by impedance measurements instead of immunochemical methods and light microscopy enables to analyze functional information, instead of the bare localization within a cell.

Outlook: *In Situ* Electroporation of Antibodies

Intracellular delivery of antibodies into cells can be used to specifically manipulate certain cellular functions. The cytoplasmic delivery of certain antibodies by chemical methods or microinjection into mammalian cells was reported to induce changes in cell morphology, which were detected microscopically (Leli et al., 1992; Didenko et al., 2005; Courtête et al., 2007). Since ECIS is extremely sensitive to changes in cell morphology with a resolution much below that of optical microscopes, *in situ* electroporation using ECIS gold-film electrodes provides a promising new tool in cell biology. Although morphological changes occur as a response to many cellular stimuli, certain types of intracellular manipulations by blocking antibodies may be of special interest. The intracellular concentration of an antibody which is required to provoke considerable cellular effects, will depend on the amount of target protein in the cell. Therefore, specific blockage of regulatory rather than structural proteins might be most promising. The efficiency of using antibodies to block regulatory proteins like transcription factors and apoptosis factors has already been reported in the literature (Lan et al., 2003; Rui et al., 2002; cp. chapter 1.2.3.2). Moreover, proteins that are associated with the function and regulation of the cytoskeleton and the formation of cell-cell or cell-substrate contacts provide interesting targets. Proteins with central roles in cell metabolism that are linked to cell motility or even apoptosis may be addressed as well. In conclusion, loading of cells with antibodies by *in situ* electroporation in combination with impedimetric detection of changes in cell morphology may provide versatile applications.

(ii) DNA

Electroporation has proven to be a versatile and efficient method for gene transfer (Neumann et al., 1982). To date, electroporation is the simplest and most efficient physical transfection method that can be performed without exposing the cells to chemical substances that affect cell viability. The low survival rate of cells after electroporation in suspension has led to the development of several *in situ* electroporation strategies that allow for gentle and efficient gene transfer into anchorage-dependent cells. The applicability of *in situ* electroporation using ECIS gold-film microelectrodes for gene transfer was evaluated in this work.

Transfection Efficiency

In situ electroporation of HEK-293 and Hep G2 cells grown on microelectrodes with the pCH1 plasmid carrying the EGFP gene yielded a transfection efficiency of ~ 60 – 70 %, while the transfection efficiency for NRK cells (~ 10 %) was rather low (Fig. 5.74). Also for other *in situ* electroporation systems using a coplanar arrangement of substrate integrated electrodes low transfection efficiencies have been reported (Jen et al., 2004; Ishibashi et al., 2007; Jain and Muthuswami, 2007). To date, *in situ* electroporation setups that pre-adsorb nucleic acids to the substrate electrode mediated by cationic polymers seem to be the most efficient systems (Yamauchi et al., 2004; Fujimoto et al., 2008; Koda et al., 2008). For HEK-293 cells transfection efficiencies of 30 % – 90 % were obtained using EGFP encoding plasmid DNA (Koda et al., 2008; Yamauchi et al., 2004).

Here, the transfection efficiency, the ratio of GFP transfected cells compared to the total cell number on both microelectrodes, could only be determined in a semi-quantitative way due to the error-prone determination of exact cell numbers. The limited transparency of the gold electrodes and the high cell density as well as the disordered growth of HEK-293 cells hampered identification of cell borders and thus the determination of the total cell number on the microelectrodes. Counting the exact number of GFP positive cells was complicated by the low fluorescence intensity of many transfected cells coexisting on the electrode with some highly fluorescent cells. The weak fluorescence of transfected cells might be due to a lowered transcriptional and translational activity in confluent cell layers as they are out of their exponential growth phase. The strong fluorescing cells residing on the electrodes sometimes revealed slightly altered, often rounded cell morphology, which is likely provoked by over-expression of GFP proteins in cytotoxic concentrations (Liu et al., 1999). Highly fluorescent and rounded cells almost detaching from the electrode were especially found within layers of transfected Hep G2 cells (Fig. 5.74 C). Since Hep G2 cells in a confluent layer typically exchange detaching apoptotic cells by cell division causing a constant turnover of cells within the cell layer, the loss of GFP transfected cells from the cell layer is very likely. In order to guarantee, a stable cell layer with a high fraction of transfected cells, the period of time during which cells are allowed to synthesize a gene product is critical. Therefore, especially in experiments using Hep G2 and HEK-293 cells that show a low cell layer stability at 100 % confluency the time frame for gene expression was limited to 24 h.

Cells expressing EGFP were not only restricted to the electrode area, but also cells in the gap between the electrodes were transfected. This can either be explained by the electric field that crosses cells between the electrodes during electroporation, as observed in dye loading studies for HEK-293 and Hep G2 cells (Fig. 5.60; Fig. 5.62), or may be attributed to cell movements and cell divisions occurring within the 24 hours of incubation between electroporation pulse and microscopy (NRK). Migration of transfected cells off the electrode was also found by other groups (Jain and Muthuswamy, 2007; Lin et al., 2004; Vassanelli et al., 2008). Vassanelli et al. (2008), for example, used an *in situ* electroporation setup based on substrate integrated electrodes for single cell electroporation. Transfected CHO cells were found next to the active electrodes 24 h after electroporation in presence of an EGFP or ECFP encoding DNA vector.

Limiting Factors for Transfection of Confluent Cell Layers

In order to guarantee a high percentage of voltage drop across the cell layer, which is required for successful electroporation, confluent cell layers were used for the transfer of DNA into NRK, HEK-293 and Hep G2 cells. By electroporation the genetic material is transferred to the cytosol by a yet not fully elucidated mechanism in which the direct interaction of DNA with the membrane during pulse application plays an important role (Rols et al., 2008; Escoffre et al., 2009) (cp. chapter 3.2.2.4). Although highly efficient delivery of fluorescent dyes was reported for all cell types, transfection efficiencies differed considerably (Fig. 5.74). The electroporation-mediated transfer of nucleic acids may depend on specific properties of the cells important for DNA accumulation and DNA translocation, like the composition of the

cell membrane, mitotic activity of the cells at the time of electrotransfection and the activity of the transcription and translation machinery of the cell.

Moreover, transfection efficiency does not only depend on the number of nucleic acid molecules that are delivered into the cytoplasm of cells. For expression of heterologous genes the foreign DNA has to gain access to the nucleus, where the transcription machinery is located. As elucidated by preceeding dye loading experiments, pulse amplitudes are not high enough to perforate the nuclear envelope (Fig. 5.58; 5.60, 5.62). Actually, subcellular structures can only be electroporated when using pulses of much higher field strength (26 – 150 kV/cm) and short pulse durations (10 – 300 ns) (Schönbach et al., 2001; Beebe et al., 2003). Free diffusion of DNA from the cytosol into the nucleus is restricted by the limitations of the nuclear pore complex, which only allows free diffusion across the nuclear envelope for molecules with a hydrodynamic diameter up to ~ 9 nm (20 – 50 kDa) (Fried and Kutay, 2003; Lechardeur and Lucas, 2006). A DNA molecule of 4 kbp, in contrast, has a diameter of about 90 – 130 nm (Sebestyen et al., 1998). Free diffusion of DNA molecules into the nucleus is reported to be limited to fragments between 200 and 310 bp (Ludke et al., 1999). An active import of Plasmid DNA into the nucleus can nonetheless occur, when special import proteins and mechanisms are present (Miller and Dean, 2008). DNA with a size of 300 – 1500 bp can be transferred by active import mechanisms. Import of DNA molecules into the nucleus is probably dependent on DNA binding proteins that contain a nuclear localization signal (NLS). The folded amino acid sequence of the NLS is recognized by specialized transport-associated proteins of the nuclear pore complex, which enables their energy dependent uptake into the nucleus. Transcription factors which bind to promoter and enhancer sequences are thought to enable nuclear import of expression vectors with many binding sites for proteins with NLS (Dean, 1997). The efficiency of nuclear import is however strongly dependent on the cell cycle (Feldherr and Atkin, 1994) and transcription activity (Dean, 1997) as well as on the size of the DNA molecule (Ludke et al., 1999). Since nuclear import is an energy dependent process, the energy status of the cell can determine the efficiency of DNA transfer into the nucleus.

Only during mitosis the nuclear envelope is decomposed and cytosolic DNA can enter the nucleus. Thus, the transfection efficiency is considerably influenced by the number of dividing cells (Colosimo et al., 2000). In confluent cell layers however, mitosis is often ceased by contact inhibition between neighbouring cells – a mechanism that prevents uncontrolled growth of tissue (Levenberg et al., 1999; Zhang et al., 1999). Contact inhibited cells remain in the G_0/G_1 phase of the cell cycle, which is also characterized by a reduced rate of gene expression. The susceptibility to contact inhibition at confluence of the cell layer and a transition to the G_0/G_1 phase of the cell cycle are dependent on the cell type (Yang et al., 1995). Cell type specific differences in transfection efficiency between NRK, HEK-293 and Hep G2 cells might therefore largely depend on the ability to perform mitosis in an already confluent cell layer. For HEK-293 and Hep G2 cells a considerable transfection was obtained, although cell layers were confluent at the time of electroporation with DNA (Fig. 5.74 B, E, F). HEK-293 cells grow in a rather disordered pattern forming multilayers at confluency, which indicates that contact inhibition is reduced. Proliferation beyond confluency, which is

obviously allowed in HEK-293 cells to a certain extent, can promote gene expression. Within confluent layers of Hep G2 single cells constantly detach from the substrate and leave free spaces for dividing cells, which maintains a high mitotic activity within the cell layer and can explain good transfection yields despite high cell densities. In contrast, NRK cells form cell layers with highly ordered cobbelstone morphology and do not further proliferate when a critical cell density is achieved (Stickel and Wang, 1987). This is the reason why most experimental protocols for transfection of adherent cells use subconfluent cells capable of undergoing mitosis and why transfection of differentiated non-dividing cells like neurons is still challenging. Most authors reporting successful gene transfer by *in situ* electroporation either used subconfluent cell layers (Zheng and Chang, 1991a; Yang et al., 1995) or subcultivation to new substrates after electroporation (Raptis and Firth, 1990).

Another barrier to efficient DNA transfer to the nucleus is its instability in the cytoplasm. Typically exogenous DNA is degraded by cytoplasmic endonucleases (Luo and Saltzman, 2000). Electroporation delivers DNA in its naked, unprotected form into the cell, which makes it highly accessible to nucleases. In contrast coating strategies with PEG or PEG-PLL block copolymers can stabilize DNA from degradation (Lee et al., 1997; Katayose et al., 1997). The structure of the cytoskeleton in a cell can moreover influence the transport of DNA molecules in the cytoplasm (Geiger et al., 2006). In addition, Transfection efficiency depends on the efficiency of the DNA expression system, the strength of promotors and enhancers on the DNA as well as the energetic status of the cell (Luo and Saltzman, 2000: Rolland et al., 1998). Actually, Rols et al. (1998) have discovered, that ATP diffuses out of the cell upon electroporation. Thus, the susceptibility of a cell on the loss of molecules essential for gene expression and intracellular DNA transport like ATP can additionally affect transfection efficiency.

Influence of DNA Size

DNA concentrations used in this work were similar to those reported in literature. Tereul et al. (1999) used 1000 – 2000 µg/ml for transfection of neurons. Müller et al. (2003) only used 10 µg/ml, whereas Golzio et al (2002) applied DNA in a concentration of 60 µg/ml, very similar to amounts chosen here. Other *in situ* electrotransfection setups used slightly lower DNA concentrations in the range of 2,5 – 30 µg/ml (Olofsson et al., 2007; Koda et al., 2008; Deora et al., 2007).

By using a rather small DNA molecule it should be analyzed if using a smaller DNA molecule can support both, the transmembrane transport supported by the electric pulse as well as nuclear transfer (Fig. 5.74 D, E). By restriction nucleases a linear fragment of 2278 bp containing all relevant sequences for efficient transfection was created, which was about 2.7 times smaller than the original plasmid with 6191 bp. Same copy numbers of the two different DNA molecules were used for electroporation experiments, so that an enhanced transfection efficiency due to different numbers of introduced genes should be excluded. Nevertheless, it has to be considered that linear DNA has an enhanced susceptibility to DNase decomposition (Neumann et al., 1982; Xie and Tsong, 1993). Actually, the use of the smaller and linear DNA fragments instead of plasmid DNA did not improve transfection efficiency (Fig. 5.74 A,

B, D, E). With both DNA types a transfection efficiency of ~ 70 % could be achieved for HEK-293 cells (Fig. 5.74 B, E). For NRK cells the transfection efficiency using the small DNA fragment was only slightly enhanced compared to that after transfection with plasmid DNA (Fig. 5.74 A, D). Probably, the size of the linear fragment was still too high to enable more efficient uptake by the nuclear pore complex.

Outlook: *In situ* Electroporation of Nucleic Acids

The expression of foreign genes after transfection into cells provides new cellular properties, which might affect cell morphology. The analysis of genetically induced changes in cell morphology with ECIS provides an interesting tool in the analysis of gene and protein function. In order to obtain meaningful results it is important that a high fraction of the cells on the electrode carries the heterologous gene and efficiently expresses the protein of interest. In principle, the highest fraction of genetically manipulated cells can be achieved using stable cell clones that are obtained by standard transfection and several rounds of selection. However the process of stable clone selection is laborious, cost and time consuming, which is not suited for screening procedures, for example. Therefore, efficient transient transfection is desirable. A direct transfection of cells grown on ECIS electrodes would be the most direct approach. In contrast to biological and chemical transfection methods electroporation does not require further reagents, except the genetic material of interest. As presented in this work as well as for other on-chip electroporation approaches, transfection efficiencies are yet quite low and moreover extremely dependent on the cell type. The highest transfection efficiency was obtained for the rather fibroblastoid cells HEK-293 and Hep G2, which are however critical with respect to their cell layer stability. These cell types might nevertheless be useful in the study of cell-cell or cell-substrate contact proteins, since overexpression of such proteins might lead to an enhanced cell layer stability and transepithelial resistance, which can be detected by ECIS readings.

Low transfection yields were, however, obtained by electroporation of confluent NRK cells. Since nuclear transfer strategies would be associated with complicated molecular modifications of the genetic material (Dean et al., 2005; Lechardeur and Lucas, 2006), these seem not to be very promising for screening approaches. As discussed above, the electroporation of subconfluent cells might enhance uptake of genetic material into the nucleus. As shown by dye loading experiments subconfluent NRK cells can be loaded with extracellular material when using slightly lower pulse amplitudes. The *in situ* electroporation of subconfluent NRK cells on microelectrodes might therefore provide a successful strategy to enhance transfection efficiency. Probably, the application of multiple electroporation steps could further enhance the amount of incorporated DNA molecules. As shown in Fig. 5.89 NRK cells on microelectrodes can be electroporated several times in intervals of 1 – 2 h, without considerably affecting the cell layer impedance.

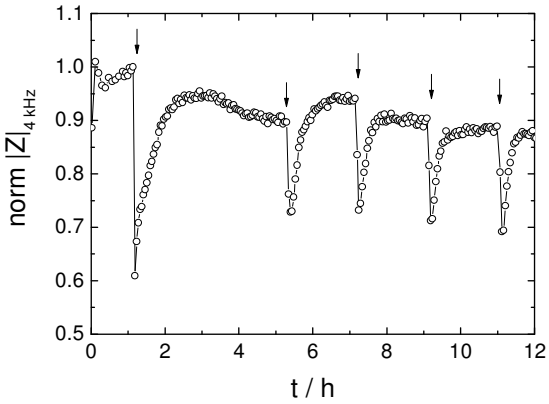

Fig. 5.89: Time course of the normalized impedance magnitude at 4 kHz for NRK cells grown on microelectrodes exposed to repeated electroporation events (arrows, 40 kHz, 4 V, 200 ms).

Alternative strategies for genetic manipulation of confluent cell layers would be based on the use of mRNA (Tereul et al., 1999) or siRNA (Jain and Muthuswami, 2007; Fujimoto et al., 2008) and thereby circumvent the transfer of genetic material to the nucleus as an essential step in transfectction.

(iii) Quantum Dot Nanoparticles

Due to their extraordinary optical properties quantum dots (QDs) have emerged as powerful imaging probes for labelling and tracking of cells as well as imaging of subcellular structures *in vitro* and *in vivo* (Delehanty et al., 2009). Additional promising applications like intracellular sensing (Zhang et al., 2010) and drug delivery (Ho and Leong, 2009; Bagalkot et al., 2007) techniques are projected for the future. Since the targeted intracellular delivery into living cells is a basic prerequisite for most of these applications, various transfer strategies have been developed. Many of them exploit endocytotic pathways, which typically entrap the nanoparticles in endolysosomal vesicles. Different strategies have extensively been pursued to enhance endocytotic uptake of QDs and other nanoparticles. Particles were decorated with receptor binding proteins (EGF, transferrin), cell penetrating peptides or antibodies or they were encapsulated with transfection reagents like liposomes (lipofectamine) or polymers (PEI) (Delehanty et al., 2009). The escape of the particles out of the endocytosed vesicles is, however, the limiting factor for intracellular targeting and sensing approaches, which require free diffusion of the ideally monodispersed particles in the cytoplasm. Alternatively, physical techniques like microinjection (Dubertret et al., 2002; Slotkin 2007) and electroporation (Derfus et al., 2004; Chen and Gerion, 2004) can be employed to deliver quantum dots directly into the cytoplasm of cells. However, especially for electroporation the studies and applications reported in the literature are limited and an *in situ* approach for electroporative transfer into anchorage-dependent cells has yet not been described.

In the scope of this work PEG-coated CdSe/ZnS core-shell quantum dot nanoparticles were successfully loaded into the cytoplasm of NRK cells grown on microelectrodes by *in situ* electroporation (Fig. 5.75 A). Loading efficiencies were similar to those obtained in experiments using 250 kDa FITC-dextran. The predominantly homogeneous distribution of the QDs among the cytoplasm indicates that they can diffuse freely and are not encapsulated

in vesicles (Fig. 5.75 C). Because of their hydrodynamic diameter of ~ 23 nm (Keren et al., 2009), which is slightly higher than the hydrodynamic diameter of 250 kDa FITC-dextran, they were too large in size to pass the nuclear pore complex so that the nucleus remained unstained. Unspecific uptake of quantum dots was low, as control cell layers that were only incubated in presence of Qdots revealed only weak cytoplasmic fluorescence (Fig. 5.75 B). However, marginal unspecific adsorption to the outer membrane, predominantly in the intercellular spaces, was detected (Fig. 5.75 D), although unspecific adsorption and uptake should be prevented by the PEG coat (Bentzen et al. 2005; Otsuka et al 2003, Xie et al., 2007).

A slight background fluorescence due to unspecifically adsorbed PEG-QDs was also observed by Derfus et al. (2004), who delivered monothiolated PEG-modified CdSe/ZnS QDs into HeLa cells by using different chemical transfection reagents as well as the physical methods microinjection and electroporation. The authors electroporated suspensions of HeLa cells in presence of PEG-QDs and afterwards seeded the cells onto glass slides for microscopic inspection. A similar protocol was used by Chen and Gerion (2004), who delivered silanized and avidin decorated QDs bearing a nuclear localization signal (NLS) or a random peptide into HeLa cells by electroporation in suspension. 24 h after electroporation they detected nuclear and perinuclear localization of the QDs in the cells, whereas a nonspecific control peptide only resulted in random distribution within the cell. Both authors reported that QDs formed aggregates of several hundred nm within the cytoplasm.

To date, only by microinjection a monodisperse intracellular distribution of the QDs (Ø 28 nm) could be achieved. Microinjection of PEG-QDs into HeLa cells produced a diffuse staining of the entire cytoplasm, while they remained excluded from the nucleus (Derfus et al., 2004). Microinjection of PEG-QDs that were conjugated with localization signals for the nucleus or mitochondria in contrast, resulted in specific labelling of these organelles. The high photostability of the quantum dots allowed to monitor the structures over a period of more than 30 min.

Derfus et al. (2004) performed the electroporation experiment in PBS at 4 °C to inhibit endocytosis and accepted a viability of only slightly above 50 %. An example for electroporation of cells with QDs under physiological conditions has been reported by Solotkin et al. (2007), who electroporated commercial phospholipid CdSe/ZnS QDs into developing mouse neural stem and progenitor cells *in vivo*. Since the aim of the experiments was to track these embryonal cells during development, migration and differentiation, a less homogeneous distribution of the QDs within the cells was not decisive.

For results presented in this work rather high concentrations of QDs (400 nM) were used, which was much higher than reported by other authors. Chen and Gerion for example used QDs in a concentration of only 10 nM. In contrast, Rosen et al. (2007) reported electroporation of hMSC cells with 8.2 nM QDs in suspension, which was not efficient.

In conclusion, the experiments presented here may be one of the first reports showing successful electroporation-assisted delivery of quantum dots into anderent cells under physiological conditions, which is an essential prerequisite for many future applications of

QDs in intracellular sensing, tracking and manipulation. However, the long-term behavior of QDs inside the cytoplasm has yet not been investigated.

Outlook: *In situ* Electroporation of Nanoparticles

Derfus et al. (2004) evaluated electroporation as a robust tool for live cell labelling, which may be used as an efficient delivery technique for whole-cell tracking and cytometry. As the results obtained in this work revealed, the ability to deliver QDs freely dispersed into the cytoplasm of living cells *in situ* may even open up new interesting possibilities, especially in intracellular targeting and tracking of biofunctionalized QDs. The use of transparent microelectrodes, for example fabricated from ITO, instead of gold having fluorescence quenching properties, will improve the microscopic quality.

However, a major concern for QDs remains their inherent cytotoxicity. Many QD preparations, that are small enough for applications like targeted delivery into organelles, molecular tracking and interaction studies, are prone to surface oxidation and leaching of heavy metal ions (Ho and Leong, 2009). The extracellular toxicity of QDs has already been monitored by "simple" ECIS readings (Male et al., 2008; Tarantola et al., 2009). But as reported in chapter 5.2 the intracellular toxicity of substances delivered to the cytoplasm by electroporation can also be monitored using ECIS. As intracellular QD toxicity might interfere with an analytical study, the impedimetric assessment of intracellular stability and cytotoxicity after *in situ* electroporation could be useful in the development of particle coating strategies suitable for *in vitro* and *in vivo* use. Also a combined approach using both, ECIS monitoring of the cell layer status and microscopic inspection of intracellular structures or optical intracellular sensing might be considered. A few examples for intracellular sensing with Qds (Zhang et al., 2010) have been published. Han et al. (2009) were able to detect different biothiols such as GSH, cysteine and homocysteine in the cytosolic fluid of Hela cells using Hg^{2+} impregnated CdTe QDs. While the Hg^{2+} coat on the QD quenches its photoluminescence in absence of the thiols, in presence of thiols the formation of a much stronger Hg-S bond with the thiols in solution promotes the detachment of Hg from the QD restoring its fluorescence. Although these authors did not report a real intracellular measurement, they could show that the system was selective for cysteine among other amino acids. A real intracellular sensing was reported by Freeman et al. (2009). They conjugated Nile blue (NB) to BSA coated MPA QDs and delivered the complex into HeLa cells by electroporation in order to sense intracellular NADH. Oxidized NB can strongly quench QDs by FRET but in presence of NADH the dye is reduced to a form in which it can not absorb the QD's emitted light in the visible region. No FRET occurs and the QD luminescence is detecable (Freeman et al., 2009).

A further example for intracellular detection with QDs was presented by Orndorff and Rosenthal (2009). Using QDs conjugated with peptide-based neurotoxins they were able to detect target proteins inside cancer cells which was proven by antibody colocalization studies.

6 *In Situ* Electrofusion of Adherent Cells on Gold-Film Electrodes

An often observed phenomenon when cells are exposed to membrane electroporating pulses is cell fusion. Electrically destabilized membranes of adjacent cells merge and form fused cells which share a common cytoplasm. This chapter shows that membrane permeabilizing *in situ* electroporation causes multiple cell fusion of HEK-293 cells grown on ECIS electrodes, when cells have been pre-incubated with certain functionalized nanoparticles or soluble polymers. Polyethyleneimine (PEI) coated superparamagnetic iron oxide (Fe_3O_4) nanoparticles (*PolyMAG*) were initially used with the aim to enhance transfection efficiency, combining the two well-established gene transfer strategies electroporation and magnetofection. Since the electrofusion enhancing effect of the *PolyMAG* nanoparticles indicated specific interactions with the cell membrane, the fusogenic properties of these particles were analyzed with emphasis on their surface chemistry.

6.1 Impedimetric Detection of *In Situ* Electrofusion

6.1.1 Combined Magnetofection and *In Situ* Electroporation

Chapter 5 introduced *in situ* electroporation as a straight-forward method to load confluent cells attached to the active working electrode with foreign molecules, like DNA for transfection. The amounts of DNA required for these electrotransfection experiments were rather high (chapter 5.5.3.4). Binding of the DNA to magnetic *PolyMAG* nanoparticles and accumulating these DNA loaded particles at the cell surface by magnetic forces before electroporation help to reduce the amount of required DNA. But even without applying an electroporation pulse these *PolyMAG* particle/DNA-complexes are known to be suitable for DNA transfer (magnetofection) (Fig. 6.1).

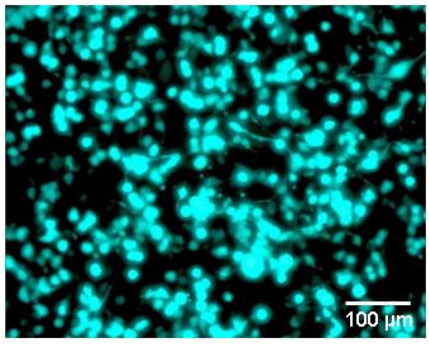

Fig. 6.1: Fluorescence micrograph of HEK-293 cells 24 h after magnetofection using pCH1 loaded *PolyMAG* particles. The pCH1 vector carries the EGFP-gene encoding the green fluorescent protein.

The concept of the magnetofection technique is to increase the local DNA concentration at the cell surface and to reduce time of exposure to the transfection medium. By application of an inhomogeneous magnetic field a quick accumulation of DNA loaded paramagnetic material targeted towards the cell layer is achieved.

Here, the magnetofection technique was combined with *in situ* electroporation to enhance the transfection efficiency of HEK-293 cells and to reduce the required DNA amount. *PolyMAG* particles were loaded with the pCH1 plasmid encoding the green fluorescent protein and were added to a confluent cell layer of HEK-293 cells (Fig. 6.2, step 1). In order to control the cell layer integrity the impedance of the cell-covered electrode was monitored before particle addition, directly after particle addition and after a 15 min incubation with the particles on a permanent magnet, as suggested by the *PolyMAG* supplier for efficient collection of the particles on the cell surface. *PolyMAG* pre-incubated cell layers were then electroporated using a pulse at 40 kHz, 4 V and 200 ms (chapter 5.1.2.1) (Fig. 6.2, step 2). The post-pulse response of the *PolyMAG* pre-incubated HEK-293 cells was monitored by impedance readings (Fig. 6.3) and the transfection efficiency was evaluated by fluorescence microscopy after 24 h (Fig. 6.4).

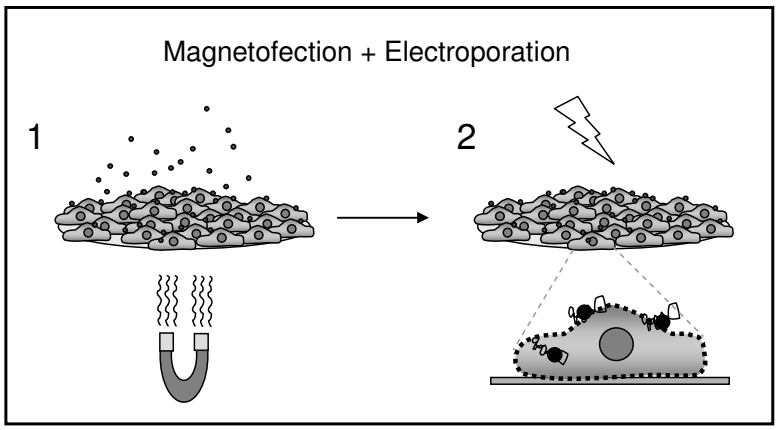

Fig. 6.2: Schematic illustration of combined magnetofection (**1**) and *in situ* electroporation (**2**) of adherent cell layers grown on gold-film electrodes. DNA loaded paramagnetic *PolyMAG* particles are pulled towards the cell layer by magnetic field application (**1**). Cell membranes of *PolyMAG* pre-incubated cells are permeabilized by an electric electroporation pulse of 40 kHz, 4 V and 200 ms (**2**) as illustrated by the cell in the right lower corner.

As becomes apparent from Fig. 6.3 A, addition of *PolyMAG* particles (●, ●) (arrow 1) leads to an increase of impedance compared to a control cell layer only subjected to serum-free medium (SFM) (○). Immediately after the medium exchange (arrow 1) the impedance for all cell layers drops below starting values to about 8.5 – 9.5 kΩ. In the following minutes the impedance of the control cell layer recovers to base line values of ~ 11 kΩ (○), whereas cell layers exposed to *PolyMAG* particles show a steep impedance increase above 15 kΩ (●, ●). After the 15 min incubation period with the cell-covered electrode exposed to a permanent magnetic field to accelerate particle sedimentation (axis break) the impedance for the cells exposed to both, DNA-free (●) and DNA-loaded *PolyMAG* particles (●), reaches a maximum

of about 16 kΩ and levels off to 12.5 kΩ. The particle-free control passes a maximum of 11.3 kΩ after magnet-incubation and remains slightly below 10 kΩ (○).

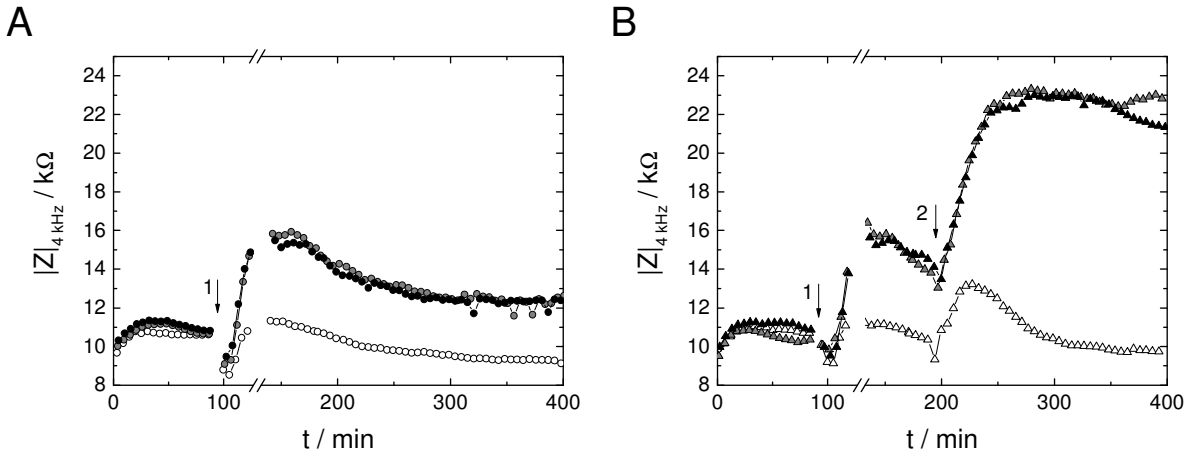

Fig. 6.3: Time course of the impedance magnitude at 4 kHz for HEK-293 cells grown on *8W1E* electrodes upon incubation (**A**) or electroporation (**B**) with DNA-free (●, ▲) and plasmid DNA (pCH1) -loaded *PolyMAG* particles (●, ▲). HEK-293 cell layers in SFM were exposed to DNA-free or DNA-loaded *PolyMAG* particles via medium exchange for *PolyMAG* or *PolyMAG*/DNA containing SFM (arrow 1). Control cell layers were only subjected to medium exchange without particles (○, △). Cells were incubated for 15 min on a permanent magnet indicated by the axis break. Cell layers in **B** were electroporated using an AC pulse of 40 kHz, 4 V and 200 ms (arrow 2). T = 37 °C.

Figure 6.3 B presents the development of the impedance at 4 kHz for HEK-293 cells before and after particle addition (arrow 1), after incubation on the permanent magnet (axis break) as well as after additional electric pulse application (arrow 2). Cell layers treated with DNA-free (●, ▲) or DNA-loaded *PolyMAG* particles (●, ▲) are compared to control cell layers without *PolyMAG* particles (○, △). After electroporation the particle-free cell layer responds with a transient impedance increase to 13.2 kΩ, typical for HEK-293 cells, and a subsequent stabilization to pre-pulse values of about 9.8 kΩ (△) (cp. chapter 5.1.2.1). In contrast, the impedance of the cell layers pre-incubated with DNA-free (▲) or DNA-loaded (▲) *PolyMAG* particles significantly increases, each reaching a plateau of 21 and 23 kΩ, respectively.

After electroporation cell layers were incubated for 24 h to allow for gene expression and then inspected by fluorescence microscopy to determine the transfection yield. Figure 6.4 presents confocal fluorescent micrographs of HEK-293 cell-covered ECIS electrodes 24 h after electroporation with DNA-loaded *PolyMAG* particles (A) compared to control cell layers (B – F).

Combining magnetofection and electroporation leads to a successful transfection of HEK-293 cells grown on the gold-film electrode yielding a transfection efficiency of roughly 60 % (A). But also some individual cells adjacent to the active electrode are transfected (~ 10 %), showing a similar transfection pattern as compared to a cell layer after magnetofection alone, where cells have been subjected to DNA-loaded *PolyMAG* particles without applying an electroporation pulse (D). Simple electroporation of DNA in solution (3 µg/ml) only reveals a negligible transfection success (C).

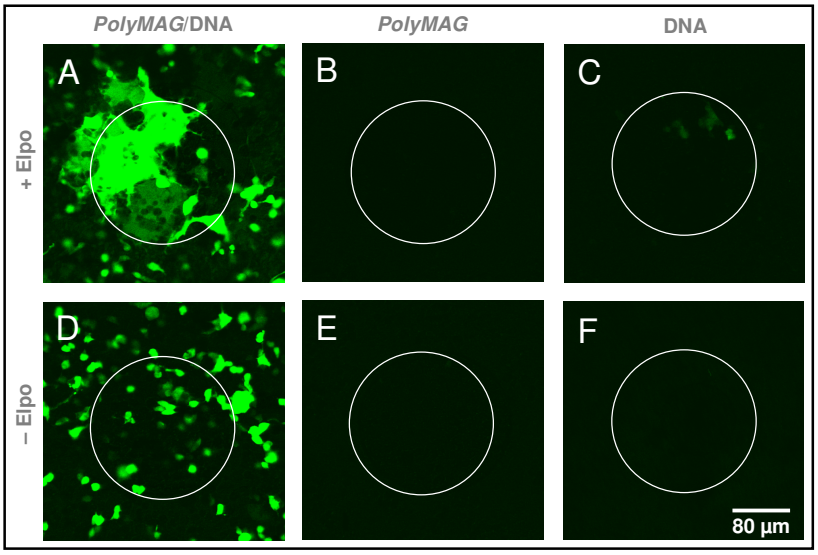

Fig. 6.4: Confocal fluorescence micrographs of HEK-293 cells taken 24 h after exposure to combined magnetofection and electroporation (**A**) or control treatments (**B** – **F**). Cell layers were pre-incubated with *PolyMAG* nanoparticles loaded with pCH1 plasmid DNA encoding EGFP (**A**, **D**), with naked *PolyMAG* particles (**B**, **E**) or pCH1 (3 µg/ml) in solution (**C**, **F**). Cell layers were electroporated using a pulse of 40 kHz, 4 V and 200 ms (+ Elpo) (**A** – **C**) or were only incubated (– Elpo) (**D** – **F**) in presence of the different transfectants.

All controls without DNA (B) or with DNA but without electroporation (E, F) do not reveal any GFP-positive cells. Interestingly, transfected cells residing on the gold-film electrode underwent a change in cell morphology. The transfected cell layer does not contain single GPF positive cells but rather two large giant cell-like structures that cover more than half of the electrode surface. The GFP-positive cellular structures are extremely inhomogeneous in size and morphology.

Phase contrast images of the same cell layers (Fig. 6.5) reveal that those cell layers exposed to *PolyMAG* particles and electroporation (A, B) show a smoother structure. For all control cell layers which were either incubated with *PolyMAG* particles or electroporated a normal cell layer morphology is observed (C – F). Thus, the impedance increase monitored after electroporation of HEK-293 cells pre-incubated with *PolyMAG* particles (Fig. 6.3 B) might be related to the observed cell morphology changes (Fig. 6.4 A and 6.5 A, B).

Finally, the significant impedance increase and the considerable changes in cell morphology after electroporation of HEK-293 cells in presence of *PolyMAG* particles shifted the focus of interest from improving transfection efficiency to elucidating the observed phenomenon of altered cell morphology. Since DNA-free and DNA-loaded particles cause the same impedimetric response, *PolyMAG* particles were typically applied in a DNA-free form in all further experiments, if not mentioned otherwise.

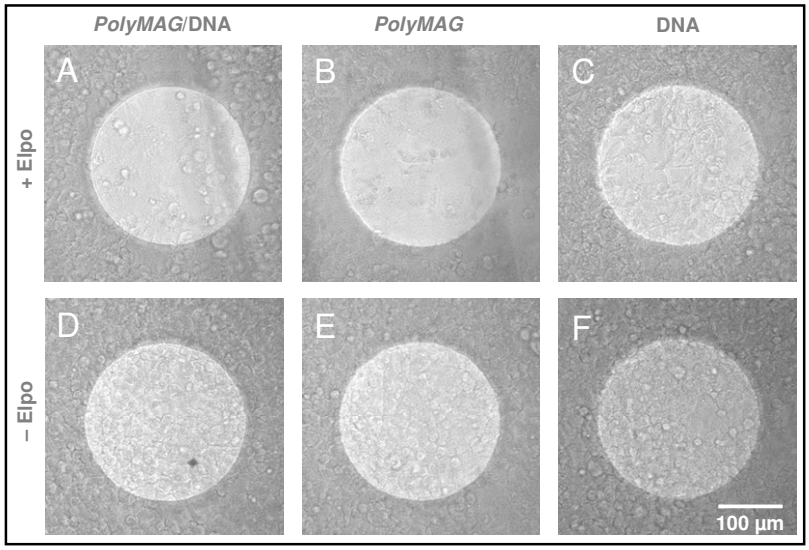

Fig. 6.5: Phase contrast micrographs of HEK-293 cells taken 24 h after exposure to combined magnetofection and electroporation (**A**) or control treatments (**B** – **F**). Cell layers were pre-incubated with *PolyMAG* nanoparticles loaded with pCH1 plasmid DNA encoding EGFP (**A**, **D**), with naked *PolyMAG* particles (**B**, **E**) or pCH1 (3 µg/ml) in solution (**C**, **F**). Cell layers were electroporated using a pulse of 40 kHz, 4 V and 200 ms (+ Elpo) (**A** – **C**) or were only incubated (– Elpo) (**D** – **F**) in presence of the different transfectants.

Experiments similar to those in Fig. 6.3 were repeated several times. The impedance magnitude at 4 kHz for HEK-293 cell layers exposed to *PolyMAG* particles and electroporation (+ *PolyMAG*, + Elpo) was determined 100 min after pulse application and compared to the impedance for control cell layers at this time, which were only incubated with *PolyMAG* particles (+ *PolyMAG*, – Elpo), remained completely untreated (– *PolyMAG*, – Elpo), or were only electroporated (– *PolyMAG*, + Elpo). The statistical summary of these experiments is presented in Fig. 6.6.

Addition of *PolyMAG* particles to HEK-293 cells yields a slightly enhanced impedance of (14.4 ± 0.2) kΩ compared to untreated cell layers with (10.9 ± 0.2) kΩ. After electroporation of particle-free HEK-293 cell layers only a minor impedance increase to (12.6 ± 0.4) kΩ can be detected, whereas electroporation of *PolyMAG* pre-incubated cell layers results in a roughly two-fold impedance increase to an average of (21.1 ± 0.4) kΩ.
As the impedance increase remains moderate when cells are exposed to the particles or the electric pulse alone, the combination of both seems to have a synergetic effect on the cell layer impedance. The onset of the process leading to elevated cell layer impedances can be selectively triggered by a spatially and temporally controlled electroporation pulse.

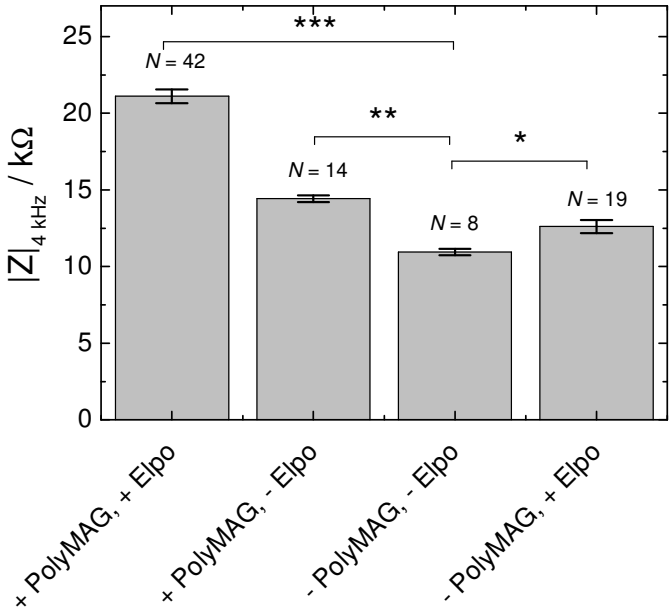

Fig. 6.6: Impedance magnitude at 4 kHz for HEK-293 cells grown on *8W1E* ECIS electrodes after exposure to *PolyMAG* nanoparticles and electroporation (40 kHZ, 4 V, 200 ms) (+ *PolyMAG*, + Elpo) compared to control cell layers. Control cell layers were either incubated with *PolyMAG* nanoparticles without electroporation (+ *PolyMAG*, – Elpo), remained completely untreated (– *PolyMAG*, – Elpo) or were only electroporated (– *PolyMAG*, + Elpo). The diagram shows the mean values and the standard errors ($\mu \pm SE$) of |*Z*| at 4 kHz recorded 100 min after electroporation (or the corresponding time point in controls) of *N* individual cell layers (+ *PolyMAG,* + Elpo: (21.1 ± 0.4) kΩ; + *PolyMAG,* – Elpo: (14.4 ± 0.2) kΩ; – *PolyMAG,* – Elpo: (10.9 ± 0.2) kΩ; – *PolyMAG,* + Elpo: (12.6 ± 0.4) kΩ). The level of statistic significance was calculated by ANOVA (*: $P \geq 0.05$; **: $P \geq 0.01$: ***: $P \geq 0.001$).

6.1.2 Electroporation Triggers the Impedance Increase of HEK-293 Cells Incubated with *PolyMAG* Particles

Membrane permeabilizing electric field pulses seem to be essential for the initiation of the fusion process (cp. Fig. 6.3 B). In order to further investigate the impact of electroporation on *PolyMAG* pre-incubated cell layers repeated electroporation pulses were applied. Figure 6.7 presents the impedance time course of *PolyMAG* pre-incubated HEK-293 cell layers subjected to none, one, two or three electroporation pulses, each interpaused by a regeneration period of about 100 min. After addition of *PolyMAG* particles ($t = 0$) cell layers need a certain time (~ 60 min) to equilibrate to stable impedance values. This stable impedance value as recorded prior to the first electroporation pulse was the basis for calculating the normalized impedance norm $|Z|_{4\ kHz}$.

After initial impedance increases due to *PolyMAG* particle addition the impedance of non-electroporated cells remains at a constant value (Fig. 6.7 A). The normalized impedance of the cell layer treated with only one electroporation pulse increases and finally stabilizes to about 1.6 (B). If a second electroporation pulse is applied to the cell layer, a second impedance increase to 1.84 can be observed (C). Application of three pulses in series only slightly enhances the cell layer impedance (D) (~ 2.0) as compared to impedance levels obtained after two electroporations (C). The extent of impedance drop immediately following an

electroporation pulse is more pronounced for the second and the third pulse than for the first pulse, indicating an increased invasiveness of the electric pulses for the cells that have already been manipulated by previous electroporation.

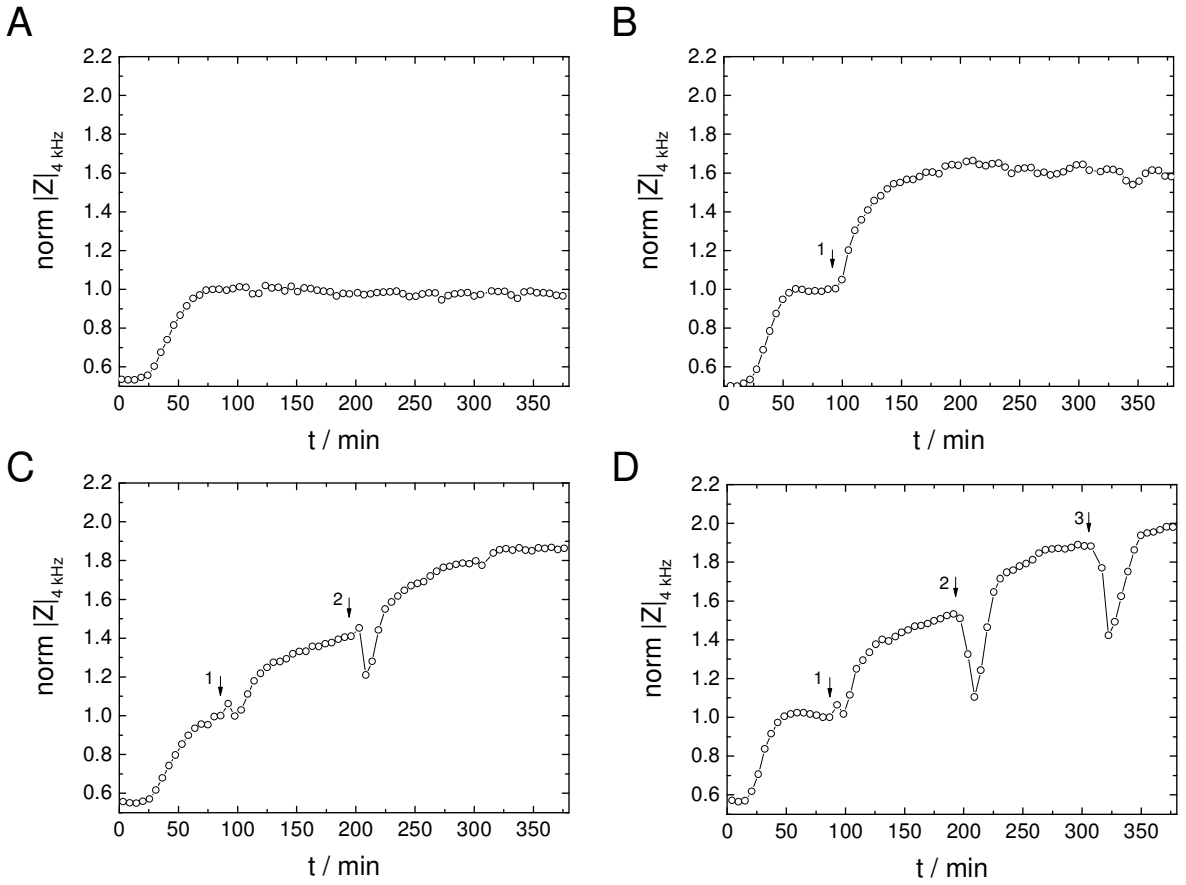

Fig. 6.7: Time course of the normalized impedance magnitude at 4 kHz for *PolyMAG* pre-incubated HEK-293 cells grown on *8W1E* ECIS electrodes before and after exposure to multiple electroporation pulses. **A:** No electroporation **B:** One electroporation pulse (arrow 1) **C:** Two electroporation pulses (arrows 1 + 2); **D:** Three electroporation pulses (arrows 1 – 3). *PolyMAG* particles have been added to the cell layers before starting the measurement ($t = 0$). All cell layers were electroporated using an AC pulse of 40 kHz, 4 V and 200 ms. Absolute impedance magnitudes were normalized to the last values before the first electroporation (A: 13.63 kΩ; B: 14.57 kΩ; C: 13.65 kΩ; D: 14.07 kΩ). $T = 37$ °C.

The mean of the normalized cell layer impedance recorded 100 min after applying one, two or three electroporation pulses is plotted in Fig. 6.8. Absolute impedance values of individual cell layers were normalized to the last impedance value before the first electroporation pulse. Figure 6.8 A reveals that the average impedance levels of *PolyMAG* pre-incubated HEK-293 cell layers rise with the number of applied electroporation pulses. After one electroporation of *PolyMAG* pre-incubated cell layers an average impedance increase to 1.47 ± 0.03 is observed. Two electroporations yield a value of 1.75 ± 0.07. Application of three electroporation pulses, each interpaused by about 100 min, elevates the average value to 2.11 ± 0.15. The rather high error of the mean after three electroporations might be ascribed to an increased instability of the cell layers after exposure to more than one electroporation. A slight increase of the normalized impedance with increasing number of electroporations is measured also for cell

layers electroporated in particle-free medium, ranging from 1.15 ± 0.03 to 1.38 ± 0.05 (Fig. 6.8 B).

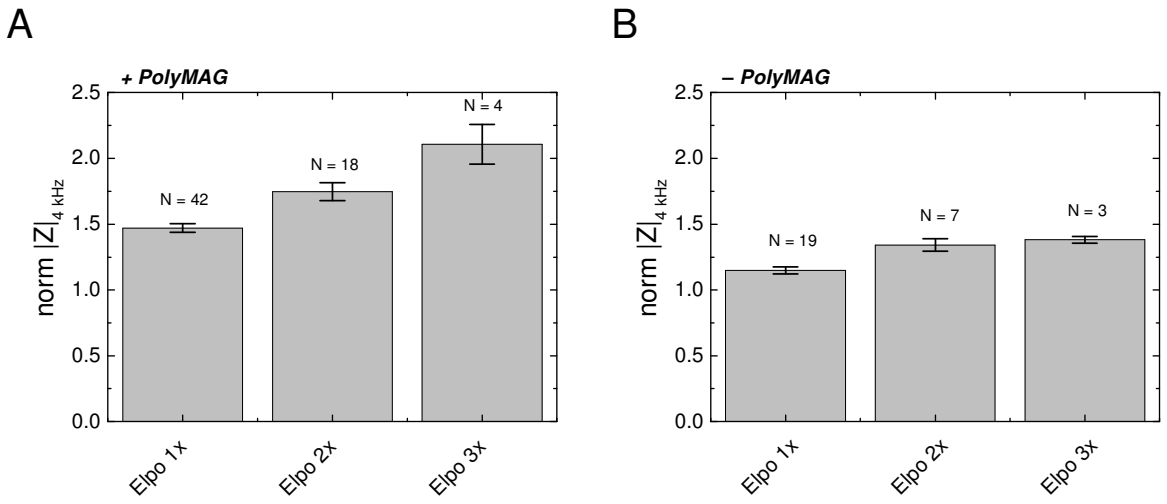

Fig. 6.8: Normalized impedance magnitude at 4 kHz for *PolyMAG* pre-incubated HEK-293 cells grown on *8W1E* ECIS electrodes after one (1 ×), two (2 ×) or three (3 ×) electroporation (Elpo) pulses of 40 kHz, 4 V and 200 ms (**A**). Control cell layers were not pre-incubated with *PolyMAG* nanoparticles (– *PolyMAG*) but subjected to one, two or three electroporation pulses (**B**). The diagram shows the mean values and the standard errors ($\mu \pm SE$) recorded 100 min after electroporation of N individual cell layers (+ *PolyMAG*: 1 ×: 1.47 ± 0.03; 2 ×: 1.75 ± 0.07; 3 ×: 2.11 ± 0.15; – *PolyMAG*: 1 ×: 1.15 ± 0.03; 2 ×: 1.34 ± 0.05; 3 ×: 1.38 ± 0.05).

Corresponding phase contrast images of *PolyMAG* pre-incubated HEK-293 cell layers after one, two or three of electroporation pulses are compared to control cells in Fig. 6.9.

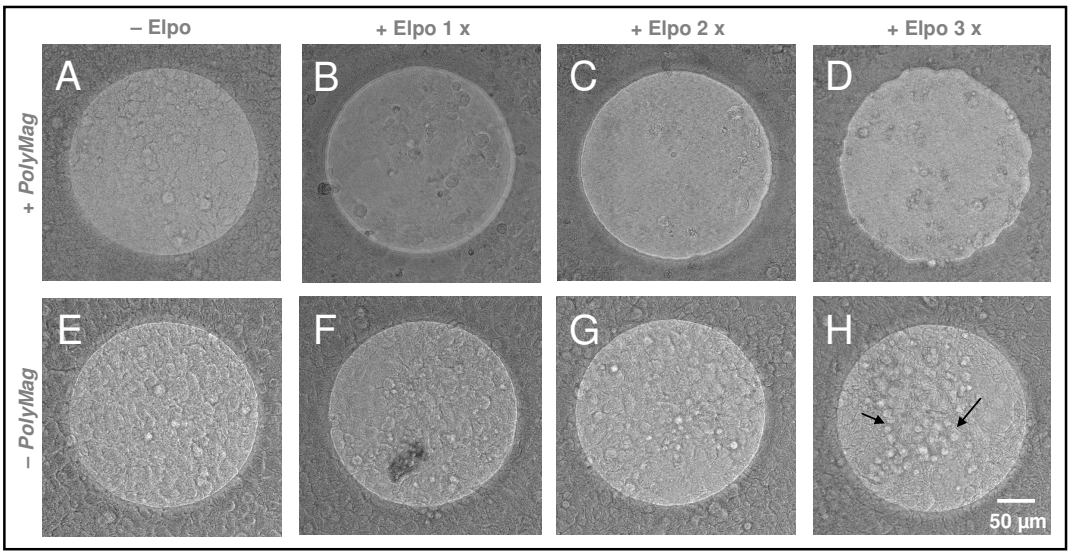

Fig. 6.9: Phase contrast micrographs of HEK-293 cells grown on *8W1E* ECIS electrodes with and without pre-incubation with *PolyMAG* nanoparticles after multiple electoporation pulses. **A** – **D:** Pre-incubation with *PolyMAG* nanoparticles (+ *PolyMAG*); **E** – **H:** Without *PolyMAG* particles (– *PolyMAG*). Cells **B** – **D**; **F** – **H** were electroporated using one, two or three AC pulse(s) of 40 kHz, 4 V and 200 ms (+ Elpo 1 ×, 2 ×, 3 ×). **A**, **E:** No pulse (– Elpo); **B**, **F:** One electroporation; **C**, **G:** Two electroporations; **D**, **H:** Three electroporations, arrows indicate damaged cells. Within a sequence of electroporation pulses cells were allowed to recover for 100 min after each individual pulse.

In an unpulsed cell layer the intercellular spaces of individual cells are visible (A, E). Control cell layers electroporated once or twice without particles show single cells with their typical morphology (F – G), but also reveal aggregates of possibly damaged cells in the center of the electrode, especially after three electroporation pulses (H, arrows). After applying up to three electroporation pulses (B – D) to particle pre-incubated cell layers individual cells and their intercellular spaces are hard to detect.

Taken together, impedimetric and microscopic results indicate that cells residing on the electrode have significantly altered their morphology after combined *PolyMAG* incubation and electroporation. Increasing impedances monitored at 4 kHz are usually based on the restriction of the paracellular current pathways beneath the cells and between neighboring cells, resulting from a reduction of the intercellular spaces. Phase contrast micrographs indicate that the typical cell layer appearance as a cobblestone pattern of individual cells vanishes after *PolyMAG* incubation / electroporation and, instead, a smoothened cell layer with hardly detectable intercellular contrast is created. These observations suggest that cells may have merged by fusing their membranes, forming giant cells (cp. Fig. 6.4; Fig. 6.5). Multi-cell fusion as a possible explanation for disappearing intercellular structures and loss of individual cell morphology together with the significant impedance increase could not be definitely proven by phase contrast microscopic techniques. Therefore, various fluorescence-based staining approaches were performed.

6.2 Microscopic Visualization of *In Situ* Electrofusion

In order to disclose the phenomenon of disappearing intercellular contrast as indicated by phase contrast micrographs, stainings of the extracellular fluid, the cell membrane or the cytoplasm were performed. The aim was to prove whether the cells have fused in the course of electroporation in presence of *PolyMAG* particles or other morphological changes have taken place. Characteristic properties of fused cells are merged cell membranes as well as mixed cytoplasms. If more than two cells fuse, multinucleate giant-cells are formed. Thus, different staining approaches were chosen to selectively label the cell membrane, the cytoplasm or the extracellular fluid in the intercellular clefts between individual cell bodies. In addition to classical staining procedures, recombinat cell lines expressing either membrane-anchored or soluble fluorescent proteins further helped to unravel the cell layer composition.

6.2.1 Staining of the Extracellular Fluid

The extracellular space was stained using membrane impermeable FITC-dextran (4 kDa). Intercellular and subcellular spaces are labeled by the green fluorescent probe, while the cell bodies remain dark. Figure 6.10 presents microscopic xy- as well as xz-sections of HEK-293 cell layers that were electroporated after incubation with *PolyMAG* nanoparticles (A – C) compared to control cell layers (D – H).

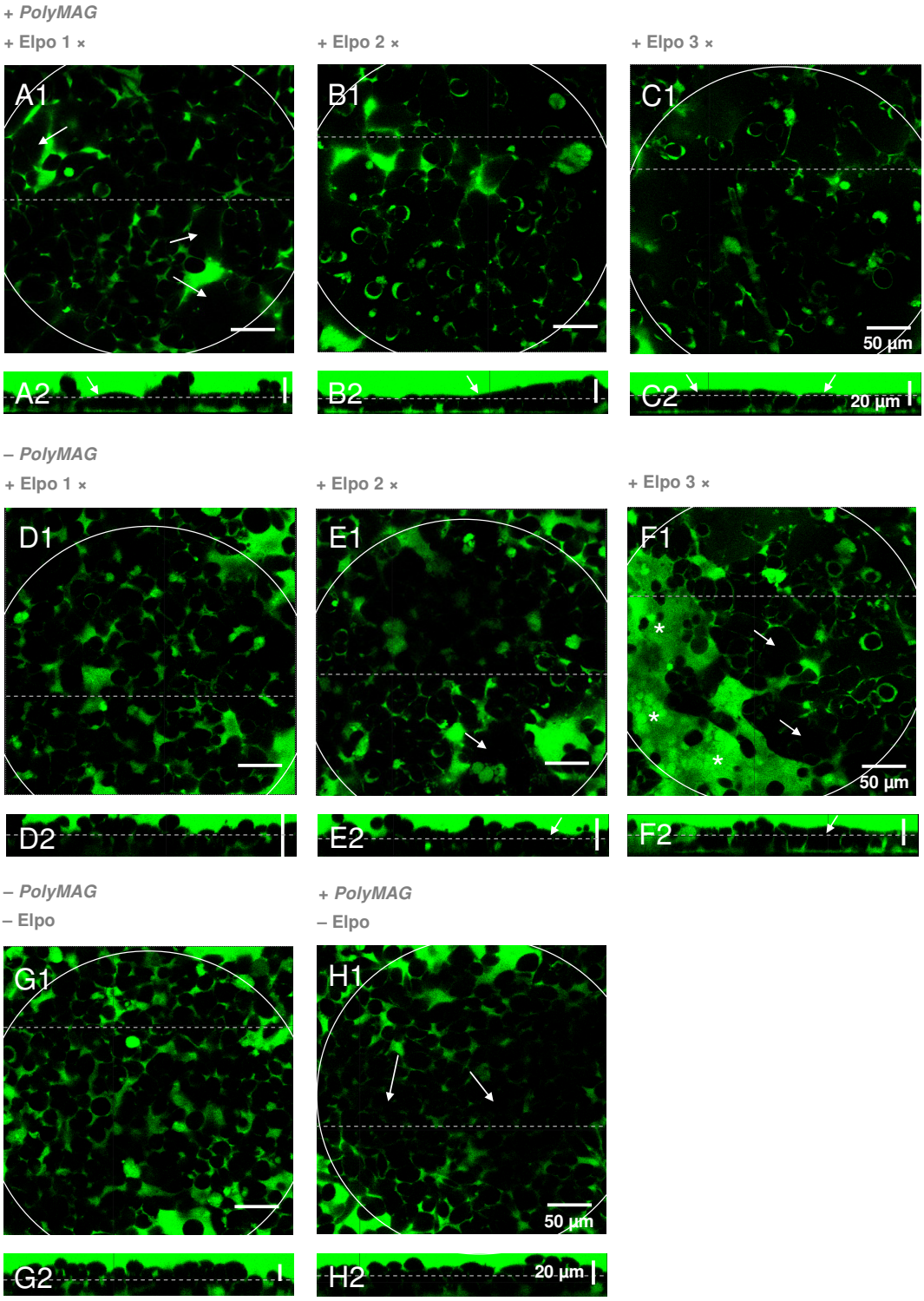

Fig. 6.10: Confocal fluorescence micrographs of HEK-293 cells grown on *8W1E* ECIS electrodes subjected to different experimental conditions. Cell layers were pre-incubated with *PolyMAG* particles (+ *PolyMAG*) (**A**, **B**, **C** and **H**) or remained particle-free (– *PolyMAG*) (**D**, **E**, **F** and **G**). Cell layers **A** – **C** and **D** – **F** were electroporated using one (**A**, **D**), two (**B**, **E**) or three (**C**, **F**) AC pulse(s) of 40 kHz, 4 V and 200 ms (+ Elpo). Cell layers G and H remained completely untreated (**G**) or were incubated with *PolyMAG* particles without electroporation (**H**) (– Elpo). Confocal xy-sections (1) and xz-sections (2) are shown after staining of the extracellular fluid with FITC-dextran. The area of the underlying active working electrode is delineated by white circles. Dashed lines illustrate positions of xz- and xy-sections in the corresponding image. Arrows indicate fused cells, asterisks (*) indicate defect sites in the cell layer.

Control cell layers that were either completely untreated (Fig. 6.10 G) or incubated with *PolyMAG* particles (H) show a typical cell layer composition for HEK-293 cells. The almost spherical morphology of individual cells can be clearly distinguished. Only in very densely packed areas the contrast between individual cells is rather low (H1). HEK-293 cells tend to form multi-layers when grown to confluence. As seen in the xz-sections about 2 – 3 cells are piled on top of each other in an irregular pattern (G2, H2).
In contrast, *PolyMAG* pre-incubated HEK-293 cell layers reveal a considerably altered morphology after electroporation (A – C). The average size of the dark cell bodies within the cell layer is increased. While a small fraction of the cells still shows a spherical morphology, enlarged cell bodies exhibit irregular, non-spherical shapes (A1, arrows). The xz-view reveals a reduced number of individual, spherical cells as well as reduced stacking of cells in the third dimension (A2). Also the enlarged size of individual cellular bodies becomes evident (A2, arrow). With increasing numbers of electroporation pulses the number of individual spherical cells further decreases (B, C). The xz-sections reveal a smoothening of the cell layer surface and disappearance of intercellular clefts (B2, C2). In the xy-sections individual cell bodies can hardly be distinguished anymore (C1).
When cell layers were electroporated without particle pre-incubation, no significant difference in cell layer composition can be detected after applying one electroporation pulse (D) compared to the untreated control (G). The cell layer shows the common irregular three-dimensional arrangement of individual cells. When two or three electroporation pulses were applied morphological alterations can also be observed for these control cell layers (E, F). Similar to *PolyMAG* pre-incubated cell layers the size of individual cell bodies seems to increase and the cell surface smoothens with increasing pulse number. However, this smoothening effect is significantly smaller than observed for *PolyMAG* pre-incubated cells. After three electroporation pulses a certain fraction of the cell layer is irreversibly damaged, leaving a FITC-dextran filled gap within the cell layer (F1, asterisks).
Since the extracellular staining can not clearly distinguish between closely adjoined cells with a narrow intercellular cleft and fused cells with merged cell membranes and shared cytoplasm, additional staining methods were applied.

6.2.2 Staining of the Cell Membrane

HEK-293 cells were subjected to different experimental conditions and subsequently stained using the membrane intercalating dye DiI (Fig. 6.11) (cp. chapter 4.4.4.4).
Control cell layers (D – F) exhibit a normal morphology and individual cells within the cell layer are distinguishable. Obviously, the dye was not able to stain the entire cell layer, since only the uppermost cells, hovering in a certain distance above the gold electrode, appearing as a red line below the cell layer, show fluorescent cell membranes (e.g. Fig. 6.11 E2).
After applying a single electroporation pulse to *PolyMAG* pre-incubated HEK-293 cell layers (A1, A2) the DiI staining reveals a reduced number of individual spherical cells when compared to control cell layers. The enlarged cell bodies, encircled by the fluorescently

labeled cell membranes, exhibit irregular shapes (A, arrows) and the surface of the cell layer smoothens (A2).

The effect of repeated membrane destabilizing electroporation pulses is even more pronounced. After two electroporation pulses the amount of intercellular membranes decreases significantly (B) and after three electroporation pulses the intercellular DiI staining almost vanishes (C1). The xz-section illustrates that large areas of the electrode are covered by one continuous membrane, which is not be interrupted by membranes separating individual cells (C2, arrow).

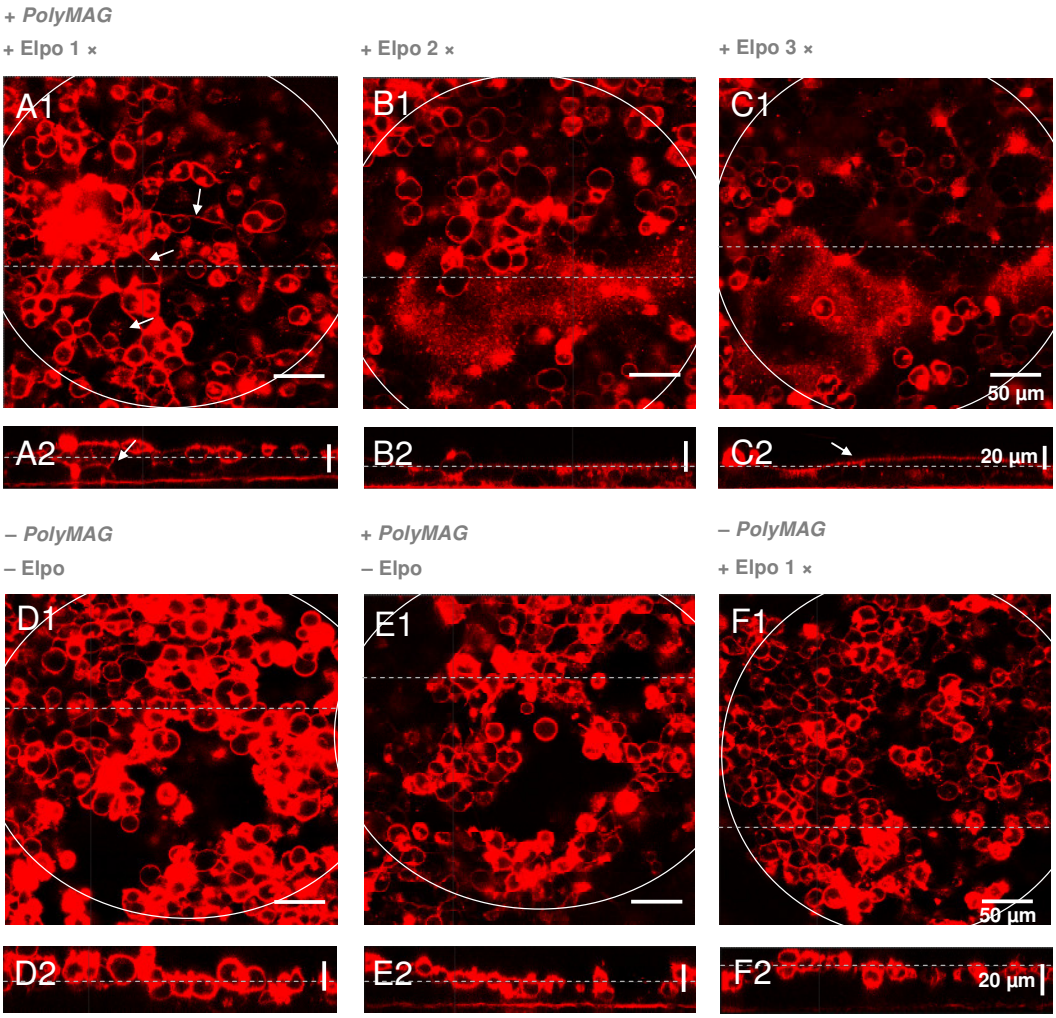

Fig. 6.11: Confocal fluorescence micrographs of DiI stained HEK-293 cells grown on *8W1E* ECIS electrodes subjected to different experimental conditions. After pre-incubation with *PolyMAG* particles (**A** – **C**) cell layers were electroporated using one (**A**), two (**B**) or three (**C**) AC pulse(s) of 40 kHz, 4 V and 200 ms. Control cell layers remained completely untreated (**D**), were incubated with *PolyMAG* particles but not electroporated (**E**) or were only electroporated without *PolyMAG* pre-incubation (**F**). Confocal xy-sections (1) and xz-sections (2) are shown. The area of the underlying active working electrode is delineated by white circles. Dashed lines illustrate positions of xz- and xy-sections in the corresponding image.

6.2.3 Staining of the Cytoplasm

In order to prove the continuity of the cytoplasm of fused cells the cytoplasm of *PolyMAG* pre-incubated cell layers was stained by a membrane-permeable calcein derivate (calcein-AM). Calcein-AM is intracellularly cleaved to its fluorescent membrane-impermeable form calcein by unspecific esterases (Fig. 6.12).

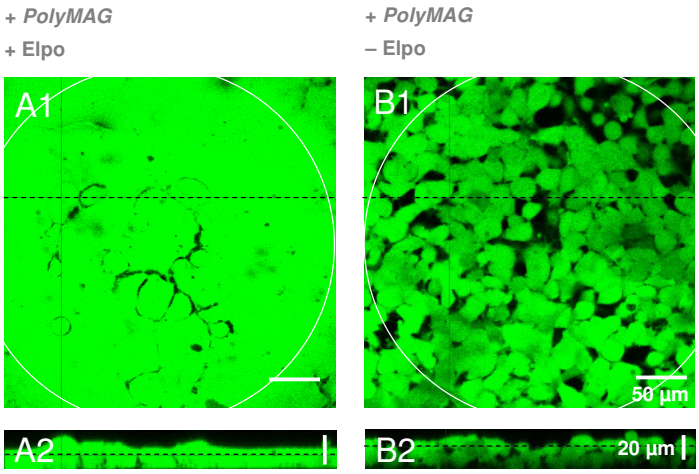

Fig. 6.12: Confocal fluorescence micrographs of calcein stained HEK cells grown on *8W1E* ECIS electrodes. After pre-incubation with *PolyMAG* particles cells were electraporated using an AC pulse of 40 kHz, 4 V and 200 ms (+ Elpo) (**A**). Control cells were not electroporated (– Elpo) (**B**). Confocal xy-sections (1) and xz-sections (2) are shown. The area of the underlying active working electrode is delineated by white circles. Dashed lines illustrate positions of xz- and xy-sections in the corresponding image.

After electroporation, *PolyMAG* pre-incubated cell layers show hardly any intercellular clefts and hardly any individual cells (A). The cell layer is formed of only few large cellular bodies resulting in a smooth surface topography (A2). In non-electroporated control cell layers individual cells can be easily distinguished due to their green cytoplasmic fluorescence, separated by non-fluorescent extracellular spaces (B). Single cells are stacked to the typical complex multi-layered cell sheet (B2).

Time consuming staining processes presented above were associated with further manipulations of the cell layer and, thus, a risk of cell layer damage during the experimental procedures. Moreover, membrane staining using DiI turned out to be too inefficient for quantitative staining of multi-layered HEK cells. Therefore, cell layers with an intrinsic fluorescence of their cell membranes or cytoplasm were used in order to circumvent the drawbacks and limitations of conventional cytochemical stainings.

6.2.4 Intrinsic Cytoplasmic Fluorescence: *In Situ* Electrofusion of HEK-EGFP Cells

A HEK cell line was created (cp. chapter 4.2.9), which stably expresses EGFP in its cytoplasm. Figure 6.13 shows electrofused HEK-EGFP cells after *PolyMAG* pre-incubation (A) as well as corresponding control cell layers (B, C, D).

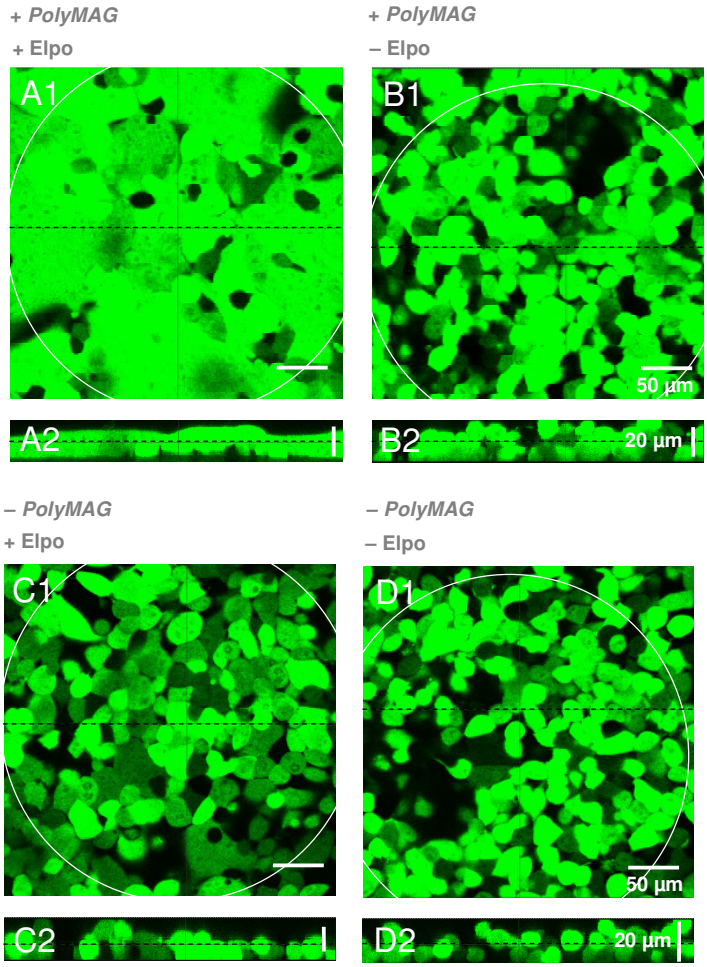

Fig. 6.13: Confocal fluorescence micrographs of HEK-EGFP cells grown on *8W1E* ECIS electrodes. Cells were pre-incubated with *PolyMAG* particles (+ *PolyMAG*) (**A**, **B**) or remained particle-free (– *PolyMAG*) (**C**, **D**). Cell layers in **A** and **C** were additionally electroporated using an AC pulse of 40 kHz, 4 V and 200 ms (+ Elpo). Cell layers in **B** and **D** were not electroporated (– Elpo). Confocal xy-sections (1) and xz-sections (2) are shown. The area of the underlying active working electrode is delineated by white circles. Dashed lines illustrate positions of xz- and xy-sections in the corresponding image.

HEK-EGFP cells show the same morphology as described for HEK-293 wild type cells. Cell layers of control populations exhibit the characteristic multi-layered structure of individual cells (B, C, D). *PolyMAG* pre-incubated and electroporated cell layers reveal the typical reduction of intercellular clefts separating individual cells and a smoothening of the cell layer, which is characteristic for the formation of giant cells (A1, A2).

6.2.5 Intrinsic Membrane Fluorescence: *In Situ* Electrofusion of HEK-EYFP/pAbcg2 Cells

To further visualize membrane fusion after *PolyMAG* pre-incubation and electroporation a recombinat HEK cell line, stably expressing a membrane located fusion protein of EYFP and the pAbcg2 membrane transporter was used (Seidl, 2008). The function of the membrane protein itself is not relevant here. The fluorescent label anchored to the membrane is the decisive property of this HEK-EYFP/pAbcg2 cell line, replacing time consuming and inefficient membrane stainings with DiI, for example.
Figure 6.14 shows HEK-EYFP/pAbcg2 cells grown on ECIS gold-film electrodes. The cells have been pre-incubated with *PolyMAG* particles (A, B) or remained particle-free (C, D). They were electroporated (A, C) or not (B, D).

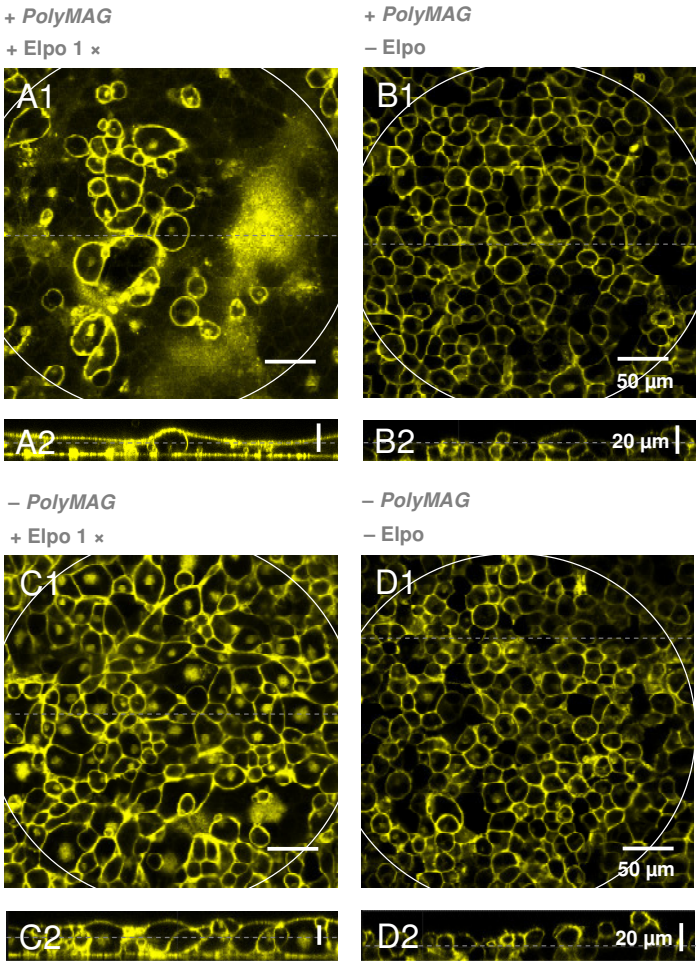

Fig. 6.14: Confocal fluorescence micrographs of HEK-EYFP/pAbcg2 cells grown on *8W1E* ECIS electrodes. Cells were pre-incubated with *PolyMAG* particles (**A**, **B**) or remained particle-free (**C**, **D**). Cell layers in **A** and **C** were additionally electroporated using an AC pulse of 40 kHz, 4 V and 200 ms (+ Elpo). Cell layers in **B** and **D** were not electroporated (– Elpo). Confocal xy-sections (1) and xz-sections (2) are shown. The area of the underlying active working electrode is delineated by white circles. Dashed lines illustrate positions of xz- and xy-sections in the corresponding image.

HEK-EYFP/pAbcg2 cells show a significant change in cell layer morphology after they have been incubated with *PolyMAG* particles and subjected to an ac electroporation pulse at

40 kHz and 4 V for 200 ms (Fig. 6.14 A). The amount of intercellular membranes decreases considerably and some giant, cell-like bodies are created (A1). Continuous membranes cover a large fraction of the electrode, generating a smooth surface topography of the entire cell layer (A2). Without electric pulse application cells exhibit their typical spherical morphology and a multi-layered composition of an intact cell sheet independent of *PolyMAG* incubation (B, D). However, enlarged cells can also be observed if particle-free cell layers are subjected to a single electroporation pulse (C), indicating that the electric pulse itself caused cell fusion of HEK-EYFP/pAbcg2 cells to some degree.

Figure 6.15 shows xy-sections across the apical, central and basal part of an untreated (A1 – D1) and a fused HEK-EYFP-pAbcg2 cell layer (A2 – D2). The picture shows that all membranes are quantitatively labeled by the membrane-anchored EYFP fusion protein.

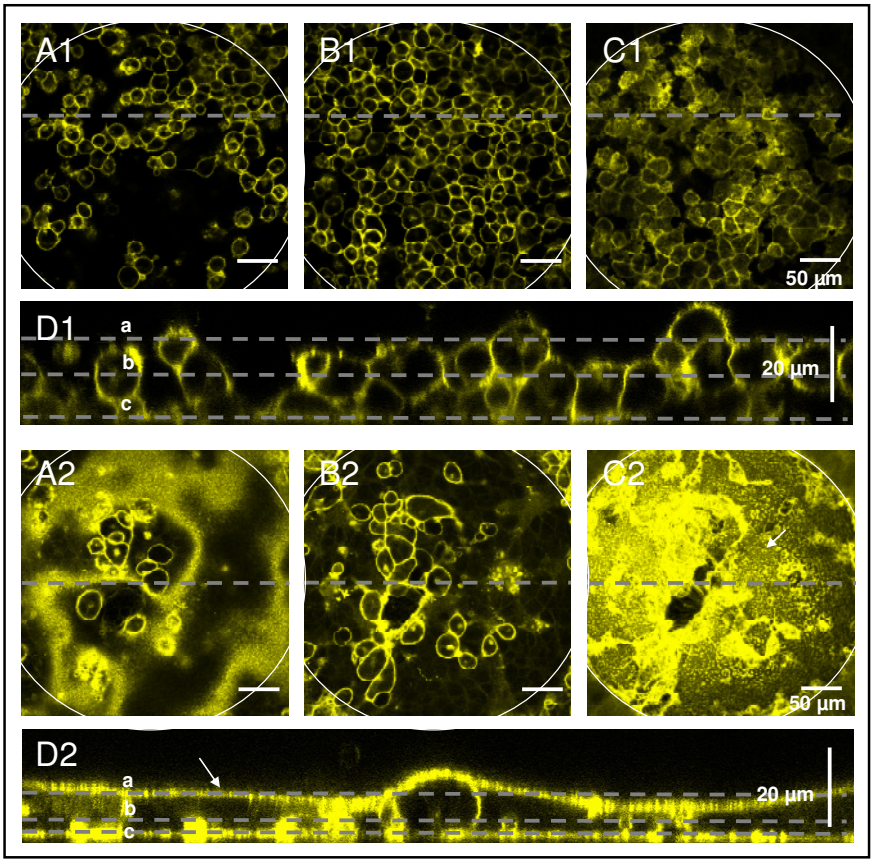

Fig. 6.15: Confocal fluorescence micrographs of the apical (**A**), central (**B**) and basal (**C**) cell layer region of control (**1**) and electrofused (**2**) HEK-EYFP/pAbcg2 cells grown on *8W1E* ECIS electrodes. Dashed lines a – c in the xz-sections (**D**) illustrate the z-position in the confocal xy-images A – C. Dashed lines in xy-sections give the position of the corresponding xz-sections (D). Electrofused cells were pre-incubated with *PolyMAG* particles and electroporated using an AC pulse of 40 kHz, 4 V and 200 ms. The area of the underlying active working electrode is delineated by a white circle.

Clear differences between the control cell layer (A1 – D1) and the *PolyMAG* incubated and electroporated cell layer (A2 – D2) are apparent in all sections across the cell layers. The apical membrane of cells exposed to *PolyMAG* particles and electroporation has merged and forms a continuous sheet covering the giant cell body (A2, D2). In the middle of the cell layer intercellular membranes which vertically intersect individual cell bodies from one another are

significantly reduced (B2, D2) when compared to the control cell layer (B1, D1). Even the basal membranes directly covering the gold electrode have fused when cells were exposed to *PolyMAG* incubation and electroporation (C2). The apical and basal membranes both show punctuate structures, presumably due to clustering of the EYFP/pAbcg2 protein (A2, C2).

The intrinsic labeling method by the membrane-linked recombinant EYFP/pAbcg2 protein makes the HEK-EYFP/pAbcg2 cells superior to gain further insights to the fate of membranes after multi-cell fusion. Figure 6.16 shows side views across *PolyMAG* incubated and electroporated HEK-EYFP/pAbcg2 cells. Large areas of the cell layer covering the electrode are fused into one continuous membrane sheet with almost no vertical intercellular membranes (A, B, E). At other regions only a few cells have fused or individual cells remained unfused (C). Additionally, intracellular bodies surrounded by membrane can be detected. These are predominantly located at the basal site of the cell layer (D, E, arrows).

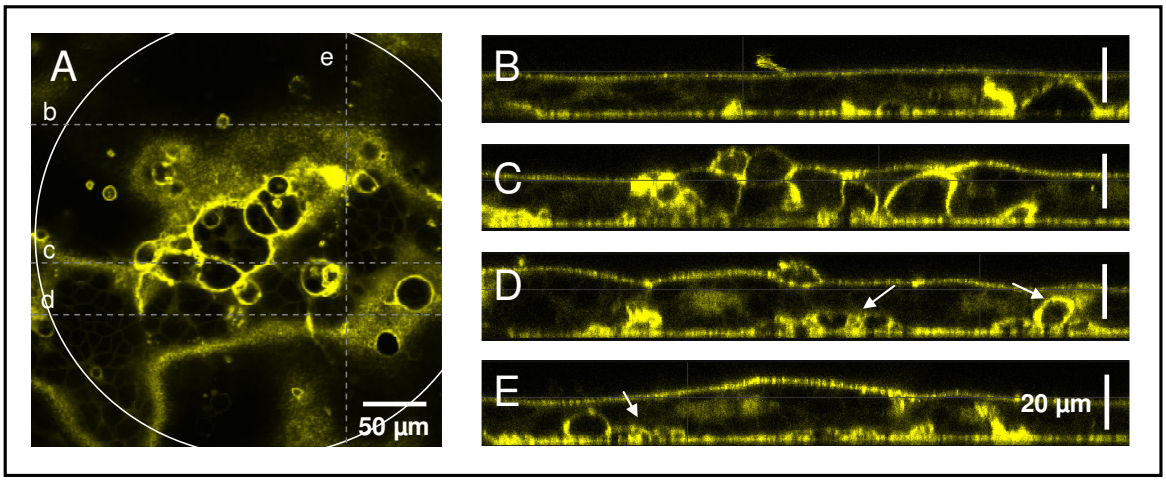

Fig. 6.16: Confocal fluorescence micrographs of HEK-EYFP/pAbcg2 cells grown on *8W1E* ECIS electrodes after pre-incubation with *PolyMAG* particles and electroporation using an AC pulse of 40 kHz, 4 V and 200 ms. Dashed lines b – e in the xy-sections (**A**) illustrate the position of the z-images **B** – **E**. The area of the underlying active working electrode is delineated by a white circle. Arrows indicate vesicle-like structures.

6.2.6 *In Situ* Electrofusion of HEK-EYFP/pAbcg2 and HEK-ECFP Cells

As shown before, valuable information is obtained from either membrane or cytoplasmic labeling. While the membrane label visualizes the position of the cell borders, the cytoplasmic stain gives information on cytoplasmic continuity and membrane integrity. Thus, labeling membrane and cytoplasm in parallel provides an increased information content. If both cellular properties are initially separated and only co-occur if cell fusion takes place, fused cells can be easily distinguished from non-fused cells.
Two different cell lines were used, the HEK-EYFP/pAbcg2 cell line with membrane anchored EYFP and the HEK-ECFP cell line with soluble ECFP expressed in the cytoplasm (cp. chapter 4.2.9). A mixed population of both cell lines was cultivated on ECIS electrodes

and subjected to *PolyMAG* pre-incubation and electroporation. CLSM images of this cell layer and the respective control cells are presented in Fig. 6.17.

The cell layer composition of non-electroporated control cell layers reveals strictly separated colonies of either membrane- or cytoplasm- labeled individual HEK cells (B, D). Electroporation of particle-free populations triggers the formation of hybrid cells, which exhibit both, membrane and cytoplasmic staining (C). The extent of membrane fusion and shared cytoplasms is even more pronounced for electroporated, *PolyMAG* pre-incubated cells, showing giant cell bodies of irregular shape (A1) and smooth cell layer topography (A2).

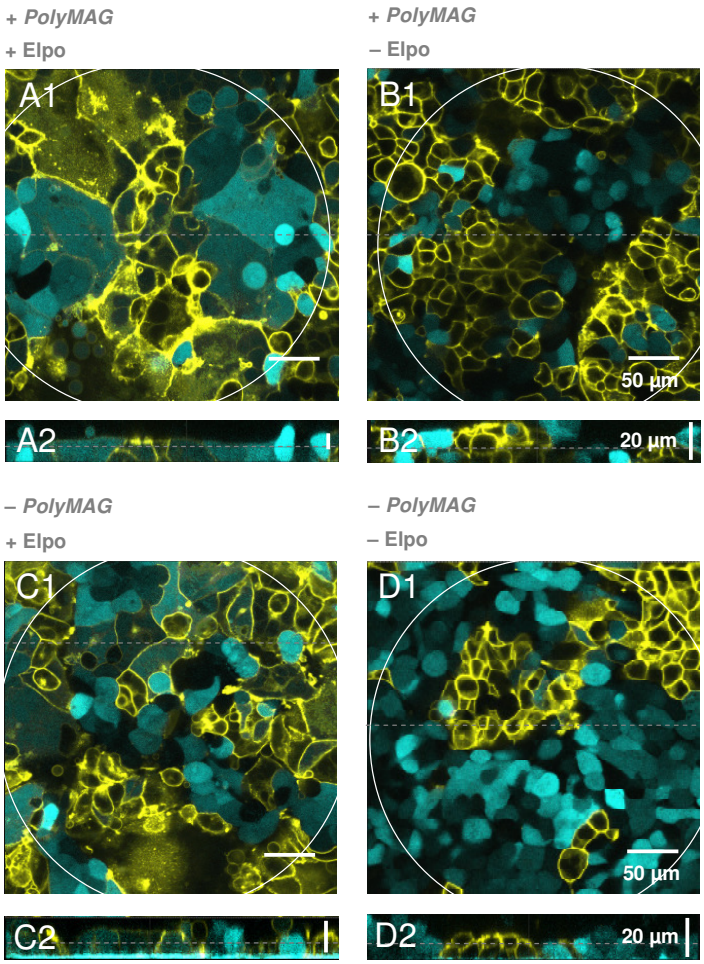

Fig. 6.17: Confocal fluorescence micrographs of mixed populations of HEK-EYFP/pAbcg2 cells and HEK-ECFP cells grown on *8W1E* ECIS electrodes. Cells were pre-incubated with *PolyMAG* particles (**A**, **B**) or remained particle-free (**C**, **D**). Cell layers in **A** and **C** were electroporated using an AC pulse of 40 kHz, 4 V and 200 ms (+ Elpo). Cell layers in **B** and **D** were not electroporated (– Elpo). Confocal xy-sections (1) and xz-sections (2) are shown. Dashed lines illustrate positions of xz- and xy-sections in the corresponding image. The area of the underlying active working electrode is delineated by white circles.

Further magnified xz- and yz-views of *PolyMAG* pre-incubated, electrofused cells are presented in Fig. 6.18. They clearly reveal that EYFP-labeled membranes cover the ECFP loaded cytoplasms (B – E, arrows). The total amount of EYFP-labeled membrane protein is determined by the number of HEK-EYFP/pAbcg2 cells on the electrode and might be significantly reduced compared to pure HEK-EYFP/pAbcg2 populations. Thus, the EYFP

fluorescence intensity of merged membranes from HEK-EYFP/pAbcg2 and HEK-ECFP cells is reduced in some regions.

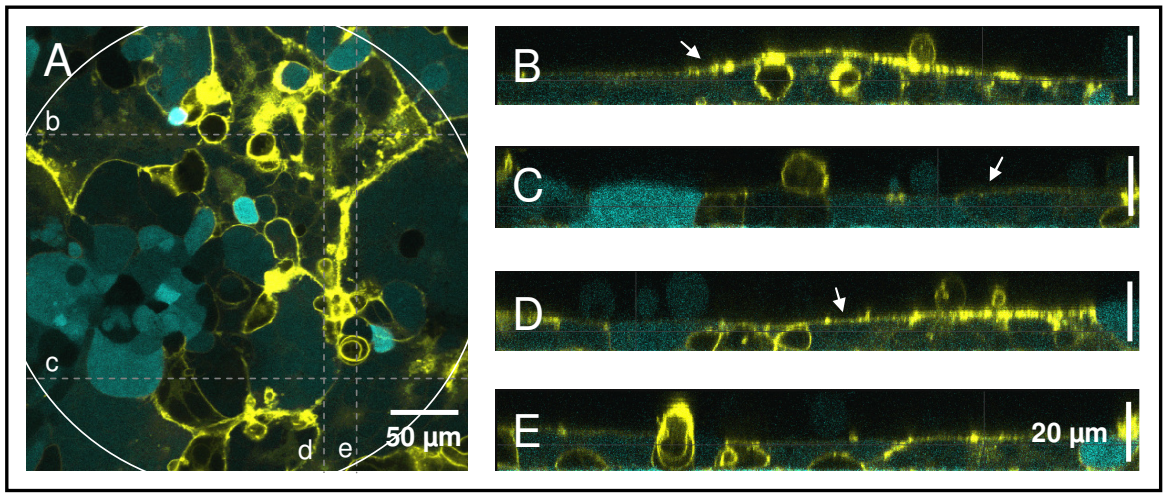

Fig. 6.18: Confocal fluorescence micrographs of electrofused HEK-EYFP/pAbcg2 and HEK-ECFP cells grown on an *8W1E* ECIS electrode (white circle) after pre-incubation with *PolyMAG* particles and electroporation using an AC pulse of 40 kHz, 4 V and 200 ms. **A:** xy-section; **B** – **E:** xz- and yz-sections of confocal xy-sections sliced in x or y-direction as illustrated by dashed lines (b – e) in A. The area of the underlying active working electrode is delineated by a white circle. Arrows mark the EYFP-labeled membrane covering cellular bodies expressing ECFP in their cytoplasm.

A summary of the microscopic proofs for cell fusion originating from combined *PolyMAG* pre-incubation and electric pulsing is given in Fig. 6.19.

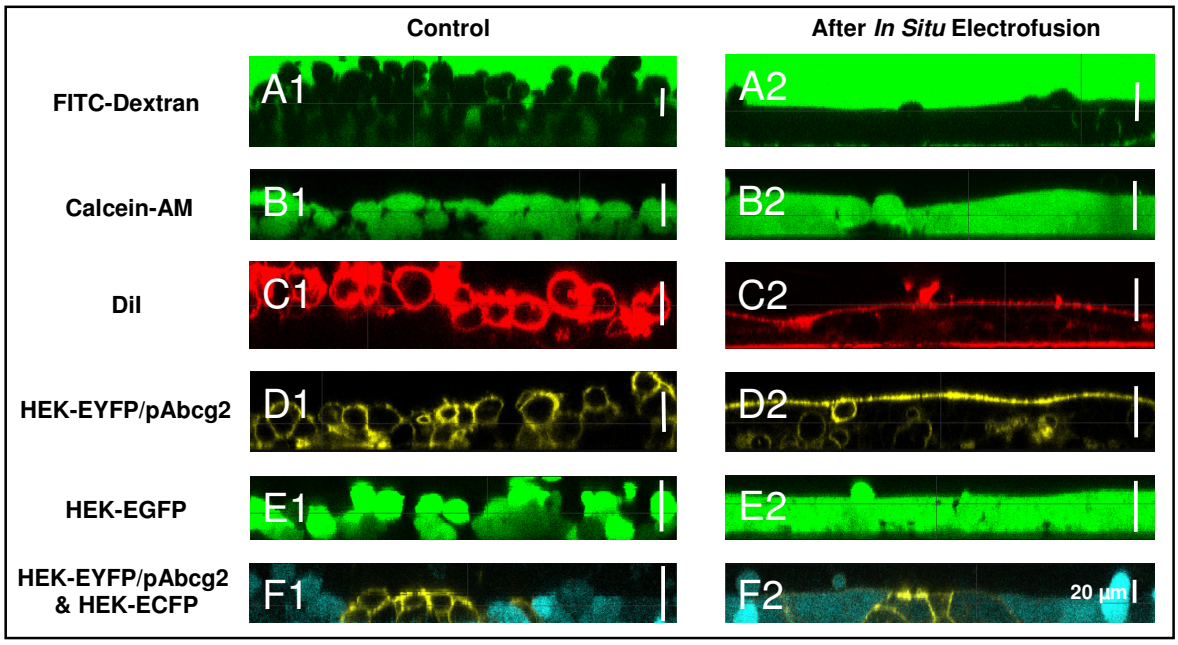

Fig. 6.19: Overview of CLSM xz-sections of differently labeled untreated (**1**) or *PolyMAG* pre-incubated and electrofused (**2**) HEK cell layers. Cytochemical stainings applied to HEK-293 wild type cells (**A** – **C**) are: **A:** Extracellular FITC-dextran; **B:** Cytoplasmic calcein; **C:** DiI stained cell membrane. Recombinant HEK cell lines exhibiting intrinsic fluorescence were: **D:** HEK-EYFP/pAbcg2; **E:** HEK-EGFP; **F:** Mixed culture of HEK-ECFP and HEK-EYFP/pAbcg2.

Since HEK-EYFP/pAbcg2 cells revealed the most detailed information about the fate of membranes within the electrofused cell layers, this cell line seemed to be the most suitable for further investigations.

6.3 Impedimetric Characterization of HEK-EYFP/pAbcg2 Cells

The fusion behavior of HEK-EYFP/pAbcg2 cells was characterized impedimetrically in order to verify their suitability for further studies.
The impedance measurements that were recorded for the cell populations shown in the CLSM micrographs above (Fig. 6.14) are presented in Fig. 6.20.

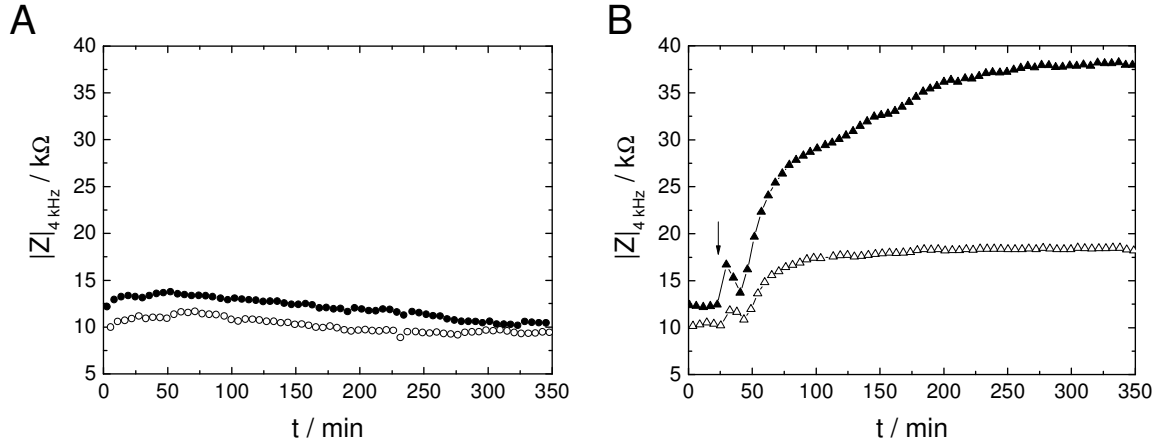

Fig. 6.20: Time course of the impedance magnitude at 4 kHz for HEK-EYFP/pAbcg2 cells grown on *8W1E* ECIS electrodes during incubation (**A**) or along an electroporation experiment (**B**). Cells have been pre-incubated with *PolyMAG* particles (●, ▲) for 20 min before starting the measurement or remained particle-free (○, △). Cell layers in B were additionally electroporated using an AC pulse of 40 kHz, 4 V and 200 ms (arrow). T = 37 °C.

Simple incubation of HEK-EYFP/pAbcg2 cells with *PolyMAG* particles slightly increases the cell layer impedance about 2 kΩ above values for control cells (Fig. 6.20 A). After electroporation of control cell layers the impedance increases from 10.2 kΩ before pulse application to about 18.5 kΩ (B). Cell layers that are pre-incubated with *PolyMAG* particles show a considerable impedance increase to almost 38 kΩ within about 200 min after electroporation. This value is much higer than the impedance obtained for fused HEK-293 wild type cells (cp. Fig. 6.3; Fig. 6.6).

Average impedance values for HEK-EYFP/pAbcg2 cell layers subjected to various conditions like the ones presented above are summarized as a bar diagram (Fig. 6.21). The mean values were calculated from impedance magnitudes $|Z|_{4\ kHz}$ measured 200 min after electric pulse application. Within this time frame most of the impedance time courses of *PolyMAG* pre-incubated and electroporated cell layers had stabilized to their plateau phase. Longer time spans were not analyzed, since some of the *PolyMAG* electrofused cell layers started to show

impedance instabilities (cp. chapter 6.4.1). The mean of $|Z|_{4\ kHz}$ for control cell layers, which were either incubated with *PolyMAG* particles, remained completely untreated or were electroporated without particles, was also calculated from the impedance magnitudes after 200 min.

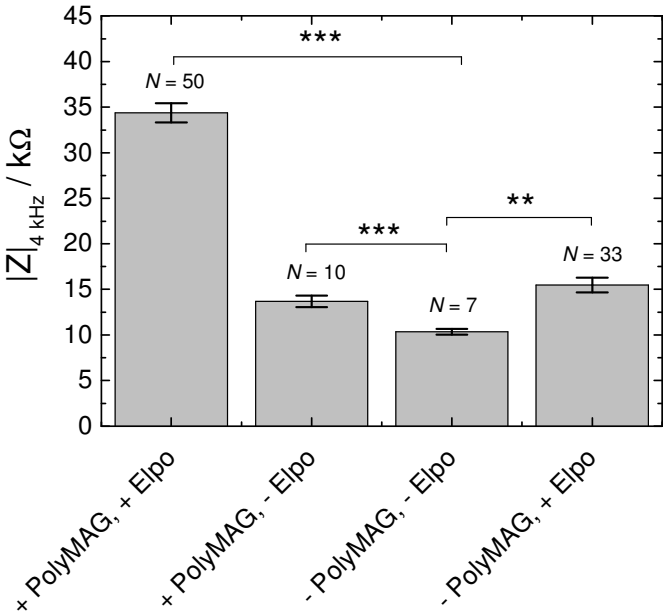

Fig. 6.21: Impedance magnitude at 4 kHz for HEK-EYFP/pAbcg2 cells grown on *8W1E* ECIS electrodes after *PolyMAG* mediated electrofusion (+ *PolyMAG*, + Elpo) compared to control cell layers. Control cell layers were either incubated with *PolyMAG* nanoparticles without electroporation (+ *PolyMAG*, – Elpo), remained completely untreated (– *PolyMAG*, – Elpo) or were only electroporated (– *PolyMAG*, + Elpo). The diagram shows the mean values and the standard errors ($\mu \pm SE$) of $|Z|_{4\ kHz}$ recorded 200 min after electroporation (or corresponding time point in controls) of N individual cell layers (+ *PolyMAG*, + Elpo: (34.4 ± 1.1) kΩ; + *PolyMAG*, – Elpo: (13.7 ± 0.6) kΩ; – *PolyMAG*, – Elpo: (10.4 ± 0.3) kΩ; – *PolyMAG*, + Elpo: (15.5 ± 0.8) kΩ). The level of statistic significance was calculated by ANOVA (**: $P \geq 0.01$; ***: $P \geq 0.001$). T = 37 °C.

A significant impedance increase to a mean value of (34.4 ± 1.1) kΩ is obtained for HEK-EYFP/pAbcg2 cell layers pre-incubated with *PolyMAG* after electroporation. Completely untreated cells show a more than three-fold lower impedance of (10.4 ± 0.3) kΩ. A slight impedance increase can be ascribed to the mere presence of *PolyMAG* particles on the cell layer, yielding a value of (13.7 ± 0.6) kΩ. When HEK-EYFP/pAbcg2 cell layers are only electroporated, the post-pulse impedance rises to (15.5 ± 0.8) kΩ, which is a considerable enhancement compared to completely untreated control cell layers.

When cell layer impedances measured 200 min after electroporation are normalized to their respective pre-pulse values the effect of the electric pulse on the impedance increase becomes apparent for particle-free and *PolyMAG* pre-incubated cells (Fig. 6.22). The electroporation of cell layers incubated with *PolyMAG* particles leads to a more than two-fold impedance increase of 2.44 ± 0.63 compared to pre-pulse conditions. Without *PolyMAG* particles this electroporation-based impedance increase is lower and only accounts for 1.52 ± 0.36.

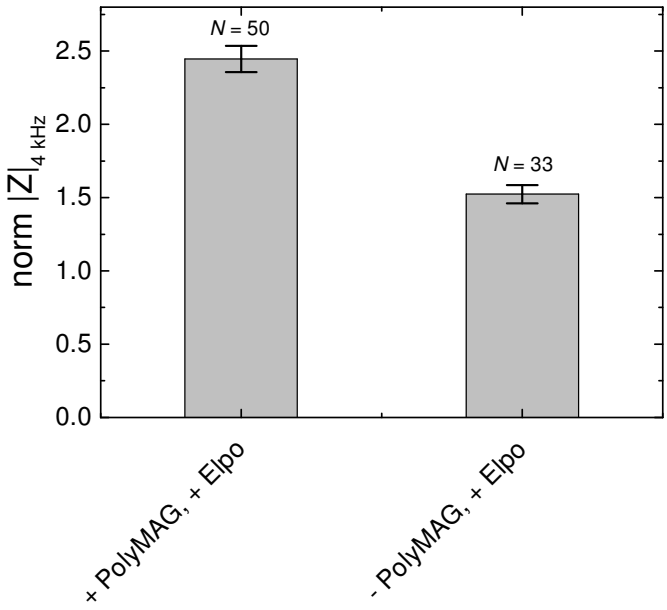

Fig. 6.22: Normalized impedance magnitudes at 4 kHz for HEK-EYFP/pAbcg2 cells grown on *8W1E* ECIS electrodes after incubation with (+ *PolyMAG*) or without (– *PolyMAG*) *PolyMAG* particles and electroporation at 40 kHz with 4 V for 200 ms (+ Elpo). The diagram shows the mean values and the standard errors ($\mu \pm SE$) of norm $|Z|_{4\ kHz}$ of *N* individual cell layers (+ *PolyMAG*: 2.44 ± 0.63, – *PolyMAG*: 1.52 ± 0.36). Absolute impedance values recorded 200 min after electroporation were each normalized to the last value before pulse application. $T = 37$ °C.

In total, the impedance increase of HEK-EYFP/pAbcg2 cells after *PolyMAG* incubation and a single electroporation pulse is considerably higher when compared to the HEK-293 wild type cells (cp. Fig. 6.6; Fig. 6.8). HEK-293 wild type cells pre-incubated with *PolyMAG* particles yielded approximately a two-fold impedance increase when subjected to three successive electroporation pulses but only a 1.5-fold increase when using one electroporation pulse. HEK-EYFP/pAbcg2 cells, in contrast, only require one electroporation pulse to reach an almost 2.5-fold increase of cell layer impedance (Fig. 6.22).
The extraordinary fusogenic response of HEK-EYFP/pAbcg2 cells appeared useful to study the particle enhanced electrofusion phenomenon, so that these cells were predominantly used in further experiments.

6.4 Cell Biological Characterization of Electrofused HEK Cells

As shown in previous chapters large continuous cell bodies can be created by particle-assisted electrofusion. This affects almost the entire cell layer on the electrode (Fig. 6.23 A). Areas of characteristic flat surface topography extended even beyond the active electrode (Fig. 6.23 A – C). Fused cell bodies were found to extend more than 50 µm beyond the active electrode in some regions.
A topographic presentation of CLSM z-stacks recorded for an electrofused HEK-ECFP cell layer (A) compared to an untreated cell layer (B) is provided in Fig. 6.24. This presentation

clearly reveals cell layer smoothening as well as a reduction of cell layer height induced by multi-cell fusion.

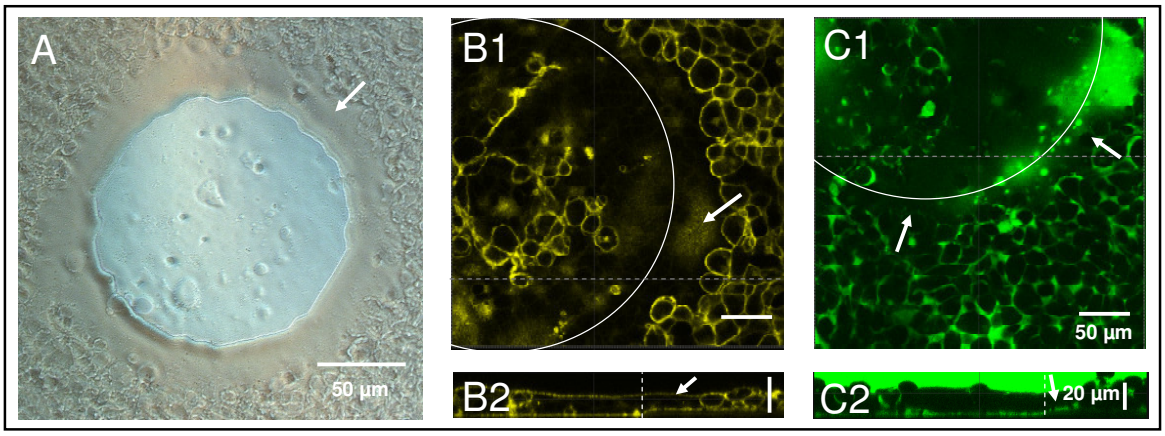

Fig. 6.23: **A:** Phase contrast micrograph of HEK-EYFP/pAbcg2 cells grown on an *8W1E* ECIS electrode after fusion by *PolyMAG* pre-incubation and electroporation (40 kHz, 4 V, 200 ms). **B** and **C:** Confocal fluorescence micrographs of HEK-EYFP/pAbcg2 cells (**B**) and HEK-293 wild type cells covered with 4 kDa FITC-dextran in $EBSS^{++}$ (**C**). Confocal xy-sections show electrofused cell layers extending beyond the electrode borders as indicated by the white circle. In xz-sections (**B2**, **C2**) the electrode border is marked by a white dashed line. Arrows indicate parts of the giant cells that extend beyond the electrode.

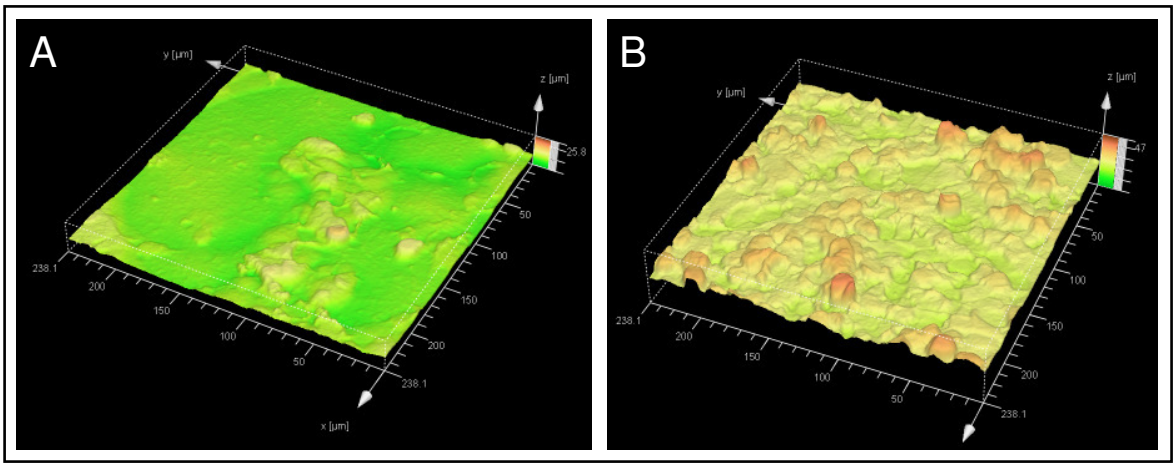

Fig. 6.24: 3D-rendering of confocal microscopic z-stacks recorded for HEK-EGFP cells grown on *8W1E* ECIS electrodes. **A:** Cell layer after fusion by *PolyMAG* pre-incubation and electroporation (40 kHz, 4 V, 200 ms); **B:** Control cells (– *PolyMAG,* – Elpo).

6.4.1 Vitality and Stability of Electrofused HEK Cells

The vitality of cells within a cell layer can be estimated by different staining techniques and microscopic documentation. For example enzymatic activity of vital cells is often addressed via selective dyes like calcein-AM, which can cross the cell membrane and is cleaved to its fluorescent derivate by intracellularly active esterases as shown in Fig. 6.12. Another approach is to detect newly synthesized biomolecules after electrofusion. Following this latter approach, HEK-EYFP/pAbcg2 cells were exposed to *PolyMAG* particles loaded with DNA encoding ECFP about one hour before electrofusion (Fig. 6.25).

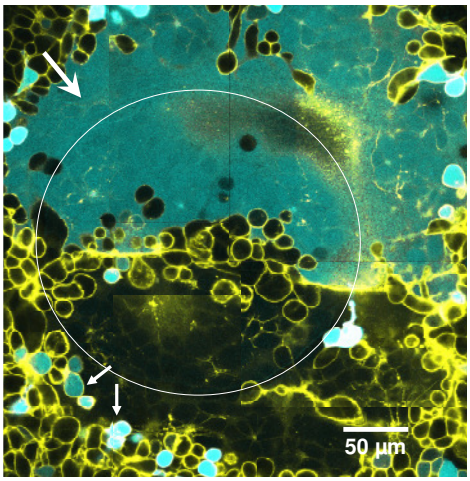

Fig. 6.25: Confocal fluorescence micrograph (composite of various single images of different xy-regions) of HEK-EYFP/pAbcg2 cells grown on an *8W1E* ECIS electrode 24 h after pre-incubation with pECFP loaded *PolyMAG* particles and *in situ* electroporation. The electrode area is delineated by the white circle. Arrows indicate ECFP expressing single cells (→) and fused cells (⟶).

After uptake of the DNA loaded particles the ECFP-gene template can be transcribed into the cyan fluorescing protein by viable cells possessing an active protein synthesis machinery. For the conditions studied here, ECFP synthesis is usually observed for some individual non-electroporated cells located beyond the active electrode due to the transfectious particles (→). Triggered by the electroporation pulse individual cells on the electrode fuse and form adherent giant cells. On the upper side of the electrode one giant cell expanding far beyond the electrode borders shows a continuous cyan fluorescence (⟶). Assuming that within the first hour before electroporation heterologous protein expression is negligible, this experiment indicates that the machinery required for protein synthesis is completely functional in fused giant cells. Additionally, this experiment demonstrates that the cytoplasms of all fused cells share functional proteins and enzymes.

Long-term impedance measurements on fused HEK-EYFP/pAbcg2 cells reveal that adherent HEK giant cells are meta-stable. Figure 6.26 shows three examples for the time course of the cell layer impedance recorded over 24 h after electroporation.

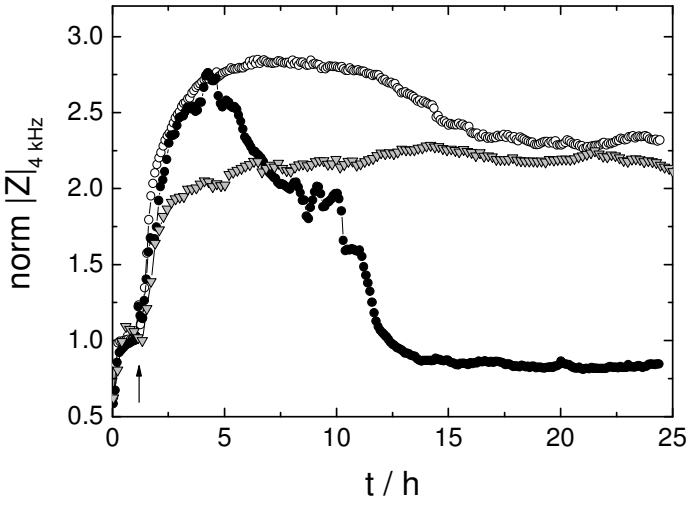

Fig. 6.26: Typical time courses of the normalized impedance magnitude at 4 kHz for HEK-EYFP/pAbcg2 cells grown on *8W1E* ECIS electrodes after *PolyMAG* pre-incubation and electroporation (40 kHz, 4 V, 200 ms) (arrow). Absolute impedance magnitudes were normalized to the last value before electroporation (○: 13.08 kΩ; ●: 12.65 kΩ; ▽: 12.32 kΩ).

The impedance of fused cell layers was observed to be stable not much longer than 24 h. Often, a spontaneous impedance drop was recorded, which occurred at variable time points after electroporation.

Confocal fluorescent micrographs of a fused HEK-EYFP/pAbcg2 cell layer after impedance breakdown are presented in Fig. 6.27. The apical cell membrane shows several defect sites appearing as black holes (arrows in A, B) and exhibits vesicular structures (F) that provide a rough surface topography to the remaining apical membrane (F, B – E, arrows).

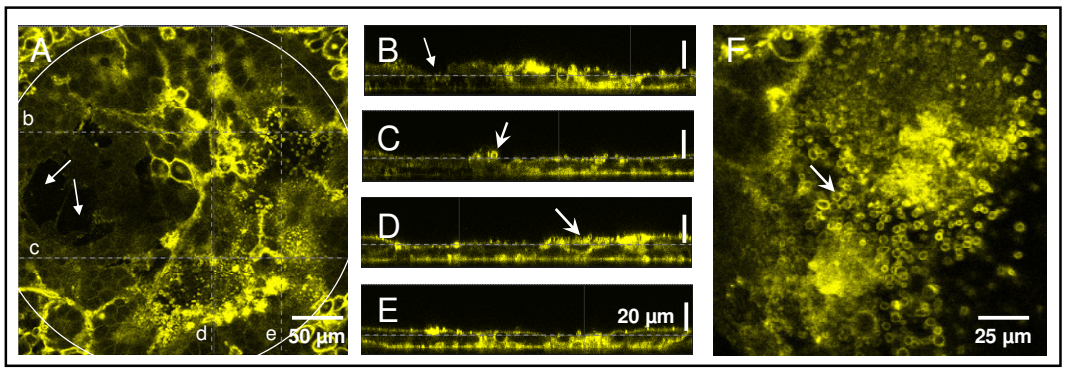

Fig. 6.27: Confocal fluorescence micrographs of HEK-EYFP/pAbcg2 cells pre-incubated with *PolyMAG* particles and electrofused on an *8W1E* ECIS electrode after impedance breakdown. **A:** xy-section along the cell layer as indicated by the dashed lines in B – E. **B** – **E:** xz- and yz-sections of sliced z-stacks as illustrated by dashed lines (b – e) in A. **F:** Magnified xy-section of the apical membrane. The area of the underlying active working electrode is delineated by the white circle (A). Arrows indicate vesicles (⟶) and holes in the cell layer (⟶).

6.4.2 Distribution of Subcellular Structures in Electrofused HEK Cells

For further characterization of fused HEK-EYFP/pAbcg2 giant cells some cellular organelles as well as the actin cytoskeleton were stained using specific cytochemical dyes. The structure and distribution of cell nuclei, mitochondria and filamentous actin was investigated by fluorescence microscopy.

6.4.2.1 Distribution of Nuclei in Electrofused HEK Cells

The nuclear DNA of fused and control HEK-EYFP/pAbcg2 cells was stained with DAPI (cp. chapter 4.4.4.5). As seen in Fig. 6.28 the nuclei of individual cells within control cell layers can be easily distinguished (B – D). They are distributed homogeneously on the electrode surface and the surrounding substrate.
In contrast, nuclei of cells after *PolyMAG* pre-incubation and electrofusion reveal a striking difference in their distribution, which is characterized by local aggregation on the electrode surface as well as on adjacent sites beyond the electrode borders (Fig. 6.28 A). Although certain individual nuclei within clustered aggregates can still be distinguished (Fig. 6.29 C),

their exact number is difficult to determine. Typically, more than about 30 nuclei can be identified in a cluster. Groups of nuclei are separated from one another or individual cells by intercellular membranes as presented in Fig. 6.29 B, C.

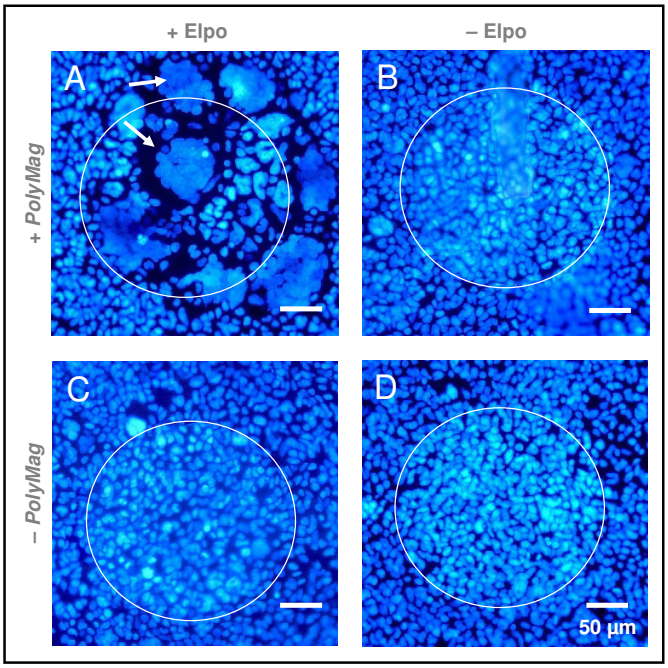

Fig. 6.28: Epifluorescence micrographs of fused (**A**) and control (**B** – **D**) HEK-EYFP/pAbcg2 cells grown on *8W1E* ECIS electrodes after staining of nuclei with DAPI. Cells were pre-incubated with *PolyMAG* particles (+ *PolyMAG*) (**A**, **B**) or remained particle-free (– *PolyMAG*) (**C**, **D**). Cell layers in A and C were electroporated using an AC pulse of 40 kHz, 4 V and 200 ms (+ Elpo). Cells in B and D were not electroporated (– Elpo). The white circles delineate the area of the active electrode. Arrows indicate aggregations of cell nuclei in fused cells.

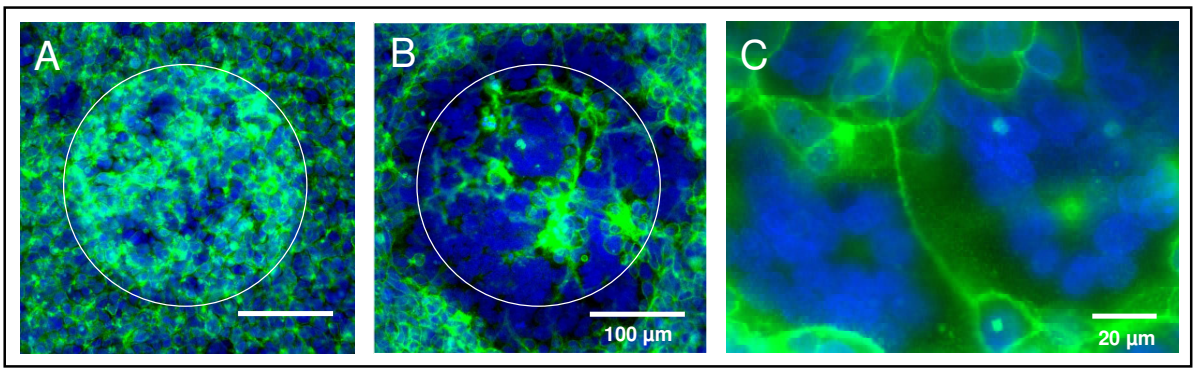

Fig. 6.29: Epifluorescence micrographs of DAPI stained HEK-EYFP/pAbcg2 cells grown on *8W1E* ECIS electrodes after *PolyMAG*-based electrofusion (**B**, **C**) compared to untreated cells (**A**). The overlays of the EYFP and the DAPI fluorescence micrographs were generated by the image analysis software *Image J*. Fluorescence of DAPI stained nuclei is presented in blue. EYFP-membrane fluorescence is presented in green. **C:** Magnified area within an electrofused cell layer.

6.4.2.2 Distribution of Mitochondria in Electrofused HEK Cells

The Mitochondria of HEK-EYFP/pAbcg2 cells were stained with *MitoTracker*® Red (cp. chapter 4.4.4.6). Stained cell layers after *PolyMAG*-based electrofusion as well as control

cells grown on ECIS electrodes were inspected by confocal fluorescence microscopy and are presented in Fig. 6.30.

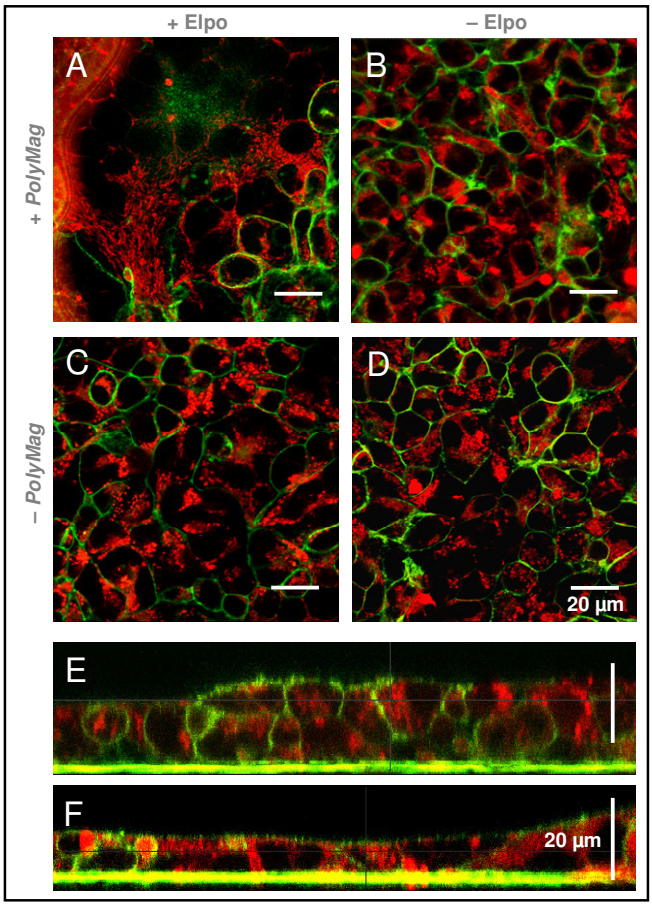

Fig. 6.30: Confocal fluorescence micrographs of fused (**A**, **F**) and control (**B** – **E**) HEK-EYFP/pAbcg2 cells grown on *8W1E* ECIS electrodes after staining of mitochondria with *MitoTracker*® Red. **A** – **D:** xy-sections. **E**, **F:** xz-sections. Cells were pre-incubated with *PolyMAG* particles (+ *PolyMAG*) (**A**, **B**, **F**) or remained particle-free (– *PolyMAG*) (**C**, **D**, **E**). Cell layers **A**, **C** and **F** were electroporated using an AC pulse of 40 kHz, 4 V and 200 ms (+ Elpo). Cells in **B**, **D** and **E** were not electroporated (– Elpo). Images show overlays of both fluorescence channels created by the image analysis software *Image J*. EYFP membrane fluorescence is presented in green, *MitoTracker*® fluorescence is presented in red.

Figure 6.30 presents overlays of the EYFP fluorescence of the membrane label and the *MitoTracker*® fluorescence for confocal xy-sections, showing only parts of the respective cell layer on the electrode. The xz-sections of fused cells (F) and untreated control cells (E) are shown as well.

In fused cells mitochondria are distributed in the entire cytoplasm of the giant cell (A, F). No aggregation or significant morphological alteration compared to control cell layers (B – E) can be detected. Mitochondria are found in the free cytoplasmic space, which is not occupied by the nuclei. Figure 6.31 shows a magnified region within an electrofused HEK-EYFP/pAbcg2 cell layer. The fact that stained mitochondria are localized between nuclear clusters indicates that nuclei have not fused (Fig. 6.31 A). Fig. 6.31 B indicates that some membrane surrounded entities – presumably created during electrofusion – do not seem to contain a nucleus (arrow).

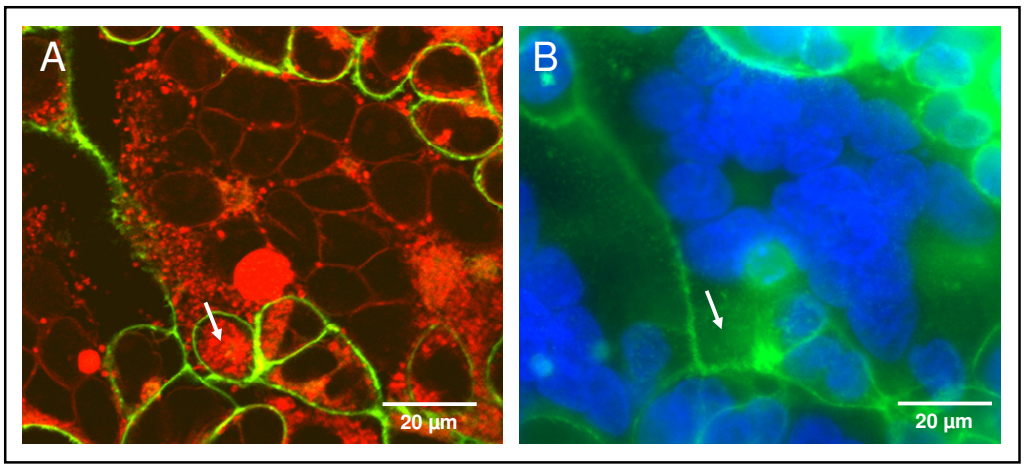

Fig. 6.31: Confocal fluorescence (**A**) and epifluorescence (**B**) micrographs of electrofused HEK-EYFP/pAbcg2 cells grown on *8W1E* ECIS electrodes after staining with *MitoTracker*® Red and DAPI. Overlays were created using the image analysis software *Image J*. Membrane fluorescence of EYFP is presented in green, mitochondria in red and nuclei are blue. The arrow marks a mitochondria-filled, nucleus-free vesicular body.

6.4.2.3 Distribution of the Actin Cytoskeleton in Electrofused HEK Cells

The actin cytoskeleton of HEK-EYFP/pAbcg2 cells was stained with TRITC labeled phalloidin (cp. chapter 4.4.4.3). Figure 6.32 presents confocal fluorescence micrographs of fused cell layers after *PolyMAG* pre-incubation and electric pulse application (A) compared to non-fused control cell layers (B – D).

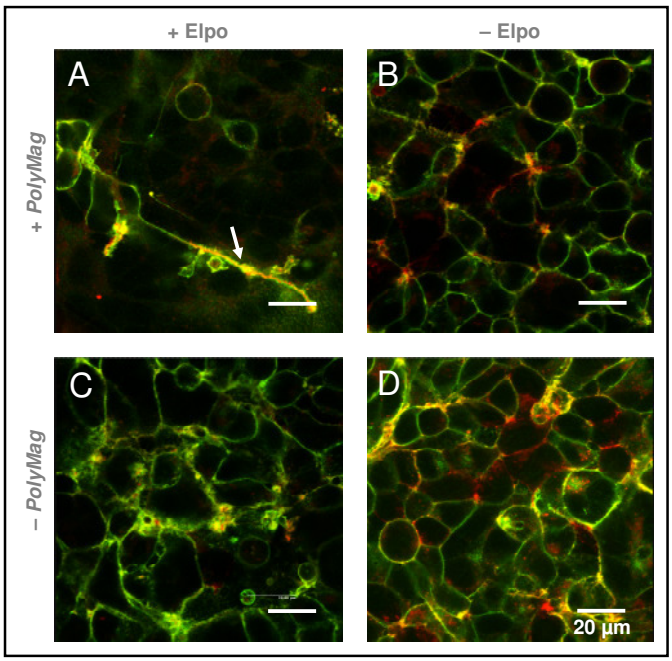

Fig. 6.32: Confocal fluorescence micrographs of fused (**A**) and control (**B** – **D**) HEK-EYFP/pAbcg2 cells grown on *8W1E* ECIS electrodes after staining of filamentous actin with TRITC-phalloidin. Cells were pre-incubated with *PolyMAG* particles (+ *PolyMAG*) (**A**, **B**) or remained particle-free (– *PolyMAG*) (**C**, **D**). Cell layers **A** and **C** were electroporated using an AC pulse of 40 kHz, 4 V and 200 ms (+ Elpo). Cells in **B** and **D** were not electroporated (– Elpo). Images show overlays of both fluorescence channels created by the image analysis software from Leica (green: Membrane fluorescence of EYFP; red: TRITC-phalloidin fluorescence). Areas of colocalization appear yellow. The arrow in A marks fused cell membranes.

The amount of cytoplasmic actin fibres is low in both, fused giant cells (A) and control cells (B – D). No distinct stress fibres spanning the cytoplasm can be observed. The actin is predominantly detected near the cell membrane co-localizing at sites of cell junctions (B – D). Also in fused cells the actin can be preferentially found in co-localization with fused membranes (A, arrow). Due to the overall low amount of filamentous actin in HEK-EYFP/pAbcg2 cells, no striking change in actin distribution after fusion is detected.

6.5 Online Monitoring of *In Situ* Cell Fusion

When cell fusion is triggered by application of an electric pulse, individual fusion events take place on the electrode surface. Microscopic images presented before (chapters 6.1 – 6.4) document the cell layer status at the end of the fusion process and in comparison to non-fused control cell layers.
In order to visualize individual fusion events taking place within one cell layer a time series of CLSM images was recorded after the fusion process was triggered electrically by electroporation. A tailor-made experimental setup allowed parallel CLSM recordings and impedance measurements. Selected images recorded at different time points before and after electroporation are shown in Fig. 6.33 A. The corresponding time course of impedance continuously monitored during the fusion process is presented in Fig. 6.33 B.

The image taken 0.5 min after electroporation during the initial impedance drop reveals only minor morphological changes of individual cells compared to pre-pulse conditions (– 2 min) but no indications of cell fusion (Fig. 6.33 A). First significant alterations of membrane structure (A) are detected 5 min after the electric trigger when the impedance of the cell layer is still below pre-pulse values (B). Major alterations with respect to the amount and distribution of membranes are observed within the first 30 min (A). In this time frame the cell layer impedance re-attains pre-pulse values (B). Afterwards local membrane alterations become less evident but specific differences or changes are hard to detect (A, 30 – 285 min). The normalized impedance shows a steep increase beyond pre-pulse values about 25 – 75 min after electroporation and finally stabilizes at around 2.5 after 200 min (B). In the last 100 min of data acquisition the impedance signal becomes instable and starts to fluctuate around the plateau value.

A

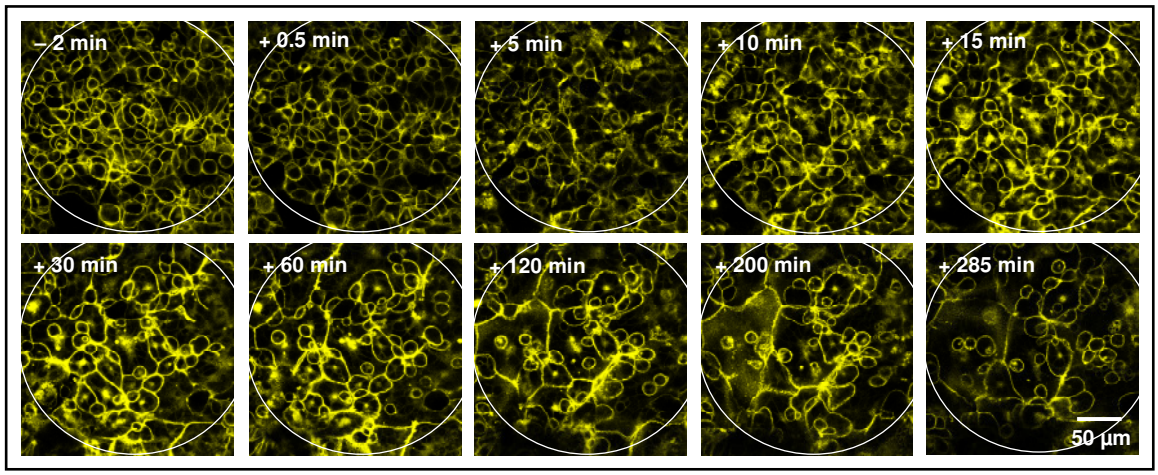

B

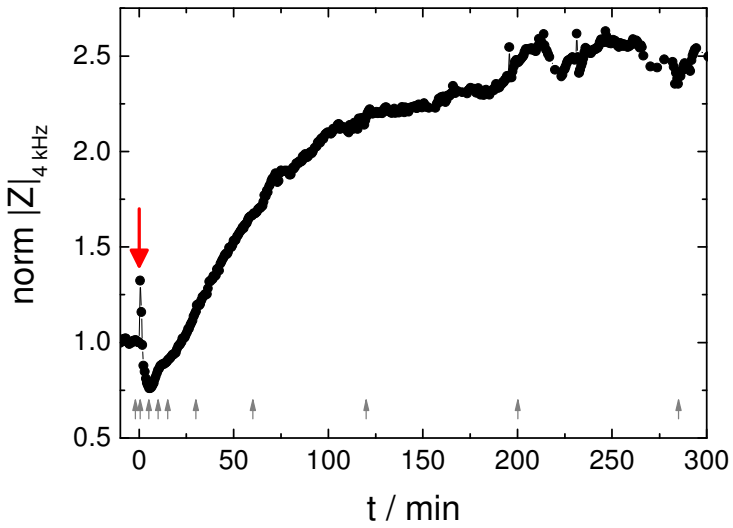

Fig. 6.33: Time series of confocal fluorescence micrographs (**A**) and the corresponding time course of the normalized impedance magnitude at 4 kHz (**B**) of HEK-EYFP/pAbcg2 cells grown on a *8W1E* ECIS electrode during the fusion process initiated by *PolyMAG* pre-incubation and electric field application (40 kHz, 4 V, 200 ms) (A: $t = 0$; B: red arrow). Time points (– 2, 0.5, 5, 10, 15, 30, 60, 120, 200 and 285 min) of CLSM image recordings are indicated by grey arrows in the graph. $T = 37$ °C.

Despite an optimal labeling of the cell layer by the recombinant EYFP fusion protein, it was very difficult to detect single membrane fusion events from confocal images (Fig. 6.33 A). To provide a sufficient time resolution data from a single confocal xy-plane have been recorded that can not correctly trace a three-dimensional process in a multi-layered cell ensemble. Impedance measurements, in contrast, provide an average measure for all individual fusion events taking place within the cell layer. Impedance measurements provide a significantly better time resolution and kinetic information on the whole fusion process and can therefore compensate for microscopic limitations.

6.6 Modeling *PolyMAG*-Mediated *In Situ* Electrofusion

PolyMAG pre-incubated cell layers start to fuse after exposure to an electroporation pulse. The associated increase of impedance magnitude can be recorded at a monitoring frequency of 4 kHz as presented in the chapters before (Fig. 6.34 A). The corresponding impedance spectrum that has been recorded for every time point can be analyzed (Fig. 6.34 B). The first spectrum recorded after electroporation (dotted line) is increased compared to the pre-pulse spectrum (○) in the range of 10^3 – 10^4 Hz, but is shifted to lower impedances in the higher frequency range above 10^4 Hz. The second impedance spectrum recorded after electric pulsing shows a similar frequency dependence as the base line spectrum, while it is still shifted to lower impedances above 10^4 Hz.

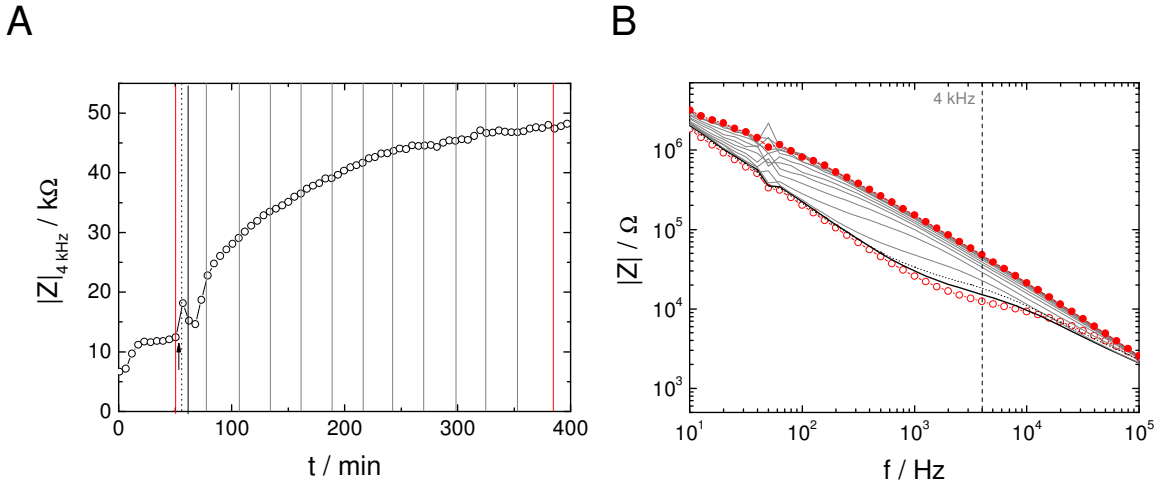

Fig. 6.34: Impedimetric measurements during the fusion process of HEK-EYFP/pAbcg2 cells. **A:** Time course of the normalized impedance magnitude at 4 kHz of *PolyMAG* pre-incubated HEK-EYFP/pAbcg2 cells grown on *8W1E* ECIS electrodes before and after electroporation (40 kHz, 4 V, 200 ms) (arrow). Red lines mark data points before and after fusion, while grey lines indicate selected time points in between. **B:** Corresponding impedance spectra for selected time points marked by lines in A. Spectra are indicated as follows: ○: before electroporation; ····: first spectrum after electroporation; ▬: second spectrum after electroporation; ●: after fusion; ▬: spectra at time points in between. T = 37 °C.

When impedance spectra of the cell layer before (○) and after (●) fusion are compared to each other striking differences in the shape of the spectra become apparent (Fig. 6.34 B). The impedance spectrum of a fused HEK-EYFP/pAbcg2 cell layer (●) shows a significant shift to higher impedances in the frequency range between 10 and 10^4 Hz (Fig. 6.34 B). In the beginning of the fusion process ($t \leq 135$ min) the shape of the impedance spectra shows strong alterations in the 4 kHz range. But as time progresses changes in the impedance spectrum are predominantly observed at lower frequencies (100 – 10^3 Hz), while the impedance changes at 4 kHz saturate. As a result, at a monitoring frequency of 4 kHz after an initial steep increase within the first hour after electroporation the impedance reaches a plateau value (A). This means that a monitoring frequency of 4 kHz is sensitive for early events in the course of the fusion process, but becomes insensitive for later fusion events. Later fusion events are more sensitively detected when using a lower monitoring frequency, which is however not sensitive at low fusion levels in the beginning of the process.

As the shape of an impedance spectrum obtained for a manipulated cell layer can provide information about the nature of cell morphology changes within the cell layer, impedance spectra of electrofused cells were analyzed by the model of Giaever and Keese (1991), which has been adapted by our group (chapter 6.6.1).

6.6.1 Analysis of Multi-Cell Fusion on ECIS Electrodes Based on the Model of Giaever and Keese

The model developed by Giaever and Keese provides three individual parameters α, R_b and C_m which can be used to describe morphological characteristics of a cell layer. Changes in cell layer impedance can be analyzed with this model in order to reveal the altered morphological properties of the manipulated cell layer (cp. Theoretical Background, chapter 3.1.3). Thus, comparison of the model parameters of untreated cell layers and manipulated cell layers can provide useful information about the mechanism behind the observed changes in cell layer impedance. The parameters α, R_b and C_m for HEK-293, HEK-EGFP and HEK-EYFP/pAbcg2 cells under different experimental conditions are presented in Tab. 6.1.

Tab. 6.1: ECIS parameters α, R_b and C_m for HEK cell lines under different conditions. Cells remained untreated (– *PolyMAG*, – Elpo), were exposed to either *PolyMAG* particles (+ *PolyMAG*, – Elpo) or electroporation (40 kHz, 4 V, 200 ms) (– *PolyMAG*, + Elpo) or were fused by exposure to both (+ *PolyMAG*, + Elpo). Parameter values were extracted from impedance spectra recorded 100 min (HEK-293, HEK-EGFP) or 200 min (HEK-EYFP/pAbcg2) after electric pulse application or equivalent time points. ECIS parameters are given as mean and standard deviation ($\mu \pm SD$) of N individual cell layers.

	HEK Cell Line	α [$\Omega^{1/2} \cdot$ cm]	R_b [$\Omega \cdot$ cm^2]	C_m [µF/cm^2]	N
– *PolyMAG*, – Elpo	HEK-293	3.1 ± 0.7	2.0 ± 0.6	2.2 ± 0.3	20
	HEK-EGFP	3.3 ± 0.6	2.0 ± 0.3	2.3 ± 0.3	7
	HEK-EYFP/pAbcg2	3.0 ± 0.6	2.0 ± 0.6	2.3 ± 0.5	48
+ *PolyMAG*, – Elpo	HEK-293	4.4 ± 0.4	3.2 ± 0.8	1.4 ± 0.4	16
	HEK-EGFP	3.70 ± 0.3	2.8 ± 0.4	2.3 ± 0.4	9
	HEK-EYFP/pAbcg2	4.4 ± 0.6	3.2 ± 0.7	2.1 ± 0.4	25
– *PolyMAG*, + Elpo	HEK-293	4.3 ± 0.7	2.0 ± 0.4	1.9 ± 0.4	15
	HEK-EGFP	4.7 ± 0.4	2.0 ± 0.1	2.1 ± 0.3	3
	HEK-EYFP/pAbcg2	7.8 ± 2.4	2.5 ± 1.7	2.0 ± 0.8	15
+ *PolyMAG*, + Elpo	HEK-293	11.7 ± 3.3	3.2 ± 0.9	1.7 ± 0.4	30
	HEK-EGFP	13.4	5.6	2.0	1
	HEK-EYFP/pAbcg2	37.6 ± 17.3	10.6 ± 10.9	2.0 ± 0.4	31

Under normal conditions **(– *PolyMAG*, – Elpo)** mean values for the three parameters α, R_b and C_m are similar for all investigated HEK cell lines. Values for α account for ~ 3 $\Omega^{1/2} \cdot$ cm and R_b was determined to ~ 2 $\Omega \cdot$ cm^2 for all three cell lines. Also the parameter C_m shows similar values slightly above 2 µF/cm^2.

Incubation of the three different HEK cell lines with *PolyMAG* particles **(+ *PolyMAG*, – Elpo)** causes slight increases of the parameters α and / or R_b. The parameter α is determined to be $(4.4 \pm 0.4)\ \Omega^{1/2} \cdot \text{cm}$ for HEK-293 and $(4.4 \pm 0.6)\ \Omega^{1/2} \cdot \text{cm}$ for HEK-EYFP/pAbcg2 cells, which is slightly enhanced compared to untreated cells (HEK-293: $(3.1 \pm 0.7)\ \Omega^{1/2} \cdot \text{cm}$; HEK-EYFP/pAbcg2: $(3.0 \pm 0.6)\ \Omega^{1/2} \cdot \text{cm}$). For HEK-EGFP cells the change in α is insignificant. R_b is increased for HEK-EGFP cells, yielding $(2.8 \pm 0.4)\ \Omega \cdot \text{cm}^2$ compared to $(2.0 \pm 0.3)\ \Omega \cdot \text{cm}^2$ without *PolyMAG* particles. The membrane capacitance C_m does not show significant changes for recombinant HEK cell lines but is decreased for HEK-293 wild type cell layers to $(1.40 \pm 0.4)\ \mu\text{F/cm}^2$.
Parameter values for HEK cell lines after electroporation in particle-free culture medium **(– *PolyMAG*, + Elpo)** were determined as well. The influence of electroporation was evaluated 100 min (HEK-293, HEK-EGFP) or 200 min (HEK-EYFP/pAbcg2) after electric pulse application, which was the required time period for reaching the plateau phase in the electrofusion process. After electroporation in particle-free medium only α changes compared to untreated cell layers. This parameter is increased to $(4.7 \pm 0.4)\ \Omega^{1/2} \cdot \text{cm}$ and $(7.8 \pm 2.4)\ \Omega^{1/2} \cdot \text{cm}$ for the recombinant HEK-EGFP and HEK-EYFP/pAbcg2 cells, respectively. Values for R_b and C_m are not significantly changed compared to untreated cells.
After *PolyMAG* assisted *in situ* electrofusion of HEK cells **(+ *PolyMAG*, + Elpo)** values for the model parameters α and R_b significantly increase whereas the parameter C_m remains in the same range as observed for control cell layers. Especially the change of α for electrofused HEK-EYFP/pAbcg2 cells yielding $(37.6 \pm 17.3)\ \Omega^{1/2} \cdot \text{cm}$ is striking. The reason for the high standard deviation can be ascribed to the considerable variations in the impedance yields after fusion (cp. Fig. 6.21). After electroporation of *PolyMAG* pre-incubated HEK-293 wild type cell layers α accounts for $(11.7 \pm 3.3)\ \Omega^{1/2} \cdot \text{cm}$. Fused HEK-EGFP cells reveal a value for α in a similar range $(13.4\ \Omega^{1/2} \cdot \text{cm})$. HEK-EGFP and HEK-EYFP/pAbcg2 cells moreover show increased R_b values which are $5.6\ \Omega \cdot \text{cm}^2$ and $10.6 \pm 10.9\ \Omega \cdot \text{cm}^2$, respectively. The individual values for the variations in R_b for electrofused HEK-EYFP/pAbcg2 cell are very high. The parameter R_b of different fused cell layers ranged between 1.7 and 46.9 $\Omega \cdot \text{cm}^2$. The change of R_b after electrofusion of HEK-293 cells is insignificant compared to untreated cells.

The following figures 6.35 and 6.36 illustrate the development of the individual model parameters during an electroporation or fusion process of HEK-293 as well as HEK-EYFP/pAbcg2 cells. The time course of the three parameters α, R_b and C_m (C, D) was extracted from the spectra of the respective time resolved impedance measurements (A, B).

Comparison of the time course of $|Z|$ at a monitoring frequency of 4 kHz after electroporation of particle-free HEK-293 cell layers (Fig. 3.35 A1) with the time course of α (Fig. 3.35 A2) reveals striking similarities. After electroporation both, $|Z|_{4\ \text{kHz}}$ and α, transiently increase and subsequently settle down to pre-pulse values after 150 min. While the membrane capacitance C_m remains almost unchanged after electroporation, R_b shows a slight initial decrease and a subsequent recovery to pre-pulse values within 100 min.

The electric trigger for initiation of the *PolyMAG* assisted *in situ* cell fusion typically recorded at 4 kHz (B1) mainly induces changes in the parameter α (B2). The electric pulse causes a slight but transient increase of the membrane capacitance C_m, which is enhanced compared to cell layers that were electroporated without *PolyMAG* particles (A2). For *PolyMAG* pre-incubated cells also the response of R_b after the electric pulse is enhanced when compared to simple electroporation. R_b drops from about 3 to about 1.5 $\Omega \cdot cm^2$ and recovers slightly above pre-pulse values within about 100 min. However, only for a few electrofusion measurements using HEK-293 cells R_b increased significantly, whereas other measurements only revealed a post-pulse recovery of R_b to slightly above or below pre-pulse conditions.

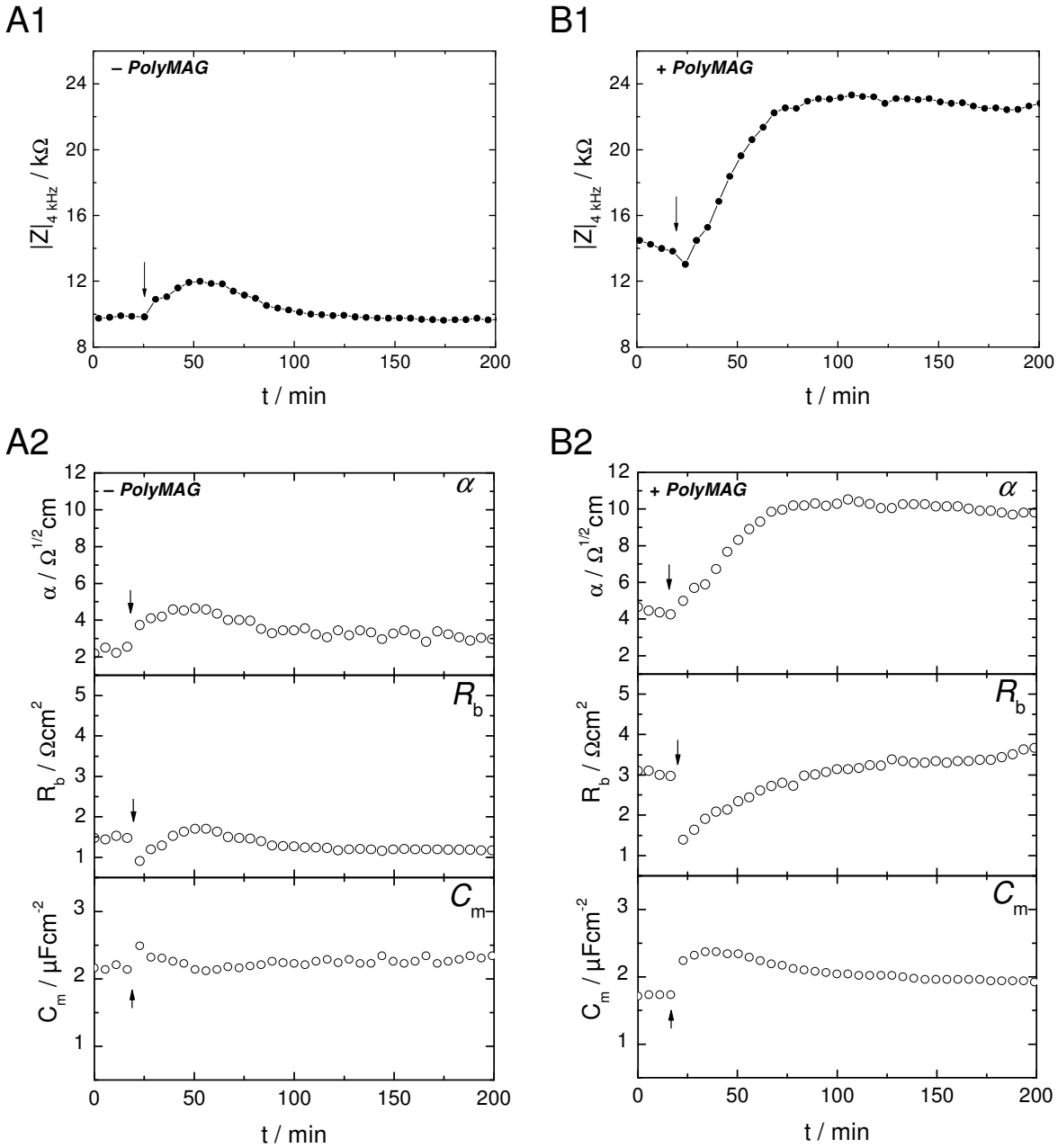

Fig. 6.35: Time course of the impedance magnitude $|Z|_{4\ kHz}$ (**A1**, **B1**) and the model parameters α, R_b and C_m (**A2**, **B2**) before and after electroporation (arrow) of particle-free (**A1**, **A2**) or *PolyMAG* pre-incubated (**B1**, **B2**) **HEK-293** cell layers. T = 37 °C.

As previously described HEK-293 cells show a rather moderate fusion response after an electroporation trigger, predominantly influencing the parameter α. A considerable extent of multi-cell fusion was observed for HEK-EYFP/pAbcg2 cells as elucidated by the enormous impedance increase monitored at 4 kHz. The time courses of impedance after simple electroporation as well as after electroporation triggered fusion of *PolyMAG* pre-incubated HEK-EYFP/pAbcg2 cell layers were analyzed with respect to the model parameters α, R_b and C_m, as previously shown for HEK-293 wild type cells. Typical time courses of |Z| at 4 kHz are shown in Fig. 6.36 A1 and B1. The development of the model parameters extracted from the impedance spectra are presented in Fig. 6.36 A2, B2.

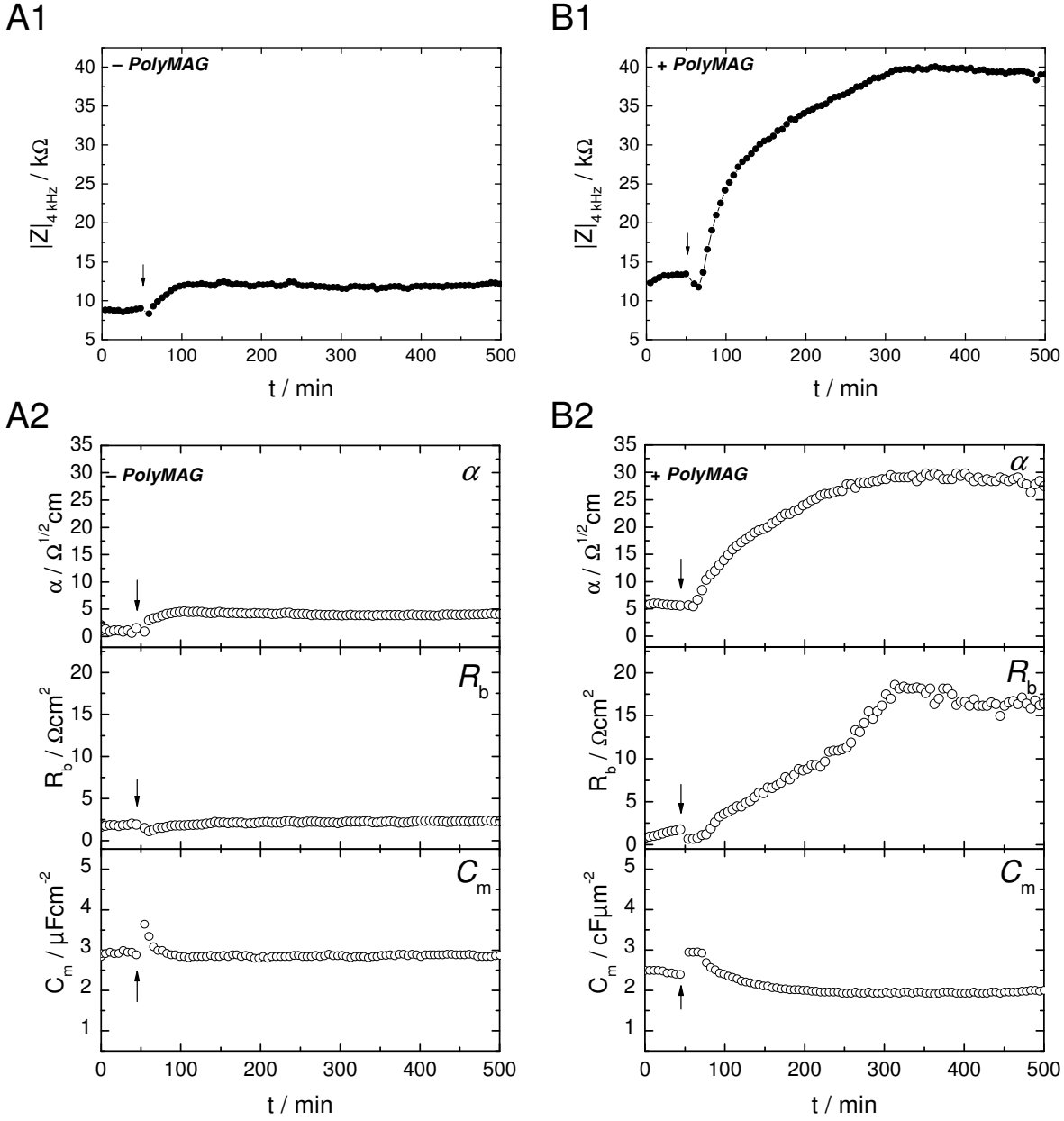

Fig. 6.36: Time course of the impedance magnitude $|Z|_{4\ kHz}$ (**A1**, **B1**) and the model parameters α, R_b and C_m (**C**, **D**) before and after electroporation (arrow) of particle-free (**A1**, **A2**) or *PolyMAG* pre-incubated (**B1**, **B2**) **HEK-EYFP/pAbcg2** cell layers. T = 37 °C.

Electroporation of HEK-EYFP/pAbcg2 cells (Fig. 6.36 A1) induces an increase of α from 1.5 $\Omega^{1/2} \cdot$ cm to a constant plateau of ~ 4 $\Omega^{1/2} \cdot$ cm within 60 min (A2). Values for R_b decrease from 1.9 to 1.3 $\Omega \cdot cm^2$ within the first 15 min after pulse application and recover to pre-pulse values in the following 60 min. The membrane capacitance transiently increases after electroporation to 3.7 $\mu F/cm^2$ but settles down again to initial values of ~ 3 $\mu F/cm^2$ within 30 min. Electric destabilization of *PolyMAG* pre-incubated HEK-EYFP/pAbcg2 also induces a transient increase of C_m (B2). Afterwards, the membrane capacitance slowly decreases by ~ 0.5 $\mu F/cm^2$ below pre-pulse values to ~ 2 $\mu F/cm^2$ within ~ 120 min. A substantial change after the electric trigger is observed for the parameters α and R_b. Values for α start to increase after electroporation with a delay of about 20 min. Over 240 min α continuously increases from ~ 5 $\Omega^{1/2} \cdot$ cm to a plateau value at ~ 29 $\Omega^{1/2} \cdot$ cm. The course of α resembles the time course of $|Z|_{4\,kHz}$ (B1). Although also R_b increases after electric pulsing, the curve development is rather linear in the first 360 min after initiating the fusion process and afterwards abruptly bends into a plateau of about 17 $\Omega \cdot cm^2$.

6.6.2 Simulation of Multi-Cell Fusion Using the Model of Giaever and Keese

In order to unravel if the observed changes of the parameters α and R_b can be correlated to the observed multi-cell fusion process, impedance spectra for fused cells were simulated assuming certain morphological changes, as they were observed by microscopic analysis of the fusion process.

6.6.2.1 Simulation Procedure

When considering initially individual cells that fuse and form polynucleated cellular bodies, morphological alterations occur, mainly due to an increasing average size of the cell bodies on the electrode surface. A reduction of the number of cellular entities by fusion will result in a decreased amount of intercellular spaces while the overall area of the cell-covered active electrode stays constant. Moreover, the surface area which is covered by one cellular body will increase on average after fusion. All these effects are schematically illustrated in Fig. 6.37. Though the illustration sketches cellular bodies as squares for simplicity, in the following considerations individual cells as well as fused cells are approximated by disk-shaped bodies with radius *r*.

The model described by Giaver and Keese (1991) (cp. chapter 3.1) provides cell layer specific parameters which describe changes in the cell-cell contacts as well as the cell-electrode junctions. Values for α and R_b are average quantities that describe the mean properties of the cells on the gold-film electrode. The model approximates cellular bodies as circular discs that hover in a certain distance above the electrode. Based on *LabView* a calculation software was developed that computes the expected changes for the parameters α and R_b when the average radius of individual cells covering an ECIS electrode with a size of 5×10^{-4} cm^2 changes.

Calculations are based on α and R_b values that were obtained from experimental data for cell layers of individual HEK cells pre-incubated with *PolyMAG* particles before fusion (Tab. 6.1, + *PolyMAG*, – Elpo).

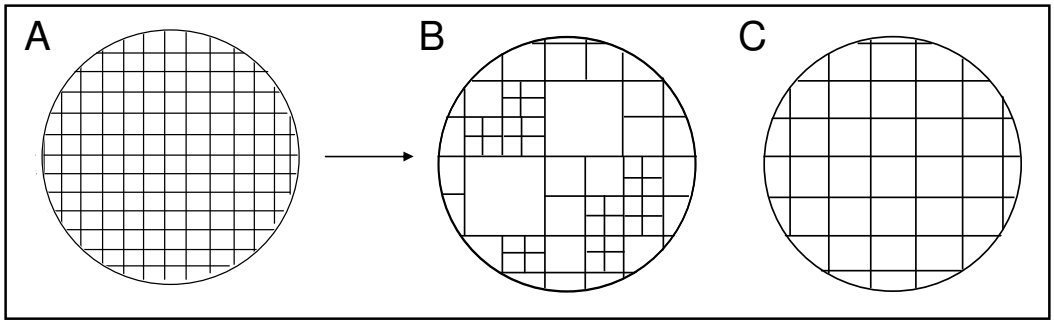

Fig. 6.37: Schematic illustration of the effect of *in situ* cell fusion on the number of intercellular clefts and the size of the cell-surface contact area. The circle with the grating sketches the electrode area covered by a cell layer of individual cells. A cellular entity is illustrated as a square for simplicity. Lines represent cell-cell contacts while white areas illustrate cell-electrode contact areas. Membrane fusion of individual small entities (**A**) results in the formation of large cellular bodies, leading to a reduction of the total length of cell-cell contacts (**B**). Since the electric impedance measurement can not distinguish local inhomogenities in the distribution of cell-cell contact sites, calculations are based on average changes of the size of cell-electrode contact areas as well as the total length of cell-cell contacts evenly distributed over the electrode area (**C**).

Calculation of R_b

R_b describes the resistance imposed by the cell-cell contacts. The specific tightness of cell-cell contacts as well as the total length of intercellular clefts covering the electrode influence the value of R_b. When initially individual cells with a certain amount of cell-cell contacts fuse and form multinucleated cell bodies, the total length of clefts within the cell layer covering the electrode will be reduced. For an ECIS electrode with a surface area of 5×10^{-4} cm^2 the resistance arising from the cell-cell contacts is expected as R_b. The resistance contribution per cm of cell-cell contacts in non-fused cells can then be determined. After fusion the reduced total length of clefts provides a new value for the resistance of cell-cell contact, which can be used to calculate the value for R_{bf}, a new parameter for the cell-cell contact resistance of fused cells.

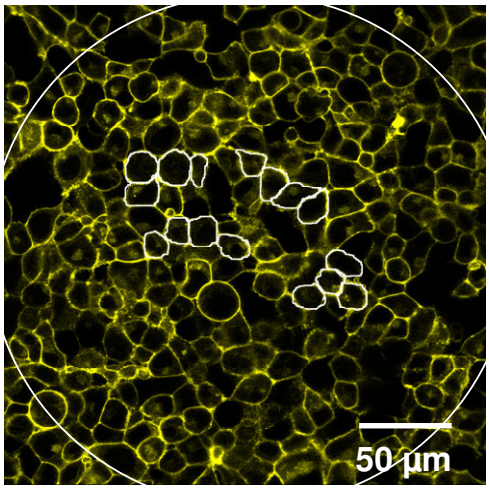

Fig. 6.38: Exemplary confocal fluorescence micrograph of a HEK-EYFP/pAbcg2 cell layer grown on an *8W1E* ECIS electrode used to determine the average HEK cell perimeter. White lines that trace the cell perimeter of some cells were inserted using the image analysis software *Image J* .

The total length of cell-cell contacts L of an intact cell layer was calculated from the average cell perimeter P of non-manipulated HEK cells. CLSM images of HEK-EYFP/pAbcg2 cells with intrinsic membrane fluorescence were analyzed by *Image J* image analysis (Fig. 6.38). Using a manually controlled tracing line the cell contours of 105 individual cells were drawn. *Image J* provides the perimeters of each cell in pixel and calculates an average value (218 ± 45). Pixel data were converted to a length scale (1 pixel = 0.2325 µm) yielding a mean perimeter P for a HEK cell of 50.69 ± 10.46 µm.
Because simulations do not consider the error of a value, further calculations do not consider error values of each quantity. According to $r = P/2\pi$, the mean radius of a HEK cell was determined as 8.07 µm (Tab. 6.2). If the cell bodies are regarded as circular discs as proposed by Giaever and Keese, the mean cell-substrate area covered by a cell is $A = \pi \cdot r^2 = 2.04 \times 10^{-6}$ cm^2. The cell number per electrode can be calculated from the electrode area and the mean area that is covered by one cell. For simplicity, cells are approximated to cover the entire electrode without gaps. This approximation seems to be justified when considering the close cell-to-cell alignment seen in the CLSM image (Fig. 6.38). Calculations do not consider cell growth in multi-layers. Thus, on average 245 cells are expected to cover one circular ECIS electrode.

Tab. 6.2: Parameters for non-fused cells used for the calculation of α and R_b after multi-cell fusion. After fusion the respective parameters (X) are indicated by the subscript f.

Parameter	Description	Value
α	impedance contribution of the cell-substrate contact area	4.37 $\Omega^{1/2} \cdot$ cm (HEK-293 + *PolyMAG*)
R_b	impedance contribution of the cell-cell contact area	3.21 $\Omega \cdot$ cm^2 (HEK-293 + *PolyMAG*)
P	cell perimeter	50.7 µm
L	total length of cell-cell contact zones	0.621 cm
r	HEK cell radius	8.07 µm
A	cell-subtrate area per cell	2.04×10^{-6} cm^2
$A_{electrode}$	surface area of *8W1E* ECIS electrode	5×10^{-4} cm^2
R_{cc}	resistance per cm of cell-cell contact	3986.8 $\Omega \cdot$ cm
n	average number of fusing cells	variable
X_f	corresponding parameter for fused cells	calculated as a function of n

The sum of the total intercellular contact sites L on an electrode is calculated by the product of the cell number per electrode and divided by two. The division is neccesary as cell-cell contacts are always shared between two cells. The calculation yields an average perimeter of 0.621 cm. *PolyMAG* pre-incubated, confluent HEK-293 cell layers for example show an R_b value of 3.21 ± 0.77 $\Omega \cdot$ cm^2. With the mean for R_b and an ECIS electrode with a surface area of 5×10^{-4} cm^2 the resistance arising from the cell-cell contact zones is calculated to be

6420 Ω. This resistance can be distributed among the total length of all intercellular contact sites of 0.621 cm for an untreated cell layer. The resulting resistance per cm of cell-cell contact then corresponds to $R_{cc} = 3986.8\ \Omega \cdot \mathrm{cm}$. Multiplying this quantity with the total length of cell-cell contacts after multi-cell fusion provides a new parameter R_{bf}, the intercellular resistance after fusion of n cells on average. The total length of cell-cell contacts after fusion L_f of n cells is obtained via the mean cell area A_f and the perimeter P_f of fused cells. A_f of fused cells is calculated by simple division of the electrode area $A_{electrode}$ by the number of cellular bodies obtained after fusion. The number of cellular bodies after fusion is calculated by dividing the number of cells before fusion by the average number of cells (n) having fused.

Calculation of α

The parameter α is defined as $\alpha = r \cdot (\delta/h)^{1/2}$ and describes the resistance of the cell-electrode junction. When cells fuse the parameter α will change due to changes in the average cell radius r, whereas the factor containing the specific conductivity δ in the cell-substrate cleft and the distance h of the basal cell membrane to the underlying electrode are assumed to be constant. For non fused cell layers the square root factor $(\delta/h)^{1/2}$ can be calculated using the mean α calculated for *PolyMAG* incubated cells and their mean cell radius as determined from microscopic images (Fig. 6.38) ($r = 8.07 \times 10^{-4}$ cm). For example for *PolyMAG* pre-incubated confluent HEK-293 cell layers data fitting provides a mean α of $(4.37 \pm 0.44)\ \Omega^{1/2} \cdot \mathrm{cm}$ and a square root factor of 5415 $\Omega^{1/2}$. The product of this factor and the mean radius of fused cellular bodies r_f finally yields the new parameter α_f for the cell layer after fusion.

Simulation of Impedance Spectra with α_f and R_{bf} for Fused Cells

All calculations described above were implemented to a *LabView* based simulation program, providing values of R_{bf} and α_f for fused cell layers as a function of the average number of fusing cells. These R_{bf} and α_f values for fused cellular bodies were then entered into an impedance spectrum simulation program. This program creates the spectra of cell-covered ECIS electrodes on the basis of the model parameters R_{bf} and α_f as well as C_m applying the mathematical model of Giaever and Keese (chapter 3.1.3). The parameter C_m is assumed to stay constant in our calculations, while α and R_b change due to multi-cell fusion. Finally, simulated impedance spectra were plotted as a function of frequency and were compared to the experimental data.

The amount of individual cells on the electrode before fusion was determined to be 245. For simulations this number was set to the maximal possible number of individual cells on the electrode. Thus, it is also the maximum number of cells which can fuse on the electrode. Fusion numbers n between 1 (no fusion) and 245 (maximal fusion) are possible. Beyond this cell number the simulation procedure is not valid. Since HEK-293 and HEK-EYFP/pAbcg2 cells revealed a different impedimetric response upon fusion, simulations were performed for both cell types individually. If simulations on the basis of the presented considerations

provide impedance spectra with a similar frequency dependence as experimentally obtained for fused cells, the model is appropriate to describe the fusion process.

6.6.2.2 Basic Simulations for *In Situ* Electrofusion

The course of the simulated parameters α_f and R_{bf} as a function of the number n of fused cells simulated on the basis of average fit parameters α, R_b and C_m for *PolyMAG* pre-incubated HEK-293 cells (n = 1) (cp. Tab. 6.1) is presented in Fig. 6.39. Parameter values for α_f and R_{bf} were simulated for n = 2, 5, 10, 20, 30, 40, 50, 100, 150, 200 and 245.

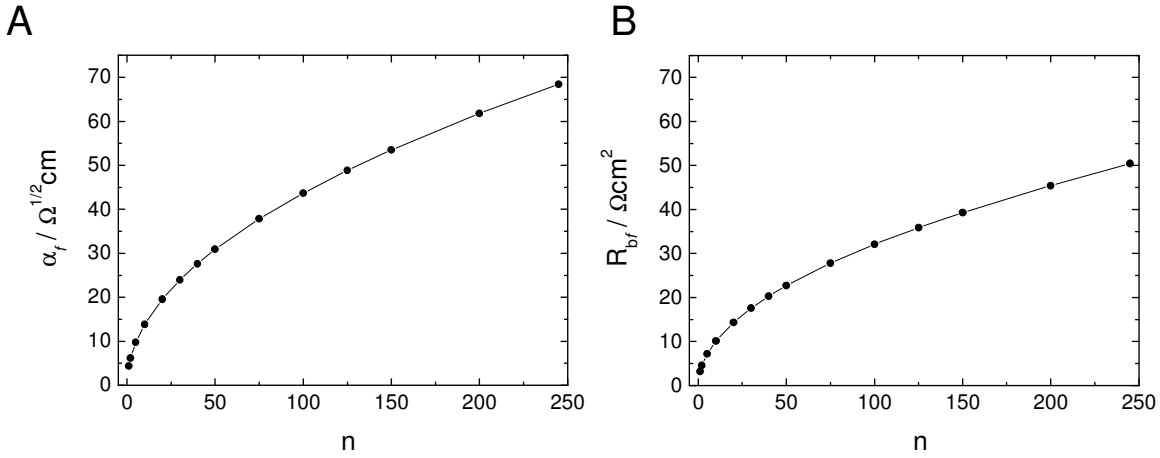

Fig. 6.39: Simulated course of α_f and R_{bf} as a function of the number of fused cells. Values of α_f (**A**) and R_{bf} (**B**) of *PolyMAG* incubated HEK-293 cell layers after *in situ* multi-cell electrofusion are plotted for n = 1, 2, 5, 10, 20, 30, 40, 50, 75, 100, 125, 150, 200 and 245 fused cells. Simulations are based on average fit parameters for *PolyMAG* pre-incubated HEK-293 cell layers with n = 1 (α: 4.37 $\Omega^{1/2} \cdot$ cm; R_b: 3.21 $\Omega \cdot$ cm^2 and C_m: 1.40 µF/cm^2) and the geometrical changes during fusion as described above.

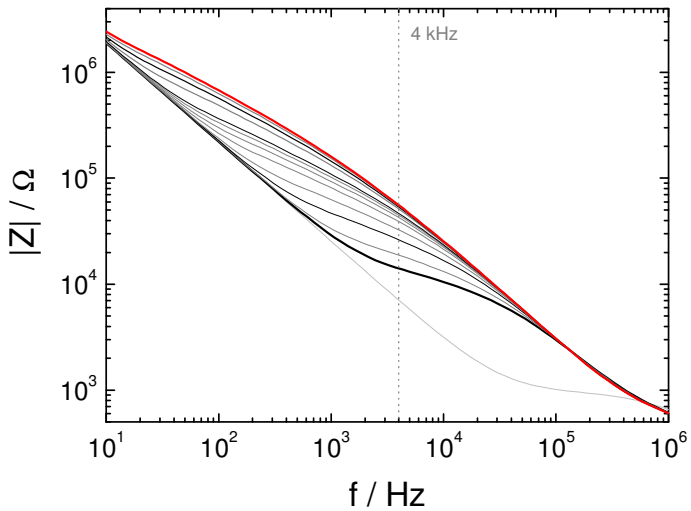

Fig. 6.40: Simulated impedance spectra for increasing degrees of HEK-293 *in situ* multi-cell electrofusion. All simulations were based on average fit parameters obtained from experimental data of *PolyMAG* pre-incubated HEK-293 cells and the geometrical changes during fusion as described above. A cell-free electrode was simulated with: A_{CPE}: 2.02 × 10^{-5} Fs^{n-1}·cm^{-2}; n_{CPE}: 0.94. For an electrode covered with HEK cells the cell-specific parameters α: 4.37 $\Omega^{1/2} \cdot$ cm; R_b: 3.21 $\Omega \cdot$ cm^2 and C_m: 1.40 µF/cm^2 were applied (▬, n = 1: No fusion). Spectra were simulated for n = 2, 5, 10, 20, 30, 40, 50, 100, 150, 200 and 245 fused cells. ▬: Maximal fusion (n = 245); ▬: Cell-free electrode.

Both parameters increase when the number of fused cells rises. The curves are parabolic, yielding maximal values of α_{Max} = 68.4 $\Omega^{1/2} \cdot$ cm and $R_{bf,\ Max}$ = 50.2 $\Omega \cdot cm^2$ for 245 fused cells. Figure 6.40 presents impedance spectra that were simulated on the basis of the parameters α_f, R_{bf} and C_m (cp. Fig. 6.39) for *PolyMAG* pre-incubated HEK-293 and HEK-EYFP/pAbcg2 cell layers for n = 2, 5, 10, 20, 30, 40, 50, 100, 150, 200 and 245. The dependence of the impedance magnitude on the number of fusing cells (n = 1 – 245) can be extracted from Fig. 6.40 and is shown in Fig. 6.41.

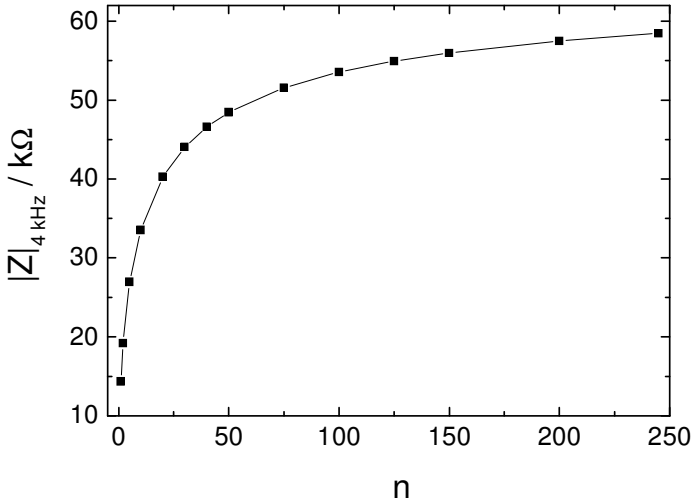

Fig. 6.41: Impedance magnitude |Z| at 4 kHz as a function of the average number of fused cells (n = 2, 5, 10, 20, 30, 40, 50, 75, 100, 125, 150, 200 and 245). Simulations are based on average fit parameters for *PolyMAG* pre-incubated HEK-293 cell layers with n = 1 and the geometrical changes during fusion as described above.

The correlation reveals a typical saturation curve with a strong increase of $|Z|_{4\ kHz}$ for up to ~ 50 fused cells. Higher fusion degrees cause a slower impedance increase at 4 kHz, leading to a plateau at 58.5 kΩ. Comparison of experimentally obtained α and R_b values as well as impedance values with the simulated data can provide the average number of fused cells on the electrode.

Similar simulations were performed for HEK-EYFP/pAbcg2 cells on the basis of average fit parameters of *PolyMAG* pre-incubated cell layers (Tab. 6.1) and the geometrical changes during fusion as described above. Similar curves as presented for HEK-293 cells (Fig. 6.39 – 6.41) were obtained. Since only slight deviations due to differences in fit data for the pre-pulse status occurred (Tab. 6.3), the respective plots are not shown here. Characteristic values for maximal fit parameters (n = 245) α_f and R_{bf} as well as for the maximal impedance magnitude $|Z|_{4\ kHz,\ Max}$ are provided in Tab. 6.3 in comparison to the values for HEK-293 cells. When all cells on the electrode fuse (n = 245) to form one polynucleated cell body the parameter $\alpha_{f\ Max}$ yields 68.4 and 68.9 $\Omega^{1/2} \cdot$ cm for HEK-293 and HEK-EYFP/pAbcg2 cells, respectively. Maximal values for R_b were calculated to be 50.2 and 49.6 $\Omega \cdot cm^2$ for the two cell lines. The maximal impedance magnitude, however, obtained from simulations for HEK-293 and HEK-EYFP/pAbcg2 cells shows considerable deviations. The smaller value for the maximal impedance magnitude $|Z|_{4\ kHz,\ Max}$ for HEK-EYFP/pAbcg2 cells (48.4 kΩ) can be ascribed to differences in the value for the basal simulation parameter C_m. If C_m for HEK-

EYFP/pAbcg2 cells is set to 1.4 instead of 2.11 µF/µm^2, the maximal impedance magnitude at 4 kHz also yields 57.8 kΩ, similar to the value for $|Z|_{4\,kHz,\,Max}$ of fused HEK-293 cells (58.5 kΩ).

Tab. 6.3: Simulated data for maximal cell fusion of *PolyMAG* pre-incubated HEK cell lines. Maximal values for $\alpha_{f\,Max}$ and $R_{bf\,Max}$ for n = 245 fused cells. Simulations are based on mean values for the parameters α and R_b of *PolyMAG* pre-incubated cell layers and the geometrical changes during fusion as described above.

cell line	$\alpha_{f\,Max}$ [$\Omega^{1/2} \cdot$ cm]	$R_{bf\,Max}$ [$\Omega \cdot$ cm^2]	$\lvert Z\rvert_{4\,kHz,\,Max}$ [kΩ]
HEK-293	68.4	50.2	58.5
HEK-EYFP/pAbcg2	68.9	49.6	48.4

6.6.2.3 Comparison of Simulated and Experimental Data

The theoretical simulation provides a method by which the degree of multi-cell fusion on a gold-film electrode can be extracted from the measured impedance. In order to estimate the exact number of fused cells the best-fit model parameters α and R_b for a given electrode were used as the basis for the simulations instead of the average fit values. Simulated spectra were then compared to experimental data as obtained 100 min after electrofusion of *PolyMAG* pre-incubated HEK-293 cells.

HEK-293 Cells

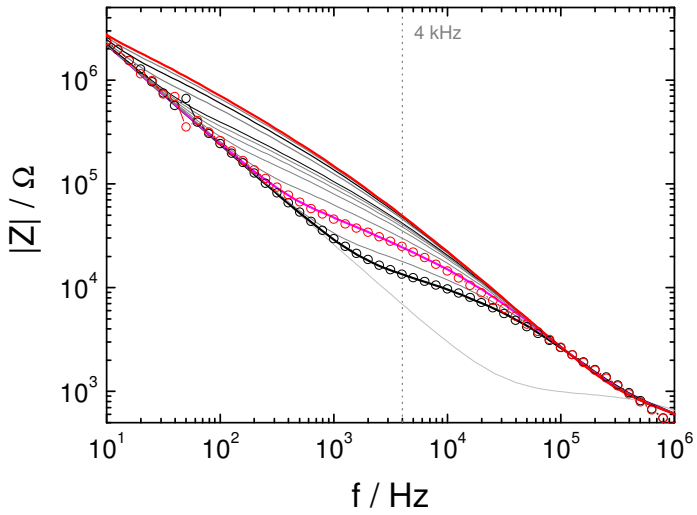

Fig. 6.42: Simulated impedance spectra for increasing degree of HEK-293 multi-cell electrofusion compared to experimental data of HEK-293 cells immediately before (○) and 100 min after (○) electrofusion. Simulations were based on fit parameters obtained from unfused *PolyMAG* pre-incubated HEK-293 cell layers with A_{CPE}: 1.48 × 10^{-5} Fs$^{n-1} \cdot$ cm^{-2}; n_{CPE}: 0.97; α: 4.7 $\Omega^{1/2} \cdot$ cm; R_b: 2.6 $\Omega \cdot$ cm^2 and C_m: 1.77 µF/cm^2 (▬, n = 1) and the geometrical changes during fusion as described above. Spectra were simulated for n = 2, 5, 10, 20, 30, 40, 50, 100, 150, 200 and 245 fused cells.: ▬: n = 5; ▬: n = 245 (maximal fusion); ▬: Cell-free electrode.

As presented in Fig. 6.42 the experimentally obtained spectrum of HEK-293 cells before fusion (○) exactly overlaps with the fitted spectrum (▬). After fusion (100 min), initiated by the electroporation pulse, the spectrum is shifted to higher impedance magnitudes (○) and

overlaps with the simulated spectrum for n = 5 fused cells (—), indicating that on average five cells have fused to form a multi-nucleate cell body.

Impedance spectra from HEK-293 fusion experiments were further analyzed with respect to the ECIS parameters α and R_b (cp. 3.1.4), which were compared to the values predicted for n = 5 by the simulation program (Tab. 6.4). Parameter values for the experimental impedance spectrum are similar to the theoretically predicted values of α = 10.5 $\Omega^{1/2} \cdot$ cm and R_b = 4.7 $\Omega \cdot cm^2$ (Tab. 6.4, experiment 1). Also the impedance at 4 kHz of the fused cell layer (24.9 kΩ) correlates well with the estimated impedance value for a simulated cell layer composed of five fused cells on average (25.3 kΩ).

However, other impedance spectra obtained from HEK-293 fusion experiments do not exactly overlap with simulated spectra. Often, the experimental spectrum of fused cells overlaps with simulated curves in the lower frequency range but slightly deviates in the higher frequency range above 5×10^3 Hz. For these data fitted values of R_b are typically lower than simulations predicted (Tab. 6.4, experiments 2 and 3), whereas the parameter α is underestimated by simulations.

Tab. 6.4: Comparison of experimental and simulated data for fused HEK-293 cells from three individual experimets.

Experiment	Data	n	α [$\Omega^{1/2} \cdot$ cm]	R_b [$\Omega \cdot cm^2$]	$\lvert Z \rvert_{4\ kHz,\ n}$ [kΩ]
1	simulated	5	10.5	4.7	25.3
	experimental		10.8	5.8	24.9
2	simulated	5	8.3	6.3	23.6
	experimental		10.5	2.2	21.0
3	simulated	5	9.4	6.5	25.7
	experimental		11.3	3.5	22.8

HEK-EYFP/pAbcg2 Cells

Since many experiments were carried out using the recombinant HEK-EYFP/pAbcg2 cell line, simulations were also performed for this cell type. Experimental impedance spectra from the highly fusogenic HEK-EYFP/pAbcg2 cells were compared to simulated spectra (Fig. 6.43).

The experimental impedance spectrum of fused HEK-EYFP/pAbcg2 cells reveals a similar frequency dependence as the simulated spectrum for fusion of n = 25 cells. Values of the ECIS model parameters and estimated impedance values for n = 25 cells used in simulation are compared in Tab. 6.5 (experiment 1). Analysis of the measured impedance spectrum provides values for the parameters α and R_b (α = 28.0 $\Omega^{1/2} \cdot$ cm; R_b = 10.0 $\Omega \cdot cm^2$) which agree well with simulated values calculated for n = 25 fused cells (α = 27.9 $\Omega^{1/2} \cdot$ cm; R_b = 8.8 $\Omega \cdot cm^2$). Additionally, impedance magnitudes at 4 kHz from simulations (34.4 kΩ) and experimental data (32.3 kΩ) show a good agreement.

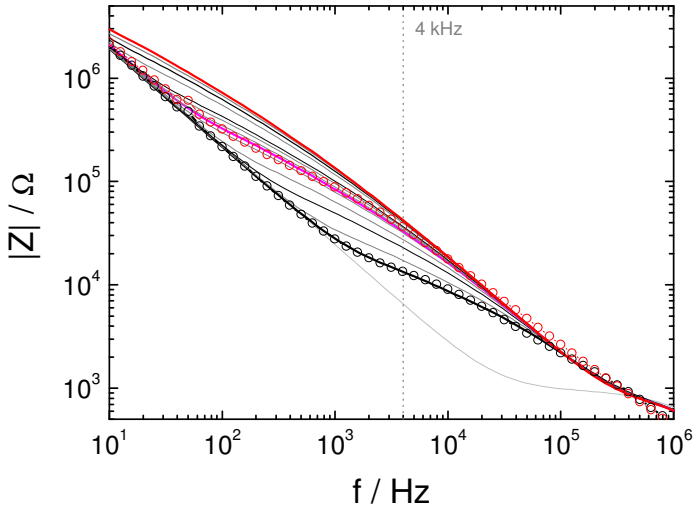

Fig. 6.43: Simulated impedance spectra for increasing degrees of HEK-EYFP/pAbcg2 *in situ* multi-cell electrofusion compared to experimental data of HEK-EYFP/pAbcg2 cells immediately before (○) and 100 min after (○) electrofusion. Simulations were based on fit parameters obtained from an unfused *PolyMAG* pre-incubated cell layer with A_{CPE}: 1.6 × 10^{-5} $Fs^{n-1}{\cdot}cm^{-2}$; n_{CPE}: 0.97 α: 5.57 $\Omega^{1/2} \cdot cm$; R_b: 1.76 $\Omega \cdot cm^2$ and C_m: 2.39 µF/cm^2 (▬, n = 1). Spectra were simulated for n = 2, 5, 10, 20, 30, 40, 50, 100, 150, 200 and 245 fused cells. ▬: n = 5; ▬: n = 245 (maximal fusion); ▬: Cell-free electrode.

Tab. 6.5: Comparison of experimental and simulated data for fused HEK-EYFP/pAbcg2 cells from three individual experiments.

Experiment	Data	n	α [$\Omega^{1/2} \cdot cm$]	R_b [$\Omega \cdot cm^2$]	$\lvert Z\rvert_{4\ kHz,\ n}$ [kΩ]
1	simulated	25	27.9	8.8	34.4
	experimental		28.0	10	32.3
2	simulated	245	60.4	46.0	46.5
	experimental		60.7	34.0	41.7
3	simulated	150	69.8	40.4	54.3
	experimental		75.3	37.5	48.1

Impedance spectra were compared to simulations for two further experimental data sets (Tab. 6.5, experiments 2 and 3). Aside from some deviations experimental values for parameters α and R_b as well as $|Z|_{4\ kHz}$ were in the same range as predicted by the simulations. However, with an increasing degree of fusion, an exact simulation of experimental spectra with an average fusion number above ~ n = 100 becomes difficult, since spectra for high fusion numbers show only slight differences.

These simulations have shown that the model is capable to describe the observed phenomenon of *in situ* multi-cell fusion. Naturally, some general assumptions were made that do not always match to the real situation on the cell-covered electrode. Especially the assumption of a perfect cell monolayer deviates from the real composition of irregular HEK multi-layers. Nevertheless, general observations as the impedance increase at 4 kHz, the associated change in the shape of the impedance spectrum for fused HEK cells as well as the increase in the parameters α and R_b elucidate a basal agreement between the experimental and

the model situation. Thus, the model might be used to extract the average number of fused cells on the electrode after *in situ* electrofusion. Since the errors of such a calculation may be considerable, the effect of experimental parameters on fusion efficiency was investigated by plotting impedance raw data at 4 kHz instead of extracting an average number of fused cells by the simulation procedure. Nevertheless, these simulations can support further investigations.

6.7 Parameters Influencing Fusion Efficiency

6.7.1 Magnetic Field

As the supplier suggests, *PolyMAG* particles should be accumulated on the cell surface by magnetic fields for efficient *PolyMAG*-based transfection. The influence of the magnetic field on the fusion process should be investigated by the following experiment. HEK-293 cells were incubated with *PolyMAG* particles and were either exposed to a magnetic field (▲) or remained unexposed (●) before triggering the fusion process by electroporation (Fig. 6.44).

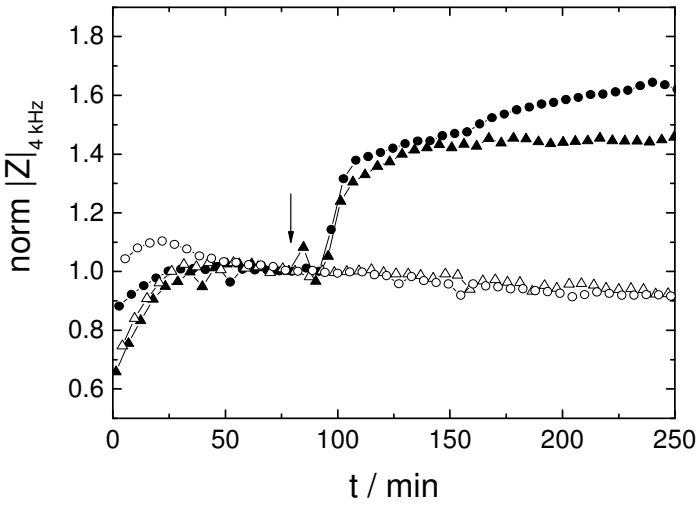

Fig. 6.44: Time course of the normalized impedance magnitude at 4 kHz before and after electroporation (arrow) of *PolyMAG* pre-incubated HEK-293 cell layers grown on *8W1E* ECIS electrodes with (▲) or without (●) particle sedimentation by magnetic field application. Control cell layers were pre-incubated with *PolyMAG* particles but were not electroporated (sedimentation without (○) or with (△) magnetic field). Absolute impedance magnitudes were normalized to the last value before electroporation (○: 13.69 kΩ; △: 14.28 kΩ; ●: 15.16 kΩ; ▲: 15.83 kΩ).

A similar impedance increase after *PolyMAG* incubation and electroporation is obtained, yielding 1.46 for cells being exposed to the magnetic field and 1.64 for the cells without incubation on the permanent magnet. Thus, pre-incubation on a permanent magnet does not enhance the fusion process. As becomes apparent from the non-electroporated control cell layers (△, ○), the magnetic field has no effect on the cell layer impedance.

Since all experiments using HEK-EYFP/pAbcg2 cells yielded high degrees of fusion without exposure to a magnetic field (chapter 6.3), all further experiments were carried out without incubating cells on the permanent magnet.

6.7.2 Electric Pulse Parameters

For standard electrofusion experiments pulse parameters that were found to be optimal for electroporation of HEK-cells (f = 40 kHz, U = 4 V and τ = 200 ms) were applied. In order to evaluate the effect of electric membrane permeabilization on fusion efficiency, the influence of pulse amplitude and pulse duration was investigated.

6.7.2.1 Pulse Amplitude

Figure 6.45 shows the influence of the pulse amplitude on *PolyMAG*-assisted *in situ* electrofusion of HEK-EYFP-pAbcg2 cells grown on ECIS electrodes.

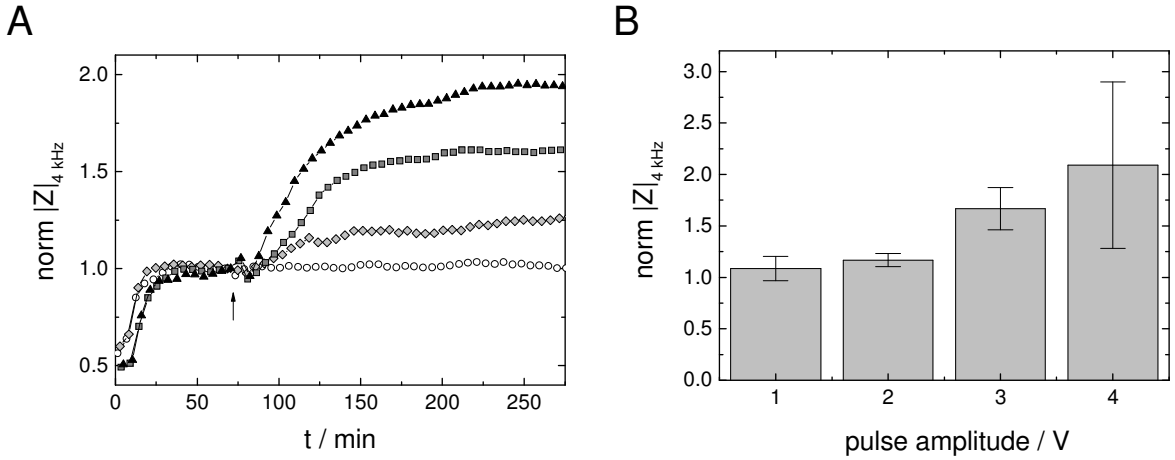

Fig. 6.45: A: Time course of the normalized impedance magnitude at 4 kHz for *PolyMAG* pre-incubated HEK-EYFP/pAbcg2 cells grown on *8W1E* ECIS electrodes before and after electroporation (arrow) at 40 kHz for 200 ms with different pulse amplitudes. ○: 1 V; ◇: 2 V; ■: 3 V; ▲: 4 V. Absolute impedance values were normalized to the last value before electroporation (1V: 16.29 kΩ; 2 V: 15.31 kΩ; 3 V: 16.74 kΩ; 4 V: 16.45 kΩ). **B:** Mean and standard deviation ($\mu \pm SD$) of normalized impedance magnitudes at 4 kHz for $N \geq 2$ individual cell layers recorded 200 min after electroporation with different pulse amplitudes (1 – 4 V) (**1 V:** 1.09 ± 0.12, N = 2; **2 V:** 1.17 ± 0.06, N = 4; **3 V:** 1.67 ± 0.21, N = 4; **4 V:** 2.09 ± 0.81, N = 4). T = 37 °C.

As shown in Fig. 6.45 A the time course of impedance increases after electroporation at 40 kHz for 200 ms in a pulse amplitude-dependent fashion. The bar diagram in Fig. 6.45 B provides average values for the cell layer impedance |Z| measured 200 min after electroporation at 40 kHz for 200 ms with varying pulse amplitudes (1 – 4 V). Electroporation of *PolyMAG* pre-incubated cell layers with a pulse amplitude of only 1 V or 2 V does not induce a considerable impedance increases compared to pre-pulse conditions (1 V: 1.09 ± 0.12; 2 V: 1.17 ± 0.06). A significant post-pulse impedance increase is observed for cell layers that are subjected to pulse amplitudes of 3 V – 4 V, yielding a more than 1.5-fold increase compared to pre-pulse impedances (3 V: 1.67 ± 0.21; 4 V: 2.09 ± 0.81).

6.7.2.2 Pulse Duration

The influence of the pulse duration on the degree of electrofusion is presented in Fig. 6.46. The normalized impedance recorded 200 min after electroporation is not significantly different for electric pulses with durations between 50 and 500 ms. All tested pulse durations were capable of inducing multi-cell fusion of HEK-EYFP/pAbcg2 cells grown on ECIS electrodes.

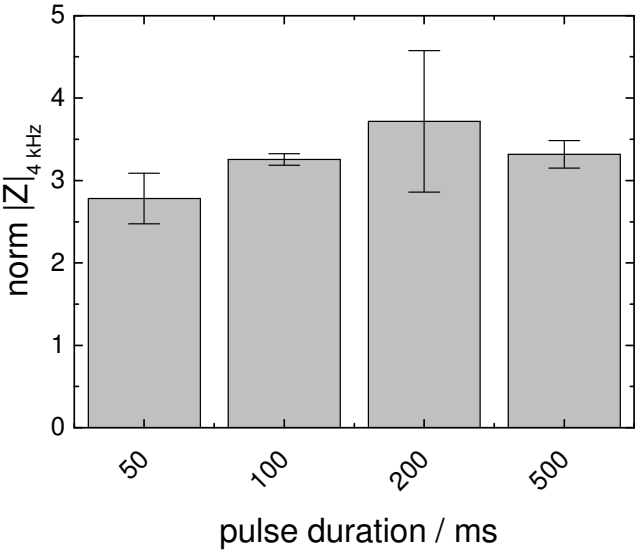

Fig. 6.46: Normalized impedance magnitude at 4 kHz for *PolyMAG* pre-incubated HEK-EYFP/pAbcg2 cell layers grown on *8W1E* ECIS electrodes after electroporation at 40 kHz with 4 V and different pulse durations of 50, 100, 200 or 500 ms. The diagram shows the mean and standard deviation ($\mu \pm SD$) of norm |*Z*| at 4 kHz of $N = 2$ individual cell layers recorded 200 min after electroporation (**50 ms:** 2.8 ± 0.3; **100 ms:** 3.3 ± 0.1; **200 ms:** 3.7 ± 0.9; **500 ms:** 3.3 ± 0.2). Absolute impedance values recorded 200 min after electroporation were each normalized to the last value before pulse application. $T = 37$ °C.

Selected epifluorescence images of electrofused HEK-EYFP/pAbcg2 cells shown in Fig. 6.47 confirm a striking multi-cell fusion for electroporation pulses of 4 V and 50, 100, 200 and 500 ms. A weak tendency of increasing fusion efficiency with increasing pulse durations can be seen, which might, however, be in the range of experimental variations. Taken together, the variation of the pulse duration between 50 and 500 ms does not significantly affect the fusion efficiency.

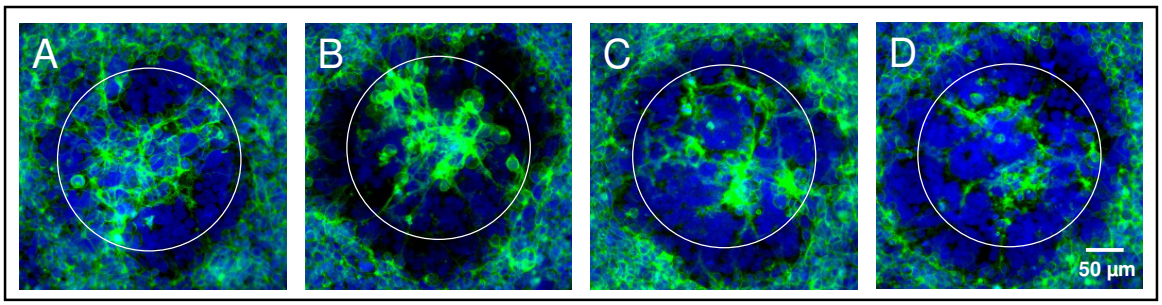

Fig. 6.47: Epifluorescence micrographs of *PolyMAG* incubated and electrofused HEK-EYFP/pAbcg2 cells grown on ECIS electrodes using electroporation pulses of varying pulse duration: **A:** 50 ms; **B:** 100 ms; **C:** 200 ms; **D:** 500 ms. Overlays of the green and blue fluorescence channel (green: membrane-linked EYFP; blue: DAPI stained nuclei) were created with the image analysis software *Image J*. White circles delineate the active electrode surface area.

6.7.2.3 Pulse Number

The effect of multiple electroporation pulses has already been described for HEK-293 wild type cells (chapter 6.1.2). Increasing numbers of electroporation pulses interpaused by a re-equilibration and fusion period of about 100 min led to enhanced fusion, as also visualized by confocal microscopy (chapter 6.2.1.2; 6.2.1.3).
Multiple electroporation of *PolyMAG* incubated HEK-EYFP/pAbcg2 cells often resulted in an abrupt impedance breakdown instead of inducing an increase in fusion yield (data not shown). However, HEK-EYFP/pAbcg2 cells that were not exposed to *PolyMAG* nanoparticles showed a considerable impedance increase after electroporation (cp. chapter 6.2.2.2). Thus, the influence of repeating electroporation pulses interpaused by regeneration times of about 100 min was investigated on particle-free cell layers (Fig. 6.48). In order to ensure similar experimental conditions as compared to experiments with *PolyMAG* particles, cells were subjected to a medium exchange in the beginning of the experiment (t = 0). The first pulse was applied after an equilibration phase of about 120 – 150 min.

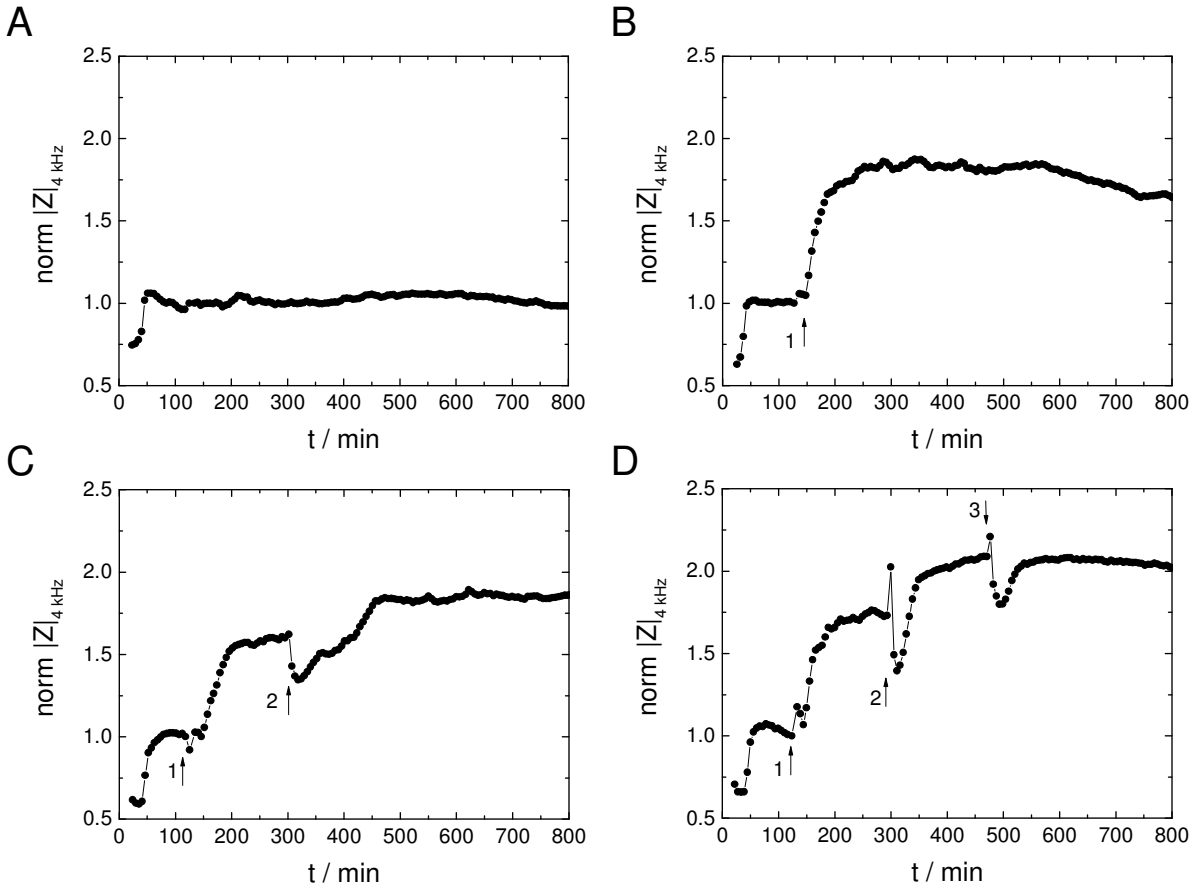

Fig. 6.48: Time course of the normalized impedance magnitude at 4 kHz for HEK-EYFP/pAbcg2 cells grown on *8W1E* ECIS electrodes after increasing numbers of electroporation pulses (arrows 1 – 3). **A:** No electroporation **B:** One electroporation (1) **C:** Two electroporations (1 + 2), **D:** Three electroporations (1 – 3). Before starting the experiment cells were subjected to a medium exchange (t = 0). Absolute impedance magnitudes are normalized to the last value before electroporation (A: 9.85 kΩ; B: 12.13 kΩ; C: 11.53 kΩ; D: 11.74 kΩ). T = 37 °C.

As shown in Fig. 6.48 repeating electroporation pulses are able to double the impedance level of the cell layer (C). While a second electroporation pulse can enhance the normalized

impedance by about 0.3 compared to a single pulse (B), a third electroporation pulse does not cause a further impedance increase (D). Here, normalized impedance values after the third electroporation are even lower than after the second electroporation trigger.

In summary, the electric pulse has to be above a critical threshold voltage to induce membrane destabilization and fusion. The pulse duration only seems to have a minor influence.

6.7.3 Fusogenic Additives

In order to reveal the role of *PolyMAG* particles in the observed electrically triggered multi-cell fusion process the characteristics and fusogenic properties of these particles were evaluated in comparison to other materials, using various polystyrene particles and soluble polymers.

6.7.3.1 *PolyMAG* Particles

PolyMAG nanoparticles are made of a superparamagnetic iron oxide (Fe_3O_4) core, which is coated with polyethylenimine (PEI) with a molecular weight of the polymer of 800 kDa. *PolyMAG* particles are described to have an average diameter of ~ 200 nm (Scherer et al., 2002). SEM analysis revealed a polydisperse size distribution between about 50 and 400 nm (Fig. 6.49 A, B).

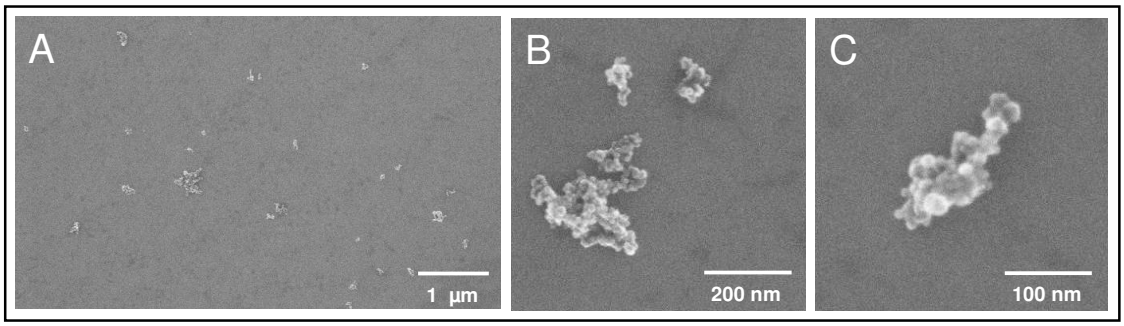

Fig. 6.49: SEM micrographs of *PolyMAG* nanoparticles on a silcon substrate. Images were kindly recorded by the NanoAnalytics GmbH, Münster.

Dynamic light scattering provided an average hydrodynamic radius of ~ 325 nm with a polydispersity index of 0.29 (see Tab. 6.6 in chapter 6.6.3.2). The PEI coating imparts a positive net charge to the particle surface. The zeta potential as a measure for the surface charge of the particles was determined to be (50.8 ± 5.5) mV (Tab. 6.6).

Localization of PolyMAG Particles Before and After Cell Fusion

PolyMAG particles were originally designed for the transfer of nucleic acids across the membrane. DNA loaded *PolyMAG* particles interact with the plasma membrane (Fig. 6.50 B, C) and are incorporated via a membrane-mediated mechanism. If the DNA load from

endocytosed *PolyMAG* particles is released and enters the nucleus, genetic information encoded on the reporter gene can be expressed (A, C).

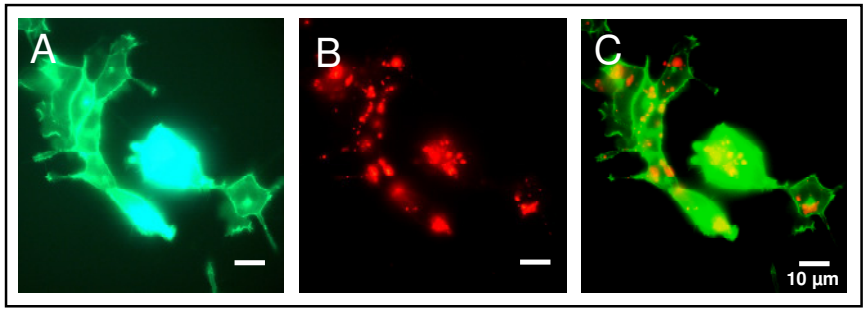

Fig. 6.50: Epifluorescence micrographs of HEK-EYFP/pAbcg2 cells 24 h after incubation with pEGFP loaded *PolyMAG* particles which were stained with EthD-1. **A:** Green channel recording EYFP fluorescence of HEK-EYFP/pAbcg2 cells and EGFP fluorescence after *PolyMAG* transfection. **B:** Red channel showing EthD-1 stained *PolyMAG* particles, **C:** Overlay of the green and red channel (*Image J*).

Thus, the fusion mediating properties of *PolyMAG* particles during electrofusion may be based on their interaction with the plasma membrane. Therefore, the location of EthD-1 stained DNA loaded *PolyMAG* particles (cp. chapter 4.3.4.4) within a confluent HEK-EYFP/pAbcg2 layer was determined after ~ 4 h of incubation with the particles by confocal fluorescence microscopy (Fig. 6.51).

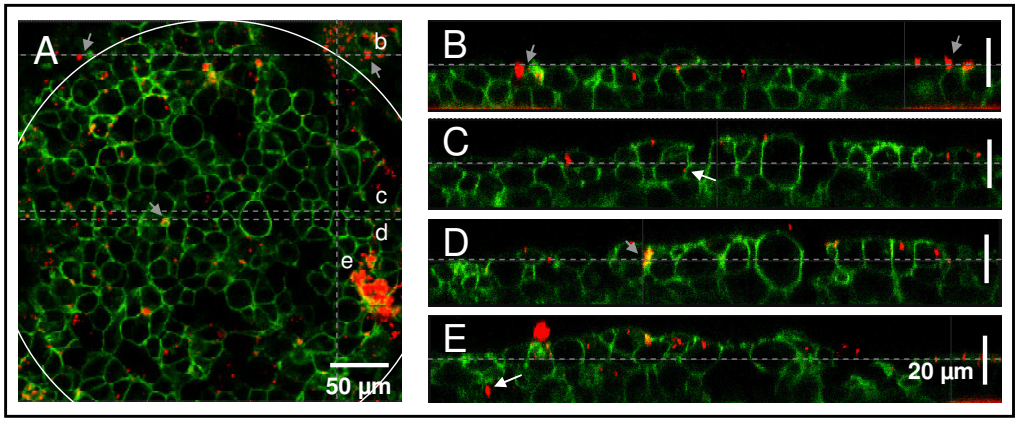

Fig. 6.51: Localization of *PolyMAG* particles before cell fusion. Confocal fluorescence xy- (**A**) and xz-sections (**B** – **D**) of HEK-EYFP/pAbcg2 cell layers grown on *8W1E* ECIS electrodes after 4 h of incubation with stained *PolyMAG* particles. *PolyMAG* particles were loaded with pCH1 plasmid DNA which was stained by EthD-1. The area of the underlying active working electrode is delineated by a white circle. Dashed lines (b – e) in A illustrate positions of the xz- and yz-sections (B – E). Arrows in grey mark particles in the apical membrane area, white arrows mark positions in the basal membrane area.

Stained, presumably aggregated particles are mainly detected on the surface of and within the uppermost cell layer of the multi-layered cell sheet. Some particles are found on the apical membranes of the uppermost cell layer (B, C) and often co-localize with the membrane as indicated by yellow spots of merged green and red fluorescence from the cell membrane and the particles (D, E). Few particles can be detected between cells in lower regions of the cell layer (C) or are already incorporated into the cell and are thus localized in the cytoplasm (D, E). In the basal region of the cell layer only a small amount of *PolyMAG* particles is detected

(E). After fusion of HEK-EYFP/pAbcg2 cells pre-incubated with *PolyMAG* particles, the particles can be mainly found associated to apical and intercellular membranes (Fig. 6.52 B, C, arrows). A considerable amount of particles is also detected within the cytoplasm of fused cells (A, D, arrows).

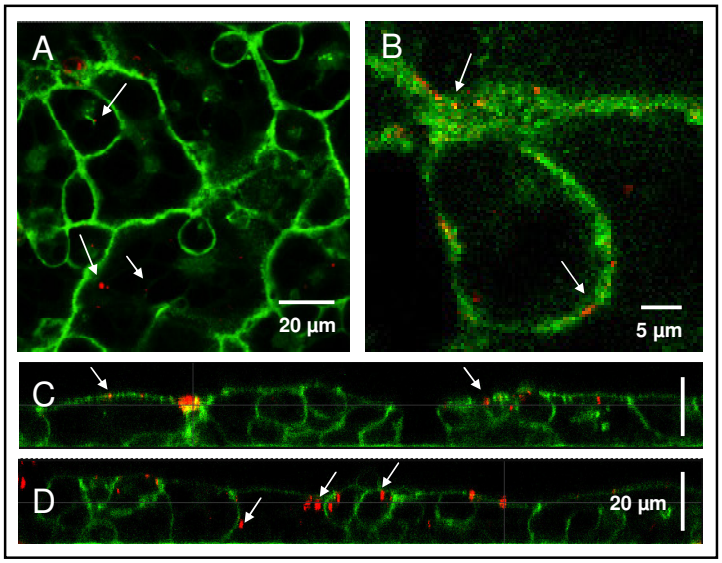

Fig. 6.52: Localization of *PolyMAG* particles after cell fusion. Confocal fluorescence xy- (**A**, **B**) and xz-sections (**C**, **D**) of HEK-EYFP/pAbcg2 cell layers grown on *8W1E* ECIS electrodes after pre-incubation with labeled *PolyMAG* particles and electrofusion. *PolyMAG* particles were loaded with pCH1 plasmid DNA which was stained by EthD-1. Cell fusion was triggered by electroporation using an AC pulse of 40 kHz, 4 V and 200 ms.

Influence of PolyMAG Concentration on Cell Fusion

The success of *PolyMAG*-assisted *in situ* electrofusion of HEK-EYFP/pAbcg2 cells was found to be dependent on particle concentration (Fig. 6.53).

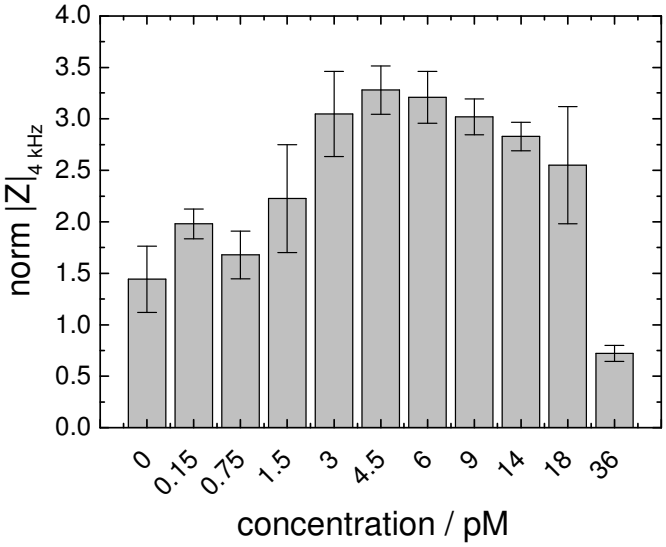

Fig. 6.53: Influence of particle concentration on fusion efficiency. Normalized impedance magnitude 4 kHz for HEK-EYFP/pAbcg2 cell layers grown on *8W1E* ECIS electrodes after electroporation. The cells were pre-incubated with different concentrations of *PolyMAG* particles. The diagram shows the mean and standard deviation ($\mu \pm SD$) of norm |Z| at 4 kHz for $N \geq 2$ individual cell layers recorded 200 min after electroporation (**0 pM:** 1.4 ± 0.3, $N = 4$; **0.15 pM:** 2.0 ± 0.1, $N = 3$; **0.75 pM:** 1.7 ± 0.2, $N = 4$; **1.5 pM:** 2.2 ± 0.5, $N = 4$; **3 pM:** 3.1 ± 0.4, $N = 2$; **4.5 pM:** 3.3 ± 0.2, $N = 2$; **6 pM:** 3.2 ± 0.3, $N = 2$; **9 pM:** 3.0 ± 0.2, $N = 6$; **14 pM:** 2.8 ± 0.1, $N = 2$; **18 pM:** 2.6 ± 0.6, $N = 2$; **36 pM:** 0.7 ± 0.2, $N = 2$). $T = 37$ °C.

With increasing particle concentrations to about 4.5 pM the averaged normalized impedance increases to slightly above 3. At higher concentrations above 6 pM average of the normalized impedance values moderately decrease again to ~ 2 and drop below 1 if particles are applied in a concentration of 36 pM. Thus, *PolyMAG* particles in appropriate concentrations significantly enhance the fusion of HEK cells.

Influence of Pre-Incubation Time with PolyMAG Particles on Cell Fusion

As *PolyMAG* particles are designed to interact with the membrane and to be incorporated into the interior of the cell by membrane-mediated uptake the time of incubation before triggering the fusion process by electric membrane destabilization may be a critical parameter for the fusion efficiency.

Figure 6.54 presents the average values for the impedance magnitude at 4 kHz, when cell layers were pre-incubated for different periods of time before pulse application. The values plotted in Fig. 6.54 have been recorded 100 min instead of 200 min after electroporation, because many cell layers in these experiments became unstable beyond 100 min after fusion, especially when they were pre-incubated for long time periods. Averages of absolute impedance values were plotted instead of normalized values, since increasing pre-pulse impedances within the cell layer equilibration phase of about 1 h would cause an underestimation of particle induced impedance increases in this time frame.

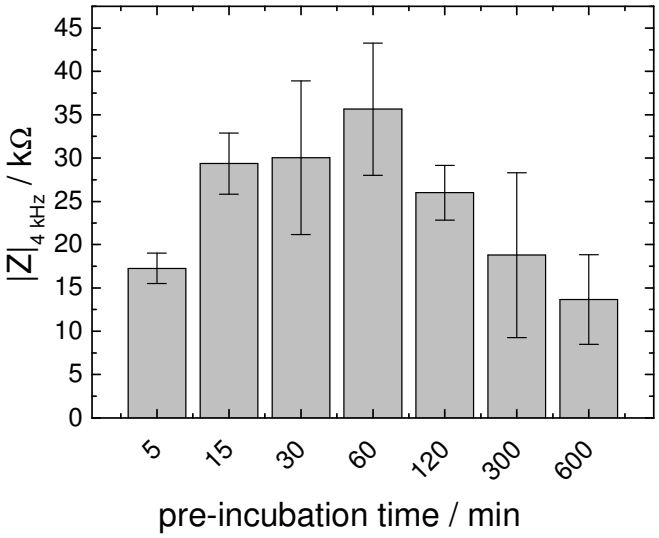

Fig. 6.54: Influence of *PolyMAG* pre-incubation time. Impedance magnitude at 4 kHz for HEK-EYFP/pAbcg2 cell layers grown on *8W1E* ECIS electrodes after pre-incubation for 5, 15, 30, 60, 120, 300 or 600 min and electroporation at 40 kHz with 4 V for 200 ms. The diagram shows the mean and standard deviation ($\mu \pm SD$) of |Z| at 4 kHz for $N \geq 2$ individual cell layers recorded 100 min after electroporation (**5 min:** (17.3 ± 1.7) kΩ, $N = 2$; **15 min:** (29.4 ± 3.5) kΩ, $N = 4$; **30 min:** (30.0 ± 8.8) kΩ, $N = 3$; **60 min:** (35.6 ± 7.6) kΩ, $N = 4$; **120 min:** (26.0 ± 3.2) kΩ, $N = 4$; **300 min:** (18.8 ± 9.5) kΩ, $N = 3$; **600 min:** (13.7 ± 5.2) kΩ, $N = 3$). $T = 37$ °C.

The pre-incubation time with *PolyMAG* nanoparticles before electric pulsing has a considerable influence on the fusion efficiency. A suitable incubation time before triggering electrofusion can be roughly estimated to be in the range of about 15 – 120 min, since above and below this time frame the impedance magnitudes are significantly lower. Although

measurements reveal a maximal impedance value after a pre-incubation time of 60 min, the exact optimum of *PolyMAG* incubation time before electric pulse application will have to be supported by further measurements.

6.7.3.2 Polystyrene Nanoparticles

The experiments presented here address the question, if other nanoparticles with similar properties as *PolyMAG* particles are able to support electrically triggered *in situ* cell fusion.
Three types of spherical polysterene nanoparticles with a core diameter of 200 nm and different surface charges were investigated with respect to their fusogenic potential. Amine or carboxylate functionalities render a positive or negative surface charge to the *FluoSphere*® nanoparticles form invitrogen, while *Polybead*® microspheres are unmodified polystyrene particles. The hydrodynamic diameter of these particles was investigated by dynamic light scattering (Tab. 6.6). The average hydrodynamic diameter of amine and carboxylate modified *FluoSpheres*® was measured to be 238 nm and 243 nm, respectively. Unmodified particles yield a diameter of 251 nm. *PolyMAG* particles whose average hydrodynamic diameter is determined to 325 nm have a polydispersity index of 0.29. The polydispersity index is a parameter to define the particle size distribution (Tscharnuter, 2006). The low polydispersity index for polystyrene nanoparticles (< 0.08) reveals their narrow size distribution. A value up to 0.7 generally indicates a medium range of polydispersity.

The zeta potential provides information on the particle surface charge (Tab. 6.6). Polyethyleneimine coated *PolyMAG* particles exhibit a zeta potential of (+ 50.8 ± 5.5) mV. Also the zeta potential of amine modified *FluoSpheres*® is positive yielding (+ 42.1 ± 5.8) mV. Unmodified *Polybead*® Microspheres show a slightly positive zeta potential of (+ 12.3 ± 7.3) mV, while the zeta potential of carboxylate modified *FluoSpheres*® is clearly negative (– 52.9 ± 6.6) mV.

Tab. 6.6: Hydrodynamic diameter and zeta potential of *PolyMAG* and further polystyrene nanoparticles.

Particle	Hydrodynamic Diameter [nm] / Polydispersity Index	Zeta Potential [mV]
PolyMAG	325 / 0.29	+ 50.8 ± 5.5
FluoSpheres®, amine	238 / 0.07	+ 42.1 ± 5.8
FluoSpheres®, carboxylate	243 / 0.04	– 52.9 ± 6.6
Polybead® Microspheres	251 / 0.02	+ 12.3 ± 7.3

Polystyrene particles were added to HEK-EYFP/pAbcg2 cells grown on ECIS electrodes in the same concentration (9 pM) as used for *PolyMAG* particles. Cell layers were incubated with particles for ~ 60 min before triggering electrofusion by electric pulse application.
The average normalized impedance at 4 kHz measured 200 min after electric pulse application for HEK-EYFP/pAbcg2 cells in presence of the various polystyrene particles in

comparison to the values obtained after electrofusion with *PolyMAG* particles or in particle-free medium is plotted in Fig. 6.55.

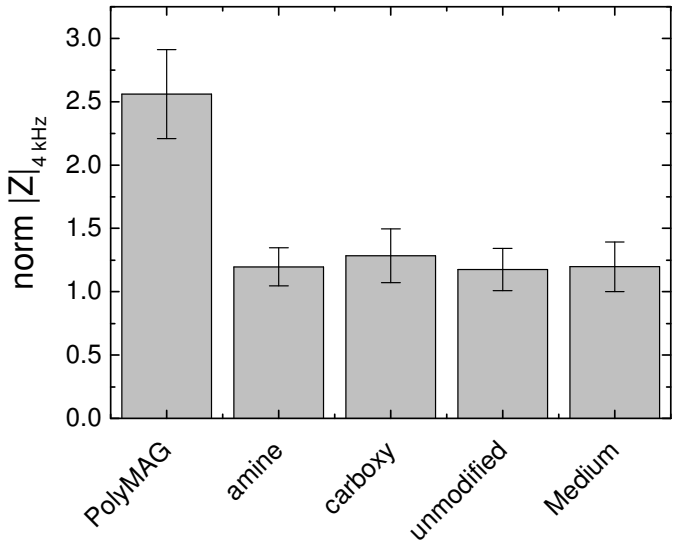

Fig. 6.55: Normalized impedance magnitude at 4 kHz measured 200 min after electroporation for $N \geq 4$ individual HEK-EYFP/pAbcg2 cell layers grown on *8W1E* ECIS electrodes. The cells were pre-incubated with *PolyMAG* or differently modified polystyrene particles in a concentration of 9 pM. Control cells were electroporated in particle-free medium. Absolute impedance magnitudes recorded 200 min after electroporation were normalized to the last value before pulse application. Mean and standard deviation ($\mu \pm SD$) are: ***PolyMAG*:** 2.56 ± 0.35, $N = 6$; ***FluoSpheres*® amine:** 1.20 ± 0.15, $N = 6$; ***FluoSpheres*® carboxy:** 1.28 ± 0.21, $N = 6$; **unmodified *Polybead*® Microspheres:** 1.18 ± 0.17, $N = 4$; **particle-free medium:** 1.20 ± 0.20, $N = 6$. $T = 37$ °C.

The mean normalized impedance 200 min after electroporation of HEK-EYFP/pAbcg2 cells pre-incubated with polystyrene particles of various surface modifications remains in the range of the particle-free control. The 2.5-fold impedance increase observed for cells incubated with *PolyMAG* particles can not be reached with any of the polystyrene particles under study.

6.7.3.3 Soluble Polymers

As described before, *PolyMAG* particles are composites of a colloidal Fe_3O_4 core and a polymeric coating of branched, polycationic polyethyleneimine (PEI). Since the outer PEI shell mainly determines the surface properties of the particles, the effect of soluble PEI was tested with respect to its fusogenic property in electrofusion experiments. *PolyMAG* particles are coated with branched PEI with an average molecular weight of 800 000 g/mol. Thus, branched PEI of a similar (750 000 g/mol) and a lower (1300 g/mol) molecular weight were tested. In order to reveal the role of polymer charge, the fusogenic effect of three other common polymers was investigated. Poly-L-lysine (PLL) is a polycationic polymer with primary amino groups. Polyethyleneglycol (PEG) with a molecular weight distribution of 1300 – 1600 g/mol is an uncharged polymer, known to induce chemical fusion of cells when applied in high concentrations above 30 % (v/v). Furthermore, polyanionic poly-L-glutamic acid (PGA; 2000 – 15 000 g/mol) served as an example for a negatively charged polymer.

Polymers were applied in the same mass concentration as present in experiments with *PolyMAG* particles (3 µg/ml).
Figure 6.56 shows the average normalized impedance at 4 kHz 200 min after electric pulsing of HEK-EYFP/pAbcg2 cells. The impedance was used as a measure for the fusogenic effect of the investigated polymers compared to *PolyMAG* particles and polymer-free medium.

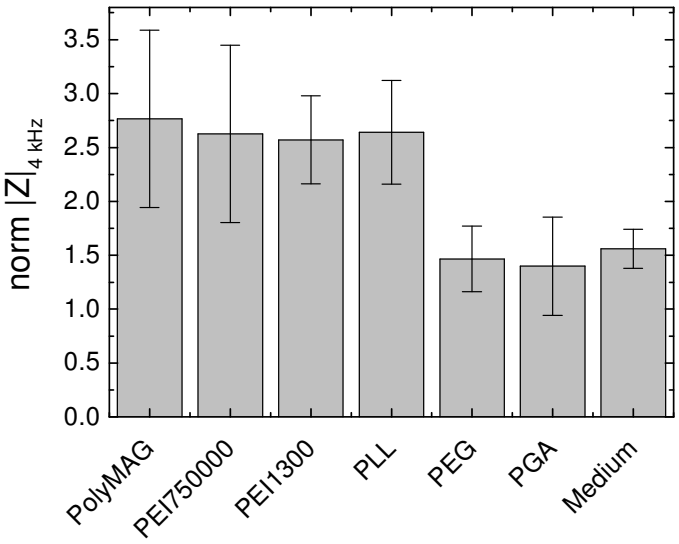

Fig. 6.56: Normalized impedance magnitude at 4 kHz measured 200 min after electroporation of $N \geq 6$ individual HEK-EYFP/pAbcg2 cell layers grown on *8W1E* ECIS electrodes. The cells were pre-incubated with *PolyMAG* particles or different soluble polymers with a concentration of 3 µg/ml. Control cells were electroporated in particle free medium. Absolute impedance magnitudes recorded 200 min after electroporation were each normalized to the last value before pulse application. Mean and standard deviation ($\mu \pm SD$) are: ***PolyMAG*:** 2.77 ± 0.82, N = 6; **PEI 750 000:** 2.63 ± 0.82, N = 8; **PEI 1300:** 2.57 ± 0.41, N = 16; **PLL:** 2.64 ± 0.48, N = 8; **PEG:** 1.47 ± 0.31, N = 10; **PGA:** 1.40 ± 0.47, N = 9; **particle-free medium:** 1.56 ± 0.18, N = 6. T = 37 °C.

The bar diagram in Fig. 6.56 illustrates that polymer solutions of PEI with a molecular weight of 750 000 and 1300 g/mol as well as PLL are able to significantly enhance the degree of *in situ* electrofusion of HEK-EYFP/pAbcg2 cells. Normalized impedances recorded 200 min after electroporation of cell layers pre-incubated with these polymers attain similar values (PEI 750 000: 2.63 ± 0.82; PEI 1300: 2.57 ± 0.41; PLL: 2.64 ± 0.48) as obtained for *PolyMAG* electrofused cells (2.77 ± 0.82).
PEG as well as PGA pre-incubated HEK-EYFP/pAbcg2 cell layers yield normalized impedance values of 1.47 ± 0.31 and 1.40 ± 0.47, respectively. These values are in the range of the control cell layers (1.56 ± 0.18) that were electroporated in particle- /polymer-free medium.

Taken together, the fusogenic effect of the *PolyMAG* nanoparticles is very likely caused by their PEI coat.

6.8 Discussion

The experiments presented in this chapter showed how ECIS electrodes can be used to induce as well as to measure *in situ* multi-cell fusion. In the following chapters the process of cell fusion as well as the possibilities and limitations of time resolved detection of multi-cell fusion with ECIS are discussed.

6.8.1 *In Situ* Electrofusion of HEK Cells Grown on ECIS Electrodes

Fusion of confluent HEK cells was first observed when cells were electroporated in presence of DNA-loaded *PolyMAG* nanoparticles with the aim of transfection (Fig. 6.4). One of the primary goals was to understand why HEK cells fuse under these circumstances, although previous experiments did not reveal such effects after simple electroporation of HEK cells without particles involved (cp. chapter 5.1.2.1). The results can be summarized as follows:

- ***Efficient in situ multi-cell fusion of HEK cells grown on ECIS electrodes was achieved by electroporation (40 kHz, 4 V, 200 ms) in presence of PolyMAG nanoparticles or the soluble cationic polymers polyethyleneimine (PEI) and poly-L-lysine (PLL).***
- ***Electroporation alone induced cell fusion with very low efficiency, while incubation with PolyMAG nanoparticles alone did not induce cell fusion.***
- ***Cell fusion depended on the pulse amplitude and the number of subsequent pulses, while the pulse duration had a minor influence.***
- ***Pre-incubation of HEK cells with the anionic polymer PGA, the neutral polymer PEG, amino or carboxy functionalized nanoparticles did not lead to cell fusion after electroporation.***

In general, the basic requirements for membrane fusion to occur are (i) destabilization of the membrane and (ii) close contact of adjacent membranes (cp. chapter 3.2.3). In this work two parameters were found to be essential to induce multi-cell fusion of HEK cells: (i) The electroporation pulse and (ii) pre-incubation with a cationic polymer (PEI, PLL).

6.8.1.1 Role of the Electroporation Pulse

The fact that electric field pulses can be used to induce membrane fusion has been known for several decades (Pohl et al., 1984). Like electroporation, electrofusion essentially depends on the destabilizing effects of electric field pulses on membranes (cp. chapter 3.2.3). Many basic biotechnological fusion protocols that are still used to date, the production of hybridoma cells for example, are based on the application of electric field pulses to cells in suspension. However, also some *in situ* fusion approaches have been published that used electroporation

pulses to induce cell fusion of adherent cells (Tab. 6.7). The experimental setups are illustrated in Fig. 1.4 (cp. chapter 1.2.3.1).

Tab. 6.7: Survey of *in situ* electrofusion experiments reported in the literature.

Publication	Cell Type	Electrofusion Setup
Teissié et al., 1982	Swiss mouse 3T3	cells on culture dish, RT (room temperature) platinum wires or stainless steel razor blades seated firmly against bottom of culture dish
Blangero and Teissié, 1983	CHO	cells on culture dish, RT parallel stainless steel electrodes
Teissié and Blangero, 1984	CHO	see Blangero and Teissié, 1983
Finaz et al., 1984	ID / CH	see Teissié et al., 1982
Teissié and Conte, 1988	CHO / HeLa	cells on microcarrier beads passed through a channel with parallel plate electrodes, 37 °C
Blangero et al., 1989	CHO	see Blangero and Teissié, 1983
Rols and Teissié, 1990	CHO	see Blangero and Teissié, 1983
Sukharev et al., 1990	L-929	cells on porous membrane grown in a monolyer addition of a second cell layer on top electric field perpendicular to the cell layer, RT
Zheng and Chang, 1990, 1991	CV-1	cells on coverslip, RT parallel stainless steel electrodes

Also this work showed that the electric field pulse is essentially required to induce multi-cell fusion. HEK-293 wild type cells as well as the recombinant cell lines HEK-EYFP/pAbcg2 and HEK-EGFP were efficiently fused using an electroporation pulse of 40 kHz, 4 V and 200 ms in presence of 9 pM *PolyMAG* particles (cp. chapter 6.2). The efficiency of cell fusion was dependend on the voltage of the electric pulse. While still significant but less cell fusion was induced by application of a 3 V pulse, cell fusion was negligible when using lower amplitudes. Comparison with previous results (cp. chapter 5.1.2.1) reveals that cell fusion and electroporation-mediated dye loading of HEK cells show similar dependencies on the pulse amplitude. Similar to fusion, electroporation of HEK cells grown on ECIS electrodes was optimal for the pulse parameter combination 40 kHz, 4 V and 200 ms. A pulse with an 3 V amplitude was suitable to load HEK cells with FITC dextran as well, however with lower efficiency (Fig. 5.10). These findings correlate well with what is reported in the literature. Electrofusion is generally induced at the same (Rols and Teissié, 1990; Dimitrov, 1995; Teissié and Ramos, 1998) or slightly higher (Abidor et al., 1993a,b) threshold voltages compared to electroporation. Membrane permeabilization and fusion efficiency both show the same sigmoidal dependency on the field strength. This is valid for cells in suspension (Teissié and Ramos, 1998) as well as for cells *in situ* (Blangero and Teissié, 1983; Rols and Teissié, 1990). As discussed before (cp. chapter 5.4.1), the pulse amplitude determines the degree of membrane permeabilization and the size of the membrane area that is permeabilized in spherical cells (cp. chapter 3.2.). Thus, with increasing pulse amplitude the membrane area

that is capable of undergoing membrane fusion increases, as long as membrane permeabilization is reversible.

Membrane permeabilization as well as cell fusion are moreover under the control of the pulse duration and the number of pulses. Pulse duration and number, both, affect the size and area density of local membrane defects. Pulse number and duration are thought to be critical for the establishment of the so-called long-lived fusogenic state that allows to initiate cell fusion even when membrane contacts are created after permeabilization (pulse-first approach) (Teissié and Ramos, 1998). For example the fusion efficiency of CHO and HeLa cells *in situ* was shown to follow a sigmoidal dependency on the pulse duration (Blangero and Teissié, 1983; Teissié and Conte, 1988). Above a critical pulse duration, however, the cell viability typically decreased considerably (Teissié et al., 1982; Teissié and Ramos, 1998). In this work no significant influence of the pulse duration on fusion efficiency was detected for electroporation pulses that lasted between 50 ms and 500 ms. Only a slight increase of cell fusion was observed for pulses with durations up to 200 ms (Fig. 6.46). The pulse durations studied here may have been too high and already in saturation, as described in the literature. Alternatively, the pre-incubation with the fusogenic material might change the dependency on the pulse duration (cp. chapter 6.8.2), vanishing the influence of pulse duration.

Also the pulse number influences the fusion yield (Teissié and Ramos, 1998). The effect of increasing pulse number on the *in situ* fusion yield of CHO and HeLa cells has been described by Blangero and Teissié (1983) and Teissié and Blangero (1984) among others. With increasing pulse number the fusion yield increased, finally reaching a plateau value. However, above a critical number of pulses the viability decreased (Teissié et al., 1982; Teissié and Ramos, 1998). As shown by experiments with *PolyMAG* pre-incubated HEK-293 cells repeated electroporation stepwise increased the normalized impedance of the cell layer (Fig. 6.7). Because the pulse applications were interpaused by a quite long period of regeneration, the experiments are, however, not fully comparable to conventional electroporation and electrofusion protocols that only pause between repetitive pulses for a few milliseconds to seconds. Electric pulses applied in short intervals have the character of pulses with a long pulse duration, since resealing may not be fully completed when the next pulse is applied (Rols and Teissié, 1998). The total time frame during which the membrane is in a permeabilized state that enables cell fusion was reported to be in the range of 5 – 20 min (Teissié and Ramos, 1998). However, the fusogenity of the membrane rapidly decreased in the first minutes after electric pulsing. Although 60 % of the membranes were still in a permeabilized state, 5 min after pulsing a fusion yield of only 12 % was observed, instead of 50 % immediately after electroporation with 80 % permeabilization. After more than 1 hour, however, which was the lag time between pulses in this work, the membranes are typically fully resealed and the cells have regenerated from the previous pulse. After each fusion step morphological rearrangements in the cell layer may have created new cell-cell contacts that allow new cell fusions upon a subsequent electroporation pulse.

The same observation of stepwise impedance increase after repeated pulse application was made for HEK-EYFP/pAbcg2 cells which were not pre-incubated with *PolyMAG* particles (Fig. 6.48). As revealed by fluorescence micrographs, also HEK-293 wild type cells fused

without *PolyMAG* preincubation in response to repeated electroporation pulses, however, with low efficiency (Fig. 6.10 E, F). These experiments show that cell fusion can be even induced by electroporation alone and emphasize the role of electric pulsing for the initiation of fusion.

Another important aspect is the orientation of the cells with respect to the electric field during electroporation (Teissié and Ramos, 1998). Only if the cells are permeabilized at sites of close membrane contact, fusion can be initiated. This is the reason why *in situ* electrofusion protocols reported in the literature applied the electric field in parallel to the surface of the cell layer (Fig. 6.57 A). The parallel wire or plate electrodes were typically firmly placed onto the bottom of the culture dish in order to guarantee a homogeneous field distribution across the lateral cell membranes. Only few other electrode setups are described that create electric field lines with other directions with respect to the cell bodies. Cells were for example grown on beads and pulsed with parallel plate electrodes when passing a flow channel (Teissié and Conte, 1988). In another approach a layer of suspended cells was added on top of an adherent cell layer that was grown on a porous filter substrate placed between two plate electrodes (Grasso et al., 1989; Sukharev et al., 1990). After pulse application suspended cells on top of the cell layer were fused with the adherent cells. Most of these setups are used for both, *in situ* electroporation as well as *in situ* electrofusion (cp. chapter 1.2.3.1; 1.2.3.3; Fig. 1.4) (Blangero and Teissié, 1983; Rols and Teissié, 1990).

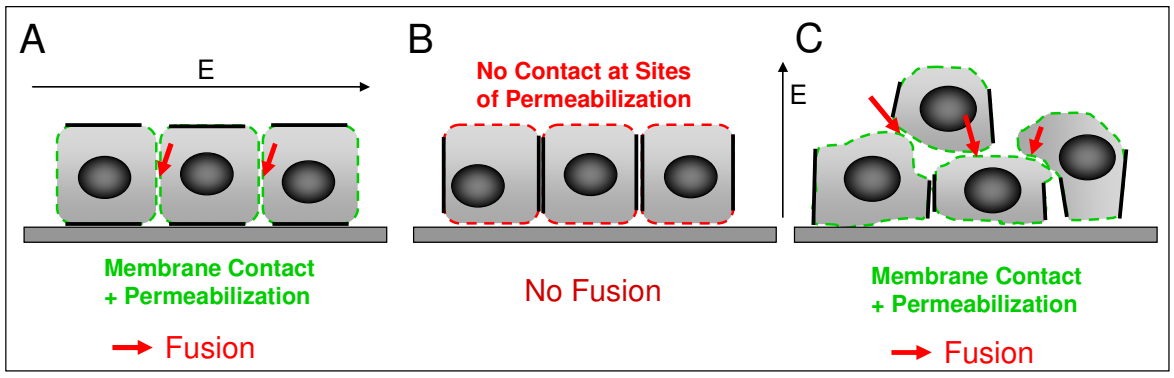

Fig. 6.57: Schematic illustration of the dependency of *in situ* fusion on the orientation of the electric field (*E*) with respect to the cell layer. **A:** Electric field in parallel to the surface of the cell layer, permeabilizing lateral cell membranes at sites of cell-cell contact. **B**, **C:** Electric field perpendicular to the surface of the cell layer, permeabilizing apical and basal membranes. Fusion only occurs, if memranes of two different cells create membrane contacts in field direction (**C**). Arrows indicate possible sites for fusion.

To demonstrate the influence of the electric field orientation with respect to the cells on the fusion efficiency Teissié and Blangero (1984) systematically altered the direction of the electric field, which was applied in parallel to the apical surface of the cell layer. They used parallel wire electrodes for the *in situ* fusion of CHO cells grown on a petri dish. The orientation of the wire electrodes was either kept constant or it was rotated by 90° between subsequent pulses to permeabilize the entire lateral membrane around the cells. When the orientation of the electric field was changed using 4 or more pulses an increased fusion yield was obtained compared to application of all pulses in the same direction. In addition, a high fraction of multinucleate cells was only obtained when the field direction was rotated.

Blangero et al. (1989) moreover reported that within a population of CHO WTT cells grown on a petri dish cells preferentially fused along the electric field lines of the electroporation pulse.
When ECIS electrodes are used for electroporation the electric field is applied perpendicular to the apical surface of the cell layer (Fig. 6.57 B, C). This results in a permeabilization of the apical and basal membrane of the cells. Since in typical cell layers the sites of cell-cell contact are predominantly located along the lateral membranes, it is rather unlikely that cell fusion is induced. Cell fusion can only occur, if such high field strengths are applied that the area of permeabilization extends also to the lateral membrane. Indeed, no cell fusion was observed under normal electroporation conditions for most cell types under study (cp. chapter 5.2). Only NIH-3T3 cells that were electroporated with a pulse of 40 kHz, 5 V and 200 ms indicated cell fusion (Fig. 5.17). While fusion of HEK-293 cells only occurred after repeated electroporation steps (Fig. 6.10), a considerable fusion of HEK-EYFP/pAbcg2 cells was already induced by simple electroporation (Fig. 6.14 C). Like HEK, NIH-3T3 are fibroblastoid cells that tend to partially grow on top of each other. Permeabilized membranes can come in contact and fuse (Fig. 6.57 C). Under this aspect it seems plausible that only for cell types, for which membranes of individual cells overlap perpendicular to the electric field, cell fusion was observed.
Fusion of HEK cells moreover exceeded the borders of the electrode (Fig. 6.23). This phenomenon may be due to the direction of the electric field lines near the electrode borders as discussed in chapter 5.4.1.

6.8.1.2 Role of Fusogenic Additives

Under natural circumstances repulsive intermembrane forces due to hydration, electrostatics and steric limitations hinder close membrane contact and intermixing of lipids. Thus, membranes typically reseal individually after electroporation. Fusion of membranes in contrast requires close proximity of neigboring cells in order to allow intermembrane lipid rearrangements. Close cell contacts can be achieved by several different methods in principle (cp. chapter 3.2.3.1, Tab. 3.4). The most prominent electrofusion setup which is used for cells in suspension tightly aligns cells by dielectrophoresis (Pohl et al., 1984). Alternatively mechanical methods were frequently used to mediate close cell contact between cells in suspension. Abidor et al. (1993a) and Li et al. (1996) for example promoted membrane contact by centrifugation. Jaroszeski et al. (1994) mechanically facilitated electrofusion by depositing cells hypobaric pressure. In a similar way Ramos et al. (2002) exposed HeLa cells to a hypobaric pressure to collect them on a filter before fusing them electrically. For fusion of adherent cells *in situ*, however, other approaches are required.
Adherent cells often form natural cell-cell contacts, that seem to be sufficient to enable cell fusion after electric destabilization of their cell membranes (cp. Tab. 6.7). Also in this work it was shown that cell fusion of adherent cells can be induced by simple electroporation

(Fig. 6.14 C; Fig. 6.17 C; Fig. 5.17 J). However, cell fusion was rather inefficient and in some cases multiple steps of electroporation were required to achieve cell fusion (Fig. 6.10 E, F).
The contact between cells adhering to a substrate can be enhanced by additional manipulation. Rols et al. (1990) showed that exposure of adherent cells to hypoosmolar medium resulted in an increased electrofusion efficiency after osmotic swelling. Aside from the laboratory fusion of adherent cells is known from biological systems. Some viruses, for example, efficiently induce multi-cell fusion (Eckert and Kim, 2001). Moreover, various processes in the development of tissues and differentiation of certain cell types include cell fusions (Ogle et al., 2005; Oren-Suissa and Podbilewicz, 2007). Specialized proteins that mediate such biological fusion processes can also be used to induce *in situ* fusion experimentally (Salsman et al., 2005).
Moreover, certain chemical substances are able to interact with membranes and induce fusion. The most prominent substance is polyethyleneglycol (PEG), which has been known to induce cell fusion ever since the 1970's (Ahkong et al., 1975; Davidon and Gerald, 1976; Lane et al., 1984). PEG is a neutral, highly hydrated polymer which induces cell agglutination, creates close membrane contacts and subsequently leads to fusion of cell membranes. It can be used to fuse cells in suspension as well as adherent cells, even without application of an electric field pulse. The detailed mechanisms underlying PEG-mediated cell fusion are, however, not fully understood (Lentz, 1994, 2007). PEG with a molecular weight between 1000 and 6000 g/mol is typically applied in concentrations of 30 – 50 %. In order to minimize the membrane damaging effect of the chemical agent the time of exposure is usually kept short (~ 1 min) (Yang and Shen, 2006).

Electrofusion in Presence of Soluble Polymers

The group of S.W. Hui showed that addition of 10 – 25 % (w/v) PEG 8000 to the electrofusion medium can enhance the fusion efficiency of suspended cells (Stoicheva and Hui, 1994; Li and Hui, 1994). Studies presented in this work did, however, not reveal such a fusion promoting effect of PEG that was applied at a non-toxic concentration of 3 µg/ml (Fig. 5.56). Concentrations were obviously too low to induce cell fusion.
Only for the polycationic polymers PEI 1300; PEI 750 000 and PLL a considerable degree of cell fusion was detected (Fig. 6.56). Although these polymers are not known to mediate cell fusion like PEG, they show strong interactions with biological membranes (Schwieger and Blume, 2007; Hong et al., 2006; Godbey et al., 1999c). Their propertiy to (i) adsorb to the membrane by electrostatic interaction, (ii) condense and shield the negative charge of nucleic acids and (iii) disrupt endosomes for cargo release into the cytoplasm are the essential reasons for their use in gene transfer and drug delivery (Godbey et al 1999a; De Smedt, et al., 1999; Thomas and Klibanov, 2003). Poly-L-lysine is moreover used as a surface coating substance that promotes cell adhesion on surfaces (Yavin and Yavin, 1974).
The pre-incubation of HEK cells with PEI and PLL may thus lead to certain membrane interactions that enhance their susceptibility for electrofusion. Since these substances have flocculating properties that lead to aggregation of vesicles (Papahadjopoulos et al., 1976; Oku et al., 1986), microorganisms (Treweek and Morgan 1976; Zeleznik et al., 2002) and

mammalian cells (Aunis and Wang, 1989) it is likely that PEI and PLL enhance intercellular membrane contacts and reduce the distance between adjacent membranes, which is beneficial for membrane fusion. Oku et al. (1986) even demonstrated the fusogenic effect of PEI on negatively charged phosphatidylserine liposomes. In addition to the strong affinity to biological membranes, the polycationic polymers PEI and PLL were shown to affect the membrane structure. Hartmann and Galla (1978) reported a strong binding of PLL to model membranes and concomittant changes of the lipid distribution. AFM studies moreover indicated that polycationic polymers like PEI and PLL cause the formation or the expansion of pre-existing defects in supported lipid membranes in a concentration rage of 1 – 3 µg/ml (Hong et al., 2006). This is about the concentration used in this work (3 µg/ml). In contrast, PEG and poly(vinlyalcohol) (PVA) did not show such effects in the same concentration range (Hong et al., 2006). The cationic polymers were not toxic to KB or rat 2 cells up to concentrations of 12 µg/ml. But leakage of LDH and luciferase as well as permeability towards propidium iodide and fluorescein was detected for polycation concentrations of 6 – 12 µg/ml (Hong et al., 2006).

A synergistic effect of PLL incubation and electroporation on the fusion efficiency of cells has been reported (Gröbner et al., 1995; Liu et al., 2000). Liu et al. (2000) studied the effect of different poly-amino acid polymers on the electrofusion of human cancer cells in suspension after dielectrophoresis. They found that the fusion yield increased up to 2-fold when cells were electrofused in presence of 15 µg/ml poly-L-lysine with a molecular mass of 233 200 g/mol. The fusion yield increased with the PLL concentration and the molecular mass of the polymer (Liu et al., 2000). Electrofusion in presence of 53 300 g/mol PLL in a concentration of 5 µg/ml resulted in a 1.5-fold increase in the fusion yield. Considerable increases in fusion yield were also obtained for poly-L-arginine and poly-L-glutamic acid. For fusion experiments presented in this work PLL with a similar molecular weight of 30 000 – 70 000 g/mol (3 µg/ml) was used (Tab. 4.12). Poly-L-glutamic acid (PGA) showed no fusogenic effect in this work (Fig. 6.56). The fusogenic effects of the positively charged polymers was predominantly ascribed to the electrostatic interactions with the negatively charged membrane (Liu et al., 2000). The interactions of cationic molecules with the membrane were found to depend on their molecular size and the charge density (Goodbey et al., 1999b; Fisher et al., 1999, 2003). PEI variants studied in this work had a molecular weight of 1300 or 750 000 g/mol, respectively. No significant differences in fusion efficiencies were detected for these variants. However, the impedance at 4 kHz becomes insensitive for high fusion degrees (cp. Fig. 6.34; Fig. 6.40). For reasonable comparison of the strong fusogenic polymers PEI, PLL and the *PolyMAG* particles a lower frequency for analysis should be chosen.

In conclusion, the cell agglutinating as well as the membrane destabilizing effect of the cationic polymers PEI and PLL might explain the fusogenic effect on HEK cells in combination with *in situ* electroporation. Probably, the polymers are able to stabilize the membrane defects that are induced by electroporation. This would also explain the low dependency of fusion on the pulse duration.

Electrofusion in Presence of Functionalized Nanoparticles

Due to the membrane permeabilizing effects, polycationic polymers like PEI and PLL are toxic in their soluble forms (Fischer et al., 1999, 2003; Choksakulnimitr et al., 1995). The complexation with DNA or immobilization on particles or other solid surfaces reduces their toxicity (Godbey et al., 1999a; Seitz et al., 2007). Various groups have bound branched PEI molecules of different molecular weights to magnetic iron oxide particles with the aim of magnetic field mediated targeting of the DNA/PEI complexes (Seitz et al., 2007; McBain et al., 2007; Plank et al., 2003).

PEI bound to the iron oxide *PolyMAG* particles showed a similar fusion efficiency as was observed for the free cationic polymers PEI and PLL (Fig. 6.56). In contrast to the PEI-coated *PolyMAG* nanoparticles, however, amine functionalized polystyrene nanoparticles did not lead to an increased fusion of HEK cells after pulsing (Fig. 6.55). For both cationic particles a positive zeta potential was measured: 50.8 ± 5.5 mV for the *PolyMAG* particles and a slightly lower value of 42.1 ± 5.8 mV for the amine functionalized polystyrene particles (Tab. 6.6).

Like *PolyMAG* nanoparticles that were found to colocalize with the cell membrane of HEK-EYFP/pAbcg2 cells (Fig.6.50; Fig. 51; Fig. 6.52), also amine functionalized polystyrene nanoparticles showed a strong affinity to the membrane of HEK-EYFP/pAbcg2 cells (Fig. 6.58). The amine functionalized particles strongly aggregated on the surface of the cell membrane, while carboxy modified particles, in contrast, showed less intense accumulation at the membrane surface, although applied in the same concentration.

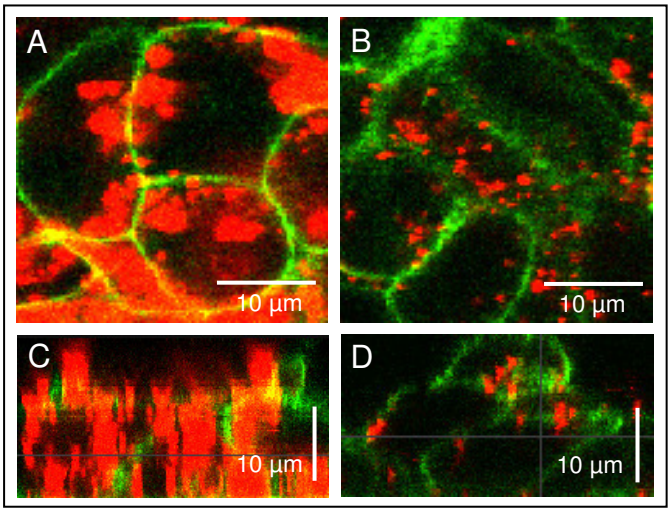

Fig. 6.58: Confocal fluorescence micrographs of HEK-EYFP/pAbcg2 cells 12 h after exposure to polystyrene particles (9 pM) with different surface modifications: **A**, **C:** amine; **B**, **D:** carboxy.

Several authors have reported that amine modified polystyrene particles are efficiently incorporated by various different cell types (Yamamoto et al., 2002; Xia et al., 2008; Jiang et al., 2010; Zupke et al., 2010). Also for nanoparticles of other materials several publications demonstrate the strong uptake of amine functionalized particles compared to other surface functionalities (Harush-Frenkel et al., 2008; Basarkar and Singh, 2009; Lee et al., 2008; Das et al., 2010).

Systematic studies on the influence of the zeta potential of amine and carboxy functionalized polystyrene particles revealed that their uptake into HeLa cells increases with increasing positive surface charge (Holzapfel et al., 2005). With increasing number of amino groups per particle the intracellular fluorescence due to uptake by HeLa, Jurkat and KG1a cells increased (Lorenz et al., 2006). Additionally, Lorenz et al. (2006) could show by SEM and confocal fluorescence analysis that already 2 h after incubation a high number of amine modified latex particles with a diameter of 330 nm has attached to the cell membrane of MSC cells. This correlates well with the strong aggregation of amine functionalized particles observed in this work (Fig. 6.58). Typically, amine functionalization results in a higher cellular uptake than functionalization with negatively charged groups, which can be mainly ascribed to the electrostatic interaction with the membrane surface (Baier et al., 2011; Mailänder and Landfester, 2009). However, also negatively charged particles are able to interact with the membrane for uptake, presumably via interaction with certain surface proteins. The fluorescence microscopic images presented in this work show that the carboxy functionalized polystyrene particles are localized at the membrane of HEK-EYFP/pAbcg2 cells, although in lower concentration than observed for amine functionalized particles (Fig. 6.58). The unmodified particles were non fluorescent and their localization with respect to the cells was therefore not detectable. According to the studies of Holzapfel et al. (2005), however, particles with low surface charge evoke only minimal interactions with the membrane and are not expected to accumulate strongly onto the cell surface. Whereas the carboxy functionalized nanoparticles revealed a strongly negative zeta potential (– 52.9.3 ± 6.6) mV, the unmodified particled only exhibited a slightly positive zeta potential of (12.3 ± 7.3) mV.
The fact that PEI-coated *PolyMAG* nanoparticles led to cell fusion, whereas amine modified paticles did not, might be ascribed to the three-dimensional arrangement of amino groups in the PEI. The flexibility of polycationic macromolecules was discussed to play an essential role for the accessibility of their charges to the cell surface (Fischer et al., 2003; Chokasakulnimitir et al., 1995). In contrast to the flexible PEI chains coating the *PolyMAG* particles, the amino groups on the surface of the polystyrene particles are tightly bound to the rigid surface, which dictates their three-dimensional arrangement. Rigid molecules were described to have more difficulties to interact with the membrane surface than flexible molecules (Ryster, 1967; Singh et al., 1992). Due to the missing flexibility the amino groups of the polystyrene nanoparticleas may not be able to stabilize membrane defects, as it is reported for PEI and PLL (Hong et al., 2006).

Since the enhanced fusion in presence of the *PolyMAG* nanoparticles has been ascribed to its PEI coat, the magnetic field expectedly proved to be not essential (Fig. 6.44). Although the magnetic field was shown to speed up *PolyMAG* particle accumulation at the cell surface (Scherer et al., 2002), particles do gather on the the cell layer by mere sedimentation as well. The pre-incubation time of cells with *PolyMAG* nanoparticles sedimenting onto the cell surface influenced the fusion yield (Fig. 6.54). Results indicate that the highest fusion yield is achieved after a certain pre-incubation time roughly between 15 and 120 min. Shorter or much longer incubation times resulted in a significantly reduced fusion yield. Since the PEI

coat stimulates endocytotic uptake, *PolyMAG* particles are removed from the cell surface as time progresses and is no longer available to mediate cell fusion. Plank et al. (2003) and Huth et al. (2004) showed that *PolyMAG* particles could be found inside of membrane invaginations near the cell surface already after 15 min. After 24 h a high fraction of particles was found inside the cell, while few were still located at the cell surface.
The low fusion efficiency after only short pre-incubation times may be explained by the equilibration time that is needed to establish close cell-cell contacts by adsoption of polycationic material to the cell surface. After addition of *PolyMAG* nanoparticles to HEK cells the cell layer impedance was initially lower compared to an equilibrated cell layer without nanoparticles (Fig. 6.3). During about 30 – 60 min after particle addition the impedance typically increased to values above that of a particle-free cell layer. Since a slight initial impedance drop and subsequent recovery to pre-pulse values were also observed after addition of particle-free medium, part of the impedance changes can be ascribed to equilibration effects after fluid exchange. The (normalized) impedance typically increased above values of particle-free cell layers, when *PolyMAG* particles (Fig. 6.3; Fig. 6.7; Fig. 6.26; Fig. 6.45 A) or soluble PEI or PLL (not shown) were added. This might indicate that the soluble or particle bound cationic polymers change the width of the intercellular spaces available for current flow by supporting the formation of unspecific, electrostatically induced cell-cell contacts. Finally the interplay between the establishment of membrane contact by adsoption of polycationic material to the cell surface and endocytotic elimination from the membrane will determine the fusogenic potential.

6.8.1.3 Influence of Heterologous Membrane Protein Overexpression in HEK-EYFP/pAbcg2 Cells

Compared to the HEK-293 wild type cell line, HEK-EYFP/pAbcg2 cells showed significantly increased fusion efficiencies. The impedance values that were obtained after fusion of *PolyMAG* preincubated cells was considerably enhanced for HEK-EYFP/pAbcg2 cells yielding average values of (34.4 ± 1.1) kΩ (Fig. 6.21), while HEK-293 wild type cell layers only gave rise to an average impedance of (21.1 ± 0.4) kΩ (Fig. 6.6) after fusion. Whereas HEK-293 wild type cells reached an 1.5-fold impedance increase compared to pre-pulse values (Fig. 6.8), HEK-EYFP/pAbcg2 cells reached an almost 2.5-fold impedance increase after electrofusion (Fig. 6.22). A 2.1-fold impedance increase of HEK-293 cell layers was only achieved, when cells were electrofused by three subsequent pulsing steps (Fig. 6.8).
The difference between these two cell lines is the overexpression of a recombinant membrane protein in HEK-EYFP/pAbcg2 cells (Seidl, 2008). The porcine Abcg2 transporter protein is an integral membrane protein with 6 transmembrane domains and three extracellular loops. The third extracellular loop consists of 74 amino acids and contains two potential sites for N-glycosylation. The EYFP tag is located intracellularily at the N-terminus of the protein. Many amino acids with a negative charge at pH 7.5 can be found in this extracellular loop (cp. Appendix *A*4) (Seidl, 2008). The overexpression of this protein may thereby render the HEK-

EYFP/pAbcg2 cells a net surface charge which is more negative than that of the HEK-293 wild type cells. A very negative charge on the cell surface is likely to foster PEI adsorbtion by electrostatic interactions. Actually, electrosttic interactions with PEI have been exploited for protein purification and separation (Burgess et al., 1975; Shibata et al., 1981; Hanora et al., 2005). PEI treated filters are for example used to adsorb ligand-free membrane receptors from ligand receptor reaction mixtures (Bruns et al., 1983). PEI-copper complexes have moreover been used to identify negatively charged sites on the surface of tissues by electron microscopy since the PEI targets the electron dense material to anionic sites on cell membranes (Pfüller et al., 1988). A higher concentration of PEI at the membrane of HEK-EYFP/pAbcg2 cells might thus enhance the promoting effects of PEI on cell fusion, which is likely based on (i) cell aggregation and (ii) stabilization of electropores.

6.8.2 Intracellular Organization of Fused HEK Cells

The previous chapters demonstrated how multi-cell fusion of HEK cells grown on ECIS electrodes is induced by electric pulse application and pre-incubation with certain polycationic materials. The intracellular organization of fused HEK cells is discussed in the following.

- ***Fused HEK-293 cells formed flat multinuclear giant cellular bodies which were viable for ~ 24 h.***
- ***Cell nuclei strongly clustered in the center of fused giant cells.***
- ***Mitochondria were homogeneously distributed among the cytoplasm of fused cells.***
- ***The actin cytoskeleton co-localized with the cell membrane.***

By application of an electric pulse of 40 kHz, 4 V and 200 ms, flat cellular bodies were created (Fig. 6.23; Fig. 6.24). *In situ* fused giant HEK cells were polynucleate. Roughly about 30 clustered cell nuclei were found in a fused cell body (Fig. 6.29 C). The formation of polynucleate cells after fusion is a well known phenomenon that occurs in suspension (Pilwat et al., 1981; Zimmermann and Vienken, 1982) as well as *in situ* (see below), especially when cell densities are high. Zimmermann et al. (2006) for example fused HEK-293 cells in suspension and created giant HEK cells that contained up to 7 nuclei after fusion.
Clustering and redistribution of nuclei is a typical phenomenon occurring after *in situ* cell fusion. Electrofusion (Blangero and Teissié, 1983; Zheng and Chang, 1990) as well as fusion induced by virusses (Okamoto et al., 1997; Wang et al., 2005), PEG mediated fusion (Kotani et al., 2002) and fusion events during tissue development (Steinberg et al., 2010) were reported to create such a reorganization of nuclei in adherent cells. Nuclei form aggregates in the center of the giant cell (Zheng and Chang, 1990; Wang et al., 2005; Bateman et al., 2000; Steinberg et al., 2010) or show a circular alignment at the outer membrane (Gasser and Möst, 1999; Kotani et al., 2002). Zheng and Chang (1990) for example found that CV-1 cells after

electrofusion on glass slides formed clusters of nuclei in the center of fused cells. About 25 % of the population formed multicellular bodies with more than 4 nuclei. Electrofusion of CHO and HeLa cells grown on petri dishes yielded multinucleate cells with up to 12 or 15 nuclei, respectively (Teissié and Conte, 1988). Steinberg et al. (2010) reported that CHO cells heterologously expressing a certain myoblast heparin-binding receptor, which is involved in myocyte fusion, form syncytia comprising several hundred nuclei. Even the creation of a syncytium consisting of more than 10^6 nuclei has been reported by using certain viral proteins for cell fusion (Salsman et al., 2005)

The cytoskeleton is assumed to play a central role in the reorganization of nuclei and other organelles (Blangero et al., 1989; Zheng and Chang, 1990, 1991). Zheng and Chang (1990) analyzed the role of microtubules (MTs) in the process of cell fusion. They could demonstrate that the microtubules are essentially participating in the formation of nuclear clusters, since the formation of nuclear aggregates was inhibited by colchicine. New MTs were synthesized at the cytoplasmic bridges in parallel bundles. The authors proposed that these MT bundles were formed by overlapping individual fibres that originate from the microtubule forming centers in participating cells. In the end of the fusion process a high concentration of MTs was found between the clustered nuclei.

The re-structuration of MTs after electrofusion was also described to reorganize the ER and mitochondria (Zheng and Chang, 1991). As found in this work mitochondria were homogeneously distributed among the cytoplasm of fused giant cells (Fig. 6.30). This indicates that the MTs, where the mitochondria are typically linked to (Heggeness et al., 1978), also participated in the re-distribution of mitochondria. However, the MTs of giant HEK cells have not been stained.

Also the actin cytoskeleton is assumed to be involved in the fusion process (Wu et al., 1994; Baumann and Sowers, 1996). Cytochemical staining of the actin cytoskeleton (Fig. 6.32) did however not reveal any significant redistribution ~ 3 h after fusion. Since HEK-293 cells do not form many stress fibers or other distinct actin structures, a certain redistribution was hard to detect. Before and after fusion the actin was predominantly found in co-localization with the membrane (Fig. 6.32). Also Blangero et al. (1989) showed that there is no particular change in the distribution of the actin cytoskeleton after electrofusion. However, they used a CHO WTT cell line, which can be cultured on substrates or in suspension. In contrast to the CHO-K1 strain this cell line does not form actin stress fibres. However, Zheng and Chang (1990) found considerable redistribution of filamentous actin after *in situ* electrofusion of CV-1 cells. While actin stress fibres partially disappeared shortly after fusion, they re-appeared after about 2 – 3 h spanning the entire giant cell.

The polynucleate cellular bodies contained active esterases (Fig. 6.12) and were able to express heterologous genes (Fig. 6.25). Both observations indicate their viability over several hours. Fused HEK cells are stable on the ECIS electrode for maximal 24 h (Fig. 6.26). After breakdown of the impedance the giant cell membrane reveals many vesicle-like structures and membrane defects (Fig. 6.27). The limited stability of electrofused HEK cells can be ascribed to several factors. The cells have already reached a critical degree of confluency when they are fused. Reaching confluency HEK cells start to overlap and form multilayers consisting of

2 – 3 cells in the third dimension. The stability of such superconfluent cell layers is low and their viability may already be limited in the terminal phase of their life cycle. The sudden mixing and interaction of cytoplasmic factors of individual cells in different cell cycle stages may cause dysregulation of normal cell functions or even induce apoptosis. A normal cell division might not be possible, since the synchronization of the centrosomes, distribution of chromosomes and definition of the cytokinesis plane are impossible. It has been described in the literature that syncytia that were formed by virus-induced (Scheller and Jasoy, 2001; Salsman et al., 2005) or PEG-induced (Huang et al., 1997) fusion undergo apoptosis. Apoptosis is likely induced either as a response to DNA abnormalities, deregulated cell homeostasis or the presence of pro-apoptotic factors due to fusion with already apoptotic cells (Huang et al., 1997; Perfettini et al., 2008). In addition, the membrane stability of large cells may be critical. Little defects or surface tension may lead to severe membrane damage. As PEI and PLL are known to destabilize membranes, constant exposure to these substances might induce leaks that lead to rupture or loss of essential cellular components.

6.8.3 Impedimetric Monitoring of Multi-Cell Fusion

This work showed that multi-cellular fusion of adherent HEK cells can be monitored *in situ* by impedance measurements.

- ***Multi-cell fusion was proven by various staining methods that label the extracellular fluid, the plasma membrane or the cytoplasm.***
- ***The fusion of HEK cells grown on ECIS electrodes led to an increase of the impedance magnitude at 4 kHz.***
- ***Cell fusion caused an increase of the parameters α and R_b which describe the impedance arising from the cell-substrate and cell-cell contacts.***
- ***The average number of fused cells on the ECIS electrode was extracted from impedance spectra by using a model approach.***

Commonly, cell fusion is detected by optical methods like microscopy or flow cytometry (Jaroszeski et al., 1995, 1998) often in combination with membrane, cytoplasmic or nuclear stainings that report on lipid and cytoplasmic mixing (Wojcieszyn, 1983; Sarkar et al., 1989; Dimitrov, 1995; Chien et al., 2009). Alternatively, biochemical approaches are used (Finaz et al., 1984; Alvarez-Dolado et al., 2003; Bär et al., 2006) which are combined with quantitative detection assays (Shinn-Thomas et al., 2008). The use of cell lines expressing recombinant proteins tagged with GFP variants to vizualize membrane fusion and cytoplasmic mixing is an appreciated method to avoid chemical stainings and to integrate biochemical recognition events (Tagawa et al., 2005; Zimmermann et al., 2006; Steinberg et al., 2010; Lin et al., 2010).

Also in this work cell fusion was proven by microscopic techniques using 4 kDa FITC-dextran as an extracellular marker (Fig. 6.10), DiI for membrane staining (Fig. 6.11) or calceinAM for cytoplasmic staining (Fig. 6.12).
Since the cytotochemical staining procedures were associated with certain experimental drawbacks as poor staining homogeneity or damage of the cell layer by the staining procedure, HEK cell lines with intrinsic membrane or cytoplasmic fluorescence were used in addition to that. Especially HEK-EYFP/pAbcg2 cells expressing an EYFP tagged recombinant membrane protein as membrane label proved to be well-suited for the microscopic detection and study of the cell fusion events (chapter 6.2.5). The use of mixed cell populations of HEK-ECFP and HEK-EYFP/pAbcg2 cells moreover demonstrated that after fusion both, membranes and cytoplasmic content, have intermixed (Fig. 6.17; Fig. 5.18). Such double marker approaches are often used to verify the exchange of cytoplasmic material after complete fusion (Popot and Fournie, 2003; Giraudo et al., 2005).

A popular parameter to quantify fusion is the fusion yield. The fusion yield is defined as the fraction of cells that have fused relative to the total number of cells. The number of fused cells can be most accurately determined by counting the number of nuclei. The ratio of nuclei in polynucleate cells as a fraction of the total number of nuclei provides the so called nucleation index (Blangero and Teissié, 1983; Teissié and Ramos, 1998; Ramos et al., 2002). Modern approaches use fluoresecence microscopy with subsequent image analysis or flow cytometry (Gabrijel et al., 2003) as well as other quantitative approaches (Shinn-Thomas et al., 2008). Fluorescence microscopic images of fused HEK-cells revealed, that the quantification of the fusion efficiency is difficult. Especially time resolved microscopy showed that individual membrane fusion events are hard to detect (Fig. 6.33 A). Confocal microscopy can only detect fusion events in one focal plane. Shifts in the cell layer due to fusion events can push membranes out of focus and bring new ones in the observed field of view. The multilayered composition of a typical HEK cell layer is one reason for such difficulties. But also in less dense cell layers problems with microscopic detection of fusion events have been described (Blangero et al., 1989). These problems typically occur when a high number of cells fuse and cell nuclei aggregate. Since the nuclei of fused cells formed dense clusters, the nucleation index could not be determined exactly (Fig. 6.28; Fig. 6.29). Concomittant membrane stains could not reveal the continuity of the membrane encompassing a cluster of nuclei, which would define it as an individual cell body. Since cell fusion is not limited to the area of the active electrode, the quantification of cell fusion has to account for that.
Only few electric detection methods for cell fusion have been reported. Abidor et al. (1993a) measured the resistance of L-929 cells that have been pelleted in a centrifuge to create close membrane contact prior to electrofusion during rotor spinning. The increase in pellet resistance correlated well with the microscopic fusion yield. They moreover showed that treatment of cells with cytochalasin affected the fusion efficiency in the same way as the pellet resistance. The fusion of vesicles with the plasma membrane during exocytosis can be measured by a patch clamp technique, that measures the membrane capacitance as a function of the membrane surface area (Zimmerberg et al., 1987, 1993). Melikyan et al. (1993) used a

similar system to study the fusion between voltage-clamped planar lipid bilayers and influenza virus infected MDCK cells. They applied a sinusoidal voltage and measured the electrical admittance in order to monitor the increase of the capacitance of the lipid bilayer after a fusion pore was formed. Bertrand et al. (1998) used a conventional transepithelial electrophysiology clamp to measure the total membrane capacitance of cell monolayers by impedance measurements. They were able to monitor the time course of capacitance changes associated with purinergenic stimulation of mucin exocytosis in clolonic globlet cell-like HT29Cl16E cells. Leikina et al. (1992) were even able to measure multi-cell fusion events in SF6 cells that overexpressed the baculoviral envelope protein. They measured quantal capacitance increases for each step of membrane surface area increase due to a fusion event with an additional cell. These changes in capacitance were detected before any morphological changes could be observed microscopically.
To date an electric method to monitor *in situ* cell fusion has not yet been described. The only report that describes the phenomenon of cell fusion that was detected by impedance measurements was published by Xing et al. (2005). Upon incubation of NIH-3T3 with arsenite (24.66 µM) they observed an unusual effect, namely an significant (~ 3-fold) but transient increase of cell layer impedance within 5 h. Stainings with Hoechst and rhodamin-phalloidin revealed that 3 h after treatment huge multinuclear cell bodies had formed. The authors concluded that cell fusion might have occurred. After 8 h, however, these cells began to decompose and apparently underwent nuclear condensation and fragmentation and finally 95 % of the cells were dead after 24 h.

As shown in this work the polycation and electric field-mediated fusion of HEK cells grown on ECIS electrodes led to a considerable impedance increase, which was stable over several hours. By monitoring the impedance magnitude at 4 kHz it was possible to evaluate the influence of electroporation parameters like pulse amplitude and duration as well as the fusogenic potential of different particle and polymer additives (cp. chapter 6.7). The establishment of a model that is able to extract the average number of fused cells from an impedance spectrum was demonstrated successfully.

6.8.3.1 Model for *In Situ* Multi-Cell Fusion

Cell fusion leads to a reduction of the amount of intercellular spaces as well as an elongation of the subcellular pathway (Fig. 6.59) which both cause an increase of cell layer impedance (Fig. 6.34 A). Indeed the analysis of the impedance spectra, that significantly altered during a fusion process (Fig. 6.34 B), revealed that the cellular parameters α and R_b are increased for electrofused HEK cells (Tab. 6.1). Especially for HEK-EYFP/pAbcg2 cells, that showed extensive multi-cell fusion, values for α and R_b increased considerably. The development of the cell layer impedance along the fusion process correlated well with the change of the parameter value α (Fig. 6.35; Fig. 6.36). Values for the parameter R_b were also found to considerably increase during the fusion process of HEK-EYFP/pAbcg2 cells (Fig. 6.36 B2).

For HEK-293 wild type cells, however, R_b only changed insignificantly after fusion (Fig. 6.35 B2; Tab. 6.1). The initial transient drop in R_b can be ascribed to the cell response after electric pulsing (cp. Fig. 6.36 A2; cp. discussion chapter 5.4.1.1).

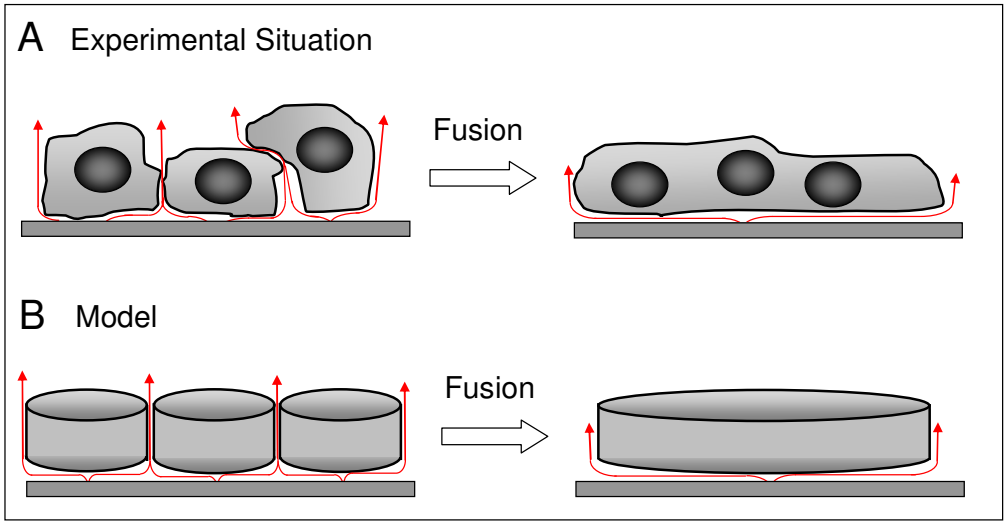

Fig. 6.59: Schematic illustration of *in situ* cell fusion. **A:** Experimental situation. **B:** Model. Arrows indicate non-invasive AC current flow.

On the basis of these observations a model was established that describes how the impedance is expected to change when a certain amount of cells fuse on the electrode (chapter 6.6.2).
However, some general assumptions had to be made that deviate from the real experimental system (chapter 6.6.2.1). The cells were approximated as circular discs that do not overlap (Fig. 6.59 B). For simulations a maximal number of 245 cells was used. This number of cells that cover the surface area of a conventional *8W1E* electrode was calculated from the average cell perimeter of HEK-EYFP/pAbcg2 cells (Fig. 6.38). The actual number of cells on the electrode in the experimental system were, however, often higher. Counting the number of DAPI stained nuclei of HEK-EYFP/pAbcg2 cells returned 342 ± 12 cells on an ECIS electrode (Fig. 6.28 D). The experiments have shown that cell fusion often exceeds the border of the electrode (Fig. 6.23). The model, in contrast, is limited to the active electrode area of 5×10^{-4} cm^2. The model is based on the assumption that cell fusion on the electrode is uniform, i.e. the size and distribution of giant cells on the electrode is homogeneous (Fig. 6.37 C). It calculates the ideal situation in which always a distinct number of cells fuses together and thereby reduces the total number of cellular bodies that all have the same size. However, experimental results show that cell fusion is often extremely non-uniform (e.g. Fig. 6.14; Fig 6.25). Often certain areas of the electrode are covered with a huge giant cell, while the the remaining part is covered with single cells. Considering such inhomogeneties would require a complicated analysis of the α and R_b behavior in heterogenous systems and the implementation of statistics.
So far the model is only suited to describe the process of fusion in rough approximation. Nevertheless, comparison of experimental data with model spectra in first approximation revealed a good correlation (Fig. 6.42; Fig. 6.43). Experimental impedance spectra of fused

HEK-293 and HEK-EYFP/pAbcg2 cells overlap with spectra that were generated on the basis of the model described in chapter 6.6.2.1. In agreement with the spectral correlation values for the model parameters α and R_b as well as the impedance magnitude at 4 kHz for experimental and simulated cell layers were very similar (Tab. 6.4; Tab. 6.5). However, in four of six cases R_b values of experimental cell layers were considerably lower than predicted by the model. In three of these cases the parameter α was underestimated by the model. These deviations might be ascribed to the inhomogenities within the cell layer and its effects on the parameter values as discussed above.

6.8.3.2 Cell Fusion Kinetics

The process of cell fusion can be generally subdivided into three phases (1) establishment of cell-cell contact, (2) mixing of membrane lipids and soluble cytoplasmic molecules and (3) cell morphology rearrangements (Blangero et al., 1989). Cell-cell contact is typically established before fusion is initiated by electric pulsing. Likely, the PEI coat of *PolyMAG* particles and PEI or PLL in solution mediate close contacts of confluent HEK cells grown on ECIS electrodes. Membrane fusion is then initiated by electric membrane destabilization. Electrofusion of cells in suspension revealed that lipid mixing and the first exchange of soluble cytoplasmic marker dyes occur within a few seconds after the electric trigger (Stenger and Hui, 1988). However, subsequent morphological rearrangements like rounding of the fused cells take several minutes to more than one hour, depending on the temperature and the amount of fusing cells (Ohno-Shosaku et al., 1985). Cells that have been electrofused *in situ* were even reported to require about 2 – 3 h until the entire fusion process is completed (Sukharev et al., 1990; Zheng and Chang, 1990, 1991).
These reports correlate well with the experimental results in this work. The entire process of HEK multi-cell fusion takes about 1 – 3 h. The exact time frame during which the impedance increased varied individually and depended on the cell type. For HEK-293 wild type cells a plateau (21.1 ± 0.4) kΩ at 4 kHz was typically reached after 50 – 100 min (cp. Fig. 6.3; Fig. 6.7). HEK-EYFP/pAbcg2 cells in contrast required between 100 and 300 min to reach a final impedance of (34.4 ± 1.1) kΩ (cp. Fig. 6.20; Fig. 6.26; Fig. 6.44; Fig. 6.45).
A typical time course of impedance for electrofusing HEK-EYFP/pAbcg2 cell layers was shown in Fig. 6.33. The time course reveals the multiphasic character of the fusion process. The entire post-pulse time course can be roughly subdivided into three phases: (i) An initial lag phase, the period between pulse application and time point where the impedance starts to increase with its maximal rate, (ii) the time period with maximal rate of impedance increase and (iii) the transition into the plateau phase. During the lag phase the impedance transiently increased above and subsequently dropped below pre-pulse values within ~ 2 min (Fig. 6.33). After about 15 min the impedance recovered to pre-pulse values. Due to the lower temporal resolution in standard measurements only a transient increase or decrease is typically observed in most impedance profiles within the first 5 – 15 min after electric pulsing.

Such lag phases have also been described in the literature (Dimitrov, 1995). They reflect the life-time of intermediate states before the actual intermixing of membrane components. Depending on the sort of fusion trigger, delay times were found to differ between several microseconds like for neurotransmitter release (Heuser et al., 1979) to minutes and hours like for HIV-1 envelope proteins induced fusion (Dimitrov et al., 1993). Delay times for electrofusion were typically found to be in the range of seconds (Abidor and Sowers, 1992; Dimitrov, 1993). They depend on the field strength and the pulse duration and are influenced by the force that mediates membrane contact, the temperature and medium viscosity (Dimitrov, 1993).

After the lag phase the subsequent stages of the fusion process, membrane merging and pore expansion are initiated. The fusion rate provides information on the time course of the subsequent stages (Dimitrov, 1995). Fusion rates can be determined from the number of cells that have fused per unit time by counting the number of cells or from the total fluorescence change per unit time by spectrofluorimetric assays (Stenger and Hui, 1988). Using ECIS measurements the fusion rate can be simply extracted from the impedance time course. The initial impedance increase per unit time starting after the lag phase was (240 ± 47) Ω/min for HEK-293 cells (N = 3) and (345 ± 108) Ω/min for HEK-EYFP/pAbcg2 cells (N = 8). The initial rate of impedance increase was slightly higher for the HEK-EYFP/pAbcg2 cells than for the HEK-293 wild type cells, although the recombinant cells typically needed more time to reach a stable impedance level. The period of maximal fusion rate varied between about 15 and 100 min. Thus, the initial maximum rate and the duration in this phase determine the value of impedance that is maximally reached. As discussed in 6.8.1.3 the heterologously expressed pAbcg2 protein in the membrane of HEK-EYFP/pAbcg2 cells may favour the fusogenic state of the membrane and therefore lead to a more pronounced fusion.

After the phase of maximal impedance increase the impedance settles and stabilizes to plateau values. A similar time course was observed by Sukharev et al. (1990), who fused suspended cells with adherent cells grown on a filter by application of an electric field pulse perpendicular to the filter substrate. The fusion index increased fastest within about the first 30 minutes and the fusion rate continuously slowed down until a plateau phase was reached after about 2 h. Blangero et al. (1989) observed that after a lag period of 10 min the most dramatic change in fusion index occurred between 20 and 30 min after electric field application. For longer incubation times of 40 – 60 min the fusion index levelled off and remained constant for up to 3 h. The authors proposed that the late establishment of fused cells may be indicative for the existence of long-lived fusogenic states, which are even present when the electric field induced permeability was not detected anymore (Blangero et al., 1989). Such long lived fusogenic states may also be responsible for the long time period that fusion of HEK cells can be observed. However, also the cytoskeleton can impose constraints that retard morphological changes. Even if the membranes are already locally fused, the cytoskeleton can hinder free expansion of the fusion pore.

The relevance of the cytoskeleton in the expansion step of the fusion process has been demonstrated by several authors (Blangero et al., 1989; Chernomordik and Sowers, 1991; Zheng and Chang, 1991). Zheng and Chang (1991) reported that although cytoplasmic

bridges were formed within ~ 15 minutes, cytoskeletal reorganizations of actin, microtubules and vimetin intermediate filaments as well as associated organelle redistributions of nuclei, the ER and mitochondria took two hours. If more than two cells fused, the process even required more than 3 hours. The fusion process was associated with considerable morphological alterations.

It was shown that destruction of the microtubules by diverse drugs increased the membrane fluidity and the diffusion of membrane lipids (Aszalos et al., 1985). Whereas the induction and expansion of electropores were reported to be independent of the cytoskeleton, the resealing step was found to be influenced by drugs that act on the cytoslekeleton (Rols and Teissié, 1992). The treatment of CHO cells with colchicine depolymerizing microtubules was found to speed up membrane resealing after electroporation and thus reduce the time frame of the fusogenic state. It was moreover found by cell cycle synchronization studies that the resealing rate of CHO cells depended on their cell cycle phase. During mitosis when the microtubules are absent from the plasma membrane, the resealing rate was increased. The organization of the microtubules was found to be markedly altered after exposure to an electrofusing pulse. 10 min after pulsing the typical membrane associated fluorescence of microtubules disappeared and was only detectable around the nuclei. Blangero et al. (1989) discussed that a depolymerisation of microtubules may occur after electric permeabilization as a result of Mg^{2+} uptake from the electroporation medium. Microinjection of Mg^{2+} was shown to induce such depolymerising effects on the MT filaments. After about one hour the microtubules had recovered to its typical structure again.

Also a rearrangement of the actin cytoskeleton has been reported to occur as a response to electric field induced *in situ* cell fusion (Zheng and Chang, 1990, 1991). After electrofusion was initiated in CV-1 cells grown on glass slides part of the actin stress fibres gradually disappeared. After 15 min a diffuse form of filametous actin appeared and actin tended to concentrate at the periphery of the cell. Complete reorganization and establishment of actin fibers that span the entire fused cell body took more than 2 h. Although the role of actin in the electrofusion process has not been elucidated yet, also studies on virus-induced cell fusion (Pontow et al., 2004; Kadiu et al., 2007) and cell fusion during tissue developmental processes like trophoblast and myotube formation (Kim et al., 2007; Peckham et al., 2008; Shibukawa et al., 2010) showed the importance of actin restructurations for cell fusion.

Although HEK cells do not have many cytoplasm spanning actin fibres (Fig. 6.32), cellular actin is concentrated at the cellular envelope underlying the cell membrane. Since the actin cytoskeleton is anchored to the membrane via membrane spanning proteins, changes in the membrane distribution may be followed by cytoskeletal rearrangements in the cell coat. The ability to rearrange the actin coat might be an essential prerequisite that extensive membrane fusion can occur. Electrofusion studies on erythrocyte ghosts have revealed that the disruption of the spectrin network, a rudimentary form of cytoskeleton underlying the membrane of erythrocytes, leads to extensive formation of giant cells (Chernomordik and Sowers, 1991).

It was proposed that cell fusion is an energy dependend process (Blangero et al., 1989; Verhoek-Koehler et al., 1983). Sukharev et al. (1990) could show that cell fusion could be

inhibited by the addition of sodium azide in combination with 2-deoxyglucose. The kinetics of cell fusion may therefore also depend on active rearrangements of the cytoskeleton.

Outlook:

Impedimetric detection of cell fusion may find applications in the study of biological fusion events. Biological cell fusion is often characterized by the formation of multinucleate syncytia, which are difficult to quantify with convenient methods. Developmental cell fusion processes, like the formation of myotubes or the trophoblast might for example be investigated with this system. In a similar way viral infections that lead to the formation of syncytia in anchorage-dependent cells can be addressed with ECIS measurements. In contrast, biotechnical applications might be limited. Hybridoma production as well as cellular transdifferentiation experiments are typically based on one-to-one fusion events of cells in suspension. For those applications tailor-made microfluidic approaches like electrofusion combined with cytometry or on-chip developments are yet favoured (Bakker-Shut et al., 1993; Skelly et al., 2009).

Since high accuracy and throuput are especially important in screening approaches the ECIS system may, however, be interesting for screenings addressing fusogens or membrane modulating agents. It has to be kept in mind that electrically induced cell fusion with ECIS electrodes will only be successful in cellular systems that form membrane contacts in the third dimension. For the electrofusion of monolayers the electric field pulse will have to be applied in parallel to the surface of the cell layer by additional electrodes.

7 Summary

This work addresses the electric manipulation, i.e. electroporation or electrofusion, of anchorage-dependent mammalian cells and the subsequent analysis of the cellular response using a well-established impedimetric biosensor (ECIS). Cells were grown to confluence on planar gold-film electrodes, which were used for the application of invasive electric AC pulses as well as for the non-invasive impedimetric monitoring of the cell layer response.

The first part of this work deals with the electroporation-assisted delivery of different classes of membrane-impermeable bioactive probes into various types of anchorage-dependent mammalian cells and the analysis of cell morphology changes by non-invasive impedance measurements. Optimal pulse parameters for electroporation of different adherent cell lines (NRK-52E, HEK-293, Hep G2, CHO, NIH-3T3) were obtained from dye loading studies with high molecular weight FITC-dextran in combination with impedance monitoring of cell layer recovery kinetics. The cell lines showed an individual impedance profile after application of the electroporation pulse. Impedance measurements with a high time resolution and time-lapse CLSM recordings revealed that within ~ 5 s after electroporation the membrane is resealed while the uptake of 250 kDa FITC-dextran is completed after ~ 3 s. Post-pulse impedance changes recorded over about 1 h after electroporation have been ascribed to changes in cell morphology. Electroporation of NRK cells in presence of membrane-impermeable cytotoxic molecules (azide, bleomycin, cytochrome c) changed the cellular impedance response profile, depending on the individual mechanism of cytotoxicity. Accompanying live/dead assays confirmed the impedimetric readout.
The experimental setup for electric manipulation and sensing was further optimized to allow for economic use of costly bioactive macromolecules, like enzymes, antibodies or nucleic acids in electroporation-assisted delivery. The miniaturized setup requires only sample volumes of less than 30 µl without influencing the loading efficiency or the quality of the ECIS measurement. After optimization of the electroporation parameters for different cell types the miniaturized microelectrode setup was used to monitor the cell layer response after loading with cytochrome c, DNase I and RNase A. Intracellular delivery of antibodies, nucleic acids and nanoparticles was proven by fluorescence microscopy. NRK and Hep G2 cells were loaded with antibodies that specifically bound to their intracellular epitopes ß-catenin, occludin and ZO-1, respectively. The *in situ* electroporation of adherent cells (NRK, Hep G2, HEK-293) in presence of plasmid DNA or a linear DNA fragment encoding fluorescent reporter genes resulted in cell type-dependent transfection efficiencies between 10% and 70 %. Moreover, NRK cells were efficiently loaded with PEGylated core-shell CdSe/ZnS quantum dots, resulting in a homogeneous cytoplasmic distribution of the probe.

The second part of this work was devoted to the use of substrate-integrated planar gold-film electrodes to induce and detect cell fusion. The electroporation of HEK-293 cells in presence

of polyethyleneimine (PEI) coated iron oxide particles designed for transfection (*PolyMAG*) led to a considerable cell fusion and the formation of polynucleate giant cells on the ECIS electrode. Multi-cell fusion was proven by specific cytochemical stainings as well as by fusing genetically engineered cell lines expressing fluorescent cytoplasmic (HEK-EGFP, HEK-ECFP) or membrane proteins (HEK-EYFP/pAbcg2). The process of multi-cell fusion was monitored electrically by ECIS readings at 4 kHz with a time resolution down to 0.6 min. Cell fusion was dependent on the HEK cell line. The experimentally obtained impedance spectra correlated well with those from theoretical simulations and provided an estimate for the average number of fused cells. Since the average number of fused cells is only an estimate for fusion efficiency, the impedance magnitude at 4 kHz was taken to evaluate different parameters, like electric pulse parameters and fusogenic additives, for their impact on cell fusion. Electric pulsing of cells in presence of negatively charged polymers and polystyrene particles did not induce fusion. In contrast, cationic soluble polymers like PEI and poly-L-lysine were shown to induce multi-cell fusion after electroporation, whereas amine modified cationic polystyrene nanoparticles had no fusogenic effect. Taken together, the fusogenic effect of *PolyMAG* particles in combination with electric pulsing has been ascribed to its polycationic and flexible PEI coat.

8 Zusammenfassung

Die elektrische Manipulation adhärenter Zellen auf leitfähigen Substraten *in situ* und die anschließende Analyse der Zellantwort mittels Impedanzspektroskopie (ECIS) standen im Vordergrund dieser Arbeit. Dazu wurden konfluente Zellschichten auf planaren Gold-Film Elektroden kultiviert, die zugleich zur Applikation invasiver AC Pulse und zur nicht-invasiven Impedanzanalyse für die Dokumentation der Zellantwort genutzt wurden.
Der erste Teil der Arbeit beschäftigte sich mit dem durch *in situ* Elektroporation vermittelten Transfer diverser bioaktiver Moleküle in adhärente Zellen und der Analyse von Zellmorphologieänderungen mit Hilfe von Zellform-sensitiven Impedanzmessungen.
Für konfluente Schichten verschiedener adhärenter Zelllinien (NRK, HEK-293, Hep G2, CHO, NIH-3T3) wurden die Elektroporationsbedingungen so optimiert, dass eine Beladung nahezu aller Zellen auf der Elektrode mit dem Indikator-Molekül FITC-Dextran (250 kDa) erfolgte, ohne dass eine irreversible Schädigung auftrat, wie anhand kontinuierlicher Impedanzmessungen nachgewiesen wurde. Als Antwort auf einen Elektroporationspuls reagieren konfluente Zellschichten verschiedener Zelllinien mit einem individuellen, zelltypischen Impedanzprofil. Impedanzmessungen mit hoher zeitlicher Auflösung zeigten, dass die Membranintegrität nach elektrischer Permeabilisierung innerhalb nur weniger Sekunden wieder hergestellt ist. Zeitaufgelöste CLSM Aufnahmen bestätigten, dass eine intrazelluläre Akkumulation von 250 kDa FITC-Dextran nur innerhalb der ersten 3 s nach einer Elektroporation erfolgte. Die bis zu 1 h andauernden Impedanzänderungen nach Elektroporation können daher auf Änderungen in der Zellmorphologie zurückgeführt werden. Das zelltypische Impedanzprofil nach Applizierung eines Elektroporationspulses kann innerhalb des Regenerationszeitraumes von etwa 1 h durch Zellreaktionen auf eingetragene, bioaktive Moleküle verändert oder überlagert werden. Das kleine anorganische Azid Ion, das Glykopeptid-Antibiotikum und Elektrochemotherapeutikum Bleomycin sowie der Apoptoseauslöser Cytochrom c wurden mittels *in situ* Elektroporation in das Cytoplasma von NRK Zellen eingetragen. Als Antwort auf diese cytotoxisch wirkenden Moleküle konnte mittels kontinuierlicher ECIS Messungen eine Abnahme der Impedanz dokumentiert werden, welche in Abhängigkeit vom Wirkmechanismus der jeweiligen Substanz zeitlich versetzt zum Eintrag in die Zelle einsetzte. Unterstützend zu den Impedanzprofilen gaben zellbiologische Färbungen mit DAPI, EthD-1 und CaAM Hinweise darauf, dass Bleomycin und Cytochrom c in NRK Zellen Apoptose induzieren.
Nach grundsätzlicher Validierung des kombinierten Elektroporations- und Sensorsystems wurde der experimentelle Aufbau für einen ökonomischen Eintrag kostenintensiver und aufwändig zu präparierender Proben miniaturisiert. Es wurde ein spezielles Elektrodenlayout entwickelt, welches es erlaubt, in einem Probenvolumen von nur 30 µl effizient zu elektroporieren und über 70 h stabil zu messen. Das miniaturisierte *in situ* Elektroporations- und Impedanzsystem wurde genutzt, um bioaktive Proteine wie Cytochrom c, RNase A und DNase I in das Cytoplasma von NRK Zellen einzutragen und deren Einfluss auf die Zellregeneration mit Hilfe nicht-invasiver Impedanzmessungen zu untersuchen. Da der

Substanzeintrag mittels *in situ* Elektroporation in Kombination mit der nicht-invasiven kontinuierlichen Impedanzmessung ein enormes Potential für die Untersuchung von Gen- und Proteinaktivitäten bedeutet, wurde die Beladung von Zellen mit Antikörpern, codierender DNA und Nanopartikeln fluoreszenzmikroskopisch untersucht. NRK Zellen konnten mit hoher Effizienz mit Antikörpern beladen werden, welche die intrazellulären Epitope ß-Catenin, Occludin und ZO-1 spezifisch binden. Die *in situ* Elektroporation von NRK, Hep G2 und HEK-293 Zellen mit codierender Plasmid- oder Fragment-DNA führte in Abhängigkeit der verwendeten Zelllinie zur Expression der fluoreszenten Reporterproteine mit Effizienzen zwischen 10 % und 70 %. Die Elektroporation von NRK Zellen in Gegenwart von Quantum Dot Nanopartikeln führte zu einer homogenen cytoplasmatischen Beladung mit Partikeln.

Der zweite Teil dieser Arbeit beschäftigte sich mit der Verwendung des ECIS basierten Elektromanipulations- und Sensorsystems zur Detektion von Zellfusionsereignissen *in situ*.

Die Elektroporation von HEK-293 Zellen in Gegenwart von zur Transfektion konzipierten, Polyethylenimin (PEI) beschichteten magnetischen Eisenoxid-Nanopartikeln (*PolyMAG*) führte zur Fusion der Zellmembranen und zur Ausbildung von polynukleären Synzytien auf der Elektrodenoberfläche. Die Fusion von HEK Zellen konnte nach spezifischer Anfärbung der Membranen, des Cytoplasmas oder des extrazellulären Raumes mikroskopisch nachgewiesen werden. Insbesondere die rekombinante Zellinie HEK-EYFP/pAbcg2 ermöglichte aufgrund ihrer intrinsischen Fluoreszenzmarkierung eine optimale mikroskopische Erfassung von Änderungen in der Membranverteilung während und nach dem Fusionsprozess. Darüber hinaus konnte der Zellfusionsprozess mit Hilfe von Impedanzmessungen bei 4 kHz mit einer zeitlichen Auflösung von bis zu 0.6 min verfolgt werden. Die Effektivität der Zellfusion erwies sich als abhängig von der eingesetzten HEK Zelllinie. Die Etablierung eines Modells auf Basis sich durch Fusion verändernder Zellparameter ermöglichte es, die Fusion von HEK Zellen auf ECIS Elektroden zu simulieren. Eine gute Übereinstimmung simulierter und experimenteller Spektren erlaubte eine Abschätzung der Zahl der im Mittel fusionierten Zellen. Für die Untersuchung der Fusionseffizienz bei Variation experimenteller Parameter, wie Einstellungen des Elektroporationspulses oder Verwendung fusogener Additive, wurde der Anstieg der Impedanz als quantitativer Indikator verwendet. Dadurch konnte sowohl die Bedeutung des elektrischen Pulses als Initiator für den Fusionsprozess als auch die entscheidende Fusions-fördernde Eigenschaft der PEI beschichteten *PolyMAG* Partikel aufgeklärt werden. Mit Fokus auf die chemischen Oberflächeneigenschaften der Partikel wurden Polystyrol Nanopartikel sowie verschiedene lösliche Polymere mit unterschiedlicher Oberflächenladung in Bezug auf ihre fusogenen Eigenschaften während der Elektropermeabilisierung untersucht. Neutrale oder negativ geladene Polymere und Partikel hatten keinen fusogenen Effekt. Polykationische, lösliche Polymere, wie PEI und PLL, induzierten einen starken Anstieg der Zellschichtimpedanz nach Pulsapplikation, wohingegen Amin-funktionalisierte Polystyrol Nanopartikel nicht zu einer Fusion der Zellen führten. Somit ließ sich schließlich die fusogene Wirkung der *PolyMAG* Partikel auf ihre polykationische und flexible Hülle aus PEI zurückführen.

9 Literature

A

Abidor, I.G., Arakelyan, V.B., Chernomordik, L.V., Chizmadzhev, Y.A., Pastushenko, V.F. and Tarasevich, M.R. (**1979**) Electric breakdown of bilayer lipid memnbranes. The main experimental facts and their qualitative discussion. *Bioelectrochem Bioenerg*, 6, 37-52.

Abidor, I.G., Barbul, A.I., Zhelev, D.V., Doinov, P., Bandrina, I.N., Osipova, E.M. and Sukharev, S.I. (**1993a**) Electrical properties of cell pellets and cell electrofusion in a centrifuge. *Biochim Biophys Acta*, 1152, 207-218.

Abidor, I.G., Li, L.H. and Hui, S.W. (**1993b**) Erythrocyte Pellets as a Model System - Osmotic phenomena, electroporation, electrofusion, membrane interactions. *Biophys J*, 64, A123-A123.

Abidor, I.G., Li, L.H. and Hui, S.W. (**1994**) Studies of cell pellets: II. Osmotic properties, electroporation, and related phenomena: membrane interactions. *Biophys J*, 67, 427-435.

Abidor, I.G. and Sowers, A.E. (**1992**) Kinetics and mechanism of cell membrane electrofusion. *Biophys J*, 61, 1557-1569.

Adam, S.A., Marr, R.S. and Gerace, L. (**1990**) Nuclear protein import in permeabilized mammalian cells requires soluble cytoplasmic factors. *J Cell Biol*, 111, 807-816.

Adel, A., Nadia, M., Mohamed, O. and Abdelhafidh, G. (**2008**) Study of thermally and chemically unfolded conformations of bovine serum albumin by means of dynamic light scattering. *Mat Sci Eng C-Bio S*, 28, 594-600.

Aden, D.P., Fogel, A., Plotkin, S., Damjanov, I. and Knowles, B.B. (**1979**) Controlled synthesis of HBsAg in a differentiated human liver carcinoma-derived cell line. *Nature*, 282, 615-616.

Ager, D.D., Phillips, J.W., Columna, E.A., Winegar, R.A. and Morgan, W.F. (**1991**) Analysis of restriction enzyme-induced DNA double-strand breaks in Chinese hamster ovary cells by pulsed-field gel electrophoresis: implications for chromosome damage. *Radiat Res*, 128, 150-156.

Ahkong, Q.F., Fisher, D., Tampion, W. and Lucy, J.A. (**1975**) Mechanisms of cell fusion. *Nature*, 253, 194-195.

Ahlemeyer, B., Klumpp, S. and Krieglstein, J. (**2002**) Release of cytochrome c into the extracellular space contributes to neuronal apoptosis induced by staurosporine. *Brain Res*, 934, 107-116.

Ai, H., Mills, D.K., Jonathan, A.S. and Jones, S.A. (**2002**) Gelatin-glutaraldehyde cross-linking on silicone rubber to increase endothelial cell adhesion and growth. *In Vitro Cell Dev Biol Anim*, 38, 487-492.

Akinc, A., Thomas, M., Klibanov, A.M. and Langer, R. (**2005**) Exploring polyethylenimine-mediated DNA transfection and the proton sponge hypothesis. *J Gene Med*, 7, 657-663.

Albermann, S. (**2004**) In situ Elektroporation adhärenter Säugerzellen. PhD thesis, Westfälische Wilhelms-Universität, Münster.

Alexander Jr., F., Price, D.T. and Bhansali, S. (**2010**) Optimization of interdigitated electrode (IDE) arrays for impedance based evaluation of Hs 578T cancer cells. *Journal of Physics: Conference Series International Conference on Electrical Bioimpedance*, I.

Alvarez-Dolado, M., Pardal, R., Garcia-Verdugo, J.M., Fike, J.R., Lee, H.O., Pfeffer, K., Lois, C., Morrison, S.J. and Alvarez-Buylla, A. (**2003**) Fusion of bone-marrow-derived cells with Purkinje neurons, cardiomyocytes and hepatocytes. *Nature*, 425, 968-973.

Anagnostopoulou, A., Cao, J., Vultur, A., Firth, K. and Raptis, L. (**2007**) Examination of gap junctional, intercellular communication by in situ electroporation on two co-planar indium-tin oxide electrodes. *Mol Oncol*, 1, 226-231.

Angelova, M.I., Hristova, N. and Tsoneva, I. (**1999**) DNA-induced endocytosis upon local microinjection to giant unilamellar cationic vesicles. *Eur Biophys J*, 28, 142-150.

Armstrong, J.K., Wenby, R.B., Meiselman, H.J. and Fisher, T.C. (**2004**) The hydrodynamic radii of macromolecules and their effect on red blood cell aggregation. *Biophys J*, 87, 4259-4270.

Arndt, S., Seebach, J., Psathaki, K., Galla, H.J. and Wegener, J. (**2004**) Bioelectrical impedance assay to monitor changes in cell shape during apoptosis. *Biosens Bioelectron*, 19, 583-594.

Aszalos, A., Yang, G.C. and Gottesman, M.M. (**1985**) Depolymerization of microtubules increases the motional freedom of molecular probes in cellular plasma membranes. *J Cell Biol*, 100, 1357-1362.

Atienza, J.M., Yu, N.C., Kirstein, S.L., Xi, B., Wang, X.B., Xu, X. and Abossi, Y.A. (**2008**) Dynamic and label-free cell-based assays using the real-time cell electronic sensing system (Reprinted from ASSAY and Drug Development Technologies, vol 4, 2006). *Genet Eng Biotechn N*, 28, 17-23.

Aunins, J.G. and Wang, D.I.C. (**1989**) Induced flocculation of animal cells in suspension culture. *Biotechnol Bioeng,* 34, 629-638.

B

Bagalkot, V., Zhang, L., Levy-Nissenbaum, E., Jon, S., Kantoff, P.W., Langer, R. and Farokhzad, O.C. (**2007**) Quantum dot-aptamer conjugates for synchronous cancer imaging, therapy, and sensing of drug delivery based on bi-fluorescence resonance energy transfer. *Nano Lett*, 7, 3065-3070.

Baier, G., Costa, C., Zeller, A., Baumann, D., Sayer, C., Araujo, P.H., Mailander, V., Musyanovych, A. and Landfester, K. (**2011**) BSA adsorption on differently charged polystyrene nanoparticles using Isothermal titration calorimetry and the influence on cellular uptake. *Macromol Biosci*, 11 ,628-638.

Bakker-Schut, T.C., Kraan, Y.M., Barlag, W., de Leij, L., de Grooth, B.G. and Greve, J. (**1993**) Selective electrofusion of conjugated cells in flow. *Biophys J*, 65, 568-572.

Bal-Price, A., Borutaite, V. and Brown, G.C. (**1999**) Mitochondria mediate nitric oxide-induced cell death. *Ann N Y Acad Sci*, 893, 376-378.

Bär, S., Takada, A., Kawaoka, Y. and Alizon, M. (**2006**) Detection of cell-cell fusion mediated by Ebola virus glycoproteins. *J Virol*, 80, 2815-2822.

Bardelli, A., Longati, P., Gramaglia, D., Basilico, C., Tamagnone, L., Giordano, S., Ballinari, D., Michieli, P. and Comoglio, P.M. (**1998**) Uncoupling signal transducers from oncogenic MET mutants abrogates cell transformation and inhibits invasive growth. *Proc Natl Acad Sci U S A*, 95, 14379-14383.

Baron, S., Poast, J., Rizzo, D., McFarland, E. and Kieff, E. (**2000**) Electroporation of antibodies, DNA, and other macromolecules into cells: a highly efficient method. *J Immunol Methods*, 242, 115-126.

Barrau, C., Teissié, J. and Gabriel, B. (**2004**) Osmotically induced membrane tension facilitates the triggering of living cell electropermeabilization. *Bioelectrochemistry*, 63, 327-332.

Basarkar, A. and Singh, J. (**2009**) Poly (lactide-co-glycolide)-polymethacrylate nanoparticles for intramuscular delivery of plasmid encoding interleukin-10 to prevent autoimmune diabetes in mice. *Pharm Res*, 26, 72-81.

Bateman, A., Bullough, F., Murphy, S., Emiliusen, L., Lavillette, D., Cosset, F.L., Cattaneo, R., Russell, S.J. and Vile, R.G. (**2000**) Fusogenic membrane glycoproteins as a novel class of genes for the local and immune-mediated control of tumor growth. *Cancer Res*, 60, 1492-1497.

Baumann, M. and Sowers, A.E. (**1996**) Membrane skeleton involvement in cell fusion kinetics: a parameter that correlates with erythrocyte osmotic fragility. *Biophys J*, 71, 336-340.

Baumann, W.H., Lehmann, M., Schwinde, A., Ehret, R., Brischwein, M. and Wolf, B. (**1999**) Microelectronic sensor system for microphysiological application on living cells. *Sensor Actuat B-Chem*, 55, 77-89.

Beavis, R.C. and Chait, B.T. (**1990**) High-accuracy molecular mass determination of proteins using matrix-assisted laser desorption mass-spectrometry. *Anal Chem*, 62, 1836-1840.

Beebe, S.J., Fox, P.M., Rec, L.J., Willis, E.L. and Schoenbach, K.H. (**2003**) Nanosecond, high-intensity pulsed electric fields induce apoptosis in human cells. *Faseb J*, 17, 1493-1495.

Belehradek, M., Domenge, C., Luboinski, B., Orlowski, S., Belehradek, J., Jr. and Mir, L.M. (**1993**) Electrochemotherapy, a new antitumor treatment. First clinical phase I-II trial. *Cancer*, 72, 3694-3700.

Bentzen, E.L., Tomlinson, I.D., Mason, J., Gresch, P., Warnement, M.R., Wright, D., Sanders-Bush, E., Blakely, R. and Rosenthal, S.J. (**2005**) Surface modification to reduce nonspecific binding of quantum dots in live cell assays. *Bioconjug Chem*, 16, 1488-1494.

Benz, R. and Zimmermann, U. (**1980**) Pulse-length dependence of the electrical breakdown in lipid bilayer-membranes. *Biochim Biophys Acta*, 597, 637-642.

Benz, R. and Zimmermann, U. (**1981**) The resealing process of lipid bilayers after reversible electrical breakdown. *Biochim Biophys Acta*, 640, 169-178.

Berg, K., Selbo, P.K., Prasmickaite, L., Tjelle, T.E., Sandvig, K., Moan, J., Gaudernack, G., Fodstad, O., Kjolsrud, S., Anholt, H., Rodal, G.H., Rodal, S.K. & Hogset, A. (**1999**) Photochemical internalization: a novel technology for delivery of macromolecules into cytosol. *Cancer Res*, 59, 1180-1183.

Berglund, D.L. and Starkey, J.R. (**1989**) Isolation of viable tumor cells following introduction of labelled antibody to an intracellular oncogene product using electroporation. *J Immunol Methods*, 125, 79-87.

Berglund, D.L. and Starkey, J.R. (**1991**) Introduction of antibody into viable cells using electroporation. *Cytometry*, 12, 64-67.

Bernhardt, J. and Pauly, H. (**1973**) On the generation of potential differences across the membranes of ellipsoidal cells in an alternating electrical field. *Biophysik*, 10, 89-98.

Bertani, G. (**1951**) Studies on lysogenesis. I. The mode of phage liberation by lysogenic Escherichia coli. *J Bacteriol*, 62, 293-300.

Berthier, E., Warrick, J., Yu, H. and Beebe, D.J. (**2008**) Managing evaporation for more robust microscale assays. Part 1. Volume loss in high throughput assays. *Lab on a Chip*, 8, 852-859.

Bertrand, C.A., Durand, D.M., Saidel, G.M., Laboisse, C. and Hopfer, U. (**1998**) System for dynamic measurements of membrane capacitance in intact epithelial monolayers. *Biophys J*, 75, 2743-2756.

Bier, M., Hammer, S.M., Canaday, D.J. and Lee, R.C. (**1999**) Kinetics of sealing for transient electropores in isolated mammalian skeletal muscle cells. *Bioelectromagnetics*, 20, 194-201.

Birschwein, M., Baumann, W., Ehret, R., Schwinde, A., Kraus, M. and Wolf, B. (**1996**) Mikrosensorische Systeme in der zellbiologischen Grundlagenforschung und der medizinischen Diagnostik. *Naturwissenschaften*, 83, 193-200.

Blangero, C. and Justin, T. (**1983**) Homokaryon production by electrofusion - a convenient way to produce a large number of viable mammalian fused cells. *Biochem Bioph Res Co*, 114, 663-669.

Blangero, C., Rols, M.P. and Teissié, J. (**1989**) Cytoskeletal reorganization during electric-field-induced fusion of Chinese hamster ovary cells grown in monolayers. *Biochim Biophys Acta*, 981, 295-302.

Bloquel, C., Fabre, E., Bureau, M.F. and Scherman, D. (**2004**) Plasmid DNA electrotransfer for intracellular and secreted proteins expression: new methodological developments and applications. *J Gene Med*, 6, 11-23.

Boccaccio, C., Ando, M., Tamagnone, L., Bardelli, A., Michieli, P., Battistini, C. and Comoglio, P.M. (**1998**) Induction of epithelial tubules by growth factor HGF depends on the STAT pathway. *Nature*, 391, 285-288.

Bodmer, J.E., English, A., Brady, M., Blackwell, K., Haxhinasto, K., Fotedar, S., Borgman, K., Bai, E.W. and Moy, A.B. (**2005**) Modeling error and stability of endothelial cytoskeletal membrane parameters based on modeling transendothelial impedance as resistor and capacitor in series. *Am J Physiol-Cell Ph*, 289, C735-C747.

Boitano, S., Dirksen, E.R. and Evans, W.H. (**1998**) Sequence specific antibodies to connexins block intercellular calcium signaling through gap junctions. *Cell Calcium*, 23, 1-9.

Boitano, S., Dirksen, E.R. and Sanderson, M.J. (**1992**) Intercellular propagation of calcium waves mediated by inositol trisphosphate. *Science*, 258, 292-295.

Bossy-Wetzel, E., Newmeyer, D.D. and Green, D.R. (**1998**) Mitochondrial cytochrome c release in apoptosis occurs upstream of DEVD-specific caspase activation and independently of mitochondrial transmembrane depolarization. *EMBO J*, 17, 37-49.

Bousse, L. (**1996**) Whole cell biosensors. *Sensor Actuat B-Chem*, 34, 270-275.

Boussif, O., Lezoualc'h, F., Zanta, M.A., Mergny, M.D., Scherman, D., Demeneix, B. and Behr, J.P. (**1995**) A versatile vector for gene and oligonucleotide transfer into cells in culture and in vivo: polyethylenimine. *Proc Natl Acad Sci U S A*, 92, 7297-7301.

Bratke, K., Luttmann, W., Michael, K. and Daniel, M. (**2006**) Der Experimentator, Immunologie. Spektrum Akademischer Verlag, Heidelberg, Berlin.

Breitenstein, D., Rommel, C.E., Mollers, R., Wegener, J. and Hagenhoff, B. (**2007**) The chemical composition of animal cells and their intracellular compartments reconstructed from 3D mass spectrometry. *Angew Chem Int Ed Engl*, 46, 5332-5335.

Brenneman, M., Gimble, F.S. and Wilson, J.H. (**1996**) Stimulation of intrachromosomal homologous recombination in human cells by electroporation with site-specific endonucleases. *P Natl Acad Sci U S A*, 93, 3608-3612.

Bright, G.R., Kuo, N.T., Chow, D., Burden, S., Dowe, C. and Przybylski, R.J. (**1996**) Delivery of macromolecules into adherent cells via electroporation for use in fluorescence spectroscopic imaging and metabolic studies. *Cytometry*, 24, 226-233.

Brownell, H.L., Lydon, N.B., Schaefer, E., Roberts, T.M. and Raptis, L. (**1998**) Inhibition of epidermal growth factor-mediated ERK1/2 activation by in situ electroporation of nonpermeant [(alkylamino)methyl]acrylophenone derivatives. *DNA Cell Biol*, 17, 265-274.

Bruchez, M., Jr., Moronne, M., Gin, P., Weiss, S. and Alivisatos, A.P. (**1998**) Semiconductor nanocrystals as fluorescent biological labels. *Science*, 281, 2013-2016.

Bruns, R.F., Lawson-Wendling, K. and Pugsley, T.A. (**1983**) A rapid filtration assay for soluble receptors using polyethylenimine-treated filters. *Anal Biochem*, 132, 74-81.

Bryant, P.E. and Johnston, P.J. (**1993**) Restriction-endonuclease-induced DNA double-strand breaks and chromosomal aberrations in mammalian cells. *Mutat Res*, 299, 289-296.

Burgess, R.R. and Jendrisak, J.J. (**1975**) A procedure for the rapid, large-scale purification of Escherichia coli DNA-dependent RNA polymerase involving Polymin P precipitation and DNA-cellulose chromatography. *Biochemistry*, 14, 4634-4638.

Buss, F., Luzio, J.P. and Kendrick-Jones, J. (**2002**) Myosin VI, an actin motor for membrane traffic and cell migration. *Traffic*, 3, 851-858.

Bustamante, M., Roger, F., Bochaton-Piallat, M.L., Gabbiani, G., Martin, P.Y. and Feraille, E. (**2003**) Regulatory volume increase is associated with p38 kinase-dependent actin cytoskeleton remodeling in rat kidney MTAL. *Am J Physiol-Renal*, 285, F336-F347.

C

Campana, L.G., Mocellin, S., Basso, M., Puccetti, O., De Salvo, G.L., Chiarion-Sileni, V., Vecchiato, A., Corti, L., Rossi, C.R. and Nitti, D. (**2009**) Bleomycin-based electrochemotherapy: clinical outcome from a single institution's experience with 52 patients. *Ann Surg Oncol*, 16, 191-199.

Campbell, C.E., Laane, M.M., Haugarvoll, E. and Giaever, I. (**2007**) Monitoring viral-induced cell death using electric cell-substrate impedance sensing. *Biosens Bioelectron*, 23, 536-542.

Capasso, J.M., Rivard, C.J. and Berl, T. (**2001**) Long-term adaptation of renal cells to hypertonicity: role of MAP kinases and Na-K-ATPase. *Am J Physiol Renal Physiol*, 280, F768-F776.

Carney, J.P. and Morgan, W.F. (**1999**) Induction of DNA double-strand breaks by electroporation of restriction enzymes into mammalian cells. *Methods Mol Biol*, 113, 465-471.

Cereijido, M., Bolivar, J.J., Gonzalezmariscal, L. and Avila, G. (**1986**) Cultured monolayers as model systems for ion-transport across epithelial and endothelial membranes – state-of-the-art lecture. *Hypertension*, 8, 22-29.

Ceriotti, L., Ponti, J., Colpo, P., Sabbioni, E. and Rossi, F. (**2007**) Assessment of cytotoxicity by impedance spectroscopy. *Biosens Bioelectron*, 22, 3057-3063.

Chakrabarti, R., Wylie, D.E. and Schuster, S.M. (**1989**) Transfer of monoclonal antibodies into mammalian cells by electroporation. *J Biol Chem*, 264, 15494-15500.

Chanana, M., Gliozzi, A., Diaspro, A., Chodnevskaja, I., Huewel, S., Moskalenko, V., Ulrichs, K., Galla, H.J. and Krol, S. (**2005**) Interaction of polyelectrolytes and their composites with living cells. *Nano Lett*, 5, 2605-2612.

Chang, C., Biedermann, K.A., Mezzina, M. and Brown, J.M. (**1993**) Characterization of the DNA double strand break repair defect in scid mice. *Cancer Res*, 53, 1244-1248.

Chang, D.C. and Reese, T.S. (**1990**) Changes in membrane structure induced by electroporation as revealed by rapid-freezing electron microscopy. *Biophys J*, 58, 1-12.

Chang, D.C., Saunders, J.A., Chassy, B.M. and Sowers, A.E. (**1992**) Overview of electroporation and electrofusion. In Chang, D.C., Chassy, B.M., Saunders, J.A., Sowers, A.E. (eds.) Guide to electroporation and electrofusion. Academic Press, San Diego.

Chen, C., Smye, S.W., Robinson, M.P. and Evans, J.A. (**2006**) Membrane electroporation theories: a review. *Med Biol Eng Comput*, 44, 5-14.

Chen, E.H. and Olson, E.N. (**2005**) Unveiling the mechanisms of cell-cell fusion. *Science*, 308, 369-373.

Chen, F.Q. and Gerion, D. (**2004**) Fluorescent CdSe/ZnS nanocrystal-peptide conjugates for long-term, nontoxic imaging and nuclear targeting in living cells. *Nano Lett*, 4, 1827-1832.

Chen, J. and Stubbe, J. (**2005**) Bleomycins: towards better therapeutics. *Nature Reviews Cancer*, 5, 102-112.

Chen, J., Ye, L., Zhang, L. and Jiang, W.G. (**2008**) Placenta growth factor, PLGF, influences the motility of lung cancer cells, the role of Rho associated kinase, Rock1. *J Cell Biochem*, 105, 313-320.

Chen, K., Obinata, H. and Izumi, T. (**2010**) Detection of G protein-coupled receptor-mediated cellular response involved in cytoskeletal rearrangement using surface plasmon resonance. *Biosens Bioelectron*, 25, 1675-1680.

Chen, S.J., Bradley, M.E. and Lee, T.C. (**1998**) Chemical hypoxia triggers apoptosis of cultured neonatal rat cardiac myocytes: Modulation by calcium-regulated proteases and protein kinases. *Mol Cell Biochem*, 178, 141-149.

Chen, W., Carbone, F.R. and McCluskey, J. (**1993**) Electroporation and commercial liposomes efficiently deliver soluble protein into the MHC class I presentation pathway. Priming in vitro and in vivo for class I-restricted recognition of soluble antigen. *J Immunol Methods*, 160, 49-57.

Chen, W. and Lee, R.C. (**1994a**) Altered ion channel conductance and ionic selectivity induced by large imposed membrane potential pulse. *Biophys J*, 67, 603-612.

Chen, W. and Lee, R.C. (**1994b**) Electromediated permeabilization of frog skeletal muscle cell membrane: Effect of voltage-gated ion channels. *Bioelectrochem Bioenerg*, 34, 157-167.

Cheng, Z.F. and Deutscher, M.P. (**2005**) An important role for RNase R in mRNA decay. *Mol Cell*, 17, 313-318.

Chernomordik, L.V. and Chizmadzhev, Y.A. (**1989**) Electrical breakdown of lipid bilayer membranes: Phenomenology and mechanism. In Neumann, E., Sowers, A.E., Jordan, C.A. (eds.) Electroporation and Electrofusion in Cell Biology. Plenum Press, London , New York.

Chernomordik, L.V. and Sowers, A.E. (**1991**) Evidence that the spectrin network and a nonosmotic force control the fusion product morphology in electrofused erythrocyte ghosts. *Biophys J*, 60, 1026-1037.

Chertkova, R.V., Sharonov, G.V., Feofanov, A.V., Bocharova, O.V., Latypov, R.F., Chernyak, B.V., Arseniev, A.S., Dolgikh, D.A. and Kirpichnikov, M.P. (**2008**) Proapoptotic activity of cytochrome c in living cells: effect of K72 substitutions and species differences. *Mol Cell Biochem*, 314, 85-93.

Chien, M.P., Lin, C.H. and Chang, D.K. (**2009**) Recruitment of HIV-1 envelope occurs subsequent to lipid mixing: a fluorescence microscopic evidence. *Retrovirology*, 6: 20.

Cho, S. and Thielecke, H. (**2007**) Micro hole-based cell chip with impedance spectroscopy. *Biosens Bioelectron*, 22, 1764-1768.

Cho, S. and Thielecke, H. (**2010**) Influence of the electrode radius on the impedance spectra of cell-covered disc electrode. *Microelectron Eng*, 87, 719-721.

Choi, Y.S., Kim, H.B., Kwon, G.S. and Park, J.K. (**2009**) On-chip testing device for electrochemotherapeutic effects on human breast cells. *Biomed Microdevices*, 11, 151-159.

Choksakulnimitr, S., Masuda, S., Tokuda, H., Takakura, Y. and Hashida, M. (**1995**) In-Vitro Cytotoxicity of macromolecules in different Cell-culture systems. *J Control Release*, 34, 233-241.

Chua, K.Y., Ramos, J.D. and Cheong, N. (**2008**) Production of monoclonal antibody by DNA immunization with electroporation. *Methods Mol Biol*, 423, 509-520.

Ciccarone, V., Chu, V., K. , Shifferli, K., Pichet, J.P., Hawley-Nelson, P., Evans, K., Roy, L. and Bennett, S. (**1999**) LipofectAMINE 2000 reagent for rapid, efficient transfection of eukaryotic cells. *Focus*, 21, 54-55.

Clapham, D.E. (**2007**) Calcium signaling. *Cell*, 131, 1047-1058.

Codina, R., Vanasse, A., Kelekar, A., Vezys, V. and Jemmerson, R. (**2010**) Cytochrome c-induced lymphocyte death from the outside in: inhibition by serum leucine-rich alpha-2-glycoprotein-1. *Apoptosis*, 15, 139-152.

Colosimo, A., Goncz, K.K., Holmes, A.R., Kunzelmann, K., Novelli, G., Malone, R.W., Bennett, M.J. and Gruenert, D.C. (**2000**) Transfer and expression of foreign genes in mammalian cells. *Biotechniques*, 29, 314-318, 320-312, 324.

Comley, J. (**2008**) Label-free detection part II: binding analysis assay. *Drug Discovery World*. Fall 2008.

Conner, S.D. and Schmid, S.L. (**2003**) Regulated portals of entry into the cell. *Nature*, 422, 37-44.

Costa, M., Dottori, M., Sourris, K., Jamshidi, P., Hatzistavrou, T., Davis, R., Azzola, L., Jackson, S., Lim, S.M., Pera, M., Elefanty, A.G. and Stanley, E.G. (**2007**) A method for genetic modification of human embryonic stem cells using electroporation. *Nat Protoc*, 2, 792-796.

Cotton, R.G. and Milstein, C. (**1973**) Letter: Fusion of two immunoglobulin-producing myeloma cells. *Nature*, 244, 42-43.

Courtête, J., Sibler, A.P., Zeder-Lutz, G., Dalkara, D., Oulad-Abdelghani, M., Zuber, G. and Weiss, E. (**2007**) Suppression of cervical carcinoma cell growth by intracytoplasmic codelivery of anti-oncoprotein E6 antibody and small interfering RNA. *Mol Cancer Ther*, 6, 1728-1735.

Cowan, C.A., Atienza, J., Melton, D.A. and Eggan, K. (**2005**) Nuclear reprogramming of somatic cells after fusion with human embryonic stem cells. *Science*, 309, 1369-1373.

Crane, J.S. and Pohl, H.A. (**1971**) Dielectrophoresis of cells. *Biophys J*, 11, 711-727.

Cristillo, A.D., Weiss, D., Hudacik, L., Restrepo, S., Galmin, L., Suschak, J., Draghia-Akli, R., Markham, P. and Pal, R. (**2008**) Persistent antibody and T cell responses induced by HIV-1 DNA vaccine delivered by electroporation. *Biochem Biophys Res Commun*, 366, 29-35.

Croons, V., Martinet, W., Herman, A.G., Timmermans, J.P. and De Meyer, G.R. (**2009**) The protein synthesis inhibitor anisomycin induces macrophage apoptosis in rabbit atherosclerotic plaques through p38 mitogen-activated protein kinase. *J Pharmacol Exp Ther*, 329, 856-864.

Cullinan, E.B., Gawron, L.S., Rustum, Y.M. and Beerman, T.A. (**1991**) Extrachromosomal chromatin: novel target for bleomycin cleavage in cells and solid tumors. *Biochemistry*, 30, 3055-3061.

D

Dabbousi, B.O., RodriguezViejo, J., Mikulec, F.V., Heine, J.R., Mattoussi, H., Ober, R., Jensen, K.F. and Bawendi, M.G. (**1997**) (CdSe)ZnS core-shell quantum dots: Synthesis and characterization of a size series of highly luminescent nanocrystallites. *J Phys Chem B*, 101, 9463-9475.

Dagher, S.F., Conrad, S.E., Werner, E.A. and Patterson, R.J. (**1992**) Phenotypic conversion of TK-deficient cells following electroporation of functional TK enzyme. *Exp Cell Res*, 198, 36-42.

Darzynkiewicz, Z., Juan, G. and Traganos, F. (**2001**) Assaying drug-induced apoptosis. *Methods Mol Biol*, 95, 241-254.

Das, M., Dhak, P., Gupta, S., Mishra, D., Maiti, T.K., Basak, A. and Pramanik, P. (**2010**) Highly biocompatible and water-dispersible, amine functionalized magnetite nanoparticles, prepared by a low temperature, air-assisted polyol process: a new platform for bio-separation and diagnostics. *Nanotechnology*, 21: 125103.

Davidson, R.L. and Gerald, P.S. (**1976**) Improved techniques for the induction of mammalian cell hybridization by polyethylene glycol. *Somatic Cell Genet*, 2, 165-176.

Davies, S. and Jiang, W.G. (**2010**) ALCAM, activated leukocyte cell adhesion molecule, influences the aggressive nature of breast cancer cells, a potential connection to bone metastasis. *Anticancer Res*, 30, 1163-1168.

de Gennes, P.G. (**1999**) Passive entry of a DNA molecule into a small pore. *Proc Natl Acad Sci U S A*, 96, 7262-7264.

De Jong, W.H. and Borm, P.J. (**2008**) Drug delivery and nanoparticles: applications and hazards. *Int J Nanomedicine*, 3, 133-149.

de Larco, J.E. and Todaro, G.J. (**1978**) Epithelioid and fibroblastic rat kidney cell clones: epidermal growth factor (EGF) receptors and the effect of mouse sarcoma virus transformation. *J Cell Physiol*, 94, 335-342.

de Lima, M.C.P., Simoes, S., Pires, P., Faneca, H. and Duzgunes, N. (**2001**) Cationic lipid-DNA complexes in gene delivery: from biophysics to biological applications. *Adv Drug Deliver Rev*, 47, 277-294.

De Smedt, S.C., Demeester, J. and Hennink, W.E. (**2000**) Cationic polymer based gene delivery systems. *Pharm Res*, 17, 113-126.

De Vuyst, E., De Bock, M., Decrock, E., Van Moorhem, M., Naus, C., Mabilde, C. and Leybaert, L. (**2008**) In situ bipolar electroporation for localized cell loading with reporter dyes and investigating gap junctional coupling. *Biophys J*, 94, 469-479.

Dean, D.A. (**1997**) Import of plasmid DNA into the nucleus is sequence specific. *Exp Cell Res*, 230, 293-302.

Dean, D.A., Strong, D.D. and Zimmer, W.E. (**2005**) Nuclear entry of nonviral vectors. *Gene Ther*, 12, 881-890.

Decrock, E., De Vuyst, E., Vinken, M., Van Moorhem, M., Vranckx, K., Wang, N., Van Laeken, L., De Bock, M., D'Herde, K., Lai, C.P., Rogiers, V., Evans, W.H., Naus, C.C. and Leybaert, L. (**2009**) Connexin 43 hemichannels contribute to the propagation of apoptotic cell death in a rat C6 glioma cell model. *Cell Death Differ*, 16, 151-163.

Delehanty, J.B., Mattoussi, H. and Medintz, I.L. (**2009**) Delivering quantum dots into cells: strategies, progress and remaining issues. *Anal Bioanal Chem*, 393, 1091-1105.

Deng, J., Schoenbach, K.H., Buescher, E.S., Hair, P.S., Fox, P.M. and Bebe, S.J. (**2003**) The effects of intense submicrosecond electrical pulses on cells. *Biophys. J.*, 84, 2709-2714.

Deora, A.A., Diaz, F., Schreiner, R. and Rodriguez-Boulan, E. (**2007**) Efficient electroporation of DNA and protein into confluent and differentiated epithelial cells in culture. *Traffic*, 8, 1304-1312.

de Pamphilis, M.L., Herman, S.A., Martinezsalas, E., Chalifour, L.E., Wirak, D.O., Cupo, D.Y. and Miranda, M. (**1988**) Microinjecting DNA into mouse ova to study DNA-replication and gene-expression and to produce transgenic animals. *Biotechniques*, 6, 662-680.

DePaola, N., Phelps, J.E., Florez, L., Keese, C.R., Minnear, F.L., Giaever, I. and Vincent, P. (**2001**) Electrical impedance of cultured endothelium under fluid flow. *Ann Biomed Eng*, 29, 648-656.

Derfus, A.M., Chan, W.C.W. and Bhatia, S.N. (**2004**) Intracellular delivery of quantum dots for live cell labeling and organelle tracking. *Adv Mater*, 16, 961-966.

Desagher, S. and Martinou, J.C. (**2000**) Mitochondria as the central control point of apoptosis. *Trends Cell Biol*, 10, 369-377.

Desmet, P., Simaels, J., Declercq, P.E. and Vandriessche, W. (**1995**) Regulatory Volume Decrease in Cultured Kidney-Cells (A6) - Role of Amino-Acids. *J Gen Physiol*, 106, 525-542.

Didenko, V.V., Ngo, H. and Baskin, D.S. (**2005**) Polyethyleneimine as a transmembrane carrier of fluorescently labeled proteins and antibodies. *Anal Biochem*, 344, 168-173.

Dimitrov, D.S. (**1993**) Kinetic mechanisms of membrane-fusion mediated by electric-fields. *Bioelectrochem Bioenerg*, 32, 99-124.

Dimitrov, D.S. (**1995**) Electroporation and electrofusion of membranes. In Lipowsky, R., Sackmann, E. (eds.) Handbook of Biological Physics. Elsevier Science B.V.

Dimitrov, D.S. (**2004**) Virus entry: molecular mechanisms and biomedical applications. *Nat Rev Microbiol*, 2, 109-122.

Dimitrov, D.S. and Jain, R.K. (**1984**) Membrane stability. *Biochim Biophys Acta*, 779, 437-468.

Dimitrov, D.S. and Sowers, A.E. (**1990**) A delay in membrane fusion: lag times observed by fluorescence microscopy of individual fusion events induced by an electric field pulse. *Biochemistry*, 29, 8337-8344.

Dimitrov, D.S., Willey, R.L., Sato, H., Chang, L.J., Blumenthal, R. and Martin, M.A. (**1993**) Quantitation of human immunodeficiency virus type 1 infection kinetics. *J Virol*, 67, 2182-2190.

Dobano, C., Widera, G., Rabussay, D. and Doolan, D.L. (**2007**) Enhancement of antibody and cellular immune responses to malaria DNA vaccines by in vivo electroporation. *Vaccine*, 25, 6635-6645.

Doherty, G.J. and McMahon, H.T. (**2009**) Mechanisms of endocytosis. *Annu Rev Biochem*, 78, 857-902.

Dressler, V., Schwister, K., Haest, C.W. and Deuticke, B. (**1983**) Dielectric breakdown of the erythrocyte membrane enhances transbilayer mobility of phospholipids. *Biochim Biophys Acta*, 732, 304-307.

Dubertret, B., Skourides, P., Norris, D.J., Noireaux, V., Brivanlou, A.H. and Libchaber, A. (**2002**) In vivo imaging of quantum dots encapsulated in phospholipid micelles. *Science*, 298, 1759-1762.

Duelli, D. and Lazebnik, Y. (**2007**) Cell-to-cell fusion as a link between viruses and cancer. *Nature Reviews Cancer*, 7, 968-976.

Duguid, J.G., Li, C., Logan, M.J., Claspell, J., Sparrow, J.T., Smith, L.C. and Rolland, A. (**1996**) Characterization of peptide DNA complexes for gene delivery. *Biophys J*, 70, 2802-2814

Durfee, T., Nelson, R., Baldwin, S., Plunkett, G., 3rd, Burland, V., Mau, B., Petrosino, J.F., Qin, X., Muzny, D.M., Ayele, M., Gibbs, R.A., Csorgo, B., Posfai, G., Weinstock, G.M. and Blattner, F.R. (**2008**) The complete genome sequence of Escherichia coli DH10B: insights into the biology of a laboratory workhorse. *J Bacteriol*, 190, 2597-2606.

E

Eckert, D.M. and Kim, P.S. (**2001**) Mechanisms of viral membrane fusion and its inhibition. *Annu Rev Biochem*, 70, 777-810.

Ehret, R., Baumann, W., Brischwein, M., Schwinde, A., Stegbauer, K. and Wolf, B. (**1997**) Monitoring of cellular behaviour by impedance measurements on interdigitated electrode structures. *Biosens Bioelectron*, 12, 29-41.

Eksioglu-Demiralp, E., Kitada, S., Carson, D., Garland, J., Andreef, M. and Reed, J.C. (**2003**) A method for functional evaluation of caspase activation pathways in intact lymphoid cells using electroporation-mediated protein delivery and flow cytometric analysis. *J Immunol Methods*, 275, 41-56.

Ende, D. and Mangold, K.M. (**1993**) Impedance Spectroscopy. *Chem. Unserer Zeit*, 27, 134-140.

Erikson, A., Andersen, H.N., Naess, S.N., Sikorski, P. and Davies Cde, L. (**2008**) Physical and chemical modifications of collagen gels: impact on diffusion. *Biopolymers*, 89, 135-143.

Escande-Geraud, M.L., Rols, M.P., Dupont, M.A., Gas, N. and Teissié, J. (**1988**) Reversible plasma membrane ultrastructural changes correlated with electropermeabilization in Chinese hamster ovary cells. *Biochim Biophys Acta*, 939, 247-259.

Escoffre, J.M., Portet, T., Wasungu, L., Teissié, J., Dean, D. and Rols, M.P. (**2009**) What is (still not) known of the mechanism by which electroporation mediates gene transfer and expression in cells and tissues. *Mol Biotechnol*, 41, 286-295.

Eulitz, D. & Mannherz, H.G. (**2007**) Inhibition of deoxyribonuclease I by actin is to protect cells from premature cell death. *Apoptosis*, 12, 1511-1521.

Eytan, G.D., Carroll, R.C., Schatz, G. and Racker, E. (**1975**) Arrangement of the subunits in solubilized and membrane-bound cytochrome c oxidase from bovine heart. *J Biol Chem*, 250, 8598-8603.

F

Fang, Y. (**2006**) Label-free cell-based assays with optical biosensors in drug discovery. *Assay Drug Dev Technol*, 4, 583-595.

Fang, Y., Ferrie, A.M., Fontaine, N.H., Mauro, J. and Balakrishnan, J. (**2006**) Resonant waveguide grating biosensor for living cell sensing. *Biophys J*, 91, 1925-1940.

Fang, Y., Ferrie, A.M. and Tran, E. (**2009**) Resonant waveguide grating biosensor for whole-cell GPCR assays. *Methods Mol Biol*, 552, 239-252.

Faurie, C., Rebersek, M., Golzio, M., Kanduser, M., Escoffre, J.M., Pavlin, M., Teissié, J., Miklavcic, D. and Rols, M.P. (**2010**) Electro-mediated gene transfer and expression are controlled by the life-time of DNA/membrane complex formation. *J Gene Med*, 12, 117-125.

Feldherr, C.M. and Akin, D. (**1994**) Role of nuclear trafficking in regulating cellular activity. *Int Rev Cytol*, 151, 183-228.

Feldman, G.J., Mullin, J.M. and Ryan, M.P. (**2005**) Occludin: Structure, function and regulation. *Adv Drug Deliver Rev*, 57, 883-917.

Felgner, J.H., Kumar, R., Sridhar, C.N., Wheeler, C.J., Tsai, Y.J., Border, R., Ramsey, P., Martin, M. and Felgner, P.L. (**1994**) Enhanced gene delivery and mechanism studies with a novel series of cationic lipid formulations. *J Biol Chem*, 269, 2550-2561.

Felgner, P.L., Gadek, T.R., Holm, M., Roman, R., Chan, H.W., Wenz, M., Northrop, J.P., Ringold, G.M. and Danielsen, M. (**1987**) Lipofection: a highly efficient, lipid-mediated DNA-transfection procedure. *Proc Natl Acad Sci U S A*, 84, 7413-7417.

Fimia, G.M. and Sassone-Corsi, P. (**2001**) Cyclic AMP signalling. *Journal of Cell Science*, 114, 1971-1972.

Finaz, C., Lefevre, A. and Teissié, J. (**1984**) Electrofusion. A new, highly efficient technique for generating somatic cell hybrids. *Exp Cell Res*, 150, 477-482.

Fischer, D., Bieber, T., Li, Y.X., Elsasser, H.P. and Kissel, T. (**1999**) A novel non-viral vector for DNA delivery based on low molecular weight, branched polyethylenimine: Effect of molecular weight on transfection efficiency and cytotoxicity. *Pharm Res*, 16, 1273-1279.

Fischer, D., Li, Y., Ahlemeyer, B., Krieglstein, J. and Kissel, T. (**2003**) In vitro cytotoxicity testing of polycations: influence of polymer structure on cell viability and hemolysis. *Biomaterials*, 24, 1121-1131.

Florian, P., Schoneberg, T., Schulzke, J.D., Fromm, M. and Gitter, A.H. (**2002**) Single-cell epithelial defects close rapidly by an actinomyosin purse string mechanism with functional tight junctions. *J Physiol*, 545, 485-499.

Förster, W. and Neumann, E. (**1989**) Gene transfer by electroporation. In Neumann, E., Sowers, A.E., Jordan, C.A. (eds.) Electroporation and electrofusion in cell biology. Plenum Press, New York, London.

Frankfurt, O.S. and Krishan, A. (**2001**) Identification of apoptotic cells by formamide-induced DNA denaturation in condensed chromatin. *J Histochem Cytochem*, 49, 369-378.

Freeman, R., Gill, R., Shweky, I., Kotler, M., Banin, U. and Willner, I. (**2009**) Biosensing and probing of intracellular metabolic pathways by NADH-sensitive quantum dots. *Angew Chem Int Ed Engl*, 48, 309-313.

Freshney, R.I. (**2005**) Culture of Animal Cells: A Manual of Basic Technique. John Wiley and Sons.

Fried, H. and Kutay, U. (**2003**) Nucleocytoplasmic transport: taking an inventory. *Cell Mol Life Sci*, 60, 1659-1688.

Friend, D.S., Papahadjopoulos, D. and Debs, R.J. (**1996**) Endocytosis and intracellular processing accompanying transfection mediated by cationic liposomes. *Biochim Biophys Acta*, 1278, 41-50.

Fujimoto, H., Kato, K. and Iwata, H. (**2008**) Electroporation microarray for parallel transfer of small interfering RNA into mammalian cells. *Anal Bioanal Chem*, 392, 1309-1316.

Fujita, Y. and Noda, Y. (**1984**) Differential scanning calorimetric studies on the thermal-denaturation of ribonuclease a in aqueous 2-methyl-2,4-pentanediol. *B Chem Soc Jpn*, 57, 1891-1896.

G

Gabriel, B. and Teissié, J. (**1994**) Generation of reactive-oxygen species induced by electropermeabilization of Chinese hamster ovary cells and their consequence on cell viability. *Eur J Biochem*, 223, 25-33.

Gabriel, B. and Teissié, J. (**1995**) Control by electrical parameters of short- and long-term cell death resulting from electropermeabilization of Chinese hamster ovary cells. *Biochim Biophys Acta*, 1266, 171-178.

Gabriel, B. and Teissié, J. (**1997**) Direct observation in the millisecond time range of fluorescent molecule asymmetrical interaction with the electropermeabilized cell membrane. *Biophys J*, 73, 2630-2637.

Gabriel, B. and Teissié, J. (**1998**) Mammalian cell electropermeabilization as revealed by millisecond imaging of fluorescence changes of ethidium bromide in interaction with the membrane. *Bioelectrochem Bioenerg*, 113-118.

Gabriel, B. and Teissié, J. (**1999**) Time courses of mammalian cell electropermeabilization observed by millisecond imaging of membrane property changes during the pulse. *Biophys J*, 76, 2158-2165.

Gabrijel, M., Repnik, U., Kreft, M., Grilc, S., Jeras, M. and Zorec, R. (**2004**) Quantification of cell hybridoma yields with confocal microscopy and flow cytometry. *Biochem Biophys Res Commun*, 314, 717-723.

Garcia-Calvo, M., Peterson, E.P., Leiting, B., Ruel, R., Nicholson, D.W. and Thornberry, N.A. (**1998**) Inhibition of human caspases by peptide-based and macromolecular inhibitors. *J Biol Chem*, 273, 32608-32613.

Garland, J., Brown, G., Beasley, J. and Brown, R. (**2000**) Apoptosis in factor-dependent haematopoietic cells is linked to calcium-sensitive mitochondrial rearrangements and cytoskeletal modulation. *Br J Haematol*, 109, 221-234.

Garland, J.M. and Rudin, C. (**1998**) Cytochrome c induces caspase-dependent apoptosis in intact hematopoietic cells and overrides apoptosis suppression mediated by bcl-2, growth factor signaling, MAP-kinase-kinase, and malignant change. *Blood*, 92, 1235-1246.

Gasser, A. and Most, J. (**1999**) Generation of multinucleated giant cells in vitro by culture of human monocytes with Mycobacterium bovis BCG in combination with cytokine-containing supernatants. *Infect Immun*, 67, 395-402.

Gazdhar, A., Fachinger, P., van Leer, C., Pierog, J., Gugger, M., Friis, R., Schmid, R.A. and Geiser, T. (**2007**) Gene transfer of hepatocyte growth factor by electroporation reduces bleomycin-induced lung fibrosis. *Am J Physiol Lung Cell Mol Physiol*, 292, L529-L536.

Gehl, J. (**2003**) Electroporation: theory and methods, perspectives for drug delivery, gene therapy and research. *Acta Physiol Scand*, 177, 437-447.

Gehl, J., Skovsgaard, T. and Mir, L.M. (**1998**) Enhancement of cytotoxicity by electropermeabilization: an improved method for screening drugs. *Anticancer Drugs*, 9, 319-325.

Gehl, J., Skovsgaard, T. and Mir, L.M. (**2002**) Vascular reactions to in vivo electroporation: characterization and consequences for drug and gene delivery. *Biochim Biophys Acta*, 1569, 51-58.

Geiger, R.C., Taylor, W., Glucksberg, M.R. and Dean, D.A. (**2006**) Cyclic stretch-induced reorganization of the cytoskeleton and its role in enhanced gene transfer. *Gene Ther*, 13, 725-731.

Ghartey-Tagoe, E.B., Morgan, J.S., Neish, A.S. and Prausnitz, M.R. (**2005**) Increased permeability of intestinal epithelial monolayers mediated by electroporation. *J Control Release*, 103, 177-190.

Ghosh, P.M., Keese, C.R. and Giaever, I. (**1993**) Monitoring electropermeabilization in the plasma membrane of adherent mammalian cells. *Biophys J*, 64, 1602-1609.

Ghosh, P.M., Keese, C.R. and Giaever, I. (**1994**) Morphological response of mammalian cells to pulsed ac fields. *Bioelectroch Bioenener*, 33, 121-133.

Giaever, I. and Keese, C.R. (**1984**) Monitoring fibroblast behavior in tissue culture with an applied electric field. *Proc Natl Acad Sci U S A*, 81, 3761-3764.

Giaever, I. and Keese, C.R. (**1991**) Micromotion of mammalian cells measured electrically. *Proc Natl Acad Sci U S A*, 88, 7896-7900.

Giaever, I. and Keese, C.R. (**1993**) A morphological biosensor for mammalian cells. *Nature*, 366, 591-592.

Gilmore, K.J., Quinn, H.E. and Wilson, M.R. (**2001**) Pinocytic loading of cytochrome c into intact cells specifically induces caspase-dependent permeabilization of mitochondria: evidence for a cytochrome c feedback loop. *Cell Death Differ*, 8, 631-639.

Giraudo, C.G., Hu, C., You, D.Q., Slovic, A.M., Mosharov, E.V., Sulzer, D., Melia, T.J. and Rothman, J.E. (**2005**) SNAREs can promote complete fusion and hemifusion as alternative outcomes. *J Cell Biol*, 170, 249-260.

Gitter, A.H., Schulzke, J.D., Sorgenfrei, D. and Fromm, M. (**1997**) Ussing chamber for high-frequency transmural impedance analysis of epithelial tissues. *J Biochem Bioph Meth*, 35, 81-88.

Glahder, J., Norrild, B., Persson, M.B. and Persson, B.R. (**2005**) Transfection of HeLa-cells with pEGFP plasmid by impedance power-assisted electroporation. *Biotechnol Bioeng*, 92, 267-276.

Glaser, R.W., Leikin, S.L., Chernomordik, L.V., Pastushenko, V.F. and Sokirko, A.I. (**1988**) Reversible Electrical Breakdown of Lipid Bilayers - Formation and Evolution of Pores. *Biochim Biophys Acta*, 940, 275-287.

Glassy, M. (**1988**) Creating hybridomas by electrofusion. *Nature*, 333, 579-580.

Glogauer, M., Lee, W. and McCulloch, C.A. (**1993**) Induced endocytosis in human fibroblasts by electrical fields. *Exp Cell Res*, 208, 232-240.

Glogauer, M. and McCulloch, C.A. (**1992**) Introduction of large molecules into viable fibroblasts by electroporation: optimization of loading and identification of labeled cellular compartments. *Exp Cell Res*, 200, 227-234.

Godbey, W.T., Barry, M.A., Saggau, P., Wu, K.K. and Mikos, A.G. (**2000**) Poly(ethylenimine)-mediated transfection: A new paradigm for gene delivery. *J Biomed Mater Res*, 51, 321-328.

Godbey, W.T., Wu, K.K. and Mikos, A.G. (**1999a**) Poly(ethylenimine) and its role in gene delivery. *J Control Release*, 60, 149-160.

Godbey, W.T., Wu, K.K. and Mikos, A.G. (**1999b**) Tracking the intracellular path of poly(ethylenimine)/DNA complexes for gene delivery. *Proc Natl Acad Sci U S A*, 96, 5177-5181.

Goldstein, J.C., Waterhouse, N.J., Juin, P., Evan, G.I. and Green, D.R. (**2000**) The coordinate release of cytochrome c during apoptosis is rapid, complete and kinetically invariant. *Nat Cell Biol*, 2, 156-162.

Golzio, M., Mora, M.P., Raynaud, C., Delteil, C., Teissié, J. and Rols, M.P. (**1998**) Control by osmotic pressure of voltage-induced permeabilization and gene transfer in mammalian cells. *Biophys J*, 74, 3015-3022.

Golzio, M., Rols, M.P. and Teissié, J. (**2004**) In vitro and in vivo electric field-mediated permeabilization, gene transfer, and expression. *Methods*, 33, 126-135.

Golzio, M., Teissié, J. and Rols, M.P. (**2002**) Direct visualization at the single-cell level of electrically mediated gene delivery. *Proc Natl Acad Sci U S A*, 99, 1292-1297.

Goodhew, P.J., Humphreys, J. and Beanland, R. (**2000**) Electron Microscopy and Analysis. Taylor and Francis, London and New York.

Gothelf, A., Mir, L.M. and Gehl, J. (**2003**) Electrochemotherapy: results of cancer treatment using enhanced delivery of bleomycin by electroporation. *Cancer Treat Rev*, 29, 371-387.

Gourlay, C.W. and Ayscough, K.R. (**2005**) The actin cytoskeleton: a key regulator of apoptosis and ageing? *Nat Rev Mol Cell Bio*, 6, 583-589.

Grabarek, J., Ardelt, B., Du, L. and Darzynkiewicz, Z. (**2002**) Activation of caspases and serine proteases during apoptosis induced by onconase (Ranpirnase). *Exp Cell Res*, 278, 61-71.

Graessmann, M. and Graessmann, A. (**1983**) Microinjection of tissue culture cells. *Methods Enzymol*, 101, 482-492.

Grafström, G., Engstrom, P., Salford, L.G. and Persson, B.R. (**2006**) 99mTc-DTPA uptake and electrical impedance measurements in verification of in vivo electropermeabilization efficiency in rat muscle. *Cancer Biother Radiopharm*, 21, 623-635.

Graham, F.L., Smiley, J., Russell, W.C. and Nairn, R. (**1977**) Characteristics of a human cell line transformed by DNA from human adenovirus type 5. *J Gen Virol*, 36, 59-74.

Graham, F.L. and van der Eb, A.J. (**1973**) A new technique for the assay of infectivity of human adenovirus 5 DNA. *Virology*, 52, 456-467.

Granot, Y., Ivorra, A., Maor, E. and Rubinsky, B. (**2009**) In vivo imaging of irreversible electroporation by means of electrical impedance tomography. *Physics in Medicine and Biology*, 54, 4927-4943.

Grasso, R.J., Heller, R., Cooley, J.C. and Haller, E.M. (**1989**) Electrofusion of individual animal cells directly to intact corneal epithelial tissue. *Biochim Biophys Acta*, 980, 9-14.

Gregoriadis, G. (**1995**) Engineering liposomes for drug delivery: Progress and problems. *Trends Biotechnol*, 13, 527-537.

Grieshaber, D., MacKenzie, R., Voros, J. and Reimhult, E. (**2008**) Electrochemical biosensors - Sensor principles and architectures. *Sensors-Basel*, 8, 1400-1458.

Gröbner, U., Velizarov, S. and Berg, H. (**1996**) Polylysine supports electrofusion. *Bioelectrochem Bioenerg*, 39, 181-184.

Gross, D., Loew, L.M. and Webb, W.W. (**1986**) Optical imaging of cell membrane potential changes induced by applied electric fields. *Biophys J*, 50, 339-348.

Gryte, D.M., Ward, M.D. and Hu, W.S. (**1993**) Real-time measurement of anchorage-dependent cell-adhesion Using a Quartz Crystal Microbalance. *Biotechnol Progr*, 9, 105-108.

Guo, X. and Szoka, F.C., Jr. (**2003**) Chemical approaches to triggerable lipid vesicles for drug and gene delivery. *Acc Chem Res*, 36, 335-341.

H

Haest, C.W., Kamp, D. and Deuticke, B. (**1997**) Transbilayer reorientation of phospholipid probes in the human erythrocyte membrane. Lessons from studies on electroporated and resealed cells. *Biochim Biophys Acta*, 1325, 17-33.

Hafner, F. (**2000**) Cytosensor Microphysiometer: Technology and recent applications. *Biosens Bioelectron*, 15, 149-158.

Haigis, M.C. and Raines, R.T. (**2003**) Secretory ribonucleases are internalized by a dynamin-independent endocytic pathway. *J Cell Sci*, 116, 313-324.

Han, A., Yang, L. and Frazier, A.B. (**2007**) Quantification of the heterogeneity in breast cancer cell lines using whole-cell impedance spectroscopy. *Clin Cancer Res*, 13, 139-143.

Han, B., Yuan, J. and Wang, E. (**2009**) Sensitive and selective sensor for biothiols in the cell based on the recovered fluorescence of the CdTe quantum dots-Hg(II) system. *Anal Chem*, 81, 5569-5573.

Hanora, A., Plieva, F.M., Hedstrom, M., Galaev, I.Y. and Mattiasson, B. (**2005**) Capture of bacterial endotoxins using a supermacroporous monolithic matrix with immobilized polyethyleneimine, lysozyme or polymyxin B. *J Biotechnol*, 118, 421-433.

Hartmann, C. (**2003**) Elektroporation von in-vitro-transkribierter RNA in adhärente Zellen. PhD thesis, Westfälische Wilhelms-Universität, Münster.

Hartmann, W. and Galla, H.J. (**1978**) Binding of polylysine to charged bilayer membranes: molecular organization of a lipid peptide complex. *Biochim Biophys Acta*, 509, 474-490.

Hartsock, A. and Nelson, W.J. (**2008**) Adherens and tight junctions: structure, function and connections to the actin cytoskeleton. *Biochim Biophys Acta*, 1778, 660-669.

Harush-Frenkel, O., Rozentur, E., Benita, S. and Altschuler, Y. (**2008**) Surface charge of nanoparticles determines their endocytic and transcytotic pathway in polarized MDCK cells. *Biomacromolecules*, 9, 435-443.

He, H., Chang, D.C. and Lee, Y.K. (**2006**) Micro pulsed radio-frequency electroporation chips. *Bioelectrochemistry*, 68, 89-97.

He, H., Chang, D.C. and Lee, Y.K. (**2008**) Nonlinear current response of micro electroporation and resealing dynamics for human cancer cells. *Bioelectrochemistry*, 72, 161-168.

Heggeness, M.H., Simon, M. and Singer, S.J. (**1978**) Association of mitochondria with microtubules in cultured cells. *Proc Natl Acad Sci U S A*, 75, 3863-3866.

Hein, M., Madefessel, C., Haag, B., Teichmann, K., Post, A. and Galla, H.J. (**1992**) Implications of a non-lamellar lipid phase for the tight junction stability. Part II: Reversible modulation of transepithelial resistance in high and low resistance MDCK-cells by basic amino acids, Ca2+, protamine and protons. *Chem Phys Lipids*, 63, 223-233.

Heitmann, V. (**2008**) Funktionelle in situ-Charakterisierung des Zell-Matrix-Kontaktes. PhD thesis, Westfälische Wilhelms-Universität, Münster.

Heo, Y.S., Cabrera, L.M., Song, J.W., Futai, N., Tung, Y.C., Smith, G.D. and Takayama, S. (**2007**) Characterization and resolution of evaporation-mediated osmolality shifts that constrain microfluidic cell culture in poly(dimethylsiloxane) devices. *Anal Chem*, 79, 1126-1134.

Hernández, J.L., Coll, T. and Ciudad, C.J. (**2004**) A highly efficient electroporation method for the transfection of endothelial cells. *Angiogenesis*, 7, 235-241.

Hernandez, L.D., Hoffman, L.R., Wolfsberg, T.G. and White, J.M. (**1996**) Virus-cell and cell-cell fusion. *Annu Rev Cell Dev Biol*, 12, 627-661.

Heuser, J.E., Reese, T.S., Dennis, M.J., Jan, Y., Jan, L. and Evans, L. (**1979**) Synaptic vesicle exocytosis captured by quick freezing and correlated with quantal transmitter release. *J Cell Biol*, 81, 275-300.

Hibino, M., Itoh, H. and Kinosita, K., Jr. (**1993**) Time courses of cell electroporation as revealed by submicrosecond imaging of transmembrane potential. *Biophys J*, 64, 1789-1800.

Hibino, M., Shigemori, M., Itoh, H., Nagayama, K. and Kinosita, K., Jr. (**1991**) Membrane conductance of an electroporated cell analyzed by submicrosecond imaging of transmembrane potential. *Biophys J*, 59, 209-220.

Hiraoka, Y., Yamada, T., Goto, M., Das Gupta, T.K. and Chakrabarty, A.M. (**2004**) Modulation of mammalian cell growth and death by prokaryotic and eukaryotic cytochrome c. *Proc Natl Acad Sci U S A*, 101, 6427-6432.

Hitchcock, S.E. (**1980**) Actin-Deoxyribonuclease-I interaction - depolymerization and nucleotide exchange. *J BiolChem*, 255, 5668-5673.

Ho, Y.P. and Leong, K.W. (**2010**) Quantum dot-based theranostics. *Nanoscale*, 2, 60-68.

Holzapfel, V., Musyanovych, A., Landfester, K., Lorenz, M.R. and Mailänder, V. (**2005**) Preparation of fluorescent carboxyl and amino functionalized polystyrene particles by miniemulsion polymerization as markers for cells. *Macromol Chem Physic*, 206 2440-2449.

Homola, J. (**2008**) Surface plasmon resonance sensors for detection of chemical and biological species. *Chem Rev*, 108, 462-493.

Hong, S.P., Leroueil, P.R., Janus, E.K., Peters, J.L., Kober, M.M., Islam, M.T., Orr, B.G., Baker, J.R. and Holl, M.M.B. (**2006**) Interaction of polycationic polymers with supported lipid bilayers and cells: Nanoscale hole formation and enhanced membrane permeability. *Bioconjugate Chem*, 17, 728-734.

Horiuchi, A., Nikaido, T., Mitsushita, J., Toki, T., Konishi, I. and Fujii, S. (**2000**) Enhancement of antitumor effect of bleomycin by low-voltage in vivo electroporation: a study of human uterine leiomyosarcomas in nude mice. *Int J Cancer*, 88, 640-644.

Huang, P., Ballal, K. and Plunkett, W. (**1997**) Biochemical characterization of the protein activity responsible for high molecular weight DNA fragmentation during drug-induced apoptosis. *Cancer Res*, 57, 3407-3414.

Huang, R., Peng, L. and Hertz, L. (**1997**) Effects of a low-voltage static electric field on energy metabolism in astrocytes. *Bioelectromagnetics*, 18, 77-80.

Hug, T.S. (**2003**) Biophysical methods for monitoring cell-substrate interactions in drug discovery. *Assay Drug Dev Technol*, 1, 479-488.

Hui and Lee (**2000**) Gene Delivery by Electroporation In Jaroszeski, M.J., Heller, R., Gilbert, R. (eds.) Electrochemotherapy, electrogenetherapy, and transdermal drug delivery.

Huth, S., Lausier, J., Gersting, S.W., Rudolph, C., Plank, C., Welsch, U. and Rosenecker, J. (**2004**) Insights into the mechanism of magnetofection using PEI-based magnetofectins for gene transfer. *J Gene Med*, 6, 923-936.

I, J

Inomata, K. and Tanaka, H. (**2003**) Protective effect of benidipine against sodium azide-induced cell death in cultured neonatal rat cardiac myocytes. *J Pharmacol Sci*, 93, 163-170.

Iordanov, M.S., Ryabinina, O.P., Wong, J., Dinh, T.H., Newton, D.L., Rybak, S.M. and Magun, B.E. (**2000**) Molecular determinants of apoptosis induced by the cytotoxic ribonuclease onconase: evidence for cytotoxic mechanisms different from inhibition of protein synthesis. *Cancer Res*, 60, 1983-1994.

Ishibashi, T., Takoh, K., Kaji, H., Abe, T. and Nishizawa, M. (**2007**) A porous membrane-based culture substrate for localized in situ electroporation of adherent mammalian cells. *Sensor Actuat B*, 128, 5-11.

Ishikawa, T., Zhu, B.L. and Maeda, H. (**2006**) Effect of sodium azide on the metabolic activity of cultured fetal cells. *Toxicol Ind Health*, 22, 337-341.

Ito, S. and Takagi, M. (**2009**) Correlation between cell cycle phase of adherent Chinese hamster ovary cells and laser phase shift determined by phase-shifting laser microscopy. *Biotechnol Lett*, 31, 39-42.

Ivorra, A. and Rubinsky, B. (**2007**) In vivo electrical impedance measurements during and after electroporation of rat liver. *Bioelectrochemistry*, 70, 287-295.

Jahnke, H.G., Rothermel, A., Sternberger, I., Mack, T.G.A., Kurz, R.G., Panke, O., Striggow, F. and Robitzki, A.A. (**2009**) An impedimetric microelectrode-based array sensor for label-free detection of tau hyperphosphorylation in human cells. *Lab on a Chip*, 9, 1422-1428.

Jain, T. and Muthuswamy, J. (**2007**) Bio-chip for spatially controlled transfection of nucleic acid payloads into cells in a culture. *Lab on a Chip*, 7, 1004-1011.

Jainchill, J.L., Aaronson, S.A. and Todaro, G.J. (**1969**) Murine sarcoma and leukemia viruses: assay using clonal lines of contact-inhibited mouse cells. *J Virol*, 4, 549-553.

Jaroszeski, M.J., Dang, V., Pottinger, C., Hickey, J., Gilbert, R. and Heller, R. (**2000**) Toxicity of anticancer agents mediated by electroporation in vitro. *Anticancer Drugs*, 11, 201-208.

Jaroszeski, M.J., Gilbert, R., Fallon, P.G. and Heller, R. (**1994**) Mechanically facilitated cell-cell electrofusion. *Biophys J*, 67, 1574-1581.

Jaroszeski, M.J., Gilbert, R. and Heller, R. (**1995**) Cytometric detection and quantitation of cell-cell electrofusion products. *Methods Mol Biol*, 48, 355-363.

Jaroszeski, M.J., Gilbert, R. and Heller, R. (**1998**) Flow cytometric detection and quantitation of cell-cell electrofusion products. *Methods Mol Biol*, 91, 149-156.

Jen, C.P., Wu, W.M., Li, M. and Lin, Y.C. (**2004**) Site-specific enhancement of gene transfection utilizing an attracting electric field for DNA plasmids on the electroporation microchip. *J Microelectromech S*, 13, 947-955.

Jiang, X.E., Dausend, J., Hafner, M., Musyanovych, A., Rocker, C., Landfester, K., Mailander, V. and Nienhaus, G.U. (**2010**) Specific effects of surface amines on polystyrene nanoparticles in their interactions with mesenchymal stem cells. *Biomacromolecules*, 11, 748-753.

Johnson, C.E., Huang, Y.Y., Parrish, A.B., Smith, M.I., Vaughn, A.E., Zhang, Q., Wright, K.M., Van Dyke, T., Wechsler-Reya, R.J., Kornbluth, S. and Deshmukh, M. (**2007**) Differential Apaf-1 levels allow cytochrome c to induce apoptosis in brain tumors but not in normal neural tissues. *Proc Natl Acad Sci U S A*, 104, 20820-20825.

Johnson, R.J., McCoy, J.G., Bingman, C.A., Phillips, G.N., Jr. and Raines, R.T. (**2007**) Inhibition of human pancreatic ribonuclease by the human ribonuclease inhibitor protein. *J Mol Biol*, 368, 434-449.

Joshi, R.P., Hu, Q., Schoenbach, K.H. and Hjalmarson, H.P. (**2002**) Improved energy model for membrane electroporation in biological cells subjected to electrical pulses. *Phys Rev E Stat Nonlin Soft Matter Phys*, 65: 041920.

Juin, P., Hueber, A.O., Littlewood, T. and Evan, G. (**1999**) c-Myc-induced sensitization to apoptosis is mediated through cytochrome c release. *Genes Dev*, 13, 1367-1381.

Jung, S.K., Gorski, W., Aspinwall, C.A., Kauri, L.M. and Kennedy, R.T. (**1999**) Oxygen microsensor and its application to single cells and mouse pancreatic islets. *Anal Chem*, 71, 3642-3649.

K

Kadiu, I., Ricardo-Dukelow, M., Ciborowski, P. and Gendelman, H.E. (**2007**) Cytoskeletal protein transformation in HIV-1-infected macrophage giant cells. *J Immunol*, 178, 6404-6415.

Kambe, M., Ioritani, N. and Kanamaru, R. (**1997**) Enhancement of chemotherapeutic effects with focused shock waves: extracorporeal shock wave chemotherapy (ESWC). *Hum Cell*, 10, 87-94.

Kanduc, D., Mittelman, A., Serpico, R., Sinigaglia, E., Sinha, A.A., Natale, C., Santacroce, R., Di Corcia, M.G., Lucchese, A., Dini, L., Pani, P., Santacroce, S., Simone, S., Bucci, R. and Farber, E. (**2002**) Cell death: apoptosis versus necrosis (review). *Int J Oncol*, 21, 165-170.

Kanduser, M., Sentjurc, M. and Miklavcic, D. (**2006**) Cell membrane fluidity related to electroporation and resealing. *Eur Biophys J Biophy*, 35, 196-204.

Kanthou, C., Kranjc, S., Sersa, G., Tozer, G., Zupanic, A. and Cemazar, M. (**2006**) The endothelial cytoskeleton as a target of electroporation-based therapies. *Mol Cancer Ther*, 5, 3145-3152.

Karczewski, J., Troost, F.J., Konings, I., Dekker, J., Kleerebezem, M., Brummer, R.J. and Wells, J.M. (**2010**) Regulation of human epithelial tight junction proteins by Lactobacillus plantarum in vivo and protective effects on the epithelial barrier. *Am J Physiol Gastrointest Liver Physiol*, 298, G851-G859.

Kartha, G. (**1967**) Tertiary structure of ribonuclease. *Nature*, 214, 234 passim.

Kashanchi, F., Duvall, J.F. and Brady, J.N. (**1992**) Electroporation of viral transactivator proteins into lymphocyte suspension cells. *Nucleic Acids Res*, 20, 4673-4674.

Katayose, S. and Kataoka, K. (**1997**) Water-soluble polyion complex associates of DNA and poly(ethylene glycol)-poly(L-lysine) block copolymer. *Bioconjug Chem*, 8, 702-707.

Kayalar, C., Ord, T., Testa, M.P., Zhong, L.T. and Bredesen, D.E. (**1996**) Cleavage of actin by interleukin 1 beta-converting enzyme to reverse DNase I inhibition. *Proc Natl Acad Sci U S A*, 93, 2234-2238.

Keese, C. and Giaever, I. (**1994**) A biosensor that monitors cell morphology with electrical fields. *IEEE Eng. Med. Bio.*, 13, 402-408.

Keese, C.R., Bhawe, K., Wegener, J. and Giaever, I. (**2002**) Real-time impedance assay to follow the invasive activities of metastatic cells in culture. *Biotechniques*, 33, 842-844, 846, 848-850.

Keese, C.R., Wegener, J., Walker, S.R. and Giaever, I. (**2004**) Electrical wound-healing assay for cells in vitro. *Proc Natl Acad Sci U S A*, 101, 1554-1559.

Keren, K., Yam, P.T., Kinkhabwala, A., Mogilner, A. and Theriot, J.A. (**2009**) Intracellular fluid flow in rapidly moving cells. *Nature Cell Biology*, 11, 1219-1224.

Kerr, J.F., Wyllie, A.H. and Currie, A.R. (**1972**) Apoptosis: a basic biological phenomenon with wide-ranging implications in tissue kinetics. *Br J Cancer*, 26, 239-257.

Keusgen, M. (**2002**) Biosensors: new approaches in drug discovery. *Naturwissenschaften*, 89, 433-444.

Khalil, I.A., Kogure, K., Akita, H. and Harashima, H. (**2006**) Uptake pathways and subsequent intracellular trafficking in nonviral gene delivery. *Pharmacol Rev*, 58, 32-45.

Kim, J.Y., Ahn, S.H., Kang, S.T. and Yoon, B.J. (**2006**) Electrophoretic mobility equation for protein with molecular shape and charge multipole effects. *J Colloid Interface Sci*, 299, 486-492.

Kim, K.W., Kim, S.H., Jang, J.H., Lee, E.Y., Park, S.W., Um, J.H., Lee, Y.J., Lee, C.H., Yoon, S., Seo, S.Y., Jeong, M.H., Lee, S.T., Chung, B.S. and Kang, C.D. (**2004**) Dendritic cells loaded with exogenous antigen by electroporation can enhance MHC class I-mediated antitumor immunity. *Cancer Immunol Immunother*, 53, 315-322.

Kim, S., Shilagardi, K., Zhang, S., Hong, S.N., Sens, K.L., Bo, J., Gonzalez, G.A. and Chen, E.H. (**2007**) A critical function for the actin cytoskeleton in targeted exocytosis of prefusion vesicles during myoblast fusion. *Dev Cell*, 12, 571-586.

Kimura, J. and Kuriyama, T. (**1990**) FET biosensors. *J Biotechnol*, 15, 239-254.

Kinosita, K., Jr. and Tsong, T.Y. (**1979**) Voltage-induced conductance in human erythrocyte membranes. *Biochim Biophys Acta*, 554, 479-497.

Kinosita, K. and Tsong, T.Y. (**1977**) Voltage-induced pore formation and hemolysis of human erythrocytes. *Biochim Biophys Acta*, 471, 227-242.

Kitamura, K., Judkewitz, B., Kano, M., Denk, W. and Hausser, M. (**2008**) Targeted patch-clamp recordings and single-cell electroporation of unlabeled neurons in vivo. *Nat Methods*, 5, 61-67.

Klenchin, V.A., Sukharev, S.I., Serov, S.M., Chernomordik, L.V. and Chizmadzhev, Y.A. (**1991**) Electrically induced DNA uptake by cells is a fast process involving DNA electrophoresis. *Biophys J*, 60, 804-811.

Koda, S., Inoue, Y. and Iwata, H. (**2008**) Gene transfection into adherent cells using electroporation on a dendrimer-modified gold electrode. *Langmuir*, 24, 13525-13531.

Koester, P.J., Tautorat, C., Beikirch, H., Gimsa, J. and Baumann, W. (**2010**) Recording electric potentials from single adherent cells with 3D microelectrode arrays after local electroporation. *Biosens Bioelectron*, 26, 1731-1735.

Kohler, G. and Milstein, C. (**1975**) Continuous cultures of fused cells secreting antibody of predefined specificity. *Nature*, 256, 495-497.

Kotani, T., Sawai, S., Kageyama, T. and Sano, M. (**2002**) Circular nuclear alignment in multinucleate PC12D cells produced by cell fusion with polyethylene glycol. *Acta Histochem Cytoc*, 35, 185-191.

Kotnik, T., Bobanovic, F. and Miklavcic, D. (**1997**) Sensitivity of transmembrane voltage induced by applied electric fields - a theoretical analysis. *Bioelectrochem Bioenerg*, 43, 285-291.

Kotnik, T., Miklavcic, D. and Slivnik, T. (**1998**) Time course of transmembrane voltage induced by time-varying electric fields-a method for theoretical analysis and its application. *Bioelectrochem Bioenerg*, 45, 3-16.

Kramer, I., Vienken, K., Vienken, J. and Zimmermann, U. (**1984**) Magneto-electro-fusion of human erythrocytes. *Biochim Biophys Acta*, 772, 407-410.

Kruidering, M., van de Water, B., Zhan, Y., Baelde, J.J., de Heer, E., Mulder, G.J., Stevens, J.L. and Nagelkerke, J.F. (**1998**) Cisplatin effects on F-actin and matrix proteins precede renal tubular cell detachment and apoptosis in vitro. *Cell Death Differ*, 5, 601-614.

Kukowska-Latallo, J.F., Bielinska, A.U., Johnson, J., Spindler, R., Tomalia, D.A. and Baker, J.R. (**1996**) Efficient transfer of genetic material into mammalian cells using Starburst polyamidoamine dendrimers. *P Natl Acad Sci U S A*, 93, 4897-4902.

Kumar, S. and Dorstyn, L. (**2009**) Analysing caspase activation and caspase activity in apoptotic cells. *Methods Mol Biol*, 559, 3-17.

Kunitz, M. (**1950**) Crystalline desoxyribonuclease; isolation and general properties; spectrophotometric method for the measurement of desoxyribonuclease activity. *J Gen Physiol*, 33, 349-362.

Kuo, M.T. (**1981**) Preferential damage of active chromatin by bleomycin. *Cancer Res*, 41, 2439-2443.

Kurata, S., Tsukakoshi, M., Kasuya, T. and Ikawa, Y. (**1986**) The laser method for efficient introduction of foreign DNA into cultured cells. *Exp Cell Res*, 162, 372-378.

Kwee, S., Nielsen, H.V. and Celis, J.E. (**1990**) Electropermeabilization of human cultured cells grown in monolayers: incorporation of monoclonal antibodies. *Bioelectrochem Bioenerg*, 23, 65-80.

L

Lan, C.Y., Tan, P.H., Cheng, J.T., Lu, H.F., Lin, M.W., Hsiao, P.N. and Lin, C.R. (**2003**) Immunoneutralization of c-Fos using intrathecal antibody electroporation attenuates chronic constrictive injury-induced hyperalgesia and regulates preprodynorphin expression in rats. *Anesthesiology*, 99, 938-946.

Lane, R.D., Crissman, R.S. and Lachman, M.F. (**1984**) Comparison of polyethylene glycols as fusogens for producing lymphocyte-myeloma hybrids. *J Immunol Methods*, 72, 71-76.

Lawen, A. (**2003**) Apoptosis-an introduction. *Bioessays*, 25, 888-896.

Lazarides.E and Lindberg, U. (**1974**) Actin Is Naturally Occurring Specific Inhibitor of Deoxyribonuclease I. *J Cell Biol*, 63, A195-A195

Lechardeur, D. and Lukacs, G.L. (**2006**) Nucleocytoplasmic transport of plasmid DNA: a perilous journey from the cytoplasm to the nucleus. *Hum Gene Ther*, 17, 882-889.

Lee, C.O. (**1981**) Ionic activities in cardiac-muscle-cells and application of ion-selective microelectrodes. *Am J Physiol*, 241, H459-H478.

Lee, G., Delohery, T.M., Ronai, Z., Brandtrauf, P.W., Pincus, M.R., Murphy, R.B. and Weinstein, I.B. (**1993**) A Comparison of techniques for introducing macromolecules into living cells. *Cytometry*, 14, 265-270.

Lee, J.E. and Raines, R.T. (**2008**) Ribonucleases as novel chemotherapeutics - The ranpirnase example. *Biodrugs*, 22, 53-58.

Lee, R.J. and Huang, L. (**1997**) Lipidic vector systems for gene transfer. *Crit Rev Ther Drug Carrier Syst*, 14, 173-206.

Lee, S.H., Bae, K.H., Kim, S.H., Lee, K.R. and Park, T.G. (**2008**) Amine-functionalized gold nanoparticles as non-cytotoxic and efficient intracellular siRNA delivery carriers. *Int J Pharm*, 364, 94-101.

Leikina, E., Onaran, H.O. and Zimmerberg, J. (**1992**) Acidic pH induces fusion of cells infected with baculovirus to form syncytia. *FEBS Lett*, 304, 221-224.

Leist, M., Single, B., Castoldi, A.F., Kuhnle, S. and Nicotera, P. (**1997**) Intracellular adenosine triphosphate (ATP) concentration: a switch in the decision between apoptosis and necrosis. *J Exp Med*, 185, 1481-1486.

Leland, P.A., Schultz, L.W., Kim, B.M. and Raines, R.T. (**1998**) Ribonuclease A variants with potent cytotoxic activity. *Proc Natl Acad Sci U S A*, 95, 10407-10412.

Leli, U., Parker, P.J. and Shea, T.B. (**1992**) Intracellular delivery of protein-kinase C-alpha or C-epsilon isoform-specific antibodies promotes acquisition of a morphologically differentiated phenotype in neuroblastoma-cells. *Febs Lett*, 297, 91-94.

Lentz, B.R. (**1994**) Polymer-induced membrane fusion: potential mechanism and relation to cell fusion events. *Chem Phy Lipids*, 73, 91-106.

Lentz, B.R. (**2007**) PEG as a tool to gain insight into membrane fusion. *Eur Biophys J Biophy*, 36, 315-326.

Levenberg, S., Yarden, A., Kam, Z. and Geiger, B. (**1999**) p27 is involved in N-cadherin-mediated contact inhibition of cell growth and S-phase entry. *Oncogene*, 18, 869-876.

Li, F., Srinivasan, A., Wang, Y., Armstrong, R.C., Tomaselli, K.J. and Fritz, L.C. (**1997**) Cell-specific induction of apoptosis by microinjection of cytochrome c. Bcl-xL has activity independent of cytochrome c release. *J Biol Chem*, 272, 30299-30305.

Li, L.H., Hensen, M.L., Zhao, Y.L. and Hui, S.W. (**1996**) Electrofusion between heterogeneous-sized mammalian cells in a pellet: Potential applications in drug delivery and hybridoma formation. *Biophys J*, 71, 479-486.

Lifson, J.D., Feinberg, M.B., Reyes, G.R., Rabin, L., Banapour, B., Chakrabarti, S., Moss, B., Wong-Staal, F., Steimer, K.S. and Engleman, E.G. (**1986**) Induction of CD4-dependent cell fusion by the HTLV-III/LAV envelope glycoprotein. *Nature*, 323, 725-728.

Lin, H.P., Vincenz, C., Eliceiri, K.W., Kerppola, T.K. and Ogle, B.M. (**2010**) Bimolecular fluorescence complementation analysis of eukaryotic fusion products. *Biol Cell*, 102, 525-537.

Lin, Y.C., Li, M., Fan, C.S. and Wu, L.W. (**2003**) A microchip for electroporation of primary endothelial cells. *Sensor Actuat a-Phys*, 108, 12-19.

Lin, Y.C., Li, M. and Wu, C.C. (**2004**) Simulation and experimental demonstration of the electric field assisted electroporation microchip for in vitro gene delivery enhancement. *Lab on a Chip*, 4, 104-108.

Link, N., Brunner, T.J., Dreesen, I.A., Stark, W.J. and Fussenegger, M. (**2007**) Inorganic nanoparticles for transfection of mammalian cells and removal of viruses from aqueous solutions. *Biotechnol Bioeng*, 98, 1083-1093.

Lips, J. and Kaina, B. (**2001**) DNA double-strand breaks trigger apoptosis in p53-deficient fibroblasts. *Carcinogenesis*, 22, 579-585.

Liu, G., Molas, M., Grossmann, G.A., Pasumarthy, M., Perales, J.C., Cooper, M.J. and Hanson, R.W. (**2001**) Biological properties of poly-L-lysine-DNA complexes generated by cooperative binding of the polycation. *J Biol Chem*, 276, 34379-34387.

Liu, H.S., Jan, M.S., Chou, C.K., Chen, P.H. and Ke, N.J. (**1999**) Is green fluorescent protein toxic to the living cells? *Biochem Biophys Res Commun*, 260, 712-717.

Liu, M., Gothe, G. and Berg, H. (**2000**) Electroporation and fusion of human cancer cells modified by amino acids and polypeptides. *Electro Magnetobiol*, 19, 331-338.

Liu, Q., Yu, J., Xiao, L., Tang, J.C., Zhang, Y., Wang, P. and Yang, M. (**2009**) Impedance studies of bio-behavior and chemosensitivity of cancer cells by micro-electrode arrays. *Biosens Bioelectron*, 24, 1305-1310.

Liu, X.S., Kim, C.N., Yang, J., Jemmerson, R. and Wang, X.D. (**1996**) Induction of apoptotic program in cell-free extracts: Requirement for dATP and cytochrome c. *Cell*, 86, 147-157.

Lo, C.M., Keese, C.R. and Giaever, I. (**1993**) Monitoring motion of confluent cells in tissue culture. *Exp Cell Res*, 204, 102-109.

Lo, C.M., Keese, C.R. and Giaever, I. (**1994**) pH changes in pulsed CO2 incubators cause periodic changes in cell morphology. *Exp Cell Res*, 213, 391-397.

Lo, C.M., Keese, C.R. and Giaever, I. (**1995**) Impedance analysis of MDCK cells measured by electric cell-substrate impedance sensing. *Biophys J*, 69, 2800-2807.

Lo, M.M., Tsong, T.Y., Conrad, M.K., Strittmatter, S.M., Hester, L.D. and Snyder, S.H. (**1984**) Monoclonal antibody production by receptor-mediated electrically induced cell fusion. *Nature*, 310, 792-794.

Lopez, A., Rols, M.P. and Teissié, J. (**1988**) P-31 NMR analysis of membrane phospholipid organization in viable, reversibly electropermeabilized Chinese-Hamster Ovary cells. *Biochemistry*, 27, 1222-1228.

Lorenz, M.R., Holzapfel, V., Musyanovych, A., Nothelfer, K., Walther, P., Frank, H., Landfester, K., Schrezenmeier, H. and Mailander, V. (**2006**) Uptake of functionalized, fluorescent-labeled polymeric particles in different cell lines and stem cells. *Biomaterials*, 27, 2820-2828.

Lu, X. and Kang, Y.B. (**2009**) Cell Fusion as a Hidden Force in Tumor Progression. *Cancer Res*, 69, 8536-8539.

Ludtke, J.J., Zhang, G.F., Sebestyen, M.G. and Wolff, J.A. (**1999**) A nuclear localization signal can enhance both the nuclear transport and expression of 1 kb DNA. *J Cell Sci*, 112, 2033-2041.

Lukas, J., Bartek, J. and Strauss, M. (**1994**) Efficient transfer of antibodies into mammalian cells by electroporation. *J Immunol Methods*, 170, 255-259.

Luo, D. and Saltzman, W.M. (**2000**) Synthetic DNA delivery systems. *Nat Biotechnol*, 18, 33-37.

Luong, J.H.T., Mulchandani, A. and Guilbault, G.G. (**1988**) Developments and applications of biosensors. *Trends Biotechnol*, 6, 310-316.

M

Macdonald, J.R. (**1992**) Impedance Spectroscopy. *Ann Biomed Eng*, 20, 289-305.

Macknight, A.C.D. (**1991**) Volume regulation in Epithelia. In Gilles, R., Bolis, L. (eds.) Volume and Osmolality in animal cells. Springer Verlag, Berlin.

Mailänder, V. and Landfester, K. (**2009**) Interaction of nanoparticles with cells. *Biomacromolecules*, 10, 2379-2400.

Majno, G. and Joris, I. (**1995**) Apoptosis, oncosis, and necrosis. An overview of cell death. *Am J Pathol*, 146, 3-15.

Male, K.B., Lachance, B., Hrapovic, S., Sunahara, G. and Luong, J.H. (**2008**) Assessment of cytotoxicity of quantum dots and gold nanoparticles using cell-based impedance spectroscopy. *Anal Chem*, 80, 5487-5493.

Malecki, J.M., Bentke, A., Ostrowska, B. and Laidler, P. (**2010**) Cytochalasin D, LY294002 and olomoucine synergize in promoting death of melanoma cells through activation of caspase-3 and apoptosis. *Melanoma Res*, 20, 52-58.

Malina, K.C.K., Cooper, I. and Teichberg, V.I. (**2009**) Closing the gap between the in-vivo and in-vitro blood-brain barrier tightness. *Brain Res*, 1284, 12-21.

Malone, R.W., Felgner, P.L. and Verma, I.M. (**1989**) Cationic Liposome-Mediated RNA Transfection. *P Natl Acad Sci USA*, 86, 6077-6081.

Manservigi, R., Spear, P.G. and Buchan, A. (**1977**) Cell fusion induced by herpes simplex virus is promoted and suppressed by different viral glycoproteins. *Proc Natl Acad Sci U S A*, 74, 3913-3917.

Marrero, M.B., Schieffer, B., Paxton, W.G., Schieffer, E. and Bernstein, K.E. (**1995**) Electroporation of Pp60(C-Src) antibodies inhibits the angiotensin-II activation of Phospholipase C-gamma-1 in rat aortic smooth-muscle cells. *J BiolChem*, 270, 15734-15738.

Marszalek, P., Liu, D.-S. and Tsong, T.Y. (**1990**) Schwan equation and transmembrane potential induced by alternating electric field. *Biophys J*, 58, 1053-1058.

Martin, S.J., Granstaff, V.E. and Frye, G.C. (**1991**) Characterization of a quartz crystal microbalance with simultaneous mass and liquid Loading. *AnalChem*, 63, 2272-2281.

Martinoia, S., Rosso, N., Grattarola, M., Lorenzelli, L., Margesin, B. and Zen, M. (**2001**) Development of ISFET array-based microsystems for bioelectrochemical measurements of cell populations. *Biosens Bioelectron*, 16, 1043-1050.

Marx, K. (**2007**) The Quartz Crystal Microbalance and the Electrochemical QCM: Applications to studies of thin polymer films, electron transfer systems, biological macromolecules, biosensors, and cells. In Steinem, C., Janshoff, A. (eds.) Piezoelectric Sensors. Springer Verlag, Berlin, Heidelberg.

Marx, K.A., Zhou, T., Montrone, A., McIntosh, D. and Braunhut, S.J. (**2007**) A comparative study of the cytoskeleton binding drugs nocodazole and taxol with a mammalian cell quartz crystal microbalance biosensor: different dynamic responses and energy dissipation effects. *Anal Biochem*, 361, 77-92.

Matsuda, T. and Cepko, C.L. (**2004**) Electroporation and RNA interference in the rodent retina in vivo and in vitro. *Proc Natl Acad Sci U S A*, 101, 16-22.

Matsushita, M., Noguchi, H., Lu, Y.F., Tomizawa, K., Michiue, H., Li, S.T., Hirose, K., Bonner-Weir, S. and Matsui, H. (**2004**) Photo-acceleration of protein release from endosome in the protein transduction system. *Febs Lett*, 572, 221-226.

McAdams, E.T., Lackermeier, A., McLaughlin, J.A., Macken, D. and Jossinet, J. (**1995**) The linear and nonlinear electrical properties of the electrode-electrolyte interface. *Biosens Bioelectron*, 10, 67-74.

McBain, S.C., Yiu, H.H.P., El Haj, A. and Dobson, J. (**2007**) Polyethyleneimine functionalized iron oxide nanoparticles as agents for DNA delivery and transfection. *J Mater Chem*, 17, 2561-2565.

McCaig, C.D., Rajnicek, A.M., Song, B. and Zhao, M. (**2005**) Controlling cell behavior electrically: current views and future potential. *Physiol Rev*, 85, 943-978.

McCaig, C.D., Song, B. and Rajnicek, A.M. (**2009**) Electrical dimensions in cell science. *J Cell Sci*, 122, 4267-4276.

McCarty, N.A. and O'Neil, R.G. (**1992**) Calcium signaling in cell volume regulation. *Physiol Rev*, 72, 1037-1061.

McCoy, M.H. and Wang, E. (**2005**) Use of electric cell-substrate impedance sensing as a tool for quantifying cytopathic effect in influenza A virus infected MDCK cells in real-time. *J Virol Methods*, 130, 157-161.

McCutchan, J.H. and Pagano, J.S. (**1968**) Enchancement of the infectivity of simian virus 40 deoxyribonucleic acid with diethylaminoethyl-dextran. *J Natl Cancer Inst*, 41, 351-357.

Mcelligott, M.A. and Dice, J.F. (**1984**) Microinjection of cultured-cells using red-cell-mediated fusion and osmotic lysis of pinosomes - a review of methods and applications. *Bioscience Rep*, 4, 451-466.

McManus, M.L., Churchwell, K.B. and Strange, K. (**1995**) Regulation of cell volume in health and disease. *N Engl J Med*, 333, 1260-1266.

Mekid, H. and Mir, L.M. (**2000**) In vivo cell electrofusion. *Biochim Biophys Acta*, 1524, 118-130.

Melikyan, G.B. and Chernomordik, L.V. (**1989**) Electrofusion of lipid bilayers. In Neumann, E., Sowers, A.E., Jordan, C.A. (eds.) Electroporation and Electrofusion in Cell Biology. Plenum Press, New York, London.

Melikyan, G.B., Niles, W.D., Peeples, M.E. and Cohen, F.S. (**1993**) Influenza hemagglutinin-mediated fusion pores connecting cells to planar membranes: flickering to final expansion. *J Gen Physiol*, 102, 1131-1149.

Michaelis, M., Cinatl, J., Anand, P., Rothweiler, F., Kotchetkov, R., von Deimling, A., Doerr, H.W., Shogen, K. and Cinatl, J., Jr. (**2007**) Onconase induces caspase-independent cell death in chemoresistant neuroblastoma cells. *Cancer Lett*, 250, 107-116.

Michaelis, S. (**2010**) Non-invasive biosensors to characterize the cell-material interface. PhD thesis, Westfälische Wilhelms-Universität, Münster.

Miklavcic, D., Mir, L.M. and Thomas Vernier, P. (**2010**) Electroporation-based technologies and treatments. *J Membr Biol*, 236, 1-2.

Miller, A.M. and Dean, D.A. (**2008**) Cell-specific nuclear import of plasmid DNA in smooth muscle requires tissue-specific transcription factors and DNA sequences. *Gene Ther*, 15, 1107-1115.

Miller, D.L., Pislaru, S.V. and Greenleaf, J.E. (**2002**) Sonoporation: mechanical DNA delivery by ultrasonic cavitation. *Somat Cell Mol Genet*, 27, 115-134.

Minami, K., Yamaguchi, Y., Ohshita, A., Kawabuchi, Y., Ohta, K., Hihara, J. and Toge, T. (**2005**) Generation of antigen-presenting cells using cultured dendritic cells and amplified autologous tumor mRNA. *Oncology*, 69, 399-407.

Minsky, M. (**1988**) Memoir on inventing the confocal scanning microscope. *Scanning*, 10, 128-138.

Mir, L.M., Banoun, H. and Paoletti, C. (**1988**) Introduction of definite amounts of nonpermeant molecules into living cells after electropermeabilization: direct access to the cytosol. *Exp Cell Res*, 175, 15-25.

Mir, L.M., Gehl, J., Sersa, G., Collins, C.G., Garbay, J.R., Billard, V., Geertsen, P.F., Rudolf, Z., O'Sullivan, G.C. and Marty, M. (**2006**) Standard operating procedures of the electrochemotherapy: Instructions for the use of bleomycin or cisplatin administered either systemically or locally and electric pulses delivered by the Cliniporator (TM) by means of invasive or non-invasive electrodes. *Ejc Suppl*, 4, 14-25.

Mir, L.M., Glass, L.F., Sersa, G., Teissié, J., Domenge, C., Miklavcic, D., Jaroszeski, M.J., Orlowski, S., Reintgen, D.S., Rudolf, Z., Belehradek, M., Gilbert, R., Rols, M.P., Belehradek, J., Jr., Bachaud, J.M., DeConti, R., Stabuc, B., Cemazar, M., Coninx, P. and Heller, R. (**1998**) Effective treatment of cutaneous and subcutaneous malignant tumours by electrochemotherapy. *Br J Cancer*, 77, 2336-2342.

Mir, L.M., Tounekti, O. and Orlowski, S. (**1996**) Bleomycin: revival of an old drug. *Gen Pharmacol*, 27, 745-748.

Mitchison, T.J. and Cramer, L.P. (**1996**) Actin-based cell motility and cell locomotion. *Cell*, 84, 371-379.

Miyauchi, K., Kim, Y., Latinovic, O., Morozov, V. and Melikyan, G.B. (**2009**) HIV enters cells via endocytosis and dynamin-dependent fusion with endosomes. *Cell*, 137, 433-444.

Mlakar, V., Todorovic, V., Cemazar, M., Glavac, D. and Sersa, G. (**2009**) Electric pulses used in electrochemotherapy and electrogene therapy do not significantly change the expression profile of genes involved in the development of cancer in malignant melanoma cells. *Bmc Cancer*, 9: 299

Mohr, J.C., de Pablo, J.J. and Palecek, S.P. (**2006**) Electroporation of human embryonic stem cells: small and macromolecule loading and DNA transfection. *Biotechnol Prog*, 22, 825-834.

Montrose-Rafizadeh, C. and Guggino, W.B. (**1990**) Cell-Volume Regulation in the Nephron. *Annu Rev Physiol*, 52, 761-772.

Moon, R.T., Kohn, A.D., De Ferrari, G.V. and Kaykas, A. (**2004**) WNT and beta-catenin signalling: diseases and therapies. *Nat Rev Genet*, 5, 691-701.

Moore, E., Rawley, O., Wood, T. and Galvin, P. (**2009**) Monitoring of cell growth in vitro using biochips packaged with indium tin oxide sensors. *Sensor Actuat B-Chem*, 139, 187-193.

Morgan, D.O. and Roth, R.A. (**1988**) Analysis of intracellular protein function by antibody injection. *Immunol Today*, 9, 84-88.

Morgan, W.F. and Day, J.P. (**1995**) The introduction of proteins into mammalian cells by electroporation. *Methods Mol Biol*, 48, 63-71.

Mülhardt, C. (**2006**) Der Experimentator, Molekularbiologie / Genomics. Spektrum Akademischer Verlag, Heidelberg, Berlin.

Müller, K.J., Horbaschek, M., Lucas, K., Zimmermann, U. and Sukhorukov, V.L. (**2003**) Electrotransfection of anchorage-dependent mammalian cells. *Exp Cell Res*, 288, 344-353.

N

Nadal, A., Martell, M., Lytle, J.R., Lyons, A.J., Robertson, H.D., Cabot, B., Esteban, J.I., Esteban, R., Guardia, J. and Gomez, J. (**2002**) Specific cleavage of hepatitis C virus RNA genome by human RNase P. *J Biol Chem*, 277, 30606-30613.

Nakagawa, K., Taya, Y., Tamai, K. and Yamaizumi, M. (**1999**) Requirement of ATM in phosphorylation of the human p53 protein at serine 15 following DNA double-strand breaks. *Mol Cell Biol*, 19, 2828-2834.

Nakashima, N., Rose, D.W., Xiao, S., Egawa, K., Martin, S.S., Haruta, T., Saltiel, A.R. and Olefsky, J.M. (**1999**) The functional role of CrkII in actin cytoskeleton organization and mitogenesis. *J BiolChem*, 274, 3001-3008.

Nemhauser, I. and Goldberg, D.J. (**1985**) Structural effects in axoplasm of Dnase-I, an actin depolymerizer that blocks fast axonal-transport. *Brain Res*, 334, 47-58.

Neumann, E. (**1989**) The relaxation hysteresis of membrane electroporation. In Neumann, E., Sowers, A.E., Jordan, C.A. (eds.) Electroporation and electrofusion in cell biology. Plenum Press, New York, London.

Neumann, E., Kakorin, S. and Toensing, K. (**1999**) Fundamentals of electroporative delivery of drugs and genes. *Bioelectrochem Bioenerg*, 48, 3-16.

Neumann, E. and Rosenheck, K. (**1972**) Permeability changes induced by electric impulses in vesicular membranes. *J Membr Biol*, 10, 279-290.

Neumann, E., Schaefer-Ridder, M., Wang, Y. and Hofschneider, P.H. (**1982**) Gene transfer into mouse lyoma cells by electroporation in high electric fields. *Embo J*, 1, 841-845.

Neumann, E., Toensing, K., Kakorin, S., Budde, P. and Frey, J. (**1998**) Mechanism of electroporative dye uptake by mouse B cells. *Biophys J*, 74, 98-108.

Neumann, E., Tonsing, K. and Siemens, P. (**2000**) Perspectives for microelectrode arrays for biosensing and membrane electroporation. *Bioelectrochem*, 51, 125-132.

Nevian, T. and Helmchen, F. (**2007**) Calcium indicator loading of neurons using single-cell electroporation. *Pflug Arch Eur J Phy*, 454, 675-688.

Newman, J. (**1966**) Resistance for flow of current to a disk. *J Electrochem Soc*, 113, 501-502

Nicholson, D.W., Ali, A., Thornberry, N.A., Vaillancourt, J.P., Ding, C.K., Gallant, M., Gareau, Y., Griffin, P.R., Labelle, M., Lazebnik, Y.A., Munday, N.A., Raju, S.M., Smulson, M.E., Yamin, T.T., Yu, V.L. and Miller, D.K. (**1995**) Identification and Inhibition of the Ice/Ced-3 Protease Necessary for Mammalian Apoptosis. *Nature*, 376, 37-43.

Niessen, C.M. (**2007**) Tight junctions/adherens junctions: basic structure and function. *J InvestDermatol*, 127, 2525-2532.

Norbury, C.J. and Zhivotovsky, B. (**2004**) DNA damage-induced apoptosis. *Oncogene*, 23, 2797-2808.

O

O'Connor, E.R., Kimelberg, H.K., Keese, C.R. and Giaever, I. (**1993**) Electrical resistance method for measuring volume changes in monolayer cultures applied to primary astrocyte cultures. *Am J Physiol*, 264, C471-C478.

Obe, G. and Johannes, C. (**1993**) Chromosomal-aberrations induced with endonucleases. *Rev Bras Genet*, 16, 849-855.

Odaka, C., Sanders, M.L. and Crews, P. (**2000**) Jasplakinolide induces apoptosis in various transformed cell lines by a caspase-3-like protease-dependent pathway. *Clin Diagn Lab Immun*, 7, 947-952.

Ogle, B.M., Cascalho, M. and Platt, J.L. (**2005**) Biological implications of cell fusion. *Nat Rev Mol Cell Biol*, 6, 567-575.

Ogura, A., Yamamoto, Y., Suzuki, O., Takano, K., Wakayama, T., Mochida, K. and Kimura, H. (**1996**) In vitro fertilization and microinsemination with round spermatids for propagation of nephrotic genes in mice. *Theriogenology*, 45, 1141-1149.

Ohno-Shosaku, T. and Okada, Y. (**1985**) Electric pulse-induced fusion of mouse lymphoma cells: roles of divalent cations and membrane lipid domains. *J Membr Biol*, 85, 269-280.

Okajima, T., Tanaka, M., Tsukiyama, S., Kadowaki, T., Yamamoto, S., Shimomura, M. and Tokumoto, H. (**2007**) Stress relaxation of HepG2 cells measured by atomic force microscopy. *Nanotechnology*, 18: 084010

Okamoto, K., Ohgimoto, S., Nishio, M., Tsurudome, M., Kawano, M., Komada, H., Ito, M., Sakakura, Y. and Ito, Y. (**1997**) Paramyxovirus-induced syncytium cell formation is suppressed by a dominant negative fusion regulatory protein-1 (FRP-1)/CD98 mutated construct: an important role of FRP-1 in virus-induced cell fusion. *J Gen Virol*, 78, 775-783.

Oku, N., Yamaguchi, N., Yamaguchi, N., Shibamoto, S., Ito, F. and Nango, M. (**1986**) The fusogenic effect of synthetic polycations on negatively charged lipid bilayers. *J Biochem-Tokyo*, 100, 935-944.

Olbrich, M., Rebollar, E., Heitz, J., Frischauf, I. and Romanin, C. (**2008**) Electroporation chip for adherent cells on photochemically modified polymer surfaces. *Appl Phys Lett*, 92: 013901.

Olive, P.L. and Banath, J.P. (**1993**) Detection of DNA double-strand breaks through the cell cycle after exposure to X-rays, bleomycin, etoposide and 125IdUrd. *Int J Radiat Biol*, 64, 349-358.

Olofsson, J., Levin, M., Stromberg, A., Weber, S.G., Ryttsen, F. and Orwar, O. (**2005**) Generation of focused electric field patterns at dielectric surfaces. *AnalChem*, 77, 4667-4672.

Olofsson, J., Levin, M., Stromberg, A., Weber, S.G., Ryttsen, F. and Orwar, O. (**2007**) Scanning electroporation of selected areas of adherent cell cultures. *Anal Chem*, 79, 4410-4418.

Oren-Suissa, M. and Podbilewicz, B. (**2007**) Cell fusion during development. *Trends in Cell Biology*, 17, 537-546.

Orlowski, S., Belehradek, J., Jr., Paoletti, C. and Mir, L.M. (**1988**) Transient electropermeabilization of cells in culture. Increase of the cytotoxicity of anticancer drugs. *Biochem Pharmacol*, 37, 4727-4733.

Orndorff, R.L. and Rosenthal, S.J. (**2009**) Neurotoxin quantum dot conjugates detect endogenous targets expressed in live cancer cells. *Nano Lett*, 9, 2589-2599.

Otsuka, H., Nagasaki, Y. and Kataoka, K. (**2003**) PEGylated nanoparticles for biological and pharmaceutical applications. *Adv Drug Deliv Rev*, 55, 403-419.

Ovcharenko, D., Jarvis, R., Hunicke-Smith, S., Kelnar, K. and Brown, D. (**2005**) High-throughput RNAi screening in vitro: from cell lines to primary cells. *RNA*, 11, 985-993.

Ow, Y.L.P., Green, D.R., Hao, Z. and Mak, T.W. (**2008**) Cytochrome c: functions beyond respiration. *Nat Rev Mol Cell Bio*, 9, 532-542.

Owicki, J.C. and Parce, J.W. (**1992**) Biosensors based on the energy metabolism of living cells: the physical chemistry and cell biology of extracellular acidification. *Biosens Bioelectron*, 7, 255-272.

P, Q

Pangburn, T.O., Petersen, M.A., Waybrant, B., Adil, M.M. and Kokkoli, E. (**2009**) Peptide- and aptamer-functionalized nanovectors for targeted delivery of therapeutics. *J Biomech Eng-T Asme*, 131: 074005.

Panke, O., Weigel, W., Schmidt, S., Steude, A. and Robitzki, A.A. (**2011**) A cell-based impedance assay for monitoring transient receptor potential (TRP) ion channel activity. *Biosens Bioelectron*, 26, 2376-2382.

Papahadjopoulos, D., Vail, W.J., Pangborn, W.A. and Poste, G. (**1976**) Studies on membrane fusion. II. Induction of fusion in pure phospholipid membranes by calcium ions and other divalent metals. *Biochim Biophys Acta*, 448, 265-283.

Park, H., Kim, D. and Yun, K.S. (**2010**) Single-cell manipulation on microfluidic chip by dielectrophoretic actuation and impedance detection. *Sensor Actuat B-Chem*, 150, 167-173.

Parker, A.L., Fisher, K.D., Oupicky, D., Read, M.L., Nicklin, S.A., Baker, A.H. and Seymour, L.W. (**2005**) Enhanced gene transfer activity of peptide-targeted gene-delivery vectors. *J Drug Target*, 13, 39-51.

Parmentier, J., Hartmann, F.J. and Fricker, G. (**2010**) In vitro evaluation of liposomes containing bio-enhancers for the oral delivery of macromolecules. *Eur J Pharm Biopharm*, 76, 394-403.

Patel, L.N., Zaro, J.L. and Shen, W.C. (**2007**) Cell penetrating peptides: intracellular pathways and pharmaceutical perspectives. *Pharm Res*, 24, 1977-1992.

Pauly, H. and Schwan, H.P. (**1959**) Über die Impedanz einer Suspension von kugelförmigen Teilchen mit einer Schale. *Z. Naturforsch., B: Anorg. Chem., Org. Chem.* , 14, 125–131.

Pavlakis, N. and Vogelzang, N.J. (**2006**) Ranpirnase – an antitumour ribonuclease: its potential role in malignant mesothelioma. *Expert Opin Biol Ther*, 6, 391-399.

Pavlin, M., Kanduser, M., Rebersek, M., Pucihar, G., Hart, F.X., Magjarevic, R. and Miklavcic, D. (**2005**) Effect of cell electroporation on the conductivity of a cell suspension. *Biophys J*, 88, 4378-4390.

Peckham, M. (**2008**) Engineering a multi-nucleated myotube, the role of the actin cytoskeleton. *J Microsc*, 231, 486-493.

Pecora, R. (**1985**) Dynamic light scattering: applications of photon correlation spectroscopy. Springer, Berlin.

Perez-Martinez, D., Tanaka, T. and Rabbitts, T.H. (**2010**) Intracellular antibodies and cancer: new technologies offer therapeutic opportunities. *Bioessays*, 32, 589-598.

Perfettini, J.L., Nardacci, R., Bourouba, M., Subra, F., Gros, L., Seror, C., Manic, G., Rosselli, F., Amendola, A., Masdehors, P., Chessa, L., Novelli, G., Ojcius, D.M., Siwicki, J.K., Chechlinska, M., Auclair, C., Regueiro, J.R., de The, H., Gougeon, M.L., Piacentini, M. and Kroemer, G. (**2008**) Critical involvement of the ATM-dependent DNA damage response in the apoptotic demise of HIV-1-elicited syncytia. *Plos One*, 3: e2458.

Peters, M.F., Knappenberger, K.S., Wilkins, D., Sygowski, L.A., Lazor, L.A., Liu, J. and Scott, C.W. (**2007**) Evaluation of cellular dielectric spectroscopy, a whole-cell, label-free technology for drug discovery on Gi-coupled GPCRs. *J Biomol Screen*, 12, 312-319.

Pfüller, U., Ichev, K., Ovtscharoff, W. and Franz, H. (**1988**) Demonstration of negative tissue charges by means of polyethyleneimine-metal complexes. *Histochemistry*, 88, 647-648.

Phez, E., Faurie, C., Golzio, M., Teissié, J. and Rols, M.P. (**2005**) New insights in the visualization of membrane permeabilization and DNA/membrane interaction of cells submitted to electric pulses. *Biochim Biophys Acta*, 1724, 248-254.

Phillips, J.W. and Morgan, W.F. (**1994**) Illegitimate recombination induced by DNA double-strand breaks in a mammalian chromosome. *Mol Cell Biol*, 14, 5794-5803.

Pilwat, G., Richter, H.P. and Zimmermann, U. (**1981**) Giant culture cells by electric field-induced fusion. *FEBS Lett*, 133, 169-174.

Plank, C., Oberhauser, B., Mechtler, K., Koch, C. and Wagner, E. (**1994**) The influence of endosome-disruptive peptides on gene transfer using synthetic virus-like gene transfer systems. *J BiolChem*, 269, 12918-12924.

Plank, C., Schillinger, U., Scherer, F., Bergemann, C., Remy, J.S., Krotz, F., Anton, M., Lausier, J. and Rosenecker, J. (**2003**) The magnetofection method: Using magnetic force to enhance gene delivery. *Biol Chem*, 384, 737-747.

Plank, C., Zauner, W. and Wagner, E. (**1998**) Application of membrane-active peptides for drug and gene delivery across cellular membranes. *Adv Drug Deliv Rev*, 34, 21-35.

Plasek, J. and Sigler, K. (**1996**) Slow fluorescent indicators of membrane potential: a survey of different approaches to probe response analysis. *J Photochem Photobiol B*, 33, 101-124.

Poghossian, A., Cherstvy, A., Ingebrandt, S., Offenhausser, A. and Schoning, M.J. (**2005**) Possibilities and limitations of label-free detection of DNA hybridization with field-effect-based devices. *Sensor Actuat B-Chem*, 111, 470-480.

Pohl, H.A. and Crane, J.S. (**1971**) Dielectrophoresis of cells. *Biophys J*, 11, 711-727.

Pohl, H.A., Pollock, K. and Rivera, H. (**1984**) The Electrofusion of Cells. *International Journal of Quantum Chemistry: Quantum Biology Symposium* 327-345

Pokutta, S. and Weis, W.I. (**2007**) Structure and mechanism of Cadherins and catenins in cell-cell contacts. *Annu Rev Cell Dev Bi*, 23, 237-261.

Pontow, S.E., Heyden, N.V., Wei, S. and Ratner, L. (**2004**) Actin cytoskeletal reorganizations and coreceptor-mediated activation of rac during human immunodeficiency virus-induced cell fusion. *J Virol*, 78, 7138-7147.

Poste, G. and Papahadjopoulos, D. (**1976**) Drug-containing lipid vesicles render drug-resistant tumor-cells sensitive to Actinomycin-D. *Nature*, 261, 699-701.

Potten and Wilson (**2004**) Apoptosis: The life and death of cells. Cambridge University Press, Cambridge.

Potter, H. and Cooke, S.W.F. (**1992**) Gene transfer into adherent cells growing on microbeads. In Chang, D.C., Chassy, B.M., Saunders, J.A., Sowers, A.E. (eds.) Guide to electroporation and electrofusion. Academic Press, San Diego.

Poupot, M. and Fournie, J.J. (**2003**) Spontaneous membrane transfer through homotypic synapses between lymphoma cells. *J Immunol*, 171, 2517-2523.

Prausnitz, M.R. (**1999**) A practical assessment of transdermal drug delivery by skin electroporation. *Adv Drug Deliv Rev*, 35, 61-76.

Prausnitz, M.R., Lau, B.S., Milano, C.D., Conner, S., Langer, R. and Weaver, J.C. (**1993**) A quantitative study of electroporation showing a plateau in net molecular transport. *Biophys J*, 65, 414-422.

Prausnitz, M.R., Milano, C.D., Gimm, J.A., Langer, R. and Weaver, J.C. (**1994**) Quantitative study of molecular transport due to electroporation: uptake of bovine serum albumin by erythrocyte ghosts. *Biophys J*, 66, 1522-1530.

Puc, M., Corovic, S., Flisar, K., Petkovsek, M., Nastran, J. and Miklavcic, D. (**2004**) Techniques of signal generation required for electropermeabilization. Survey of electropermeabilization devices. *Bioelectrochemistry*, 64, 113-124.

Puc, M., Kotnik, T., Mir, L.M. and Miklavcic, D. (**2003**) Quantitative model of small molecules uptake after in vitro cell electropermeabilization. *Bioelectrochemistry*, 60, 1-10.

Puck, T.T. (**1957**) The genetics of somatic mammalian cells. *Adv Biol Med Phys*, 5, 75-101.

Qiao, J., Huang, F., Naikawadi, R.P., Kim, K.S., Said, T. and Lum, H. (**2006**) Lysophosphatidylcholine impairs endothelial barrier function through the G protein-coupled receptor GPR4. *Am J Physiol Lung Cell Mol Physiol*, 291, L91-L101.

R

Rahman, A.R.A., Lo, C.M. and Bhansali, S. (**2006**) A micro-electrode array biosensor for impedance spectroscopy of human umbilical vein endothelial cells. *Sensor Actuat B-Chem*, 118, 115-120.

Rahman, A.R.A., Price, D.T. and Bhansali, S. (**2007**) Effect of electrode geometry on the impedance evaluation of tissue and cell culture. *Sensor Actuat B-Chem*, 127, 89-96.

Raicu, P. and Mixich, F. (**1992**) Cytogenetic effects of sodium azide encapsulated in liposomes on heteroploid cell cultures. *Mutat Res*, 283, 215-219.

Raines, R.T. (**1998**) Ribonuclease A. *Chem Rev*, 98, 1045-1065.

Rajnicek, A.M., Foubister, L.E. and McCaig, C.D. (**2006a**) Growth cone steering by a physiological electric field requires dynamic microtubules, microfilaments and Rac-mediated filopodial asymmetry. *J Cell Sci*, 119, 1736-1745.

Rajnicek, A.M., Foubister, L.E. and McCaig, C.D. (**2006b**) Temporally and spatially coordinated roles for Rho, Rac, Cdc42 and their effectors in growth cone guidance by a physiological electric field. *J Cell Sci*, 119, 1723-1735.

Ramos, C., Bonenfant, D. and Teissié, J. (**2002**) Cell hybridization by electrofusion on filters. *Anal Biochem*, 302, 213-219.

Ramos, C. and Teissié, J. (**2000**) Electrofusion: a biophysical modification of cell membrane and a mechanism in exocytosis. *Biochimie*, 82, 511-518.

Rao, J.Y., Jin, Y.S., Zheng, Q.L., Cheng, J., Tai, J. and Hemstreet, G.P. (**1999**) Alterations of the actin polymerization status as an apoptotic morphological effector in HL-60 cells. *J Cell Biochem*, 75, 686-697.

Raptis, L., Balboa, V., Hsu, T., Vultur, A., Turkson, J., Jove, R. and Firth, K.L. (**2003**) In situ electroporation of large numbers of cells using minimal volumes of material. *Anal Biochem*, 317, 124-128.

Raptis, L. and Firth, K. (**2008**) Electrode assemblies used for electroporation of cultured cells. In Li, S. (ed.) Electroporation Protocols: Preclinical and Clinical Gene Medicine. Humana Press 2008.

Raptis, L. and Firth, K.L. (**1990**) Electroporation of adherent cells in situ. *DNA Cell Biol*, 9, 615-621.

Raptis, L., Firth, K.L., Tomai, E. and Forkert, P.G. (**2000**) Improved procedure for examination of gap junctional intercellular communication by in situ electroporation on a partly conductive slide. *Biotechniques*, 29, 222-224, 226.

Raptis, L.H., Brownell, H.L., Liu, S.K., Firth, K.L., MacKenzie, L.W., Stiles, C.D. and Alberta, J.A. (**1995a**) Applications of electroporation of adherent cells in situ, on a partly conductive slide. *Mol Biotechnol*, 4, 129-138.

Raptis, L.H., Firth, K.L., Brownell, H.L., Todd, A., Simon, W.C., Bennett, B.M., MacKenzie, L.W. and Zannis-Hadjopoulos, M. (**1995b**) Electroporation of adherent cells in situ for the introduction of nonpermeant molecules. *Methods Mol Biol*, 48, 93-113.

Raptis, L.H., Liu, S.K.-W., Firth, K.L., Stiles, C.D. and Alberta, J.A. (**1994**) Electroporation of Peptides into Adherent Cells In Situ. *BioTechniques*, 18, 104-114.

Reddy, L., Wang, H.S., Keese, C.R., Giaever, I. and Smith, T.J. (**1998**) Assessment of rapid morphological changes associated with elevated cAMP levels in human orbital fibroblasts. *Exp Cell Res*, 245, 360-367.

Redepenning, J., Schlesinger, T.K., Mechalke, E.J., Puleo, D.A. and Bizios, R. (**1993**) Osteoblast Attachment Monitored with a Quartz-Crystal Microbalance. *Analytical Chemistry*, 65, 3378-3381.

Rehder, D., Iden, S., Nasdala, I., Wegener, J., Brickwedde, M.K., Vestweber, D. and Ebnet, K. (**2006**) Junctional adhesion molecule-a participates in the formation of apico-basal polarity through different domains. *Exp Cell Res*, 312, 3389-3403.

Riske, K.A. and Dimova, R. (**2005**) Electro-deformation and poration of giant vesicles viewed with high temporal resolution. *Biophys J*, 88, 1143-1155.

Rodriguez, M., Torrent, G., Bosch, M., Rayne, F., Dubremetz, J.F., Ribo, M., Benito, A., Vilanova, M. and Beaumelle, B. (**2007**) Intracellular pathway of Onconase that enables its delivery to the cytosol. *J Cell Sci*, 120, 1405-1411.

Rogakou, E.P., Nieves-Neira, W., Boon, C., Pommier, Y. and Bonner, W.M. (**2000**) Initiation of DNA fragmentation during apoptosis induces phosphorylation of H2AX histone at serine 139. *J Biol Chem*, 275, 9390-9395.

Rolland, A.P. (**1998**) From genes to gene medicines: recent advances in nonviral gene delivery. *Crit Rev Ther Drug Carrier Syst*, 15, 143-198.

Rols, M.-P., Golzio, M., Delteil, C. and Teissié, J. (**2000**) In vitro delivery of drugs and other molecules to cells. In Jaroszeski, M.J., Heller, R., Gilbert, R. (eds.) Methods in Molecular Medicine: Electrically mediated Delivery of Molecules to Cells. Humana Press, Totowa, NJ.

Rols, M.P. (**2006**) Electropermeabilization, a physical method for the delivery of therapeutic molecules into cells. *Biochim Biophys Acta*, 1758, 423-428.

Rols, M.P. (**2008**) Mechanism by which electroporation mediates DNA migration and entry into cells and targeted tissues. *Methods Mol Biol*, 423, 19-33.

Rols, M.P., Delteil, C., Golzio, M., Dumond, P., Cros, S. and Teissié, J. (**1998a**) In vivo electrically mediated protein and gene transfer in murine melanoma. *Nat Biotechnol*, 16, 168-171.

Rols, M.P., Delteil, C., Golzio, M. and Teissié, J. (**1998b**) Control by ATP and ADP of voltage-induced mammalian-cell-membrane permeabilization, gene transfer and resulting expression. *Eur J Biochem*, 254, 382-388.

Rols, M.P., Femenia, P. and Teissié, J. (**1995**) Long-lived macropinocytosis takes place in electropermeabilized mammalian cells. *Biochem Biophys Res Commun*, 208, 26-35.

Rols, M.P. and Teissié, J. (**1989**) Ionic-strength modulation of electrically induced permeabilization and associated fusion of mammalian cells. *Eur J Biochem*, 179, 109-115.

Rols, M.P. and Teissié, J. (**1990a**) Electropermeabilization of mammalian cells. Quantitative analysis of the phenomenon. *Biophys J*, 58, 1089-1098.

Rols, M.P. and Teissié, J. (**1990b**) Modulation of electrically induced permeabilization and fusion of Chinese hamster ovary cells by osmotic pressure. *Biochemistry*, 29, 4561-4567.

Rols, M.P. and Teissié, J. (**1992**) Experimental evidence for the involvement of the cytoskeleton in mammalian cell electropermeabilization. *Biochim Biophys Acta*, 1111, 45-50.

Rols, M.P. and Teissié, J. (**1998**) Electropermeabilization of mammalian cells to macromolecules: control by pulse duration. *Biophys J*, 75, 1415-1423.

Roos, W.P. and Kaina, B. (**2006**) DNA damage-induced cell death by apoptosis. *Trends Mol Med*, 12, 440-450.

Rosen, A.B., Kelly, D.J., Schuldt, A.J., Lu, J., Potapova, I.A., Doronin, S.V., Robichaud, K.J., Robinson, R.B., Rosen, M.R., Brink, P.R., Gaudette, G.R. and Cohen, I.S. (**2007**) Finding fluorescent needles in the cardiac haystack: tracking human mesenchymal stem cells labeled with quantum dots for quantitative in vivo three-dimensional fluorescence analysis. *Stem Cells*, 25, 2128-2138.

Rosenberg, H.F. (**2008**) RNase A ribonucleases and host defense: an evolving story. *J Leukoc Biol*, 83, 1079-1087.

Rosemberg, Y. & Korenstein, R. (**1990**) Electroporation of the photosynthetic membrane: A study by intrinsic and external optical probes. *Biophys J*, 58, 823-832.

Rubtsova, S.N., Kondratov, R.V., Kopnin, P.B., Chumakov, P.M., Kopnin, B.P. and Vasiliev, J.M. (**1998**) Disruption of actin microfilaments by cytochalasin D leads to activation of p53. *Febs Lett*, 430, 353-357.

Rui, M., Chen, Y., Zhang, Y. and Ma, D. (**2002**) Transfer of anti-TFAR19 monoclonal antibody into HeLa cells by in situ electroporation can inhibit the apoptosis. *Life Sci*, 71, 1771-1778.

Ryser, H.J.P. (**1967**) A membrane effect of basic polymers dependent on molecular size. *Nature*, 215, 934-936.

S

Salsman, J., Top, D., Boutilier, J. and Duncan, R. (**2005**) Extensive syncytium formation mediated by the reovirus FAST proteins triggers apoptosis-induced membrane instability. *J Virol*, 79, 8090-8100.

Sarkar, D.P., Morris, S.J., Eidelman, O., Zimmerberg, J. and Blumenthal, R. (**1989**) Initial stages of influenza hemagglutinin-induced cell fusion monitored simultaneously by two fluorescent events: cytoplasmic continuity and lipid mixing. *J Cell Biol*, 109, 113-122.

Satkauskas, S., Bureau, M.F., Mahfoudi, A. and Mir, L.M. (**2001**) Slow accumulation of plasmid in muscle cells: supporting evidence for a mechanism of DNA uptake by receptor-mediated endocytosis. *Mol Ther*, 4, 317-323.

Sato, E., Suzuki, T., Hoshi, N., Sugino, T. and Hasegawa, H. (**2008**) Sodium azide induces necrotic cell death in rat squamous cell carcinoma SCC131. *Med Mol Morphol*, 41, 211-220.

Sato, M. (**2005**) Intraoviductal introduction of plasmid DNA and subsequent electroporation for efficient in vivo gene transfer to murine oviductal epithelium. *Mol Reprod Dev*, 71, 321-330.

Saulis, G., Satkauskas, S. and Praneviciute, R. (**2007**) Determination of cell electroporation from the release of intracellular potassium ions. *Anal Biochem*, 360, 273-281.

Saulis, G. & Praneviciute, R. (**2005**) Determination of cell electroporation in small-volume samples by using a mini potassium-selective electrode. *Anal Biochem*, 345, 340-342.

Saulis, G., Venslauskas, M.S. and Naktinis, J. (**1991**) Kinetics of pore resealing in cell-membranes after electroporation. *Bioelectrochem Bioenerg*, 26, 1-13.

Saxena, N.K., Sharma, D., Ding, X., Lin, S., Marra, F., Merlin, D. and Anania, F.A. (**2007**) Concomitant activation of the JAK/STAT, PI3K/AKT, and ERK signaling is involved in leptin-mediated promotion of invasion and migration of hepatocellular carcinoma cells. *Cancer Res*, 67, 2497-2507.

Saxena, S.K., Rybak, S.M., Winkler, G., Meade, H.M., Mcgray, P., Youle, R.J. and Ackerman, E.J. (**1991**) Comparison of RNases and Toxins upon injection into Xenopus oocytes. *J Biol Chem*, 266, 21208-21214.

Schaft, N., Dorrie, J., Muller, I., Beck, V., Baumann, S., Schunder, T., Kampgen, E. and Schuler, G. (**2006**) A new way to generate cytolytic tumor-specific T cells: electroporation of RNA coding for a T cell receptor into T lymphocytes. *Cancer Immunol Immunother*, 55, 1132-1141.

Scheid, A. and Choppin, P.W. (**1973**) Isolation and purification of the envelope proteins of Newcastle disease virus. *J Virol*, 11, 263-271.

Scheller, C. and Jassoy, C. (**2001**) Syncytium formation amplifies apoptotic signals: a new view on apoptosis in HIV infection in vitro. *Virology*, 282, 48-55.

Scherer, F., Anton, M., Schillinger, U., Henke, J., Bergemann, C., Kruger, A., Gansbacher, B. and Plank, C. (**2002**) Magnetofection: enhancing and targeting gene delivery by magnetic force in vitro and in vivo. *Gene Ther*, 9, 102-109.

Schieffer, B., Paxton, W.G., Chai, Q., Marrero, M.B. and Bernstein, K.E. (**1996**) Angiotensin II controls p21ras activity via pp60c-src. *J Biol Chem*, 271, 10329-10333.

Schimmer, A.D., Pedersen, I.M., Kitada, S., Eksioglu-Demiralp, E., Minden, M.D., Pinto, R., Mah, K., Andreeff, M., Kim, Y., Suh, W.S. and Reed, J.C. (**2003**) Functional blocks in caspase activation pathways are common in leukemia and predict patient response to induction chemotherapy. *Cancer Res*, 63, 1242-1248.

Schmidt, E., Leinfelder, U., Gessner, P., Zillikens, D., Brocker, E.B. and Zimmermann, U. (**2001**) CD19+ B lymphocytes are the major source of human antibody-secreting hybridomas generated by electrofusion. *J Immunol Methods*, 255, 93-102.

Schoenbach, K.H., Beebe, S.J. and Buescher, E.S. (**2001**) Intracellular effect of ultrashort electrical pulses. *Bioelectromagnetics*, 22, 440-448.

Schönenberger, C., Schutz, A., Franco-Obregon, A. & Zenobi-Wong, M. (**2011**) Efficient electroporation of peptides into adherent cells: investigation of the role of mechano-growth factor in chondrocyte culture. *Biotechnol Lett*, 33, 883-888.

Schöning, M.J. and Poghossian, A. (**2002**) Recent advances in biologically sensitive field-effect transistors (BioFETs). *Analyst*, 127, 1137-1151.

Schrimpf, G. (2002) Gentechnische Methoden. Spektrum Akademischer Verlag, Heidelberg, Berlin.

Schwieger, C. and Blume, A. (**2007**) Interaction of poly(L-lysines) with negatively charged membranes: an FT-IR and DSC study. *Eur Biophys J*, 36, 437-450.

Schwister, K. and Deuticke, B. (**1985**) Formation and properties of aqueous leaks induced in human erythrocytes by electrical breakdown. *Biochim Biophys Acta*, 816, 332-348.

Sebestyen, M.G., Ludtke, J.J., Bassik, M.C., Zhang, G., Budker, V., Lukhtanov, E.A., Hagstrom, J.E. and Wolff, J.A. (**1998**) DNA vector chemistry: the covalent attachment of signal peptides to plasmid DNA. *Nat Biotechnol*, 16, 80-85.

Seidl, M. (**2008**) Abcg2 an der porcinen Blut-Hirn-Schranke (Methoden zur funktionellen Charakterisierung). PhD thesis, Westfälischen Wilhelms-Universität Münster.

Semwogerere, D. and Weeks, E.R. (**2005**) Confocal Microscopy *Encyclopedia of Biomaterials and Biomedical Engineering*. Taylor and Francis.

Senda, M., Takeda, J., Abe, S. and Nakamura, T. (**1979**) Induction of cell fusion of plant protoplasts by electrical stimulation. *Plant Cell Physiol*, 20, 1441-1443.

Sersa, G., Cemazar, M. and Snoj, M. (**2009**) Electrochemotherapy of tumours. *Curr Oncol*, 16, 34-35.

Sersa, G., Stabuc, B., Cemazar, M., Jancar, B., Miklavcic, D. and Rudolf, Z. (**1998**) Electrochemotherapy with cisplatin: potentiation of local cisplatin antitumour effectiveness by application of electric pulses in cancer patients. *Eur J Cancer*, 34, 1213-1218.

Sharma, A. and Sharma, U.S. (**1997**) Liposomes in drug delivery: progress and limitations. *Int J Pharm*, 154, 123-140.

Shibata, T., Cunningham, R.P. and Radding, C.M. (**1981**) Homologous pairing in genetic recombination. Purification and characterization of Escherichia coli recA protein. *J BiolChem*, 256, 7557-7564.

Shibukawa, Y., Yamazaki, N., Kumasawa, K., Daimon, E., Tajiri, M., Okada, Y., Ikawa, M. and Wada, Y. (**2010**) Calponin 3 regulates actin cytoskeleton rearrangement in trophoblastic cell fusion. *MolBiol Cell*, 21, 3973-3984.

Shinn-Thomas, J.H., Scranton, V.L. and Mohler, W.A. (**2008**) Quantitative assays for cell fusion. *Methods Mol Biol*, 475, 347-361.

Shulga, A.A., Sandrovsky, A.C., Strikha, V.I., Soldatkin, A.P., Starodub, N.F. and Elskaya, A.V. (**1992**) Overall characterization of Isfet-based glucose biosensor. *Sensor Actuat B-Chem*, 10, 41-46.

Silva, J., Chambers, I., Pollard, S. and Smith, A. (**2006**) Nanog promotes transfer of pluripotency after cell fusion. *Nature*, 441, 997-1001.

Singh, A.K., Kasinath, B.S. and Lewis, E.J. (**1992**) Interaction of polycations with cell-surface negative charges of epithelial-cells. *Biochim Biophys Acta*, 1120, 337-342.

Sjaastad, M.D., Lewis, R.S. and Nelson, W.J. (**1996**) Mechanisms of integrin-mediated calcium signaling in MDCK cells: Regulation of adhesion by IP3 and store-independent calcium influx. *Mol Biol Cell*, 7, 1025-1041.

Skelley, A.M., Kirak, O., Suh, H., Jaenisch, R. and Voldman, J. (**2009**) Microfluidic control of cell pairing and fusion. *Nat Methods*, 6, 147-152.

Slotkin, J.R., Chakrabarti, L., Dai, H.N., Carney, R.S.E., Hirata, T., Bregman, B.S., Gallicano, G.I., Corbin, J.G. and Haydar, T.F. (**2007**) In vivo quantum dot labeling of mammalian stem and progenitor cells. *Dev Dynam*, 236, 3393-3401.

Smets, I., Ameloot, M., Steels, P. and Van Driessche, W. (**2002**) Loss of cell volume regulation during metabolic inhibition in renal epithelial cells (A6): role of intracellular pH. *Am J Physiol-Cell Ph*, 283, C535-C544.

Solly, K., Wang, X., Xu, X., Strulovici, B. and Zheng, W. (**2004**) Application of real-time cell electronic sensing (RT-CES) technology to cell-based assays. *Assay Drug Dev Technol*, 2, 363-372.

Soreq, H. and Seidman, S. (**1992**) Xenopus Oocyte Microinjection - from Gene to Protein. *Method Enzymol*, 207, 225-265.

Sowers, A.E. (**1983**) Fusion of mitochondrial inner membranes by electric fields produces inside-out vesicles. Visualization by freeze-fracture electron microscopy. *Biochim Biophys Acta*, 735, 426-428.

Sowers, A.E. (**1984**) Characterization of electric field-induced fusion in erythrocyte ghost membranes. *J Cell Biol*, 99, 1989-1996.

Sowers, A.E. (**1985**) Movement of a fluorescent lipid label from a labeled erythrocyte membrane to an unlabeled erythrocyte membrane following electric-field-induced fusion. *Biophys J*, 47, 519-525.

Sowers, A.E. and Lieber, M.R. (**1986**) Electropore diameters, lifetimes, numbers, and locations in individual erythrocyte ghosts. *FEBS Lett*, 205, 179-184.

Spegel, C., Heiskanen, A., Skjolding, L.H.D. and Emneus, J. (**2008**) Chip based electroanalytical systems for cell analysis. *Electroanal*, 20, 680-702.

Sriperumbudur, K.K., Koester, P.J., Stubbe, M., Tautorat, C., Held, J., Baumann, W. and Gimsa, J. (**2009**) Local electroporation of single adherent cells by micro-structured needle electrodes *COMSOL Conference* Bangalore.

Steinberg, F., Gerber, S.D., Rieckmann, T. and Trueb, B. (**2010**) Rapid fusion and syncytium formation of heterologous cells upon expression of the FGFRL1 receptor. *J BiolChem*, 285, 37704-37715.

Steitz, B., Hofmann, H., Kamau, S.W., Hassa, P.O., Hottiger, M.O., von Rechenberg, B., Hofmann-Amtenbrink, M. and Petri-Fink, A. (**2007**) Characterization of PEI-coated superparamagnetic iron oxide nanoparticles for transfection: size distribution, colloidal properties and DNA interaction. *J Magn Magn Mater*, 311, 300-305.

Stenger, D.A. and Hui, S.W. (**1986**) Kinetics of ultrastructural changes during electrically induced fusion of human erythrocytes. *J Membr Biol*, 93, 43-53.

Stenger, D.A. and Hui, S.W. (**1988**) Human erythrocyte electrofusion kinetics monitored by aqueous contents mixing. *Biophys J*, 53, 833-838.

Stenger, D.A. and Hui, S.W. (**1989**) Electrofusion kinetics: studies using electron microscopy and fluorescence contents mixing. In Neumann, E., Sowers, A.E., Jordan, C.A. (eds.) Electroporation and Electrofusion in Cell Biology. Plenum Press, New York, London.

Stickel, S.K. and Wang, Y.L. (**1987**) Alpha-actinin containing aggregates in transformed-cells are highly dynamic structures. *J Cell Biol*, 104, 1521-1526.

Stoicheva, N.G. and Hui, S.W. (**1994**) Electrically induced fusion of mammalian cells in the presence of polyethylene glycol. *J Membr Biol*, 141, 177-182.

Stolwijk, J. (**2006**) In situ Elektroporation adhärenter Zellen auf leitfähigen Substraten. Diploma thesis, Westfälische Wilhelms-Universität Münster.

Strömberg, A., Ryttsen, F., Chui, D.T., Davidson, M., Eriksson, P.S., Wilson, C.F., Orwar, O. and Zare, R.N. (**2000**) Manipulating the genetic identity and biochemical surface properties of individual cells with electric-field-induced fusion. *Proc Natl Acad Sci U S A*, 97, 7-11.

Stulen, G. (**1981**) Electric field effects on lipid membrane structure. *Biochim Biophys Acta*, 640, 621-627.

Subramanian, A., Ranganathan, P. and Diamond, S.L. (**1999**) Nuclear targeting peptide scaffolds for lipofection of nondividing mammalian cells. *Nat Biotechnol*, 17, 873-877.

Sudhof, T.C. and Rothman, J.E. (**2009**) Membrane fusion: grappling with SNARE and SM proteins. *Science*, 323, 474-477.

Sugar, I.P., Forster, W. and Neumann, E. (**1987**) Model of cell electrofusion. Membrane electroporation, pore coalescence and percolation. *Biophys Chem*, 26, 321-335.

Sukharev, S.I., Bandrina, I.N., Barbul, A.I., Fedorova, L.I., Abidor, I.G. and Zelenin, A.V. (**1990**) Electrofusion of fibroblasts on the porous membrane. *Biochim Biophys Acta*, 1034, 125-131.

Sukharev, S.I., Klenchin, V.A., Serov, S.M., Chernomordik, L.V. and Chizmadzhev Yu, A. (**1992**) Electroporation and electrophoretic DNA transfer into cells. The effect of DNA interaction with electropores. *Biophys J*, 63, 1320-1327.

Sukhorukov, V.L., Mussauer, H. and Zimmermann, U. (**1998**) The effect of electrical deformation forces on the electropermeabilization of erythrocyte membranes in low- and high-conductivity media. *J Membr Biol*, 163, 235-245.

Sukhorukov, V.L., Reuss, R., Endter, J.M., Fehrmann, S., Katsen-Globa, A., Gessner, P., Steinbach, A., Muller, K.J., Karpas, A., Zimmermann, U. and Zimmermann, H. (**2006**) A biophysical approach to the optimisation of dendritic-tumour cell electrofusion. *Biochem Biophys Res Commun*, 346, 829-839.

Sun, T. and Morgan, H. (**2010**) Single-cell microfluidic impedance cytometry: a review. *Microfluid Nanofluid*, 8, 423-443.

Sundquist, T., Moravec, R., Niles, A., O'Brien, M. and Riss, T. (**2006**) Timing your apoptosis assays *Promega CELL NOTES*, 18-21.

Sung, W. and Park, P.J. (**1997**) Dynamics of pore growth in membranes and membrane stability. *Biophys J*, 73, 1797-1804.

T

Tagawa, A., Mezzacasa, A., Hayer, A., Longatti, A., Pelkmans, L. and Helenius, A. (**2005**) Assembly and trafficking of caveolar domains in the cell: caveolae as stable, cargo-triggered, vesicular transporters. *J Cell Biol*, 170, 769-779.

Tait, S.W. and Green, D.R. (**2010**) Mitochondria and cell death: outer membrane permeabilization and beyond. *Nat Rev Mol Cell Biol*, 11, 621-632.

Takagi, M., Hayashi, H. and Yoshida, T. (**2000**) The effect of osmolarity on metabolism and morphology in adhesion and suspension chinese hamster ovary cells producing tissue plasminogen activator. *Cytotechnology*, 32, 171-179.

Tang, M.X., Redemann, C.T. and Szoka, F.C. (**1996**) In vitro gene delivery by degraded polyamidoamine dendrimers. *Bioconjugate Chem*, 7, 703-714.

Tao, W., Wilkinson, J., Stanbridge, E.J. and Berns, M.W. (**1987**) Direct gene transfer into human cultured cells facilitated by laser micropuncture of the cell membrane. *Proc Natl Acad Sci U S A*, 84, 4180-4184.

Tarantola, M., Marel, A.K., Sunnick, E., Adam, H., Wegener, J. and Janshoff, A. (**2010**) Dynamics of human cancer cell lines monitored by electrical and acoustic fluctuation analysis. *Integr Biol (Camb)*, 2, 139-150.

Tarantola, M., Pietuch, A., Schneider, D., Rother, J., Sunnick, E., Rosman, C., Pierrat, S., Sonnichsen, C., Wegener, J. and Janshoff, A. (**2010**) Toxicity of gold-nanoparticles: Synergistic effects of shape and surface functionalization on micromotility of epithelial cells. *Nanotoxicology,*3*,* 213-222.

Tarantola, M., Schneider, D., Sunnick, E., Adam, H., Pierrat, S., Rosman, C., Breus, V., Sonnichsen, C., Basche, T., Wegener, J. and Janshoff, A. (**2009**) Cytotoxicity of metal and semiconductor nanoparticles indicated by cellular micromotility. *ACS Nano*, 3, 213-222.

Tarek, M. (**2005**) Membrane electroporation: a molecular dynamics simulation. *Biophys J*, 88, 4045-4053.

Teissié, J. (**1988**) Effects of electric fields and currents on living cells and their potential use in biotechnology – a survey. *Bioelectrochem Bioenerg*, 20, 133-142.

Teissié, J. (**2007**) Biophysical effects of electric fields on membrane water interfaces: a mini review. *Eur Biophys J*, 36, 967-972.

Teissié, J. and Blangero, C. (**1984**) Direct experimental evidence of the vectorial character of the interaction between electric pulses and cells in cell electrofusion. *Biochim Biophys Acta*, 775, 446-448.

Teissié, J. and Conte, P. (**1988**) Electrofusion of large volumes of cells in culture .I. Anchorage-dependent strains. *Bioelectrochem Bioenergs*, 19, 49-57.

Teissié, J., Eynard, N., Gabriel, B. and Rols, M.P. (**1999**) Electropermeabilization of cell membranes. *Adv Drug Deliver Rev*, 35, 3-19.

Teissié, J., Golzio, M. and Rols, M.P. (**2005**) Mechanisms of cell membrane electropermeabilization: a minireview of our present (lack of ?) knowledge. *Biochim Biophys Acta*, 1724, 270-280.

Teissié, J., Knutson, V.P., Tsong, T.Y. and Lane, M.D. (**1982**) Electric pulse-induced fusion of 3T3 cells in monolayer culture. *Science*, 216, 537-538.

Teissié, J. and Ramos, C. (**1998**) Correlation between electric field pulse induced long-lived permeabilization and fusogenicity in cell membranes. *Biophys J*, 74, 1889-1898.

Teissié, J. and Rols, M.P. (**1986**) Fusion of mammalian-cells in culture is obtained by creating the contact between cells after their electropermeabilization. *Biochem Bioph Res Co*, 140, 258-266.

Teissié, J. and Rols, M.P. (**1993**) An experimental evaluation of the critical potential difference inducing cell membrane electropermeabilization. *Biophys J*, 65, 409-413.

Teissié, J. and Rols, M.P. (**1994**) Manipulation of cell cytoskeleton affects the lifetime of cell membrane electropermeabilization. *Ann N Y Acad Sci*, 720, 98-110.

Tekle, E., Astumian, R.D. and Chock, P.B. (**1991**) Electroporation by using bipolar oscillating electric-field - an improved method for DNA transfection of NIH 3T3 cells. *P Natl Acad Sci USA*, 88, 4230-4234.

Temsamani, J. and Vidal, P. (**2004**) The use of cell-penetrating peptides for drug delivery. *Drug Discov Today*, 9, 1012-1019.

Teruel, M.N., Blanpied, T.A., Shen, K., Augustine, G.J. and Meyer, T. (**1999**) A versatile microporation technique for the transfection of cultured CNS neurons. *J Neurosci Methods*, 93, 37-48.

Thévenot, D.R., Toth, K., Durst, R.A. and Wilson, G.S. (**2001**) Electrochemical biosensors: recommended definitions and classification. *Biosens Bioelectron*, 16, 121-131.

Thomas, M. and Klibanov, A.M. (**2003**) Non-viral gene therapy: polycation-mediated DNA delivery. *Appl Microbiol Biotechnol*, 62, 27-34.

Thornberry, N.A. and Lazebnik, Y. (1998) Caspases: enemies within. *Science*, 281, 1312-1316.

Tieleman, D.P. (**2004**) The molecular basis of electroporation. *BMC Biochem*, 5: 10.

Tinel, H., Kinne-Saffran, E. and Kinne, R.K. (**2000**) Calcium signalling during RVD of kidney cells. *Cell Physiol Biochem*, 10, 297-302.

Tinoco, I., Sauer, K., Wang, J.C. and Puglisi, J.D. (**2002**) Physical Chemistry: Principles and Applications in Biological Sciences. Prentice Hall.

Tiruppathi, C., Yan, W., Sandoval, R., Naqvi, T., Pronin, A.N., Benovic, J.L. and Malik, A.B. (**2000**) G protein-coupled receptor kinase-5 regulates thrombin-activated signaling in endothelial cells. *Proc Natl Acad Sci U S A*, 97, 7440-7445.

Toprak, M.S., McKenna, B.J., Waite, J.H. and Stucky, G.D. (**2007**) Control of size and permeability of nanocomposite microspheres. *Chem Mater*, 19, 4263-4269.

Tounekti, O., Kenani, A., Foray, N., Orlowski, S. and Mir, L.M. (**2001**) The ratio of single- to double-strand DNA breaks and their absolute values determine cell death pathway. *Brit J Cancer*, 84, 1272-1279.

Tounekti, O., Pron, G., Belehradek, J. and Mir, L.M. (**1993**) Bleomycin, an Apoptosis-Mimetic Drug That Induces 2 Types of Cell-Death Depending on the Number of Molecules Internalized. *Cancer Res*, 53, 5462-5469.

Trabulo, S., Cardoso, A.L., Mano, M. and de Lima, M.C.P. (**2010**) Cell-Penetrating Peptides: Mechanisms of Cellular Uptake and Generation of Delivery Systems. *Pharmaceuticals*, 3 961-993.

Treeratanapiboon, L., Psathaki, K., Wegener, J., Looareesuwan, S., Galla, H.J. and Udomsangpetch, R. (**2005**) In vitro study of malaria parasite induced disruption of blood-brain barrier. *Biochem Biophys Res Commun*, 335, 810-818.

Treweek, G.P. and Morgan, J.J. (**1977**) Polymer flocculation ofbacteria - mechanism of Escherichia coli aggregation by polyethyleneimine. *J Colloid Interf Sci*, 60, 258-273.

Trisciuoglio, D., Uranchimeg, B., Cardellina, J.H., Meragelman, T.L., Matsunaga, S., Fusetani, N., Del Bufalo, D., Shoemaker, R.H. and Melillo, G. (**2008**) Induction of apoptosis in human cancer cells by candidaspongiolide, a novel sponge polyketide. *J Natl Cancer Inst*, 100, 1233-1246.

Tsoneva, I., Nikolova, B., Georgieva, M., Guenova, M., Tomov, T., Rols, M.P. and Berger, M.R. (**2005**) Induction of apoptosis by electrotransfer of positively charged proteins as Cytochrome C and Histone H1 into cells. *Biochim Biophys Acta*, 1721, 55-64.

Tsong, T.Y. (**1991**) Electroporation of cell membranes. *Biophys J*, 60, 297-306.

U, V

Uchida, M., Li, X.W., Mertens, P. and Alpar, H.O. (**2009**) Transfection by particle bombardment: Delivery of plasmid DNA into mammalian cells using gene gun. *Bba-Gen Subjects*, 1790, 754-764.

Ueki, T., Uemura, H., Nagashima, Y., Ohta, S., Ishiguro, H. and Kubota, Y. (**2008**) Antitumour effect of electrochemotherapy with bleomycin on human prostate cancer xenograft. *Bju International*, 102, 1467-1471.

Umezawa, H., Maeda, K., Takeuchi, T. and Okami, Y. (**1966**) New antibiotics, bleomycin A and B. *J Antibiot (Tokyo)*, 19, 200-209.

Urlaub, G. and Chasin, L.A. (**1980**) Isolation of Chinese hamster cell mutants deficient in dihydrofolate reductase activity. *Proc Natl Acad Sci U S A*, 77, 4216-4220.

Ushio-Fukai, M., Griendling, K.K., Akers, M., Lyons, P.R. and Alexander, R.W. (**1998**) Temporal dispersion of activation of phospholipase C-beta1 and -gamma isoforms by angiotensin II in vascular smooth muscle cells. Role of alphaq/11, alpha12, and beta gamma G protein subunits. *J BiolChem,* 273, 19772-19777.

Uzgiris, E.E. (**1980**) Laser Doppler Methods in Electrophoresis. *Prog Surf Sci*, 10, 53-164.

Van den Bosch, G.A., Ponsaerts, P., Nijs, G., Lenjou, M., Vanham, G., Van Bockstaele, D.R., Berneman, Z.N. and Van Tendeloo, V.F. (**2005**) Ex vivo induction of viral antigen-specific CD8 T cell responses using mRNA-electroporated CD40-activated B cells. *Clin Exp Immunol*, 139, 458-467.

Van Driessche, A., Ponsaerts, P., Van Bockstaele, D.R., Van Tendeloo, V.F. and Berneman, Z.N. (**2005**) Messenger RNA electroporation: an efficient tool in immunotherapy and stem cell research. *Folia Histochem Cytobiol*, 43, 213-216.

Van Itallie, C.M., Fanning, A.S., Bridges, A. and Anderson, J.M. (**2009**) ZO-1 stabilizes the tight junction solute barrier through coupling to the perijunctional cytoskeleton. *Mol Biol Cell*, 20, 3930-3940.

Vanbever, R. and Preat, V.V. (**1999**) In vivo efficacy and safety of skin electroporation. *Adv Drug Deliv Rev*, 35, 77-88.

Varkouhi, A.K., Scholte, M., Storm, G. and Haisma, H.J. (**2010**) Endosomal escape pathways for delivery of biologicals. *J Control Release*, in press.

Vassanelli, S., Bandiera, L., Borgo, M., Cellere, G., Santoni, L., Bersani, C., Salamon, M., Zaccolo, M., Lorenzelli, L., Girardi, S., Maschietto, M., Dal Maschio, M. and Paccagnella, A. (**2008**) Space and time-resolved gene expression experiments on cultured mammalian cells by a single-cell electroporation microarray. *N Biotechnol*, 25, 55-67.

Vaux, D.L. (**1993**) Toward an understanding of the molecular mechanisms of physiological cell death. *Proc Natl Acad Sci U S A*, 90, 786-789.

Verhoef, K., Koken, S.E. and Berkhout, B. (**1993**) Electroporation of the HIV Tat trans-activator protein into cells. *Anal Biochem*, 210, 210-214.

Verhoek-Kohler, B., Hampp, R., Ziegler, H. and Zimmermann, U. (**1983**) Electro-fusion of mesophyll protoplasts of Avena sativa - determination of the cellular adenylate-level of hybrids and Its influence on the fusion process. *Planta*, 158, 199-204.

Verma, A. and Stellacci, F. (**2010**) Effect of surface properties on nanoparticle-cell interactions. *Small*, 6, 12-21.

Vienken, J., Zimmermann, U., Ganser, R. and Hampp, R. (**1983**) Vesicle Formation during Electro-Fusion of Mesophyll Protoplasts of Kalanchoe-Daigremontiana. *Planta*, 157, 331-335.

Vier, J., Linsinger, G. and Hacker, G. (**1999**) Cytochrome c is dispensable for Fas-induced caspase activation and apoptosis. *Biochem Bioph Res Co*, 261, 71-78.

Voldman, J. (**2006**) Electrical forces for microscale cell manipulation. *Annu Rev Biomed Eng*, 8, 425-454.

von Wedel-Parlow, M., Galla, H.J. and Wolte, P. (**2009**) Regulation of major efflux transporters under inflammatory conditions at the blood-brain barrier in vitro. *J Neurochem*, 111, 111-118.

W

Wang, E., Yin, Y., Zhao, M., Forrester, J.V. and McCaig, C.D. (**2003**) Physiological electric fields control the G1/S phase cell cycle checkpoint to inhibit endothelial cell proliferation. *Faseb Journal*, 17, 458-460.

Wang, J., Wei, Q., Wang, C.Y., Hill, W.D., Hess, D.C. and Dong, Z. (**2004**) Minocycline up-regulates Bcl-2 and protects against cell death in mitochondria. *J Biol Chem*, 279, 19948-19954.

Wang, P., Xu, G.X., Qin, L.F., Xu, Y., Li, Y. and Li, R. (**2005**) Cell-based biosensors and its application in biomedicine. *Sensor Actuat B-Chem*, 108, 576-584.

Wang, W., Jobbagy, Z., Bird, T.H., Eiden, M.V. and Anderson, W.B. (**2005**) Cell signaling through the protein kinases cAMP-dependent protein kinase, protein kinase C epsilon, and RAF-1 regulates amphotropic murine leukemia virus envelope protein-induced syncytium formation. *J Biol Chem*, 280, 16772-16783.

Weaver, J.C. and Chizmadzhev, Y.A. (**1996**) Theory of electroporation: A review. *Bioelectrochem Bioenerg*, 41, 135-160.

Weaver, J.C. and Powell, K.T. (**1989**) Theory of electroporation. In Neumann, E., Sowers, A.E., Jordan, C.A. (eds.) Electroporation and Electrofusion in Cell Biology. Plenum Press, New York, London.

Weaver, J.C., Vaughan, T.E. and Chizmadzhev, Y. (**1999**) Theory of electrical creation of aqueous pathways across skin transport barriers. *Adv Drug Deliv Rev*, 35, 21-39.

Wegener, J. (**2003**) ECIS: Ein variabel einsetzbares elektrochemisches Verfahren - Lebende Zellen als Sensoren. *Forschunsjournal der Westfälischen Wilhelms-Universität Münster*, 11-17.

Wegener, J. (**2009**) Impedance Analysis of Cell Junctions. In Fuchs, H. (ed.) *Nanotechnology*. WILEY-VCH Verlag GmbH and Co. KGaA, Weinheim.

Wegener, J., Abrams, D., Willenbrink, W., Galla, H.J. and Janshoff, A. (**2004**) Automated multi-well device to measure transepithelial electrical resistances under physiological conditions. *Biotechniques*, 37, 590, 592-594, 596-597.

Wegener, J., Hakvoort, A. & Galla, H.J. (**2000a**) Barrier function of porcine choroid plexus epithelial cells is modulated by cAMP-dependent pathways in vitro. *Brain Res*, 853, 115-124.

Heitmann, V. and Wegener, J. (**2007**) Monitoring cell adhesion by piezoresonators: Impact of increasing oscillation amplitudes. *Anal Chem*, 79, 3392-3400.

Wegener, J., Janshoff, A. and Galla, H.J. (**1998**) Cell adhesion monitoring using a quartz crystal microbalance: comparative analysis of different mammalian cell lines. *Eur Biophys J Biophy*, 28, 26-37.

Wegener, J., Keese, C.R. and Giaever, I. (**2000b**) Electric cell-substrate impedance sensing (ECIS) as a noninvasive means to monitor the kinetics of cell spreading to artificial surfaces. *Exp Cell Res*, 259, 158-166.

Wegener, J., Keese, C.R. and Giaever, I. (**2002**) Recovery of adherent cells after in situ electroporation monitored electrically. *Biotechniques*, 33, 348, 350, 352.

Wegener, J., Seebach, J., Janshoff, A. and Galla, H.J. (**2000c**) Analysis of the composite response of shear wave resonators to the attachment of mammalian cells. *Biophys J*, 78, 2821-2833.

Wegener, J., Sieber, M. and Galla, H.J. (**1996**) Impedance analysis of epithelial and endothelial cell monolayers cultured on gold surfaces. *J Biochem Biophys Methods*, 32, 151-170.

Wehner, F., Olsen, H., Tinel, H., Kinne-Saffran, E. and Kinne, R.K. (**2003**) Cell volume regulation: osmolytes, osmolyte transport, and signal transduction. *Rev Physiol Biochem Pharmacol*, 148, 1-80.

Weidenfeller, C., Schrot, S., Zozulya, A. and Galla, H.J. (**2005**) Murine brain capillary endothelial cells exhibit improved barrier properties under the influence of hydrocortisone. *Brain Res*, 1053, 162-174.

Weill, C.O., Biri, S., Adib, A. and Erbacher, P. (**2008**) A practical approach for intracellular protein delivery. *Cytotechnology*, 56, 41-48.

Weiss, M., Elsner, M., Kartberg, F. and Nilsson, T. (**2004**) Anomalous subdiffusion is a measure for cytoplasmic crowding in living cells. *Biophys J*, 87, 3518-3524.

White, S.R., Williams, P., Wojcik, K.R., Sun, S., Hiemstra, P.S., Rabe, K.F. and Dorscheid, D.R. (**2001**) Initiation of apoptosis by actin cytoskeletal derangement in human airway epithelial cells. *Am J Respir Cell Mol Biol*, 24, 282-294.

Wilhelm, S., Roloff, S. and Hacker, G. (**1997**) Inhibition of etoposide-induced apoptotic events by azide. *Immunol Lett*, 59, 53-59.

Wilkins, D.K., Grimshaw, S.B., Receveur, V., Dobson, C.M., Jones, J.A. and Smith, L.J. (**1999**) Hydrodynamic radii of native and denatured proteins measured by pulse field gradient NMR techniques. *Biochemistry*, 38, 16424-16431.

Winegar, R.A., Phillips, J.W., Youngblom, J.H. and Morgan, W.F. (**1989**) Cell electroporation is a highly efficient method for introducing restriction endonucleases into cells. *Mutat Res*, 225, 49-53.

Wojchowski, D.M. and Sytkowski, A.J. (**1986**) Hybridoma production by simplified avidin-mediated electrofusion. *J Immunol Methods*, 90, 173-177.

Wojcieszyn, J.W., Schlegel, R.A., Lumley-Sapanski, K. and Jacobson, K.A. (**1983**) Studies on the mechanism of polyethylene glycol-mediated cell fusion using fluorescent membrane and cytoplasmic probes. *J Cell Biol*, 96, 151-159.

Wolf, H., Rols, M.P., Boldt, E., Neumann, E. and Teissié, J. (**1994**) Control by pulse parameters of electric field-mediated gene transfer in mammalian cells. *Biophys J*, 66, 524-531.

Wolf, P., Rothermel, A., Beck-Sickinger, A.G. and Robitzki, A.A. (**2008**) Microelectrode chip based real time monitoring of vital MCF-7 mamma carcinoma cells by impedance spectroscopy. *Biosens Bioelectron*, 24, 253-259.

Wu, M.H., Smith, S.L. and Dolan, M.E. (**2001**) High efficiency electroporation of human umbilical cord blood CD34+ hematopoietic precursor cells. *Stem Cells*, 19, 492-499.

Wu, Y., Rosenberg, J.D. and Sowers, A.E. (**1994**) Surface shape change during fusion of erythrocyte membranes is sensitive to membrane skeleton agents. *Biophys J*, 67, 1896-1905.

Wu, Y.C., Wang, P., Ye, X.S., Zhang, Q.T., Li, R., Yan, W.M. and Zheng, X.X. (**2001**) A novel microphysiometer based on MLAPS for drugs screening. *Biosens Bioelectron*, 16, 277-286.

X, Y

Xia, T., Kovochich, M., Liong, M., Zink, J.I. and Nel, A.E. (**2008**) Cationic polystyrene nanosphere toxicity depends on cell-specific endocytic and mitochondrial injury pathways. *ACS Nano*, 2, 85-96.

Xiao, C., Lachance, B., Sunahara, G. and Luong, J.H. (**2002**) Assessment of cytotoxicity using electric cell-substrate impedance sensing: concentration and time response function approach. *Anal Chem*, 74, 5748-5753.

Xiao, C. and Luong, J.H. (**2003**) On-line monitoring of cell growth and cytotoxicity using electric cell-substrate impedance sensing (ECIS). *Biotechnol Prog*, 19, 1000-1005.

Xiao, C. and Luong, J.H. (**2005**) Assessment of cytotoxicity by emerging impedance spectroscopy. *Toxicol Appl Pharmacol*, 206, 102-112.

Xiao, M., Velizarov, S., Gluck, B. and Berg, H. (**1996**) Modification of electrofusion by proteins. *Bioelectrochem Bioenerg*, 41, 161-166.

Xie, J., Xu, C., Kohler, N., Hou, Y. and Sun, S. (**2007**) Controlled PEGylation of monodisperse Fe_3O_4 nanoparticles for reduced non-specific uptake by macrophage cells. *Adv Mater*, 19, 3163-3166.

Xie, T.D. and Tsong, T.Y. (**1993**) Study of mechanisms of electric field-induced DNA transfection. V. Effects of DNA topology on surface binding, cell uptake, expression, and integration into host chromosomes of DNA in the mammalian cell. *Biophys J*, 65, 1684-1689.

Xing, J.Z., Zhu, L., Jackson, J.A., Gabos, S., Sun, X.J., Wang, X.B. and Xu, X. (**2005**) Dynamic monitoring of cytotoxicity on microelectronic sensors. *Chem Res Toxicol*, 18, 154-161.

Xu, Y. and Szoka, F.C., Jr. (**1996**) Mechanism of DNA release from cationic liposome/DNA complexes used in cell transfection. *Biochemistry*, 35, 5616-5623.

Yamamoto, N., Fukai, F., Ohshima, H., Terada, H. and Makino, K. (**2002**) Dependence of the phagocytic uptake of polystyrene microspheres by differentiated HL60 upon the size and surface properties of the microspheres. *Colloid Surface B*, 25, 157-162.

Yamauchi, F., Kato, K. and Iwata, H. (**2004**) Spatially and temporally controlled gene transfer by electroporation into adherent cells on plasmid DNA-loaded electrodes. *Nucleic Acids Res*, 32: e187.

Yanase, Y., Suzuki, H., Tsutsui, T., Hiragun, T., Kameyoshi, Y. and Hide, M. (**2007**) The SPR signal in living cells reflects changes other than the area of adhesion and the formation of cell constructions. *Biosens Bioelectron*, 22, 1081-1086.

Yang, J. and Shen, M.H. (**2006**) Polyethylene glycol-mediated cell fusion. *Methods Mol Biol*, 325, 59-66.

Yang, N.S., Burkholder, J., Roberts, B., Martinell, B. and McCabe, D. (**1990**) In vivo and in vitro gene transfer to mammalian somatic cells by particle bombardment. *Proc Natl Acad Sci U S A*, 87, 9568-9572.

Yang, T.A., Heiser, W.C. and Sedivy, J.M. (**1995**) Efficient in situ electroporation of mammalian cells grown on microporous membranes. *Nucleic Acids Res*, 23, 2803-2810.

Yao, L., McCaig, C.D. and Zhao, M. (**2009**) Electrical signals polarize neuronal organelles, direct neuron migration, and orient cell division. *Hippocampus*, 19, 855-868.

Yavin, E. and Yavin, Z. (**1974**) Attachment and culture of dissociated cells from rat embryo cerebral hemispheres on polylysine-coated surface. *J Cell Biol*, 62, 540-546.

Yorifuji, T. and Mikawa, H. (**1990**) Co-transfer of restriction endonucleases and plasmid DNA into mammalian-cells by electroporation - effects on stable transformation. *Mutat Res*, 243, 121-126.

Yu, H.Y. and Berg, H. (**1998**) Electrofusion of protoplasts modified by protein adsorption. *Bioelectrochem Bioenerg*, 44, 233-236.

Z

Zabner, J. (**1997**) Cationic lipids used in gene transfer. *Adv Drug Deliver Rev*, 27, 17-28.

Zaharoff, D.A., Henshaw, J.W., Mossop, B. and Yuan, F. (**2008**) Mechanistic analysis of electroporation-induced cellular uptake of macromolecules. *Exp Biol Med (Maywood)*, 233, 94-105.

Zale, S.E. and Klibanov, A.M. (**1986**) Why does ribonuclease irreversibly inactivate at high temperatures? *Biochemistry*, 25, 5432-5444.

Zelenin, A.V., Titomirov, A.V. and Kolesnikov, V.A. (**1989**) Genetic transformation of mouse cultured cells with the help of high-velocity mechanical DNA injection. *FEBS Lett*, 244, 65-67.

Zeleznik, M.J., Segatta, J.M. and Ju, L.-K. (**2002**) Polyethyleneimine-induced flocculation and flotation of cyanobacterium Anabaena flos-aquae for gas vesicle production. *Enzyme Microb Tech*, 949–953.

Zelphati, O., Wang, Y., Kitada, S., Reed, J.C., Felgner, P.L. and Corbeil, J. (**2001**) Intracellular delivery of proteins with a new lipid-mediated delivery system. *J Biol Chem*, 276, 35103-35110.

Zha, X., Pierini, L.M., Leopold, P.L., Skiba, P.J., Tabas, I. and Maxfield, F.R. (**1998**) Sphingomyelinase treatment induces ATP-independent endocytosis. *J Cell Biol*, 140, 39-47.

Zhang, F., Ali, Z., Amin, F., Riedinger, A. and Parak, W.J. (**2010**) In vitro and intracellular sensing by using the photoluminescence of quantum dots. *Anal Bioanal Chem*, 397, 935-942.

Zhang, H.S., Postigo, A.A. and Dean, D.C. (**1999**) Active transcriptional repression by the Rb-E2F complex mediates G1 arrest triggered by p16INK4a, TGFbeta, and contact inhibition. *Cell*, 97, 53-61.

Zhang, L. (**1994**) Polymer-supported electrofusion of Barley protoplasts - a synergistic effect. *Bioelectrochem Bioenerg*, 34, 109-113.

Zhang, S., Li, J., Lykotrafitis, G., Bao, G. and Suresh, S. (**2009**) Size-dependent endocytosis of nanoparticles. *Adv Mater*, 21, 419-424.

Zhao, M., Forrester, J.V. and McCaig, C.D. (**1999**) A small, physiological electric field orients cell division. *Proc Natl Acad Sci U S A*, 96, 4942-4946.

Zhao, M., Song, B., Pu, J., Wada, T., Reid, B., Tai, G.P., Wang, F., Guo, A.H., Walczysko, P., Gu, Y., Sasaki, T., Suzuki, A., Forrester, J.V., Bourne, H.R., Devreotes, P.N., McCaig, C.D. and Penninger, J.M. (**2006**) Electrical signals control wound healing through phosphatidylinositol-3-OH kinase-gamma and PTEN. *Nature*, 442, 457-460.

Zheng, Q.A. and Chang, D.C. (**1990**) Dynamic changes of microtubule and actin structures in CV-1 cells during electrofusion. *Cell Motil Cytoskeleton*, 17, 345-355.

Zheng, Q.A. and Chang, D.C. (**1991a**) High-efficiency gene transfection by in situ electroporation of cultured cells. *Biochim Biophys Acta*, 1088, 104-110.

Zheng, Q.A. and Chang, D.C. (**1991b**) Reorganization of cytoplasmic structures during cell fusion. *J Cell Sci*, 100, 431-442.

Zhou, J., Liu, Q. and Wang, P. (**2009**) Field effect transistor (FET) as cell-based biosensors. In Wang, P., Liu, Q. (eds.) Cell-Based Biosensors: Principles and Aplications. Artech House Publishers.

Ziegler, C. (**2000**) Cell-based biosensors. *Fresenius J Anal Chem*, 366, 552-559.

Zimmerberg, J. (**1993**) Simultaneous electrical and optical measurements of individual membrane fusion events during exocytosis. *Methods Enzymol*, 221, 99-112.

Zimmerberg, J., Curran, M., Cohen, F.S. and Brodwick, M. (**1987**) Simultaneous electrical and optical measurements show that membrane-fusion precedes secretory granule swelling during exocytosis of beige mouse mast-cells. *P Natl Acad Sci USA*, 84, 1585-1589.

Zimmermann, D., Terpitz, U., Zhou, A., Reuss, R., Müller, K., Sukhorukov, V.L., Gessner, P., Nagel, G., Zimmermann, U. and Bamberg, E. (**2006**) Biophysical characterisation of electrofused giant HEK293-cells as a novel electrophysiological expression system. *Biochem Biophys Res Commun*, 348, 673-681.

Zimmermann, U. (**1982**) Electric field-mediated fusion and related electrical phenomena. *Biochim Biophys Acta*, 694, 227-277.

Zimmermann, U., Pilwat, G. and Riemann, F. (**1974**) Dielectric breakdown of cell membranes. *Biophys J*, 14, 881-899.

Zimmermann, U., Scheurich, P., Pilwat, G. and Benz, R. (**1981**) Cells with manipulated functions - new perspetives for cell biology, medicine, and technology *Angew. Chem.-Int. Edit. Engl.*, 20, 325-344.

Zimmermann, U. and Vienken, J. (**1982**) Electric field-induced cell-to-cell fusion. *J Membr Biol*, 67, 165-182.

Zimmermann, U., Vienken, J. and Pilwat, G. (**1980**) Development of drug carrier systems - electrical-field induced effects in cell-membranes. *Bioelectrochem Bioenerg*, 7, 553-574.

Zuhorn, I.S., Kalicharan, R. and Hoekstra, D. (**2002**) Lipoplex-mediated transfection of mammalian cells occurs through the cholesterol-dependent clathrin-mediated pathway of endocytosis. *J BiolChem*, 277, 18021-18028.

Zupke, O., Distler, E., Baumann, D., Strand, D., Meyer, R.G., Landfester, K., Herr, W. and Mailander, V. (**2010**) Preservation of dendritic cell function upon labeling with amino functionalized polymeric nanoparticles. *Biomaterials*, 31, 7086-7095.

Web Links

http://www.biophysics.com/

http://www.btxonline.com/

http://www.dsmz.de/

10 Appendix

A1 Abbreviations

AC	alternating current
Ac	Acetate
ad	(Lat.: *ad*) up to
ANOVA	analysis of variance
BLM	bleomycin
bp	base pairs
BSA	bovine serum albumin
CaAM	calcein acetoxymethylester
cAMP	cyclic adenosine monophosphate
CHO	chinese hamster ovary
CLSM	confocal laser scanning microscope
cp.	(Lat.: *compare*) compare
CPE	constant phase element
CPP	cell penetrating peptide
DAPI	4', 6-diamidino-2-phenylindole
DC	direct current
dd	double deionized
DEAE	diethylaminoethyl
DLS	dynamic light scattering
DMEM	Dulbecco's Modified Eagle's Medium
DMSO	dimethylsulfoxide
DMR	dynamic mass redistribution
DNA	desoxyribonucleic acid
DiI	1,1'-dioctadecyl-3,3,3',3'-tetramethylindocarboxycyanine
DMF	dimethylformamide
DSB	double strand breaks
DSMZ	*Deutsche Sammlung von Mikroorganismen und Zellkulturen*
E. coli	*Escherichia coli*
$EBSS^{++}$	Earle's balanced salt solution
ECIS	electric cell-substrate impedance sensing
ECFP	enhanced cyan fluorescent protein
EDTA	ethylenediaminetetraacetic acid
e.g.	(Lat.: *exempli gratia*) for example
EGFP	enhanced green fluorescent protein
em.	emission
EnFET	enzyme field-effect transistor
et al.	(Lat.: *et alii*) and others
EthD	ethidium homodimer
ex.	extinction
EYFP	enhanced yellow fluorescent protein
FCS	fetal calf serum
FG	frequency generator
FET	field-effect transistor
Fig.	figure
FITC	fluorescein isothiocyanate
FRET	Förster resonance energy transfer
G418	geneticin
GST	glutathione-S-transferase
Hep	hepatocellular

HEK	human embryonic kidney
HIV	human immunodeficiency virus
IA	impedance analyzer
IDEs	interdigitated electrodes
i.e.	(Lat.: *id est*) that is
Im	imaginary fraction of a complex quantity
IS	impedance spectroscopy
ISFET	ion selective field-effect transistor
ITO	indium tin oxide
LAPS	light addressable potentiometric sensor
LED	light-emitting diode
LB	lysogeny broth
MDCK	Madin-Darby canine kidney
MPA	mercapto propionic acid
mRNA	messenger ribonucleic acid
NADH	nicotineamid adenine dinucleotid (reduced form)
n.d.	not determined
NLS	nuclear localisation signal
norm |Z|	normalized impedance magnitude (|Z|)
NPC	nuclear pore complex
NRK	normal rat kidney
OD	optical density
PAMAM	polyamidoamin
PBS^{--}	phosphate buffered saline (without Ca^{2+} and Mg^{2+})
PBS^{++}	phosphate buffered saline (with Ca^{2+} and Mg^{2+})
p.a.	(Lat.: *pro analysi*) for analysis
PC	personal computer
PDMS	polydimethylsiloxane
PGA	poly-L-glutamic acid
PEG	polyethyleneglycol
PEI	polyethyleneimine
PFA	paraformaldehyde
PLC	phospholipase C
PLL	poly-L-lysine
PMMA	polymethylmethacrylate
PMT	photomultiplier tube
QCM	quartz crystal microbalance
QD	quantum dot
Re	real fraction of a complex quantity
RNA	ribonucleic acid
RNase	ribonuclease
RPMI	Roswell Park Memorial Institute
RWG	resonant waveguide grating
rms	root mean square
ROS	reactive oxygen species
RT	room temperature
RT-CES	real-time cell electronic sensing system
rpm	rounds per minute
RVD	regulation volume decrease
SD	standard deviation
SDS	sodium dodecyl sulfate
SEM	scanning electron microscopy
SAM	self assembling monolayer
SFM	serum-free medium
SPR	surface plasmon resonance
SSB	single strand breaks

SV40	Simian virus 40
Tab.	table
TAE	Tris-acetate-EDTA
TER	transepithelial resistance
tRNA	transfer ribonucleic acid
TRITC	Tetramethylrhodamin isothiocyanate
U	Unit
UV	ultraviolet
VIS	visual
ZO-1	zona occludens protein 1
8W1E	eight wells, one electrode

A2 Symbols

A	area; CPE parameter
C	capacitance
C_m	specific membrane capacitance (ECIS model)
E	electric field
d	distance
d_h	hydrodynamic diameter
F	flow across the membrane; fractional voltage drop across the cell layer
f	frequency, shape factor
g	gravitational acceleration
g	factor in electroporation
I	current
i	imaginary factor
k	time constant
L	inductance
M	normal to the membrane surface
M_w	molecular weight
N	number of experiments; pulse number
n	CPE parameter; number of fusing cells
P	permeability coefficient
R	resistance
R_b	specific barrier resistance (ECIS model)
r_h	hydrodynamic radius
r	radius
S	concentration of substance S
T	pulse duration; temperature
t	time
U	voltage
Z	impedance
Z'	resistance (real fraction of the complex impedance)
Z''	reactance (imaginary fraction of the complex impedance)
$\|Z\|$	impedance magnitude
α	parameter for cell-substrate junction (ECIS model)
Δ	difference
λ	wavelength
μ	mean value
ξ	Osmolality
ρ	specific resistivity
σ	specific conductivity

τ	charging time
Φ	angle
φ	phase shift
Ψ	membrane potential
ω	angular frequency
χ^2	chi square function
×	-times
Ø	diameter

A3 Supplementary Figures and Tables

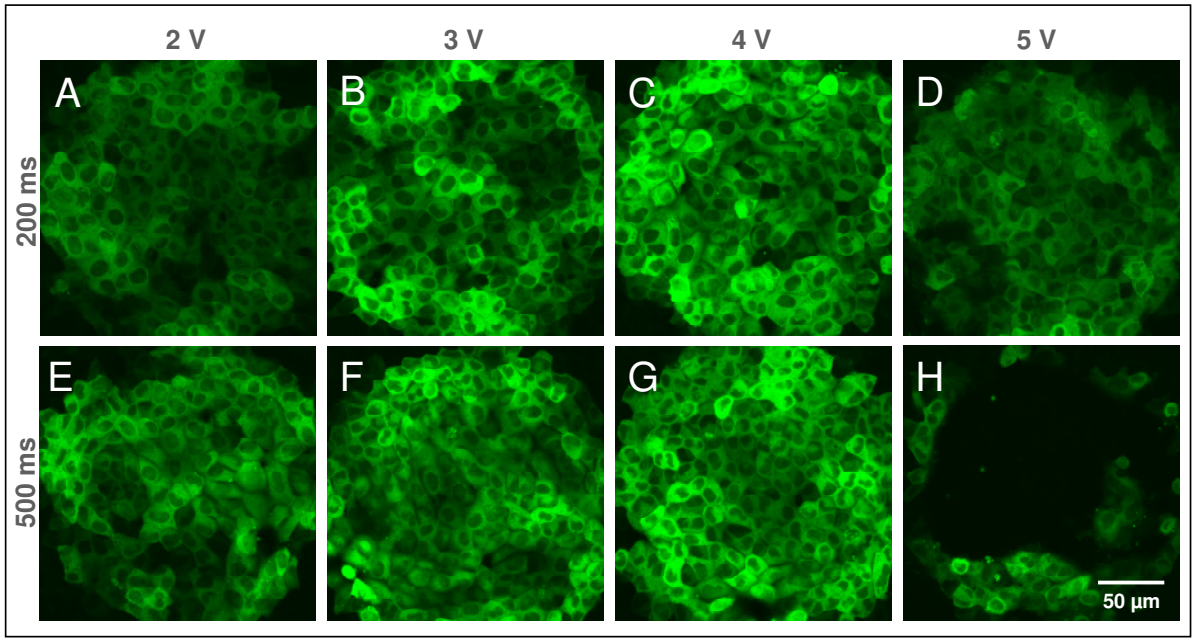

Fig. A 1: Confocal fluorescence micrographs of confluent **NRK** cell layers grown on *8W1E* ECIS electrodes after electroporation in EBSS^{++} with 250 kDa FITC-dextran (2 mg/ml). All cell layers were electroporated using an AC pulse of 40 kHz and discrete combinations of pulse parameters. **A:** 200 ms, 2 V; **B:** 200 ms, 3 V; **C:** 200 ms, 4 V; **D:** 200 ms, 5 V; **E:** 500 ms, 2 V; **F:** 500 ms, 3 V; **G:** 500 ms, 4 V; **H:** 500 ms, 5 V.

Tab. A 1: Specifications of epifluorescence filters for the used microscopes.

Microscope	Modes of Microscopy	Filter Specifications Excitation / Dicroic Mirror / Emission Filters
Leica DM IRB	Phase Contrast Epifluorescence	Filter Cube I3: BP 450 – 490 nm / 510 nm / LP 515 nm Filter Cube N2.1: BP 515 – 560 nm / 580 nm / LP 590 nm Filter Cube A: 340 – 380 nm / 400 nm / LP 425nm
Nikon Diaphot	Phase Contrast Epifluorescence	B: BP 420 – 490 nm / 510 nm / LP 520 nm G: BP 510 – 560 nm / 580 nm / LP 590 nm UV-2A: 330 – 380 nm / 400 nm / LP 420 nm
Leica TCS SL	Phase Contrast Epifluorescence Confocal Laser Scanning	Filter Cube I3: BP 450 – 490 nm / 510 nm / LP 515 nm Filter Cube N2.1: BP 515 – 560 nm / 580 nm / LP 590 nm Filter Cube A: 340 – 380 nm / 400 nm / LP 425nm
Nikon Eclipse 90i	Phase Contrast Epifluorescence Confocal Laser Scanning	340 – 380 nm / 400 nm / 435 – 485 nm 465 – 495nm / 505 nm / 515 – 555 nm 540/25 nm / 565 nm / 605/55 nm

Tab. A 2: Overview of probes introduced into adherent cells by *in situ* electroporation. LY: Lucifer Yellow; FM: Fluorescence microscopy; LM: Light microscopy; EM: Electron microscopy; FC: Flow cytometry; TEER: Transepithelial/endothelial resistance; IP: Immuno prezipitation; IS: Immuno staining; WB: Western Blot, RL: Radiolabeling.

Molecule	Setup	Detection	Literature
Dyes			
LY	ECIS	FM	Wegener et al., 2002
LY	ITO electrodes	FM	Raptis and Firth, 1994
LY	plate electrodes	FM	Bright et al., 1996
LY	ITO small volume	FM	Raptis et al., 2003
fluorescein dextran	plate electrodes	FM	Bright et al., 1996
Trypan Blue	plate electrodes	LM, EM	Escande-Geraud et al., 1988
Calcein	filter in cuvette	FM, FC, TEER	Ghartey-Tagoe et al., 2005
Fluoresceindiphosphate	capillary electrode	FM	Olofsson et al., 2005
Fluorescein dextrans	slider electrode	FM	De Vyst et al., 2007
Proteins & Peptides			
Peptides	ITO electrodes	LM	Bardelli et al., 1998
SH2 domain of HGF	ITO electrodes	LM, RB	Boccaccio et al., 1998
Grb2-SH2 peptide	ITO, small volume	WB	Raptis et al., 2003
Synthetic peptides	ITO electrodes	RB	Giorgetti-Peraldi et al., 1997
SH2 / SH3 -GST	ITO electrodes	IP	Nakashima et al., 1999
STAT-3 peptides	ITO electrodes	WB, apoptosis assay, FC	Anagnostopoulou et al., 2006
Heparin	wire electrodes	propagation of Ca^{2+}, FM	Boitano et al., 1992
BSA-FITC	filter in cuvette	FM, FC, TEER	Ghartey-Tagoe et al., 2005
MGF	ITO	FM, FC	Schoeneberger et al., 2010
Antibodies			
Fluorescein labeled IgG	plate electrodes	FM	Bright et al., 1996
Anti phosphotyrosine Anti GLUT-1	plate electrodes	2-deoxyglucose uptake	Bright et al., 1996
Anti-PLC, -Gα, -Gβ	BTX	WB	Ushio-Fukai et al., 1998
Anti-c-Fos	BTX	Luciferase assay	Lan et al., 2003
Anti-TFAR19	BTX	FM, WB, apoptosis assay	Rui et al., 2002
Anti-pp60$^{c\text{-}src}$	BTX	IP, chromatography, WB	Schieffer et al., 1996
Anti-vimetin antibodies	platinum foils	IF	Kwee et al., 1990
Chicken IgG	ITO electrodes	IF	Raptis and Firth, 1990
Chemical substances			
^{32}P- ATP	plate electrodes	RB	Bright et al., 1996
^{32}P- GTP	ITO electrodes	RB	Brownell et al., 1997
^{32}P- ATP and GTP	ITO small volume	RB	Tomai et al., 2003
Acrylophenone derivatives	ITO electrodes	WB, IS, FM	Brownell et al., 1998
DNA			
pDSRed1-C1	filter, PDMS mask	FM	Ishibashi et al., 2007
pEGFP-N1	IDES	FM	Jen et al., 2004
pCH110 / ß-gal	filter on electrode	ß-gal colorimetric assay	Klenchin et al., 1991
pEGFP-C1, pDSRed2-C1	dendrimer coated electrode	FM	Koda et al., 2008
pEGFP-C1	filter	FC	Müller et al., 2003
pmax GFP plasmid	capillary	FM	Olofsson et al., 2007
pEGFP-C1, pDSRed-C1	PEI coated electrode	FM	Yamauchi et al., 2004
pH3Luc, pCMV-Luc pSV2ALAA5', pRSVlacZ	filter in cuvette	ß-gal colorimetric assay	Yang et al., 1995
RSV-ß-gal, CMV-ß-gal	wire electrodes	ß-gal colorimetric assay	Zheng and Chang, 1990
mRNA			
mRNA for: GFP, CFP, YFP, Esastase-GFP, Mirystoyl, Palmitoyl-GFP	microinjector	FM, patch clamp	Tereul et al., 1999
siRNA			
siRNA	RNA on PEI	FC, FM	Fujimoto et al., 2008
labeled siRNA	electrode array	FM	Jain and Muthuswami, 2007

A4 Eukaryotic Expression Vectors and Sequences

A4.1 pCH1

The eukaryotic expression vector pCH1 was cloned by C. Hartmann (Hartmann, 2003) from pcDNA3 (A-150228, Invitrogen, Darmstadt) with the EGFP gene insert from pEGFP-N1 (Cat. #6085-1, Clontech, Moutain View / CA, USA) by digestion of pcDNA3 with *Eco*RI and *Not*I and final ligation.

Characteristics:
Size: 6191 bp
T7 promoter: 864-882
CMV-promoter: 209-836
EGFP-gene: 988-1707
BGH PolyA: 1763-1994
Relevant restriction sites: *Bgl*II: pos. 12
*Dra*III: pos. 2285

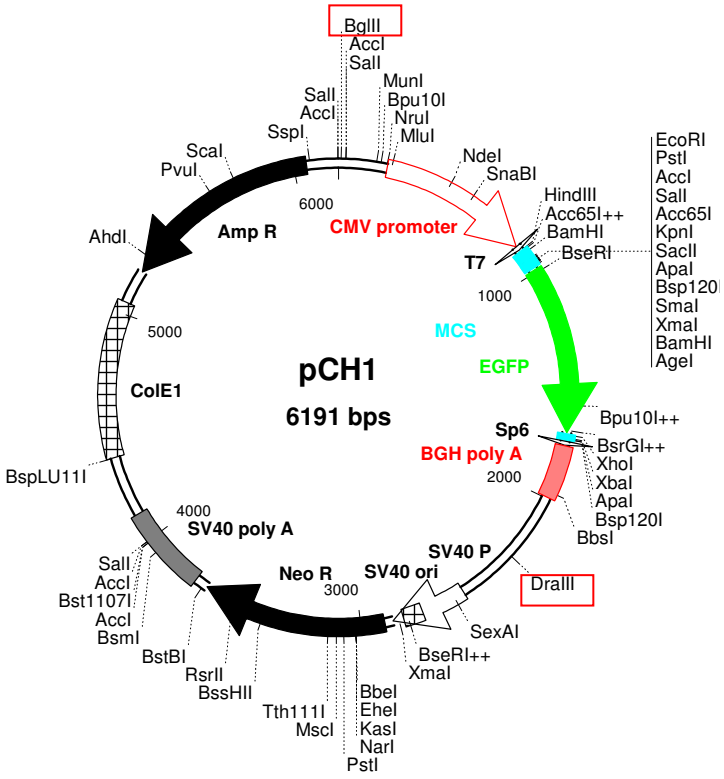

Sequence of the EGFP Gene:

ATGGTGAGCA	AGGGCGAGGA	GCTGTTCACC	GGGGTGGTGC	CCATCCTGGT	CGAGCTGGAC
GGCGACGTAA	ACGGCCACAA	GTTCAGCGTG	TCCGGCGAGG	GCGAGGGCGA	TGCCACCTAC
GGCAAGCTGA	CCCTGAAGTT	CATCTGCACC	ACCGGCAAGC	TGCCCGTGCC	CTGGCCCACC
CTCGTGACCA	CCCTGACCCA	CGGCGTGCAG	TGCTTCAGCC	GCTACCCCGA	CCACATGAAG
CAGCACGACT	TCTTCAAGTC	CGCCATGCCC	GAAGGCTACG	TCCAGGAGCGCA	CCATCTTCTT
CAAGGACGAC	GGCAACTACA	AGACCCGCGC	CGAGGTGAAG	TTCGAGGGCG	ACACCCTGGT
GAACCGCATC	GAGCTGAAGG	GCATCGACTT	CAAGGAGGAC	GGCAACATCC	TGGGGCACAA
GCTGGAGTAC	AACTTCAACA	GCCACAACGT	CTATATCATG	GCCGACAAGC	AGAAGAACGG
CATCAAGGTG	AACTTCAAGA	TCCGCCACAA	CATCGAGGAC	GGCAGCGTGC	AGCTCGCCGA
CCACTACCAG	CAGAACACCC	CCATCGGCGA	CGGCCCCGTG	CTGCTGCCCG	ACAACCACTA
CCTGAGCACC	CAGTCCGCCC	TGAGCAAAGA	CCCCAACGAG	AAGCGCGATC	ACATGGTCCT
GCTGGAGTTC	GTGACCGCCG	CCGGGATCAC	TCTCGGCATG	GACGAGCTGT	ACAAGTAAAG CG

A4.2 pEYFP-Actin

Cat. #6902-1, Clontech, Moutain View / CA, USA

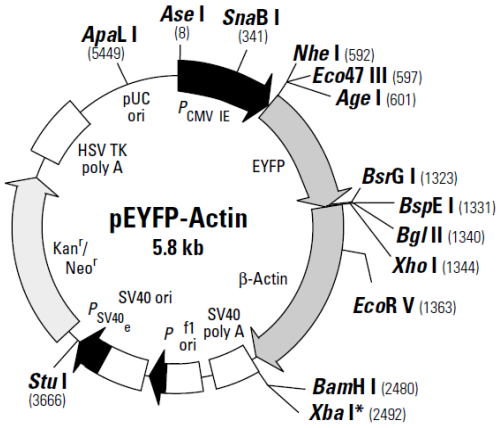

A4.3 pEGFP-N1

Cat. #6085-1, Clontech, Moutain View / CA, USA

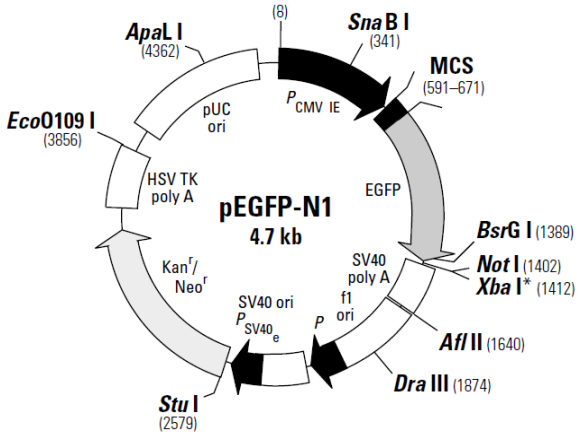

A4.4 pECFP-N1

Cat. #6900-1, Clontech, Moutain View / CA, USA

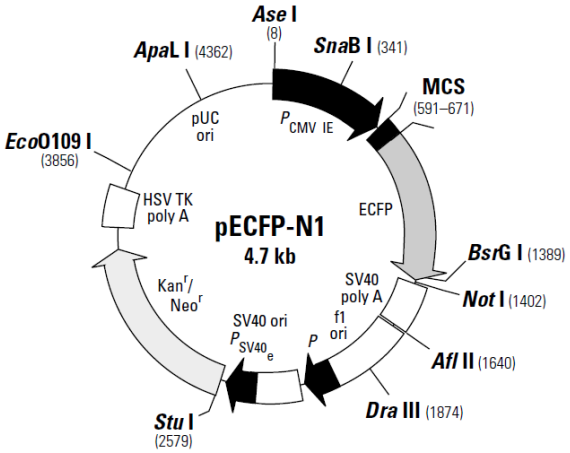

A4.5 pEYFP/pAbcg2

The eukaryotic expression vector pEYFP/pAbcg2 was created by M. Seidl (Seidl, 2008) cloning pEYFP-C1 (Cat. #6005-1, Clontech, Moutain View / CA, USA) with the coding sequence of pAbcg2 (NM_214010.1, NCBI).

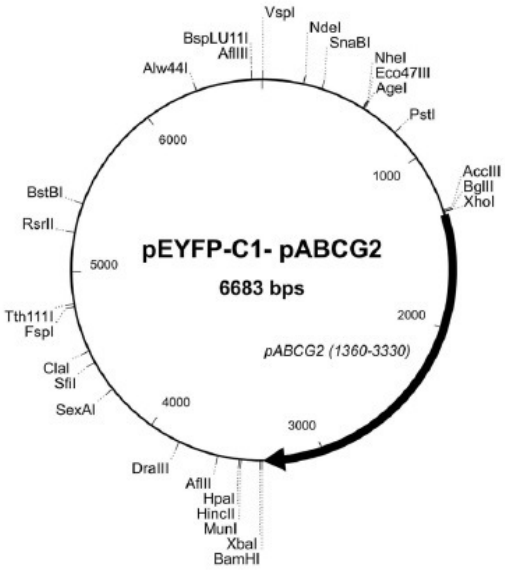

Schematic structure and amino acid sequence of pAbcg2 (Seidl, 2008):

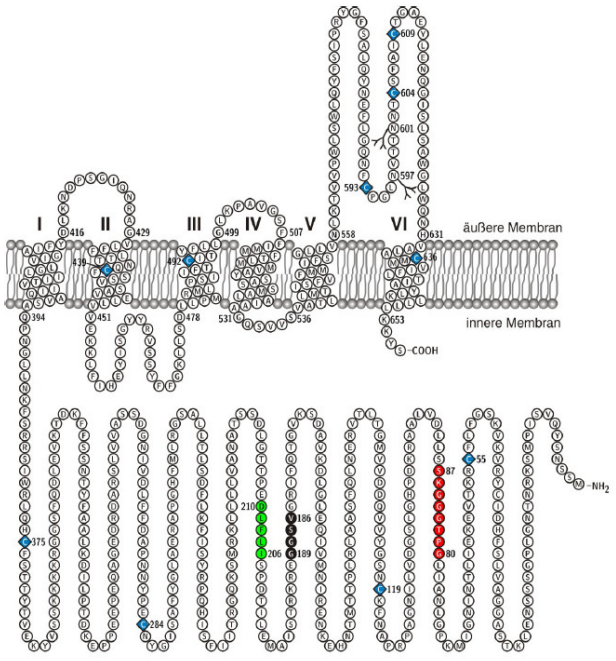

A	alanine	M	methionine
C	cysteine	N	asparagine
D	aspartate	P	proline
E	glutamate	Q	glutamine
F	phenylalanine	R	arginine
G	glycine	S	serine
H	histidine	T	threonine
I	isoleucine	V	valine
K	lysine	W	tryptophane
L	leucine	Y	tyrosine

A5 Chemical Structures

A5.1 Fluorescent Dyes

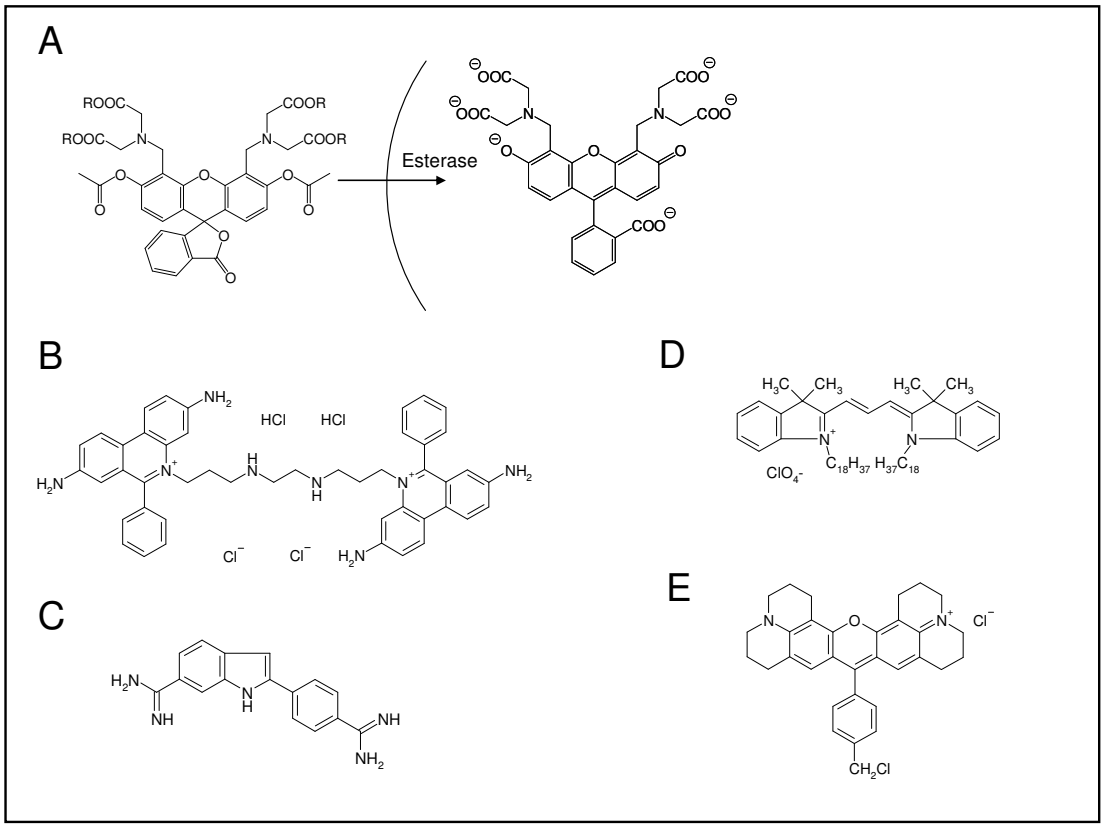

Fig. A 2: Chemical structures of **A:** Non-fluorescent CaAM (left) and Calcein (right) after esterase cleavage of CaAM within viable cells (R=CH_2OCOCH_3); **B:** Ethidium homodimer (EthD-1); **C:** DAPI; **D:** DiI C_{18}; **E:** *MitoTracker*® Red CHXRos.

A5.2 Cytotoxic Probes

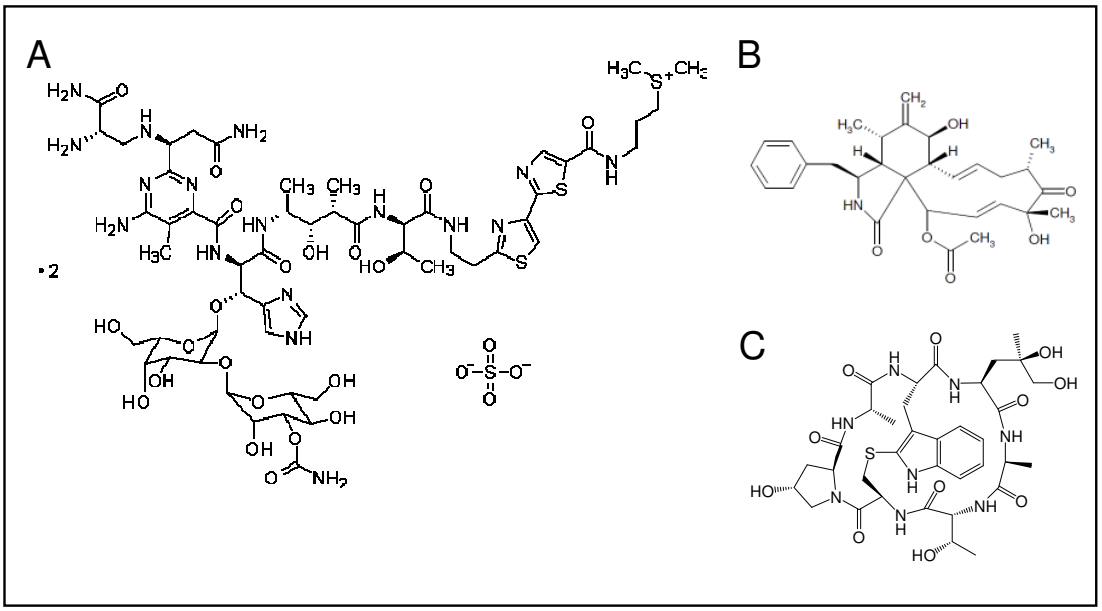

Fig. A 3: Chemical structures of **A:** Bleomycin; **B:** Cytochalasin D and **D:** Phalloidin.

A5.3 Functional Soluble Polymers

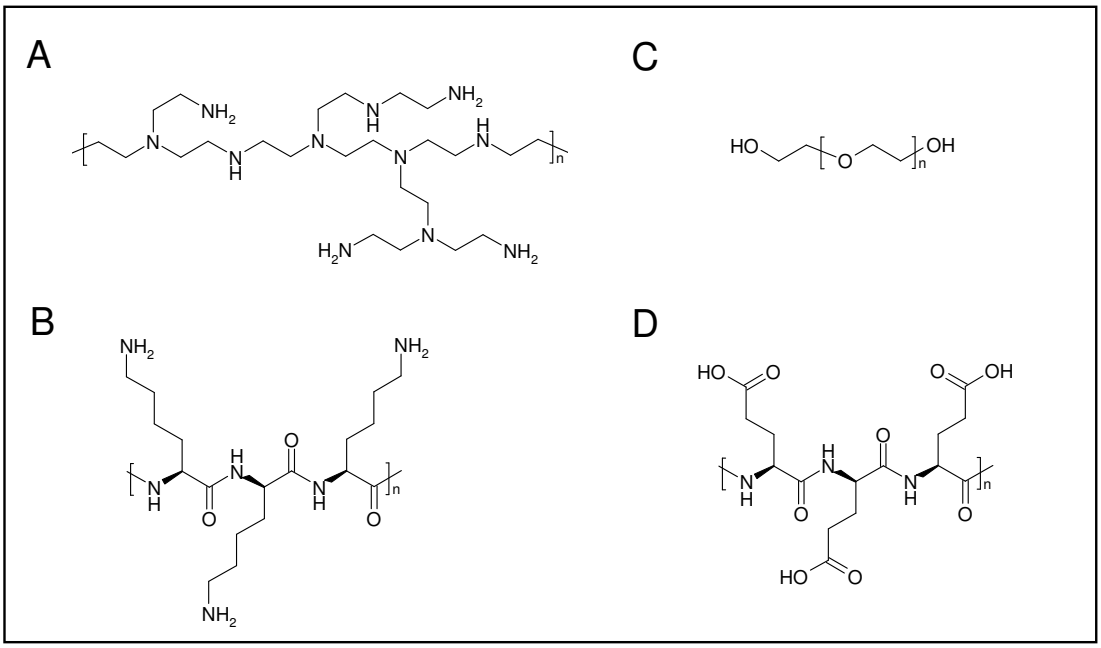

Fig. A 4: Chemical structures of **A:** Branched Polyethylenimine (PEI); **B:** Poly-L-lysine (PLL); **C:** Polyethyleneglycol (PEG); **D:** Poly-L-glutamic acid (PGA).

A6 Materials and Instrumentation

A6.1 Materials for Molecular Biological Work

Agarose	Sigma Aldrich GmbH, Deisenhofen
Ampicilin	Sigma Aldrich GmbH, Deisenhofen
DNA ladder 1 kb	Gibco BRL , Rockville, MD, USA
E. coli ElectroMAX™ DH10B™	Invitrogen GmbH, Darmstadt
E. coli OneShot® TOP10F'	Invitrogen GmbH, Darmstadt
Ethanol	Sigma Aldrich GmbH, Deisenhofen
Ethidiumbromide	Roth GmbH, Karlsruhe
Formaldehyde (37%)	Merck KGaA, Darmstadt
Isopropyl alcohol	Merck KGaA, Darmstadt
Kanamycin	Sigma Aldrich GmbH, Deisenhofen
Loading Dye	Fermentas, St. Leon-Rot
Paper filter	Machery-Nagel GmbH & CoKG, Düren
Peptone	Life Technologies, Paisley ,GB
Phenol-chloroform-isoamylalkohol (25:24:1)	Sigma Aldrich GmbH, Deisenhofen
QiagenMaxiPrepKit	Qiagen GmbH, Hilden
QiagenSpinKit	Qiagen GmbH, Hilden
Restriction enzymes *Bgl*II *Dra*III	New England Biolabs GmbH, Frankfurt
Restriction enzyme buffer	New England Biolabs GmbH, Frankfurt
Sodium acetate	Sigma Aldrich, Deisenhofen
Sodium chloride	Merck, Darmstadt
Tris (Base)	ICN Biomedicals GmbH, Eschwege
Titriplex III (EDTA)	Merck KGaA, Darmstadt
Yeast extract	Life Technologies GmbH, Frankfurt

A6.2 Materials for Cell Biological and Biophysical Work

Anti-ß-catenin from rabbit		Sigma Aldrich GmbH, Deisenhofen
Anti-occludin from rabbit		Zymed Laboratories, San Francisco / CA, USA
Anti-ZO-1 from rabbit		Zymed Laboratories, San Francisco / CA, USA
Anti-F_c rabbit *AlexaFluor*® 488 from goat		MoBiTec, Molecular Probes, Leiden , NL
Anti-F_c mouse *AlexaFluor*® 568 from goat		MoBiTec, Molecular Probes, Leiden, NL
AquaPolymount embedding solution		Polysciences, Warrington / PA, USA
Bleomycinsulfate		Sigma Aldrich GmbH, Steinheim
Bovine serum albumin		Sigma Aldrich GmbH, Deisenhofen
Butane / propane camping gas		Cavagna Group S.p.A., Viadana di Calvasano, I
Caspase inhibitor AC-DEVD-CHO		Sigma Aldrich GmbH, Steinheim
Calcium chloride-hexahydrate		Merck KGaA, Darmstadt
Calcium sulfate		Merck KGaA, Darmstadt
Cell culture media	Alpha Medium	Biochrom AG, Berlin
	DMEM	
	Ham's F12	
	RPMI	
Carbondioxide		Westfalen Gas AG, Münster / Regensburg
Cytochalasin D		Sigma Aldrich GmbH, Steinheim
Cytochrome c from equine heart		Sigma Aldrich GmbH, Steinheim
DAPI		Sigma Aldrich GmbH, Deisenhofen
Deionized Water		Millipore GmbH, Schwalbach
DiI		Fluka Chemie GmbH, Oberhaching
Disodium hydrogenphosphate-dihydrate		Merck KGaA, Darmstadt
DMF		Sigma Aldrich GmbH, Deisenhofen
DNase I		Roche, Basel, CH
$EBSS^{++}$		Sigma Aldrich GmbH, Deisenhofen
EDTA		Sigma Aldrich GmbH, Steinheim
Electrode arrays *8W1E*		Applied Biophysics Inc. Troy / NY, USA
Electrode arrays custom-made (micro-electrodes)		Applied Biophysics Inc. Troy / NY, USA
Ethanol		Merck KGaA, Darmstadt
Fetal calf serum		Biochrom AG, Berlin
FITC-dextran (4 kDa / 250 kDa)		Sigma Aldrich GmbH, Deisenhofen
FluoSpheres®, amine		Invitrogen, Karlsruhe
FluoSpheres®, carboxy		Invitrogen, Karlsruhe
G418		InvivoGen, San Diego / CA, USA
Gelatin		Sigma Aldrich GmbH, Deisenhofen
D-Glucose		Sigma Aldrich GmbH, Steinheim
L-Glutamine		Biochrom AG, Berlin
Glutaraldehyde		Merck KGaA, Darmstadt
Isopropyl alcohol		Merck KGaA, Darmstadt
Lipofectamine 2000®		Invitrogen GmbH, Karlsruhe
LIVE/DEAD® viability/cytotoxicity kit (L3224)		Invitrogen GmbH, Karlsruhe
Magnesium chloride-hexahydrate		Merck KGaA, Darmstadt
MitoTracker® Red CHXRos		Invitrogen GmbH, Darmstadt
Penicillin / Streptomycin solution		Biochrom AG, Berlin
Polybead® Microspheres		Polysciences Inc., Warrington / PA, USA
Polyethyleneimine solution M_w 1300 (482595)		Sigma Aldrich GmbH, Steinheim
Polyethyleneimine solution M_w 750 000 (181978)		Sigma Aldrich GmbH, Steinheim
Poly-L-glutamic acid (81326)		Sigma Aldrich GmbH, Steinheim
Polyethyleneglycol *Hybri-Max*™ waxy solid (P7777)		Sigma Aldrich GmbH, Steinheim
Poly-L-lysine (P29155)		Sigma Aldrich GmbH, Steinheim
PolyMAG iron oxide nanoparticles		Chemicell GmbH, Berlin
Potassium chloride		Merck KGaA, Darmstadt
Potassium dihydrogenphosphate		Merck KGaA, Darmstadt

Quantum dots *Qtracker* (Q21031 MP)	Invitrogen GmbH, Darmstadt
RNase A	Roche, Basel, CH
Saccharose	Sigma Aldrich GmbH, Steinheim
Silicone glue	Warenimport und Handels GmbH, Vienna, A
Silver conductive adhesive	Epoxy GmbH, Fürth / Odenwald
Sodium azide	Merck KGaA, Darmstadt
Sodium chloride	Merck KGaA, Darmstadt
Sodium hydroxyde	Merck KGaA, Darmstadt
Sylgard® 184 Silicone Elastomer Kit	Dow Corning Corp., Michigan / MI, USA
Teflon weights	Fine Mechanical Workshop of the Chemical Institute, Münster
TRITC-phalloidin	Sigma Aldrich GmbH, Deisenhofen
Triton-X-100	Sigma Aldrich GmbH, Steinheim
Trypsine	Biochrom AG, Berlin

A6.3 Instrumentation and Consumables

48-*well* cell culture plates	Corning Costar GmbH, Bodenheim
8W1E ECIS arrays	Applied Biophys. Inc., Troy / NY, USA
Aluminium foil quality S	Roth GmbH, Karlsruhe
Argon plasma cleaner PDC 32G-2	Harrick Plasma, New York, USA
Autoclave DX-45	Systec GmbH, Wettenberg
Bürker hemacytometer	LO-Laboroptik GmbH, Friedrichsdorf
Bunsen burner (for cell culture)	Fireboy Tecnomare, Fernwald
CCD camera for ethidium bromide gels	Inats Science Imaging Instruments GmbH, Göttingen
CCD camera Leica fluorescence microscope	Leica Microsystems GmbH, Wetzlar
CCD camera Nikon fluorescence microscope F-301	Nikon Instruments Europe, Amstelveen, NL
Cell culture dishes	Greiner Bio-One GmbH, Frickenhausen
Cell culture flasks (25 cm^2)	Nunc GmbH & CoKG, Wiesbaden-Bieberach
Cell culture flasks (Jet BIOFIL®) (12.5 cm^2)	JET Bio-Chemicals Int., Inc., Canada
Centrifuge Heraeus Multifuge 1S-R (for cell culture)	Thermo Fisher Scientific GmbH, Munich
Centrifuges 5415 C und 5804 R (for molecular biology)	Eppendorf GmbH, Hamburg
Centrifuge Mikro Rapid/K 1306 (for molecular biology)	Andreas Hettich GmbH Co.KG, Tuttlingen
Centrifuge J2-21 (for molecular biology)	Beckmann GmbH, München
Conductivity cell inoLab multi 720	WTW GmbH, Weilheim, Weilheim
Confocal laser scanning microscope CLSM TCS SL	Leica Microsystems GmbH,Wetzlar
Confocal laser scanning microscope Eclipse90i	Nikon Instruments Europe, Amstelveen, NL
Coverglasses	Menzel GmbH & Co. KG, Braunschweig
Cryovials (1.8 ml)	Nunc GmbH & CoKG, Wiesbaden-Bieberach
Disposable pipettes (1, 5, 10, 25 ml)	Sarstedt AG & Co., Nümbrecht
ECIS1600R	Applied Biophysics Inc., Troy / NY, USA
Flow hood *LaminAir®*	Holten, Gydevang, Denmark
Flow hood *HERAsafe®*	Thermo Fisher Scientific GmbH, Munich
Fluorescence microscope DM IRB	Leica Microsystems GmbH, Wetzlar
Frequency generator 33120 A	HP-Agilent, Böblingen
Gel electrophoresis chamber	Biorad Laboratories GmbH, München
Greiner tubes (10 mL and 50 mL)	Greiner Bio-One GmbH, Frickenhausen
Impedance analyzer SI-1260	Solartron Instruments, Farnsborough,GB
Incubator Heraeus BB15 function line (cell culture)	Thermo Fisher Scientific GmbH, Munich
Incubator BB 6220 CU (cell culture)	Heraeus Holding GmbH, Hanau
Incubator IG 150 (cell culture)	Jouan GmbH, Unterhaching
Incubator Innova 4230 (microbiology)	New Brunswick Scientific GmbH, Nürtingen
LabTek No. 1 chambered coverglasses	Nunc GmbH, Wiesbaden-Bieberach
Laminar flow BSB 6A and BSB 4A	Gelaire Flow Laboraties, Meckenheim

Latex gloves	Roth GmbH & Co. KG, Karlsruhe
MagnetoFACTOR plate 96	Chemicell GmbH, Berlin
Osmometer 030	Gonotech GmbH, Berlin
PMMA cuvettes	Brand GmbH & CoKG, Wertheim
Phase contrast microscope Diaphot TMD	Nikon GmbH, Düsseldorf
pH-Meter inoLab multi 720	WTW GmbH, Weilheim
Pipette tips	Sarstedt AG & Co., Nümbrecht
Power supply 250/25 (for gel electrophoresis)	Biorad Laboratories GmbH, München
Reaction tubes (0.5 – 2 mL)	Eppendorf AG, Hamburg
Sterile filters (pore diameter: 0.2 µm)	Sartorius Stedim Biotech GmbH, Göttingen
Sterilisator UT 6120	Heraeus Instruments GmbH, Düsseldorf
Shake 4450-1CE	Thermo Fisher Scientific GmbH, Karlsruhe
Thermostat MWG Lauda RM6	Lauda GmbH & Co. KG, Lauda-Königshofen
Ultrasonic bath (Sonorex Digitech)	Bandelin Electronic GmbH & Co. KG, Berlin
UV-illuminator	Isel Germany AG, Eiterfeld
UV-spectrometer UV-2100	Shimatsu Deutschland GmbH, Düsseldorf
Vortexer	IKA Labortechnik GmbH & Co. KG, Staufen
Water bath GFL	Julabo Labortechnik GmbH, Seelbach
Zetasizer Nano ZS	Malvern Instruments, Malvern, UK

A6.4 Software

Impedance data acquisition and analysis	ECIS 1600R software	http://www.biophysics.com/
	LabView based software	J. Wegener
Image analysis	*Image J*	http://www.macbiophotonics.ca/
	Leica software	Leica Microsystems GmbH, Wetzlar

Eidesstattliche Erklärung

Hiermit erkläre ich an Eides statt, dass ich die vorliegende Arbeit selbstständig und nur unter Zuhilfenahme der angegebenen Mittel angefertigt habe.

Regensburg, den 31. Mai 2011